

PARTICLE TECHNOLOGY SERIES

# **PARTICLE CHARACTERIZATION: LIGHT SCATTERING METHODS**

**Renliang Xu**

---

Kluwer Academic Publishers

# **Particle Characterization: Light Scattering Methods**

# Particle Technology Series

Series Editor

Professor Brian Scarlett  
*Technical University of Delft*

The Kluwer Particle Technology Series of books is the successor to the Chapman and Hall Powder Technology Series. The aims are the same, the scope is wider. The particles involved may be solid or they may be droplets. The size range may be granular, powder or nano-scale. The accent may be on materials or on equipment, it may be practical or theoretical. Each book can add one brick to a fascinating and vital technology. Such a vast field cannot be covered by a carefully organised tome or encyclopaedia. Any author who has a view or experience to contribute is welcome. The subject of particle technology is set to enjoy its golden times at the start of the new millennium and I expect that the growth of this series of books will reflect that trend.

# Particle Characterization: Light Scattering Methods

by

RENLIANG XU

*Beckman Coulter,  
Miami, U.S.A.*

KLUWER ACADEMIC PUBLISHERS  
NEW YORK, BOSTON, DORDRECHT, LONDON, MOSCOW



eBook ISBN: 0-306-47124-8  
Print ISBN: 0-792-36300-0

©2002 Kluwer Academic Publishers  
New York, Boston, Dordrecht, London, Moscow

All rights reserved

No part of this eBook may be reproduced or transmitted in any form or by any means, electronic, mechanical, recording, or otherwise, without written consent from the Publisher

Created in the United States of America

Visit Kluwer Online at: <http://www.kluweronline.com>  
and Kluwer's eBookstore at: <http://www.ebooks.kluweronline.com>

# CONTENTS

---

Preface	xiii
Acknowledgements	xvii
<b>Chapter 1</b>	<b>PARTICLE CHARACTERIZATION</b>
<b>- An Overview</b>	1
1.1. Particles and Their Characterization	1
1.2. A Survey of Particle Characterization Technologies	7
1.2.1. Sieve Analysis	7
1.2.2. Sedimentation Methods	10
1.2.3. The Electrical Sensing Zone Method	12
1.2.4. Image Analysis	14
Microscopic Methods	14
Holographic Method	16
1.2.5. Chromatographic Methods	18
Size Exclusion Chromatography	18
Hydrodynamic Chromatography	19
Field Flow Fractionation	20
1.2.6. Submicron Aerosol Sizing and Counting	21
1.2.7. Acoustic Analysis	22
Acoustic Spectroscopy	22
Electroacoustic	23
1.2.8. Gas Sorption	24
1.2.9. Other Characterization Methods	25
Mercury Porosimetry and Capillary Flow Porometry	25
Streaming Potential Measurement	26
Pulsed Field Gradient Nuclear Magnetic Resonance	26
Dielectric Spectroscopy	26
1.3. Data Presentation and Statistics	28
1.3.1. Data Presentation Formats	28
1.3.2. Basic Statistical Parameters	34
1.3.3. Mean Values	37
The Moment-Ratio Notation	37
The Moment Notation	40
1.3.4. Quality of Measurement	41
1.3.5. Shape Effect in Size Characterization	43
1.4. Sample Handling	46
1.4.1. Sample Reduction	46
Liquid Sample Reduction	47

	Solid Sample Reduction	47
1.4.2.	Sample Dispersion	49
	Liquid Sample Dispersion	49
	Solid Sample Dispersion	52
References		53

## **Chapter 2      LIGHT SCATTERING**

	<b>- The Background Information</b>	56
2.1.	Light Scattering Phenomena and Technologies	56
2.2.	Light Scattering Theory - an Outline	61
2.2.1.	Scattering Geometry	61
2.2.2.	Scattering Intensity from a Single Particle	63
	The Rigorous Solution: Mie Theory	66
	The Zeroth-order Approximation: Rayleigh Scattering	69
	The First-order Approximation: RDG Scattering	71
	The Large-end Approximation: Fraunhofer Diffraction	73
	Numerical Approaches	81
2.2.3.	Time-Averaged Scattering Intensity of Particles	82
2.2.4.	Scattering Intensity Fluctuations of Particles	83
	Doppler Shift	84
	ACF and Power Spectrum	86
2.3.	Other Light Scattering Technologies	89
2.3.1.	Static Light Scattering	90
2.3.2.	Focused Beam Reflectance	95
2.3.3.	Time-of-Flight (TOF) Measurement	96
2.3.4.	Time-of-Transition (TOT) Measurement	97
2.3.5.	Turbidimetry	98
2.3.6.	Back Scattering Measurement	99
2.3.7.	Frequency Domain Photon Migration (FDPM)	100
2.3.8.	Phase Doppler Anemometry (PDA)	101
References		105

## **Chapter 3      LASER DIFFRACTION**

	<b>- Sizing from Nanometers to Millimeters</b>	111
3.1	Introduction	111
3.2.	Instrumentation	125
3.2.1.	Light Source	126
3.2.2.	Collecting Optics	128
3.2.3.	Detecting System	134
3.2.4.	Sample Module	139
3.2.5.	Instrument Calibration and Verification	143
3.3.	Data Acquisition and Analysis	148

3.3.1.	Data Acquisition	149
	Instrument Alignment and Validation	149
	Sample Preparation and Introduction	150
	Air Bubbles in Liquid Dispersion	150
3.3.2.	Data Analysis	151
3.3.3.	Refractive Index Effects	159
3.3.4.	Concentration Effects	163
3.4.	Accuracy of Laser Diffraction Technology	165
3.4.1.	Resolution and Precision	165
3.4.2.	Bias and Shape Effects	168
	References	177

## **Chapter 4 OPTICAL PARTICLE COUNTING**

	<b>- Counting and Sizing</b>	182
4.1.	Introduction	182
4.2.	Instrumentation	183
4.2.1.	Light Source	185
4.2.2.	Optics of the Volumetric Instrument	186
	Light Scattering OPC	186
	Light Extinction OPC	187
	Combined Optics	189
4.2.3.	Optics of the In-situ Spectrometer	189
4.2.4.	Sample Handling	191
	Sample Acquisition	191
	Sample Delivering in Volumetric Measurement	192
4.2.5.	Electronic Systems	198
4.3.	Data Analysis	199
4.3.1.	Optical Response	199
4.3.2.	Lower Sizing Limit	207
4.3.3.	Accuracy in Particle Sizing	208
	Calibration Particles	208
	Sample Particles	210
4.3.4.	Particle Size Resolution	211
4.3.5.	Particle Counting Efficiency and Accuracy	213
4.3.6.	Data Analysis of Liquid Monitor	217
	References	220

## **Chapter 5 PHOTON CORRELATION SPECTROSCOPY**

	<b>-Submicron Particle Characterization</b>	223
5.1.	Introduction	223
5.2.	Instrumentation	225
5.2.1.	Light Source	226

5.2.2.	Delivering Optics	227
5.2.3.	Sample Module	229
5.2.4.	Collecting Optics	230
5.2.5.	Detector	233
5.2.6.	Electronics	235
5.2.7.	Correlator	235
5.2.8.	Experimental Considerations	239
	Sample Quality	239
	Particle Concentration	240
	Instrument Condition	241
	ACF Delay Time	241
	Scattering Angle	241
	Measurement Time	241
	ACF Quality	242
5.2.9.	Multiangle Measurement	242
5.3.	Data Analysis	246
5.3.1.	Analysis of Characteristic Decay Constant	247
	Cumulants Method	249
	Functional Fitting	250
	Inversion of Laplace Integral Equation	251
	Judgment of the Computed Distribution	256
	Data Analysis of Multiangle Measurement	257
5.3.2.	Analysis of Diffusion Coefficient	259
5.3.3.	Analysis of Particle Size	262
	Concentration Effect	262
	Absorption Effect	264
	Hydrodynamic Effect	265
	Multiangle Analysis – Fingerprint	267
	Particle Shape Effect	268
	Distribution Type	269
5.3.4.	Analysis of Molecular Weight	270
5.3.5.	Accuracy and Resolution	270
5.4.	PCS Measurement in Concentrated Suspensions	272
5.4.1.	Fiber Optic PCS	273
5.4.2.	Cross Correlation Function Measurement	276
5.4.3.	Diffusing Wave Spectroscopy (DWS)	280
	References	283
 <b>Chapter 6 ELECTROPHORETIC LIGHT SCATTERING</b>		
	<b>- Zeta Potential Measurement</b>	289
6.1.	Introduction	289
6.2.	Zeta Potential and Electrophoretic Mobility	290

6.2.1.	Zeta Potential	290
6.2.2.	Electrophoretic Mobility	295
6.2.3.	Electrophoretic Light Scattering	299
6.3.	Instrumentation	299
6.3.1.	Heterodyne Measurement	300
6.3.2.	Frequency Shifter	304
6.3.3.	Sample Cell	307
	Capillary ELS Cells	308
	Parallel-Plate ELS Cells	315
6.3.4.	Electric Field	317
6.3.5.	Multiangle Measurement	319
6.3.6.	Signal Processing	321
6.3.7.	Experimental Considerations	321
	Sample Preparation	322
	Particle Size and Concentration Limits	322
	Experimental Noises	323
	Mobility Controls	323
6.4.	Data Analysis	323
6.4.1.	ACF and Power Spectrum	323
6.4.2.	Spectrum Range and Resolution	330
6.4.3.	Accuracy of Electrophoretic Mobility Measurement	334
6.4.4.	Applications	335
6.5.	Phase Analysis Light Scattering (PALS)	337
	References	341
Appendix I:	Symbols and Abbreviations	344
Appendix II:	ISO and ASTM Standards	349
Appendix III:	Instrument Manufacturers	352
Appendix IV:	Scattering Functions of a Sphere	353
Appendix V:	Scattering Factors for Randomly Oriented Particles	355
Appendix VI:	Physical Constants of Common Liquids	356
Appendix VII:	Refractive Index of Substances	361
Author Index		379
Subject Index		391

## PREFACE

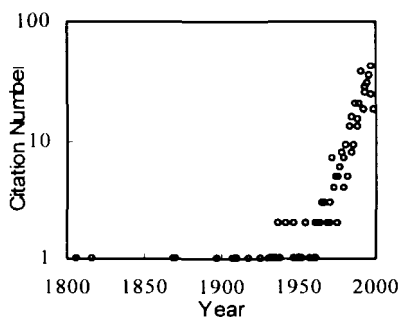
The importance of particle characterization in both the research and development, and the manufacture and quality control of materials and products that we use in our everyday lives is, in some sense, invisible to those of us not directly involved with these activities. Few of us know how particle size, shape, or surface characteristics can influence, for example, the efficacy of a pain-reliever, or the efficiency of a catalytic converter, or the resolution of a printer. The ever-increasing demand for standardization (promoted in large part by organizations such as ISO) has led to a greater awareness of the many ways in which the characteristics of a particle can impact the quality and performance of the objects that make up so much of the world that surrounds us.

Particle characterization has become an indispensable tool in many industrial processes, where more and more researchers rely on information obtained from particle characterization to interpret results and to guide or determine future directions or to assess the progress of their investigations. The study of particle characterization, as well as the other branches of particle science and technology, has traditionally not received much emphasis in higher education, especially in the USA. The subject of particle characterization might be covered in a chapter of a text, or a short section taught in one of the courses in the departments of chemical engineering or material science. There are only a handful of journals, all having low impact factors (the ratio of the number of citation to the number of published articles for a specific journal) in the field of particle characterization. Thus, unlike other branches of engineering, the knowledge of particle characterization, or even particle technology in general, cannot be accessed systematically through a college education. In most cases, such knowledge is accumulated through long years of experience.

During the past decade, particle science and technology have advanced to the extent that the National Science Foundation established an engineering research center in Gainesville, Florida, dedicated to the promotion of fundamental research and exploration of industrial applications of particle science and technology. Meanwhile, due to the evolution of other modern technologies, e.g., lasers, computers and automation, the methods involved in particle characterization have changed considerably. Several conventional particle characterization methods, such as sieve analysis and sedimentation analysis, have gradually been replaced by non-invasive methods based on light-matter interaction. New applications that use these non-invasive methods to

characterize various particulate systems appear daily. In recent years many new national and international standards have been and are still been established. The number of publications related to particle characterization technologies is increasing rapidly. This last fact is partially reflected in the following graph which shows a plot of the literature cited in this book versus the year of publication. Even so, there is still a lack of educational material related to these new particle characterization technologies.

During the past four years, while teaching industrial short courses in particle characterization, I have found that it is increasingly difficult for many industrial users (or even academic researchers) to find collective literature regarding the principles, instrumentation, and applications of modern particle characterization technology. Books covering these areas are thus in high demand.



I entered the field of particle characterization unknowingly almost thirty years ago, when high school graduates in China were distributed to different work places. I was assigned to a coking plant to do sieve analysis of coal and coke using sieves up to mesh size 5. I did not realize that I was doing particle analysis as I was manually sampling and sieving a few hundred kilograms of coke and coal chunks daily. After the Cultural

Revolution I was admitted to the university through the heavy competition among the millions of youth after higher education in China had been halted for more than ten years. I chose to major in optics, but was again unknowingly placed in the chemistry department. After having studied and researched light scattering, polymer physics, and colloid science over the following twelve years in three countries, I came back to the field of particle characterization, knowingly and willingly, with a higher level of understanding.

The present book is intended to cover the theory and practice of one important branch in modern particle characterization technology — light scattering methods. The topics include several major scattering techniques used in today's particle characterization field. This book is intended mainly for industrial users of scattering techniques who characterize a variety of particulate systems, and for undergraduate or graduate students studying chemical engineering, material sciences, physical chemistry, or other related fields. To keep the book in a concise format, many theoretical derivations have been omitted, but references where interested readers can find more details are provided. The book is organized in a modular form - each chapter is relatively self-contained. The book's main goal is to introduce both the principles and



applications of the various light scattering methods. Therefore, the details and design of commercial instruments are not included. Actually, the mention of any particular commercial instrument is avoided except in instances when experimental results are used to demonstrate the relevant technology, or in a reference citation. A list of the current manufacturers of light scattering instruments is provided in the appendix if more information is desired.

RENLIANG XU  
(ren.xu@prodigy.net)  
(ren.xu@coulter.com)

Miami, Florida, USA  
January, 2000

## **ACKNOWLEDGEMENTS**

I would like to express my gratitude to Benjamin Chu, who introduced me to the fields of light scattering and polymer science, and to Beckman Coulter Inc., for continuous support throughout the writing of the manuscript. Special appreciation shall be addressed to Hillary Hildebrand, who made many suggestions, patiently read the entire manuscript, and helped me in polishing the book for its readability with his linguistic talent and skill.

## CHAPTER 1

### PARTICLE CHARACTERIZATION

#### *An Overview*

#### 1.1. Particles and Their Characterization

What is a particle? According to Merriam-Webster's Collegiate® Dictionary (10th Edition), a particle is "a minute quantity or fragment," or "a relatively small or the smallest discrete portion or amount of something." Because the word "small" is relative to "something," a particle can be as small as a quark in a quantum well or as large as the sun suspended in Milky Way. In the vastness of the universe, the sun is really just a small particle! Thus, the range of sciences and technologies that study particles stretches from astrophysics to high-energy physics. A person who knows nothing about particle characterization may think that this is a part of particle physics and that all particle physicists are actually studying only micron-sized particles. Therefore, we have to define the type of particles which interest us; otherwise, you might have a situation in which a technician in the paint industry who works on pigments joins the American Physical Society's Particle Physics Division and finds himself like Gulliver among the Lilliputians. Even when studying particles of similar dimension, astronomers have different approaches to characterize particles in the sky when compared with their industrial counterparts even though both of them may use the same principle, for example, light scattering.

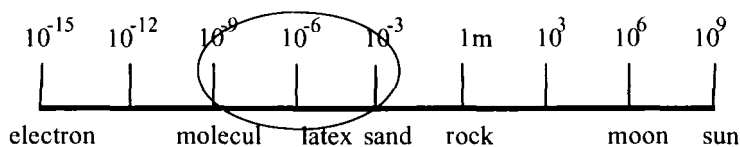


Figure 1.1. Dimension of particles.

The particles covered in this book have dimensions ranging from a few nanometers to a few millimeters, even though the upper end of particle size in many industrial applications may extend into the range of centimeters. In mining industries, particles as large as 20 cm often need to be characterized; however, in this book we will concentrate only on particles in the range described above - a few nanometers to a few millimeters - from

macromolecules to sand grains. We collectively call these particles industrial particles. In this regime, particles may exist in some very different forms. Particles can be natural or synthetic macromolecules in linear form or in networks, such as proteins, gels, DNAs, and latexes. Particles can also be ensembles of small inorganic or organic molecules, such as micelles or liposomes; they can even be pieces of “space”, such as bubbles in liquid or solid foams. More typically, they may be just minute pieces of bulk materials, such as metal oxides, sugars, pharmaceutical powders, or even the non-dairy creamer one puts in coffee. They may be household dust, hay fever pollen, asbestos fibers, magnetic tape, paper products, automobile paint, or drug products. The existence of particulate materials is almost universal, from the materials used in household appliances to the ingredients in food and drink, and from transportation vehicles to clothing. Particles and particle technologies have a profound impact on everyday lives. It is safe to say that everyone has dealt with particles in some way, at sometime, in someplace in his or her everyday life. In the US alone, the industrial output impacted by particulate systems was almost one trillion dollars in 1993 for these ten major industries alone, not even including agricultural products:

- Hybrid microelectronics
- Coal
- Construction materials
- Metal and minerals
- Cleaning and cosmetics
- Drugs
- Textile products
- Paper and allied products
- Food and beverages
- Chemicals and allied products

Within these industries there are many processes that rely heavily on the applications of particle technologies. For example, during paste manufacturing, the particle size and size distribution have to be tightly controlled because too fine a distribution will cause blistering during sintering and too coarse a distribution will lead to electrical leakage. The size and size distribution of film additives, adhesives, pigment particles all affect their corresponding product quality. The gloss and hiding power of paints are affected by the presence of a few large particles and by the total fraction of small particles, respectively. Other examples of industrial processes affected by particle characteristics are:

- |                    |                 |            |
|--------------------|-----------------|------------|
| Adhesion           | Catalysis       | Detergency |
| Electro-deposition | Food processing | Grinding   |

Ion exchange	Lubrication	Ore flotation
Polymerization	Precipitation	Road surfacing
Sewage disposal	Soil conditioning	Sugar refining
Water clarification		

Industrial particles cover a broad range of sizes. For example, contaminants can cover five orders of magnitude in size, and powder products typically cover seven orders from decimeters to submicrons.

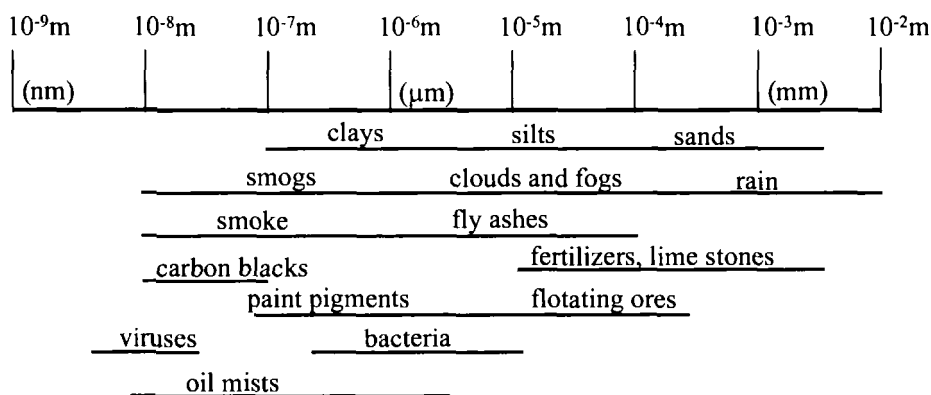


Figure 1.2. Dimension of industrial particles.

Figure 1.2 lists some typical industrial particles and their approximate size ranges. In this size regime, a particle may be either a molecule of high molecular weight, e.g., a macromolecule, or a group of molecules. The latter can be either molecular associations such as liposomes or micelles that are thermodynamically stable and reversible in solution, or more typically, just different forms of particles. From the viewpoint of physical chemistry, industrial particulate systems, regardless of their chemical compositions and practical applications are dispersions, except for macromolecule solutions.

According to the physical phase of particles and the surrounding media, we can construct the following matrix (Table 1.1) to classify dispersion systems. In Table 1.1 the first line in each box contains the common terminology used for that system and some examples are included in the second line. In particle characterization, most attention and interest concern the dispersions of particles in liquid and in gas (the right two columns in the matrix). Especially, dry powders, colloidal suspensions, aerosols and emulsions are prevalent in many fields and have the most applications in industry or academia.

Table 1.1. Particulate systems

a) Dispersions				
		Dispersion Medium		
		Solid	Liquid	Gas
Dispersed Phase	Solid	Solid Suspension (pigmented plastic)	Suspension (paint, toothpaste)	Dry Powder (dust, flour)
	Liquid	Solid Emulsion (pearl, opal)	Emulsion (milk, mayonnaise)	Liquid Aerosol (fog, mist)
	Gas	Solid Foam (expanded polystyrene)	Foam (shave cream)	
b) Macromolecule Solutions				

Regardless of its physical formation, a particulate system has two properties that distinguish it from its corresponding bulk form:

1. When compared with the bulk form for the same volume or weight there is a large number of particles in the particulate form. Each individual particle may have different physical properties. The ensemble behavior is usually what is macroscopically observable, and is often different from that of the bulk material. The macroscopic properties are derived from the contributions of individual particles. If one property is the same for all particles in the system, the system is called *monodisperse* for the concerned property. If all or some particles in the system have different values for the property of interest, the system is called *polydisperse* for that property. Another term, *pausidisperse*, is sometimes used to describe situations where there are a few distinct groups within a system. In this case all particles have the same value for the property concerned within each group but different values between the groups. Although the terms polydisperse and monodisperse are most often used when describing particle size, they can also be used to describe any property of a particle, such as zeta potential, color, porosity, etc.

2. The specific surface area (surface area per unit mass) of such particles is so large that it leads to many significant interfacial phenomena, such as surface interaction with the surrounding medium and neighboring particles. These phenomena will be non-existent for the same material in the bulk form. For example, a spherical particle of density  $2 \text{ g/cm}^3$  will have a specific surface area of  $3 \text{ cm}^2/\text{g}$  if its diameter is 1 cm. The specific surface area will increase to  $3 \times 10^6 \text{ cm}^2/\text{g}$  if the diameter is reduced to 10 nm. This example illustrates how a particle's dimension determines its surface area, which consequently determines the thermodynamic and kinetic stability of a given particulate system.

It is these two characteristics that make particle science and technology unique from manufacture, fabrication, mixing, classification, consolidation, transport, and storage, to characterization, when compared with other branches

of engineering. In particle characterization, almost every sophisticated technique has been developed and advanced to address the complexities caused by the polydispersity of particle systems. If all constituents of the system have same properties, there would hardly be any need for an advanced characterization technology. All that would be required is some way to measure the macroscopic behavior and properties of one single particle, no matter how big or small that particle is.

Generally speaking, for a particulate sample, there are two types of properties. One is the properties of the material, such as its elemental composition, molecular structure or crystal structure, which are independent of macroscopic form of presence. Whether it is in a bulk form (solid or liquid) or a particulate form, these properties will not vary. The other class of properties, such as the geometrical properties of individual particles (size, shape, and surface structure), is closely associated with the fact that the material is in a particulate form. For particulate material, besides the properties of individual particles, many bulk characteristics, such as explosibility, conveyability, gas permeability, and compressibility of powders, are also related to the fact that the material is in the particulate form. These properties will not be present if the material is in the bulk form. If we dedicate the phrase “particle characterization” for measurements related to the second type properties, then the phrase “particle analysis” can be, as it often is, used for measurements related to the first type properties. The technologies used in particle analysis are quite different from those used for particle characterization. Common technologies used in particle analysis are various types of mass spectroscopy, x-ray crystallography, electron diffraction, electron energy loss spectroscopy, infrared microspectrophotometry, etc. We will not discuss these technologies and focus only on the ones used for particle characterization. We also will not discuss concentration dependence of particle characteristics, although many properties of particulate systems are related to concentrations of certain components in the diluent or even the concentration of the particles themselves.

Most physical properties of a particulate system are ensembles or statistical values of the properties from their individual constituents. Commonly evaluated particle geometrical properties are counts, dimension (size and distribution), shape (or conformation), and surface features (specific area, charge and distribution, porosity and distribution). Of these properties, characterization of particle size and surface features is of key interest. The behavior of a particulate system and many of its physical parameters are highly size-dependent. For example, the viscosity, flow characteristics, filterability of suspensions, reaction rate and chemical activity of a particulate system, the stability of emulsions and suspensions, abrasiveness of dry powders, color and finish of colloidal paints and paper coatings, strength of ceramics, are all dependent on particle size distribution. Out of necessity, there are many

technologies that have been developed and successfully employed in particle characterization, especially ones for sizing particles from nanometers to millimeters. There were more than 400 different methods applied in measurement of particle size, shape and surface area in 1981 [1]. Prior to the adoption of light-based and other modern technologies, most particle sizing methods relied on either the physical separation of a sample, such as sieve analysis, or the analysis of a limited number of particles, as in the microscopic method. The results from separation methods consist of ensemble averages of the property of each fraction, and the results from microscopic methods provide two-dimensional size information from the limited number of particles examined. During the last two decades, because of the birth and commercialization of lasers and microelectronics (including computers), the science and technology of particle characterization has been greatly advanced. Today, many new and sophisticated technologies have been successfully developed and applied in particle characterization. Some previously popular characterization methods are now being phased out in many fields.

We can classify the analytical methods used in particle characterization into *ensemble* and *non-ensemble* methods according to whether one detects signals or gathers information from particles of different properties or particles of the same property in the sample during each measurement. There are advantages and disadvantages for both ensemble and non-ensemble methods. These are often complementary to each other. The advantages of ensemble methods, such as fast and non-intrusive measurement, are just the deficiencies of non-ensemble methods, namely time consuming analysis and sample destruction. In an ensemble method, since the signal is detected from particles having different properties, an information retrieval process that often involves modeling has to be used to convert the signal into a result. Two common ensemble methods used in particle size determination are photon correlation spectroscopy and laser diffraction.

On the other hand, as opposed to the low resolution of ensemble methods, non-ensemble methods have the advantage of high resolution. For non-ensemble methods, the material has to be separated or fractionated into separate components according to a certain property of the material prior to the measurement. Thus, all non-ensemble methods are comprised of a separation or fractionation mechanism. Technologies such as sieving, size exclusion chromatography, or field-flow fractionation are all methods of separation. Additional detection schemes, which often involve completely different technologies, are still needed to complete the measurement. Depending on the method and the completeness of separation, a measurement may detect or sense only one particle at a time or a group of particles having the same property value according to how they are separated or fractionated. Two typical methods used to size one particle at a time are optical particle counting and the Coulter



Principle (electrical sensing zone method). The signal such obtained usually has a one-to-one correspondence to the property being measured.

The choice of a proper analytical method for particle characterization wholly depends on the requirement of the application and the accessibility to a suitable analytical technique. Users often have to make a compromise when choosing the best method for their particulate materials.

## **1.2. A Survey of Particle Characterization Technologies Other Than Light Scattering Methods**

In this section, we describe common particle characterization methods other than light scattering methods presently used in various industrial applications. Also included are a few not yet commercialized methods. There are several monographs in which the reader can find more detail regarding some of these technologies [2,3,4,5,6,7].

Listed for each method are its principles, overall application range, advantages and disadvantages, and major references for the method. Only the original article published when the technology was first invented, or one or two latest articles are cited for each. With today's internet connection and search engines there should be little difficulty in finding relevant references from the ever-expanding ocean of literature. At the end of the section there is a table which summarizes particle sizing methods according to their applicable sizing ranges.

### **1.2.1. SIEVE ANALYSIS - FRACTIONATION AND SIZING (5 $\mu\text{m}$ -10 cm)**

Sieve analysis is probably one of the oldest sizing technologies. It may have been used as far back as prehistoric time in the preparation of foodstuffs. Even the early version of the modern woven wire sieves can be traced back to the sixteenth century [8]. Sieve analysis uses a test sieve (or a set of test sieves), that has a screen with many (presumably) uniform openings to classify materials into different fractions. The fraction of material that is larger than the opening of the screen will be retained on the screen and the fraction that is smaller than the opening will pass through. Sieves are usually designated by a "mesh" number, which is related to the number of parallel wires per inch in the weave of the sieve. The openings are either gaps between the woven wires in a wire-cloth sieve (also called woven-wire sieve) where the screen is a piece of metal or nylon cloth, or perforated holes in a metal plate in a punched-plate sieve, or photo-etched holes in a metal sheet in an electroformed sieve. Sieve screens can be made using different materials. The sizing range for the wire-cloth sieve is typically from 20  $\mu\text{m}$  to a few inches, and for the electroformed sieves it is from 5  $\mu\text{m}$  to a few tenths of a millimeter. The most common shape

of the openings is square, but some electroformed and punched-plate sieves have circular openings. Sieves with openings of other shapes (diamond, rectangle, hexagon, slotted) are also in use. The following table lists the ISO (International Organization for Standardization) and ASTM (American Society for Testing and Materials) standard sieve series.

Table 1.2. Standard sieve series

ISO (mm)	ASTM (mesh)	ISO (mm)	ASTM (mesh)	ISO (mm)	ASTM (mesh)
125	5"	7.1	-	0.425	No.40
112	-	6.7	0.265"	0.400	-
106	4.24"	6.3	¼"	0.355	No.45
100	4"	5.6	No. 3½	0.315	-
90	3½"	5.0	-	0.300	No.50
80	-	4.75	No.4	0.280	-
75	3"	4.50	-	0.250	No.60
71	-	4.00	No.5	0.224	-
63	2½"	3.55	-	0.212	No.70
56	-	3.35	No.6	0.200	-
53	2.12"	3.15	-	0.180	No.80
50	2"	2.80	No.7	0.160	-
45	1¼"	2.50	-	0.150	No.100
40	-	2.36	No.8	0.140	-
37.5	1½"	2.24	-	0.135	No.120
35.5	-	2.00	No.10	0.112	-
31.5	1¼"	1.80	-	0.106	No.140
28.0	-	1.70	No.12	0.100	-
26.5	1.06"	1.60	-	0.090	No.170
25.0	1"	1.40	No.14	0.080	-
22.4	7/8"	1.25	-	0.075	No.200
20.0	-	1.18	No.16	0.071	-
19.0	¾"	1.12	-	0.063	No.230
18.0	-	1.00	No.18	0.056	-
16.0	5/8"	0.900	-	0.053	No.270
14.0	-	0.850	No.20	0.050	-
13.2	0.530"	0.800	-	0.045	No.325
12.5	½"	0.710	No.25	0.040	-
11.2	7/16"	0.630	-	0.038	No.400
10.0	-	0.600	No.30	0.036	-
9.5	3/8"	0.560	-	0.032	No.450
9.0	-	0.500	No.35	0.025	No.500
8.0	5/16"	0.450	-	0.020	No.635

In Table 1.2, the left column is the sieve series as defined in ISO 565 [9], and ISO 3310 [10] with the nominal openings given in millimeters, and the same as the sieve number. The ASTM series, which is defined in the ASTM Standard

El 1 [11], is listed in the right column; the nominal openings correspond to the openings in the ISO series. Many countries also have their own standard test sieve series corresponding to part of the ISO series. A partial list of other country's standards includes Australia (AS 1152), Britain (BS 410), Canada (CGS-8.2-M88), French (NFX 11-501), Germany (DIN 4188), India (IS 460), Ireland (I.S. 24), Italy (UNI 2331), Japan (JIS Z 8801), Portugal (NP 1458), and South Africa (SABS 197).

Because of the simplicity of the principle, the equipment, and the analytical procedure, sieve analysis has been widely used in almost every field that requires the sizing of particles larger than a few tens of microns. There are more ASTM and international standards pertaining to sieve analysis than for any other technology in particle characterization. Sieve analysis can be used for dry powders as well as wet slurries. The amount of material needed for each analysis can be as large as 50-100 kg in coke analysis or as small as a few grams in dust analysis. To help in sorting particles on the screen pass the openings, one or several of the following means are used to generate vertical or horizontal motion in the sieve frame or particles: electromagnetic, mechanical, or ultrasonic. Additional forces may also be used to help the sieving process, such as liquid flow, air jet, and vibrating air column. Many types of automated sieving equipment are available to increase working efficiency and reduce the operator dependence of hand sieving.

Despite its wide usage, there are several inherent drawbacks in this seemingly rugged and simple method. The openings on a sieve are actually three-dimensional considering the round woven wires. However, fractionation by sieving is a function of two dimensions only. Two rods of the same diameter but different lengths may yield the same result. Whether a three-dimensional particle of any shape can pass through an opening depends on the orientation of the particle, which in turn depends on the mechanics of shaking the sieve or the particle itself, as well as the time length of such shaking. Typically, result from sieve analysis varies with the method of moving the sieve or particles, the geometry of sieve surface (sieve type, fractional open area, etc.), the time length of operation, the number of particles on the sieve, and the physical properties of particles (such as their shape, stickiness, and brittleness). In addition, the actual size of openings can have large variations from the nominal size. Especially, in the case of wire-cloth sieves of high mesh numbers, such variation can be substantial. For example, for sieves with a mesh number higher than 140 mesh, the average opening can have  $\pm 8\%$  tolerance, while the tolerance for the maximum opening may be as large as  $\pm 60\%$ . The above facts and others limit the accuracy and precision of sieve analysis and are the reasons for this technology being widely replaced by light scattering methods, especially for sizing particles smaller than a few millimeters.

### 1.2.2. SEDIMENTATION METHODS - SIZING (0.05-100 $\mu\text{m}$ )

Sedimentation is another classical particle classification and sizing method for liquid-born particles. Sedimentation methods are based on the rate of settling of particles in a liquid at rest under a gravitational or centrifugal field. The relationship between settling velocity and particle size is reduced to the Stokes equation at low Reynolds numbers:

$$d_{st} = \sqrt{\frac{18\eta u}{(\rho_s - \rho_l)g}}. \quad (1.1)$$

In Eq. 1.1,  $d_{st}$  is the Stokes diameter which is equal to the equivalent diameter of a spherical particle that has the same density and free-falling velocity as the real particle in the same liquid under laminar flow conditions. The quantities  $\eta$ ,  $u$ ,  $\rho_s$ ,  $\rho_l$ , and  $g$  are the viscosity of suspension liquid, the particle settling velocity, the effective particle density, the liquid density, and the acceleration, respectively. In the gravitational sedimentation methods,  $g$  is the gravitation acceleration and in the centrifugal sedimentation methods,  $g$  ( $= \omega^2 r$ , with  $\omega$  and  $r$  being the angular velocity of centrifugation and the radius where particles are being measured, respectively) is the centrifugal acceleration.

Depending on the position of the particles at the beginning of the measurement, there are homogeneous methods where particles are uniformly distributed and line-start methods where particles at the beginning are concentrated in a thin layer on top of the solid-free medium (see Figure 1.3). Depending on the location of measurement, there are incremental methods where the measurement for the amount of solids is determined from a thin layer at a known height and time and cumulative methods where the rate at which solids settle out of suspension is determined. Therefore, based on different combinations of the force field, the location of measurement in the suspension, and the distribution of particles at the start of the measurement, there are eight experimental arrangements. Since sedimentation is in principle a classification process, it needs some additional measurement to determine the physical property of particles in order to obtain particle concentration corresponding to certain sizes of particles. Traditionally, there are measurements based on particle mass, such as the pipette method, decanting method, and sedimentation balance method; measurements based on suspension density, such as the methods using manometers, aerometers, or various divers; and measurements based on particle attenuation or scattering to radiation of light or x-rays. All methods require calibration of the sedimentation device and concentration detection.

The foundation of a sedimentation experiment to deduce particle size information is the Stokes equation, which is valid for a single spherical particle settling slowly in a fluid of infinite extent without the interference of other forces or motions. To satisfy these conditions, the experiment should only be performed at low concentrations and for particles in a certain size range. At high concentrations there exists interactions or mutual interference between the particles. Laminar flow can not be maintained either for very large particles, whose velocities are so large that eddies or turbulence will form, or for very small particles, where disturbance to free settling due to the Brownian motion of particles is too great. The settling of particles should be at low Reynolds numbers, e.g., less than 0.25 if the error in Stokes diameter is not to exceed 3%. The commonly accepted maximum volume concentration is 0.2%, and the wall-to-wall distance in the sedimentation vessel is at least 0.5 cm so as to reduce the wall effects. The size range is dependent upon the density difference between the liquid and the particle as well as the liquid viscosity; in centrifugal sedimentation, it also depends on the rotational speed of the centrifuge. For most samples in aqueous suspension, the achievable size range in a gravitational sedimentation experiment is approximately 0.5-100  $\mu\text{m}$  and in a centrifugal sedimentation experiment it is approximately 0.05-5  $\mu\text{m}$ .

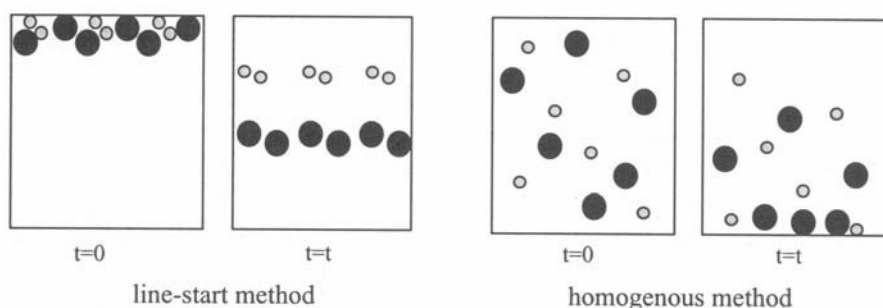


Figure 1.3. Sedimentation separation processes.

Sedimentation methods have been widely used during the past and many product specifications and industrial standards have been established based on these methods. However, there are intrinsic limitations associated with sedimentation. For a non-spherical particle, its orientation is random at low Reynolds numbers so it will have a wide range of settling velocities. As the Reynolds number increases, the particle will tend to orient itself to create maximum drag and will settle at the slowest velocity. Thus, for a polydisperse sample of non-spherical particles, there will be a bias in the size distribution toward larger particles and the result obtained will be broader than the real distribution. Also, all samples analyzed using sedimentation must have a

uniform and known density, otherwise particles of different sizes may settle at the same velocity because of density variations.

Due to these disadvantages, especially the long and tedious analysis procedures involved in the pipette methods, sedimentation balance method, and diver method, these widespread devices and methods have been replaced with modern technologies that do not depend on separation. The current versions of sedimentation that are still widely used are primarily centrifugal sedimentation using light or x-ray detection [12].

### 1.2.3. THE ELECTRICAL SENSING ZONE METHOD (ESZ, THE COULTER PRINCIPLE) - COUNTING AND SIZING (0.4-1200

Since its invention in the early 1950's [13], the Coulter principle has been so widely accepted in the field of medical technology that presently over 98% of automated cell counters incorporate the Coulter principle. Besides counting blood cells for which the Coulter Principle was originally invented, this method can be used to count and size any particulate material that can be suspended in an electrolyte solution. During the past fifty years, the method has been utilized to characterize thousands of different industrial particulate materials. Over 7000 references to the uses of various COULTER COUNTER<sup>®</sup> models have been documented [14].

In an electrical sensing zone experiment, a tube with an orifice or aperture is placed in an electrolyte solution containing the particles of interest in low concentration. The device has two electrodes, one inside and the other outside the orifice (see Figure 1.4). The aperture creates what is called a "sensing zone." Particles pass through the aperture when the liquid is drawn from one side. As a particle passes through the sensing zone, a volume of the electrolyte equivalent to the immersed volume of the particle is displaced from the sensing zone. This causes a short-term change in the resistance across the aperture. This resistance change can be measured either as a voltage pulse or a current pulse. By measuring the number of pulses and their amplitudes, one can obtain information about the number of particles and the volume of each individual particle. The number of pulses detected during measurement is the number of particles measured, and the amplitude of the pulse is proportional to the volume of the particle:

$$U = \frac{V\rho_o if}{\pi^2 R^4}. \quad (1.2)$$

In Eq. 1.2,  $U$ ,  $V$ ,  $\rho_0$ ,  $i$ ,  $f$ , and  $R$  are the amplitude of the voltage pulse, the particle volume, electrolyte resistivity, aperture current, particle “shape” factor, and aperture radius, respectively. If a constant particle density is assumed, the pulse height is proportional to the particle mass. The measured particle size can be channelyzed using the pulse height analyzer circuit, and a particle size distribution is thus obtained. The electrical response of the instrument is essentially independent of shape for particles of the same volume, both in theory and in practice. A typical measurement takes less than a minute, as counting and sizing rates of up to 10,000 particles per second are possible. The accuracy of size measurements is usually within 1-2%. Calibration can be performed using known size standards or by the mass balance method [15].

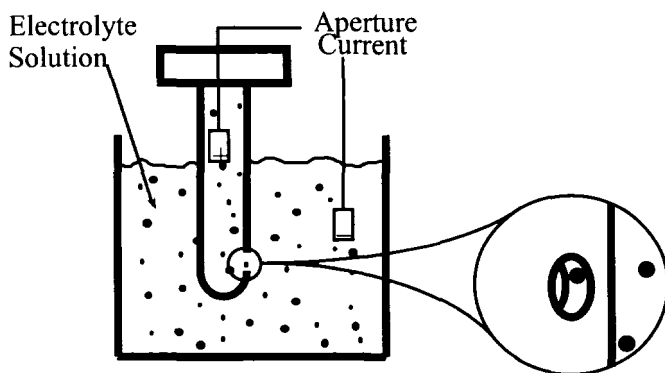


Figure 1.4. Schematic of the electrical sensing zone analyzer.

The lower size limit of this method is defined by the ability to discriminate all kinds of noise from the signal generated from particles passing through the aperture. One source of interference is electronic noise generated mainly within the aperture itself. Although apertures smaller than  $15\text{ }\mu\text{m}$  have been produced, electrical and environmental noise prevents these small apertures from routine use in sizing small particles. The upper size limit is set by the ability to suspend particles uniformly in the sample beaker. Since each aperture can be used to measure particles within a size range of 2% to 60% of its nominal diameter, (i.e., a dynamic range of 30:1 with aperture size typically ranging from  $20\text{ }\mu\text{m}$  to  $2000\text{ }\mu\text{m}$ ), an overall particle size range of  $0.4\text{ }\mu\text{m}$  to  $1200\text{ }\mu\text{m}$  is possible. However, the method is limited to those particles that can be suitably suspended in an electrolyte solution, either aqueous or non-aqueous. The upper limit therefore may be  $500\text{ }\mu\text{m}$  for sand but only  $75\text{ }\mu\text{m}$  for tungsten carbide because of their different densities. In order to suspend some large particles it may be necessary to add a thickening agent such as glycerol or sucrose to raise the diluent viscosity. A thickening agent will also help reduce the noise generated

by the turbulent flow of low viscosity electrolyte solutions as they pass through apertures with diameters larger than 400  $\mu\text{m}$ . If particles to be measured cover a wider range than what any single aperture can measure, two or more apertures will have to be used, and the test results can be overlapped to provide a complete particle size distribution.

The advantages of the method are that it measures a particle's volume, and the result will hardly be biased due to the shape of particle, except in certain extreme cases and that it can also simultaneously count and size with very high resolution and reproducibility. However, the limitation or drawback of this method is that the particles that can be analyzed are restricted to those that can be dispersed in an electrolyte solution and still retain their original integrity [15].

#### 1.2.4. IMAGE ANALYSIS

##### *Microscopic Methods - Morphology Study and Sizing (0.001-200 $\mu\text{m}$ )*

Microscopic analyses are and have always been indispensable tools in particle studies. For example, in 1827 the English botanist Robert Brown discovered the random thermal motion of flower pollen particles in suspension now known as "Brownian motion" using an optical microscope. A simple optical microscope can provide visual observation and inspection of individual particles' features and dimensions down to the micron range. Microscopes are also widely used in preparation of samples for other particle characterization techniques to check whether particles have been properly dispersed.

All microscopic methods include an image capture procedure and an image process and analysis procedure. The image capture procedure can be accomplished using illumination of light (optical microscopy, OM) or by the bombardment of electrons (electron microscopy, EM). Depending on the energy of the electrons and the way the electrons are collected, the technology can be classified as transmission electron microscopy (TEM) or scanning electron microscopy (SEM). One of the newer members of the EM family used for particle characterization is known as Scanning Transmission Electron Microscopy with Atomic Number (Z) Contrast (STEM with Z contrast). This technique utilizes a small probe ( $\sim 2 \text{ \AA}$ ) to scan across the specimen. The incoherent scattering of electrons, which is detected by a parallel electron energy loss detector, is collected using a high angle annular detector. The scattering intensity is proportional to the square of the atomic number of the element in the scanning area. STEM with Z contrast has very high atomic scale resolution and can reveal information on the exact location of atomic sites and chemical composition at a surface or interface [16].

In optical microscopy, either reflected or transmitted light can be used to capture an image; but for smaller particles, only transmission microscopes,



especially ones using polarized light in which silhouettes are seen, are suitable. Image resolution, laterally and axially, can be further enhanced using confocal laser scanning microscopy (CLSM), in which the fluorescence blur from out-of-focus structure is reduced through confocal optics that focuses light to a spot on a particular volume element (voxel) of the sample at some chosen depth one at a time [17]. Particle porosity information can also be obtained using CLSM. Figure 1.5 depicts the similarities and differences between CLSM and optical and electron microscopes. Other modifications to conventional optical microscopy, such as differential interference contrast microscopy (DICM), are also used in particle characterization. The practical lower size limit with acceptable precision for conventional optical microscopy is around 3  $\mu\text{m}$ . With development of near-field scanning optical microscopy (NSOM), in which a fiber-optic probe is placed near the sample surface so the emerging light interacts with the sample before diffraction effects degrade the resolution. With enhanced resolution, the lower detection limit is further reduced to the submicron range [18]. There is no theoretical upper size limit. If particles are larger than a few hundreds of microns, a microscope is not needed; a simple magnifying glass is more than adequate. The size range for TEM is about 0.001-5  $\mu\text{m}$  and for SEM is about 0.02-200  $\mu\text{m}$ . SEM has a depth of focus few hundreds times more than that of optical microscopy and therefore much more information about the surface texture of particles can be obtained. Calibration is needed for all microscopic methods, and is commonly accomplished using known size spheres, graticules, or calibration gratings.

In capturing images, one has to be careful in sample preparation so that representative particles from the sample are both taken and seen; there should be a minimum number of particles touching each other, and any staining, shadowing or coating of particles should not lead to incorrect information.

Conventionally, captured images from microscopic measurements are recorded on photographic papers followed by manual study of the shape, size or surface morphology of the particles in the images. Recently, using computer automation, images can be viewed directly on a monitor or digitized and recorded into computer files, typically containing 512 $\times$ 512 or 1024 $\times$ 1024 pixels and 256 gray levels. These images then can be reprocessed (e.g., by image enhancement) and analyzed using an image analysis program. Particle dimensional measurement (size, area, and cord length), particle count, shape analysis, and even fractal analysis can be accomplished by image analysis [19]. In addition to optical microscopes, SEM and TEM, and scanning probe microscopes such as the scanning tunneling microscope (STM) and the atomic force microscope (AFM), are also used, primarily in academia, to characterize particle size and surface structure.

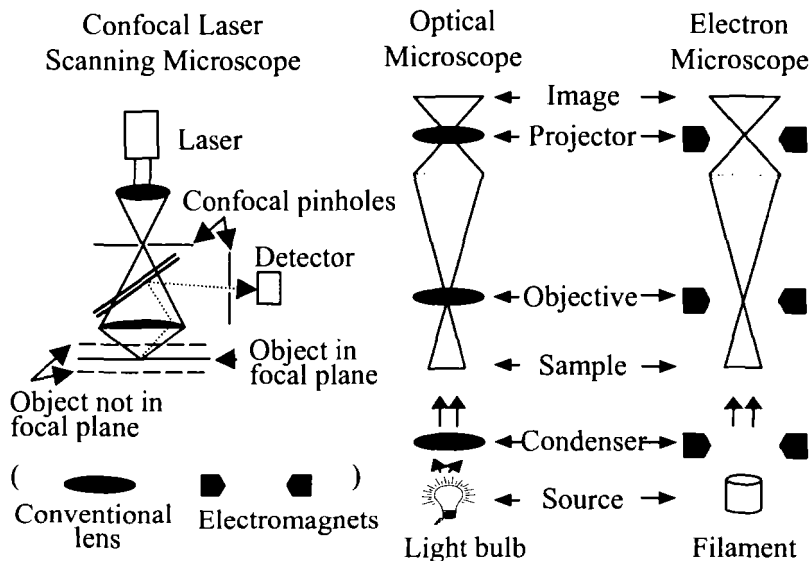


Figure 1.5. Schematics of optical and electron microscopes.

Microscopic analysis has advantages over other methods in that it can provide information on size, shape, surface texture and some optical properties of individual particles in a broad size range and in great detail [20]. Microscopic analysis has often been the final judge of the size of monodisperse standard reference materials. However, the disadvantages of microscopic methods are also obvious. First, in most cases, they only yield information from the 2-D projected areas of particles. Particle orientation in the prepared sample can alter the result significantly. Also, in electron microscopy, unless the newly developed “freeze-fracture” technique is used, it can only analyze dried particles which sometimes have different sizes, shapes, or even different masses when compared with those in suspension, especially for colloidal associates or aggregates. The biggest drawback is that in spite of modern automated image analysis the number of particles in focus that can be inspected in any field of view is limited. Thus, for a polydisperse sample, an adequate statistical representation of the entire sample can be an exhaustive, if not impossible, task.

#### *Holographic Method – Sizing (0.3-1000 $\mu\text{m}$ )*

The holographic method is a relatively new imaging technique developed about three decades ago. Since then, this method has been used in the study of airborne and liquid-borne particulate systems in their real world environments [21]. In a holographic experiment, images are formed in a two-step process. In the first step, a collimated coherent light is used to illuminate the sample. A hologram is formed by the far-field diffraction patterns of all the particles in the

illuminated sample volume with the coherent illuminating light as the background. Many individual diffraction patterns overlap in the 2-D hologram. In the second step, the hologram is again illuminated by a coherent light source and a stationary image of all the particles at their original locations in the volume is created. This 3-D image can be studied and restudied by focusing the viewing plane on particles at different locations and new 2-D images of particles can then be viewed or recorded. The same image analysis tools used in microscopic studies can be used to analyze these holographic images to determine characteristics of the particles. Figure 1.6 illustrates how a holographic image is recorded and redisplayed.

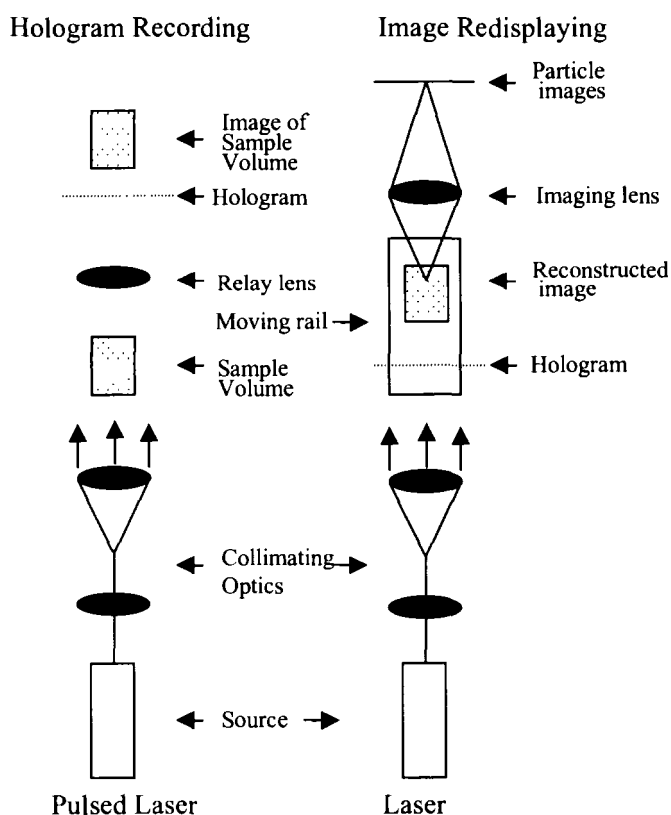


Figure 1.6. Holographic imaging.

Since a hologram is recorded using a pulsed laser of a very short duration and since the particles are recorded in their real environment (suspension, aerosol, etc.), this method effectively records the sample at one particular moment. A more detailed study can be performed in the second step at some later time. This

method can provide information on particle size, shape, and even the particle orientations in real space. Using a modified recording process and special mathematics, this technique even can measure the motion (velocity) of particles [22].

### 1.2.5. CHROMATOGRAPHIC METHODS

In chromatographic methods of particle characterization, a sample is injected or placed at one location; it is then moved by a carrier, often a type of liquid, and passed through a chromatographic path. During the passage, these particles are retained by, or interact with, the chromatographic barriers differently, based on a certain property of the particle that is related to size, and are thus fractionated. The fractionated particles are then detected by various detection methods. All chromatographic analyzers need calibrations for both retention time and concentration determination. Although there are many different devices that can be used to detect effluent materials, based either on their chemical composition or their physical properties, the detectors used in particle characterization are usually some types of light scattering or UV-vis sensors. Depending on the form of chromatographic passage and the property of interest, there are several different techniques:

#### *Size Exclusion Chromatography (SEC) – Fractionation and Sizing (0.001-0.5 $\mu\text{m}$ )*

Also known as gel permeation chromatography (GPC), SEC is a mature and well-accepted technique for characterizing both synthetic and biological macromolecules. This method uses a column packed with porous gel beads having a uniform pore size. A carrier liquid is passed through the column, and depending on the relative size or hydrodynamic volume of the polymer chains passing through the column with respect to the pore size of the gel beads, the chains are fractionated in an entropically controlled fashion. The larger ones, since they are too large to enter the pores and so flow straight through the voids between the gel beads, are eluted first. Those that can enter the packing material will be retained in the pores according to the pore volume that can be accessed. The smaller the chain, the larger the pore volume that can be accessed and the longer the delay. Using standard materials to calibrate the retention time as a function of molecular weight and using a detection scheme in which the signal response is proportional to the effluent mass of polymer, SEC is one of the more popular ways to determine the molecular weight of macromolecules. The application of SEC to particle size characterization is based on the same principle as that employed for polymer chains. It is mainly used for fractionating and sizing submicron colloidal particles. The limitations of the technique arise from particle-packing interaction and loss of sample via

entrapment of aggregates or larger particles by the packing beads. The efficiency of separation decreases when particle size exceeds about half a micron. Elution band broadening of each size of particle determines the low resolution limit of this method when applied to particle sizing [23,24],

*Hydrodynamic Chromatography (HDC) – Fractionation and Sizing (packed-column HDC 0.03-2  $\mu\text{m}$ , capillary HDC 0.02-50  $\mu\text{m}$ )*

Hydrodynamic chromatography fractionates particles utilizing the hydrodynamic interaction between particles and the liquid flow profile in the elution path. When a liquid flows through a narrow path there will be a flow profile in which the flow velocity nearer the wall will be slower than that in the middle of the stream. Meanwhile, particles can only move in the spaces between the walls. Larger particles will be confined in spaces further away from the wall than smaller particles because of their volumes. Figure 1.7 illustrates an ideal situation for spheres flowing through a capillary. In this case, the flow profile is parabolic. Larger particles will experience relatively higher velocities than smaller ones because of their accessible locations. Thus, particles of different sizes are fractionated. Practically, there are two types of HDC. One uses a non-porous bead-packed column. The hydrodynamic interaction occurs between particles and the curved bead surfaces. This type of HDC fractionates mainly submicron particles with limited resolution; thus the applications are limited [25]. The other type of HDC uses a long capillary as the chromatography column. The hydrodynamic interaction occurs between the long capillary wall and the particles. Capillaries can have different lengths and diameters depending on the particle size range to be fractionated. For a particular capillary, the dynamic sizing range is approximately 100:1. For example, a capillary with an internal diameter of 400  $\mu\text{m}$  can be used to fractionate particles from 0.5  $\mu\text{m}$  to 30  $\mu\text{m}$ . Capillary HDC has been used to fractionate solid suspensions as well as emulsion droplets with considerably higher resolution than packed-column HDC. In the submicron range, it can resolve size differences as small as 10% in diameter [26].

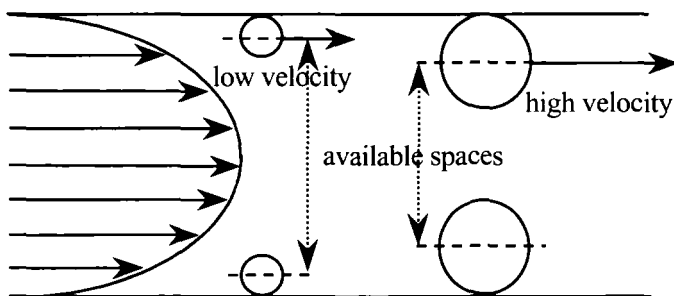


Figure 1.7. Hydrodynamic fractionation.

### *Field Flow Fractionation – Fractionation and Sizing (0.001-500 $\mu\text{m}$ )*

Although in the ideal case of Figure 1.7, capillary HDC can separate particles according to the flow profile and the location of the center-of-mass of spheres, there are many other factors leading to deviations in the real situation from the ideal situation. For example, although smaller particles can access spaces near the wall where larger particles are excluded, the same small particles can also travel through the central locations where the larger particles are. Brownian motion further ensures that particles will occupy all the available radial positions. Thus, elution line broadening is unavoidable, and that limits the resolution and efficiency of HDC. Compared to HDC, field flow fractionation (FFF) is a much more versatile technique in terms of separation range, selectivity, and resolution. Since the proposal of the FFF idea in the 1960's [27], the technology has evolved into a group of methods that have been applied to a broad range of particulate systems. A typical FFF device is composed of a flat, ribbon like (wide but thin) open channel into which the sample is injected and from which the fractionated components of the sample are eluted. A field is applied perpendicularly to the channel, and a detection scheme is used to measure the effluent (Figure 1.8).

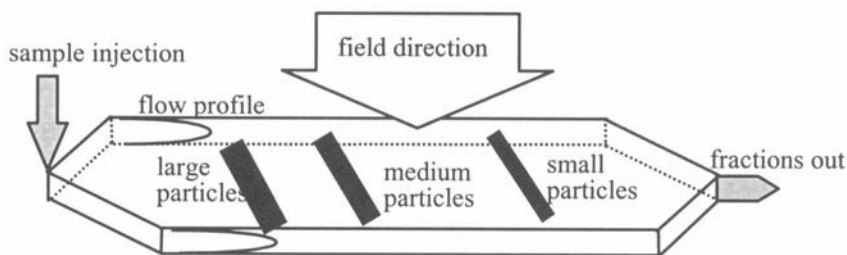


Figure 1.8. Field flow fractionation channel.

As in HDC, a liquid carrier flowing in the channel will have a parabolic flow profile due to the channel geometry; the liquid near the walls of the channel will have near-zero velocities and its velocity reaches a maximum at the center of the channel. After the sample is introduced into the channel, the flow is stopped momentarily and the external field is applied. This field can take a variety of forms. The common ones are centrifugal, thermal, electric, magnetic, flow, gravitational, or the opposed flow sample concentration technique. In addition, there can be different operating modes for each field, such as in steric and hyperlayer sedimentation FFF. The purpose of the applied field is to partition particles into different velocity streamlines in the liquid flow according to their size. Completion of this process is based on the response of the particles to the applied field, due to one of particle's properties. For example, under a thermal

field particles diffuse from the hot wall to the cold wall according to their thermal diffusion coefficient and mass, whereas under a centrifugal field particles are pushed to the outer wall according to their density and mass. Once the particle partition in the different layers is established, the liquid flow will then carry the particles out at different elute times due to the flow velocity differences at different streamlines. If small particles are partitioned and concentrated at the center of the channel after the field is applied, then small particles will have a shorter retention time and large particles will have a longer retention time (as described in Figure 1.8). The opposite situation will occur if large particles accumulate at the center of the channel [28,29].

Although the FFF technique has been demonstrated in sizing of a variety of particles across a size range of over five orders of magnitude (from 1 nm to 500  $\mu\text{m}$ ), and though research and development still continues, its commercialization has not been successful. During the past decade, a few commercial instruments have been manufactured and marketed. They are not popular and their main applications are limited to academia.

#### 1.2.6. SUBMICRON AEROSOL SIZING AND COUNTING (0.001-1 $\mu\text{m}$ )

Submicron aerosol particles exist abundantly in the atmosphere, but because of their sizes and concentrations, common sizing and counting methods are not suitable in the direct measurement of submicron aerosols. The common procedure to characterize submicron particles has two steps. In the first step, aerosol particles are fractionated (or classified) according to their size. These fractionated particles then pass through a container of evaporative liquid. Vapor condenses onto the aerosols leading to much larger size particles ( $\sim 10 \mu\text{m}$ ) which can then be detected and counted by an optical counter. Two schemes can be used to fractionate submicron aerosols. In the first scheme, called the diffusion battery method, particles pass through a stack of mesh screens. Because of diffusion they will collide with, and be captured by, the screen wires. Small particles will be captured first because they diffuse quickly and many more collisions with the screen wires will occur. Large particles will be captured by the consequent screens. Aerosol particles between 5 nm and 200 nm can be fractionated using the diffusion battery method. In the second scheme, called differential mobility analysis, particles are first charged and then carried by a sheath flow passing through an electric field. Particles are fractionated based on their differential electrical mobilities, and thus different velocities, both of which are related to their sizes. Particles between 1-1000 nm in diameter can be fractionated in this way [30,31,32].

## 1.2.7. ACOUSTIC ANALYSIS [33]

Many of the technologies listed above can be used only with dilute suspensions. However, there are instances where particle characterization has to be performed in a concentrated phase in which dynamic processes such as aggregation, agglomeration, or flocculation may occur at a much faster rate. In other instances, such as in emulsion systems, dilution just is not feasible because the system may change due to the dilution process. The analysis of such concentrated samples is especially important in on-line processes where particles naturally exist in concentrated states. Since sound waves can travel through concentrated suspensions, ultrasonic analysis provides a mean to characterize particulate systems at concentrations up to 60% by volume [34].

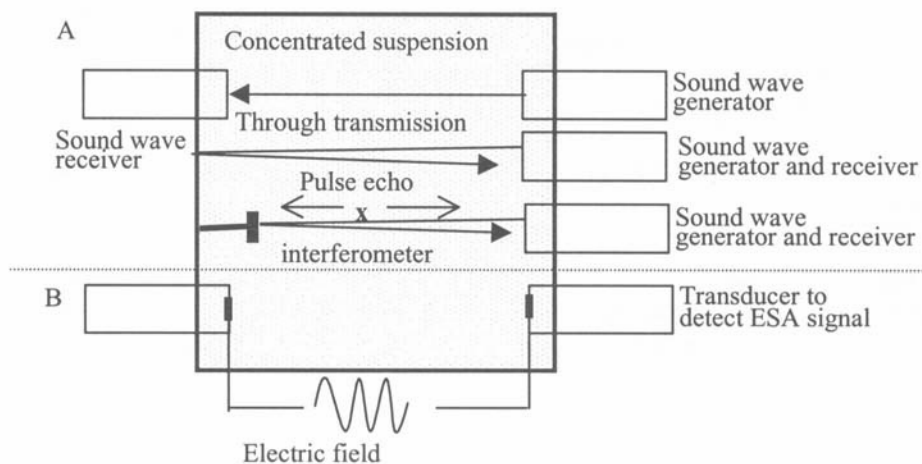


Figure 1.9. Schematics of acoustic attenuation (A) and electroacoustic effect (B) detection.

#### Acoustic Spectroscopy – Sizing (0.01-1000 $\mu\text{m}$ )

Acoustic attenuation spectroscopy is based on the measurement of the attenuation of sound waves as a function of their frequency, typically from 1 to 150 MHz. Sound waves of various frequencies are transmitted by an ultrasonic transducer through the concentrated suspension; another ultrasonic transducer receives the attenuated plane waves. Three techniques are generally used in the detection of the spectrum: through transmission, pulse echo, and interferometry (see Figure 1.9). The measured attenuation spectrum constitutes a signature for the particular suspension (its size distribution and concentration). The attenuation is due to wave interactions with both the liquid medium and any particles dispersed in the liquid. A particle presents a discontinuity to the propagation of sound. The attenuation of the sound wave is mainly the result of entrainment (when particles are much smaller than the wavelength of sound), resonance (when particles have the same dimension as the wavelength of sound)



and scattering (when particles are much larger than the wavelength of sound). Absorption also occurs when particles move relative to the suspending medium. If the physical properties of the system, such as material density, are known, the attenuation can be predicted and modeled (assuming a plane incident wave applied to a two-phase system of spheres without multiple scattering) through a set of fundamental wave equations [35,36]. Using scattering matrix conversion techniques, a particle size distribution can be determined from the attenuation spectrum. Acoustic spectroscopy can be used to size particles from 0.01 to 1000  $\mu\text{m}$  over a wide concentration range (0.5-50% by volume), and in a relatively short time (typically a few minutes). However, in applying acoustic spectroscopy, one needs to know the mechanical, transport and thermodynamic properties of the system (both particles and medium) with accuracy better than 5%. These parameters include the density, the sound attenuation coefficient (as a function of frequency), the coefficient of thermal expansion, the thermal conductivity, heat capacity, liquid viscosity, and the particle shear rigidity. Changes in even one of these parameters will alter the result, sometimes significantly. In addition, since the matrix conversion is multi-dimensional, to find a true, not-presumed solution for the particle size distribution is difficult even with modern computing power. Thus, an analytical formula, in which only a few parameters need to be fitted, such as a log-normal distribution (single-modal or multi-modal), is often used.

Besides measuring the attenuation of acoustic waves, another type of acoustic spectroscopy has been demonstrated to be able to size particles in the range from 0.1 to 30  $\mu\text{m}$ . In this technique, the transit time (hence, the velocity) of pulsed multiple frequency ultrasonic waves passing through a concentrated suspension (up to 10 v%) is measured. The frequencies applied (50 kHz - 50 MHz) in this technique are lower than those in the attenuation measurement so that a longer operational distance between the ultrasonic source and detector can be used [37]. The zeta potential of the particles in suspension can also be determined using an acoustic instrument if additional devices are used to measure the colloid vibration potential in the acoustic field.

#### *Electroacoustic Spectral Analysis – Zeta Potential Determination and Sizing (0.1-100 $\mu\text{m}$ )*

Different from acoustic attenuation spectroscopy, in electroacoustic spectral analysis, sound waves are generated by an applied high frequency electric field across a colloidal suspension and subsequently detected. This is called the electrokinetic sonic amplitude effect (ESA) [38]. These sound waves arise because the alternating electric field pushes the suspended particle forwards and backwards. By measuring the magnitude and phase angle of the sound waves at multiple frequencies (typically from 1-10 MHz), the particle dynamic mobility,  $\mu_d$ , can be determined, provided the concentration and the density of the

particles are known. From the dynamic mobility, the zeta potential of particles and the particle size distribution can be derived, assuming all particles have the same zeta potential and the distribution obeys certain predetermined analytical forms [39]. The concentration of the suspension that can be characterized ranges from less than one to up to sixty volume percent. This technology has been successfully applied to many concentrated suspensions. However, its main limitation is that the particles have to be charged, have a sufficient density difference from the medium, and are small enough that significant movement can be generated.

### 1.2.8. GAS SORPTION – SURFACE AREA AND PORE SIZE DETERMINATION

Gas sorption (both adsorption and desorption) at the clean surface of dry solid powders is the most popular method for determining the surface area of these powders as well as the pore size distribution of porous materials. In a gas sorption experiment, the material is heated and degassed by vacuum force or inert gas purging to remove adsorbed foreign molecules. Controlled doses of an inert gas, such as nitrogen, krypton, or argon, are introduced and the gas is adsorbed, or alternatively, withdrawn and desorbed. The sample material is placed in a vacuum chamber at a constant and very low temperature, usually at the temperature of liquid nitrogen (-195.6 °C), and subjected to a wide range of pressures, to generate adsorption and desorption isotherms. The amounts of gas molecules adsorbed or desorbed are determined by the pressure variations due to the adsorption or desorption of the gas molecules by the material (the adsorbent). Various amounts of gas molecules will be adsorbed or desorbed at different doses (creating different pressures in the chamber) of the gas (the adsorbate). Knowing the area occupied by one adsorbate molecule,  $\sigma$  (for example,  $\sigma = 16.2 \text{ \AA}^2$  for nitrogen), and using an adsorption model, the total surface area of the material can be determined. There are several adsorption models [40]. The most well known and most widely used is the BET equation for multilayer adsorption [41]:

$$\frac{P}{n(P_0 - P)} = \frac{1}{cn_m} + \frac{c-1}{cn_m} \frac{P}{P_0}. \quad (1.3)$$

In Eq. 1.3,  $P$ ,  $P_0$ ,  $c$ ,  $n$ ,  $n_m$  are the adsorption pressure, the saturation vapor pressure, a constant, the amount adsorbed (moles per gram of adsorbent) at the relative pressure  $P/P_0$ , and the monolayer capacity (moles of molecules needed to make a monolayer coverage on the surface of one gram of adsorbent),

respectively. Through the slope and intercept of a plot of  $P/[n(P_0-P)]$  against  $(P/P_0)$ ,  $n_m$  can be resolved. The specific surface area,  $S$ , can then be derived:

$$S = N_A n_m \sigma. \quad (1.4)$$

In Eq. 1.4,  $N_A$  is Avogadro's number. The specific surface area that can be determined by gas sorption ranges from 0.01 to over 2000 m<sup>2</sup>/g. Determination of pore size and pore size distribution of porous materials can be made from the adsorption/desorption isotherm using an assessment model, such as the t-plot, the MP method, the Dubinin-Radushkevich method and the BJH model, etc. [42], suitable for the shape and structure of the pores. The range of pore sizes that can be measured using gas sorption is from a few Ångstroms up to about half a micron.

### 1.2.9. OTHER CHARACTERIZATION METHODS

There are many other particle characterization techniques. Although they are not as common as the one listed above, they all have unique features that can be used in certain niches. Some of these are listed here along with their major features and references.

#### *Mercury Porosimetry and Capillary Flow Porometry – Pore Size Determination*

In a mercury porosimetry measurement, pressure is used to force mercury into filling the pores and voids of the material. The method is based on the capillary rise phenomenon which exists when a non-wetting liquid climbs up a narrow capillary. As the pressure is increased, mercury infiltrates the pores to occupy a subset of the total pore space, the extent of which depends on the applied external pressure. The injected volume of mercury as a function of pressure is recorded. The pore size and distribution can be resolved using the Young and Laplace model [43]. The pore sizes that can be determined by mercury porosimetry range from a few nanometers to a few hundreds of microns. The method is invasive in that not all the mercury will be expelled from the pores and pores may collapse as a result of the high pressures. Due to this and environmental concerns about mercury pollution mercury porosimetry method is becoming less popular.

In a capillary flow porometer, a sample is first fully wetted by a liquid of low surface tension and low vapor pressure and then a flow of air (or other gas) at a certain pressure is established through the sample until the “bubble point” (the pressure at which the largest pores are emptied of fluid) is reached. The flow pressure is then continuously increased and the flow of air or gas is measured until all the pores are emptied. The pore size range that can be determined is from some tens of nanometers to a few hundreds of microns [44].

Choosing a porometer or a porosimeter depends upon what information about the material is sought and upon what type of pores the material contains. Porometry is best for determining "through" pore (pores having two openings) diameter, distribution and permeability since it characterizes only "through" pores and yields no useful information about "dead-end" pores. Porosimeters are useful for determining the total "through" and "non-through" (or "dead-end") pore volume of a material.

#### *Streaming Potential Measurement – Zeta Potential Determination*

When external pressure forces an electrolyte solution through a capillary, or through a bundle of fibers, or through a plug of porous material, some displacement of charge will take place. The displacement is in the same direction as the liquid flow and results in a streaming potential between the ends of the sample. From the streaming potential, information on the zeta potential of the material can be obtained. This is very useful in the determination of zeta potential for fibers, membranes, textiles, and other larger particles when an electrophoretic mobility measurement is not feasible [45,46].

#### *Pulsed Field Gradient Nuclear Magnetic Resonance (PFG-NMR) – Diffusion Coefficient Determination*

In a PFG-NMR measurement, a radio frequency pulse is applied to rotate the magnetization of the nuclear spins of the sample into the transverse plane that is held perpendicular to the main homogeneous magnetic field. The positions of the nuclear spins are subsequently labeled by imposing a linear magnetic field gradient for a short time period. Then a second pulse is applied which inverts the phase of the local magnetization in the sample. After applying a second magnetic field gradient pulse, the spin echo is recorded. Diffusion of spins along the direction of the magnetic field gradient in the time span between the gradient pulses causes irreversible loss of phase coherence, from which the self-diffusion coefficient of the sample can be obtained. A size distribution can then be resolved from the diffusion coefficient. During the past few years, this academic technique has been shown to be able to study not only the diffusion of small molecules but also the diffusion of particles such as micelles and latexes up to 100 nm [47].

#### *Dielectric Spectroscopy – Surface Characterization of Liquid-borne Colloids*

When an oscillatory electric field is applied to a colloidal suspension, the electric double layer around the particle will be polarized. The complex dielectric properties of the suspension, the loss factor, and the relative permittivity are determined by performing several isothermal scans as a function of frequency in the range of  $100\text{--}10^{10}$  Hz. The dielectric relaxation of particles can be determined through the dielectric spectroscopy and the

characteristics of the particle surface can be obtained more sensitively than from an electrophoresis measurement [48].

The sizing methods described in this section as well as in the following chapters are plotted in Figure 1.10 as a function of their applicable size range as the conclusion of this section.

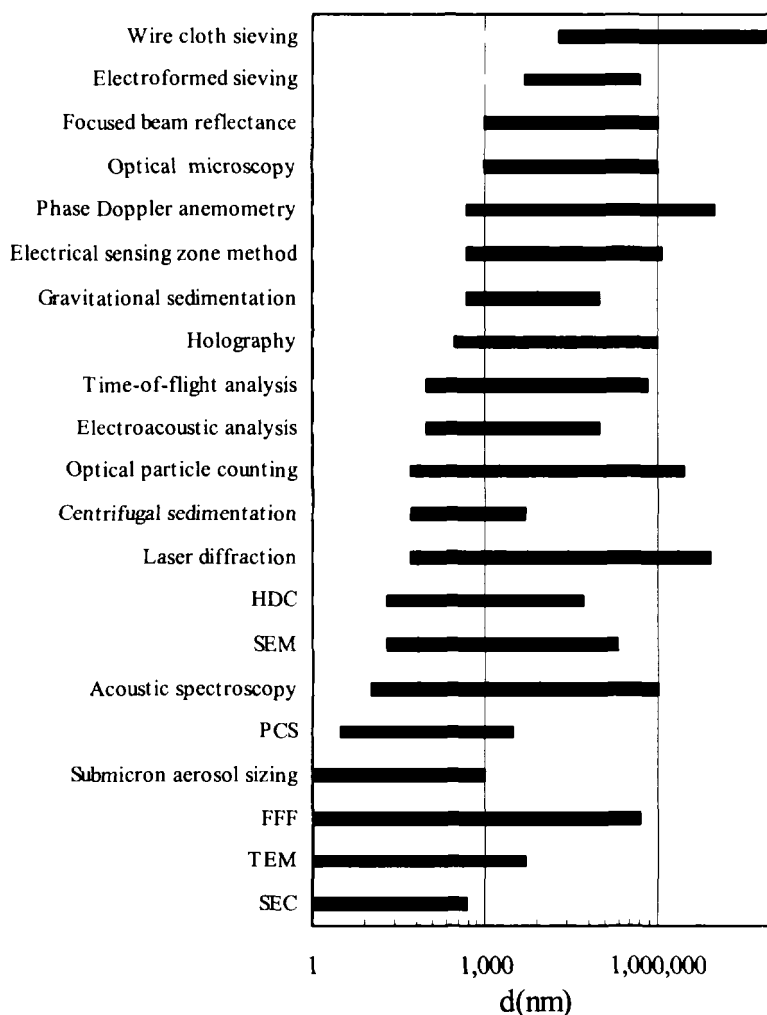


Figure 1.10. Particle sizing methods.

### 1.3. Data Presentation and Statistics

In particle characterization, data often are in a form of  $q(x)\Delta x$ , where  $q(x)$  is a proportional amplitude or concentration (relative or absolute) measure of particles having the variable  $x$ .  $x$  is the primary property being measured. In the other words,  $q(x)$  is the density distribution of particles having the variable  $x$ .  $q(x)$  can be discrete or continuous depending on the measurement and the data interpretation process used. Commonly,  $q(x)\Delta x$  represents either the percentage or absolute number, length, surface area, or volume of particles within the range  $\Delta x$ , where  $x$  might be used to refer to one of the following properties: particle volume, particle size, pore size, pore volume, particle surface area, or particle mobility. Depending on the application, both  $q(x)$  and  $x$  can be transformed using different weightings into other variables. No matter which technology is used to obtain the result, correct data presentation using appropriate statistics is the last important step in the whole characterization procedure. There are different ways to present information from the same data set. The nomenclature and terminology used in the field of particle characterization are different depending on the industry and country of origin, and thus are often confusing. A very simple example is the symbol used for particle diameter: in the US and some other countries,  $d$  is used for particle diameter, but in Germany and other European countries,  $x$  is preferred [49]. Another example is the definition of different mean values. In some cases the entire system used to define these mean values may be different [50].

In the following we will first list the ways  $q(x)$  can be presented, followed by the basic statistic values that can be calculated from  $q(x)$ . Finally, the definitions for various mean values are given.

#### 1.3.1. DATA PRESENTATION FORMATS

In particle characterization experiments,  $q(x)$  is obtained at the  $x$  values that result either from a calibrated direct measurement or from a conversion process involving predetermined  $x$  values. In the other words, the  $x$  values may be preset, extracted, or measured directly. The choices of the  $x$  values where  $q(x)$  are to be obtained depend on the characterization technology and the property of the sample. From a statistical point of view, the  $x$  values should be arranged in a way that the distances (or steps) between consecutive  $x$  values are all the same or similar (i.e.,  $\Delta x$  is spaced more or less equally) thus giving a good representation of the true distribution. Although, because of the nearly infinite number of particles in a sample, the distribution function  $q(x)$  can be continuous or discrete, but the data points (the locations of  $x$ ), sampled from  $q(x)$  in an experiment are often finite, except in chromatography and a few other methods where a continuous measurement of  $q(x)$  is possible. Thus, except when an

analytical distribution form is used to represent the distribution, most data will be in discrete forms and any statistics will be computed using these discrete values. Most particulate systems are polydisperse with a broad distribution in the property measured. The  $x$  values are then commonly equally spaced on a logarithmic scale so that information across the whole distribution can be revealed evenly. Suppose, for example, in a particle size measurement, the size range of the particles is from 100 nm to 100  $\mu\text{m}$ ; if the size steps are spaced linearly, i.e., the size population is measured in equally spaced size steps, information about the small particles cannot be revealed. In this example, if one measures 100 data points, each step will be approximately 1  $\mu\text{m}$ , and no detail will be obtained regarding the size distribution from 100  $\mu\text{m}$  to 1  $\mu\text{m}$ . If instead the size steps are spaced logarithmically, the size distribution in each decade of the size range will be revealed with similar resolution; i.e., there will be 33 data points in the size range from 100 nm to 1  $\mu\text{m}$ , as well as in the ranges from 1  $\mu\text{m}$  to 10  $\mu\text{m}$  and from 10  $\mu\text{m}$  to 100  $\mu\text{m}$ . In order to also satisfy the requirement of having equally spaced data points (discussed earlier), the statistics have to be calculated based on the logarithms of the values, not the values themselves. Thus, in particle characterization, statistics can be calculated either arithmetically or geometrically [51]. Arithmetic calculation is applied to  $x$  values that are linearly spaced and has conventional meaning used in some scientific disciplines. For example, the arithmetic number mean  $\bar{x}_a$  of  $N$  particles, in which there are  $n_1$  particles having the variable  $x_1$ ,  $n_2$  particles having the variable  $x_2$ , (and so on), is:

$$\bar{x}_a = \frac{\sum_i n_i x_i \Delta x_i}{\sum_i n_i \Delta x_i} = \frac{1}{N} \sum_i n_i x_i. \quad (1.5)$$

In Eq. 1.5,  $N = \sum n_i$  and the second equality applies when all  $\Delta x_i$  are the same. Actually, there is an approximation in the first equality if  $\bar{x}_a$  is meant to be close to the real mean value of the sample. Since from experiment, one only has information for the density distribution at the measured  $x_i$  values, one does not know the density distribution at those non-measured  $x_i$  values. These values might be zero or any non-negative value. In most real particulate systems, distributions have smooth variations. If the number of sampling points is not too small, one may make an assumption that all density distribution values in the neighborhood of the measured  $x_i$  values are the same as that at the measured  $x_i$  values. Under this assumption, the measured distribution can be represented by a histogram where the  $q(x)$  values from  $x_{i-1}$  to  $x_i$ , or from  $x_i$  to  $x_{i+1}$ , (or more commonly from  $(x_{i-1}+x_i)/2$  to  $(x_i+x_{i+1})/2$ ) take the  $q(x)$  value at  $x_i$ . A histogram

is then composed of a successive series of rectangular columns, where each column represents the quantity  $q(x_i)\Delta x_i$ . When  $i$  is very large, i.e.,  $\Delta x_i \rightarrow dx_i$ , such as when using fractionation technologies where the measurement is often nearly continuous, the histogram becomes a continuous curve. Another approximation commonly followed is a conversion from the histogram to a continuous curve. This approximation involves an interpolation that connects the central points of successive columns by straight lines so that a smooth density distribution curve can be displayed although all statistical parameters may still have to be calculated using the original histogram. Figure 1.11 shows a histogram from a laser diffraction measurement of a trimodal polystyrene latex suspension and the smoothed volume percentage distribution.

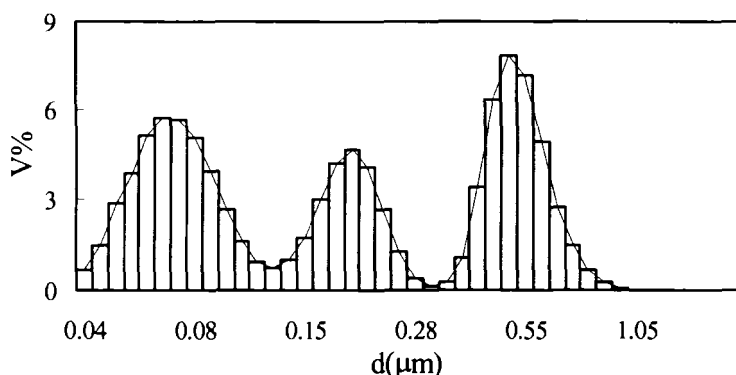


Figure 1.11. Histogram and smoothed distribution.

The geometric mean of a series of values  $x_1, x_2, \dots, x_N$ , in the definition of statistics, is the  $N^{\text{th}}$  root of the product of the  $N$  values of the variable:

$$\bar{x}_g = (x_1^{n_1} x_2^{n_2} \dots x_i^{n_i})^{\frac{1}{N}}. \quad (1.6)$$

In terms of the logarithms of the above equation:

$$\text{Log}(\bar{x}_g) = \frac{1}{N} \sum_i n_i \log(x_i). \quad (1.7)$$

Eq. 1.7 has the analogy of Eq. 1.5 except now the calculation is based on the logarithm of the data. It is often used when the data are arranged logarithmically, i.e., the logarithm of the  $x$  channels being more or less linearly



spaced. Obviously, these two types of statistics give different results because they are based on differently “scaled” information. It can be proved that the arithmetic mean is always larger than its corresponding geometric mean for any polydisperse system.

Besides the fractional form  $q(x)$ , also called differential form, as discussed above, the distribution can also be represented in a cumulative form (partial integration form). In the cumulative form,  $Q(x_i)$  represents the summation of all differential  $q(x)$  values whose corresponding values of  $x$  are smaller than  $x_i$ . In a mathematical form, there exists the relationship

$$Q(x_i) = \sum_{n=1}^i q(x_n) \Delta x_n = \int_{x_{\min}}^{x_i} q(x) dx. \quad (1.8)$$

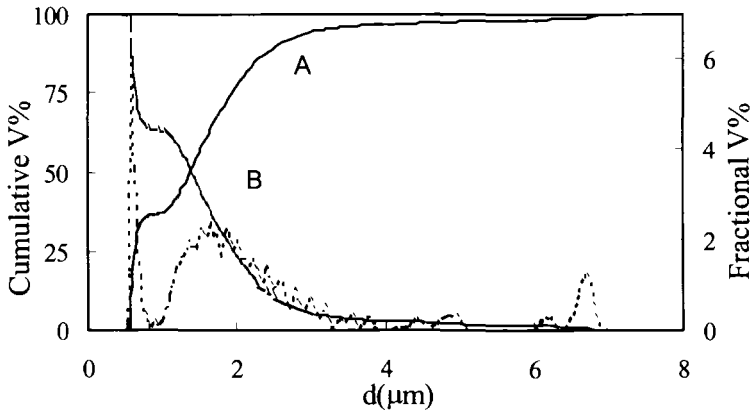


Figure 1.12. Cumulative and differential distributions. Dotted line: Fractional (or differential) volume distribution with the right ordinate. A: Cumulative-undersize distribution with the left ordinate. B: Cumulative-oversize distribution with the left ordinate.

In histogram form, the cumulative distribution can be obtained by summing all the columns from the smallest  $x$  value up to the point  $i$  from the fractional (or density, or differential) distribution. This representation of the cumulative term is also called the “cumulative-undersize” distribution, in contrast to the “cumulative-oversize” distribution, wherein the summation is performed from  $x_{\max}$  to  $x_i$ . For percentage distributions, there exists the relation  $Q(x_i)_{\text{cumulative-undersize}} = 1 - Q(x_i)_{\text{cumulative-oversize}}$ . Because of the integration relation between the fractional distribution and the cumulative distribution, the absolute values of the maximum and minimum slopes in the cumulative distribution correspond to the

peak and minimum values in the fractional distribution, respectively. Figure 1.12 shows a particle size distribution presented in three different forms.

For a cumulative distribution, the result will be independent of whether the abscissa is linearly or logarithmically scaled since  $Q(x_i)$  represents the total amount smaller than  $x_i$ ; thus,  $Q(x_i) = Q(\log(x_i))$ . However, in a differential distribution, a recalculation is needed when the abscissa is transformed in order to keep the area in each column of the histogram constant:

$$q(\log(x_i)) = q(x_i)\Delta x_i / \Delta \log(x_i). \quad (1.9)$$

There are three ways to present a distribution: tabulate, graphic, and functional. Tabulate forms are the listing of experiment results, the data points, or other values transformed from the data points. In a graphic representation, the physical property chosen to characterize particles is plotted on the abscissa and the dependent variable is plotted on the ordinate. In the pre-computer era, graphic forms were often used to determine the statistic parameters besides serving as a presentation tool. For a data set of 100 points, to manually calculate the standard deviation (distribution broadness) without even a calculator would be a tedious job. Depending on the type of distribution, several graphic papers, such as probability graph paper, were commonly used to plot the data and estimate statistical parameters. With the ever-advancing computer hardware and software, the graphic form has becoming purely a presentation tool and graphic papers are needed less and less.

The same is true for functional forms. An analytical function can be characterized by a few parameters. Once these parameters are determined, all statistical values are determined. Thus, fitting the parameters of a chosen function from the experiment result to represent the real distribution was a popular method in particle characterization, especially for ensemble methods in which  $q(x)$  is not directly measured but determined through a certain conversion process. Of course, a real distribution may not be describable by an equation, especially for multimodal distributions. Even if a real distribution is close to an analytical function, it may not be one of the common forms and may not be fitted by only two or three variables. However, fitting a function can be easily achieved using simple computation means and these fitted parameters can be used in the quality control of products or processes. Recently, even in moderately complicated computational processes in particle characterization, the actual computing times are much less or only slightly more than the time needed for the user interface, e.g., data input, report printing, etc. Most modern technologies in particle characterization have adopted methods that directly compute distributions without any assumptions about the forms of distribution. However, these analytical forms still have reasons for their persistence in particle characterization. They may be used for simulation purposes or for

comparisons with existing data or pre-determined quality control specifications. In Table 1.3, several common unimodal distribution functions are listed along with their arithmetic mean and mode values.

Table 1.3. Common distribution functions

Differential Distribution Form	Mean	Mode
<b>Normal Distribution (Gaussian Distribution)</b>		
$q(x) = \frac{1}{\sqrt{2\pi}\sigma} \exp\left(-\frac{(x-a)^2}{2\sigma^2}\right)$	a	a
<b>Log-normal Distribution</b>		
$q(x) = \frac{1}{\sqrt{2\pi \ln\left(\frac{\sigma^2}{a^2} + 1\right)}x} \exp\left(-\frac{\left(\ln\left(\frac{x}{a} \sqrt{\frac{\sigma^2}{a^2} + 1}\right)\right)^2}{2 \ln\left(\frac{\sigma^2}{a^2} + 1\right)}\right)$ $q(x) = \frac{1}{\sqrt{2\pi x \sigma_{\ln(x)}}} \exp\left(-\frac{(\ln(x) - a_{\ln(x)})^2}{2\sigma_{\ln(x)}^2}\right)$	a	$\frac{a^4}{(\sigma^2 + a^2)^{3/2}}$
<b>Rosin-Rammler-Sperling-Bennet Distribution</b>		
$q(x) = nbx^{n-1} \exp(-bx^n)$	$\frac{\Gamma\left(\frac{1}{n} + 1\right)}{\sqrt[n]{b}}$	$\sqrt[n]{\frac{n-1}{bn}}$
<b>Schulz-Zimm Distribution</b>		
$q(x) = \left(\frac{\sigma}{a}\right)^{\sigma+1} \frac{x^\sigma}{\Gamma(\sigma+1)} \exp\left(-\frac{\sigma x}{a}\right)$	$\frac{a(\sigma+1)}{\sigma}$	a
<b><math>\beta</math> Distribution</b>		
$q(x) = \frac{x^m (a-x)^n}{B(m+1, n+1)} \quad x < a,$ (negatively skewed when $m > n$ )	$\frac{a(m+1)}{(n+m+2)}$	$\frac{am}{m+n}$

Table 1.4. Data presentation formats

	Tabular	Graphic	Functional
Cumulative	Linear/Logarithm	Linear/Logarithm	Q(x)
Differential	Linear/Logarithm	Linear/Logarithm	q(x)

In Table 1.3,  $\sigma$  is the standard deviation of the distribution (see Eq. 1.10 below), and  $\Gamma(\alpha)$  and  $B(m,n)$  are  $\Gamma$  function and B function, respectively. The log-normal distribution is presented in two forms. In one formula, the variables are the mean value  $a$  and the standard deviation  $\sigma$  in the linear scale; and in the second formula, the one more commonly seen in the particle characterization

literature, the variables are the mean value of  $\ln(x)$ ,  $a_{\ln(x)}$ , and the standard deviation of  $\ln(x)$ ,  $\sigma_{\ln(x)}$ . Table 1.4 summarizes all data presentation formats.

### 1.3.2. BASIC STATISTICAL PARAMETERS [52]

Mean:

The mean is an average over the whole distribution. There are different types of means that can be calculated from the same set of data. See the next subsection (Section 1.3.3) for a more detailed discussion.

Median:

The median is the  $x$  value that divides the population into two equal halves. Just like the mean value, populations with different weightings will have different median values.

Mode:

The mode is the most common value of the distribution, i.e., the highest point of the distribution curve. It is also commonly called the peak value. If there are more than one high frequency region in the distribution, the distribution is called multi-modal.

Variance( $\sigma^2$ ):

A measure of distribution broadness defined as, for arithmetic and geometric, respectively:

$$\sigma^2 = \frac{\sum_{i=1}^N (x_i - \bar{x})^2}{N - 1}, \quad (1.10)$$

$$\sigma_g^2 = \text{anti log} \left( \frac{\sum_{i=1}^N (\log(x_i / \bar{x}))^2}{N - 1} \right). \quad (1.11)$$

Standard Deviation ( $\sigma$ ):

The square root of the variance. Note that the geometric standard deviation is not a standard deviation in its true sense.

Coefficient of Variation (arithmetic statistics only):

The coefficient of variation (CV) is the standard deviation divided by the mean. It relates the breadth of the distribution to the mean in percentage.

Skewness ( $g_1$ ):

Skewness is the degree of distortion from a symmetrical distribution. If on one side of the mean has extreme values but the other does not, the distribution is said to be skewed. If the dispersion of  $q(x)$  on either side of the mean are roughly symmetrical (i.e. one is a mirror reflection of the other), the distribution is said to be not skewed. When a distribution is perfectly symmetrical the skewness ( $g_1$ ) is equal to zero. For a right-skewed distribution there is a long tail at the right side and a steep rise at the left side, and the skewness is positive. For a left-skewed distribution the skewness is negative and the tail is on the left with the bulk of the distribution on the right (Figure 1.13). The second approximate equality in Eq. 1.12 is held when  $N$  is large.

$$g_1 = \frac{N}{(N-1)(N-2)} \sum_{i=1}^N \left( \frac{x_i - \bar{x}}{\sigma} \right)^3 \approx \frac{\sum_{i=1}^N (x_i - \bar{x})^3}{\sigma^3 N}. \quad (1.12)$$

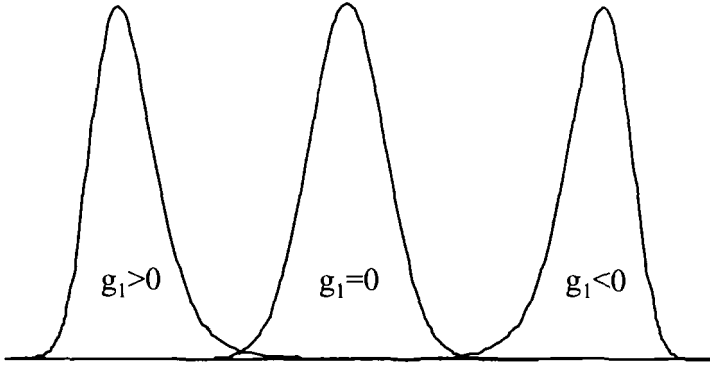


Figure 1.13. Distribution skewness.

kurtosis ( $g_2$ ):

Kurtosis is a measure of the weight of the tails of a distribution or the peakedness of a distribution. A normal distribution is defined as having zero kurtosis (mesokurtic). When  $q(x)$  values are closer to the mean, the distribution is narrower or sharper than the normal distribution and the kurtosis ( $g_2$ ) is positive (leptokurtic). When  $q(x)$  values tend towards the extremes, the distribution is broader than the normal distribution and the kurtosis is negative (platykurtic). These three situations are illustrated in Figure 1.14. The second approximate equality in Eq. 1.13 is held when  $N$  is large.

$$g_2 = \frac{N(N+1)}{(N-1)(N-2)(N-3)} \sum_{i=1}^N \left( \frac{x_i - \bar{x}}{\sigma} \right)^4 - \frac{3(N-1)^2}{(N-2)(N-3)} \quad (1.13)$$

$$\approx \frac{\sum_{i=1}^N (x_i - \bar{x})^4}{\sigma^4 N} - 3$$

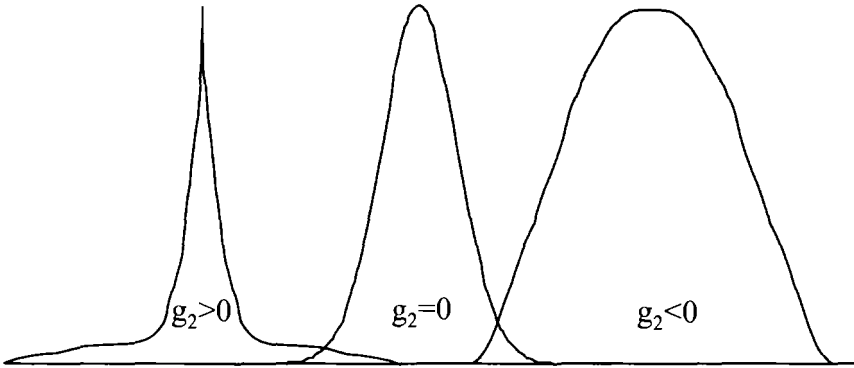


Figure 1.14. Distribution kurtosis.

$x_{w\%}$ :

The  $x$  value at which  $w\%$  of particles has smaller  $x$  values. It is most commonly used in diameter distribution presentation, in which  $d_{w\%}$  means the diameter at which  $w\%$  of particles is smaller (cumulative undersize by volume.)

It is obvious that in Eqs. 1.10 - 1.13, when  $\bar{x}$  is different, it will result in different values of the standard deviation, skewness and kurtosis. In general, these values are all different between arithmetic statistics and geometric statistics. From the definitions of arithmetic mean, median, and mode, one can predict that for positively skewed distributions that account for most of the industrial particulate systems, mode < median < mean. The degree of spread in these three values depends on the symmetry of the distribution. For completely symmetric distributions, these three values overlap.

### 1.3.3. MEAN VALUES

Many times, a simple and concise value is used to represent a certain property of a group of particles, e.g., the sample. This value should be a measure of some central tendency, unaffected by a relatively few extreme values in the tails of the distribution. This value is the so-called mean value. The mean value is a certain type of average taken over the whole distribution. For example, if there are ten spheres of diameters from 1 to 10, the sum of their diameters from the distribution can be represented by ten spheres each of diameter 5.5; but the sum of their volumes has to be represented by ten spheres each having a diameter of 6.72. Due to their nature, each particle characterization technology will “see” the same system differently. In the language of statistics, different technologies see particles through different “weighting factors.” For example, when using TEM, one measures particles on the basis of their number, but when using laser diffraction one detects the light scattering intensity of particles on the basis of their volume. Thus, if one calculates the mean value of a distribution using the “native weighting” of the measurement, i.e., without converting it to the same base, no valid comparison can be made from results of two different measurement technologies, even for spheres [53]. Again, due to the lack of computing power, historically it was difficult to perform weighting factor conversions. Additionally, in practice, various applications may need representations with different weighting factors. Different mean values thus have to be defined and used. There are two systems commonly in use in defining and calculating mean *size* values. See Section 2.3 for another convention used in defining mean values.

#### *The Moment-Ratio Notation [50]*

In this system of notation, mean size values are expressed as the ratio between two moments of the number density distribution of parameter  $x$ . Here,  $x$  is a characteristic parameter, most commonly the diameter  $d$  (or  $x$ ) but it can also be some other parameter. The term  $\bar{D}_{p,q}$  is used to designate a mean value obtained from summing discrete individual  $x$  values to the power of  $p$  ( $x^p$ ), which represents the relationship between the measured signal and the particle parameter  $x$ . The value of the  $x^p$  summation is then normalized by a summation of  $x$  values to the power of  $q$ , which represents the relation between the weighting of each particle to its parameter  $x$  in the measurement [54]:

$$\bar{D}_{p,q} = \left( \frac{\sum_{i=1}^N x_i^p}{\sum_{i=1}^N x_i^q} \right)^{\frac{1}{p-q}} \quad p \neq q, \quad (1.14)$$

$$\bar{D}_{p,q} = \exp \left( \frac{\sum_{i=1}^N x_i^p \ln(x_i)}{\sum_{i=1}^N x_i^p} \right) \quad p = q, \quad (1.15)$$

$$\bar{D}_{p,q} = (\bar{D}_{p,c})^{\frac{p-c}{p-q}} / (\bar{D}_{q,c})^{\frac{q-c}{p-q}} \quad p \neq q. \quad (1.16)$$

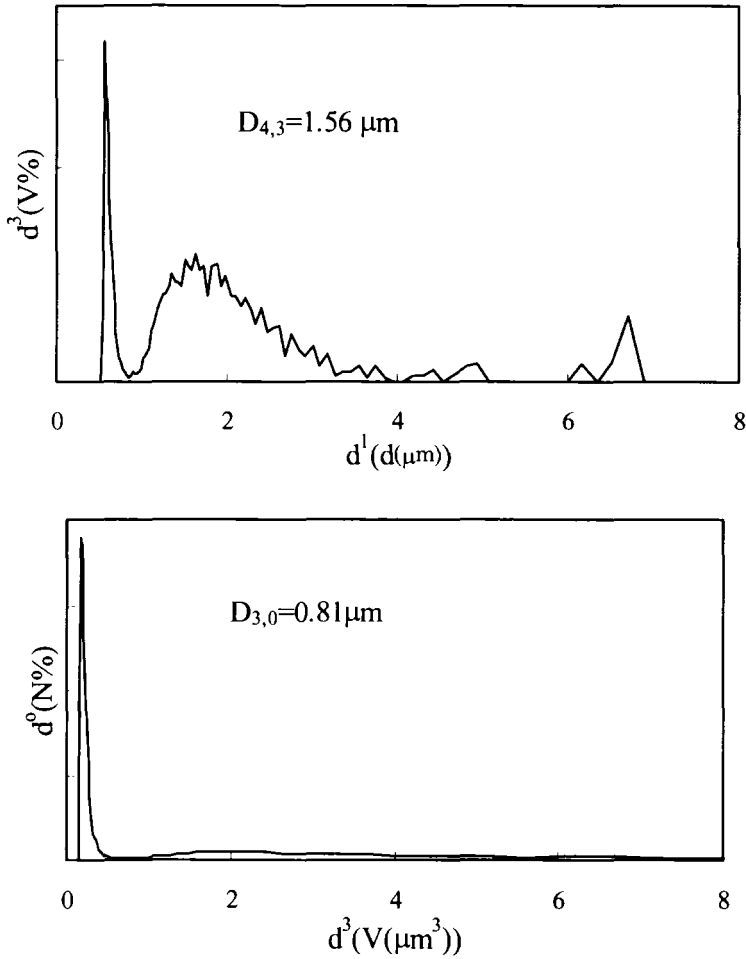


Figure 1.15. Different graphic presentations of a size distribution and their mean values. In the top graph,  $p = 4$  and  $q = 3$  and the bottom one,  $p = 3$  and  $q = 0$ .



In graphic presentation,  $\bar{D}_{p,q}$  is the arithmetic mean when plotting  $x^q$  as a function of  $x^{p-q}$  after extraction of a proper root. For a particle size distribution, when the exponential term of  $d^q$  is equal to 1, 2, or 3, the term  $d^q$  is length, surface, or volume weighted, respectively. The same is true for  $d^{p-q}$ . Figure 1.15 shows a particle size distribution plotted in two forms and their corresponding arithmetic mean  $\bar{D}_{p,q}$ .

In the above definitions,  $p$  and  $q$  are restricted to integer values. The last equality (Eq. 1.16) is particularly useful when a specific mean value cannot be measured directly but the other two mean values are measurable. For example, if one uses an electron microscope to measure particles, one will measure the diameters with a graticule, add them up and divide the sum by the number of particles to get an average result. This will then be  $\bar{D}_{1,0}$ ; i.e., the number average. If one then does an image analysis the area of particles is what most important.  $\bar{D}_{2,0}$  will be generated from the image analysis by adding all projected areas and dividing the sum by the total number of particles analyzed. Likewise, in a Coulter Principle measurement, one would get  $\bar{D}_{3,0}$ , and in a laser scattering experiment, one would get  $\bar{D}_{4,3}$ . The table below illustrates one example of how large the difference in the  $\bar{D}_{p,q}$  values can be, even for a very simple system. In this example we assume that there is a particle system that consists of four spherical particles with diameters of 1, 2, 3, and 10, respectively (the unit is irrelevant here). In size measurements their corresponding  $\bar{D}_{p,q}$  values are as follows:

Table 1.5.  $\bar{D}_{p,q}$  values of a simple system

$\bar{D}_{0,0} = 2.78$	$\bar{D}_{1,1} = 5.65$	$\bar{D}_{3,2} = 9.08$	$\bar{D}_{6,3} = 9.88$
$\bar{D}_{1,0} = 4.00$	$\bar{D}_{2,1} = 7.13$	$\bar{D}_{4,2} = 9.41$	$\bar{D}_{4,4} = 9.87$
$\bar{D}_{2,0} = 5.34$	$\bar{D}_{3,1} = 8.05$	$\bar{D}_{5,2} = 9.58$	$\bar{D}_{5,4} = 9.93$
$\bar{D}_{3,0} = 6.37$	$\bar{D}_{4,1} = 8.57$	$\bar{D}_{6,2} = 9.67$	$\bar{D}_{6,4} = 9.95$
$\bar{D}_{4,0} = 7.08$	$\bar{D}_{5,1} = 8.90$	$\bar{D}_{3,3} = 9.55$	$\bar{D}_{5,5} = 9.96$
$\bar{D}_{5,0} = 7.58$	$\bar{D}_{6,1} = 9.10$	$\bar{D}_{4,3} = 9.74$	$\bar{D}_{6,5} = 9.98$
$\bar{D}_{6,0} = 7.94$	$\bar{D}_{2,2} = 8.42$	$\bar{D}_{5,3} = 9.83$	$\bar{D}_{6,6} = 9.99$

We can see from the above table that the mean sizes can be quite different if one uses an electron microscope ( $\bar{D}_{1,0} = 4.00$ ), or a laser diffraction instrument ( $\bar{D}_{4,3} = 9.74$ ) to measure this four-particle system. The difference between a number-averaged mean ( $q = 0$ ) and a mass-averaged mean ( $q = 3$ ) resides in the fact that in the number average the mean value represents values from particles with the largest population while in the mass average the mean value represents more from particles with the largest size. The same is true for a real distribution. A number distribution may be completely different from its corresponding mass

distribution. Figure 1.16 shows the same differential volume distribution as that in Figure 1.12 but with an additional curve showing the differential number distribution. Table 1.6 lists the values for a few statistical parameters.

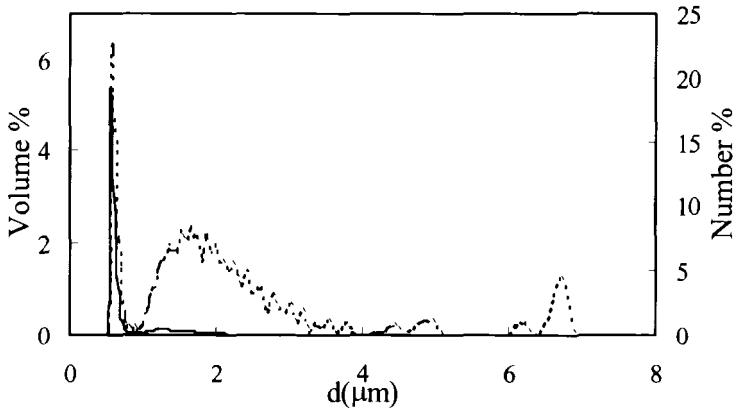


Figure 1.16. Number (solid line) and volume (dashed line) distributions of the same sample.

Table 1.6. Statistics of the distribution in Figure 1.16 (all values are in  $\mu\text{m}$ )

	Volume Weighted		Number Weighted	
	Arithmetic	Geometric	Arithmetic	Geometric
Mean	$\bar{D}_{4,3} = 1.56$	$\bar{D}_{3,3} = 1.24$	$\bar{D}_{1,0} = 0.68$	$\bar{D}_{0,0} = 0.65$
Median	1.37	1.37	0.60	0.60
Mode	0.58	0.58	0.56	0.56
SD	1.09	1.86	0.28	1.30

*The Moment Notation [55]*

In this convention, mean size values are defined through the moments of different types of distributions (e.g., number, length, surface, or volume distribution). For distributions in histogram form, the  $k^{\text{th}}$  complete moment  $M$  of a density distribution is defined as:

$$M_{k,r} = \frac{1}{k+1} \sum_{i=1}^N q_{r,i} (x_i^{k+1} - x_{i-1}^{k+1}) \quad k \neq -1, \quad (1.17)$$

$$M_{k,r} = \sum_{i=1}^N q_{r,i} \ln\left(\frac{x_i}{x_{i-1}}\right) \quad k = -1 \quad (1.18)$$

where the first subscript,  $k$ , of  $M$  indicates the power of the size parameter  $x$ , and the second subscript,  $r$ , of  $M$  describes the type of the density distribution.  $q_{r,i}$  is the average height of a density distribution in the  $i^{\text{th}}$  interval. When  $r = 0$ ,  $q_r$  is a normalized number distribution; and when  $r = 1, 2$ , or  $3$ ,  $q_r$  is a normalized length, surface or volume (or mass) distribution, respectively. Using these moments, the mean values are defined as:

$$\bar{x}_{k,r} = \sqrt[k]{M_{k,r}}. \quad (1.19)$$

Depending on the numbers chosen for the subscripts  $k$  and  $r$ , different mean values may be defined. These two systems can be related to each other for arithmetic mean values only since there is no definition of geometric mean values in the moment notation. Their relations can be summarized in the following table for the mean values commonly used.

Table 1.7. Comparison of two mean value notation systems

Name	Moment-Ratio System	Moment System
Geometric mean $x$	$\bar{D}_{0,0}$	
Arithmetic mean $x$	$\bar{D}_{1,0}$	$\bar{x}_{1,0}$
Length-weighted geometric mean $x$	$\bar{D}_{1,1}$	
Mean surface $x$	$\bar{D}_{2,0}$	$\bar{x}_{2,0}$
Length-weighted mean $x$	$\bar{D}_{2,1}$	$\bar{x}_{1,1}$
Surface-weighted mean $x$ (Sauter mean)	$\bar{D}_{3,2}$	$\bar{x}_{1,2}$
Mean volume $x$	$\bar{D}_{3,0}$	$\bar{x}_{3,0}$
Volume-weighted geometric mean $x$	$\bar{D}_{3,3}$	
Volume-weighted mean $x$ (De Brouckere mean)	$\bar{D}_{4,3}$	$\bar{x}_{1,3}$

#### 1.3.4. QUALITY OF MEASUREMENT

Quality in a particle characterization measurement can be defined using the term “accuracy”, which is composed of both bias and precision [56]. Bias is a measure of how the determined value compares with the “true” value. This true value may be established through other (certified) reference measurement methods or simply unknown. The best way to avoid bias, including bias in instrumentation, sampling and operation, is to verify the whole measurement process or to calibrate the instrument using a reference material. Reference materials can be user’s own product reference, a national standard reference material, or a secondary reference material traceable to the national standard [57]. Bias is also often associated with the inherent resolution of each technology. Figure 1.17 shows a comparison of the particle size distribution of a polystyrene latex sample measured using the electrical sensing zone method and the laser diffraction method. Although the mean values from the two methods

are very close, the difference in the size distributions is due to the difference in resolution of these two methods.

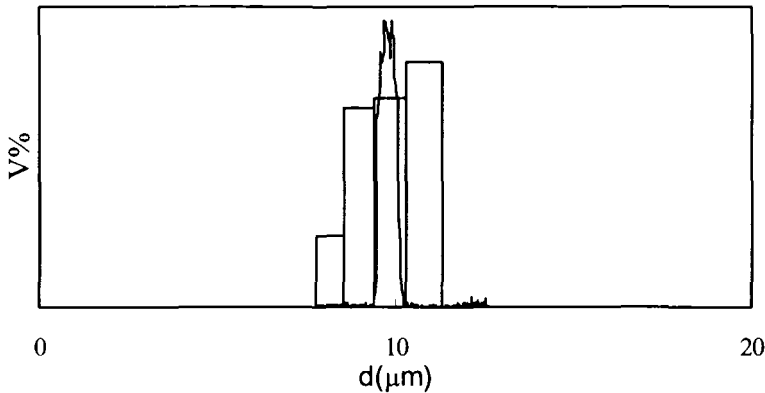


Figure 1.17. Size distributions of a latex sphere sample of narrow distribution obtained from electrical sensing zone (the narrow peak in the center,  $d = 9.83 \mu\text{m}$ ,  $\text{SD} = 0.41 \mu\text{m}$ ) and laser diffraction measurements (the four-rectangle histogram,  $d = 9.87 \mu\text{m}$ ,  $\text{SD} = 1.88 \mu\text{m}$ ).

Precision is the degree of agreement from one measurement to another. According to the condition of comparison, there are three terms related to precision:

- 1) Standard deviation is defined as the degree of agreement in the results from repeated measurements on the same instrument by the same operator;
- 2) Reproducibility is defined as the degree of agreement in the results from repeated measurements on the same instrument but by different operators following the same operational procedure;
- 3) Repeatability is defined as the degree of agreement in the results from measurements with the same conditions but by different operators using different instruments that may or may not be at the same location.

In measuring particle size distributions, besides errors introduced due to imperfection in instrument design and malfunctions of instrument (not in proper working condition, inappropriate setup, abuse of the instrument, or the wrong choice of data interpretation model, etc.), there are several other error sources that should be mentioned. Improper sampling and sample dispersion commonly introduce errors. The former may be non-representative sampling from the batch sample or non-uniform sampling during measurement; the latter may be inadequate or wrong dispersion procedure, causing agglomeration, attrition, swelling, or air bubbles. Generally, the possibility of sampling error increases with increasing particle size; conversely the possibility of dispersion error increases with decreasing particle size [58].

### 1.3.5. SHAPE EFFECT IN SIZE CHARACTERIZATION

For a sphere, a cube, or polygons of certain shapes, one can use one unique number to characterize their dimension. For most three-dimensional particles, however, one will need more than one parameter to describe dimension. Can we choose just a few parameters to describe a three-dimensional particle? The answer is yes for objects with regular shapes such as a parallelepiped (2 or 3 dimensional parameters) or a cylinder (2 dimensional parameters). However, for the irregularly shaped particles often encountered in the real world, e.g., a grain of sand or a broken piece of glass, one will need a large number of dimensional parameters in order to exactly describe the particle. If we are dealing with just a few particles, then it might be possible, though difficult, to obtain all the parameters necessary to characterize the dimensions of particles. However, when we are talking about millions of particles, the ability to describe them individually is just not practical. Only one parameter (or at most two parameters) should be used to "characterize" each particle. We call one of these parameters "size." This brings us to the conclusion that the definition we employ to define "size" will affect the answer we obtain. In fact, there are many different definitions when using a single parameter to describe a three-dimensional irregular particle. The most common one is to use an equivalent spherical representation, since a sphere is a three-dimensional object requiring only one parameter, the diameter, to characterize it. However, now that all the dimensional information of particle is condensed into a single number, you must keep in mind that this single number will now contain distorted or summarized information about the particle, with the degree of distortion being related to the particle's shape. This is a derived value that depends upon the measured property. This can be illustrated by an example of equivalent spheres for cylinders.

The volume equivalent diameter ( $d$ ) of a sphere calculated from a cylindrical particle is:

$$d = (6r^2h)^{1/3} \quad (1.20)$$

where  $r$  is the radius of the cylinder and  $h$ , the height. The figure below shows how the equivalent diameter  $d$  varies with change in the cylinder's height for a cylinder with a given radius ( $r = 10$ ).

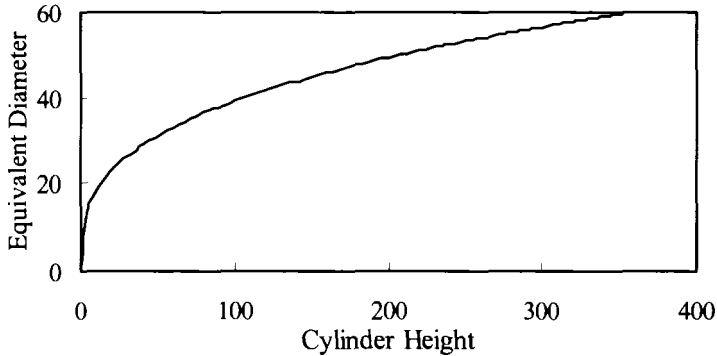


Figure 1.18. Equivalent spherical diameter as a function of cylinder height.

We observe that for cylindrical particles having the same radius but with heights varying 200 fold (2-400), their equivalent spherical diameters change only 6 fold ( $\approx 10$ -60). This equivalent spherical diameter would be obtained if one were to use a Coulter counter to measure them. If one were to use a sieve to analyze these same cylinders, the result might indicate that all the cylinders were smaller than about 20 units in diameter without much differentiation, if all cylinders stood upright on the sieve. However, if one were to use sedimentation to analyze them, the differentiation would be much bigger due to different settling velocities between particles of various lengths. In a microscopic analysis, the differentiation will come from the projected areas of cylinders. Thus, particle size distributions obtained from these four analysis means will not be the same. Even with this simple comparison, we can see differences when using various techniques for non-spherical particles.

There are many different definitions in converting three-dimensional irregular-shaped particles into equivalent spheres. The following definitions are just a few often appearing in the literature:

- $d_{\max}$ : Sphere of same maximum length
- $d_{\min}$ : Sphere of same minimum length
- $d_w$ : Sphere of same weight
- $d_v$ : Sphere of same volume
- $d_s$ : Sphere of same surface area
- $d_{\text{sieve}}$ : Sphere of same sieve aperture
- $d_{\text{sed}}$ : Sphere of same sedimentation rate

The volume equivalent sphere is the one used in most sizing technologies involving volumetric measurement and the area equivalent circle is used often

in technologies involving projected area measurement. The uniqueness of spheres has resulted in this being the universal particle shape: they are identical in any orientation; they have the smallest “maximum size,” the smallest surface area, and the smallest “maximum projected area” for any given volume. However, the method one uses to measure irregularly shaped particles will affect the result to be obtained in the form of equivalent spherical diameters. Spherical diameter distributions and average diameters obtained using different technologies will have different biases and deviation from the true equivalent diameters because of both shape sensitivity to the technology and weighting effects on different particles in the sample. Simply put, we are “seeing” a different view of the system that is measured. One technique may pay more attention to large particles and another technique may pay more attention to small particles. Which result is correct? The answer is that they are all correct results (disregarding all measurement errors or uncertainties) but from different viewpoints [59].

From the above analysis, we know that in order to compare results, whether the mean value or the distribution, obtained from different technologies, the results must be converted to the same basis, i.e., the same weighting. However, such conversion is based on an assumption that both technologies in the comparison have the same sensitivity over the entire size range and the same bias from the real shape to the equivalent diameter. Otherwise, the results will still be different even after conversion. For example, in a laser diffraction measurement the scattered light from large particles will be buried in the experimental noise and undetectable if the measurement is performed at large scattering angles, while in a Coulter Principle measurement, the signals from small particles will be below the noise level if a large orifice is used. No matter what type of conversion is performed, the results from the two measurements will never match because a different bias has been introduced. One has to keep in mind that during the transformation the experimental error is also transformed. For example, if in an electron microscope measurement there is a  $\pm 3\%$  error in the mean size, when the number mean size is converted to a mass mean size the error will be cubed and become  $\pm 27\%$ ! The same is true for the distribution, assuming the original number distribution has the same uncertainty for the amplitude of each size class, after being transformed to a volume distribution, the error will be amplified by different degrees: the larger the particle, the larger the error in the volume distribution. Of course, in a reverse transformation, a  $\pm 3\%$  uncertainty in the mass mean size will be reduced to  $\pm 1.5\%$  in the number mean size. Another often-used conversion is from mass% to volume% or vice versa. In this conversion, if all particles have the same density, then the two distributions will have the same shape, i.e. mass% = volume%.

Although most modern particle characterization methods are developed, validated and presumably used for spherical particles or equivalent spherical particles, real particles are rarely such ideal. In many instances, particle shape affects powder packing, bulk density, and many other macroscopic properties. Shape characterization of particulate systems only scatters in the literature [60], since there are hardly any universal methodologies available. Several methods exist that use shape coefficients, shape factors, Fourier analysis, or fractal analysis to semi-quantitatively describe shape [1].

## **1.4. Sample Handling**

Obtaining a representative sample and properly dispersing particles in the sample so that they can be measured are the two most important steps before any particle characterization technology can be applied to a particulate material. Without a well-prepared representative sample, the result, no matter how good it is, will be meaningless and irrelevant, and may be often misleading, no matter how good the instrument is.

### **1.4.1. SAMPLE REDUCTION**

With very few exceptions, the characterization of particulate material has to be made by the examination of a small fraction of that material. Obtaining a representative sample and reducing it to an appropriate amount, typically in the range of grams, is thus essential. Furthermore, in many technologies, not every particle put into the instrument will be sensed: i.e., the signal may only come from a part of the sample in the sample cell. The amount of particles actually being “measured” may be only in the range of milligrams. The probability that the measured particles perfectly represent the bulk material is remote. Many factors affect the representativeness of the bulk material in each sample preparation stage. For example, when a powder is poured into a heap, size separation or partitioning occurs, with the fine particles being located at the center of the heap. When a container of powder is subjected to vibration the fine particles percolate through the coarse particles, and when a powder flows out of a hopper it may have the tendency to unmix. Fine powders suspended in liquid media often tend to partition, meaning that larger particles will migrate downward while smaller particles remain in suspension. Although sample handling is only one step in the overall process of characterizing the size distribution of a sample, care in preparation will lead to a good representative sample when size analysis is performed. The process of reduction from bulk to measurement sample should be implemented in stages because it often entails a reduction from tons or liters of material to fractions of an ounce or milliliters, as shown in the following table:



Table 1.8. Sample amount

Bulk	— <sup>1</sup> →	Laboratory	Sample	— <sup>2</sup> →	Analysis	Sample	— <sup>3</sup> →	Measurement	Sample
(10 <sup>n</sup> Kg)		(Kg)			(g)			(mg)	

The processes listed in Table 1.8 (1:sampling, 2:sample reduction, and 3:sample measurement) regarding the quantity of material can be the basis for a lengthy discussion. To avoid this, we will only summarize the second process, sample reduction, in this section. Discussion of the third process (sample measurement) will be touched upon in subsequent chapters.

### *Liquid Sample Reduction*

Sampling powders suspended in a liquid medium that is not homogenous requires the use of rotational devices such as rollers, magnetic stirrers, tube rotators, manual inversion, and aspiration with pipettes, etc. These external devices are generally used to keep particles in suspension while attempting to draw an analysis sample. The most common method is to use a magnetic stir bar in a glass beaker containing the sample and to draw liquid with a pipette as the stir bar rotates. Even though these techniques are effective in obtaining a good representative sample from a liquid suspension, for powder samples the overall sampling process will be representative only when the solid sampling, performed before the powder is suspended, is performed correctly.

### *Solid Sample Reduction*

In sample reduction of non-flowing powders, such as fine cohesive solids, sticky or moist materials, or fibrous solids, since these materials do not have a tendency to segregate but may not be uniform, it is quite necessary to pass these materials through a mixer or to shake the sample in a container using different modes of shaking. Surface sampling with a scoop usually yields a good representation of the laboratory sample. If more than one analysis sample is taken and analyzed separately, the variations in the results are usually minimal. Another method which can be used is called *Cone and Quartering*, which involves pouring the material into a conical heap then flattening and cutting the heap into four equal parts. One of the four parts is taken. It can be repeated until the final quantity reaches the desired amount. If symmetry does not exist in the flattening and cutting of the heap size error will occur. This method is greatly dependent on the skill of the operator.

Free-flowing material will segregate by particle size. When poured or stored in a container, the fines tend to percolate to the center and coarse particles will roll down to the outside. Thus it is not recommended to remove a

sample directly from the surface or to use the cone and quartering method due to the tendency to segregate. A good representative sample can be obtained by implementing one of the following three common laboratory sample reduction procedures.

*Spinning Riffler.* A spinning riffler is a rotary sample divider. The sample fills a mass flow hopper so that no heaps are present and then falls from the hopper into collection boxes that are set in circular motion. A vibratory feeder supplies a constant flow rate. This method yields the most accurate results among the many sample reduction devices.

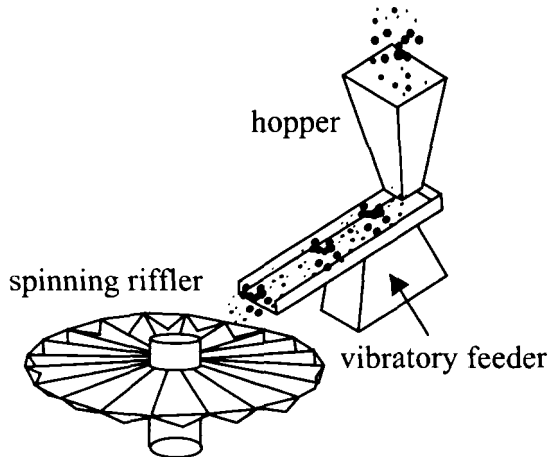


Figure 1.19. A spinning riffler.

*Chute Splitter.* The sample is placed in a V-shaped trough and migrates down a series of chutes that alternately feed two trays placed on each side of the trough. The sample is poured into chutes and repeatedly halved until a desired amount of sample is obtained. Satisfactory sample division can be obtained only if an operator loads the sample into the trough carefully without segregation occurring.

*Table Sampling.* The sample is fed onto the top of an inclined plane. The sample stream flows downward and is broken up into fractions as it encounters prisms and holes. The drawback of this device is that it depends upon the initial feed being uniformly distributed and completely mixed after each separation. Thus, accuracy is low since any error is compounded at each separation.

In using these devices, one should try to make the sample stream as homogenous as possible and size gradation of the material from one part of the

stream to another should not vary. This can be done by moving the pour point around to prevent any conical heaps from forming.

#### 1.4.2. SAMPLE DISPERSION

Dispersion is a process in which particles are homogeneously suspended by the medium and after which the particles are available to be examined individually. Dispersion can make or break the analysis, regardless of the particle analyzer being used. Thus, sufficient attention has to be paid to sample dispersion before introducing the sample into the instrument [61].

##### *Liquid Sample Dispersion*

Liquid sample dispersion occurs when a dry powder is suspended in a liquid medium before analysis. The medium can be either aqueous or non-aqueous. Characteristics of the dry powder dictate what medium is to be utilized as a diluent. Factors such as solubility, reactivity, suspendibility and the intended end-use govern the choice of media. For example, when determining the particle size distribution of a sample of fertilizer, which is soluble in water, a non-aqueous medium such as isopropanol is an appropriate choice. Many pharmaceutical powders such as niacin are water-soluble and also require the use of non-aqueous media. If the particles dissolve in the diluent that must be used, then a saturated solution has to be prepared by dissolving a large amount of sample in the diluent until the saturation level is reached and that any additional material will not be further dissolved. There should not be any chemical reaction between the sample and the diluent or between the diluent and the sample's suspension fluid. Many powders can be highly reactive with certain media. For instance, lithium hydride explodes on contact with water; on the other hand, cement cures in water. Physical changes to the particles, such as agglomeration, flocculation, aggregation, clumping, shrinking, or swelling, should not exist if the medium is chosen correctly. In addition, the integrity of the diluent has to be considered. Will the diluent absorb unwanted water? Will the diluent allow growth of bacteria or yeast? Is the diluent chemically pure? Is it free of interfering particles? All these have to be considered when choosing a proper diluent. The suspendibility of large or heavy powders in a medium may prompt one to use a highly viscous solvent such as glycerol. However, if the viscosity is too high, the suspension may entrap bubbles and the particles may not be homogeneously dispersed. The above examples illustrate why it is sometimes beneficial to select a non-aqueous medium over an aqueous one. Nevertheless, aqueous systems have advantages in that they provide effective dispersion, and require fewer precautions in handling and disposal of waste, as well as the fact that the use of water is far less costly than any organic solvent.

Another issue in choosing a proper diluent is its suitability for the chosen characterization technology and instrument. For example, the degradation effect of the diluent to parts of the instrument may need to be checked; the color and refractive index of the diluent must be chosen so as not to affect measurement using light scattering technologies.

The techniques that are used in dispersing powders into both aqueous and non-aqueous media are quite similar. The first task in dispersing a dry powder that is to be suspended in a liquid is the actual wetting of the sample with the diluent or a dispersant, if needed. Dispersants, ionic (anionic or cationic) or non-ionic, aid the wetting of particles and in the stabilization of the suspension. Aqueous surfactants are primarily responsible for reducing surface tension, hence aiding in the dispersion of powders in aqueous systems. However, concentrations of dispersants must be low. Otherwise, their properties are reduced or even inverted (i.e., causing aggregation or flocculation). In dispersing powders into a non-aqueous medium it is critical to select an organic solvent that is a good diluent as well as a dispersant, although there are many organic dispersant aids that can be used with organic solvents.

Gentle spatulation to break up large clumps of the resulting paste before adding the diluent further aids the dispersion process. Once the diluent is added, a sample of the slurry can be placed on a slide for a microscopic evaluation of the effectiveness of the dispersion. If the sample is well dispersed the use of a magnetic stir bar is suggested to keep the sample fully dispersed so that a good representative sample can be drawn for analysis while stirring is in progress. In some cases, such as heavily aggregated pigments or earths, it is often necessary to use an ultrasonic probe or bath. Ultrasonics must be used with caution since it can cause aggregation, shattering, and heating if the duration is too long or the ultrasonic power is too strong, hence altering sample integrity. In dispersing magnetic particles a degaussing coil or heating of the sample may be needed. In some cases special care must be taken so that the particles are not damaged. For example, when dispersing emulsions the use of dispersants and sonication can cause de-emulsification; when dispersing liposomes the use of dispersants and sonication can disrupt or rupture the liposome wall. There are two mechanisms to create a stable dispersion of particles while in suspension: surface charge stabilization and steric stabilization. There are several ways to induce surface stabilization for particles dispersed in an aqueous medium:

*Addition of Surfactants.* The most common and effective way to introduce surface charge and to wet particle surface is by reducing hydrophobicity. Most surfactants have a hydrophobic part that will be adsorbed onto the particle surface and a hydrophilic part that will extend into the medium, allowing the particle to be wetted and charged, and thus repel each other. Surfactants are classified as anionic which impart negative charge, cationic which impart

positive charge, amphoteric which impart both negative and positive charge, and nonionic which wet particle without imparting charge.

*pH Adjustment.* In this method surface charges are introduced by adjusting the pH. Amine ( $\text{NH}_3$ ), hydroxyl ( $\text{OH}$ ), and carboxyl groups ( $\text{COOH}$ ) (which are the most common surface groups) all adsorb a hydrogen ion below their isoelectric pH value resulting in a positive charge on the group: ( $\text{NH}_4^+$ ), ( $\text{OH}_2^+$ ), ( $\text{COOH}^+$ ); or lose a hydrogen ion above their isoelectric pH value resulting in a negative charge on the group: ( $\text{NH}_2^-$ ), ( $\text{O}^-$ ), ( $\text{COO}^-$ ). Typically, 2 pH units above or below the isoelectric pH value will result in stabilization, due to the increase in surface charge, corresponding to a change in zeta potential of approximately  $\pm 30$  mV.

*Addition of Common Ions.* Here a solution containing dissolved ions which are the same as ones found in the sample's molecular lattice may help disperse the sample by adsorbing and charging the surface of the particles.

*Addition of Multiply-charged Ions.* For ionic particles or particles with polar bonds in water, multiply-charged ions which are not part of the crystal lattice may adsorb to create a surface charged with soluble salts (examples: polyphosphates; hexametaphosphate, pyrophosphate, polysilicate ions).

For nonpolar organic particles in polar organic media, the surface can be charged by adsorbing a neutral ion-pair. Dissociation then occurs with one part of the ion-pair desorbing, leaving a charged particle. For example, adsorbed trimethyldodecylamine hydroxybenzoate dissociates into a positive quaternary amine and a negative polar organic acid and thus charges the particle surface. However, for an organic suspension, steric stabilization may be more effective. Steric stabilization can be accomplished using nonionic dispersants or block copolymers. The optimum structure has an anchor region that adsorbs strongly onto the organic solid and another region that is highly soluble in the liquid. An example of a nonionic dispersant is the polyethylene oxide chains.

A combination of wetting the sample with a dispersant followed by spatulation and sonication has proven to give the best dispersions. There are monographs dedicated to sample dispersion [3,62]. Especially useful is Appendix A in [3]. The following is a practical recipe for dispersing dry powders in liquid:

*Dispersant Check.* Use a watch glass or a weighing boat to determine which dispersant has the best interaction with the particles.

*Wetting.* Add just enough dispersant or diluent to the sample to form a thick paste.

*Spatulate.* Use a spatula or rubber policeman to mull the sample and dispersant into a paste.

*Add Diluent.* Add diluent to form a slurry.

*Optical Check.* Use a microscope to visually check the status of dispersion.

*Add Energy to the System.* Use sonication (usually best), stirring, heat, etc., to deagglomerate difficult particles, if needed.

*Optical Check.* Use a microscope to visually check the status of the dispersion. If dispersion appears incomplete, then either try another dispersant or add more energy to the system, taking care not to disrupt the integrity of the particles. If dispersion appears complete, then continue.

*Check for Stability.* Sometimes, the sample may reagglomerate or flocculate over time due to dilution, change in pH, ionic concentration, or improper dispersant. If this happens the dispersion is not stable. In this case different approaches such as the use of different dispersants or different conditions such as a change in pH, ionic concentration, etc. have to be used.

*Sampling.* While adding sample to the sample vessel, always try to obtain a representative sample with each addition. Use a stir bar while sampling in order to keep particles suspended or use pipette aspiration.

### *Solid Sample Dispersion*

Solid sample dispersion is the attempt to disperse a dry powder with the intent of suspending it in air. As previously mentioned, many dry powders encounter problems of solubility, reactivity and suspendibility when suspended in liquid media. Due to these problems, analysis of dry systems is often an unavoidable alternative as well as being a preference. In many instances, the selection of solid sample dispersion is totally dependent on the end use of the product. For example, particle size measurement of flour must be carried out using a dry system, hence requiring solid sample dispersion. Dry powders that are free flowing, anti-caking and anti-clogging require no external dispersion aids. However, if these conditions do not hold true external dispersion aids (additives having a much smaller or distinguishable size from the sample so that its overall effect on particle size measurement is negligible), such as fumed silica, tricalcium phosphate, and carbon black are available. Fumed silica, when added and mixed to particulate systems in a ratio of 0.5-1 wt%, can help the flow of dry powder because of its “ball bearing” effect. The same mixing ratio (0.5-1 wt%) can be used for tricalcium phosphate. Sometimes, antistatic aids such as sprays and a static bar are needed to eliminate static charges.

## REFERENCES

- 1 Kaye, B. H., in *Particle Size Analysis 1981*, Eds. Stanley-Wood, N., Alien, T., John Wiley and Sons, New York, 1982, pp3.
- 2 Alien, T., *Particle Size Measurement, Vol.1 and Vol.2*, 5<sup>th</sup> Ed., Chapman & Hall, London, 1997.
- 3 Bernhardt, C., *Particle Size Analysis: Classification and Sedimentation Methods*, Chapman & Hall, London, 1994.
- 4 *Liquid and Surface-Borne Particle Measurement Handbook*, Eds. Knapp, J. Z., Barber, T. A., Lieberman, A., Marcel Dekker, New York, 1996.
- 5 *Particle Size Distribution I*, Ed. Provder, T., American Chemical Society, Washington D.C., ACS Symp. Series 332, 1987.
- 6 *Particle Size Distribution II*, Ed. Provder, T., American Chemical Society, Washington D.C., ACS Symp. Series 472, 1991.
- 7 *Particle Size Distribution III*, Ed. Provder, T., American Chemical Society, Washington D.C., ACS Symp. Series 693, 1998.
- 8 Heywood, H., in *Proc. Particle Size Analysis Conf.*, Eds. Groves, M. J., Wyatt-Sargent, J. L., Soc. Anal. Chem., 1970, pp. 156-177.
- 9 *ISO 565:1990 Test Sieves -- Metal Wire Cloth, Perforated Metal Plate and Electroformed Sheet -- Nominal Sizes of Openings*, International Organization for Standardization (ISO), Genève, 1990.
- 10 *ISO 3310:1990 Test Sieves -- Technical Requirements and Testing*, International Organization for Standardization (ISO), Genève, 1990.
- 11 *ASTM Standard E11-95: Specification for Wire Cloth and Sieves for Testing Purposes*, American Society for Testing and Materials, West Conshohocken, 1995.
- 12 Allen, T., A Review of Sedimentation Methods of Particle Size Analysis, in *Proc. Conf. Part. Size Analysis*, Loughborough, 1991.
- 13 Coulter, W. H., Means for Counting Particles Suspended in a Fluid, *US Patent 2,656,508*, 1953.
- 14 *Industrial and Scientific Bibliography; Medical and Biological Bibliography*, Coulter Electronics Ltd, Luton, 1994.
- 15 Lines, R. W., The Electrical Sensing Zone Method, in *Liquid and Surface-Borne Particle Measurement Handbook*, Eds. Knapp, J. Z., Barber, T. A., Lieberman, A., Marcel Dekker, New York, 1996, Chpt.4, pp.113-154.
- 16 Pennycook, S. J., Boatner, L. A., Chemically Sensitive Structure-Imaging with a Scanning Transmission Electron Microscope, *Nature*, 1988, 336, 565-567.
- 17 Möller, T., Confocal Laser Scanning Microscopy and its Application in Liposomal Research, in *Particle and Surface Characterization Methods*, Eds. Müller, R. H., Mehnert, W., Medpharm Scientific Publishers, Stuttgart, 1997, Chpt.6, pp.85-98.
- 18 Shik, H., Dunn, R. C., Near-field Scanning Optical Microscopy, *Anal. Chem.*, 1999, 71, 23A-28A.
- 19 Inoue, S., *Video Microscopy*, Plenum Press, New York, 1986.
- 20 McCrone, W. C., Delly, J. G., *The Particle Atlas Electronic Edition*, Microdataware, Hayward, 1992.
- 21 Vokram, C. S., *Particle Field Holography*, Cambridge University Press, London, 1992.
- 22 Menzel, R., Shofner, F. M., An Investigation of Fraunhofer Holography for Velocity Applications, *Appl. Opt.*, 1970, 9, 2073-2079.
- 23 Yau, W. W., Kirkland, J. J., Bly, D. D., *Modern Size Exclusion Chromatography*, John Wiley and Sons, New York, 1979.
- 24 Kirkland, J. J., New Separation Methods for Characterizing the Size of Silica Sols, *Adv. Chem. Ser.* 1994, 234, 287-308.

- 
- 25 Revillion, A., Alternatives to Size Exclusion Chromatography, *J. Liq. Chromatogr.* 1994, 17, 2991-2994.
  - 26 Ramos, J.G. dos, Silebi, C. A., in *Particle Size Distribution II*, Ed. T. Provder, ACS Symp. Series 472, American Chemical Society, Washington D.C., 1991, pp. 292.
  - 27 Giddings, J. C., A New Separation Concept Based on a Coupling of Concentration and Flow Nonuniformities, *Sep. Sci.*, 1966, 1, 123-125.
  - 28 Giddings, J. C., *Unified Separation Science*, Wiley, New York, 1991.
  - 29 Williams, P. S., Giddings, J. C., Theory of Field-Programmed Field Flow Fractionation with Correction for Steric Effects, *Anal. Chem.* 1994, 66, 4215-4228.
  - 30 Raes, F., Plomp, A., Comparison of Two Condensation Nucleus Counters (TSI Model 3020): Calibration of the Photometric Mode, *J. Aerosol Sci.*, 1983, 14, 394-396.
  - 31 Winkelmayr, W., Reischl, G. P., Linder, A. O., Berner, A., A New Electromobility Spectrometer for the Measurement of Aerosol Size Distribution in the Size Range from 1 to 1000 nm, *J. Aerosol Sci.*, 1991, 22, 289-296.
  - 32 De La Mora, J., De Juan, L., Eichler, T., Rosell, J., Differential Mobility Analysis of Molecular Ions and Nanometer Particles, *Trends Anal. Chem.*, 1998, 17, 328-339.
  - 33 *Handbook on Ultrasonic and Dielectric Characterization Techniques for Suspended Particulates*, Eds. Hackley, V. A., Texter, J., The American Ceramic Society, Westerville, 1998.
  - 34 Dukhin, A. S., Goetz, P. J., Acoustic and Electroacoustic Spectroscopy, *Langmuir*, 1996, 12, 4336-4344.
  - 35 Dukhin, A. S., Ohshima, H., Shilov, V. N., Goetz, P. J., Electroacoustics for Concentrated Dispersions, *Langmuir*, 1999, 15, 3445-3451.
  - 36 McClements, D. J., Principles of Ultrasonic Droplet Size Determination in Emulsions, *Langmuir*, 1996, 12, 3454-3461.
  - 37 Coghill, P. J., Millen, M. J., Sowerby, B. D., On-line Particle Size Analysis Using Ultrasonic Velocity Spectroscopy, *Part. Part. Syst. Charact.*, 1997, 14, 116-121.
  - 38 Oja, T., Petersen, G., Cannon, D., Measurement of Electro-Kinetic Properties of a Solution, *US Patent 4,497,208*, 1985.
  - 39 O'Brien, R. W., Cannon, D. W., Rowlands, W., Electroacoustic Determination of Particle Size and Zeta Potential, *J. Colloid Interface Sci.* 1995, 173, 406-418.
  - 40 Gregg, S. J., Sing, K. S. W., *Adsorption. Surface Area and Porosity*, 2<sup>nd</sup> Ed., Academic Press, New York, 1982.
  - 41 Brunauer, S., Emmett, P. H., Teller, E., Adsorption of Gases in Multimolecular Layers, *J. Am. Chem. Soc.*, 1938, 60, 309-319.
  - 42 Dubinin, M. M., Stoeckli, H. F., Homogenous and Heterogeneous Micropore Structures in Carbonaceous Adsorbents, *J. Colloid Interface Sci.*, 1980, 75, 34-42.
  - 43 Adamson, A. W., *Physical Chemistry of Surfaces*, 2<sup>nd</sup> Ed., Interscience, New York, 1967.
  - 44 *British Standard 7591: Porosity and Pore Size Distribution of Materials Part 4: Method of Evaluation by Liquid Expulsion*, BSI, London 1993.
  - 45 Ribitsch, V., Jacobasch, H.-J., Boerner, M., Streaming Potential Measurements of Films and Fibres, in *Advance in Measurement and Control of Colloidal Processes*, Eds., Williams, R. A., de Jaeger, N. C., Butterworth-Heinemann, London, 1991, pp.354-365.
  - 46 Furusawa, K., Sasaki, H., Nashima T., Electro-osmosis and Streaming Potential Measurement, in *Surfactant Science Series 76: Electrical Phenomena at Interfaces*, Eds. Ohshima, H., Furusawa, K., Marcel Dekker, New York, 1998, Chpt.9, pp.225-244.
  - 47 Blees, M. H., Geurts, J. M., Leyte, J. C., Self-Diffusion of Charged Polybutadiene Latex Particles in Water Measured by Pulsed Field Gradient NMR, *Langmuir*, 1996, 12, 1947-1957.



- 
- 48 Miller, J. F., Velev, O., Wu, S. C. C., Ploehn, H. J., A Combined Instrument for Phase Analysis Light Scattering and Dielectric Spectroscopy, *J. Colloid Interface Sci.*, 1995, 174, 490-499.
  - 49 *ISO 9276-1 Representation of Results of Particle Size Analysis Part 1: Graphical Representation*, International Organization for Standardization (ISO), Genève, 1990.
  - 50 Alderliesten, M., Mean Particle Diameter, Part I: Evaluation of Definition Systems, *Part. Part. Syst. Charact.* 1990, 7, 233-241.
  - 51 Herdan, G., *Small Particle Statistics*, Butterworths, London, 1960.
  - 52 Young, H. D., *Statistical Treatment of Experimental Data: an Introduction to Statistical Methods*, Waveland Press, Prospect Heights, 1996.
  - 53 Lange, H., Comparative Test of Methods to Determine Particle Size and Particle Size Distribution in the Submicron Range, *Part. Part. Syst. Charact.*, 1995, 12, 148-157.
  - 54 Alderliesten, M., Mean Particle Diameter, Part II: Standardization of Nomenclature, *Part. Part. Syst. Charact.*, 1991, 8, 237-241.
  - 55 Leschonski, K., Representation and Evaluation of Particle Size Analysis Data, *Part. Charact.* 1984, 1, 89-95.
  - 56 *ASTM Standard D2777, Standard Practice for Determination of Precision and Bias of Applicable Methods of Committee D19 on Water*, American Society for Testing and Materials, West Conshohocken, 1994.
  - 57 Xu, R., Reference Materials in Particle Measurements, in *Liquid and Surface-Borne Particle Measurement Handbook*, Eds. Knapp, J. Z., Barber, T. A., Lieberman, A., Marcel Dekker, New York, 1996, Chpt.16, pp.709-720.
  - 58 Paine, A. J., Error Estimates in the Sampling from Particle Size Distribution, *Part. Part. Syst. Charact.*, 1993, 10, 26-32.
  - 59 Scarlett, B., Measurement of Particle Size and Shape, Some Reflections on the BCR Reference Material Programme, *Part. Charact.*, 1985, 2, 1-6.
  - 60 Hawkins, A. E., *The Shape of Powder-Particle Outlines*, John Wiley, New York, 1993.
  - 61 Polke, R., Schäfer, M., Scholz, N., Preparation Technology for Fine Particle Measurement, *Part. Part. Syst. Charact.*, 1991, 8, 1-7.
  - 62 Nelson, R. D., *Dispersing Powders in Liquids*, Elsevier, New York, 1988.

## LIGHT SCATTERING

### *The Background Information*

#### 2.1. Light Scattering Phenomena and Technologies

Light is electromagnetic radiation in the frequency range from approximately  $10^{13}$  Hz (infrared) to  $10^{17}$  Hz (ultraviolet) or the wavelength range from 3 nm to 30,000 nm. The conversion between frequency and wavelength of light can be made using the speed of light ( $c = 3 \times 10^8$  m/s in *vacuo*):

$$c = \lambda \nu. \quad (2.1)$$

Visible light is the part of the electromagnetic radiation to which the human eye is sensitive. When white light, which contains a range of wavelengths, is separated by wavelength, each wavelength is perceived to correspond to a different color. The wavelength of visible light ranges from ~400 nm (violet or purple) to ~750 (red) nm [1]. As light propagates it has the characteristics of both a transverse wave (a light wave) as well as a particle (a photon). As a wave, light have wave-like properties such as frequency, wavelength, and interference; as a particle, light have particle-like properties such as momentum, velocity, and position. In most of the discussions in this text, we discuss situations where the dimension of a light beam is larger than that of the particulate material though the sizes of the particles can be much smaller, as well as larger than the wavelength of light. In these cases, descriptions from geometric optics are no longer sufficient to describe the behavior of scattered light, and more sophisticated theories have to be used.

When a light beam illuminates a piece of matter having a dielectric constant different from unity, light will be absorbed or scattered, or both, depending on the wavelength of light and the optical properties of the material. The net result of the absorption and scattering caused by the material is known as the extinction of incident light,

$$\text{Extinction} = \text{Absorption} + \text{Scattering}. \quad (2.2)$$

When light interacts with the electrons bound in the material so as to re-radiate light, scattering is observed. The detected scattering is from particle(s) in a

scattering volume, the cross section between the beam and the detection cone. The absorbed light energy that becomes the excitation energy of particles will be dissipated mostly through thermal degradation (i.e., converted to heat) or lost through a radiative decay producing fluorescence or phosphorescence depending on the electronic structure of the material. Because many materials exhibit strong absorption in the infrared and ultraviolet regions, which greatly reduces scattering intensity, most light scattering measurements are performed using visible light. Scattering is only observed when a material is in itself heterogeneous, either due to local density fluctuations in the pure material or due to the optical heterogeneity for dispersed particles in a medium. In a perfectly homogeneous and isotropic material the radiation scattered by individual molecules interferes destructively, and so no scattering is observed.

Scattering intensity from a unit volume of material that is illuminated by a unit flux of light is a function of the complex refractive index ratio between the material and its surrounding medium along with various other properties of the material. In the regime of Rayleigh scattering, where particle dimension is much smaller than the wavelength of light, the scattering intensity,  $I_s$ , is inversely proportional to the fourth power of the wavelength when the same material is illuminated by light of different wavelengths but having the same intensity; i.e., the shorter the wavelength, the stronger the scattering:

$$I_s \propto I_0/\lambda^4. \quad (2.3)$$

In fact, this wavelength dependence on scattering power was the first observed scattering phenomenon in nature. The reason that the sky is bluest at midday is because one sees primarily the shorter wavelength portion of the sunlight scattered by particles (dust, vapor droplets, etc.) in the atmosphere, while the longer wavelengths contribute much less to the observed scattering due to their weaker scattering power. At sunrise or sunset, the situation is just the opposite and one sees mainly transmitted sunlight in which the longer wavelengths in the sunlight contribute much more than those of shorter wavelength. The sunlight transmitted through the atmosphere traverses different pathlengths during sunrise and sunset, and most of the shorter wavelength portion of the spectrum is scattered away, hence more of the longer wavelength portion reaches the earth. Thus one observes a color change in the sun from orange, to red, to deep red during dusk, and from deep red, to red, to orange at dawn. Utilizing this wavelength dependence, we use red as the color for traffic stop lights and the color red in traffic control warning signs because red light has the least scattering power in the visible light spectrum, thus allowing the transmitted light to go through fog, rain, and dust particles and reach the intended detector: in this case the human eye. Remember that the first traffic light was established in U.K. where fog and rain are quite common.

Attempts to explain natural scattering phenomena can be traced back to early in the eleventh century and an Arabic physicist Ibn-al-Haitham, known as Alhazen of Basra, through the Italian Renaissance and the famous Italian painter, architect, musician, and engineer Leonardo Da Vinci, to Sir Issac Newton in the seventeenth century. The first systematic studies of scattering effects and the development of explanations took place in the 1860's by John Tyndall who analyzed suspensions and aerosols [2]. It was perhaps when John Strutt (Lord Rayleigh) observed and studied scattering from natural phenomena in the 1870's [3], that a solid foundation of light scattering, as a branch of the science of the nature of light, was laid. Scattering theories were further developed by the grand masters of physics such as Ludvig Lorenz [4], Gustav Mie [5], Peter Debye [6], and Albert Einstein [7] around the turn of the century along with the establishment of Maxwell's electromagnetic theory. During the twentieth century, light scattering theories, involving time-averaged scattering intensity and intensity fluctuation, were further developed. With the establishment of quantum mechanics, light scattering became a mature field of science enabling the numerical computation of scattering problems and experimental applications in studies of liquid and macromolecule solutions.

In the past few decades the use of light scattering as a tool in many branches of material studies has flourished and has penetrated into different fields of sciences both theoretically and experimentally. To a large extent, this is associated with the development and commercialization of several new technologies, especially the laser and microelectronic devices, including the computer. As an example, the photon correlation experiment was pioneered in the 1950's, yet the popularity of this technology was made possible only after coherent light sources from lasers became available at low cost in the 1970's. Resolving the distribution of Brownian motion in a macromolecule solution or a particle suspension by photon correlation spectroscopy was practical only when microelectronics the computation became fast enough so that a user did not have to wait hours for the result. Also, using the T-matrix or discrete dipole moment methods to compute scattering patterns from irregularly shaped particles was not feasible until the clock-time of a computer exceeded a few hundred megahertz.

Used as a general term, "light scattering" can be encountered in several branches of the physical sciences, such as optics, physical chemistry, material science, fluid dynamics and solid physics. There are many ways to use light scattering phenomena to study various properties of materials. Each has its own terminology, expertise, applications, and techniques of measurement, and each involves different disciplines in the physical sciences. In the measurement of scattering intensity fluctuations as a function of time, there is transient light scattering, dynamic light scattering and diffusing wave light scattering. There is static light scattering and turbidity measurements based on time-averaged

scattering intensity, and there is phase Doppler analysis for phase analysis of scattered light. For measurements performed under an additional applied field, there is electrophoretic light scattering, electric field light scattering, and forced Rayleigh scattering, etc. For measurement of optically anisotropic material, there is circular dichroism light scattering. For measurements other than in liquid and air there is surface Raman scattering, surface evanescent scattering and solid scattering, etc.

Depending on whether the frequency of scattered light to be detected is the same as that of the incident light, a light scattering experiment may be described as elastic (ELS), quasi-elastic (QELS), or as inelastic light scattering (IELS). In ELS, the scattering signal to be detected is the time-averaged light intensity and thus its frequency deviation from the incident light is often not measured. The intensity of scattered light is a function of the optical properties of the particles and the medium, the dimension and mass of the particles, sample concentration, and observation angle and distance. Information regarding particles is obtained through their static status in an ELS measurement. In QELS, the frequency of scattered light to be detected is slightly different from that of the incident light, typically in the range of a few Hz to a few hundred Hz (remember that the frequency of visible light is in the range of  $10^{14}$  Hz). The frequency difference comes from the translational and rotational motions of the particles and its value is directly related to the particles' motions. QELS is often employed in studying the motions of particles and other information regarding the particles may also be revealed through their motions. In IELS, the scattered frequency differs by an amount much larger than a few hundred Hz from that of the incident light due to the involvement of other forms of energy, such as the vibrational and rotational energy of scatterers in Raman scattering and photon-phonon interaction in Brillouin scattering. IELS scattering signals are extremely weak for scatterers of large mass when compared to signals from ELS or QELS and thus not many applications have been found in particle characterization. IELS is often used in the structural study of molecules and liquids.

The following table lists light scattering technologies used for studying particulate materials in liquid and air excluding at or near the particle's surface. There are excellent monographs covering a variety of topics of light scattering, in addition to many more articles in hundreds of other journals and magazines. Although several light scattering technologies (as well as the basic theories of light scattering) are described in the present book, there are others that are not included because they are less common or immature as applied in particle characterization.

Table 2.1. Light scattering technologies

Scattering Frequency Change	Name	Signal	Main Applications	External Field
Elastic	Static LS (including diffraction) [8,9,10,11,12,13]	Angular scattering intensity pattern	Sizing, particle and macromolecule study	No or Flow
	Optical counting [14]	Single particle scattering	Sizing, counting	Flow
	Focused Beam Reflectance [15,16]	Back scattering using a rotating beam	Sizing	Flow
	Time-of-Transition [17]	Transmission using a rotating beam	Sizing	Flow
	Time-of-Flight [18]	Scattering of accelerating aerosols	Sizing	Flow
	Optical Space-Frequency Analysis [19]	Scattering from masked incoherent light	Sizing	Flow
	Turbidimetry [20]	Transmission	Sizing, composition study	No
	Transient LS [21,22]	Scattering intensity variation in an applied field	Shape study	Electric field
	Forced Rayleigh LS [23,24]	Fringe pattern change due to diffusion	Diffusion study	Intense pulses of light
	Resonance LS [25]	Enhanced scattering due to absorption change	Aggregation study	No
	Flow Cytometry [26,27,28]	Single particle fluorescence and scattering	Cell analysis	Flow
	Pulse Displacement [29]	Refraction and reflection pulses	Sizing and flow velocity study	Flow
Quasi-elastic	PCS (including DWS) [30,31,32,33,34,35,36,37,38,39,40]	Scattering intensity fluctuations	Diffusion study, sizing	No
	Electrophoretic LS [41] (including spectrum analysis [42])	Scattering intensity fluctuations	Mobility and diffusion study, sizing	Electric field
	Phase Doppler [43,44,45,46,47,48]	Scattering frequency shift and phase delay	Sizing, counting, flow velocity study	Flow
	Phase Analysis [49,50]	Scattering phase change	Mobility study	Electric field
	Photon Migration [51]	Optical diffusion of intensity modulated light	Sizing	No
	QELS-SEF [52]	Scattering intensity fluctuations in a sinusoidal field	Dynamic property study	Electric field
	Modulated Dynamic LS [53,54]	Scattering intensity fluctuations of a single particle	Particle mass, diffusion, velocity and shape study	Flow
Inelastic	RCS [55]	Raman scattering intensity fluctuations	Dynamics and composition study	No

In Table 2.1, PCS stands for photon correlation spectroscopy; DWS for diffusing-wave spectroscopy; QELS-SEF for quasi-elastic light scattering-

sinusoidal electric field; and RCS for Raman correlation spectroscopy. References are given for the technologies in the table so interested readers can find more details from these references if desired. In these references and the ones cited in the following chapters, readers can also find derivations for many equations associated with technologies presented in this text, which have been skipped due to the intended purpose of the book.

It is certain that even persons with a strong scientific background may be confused by all of these different specialties and hardly anyone can become an expert in all light scattering technologies. In addition, the diversity of the light scattering terminology used in different scientific fields sometimes causes more confusion in the literature. For example, the names of the technologies listed in the above table may appear differently in different literature. In the present text, we will only discuss those scattering technologies that have been used to characterize a broad range of air-borne and liquid-borne particulate materials.

## 2.2. Light Scattering Theory - an Outline

There are a few excellent monographs that describe the time-averaged and intensity fluctuation scattering theories. The theories outlined in this section are by no means in great detail but only for the practical purpose that certain theoretical knowledge of light scattering is needed in order to proceed to the following chapters of various technologies. We will start with the scattering geometry and a few basic definitions, followed by the basic theories for time-averaged scattering intensity and intensity fluctuation. These serve as the foundation of the later theories developed in the applications of light scattering in a variety of particle characterization technologies.

### 2.2.1. SCATTERING GEOMETRY

Figure 2.1 is a basic scheme for light scattering geometry in the laboratory frame. In Figure 2.1,  $\mathbf{k}_0$  is the wave vector of the incident light (with intensity  $I_0$ ) of wavelength  $\lambda$  ( $= \lambda_0/n_0$  with  $n_0$  being the refractive index of the medium and  $\lambda_0$  being the incident light wavelength in *vacuo*) propagating along the X direction. The magnitude of  $\mathbf{k}_0$  is the wave number of the incident light,  $|\mathbf{k}_0| = 2\pi/\lambda$ . For non-polarized light, the electric vector is randomly oriented. For polarized light, the electric vector is oriented in a particular direction. For theoretical simplification and practical convenience, the direction of polarization is set either perpendicular to a hypothetical tabletop in the Z direction, termed vertically polarized ( $E_v$ ), or parallel to the tabletop, termed horizontally polarized ( $E_h$ ). Most of the incident light will be transmitted, passing through the scattering volume containing the particles unless the



particle concentration is so high that multiple scattering occurs, in which the light scattered from one particle serves as the incident light of another particle, or if the particles are highly absorbing. Light encountered by the particles will be scattered in all directions. As will be described throughout the book, both the scattering intensity and intensity fluctuations are a function of scattering direction, relative to the direction of the incident light. Therefore, the scattering direction has to be specified. Normally, it is specified as the direction that is at an angle  $\theta$  with respect to the X direction and an angle  $\phi$  with respect to the Z direction. The angle  $\theta$  is called the scattering angle. The plane formed by the propagation directions of the incident, transmitted, and scattered light defines the scattering plane. Unless otherwise stated, the azimuthal angle  $\phi$  is assumed to be  $90^\circ$  and the scattering plane is the plane where  $\phi = 90^\circ$ . The terms  $\mathbf{k}_s$  ( $|\mathbf{k}_s| \approx |\mathbf{k}_o|$ ) and  $I_s$  are the wave vector and intensity of scattered light, respectively. Another parameter that appears very often in light scattering theory is the vector of momentum-transfer,  $\mathbf{K}$ , also commonly called the scattering vector, which is the result of the momentum transfer between the incident light and a particle. The magnitude of  $\mathbf{K}$  ( $= |\mathbf{K}| = |\mathbf{k}_o - \mathbf{k}_s|$ ) is:

$$\begin{aligned} K &= \sqrt{|\mathbf{k}_o - \mathbf{k}_s|^2} = \sqrt{k_o^2 + k_s^2 - 2\mathbf{k}_o \cdot \mathbf{k}_s} \\ &\approx \sqrt{4k_o^2 \sin^2(\theta/2)} = \frac{4\pi n_o \sin(\theta/2)}{\lambda_o}. \end{aligned} \quad (2.4)$$

In almost all light scattering experiments, a collimated light source (polarized or non-polarized) at a distance much larger than the dimension of the particles, is used to illuminate the sample. Scattering intensity is detected at a far field (the distance,  $r$ , between the detector and particles is also much larger than the dimension of the particles). Thus, both incident light and scattered light behave as a plane-wave making the theoretical description simple. The cross section between the incident light and the viewing cone of the detector defines the scattering volume. In the scattering volume, there may be only one particle, as in the case of optical particle counting, or many particles as in other scattering experiments. Scattering results from alterations to the electric field from all particles in the scattering volume illuminated by the incident light. Since particles scatter light in all directions, the intensity received by the detector is proportional to its detecting area and inversely proportional to the square of its distance from the scatterers. Although the suspension medium (air or liquid) also scatters light, the scattering from air or any homogeneous liquid can almost always be neglected when compared with the magnitude of the scattering from the particles. Some exceptions to this exist such as when an inhomogeneous



medium is used, or when the mass of the particle is comparable to that of the medium molecules.

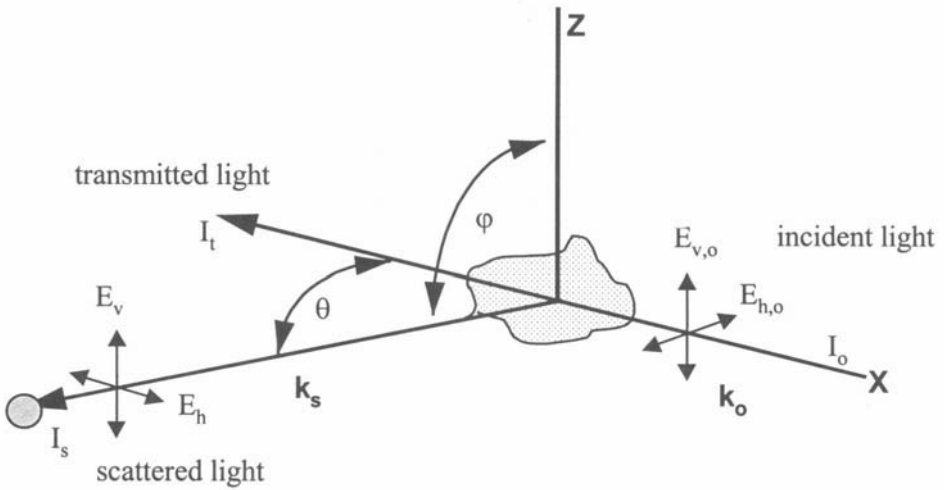


Figure 2.1. Scattering geometry.

### 2.2.2. SCATTERING INTENSITY FROM A SINGLE PARTICLE

In the following discussion, the incident light is assumed to be a collimated beam having a plane wave front and of uniform intensity. Light from many sources, such as a He-Ne laser, has a Gaussian intensity profile. The “spot size” (diameter) of the beam is characterized as the circular region having a radius twice the standard deviation ( $2\sigma$ ). Most of the light power is within this region and the light intensity at the radius  $2\sigma$  from the beam center falls off to 0.135 of the maximum intensity. For Gaussian or divergent beams all formulas given have to be modified accordingly, leading to generalized theories having more complicated formulas (for instance, to the generalized Mie theory) [56,57,58,59]. For this reason, one important target in designing the optics of a light scattering instrument is to make the beam intensity homogeneous and to reduce the beam divergence to a minimum.

In the plane-wave solution of Maxwell’s equations, the electric vector of light is transverse and composed of two polarization components,  $E_v$  and  $E_h$ , that are orthogonal to each other. Both the incident light and the scattered light can be fully characterized (in terms of intensity, polarization and phase) by a set of Stokes parameters,  $S(I_v, I_h, U, V)$ , defined by:

$$I_v = E_v E_v^* ; \quad (2.5a)$$

$$I_h = E_h E_h^*; \quad (2.5b)$$

$$U = E_v E_h^* + E_h E_v^*; \quad (2.5c)$$

$$V = i(E_v E_h^* - E_h E_v^*), \quad (2.5d)$$

where an asterisk denotes the conjugate complex value. The Stokes parameters of scattered light are homogeneous linear functions of those of incident light by a 4x4 transform matrix  $\mathbf{F}$  that has 16 elements [60]. All elements in the  $\mathbf{F}$  matrix are combinations of four complex amplitude functions  $S_1$ ,  $S_2$ ,  $S_3$ , and  $S_4$  that can be computed using different scattering theories.

$$\begin{pmatrix} |S_1|^2 & |S_4|^2 & \frac{1}{2}(S_1 S_4^* + S_4 S_1^*) & \frac{i}{2}(S_1 S_4^* - S_4 S_1^*) \\ |S_3|^2 & |S_2|^2 & \frac{1}{2}(S_2 S_3^* + S_3 S_2^*) & \frac{i}{2}(S_3 S_2^* - S_2 S_3^*) \\ (S_3 S_1^* + S_1 S_3^*) & (S_2 S_4^* + S_4 S_2^*) & \frac{1}{2}(S_1 S_2^* + S_2 S_1^* + S_3 S_4^* + S_4 S_3^*) & \frac{i}{2}(S_3 S_4^* - S_4 S_3^* + S_1 S_2^* - S_2 S_1^*) \\ i(S_3 S_1^* - S_1 S_3^*) & i(S_2 S_4^* - S_4 S_2^*) & \frac{i}{2}(S_2 S_1^* - S_1 S_2^* + S_3 S_4^* - S_4 S_3^*) & \frac{1}{2}(S_1 S_2^* + S_2 S_1^* - S_3 S_4^* - S_4 S_3^*) \end{pmatrix} \quad (2.6a)$$

The relationship between the incident light and scattered light can be presented by the following matrix equation:

$$\mathbf{S}_{\text{scattered}}(I_v, I_h, U, V)_{4 \times 1} = \mathbf{F}_{4 \times 4} \cdot \mathbf{S}_{\text{incident}}(I_{v_0}, I_{h_0}, U_0, V_0)_{4 \times 1} / k_0^2 r^2. \quad (2.6b)$$

The subscripts denote the dimension of the matrices. The denominator in Eq. 2.6b results from the fact that scattering detection is made at some distance,  $r$ , from the scattering center. The amplitude functions are functions of the size, shape, orientation, and optical properties of the particle and of the scattering angle. Once the amplitude functions are determined, one can obtain from the matrix  $\mathbf{F}$  characteristics of the scattered light. In the cases when both  $S_3$  and  $S_4$  are nil, the relationships between the incident and scattered light intensities are simple:

$$I_v = |S_1|^2 I_{v_0} / k_0^2 r^2, \quad (2.7a)$$

$$I_h = |S_2|^2 I_{h_0} / k_0^2 r^2. \quad (2.7b)$$

Now the task is to compute the amplitude functions for different types of particles.

Another concept often used in dealing with the interaction of radiant energy and matter is the scattering cross section. In light scattering, the angular scattering cross section of a particle is defined as that cross section of an incident beam, acted on by the particle, having an area such that the power flowing across it is equal to the power scattered by the particle per solid angle at a scattering angle  $\theta$ . The total scattering cross section of a particle corresponds to the total power scattered in all direction. The magnitude of total scattering cross section at a unit irradiance of visible light is about  $10^{-26} \text{ cm}^2$  for a gas molecule and  $10^{-14} \text{ cm}^2$  for a 50 nm latex particle. The scattering intensity detected at a far field is the result of the scattered electric field from different portions of any particle that is homogeneously illuminated by the incident beam. Because the scattered fields from different portions of the particle interfere with each other, one has to solve the complete set of Maxwell's equations for the entire particle in order to obtain the scattering intensity at any scattering angle. Ever since Gustav Mie derived the rigorous formula describing the scattering from spheres of arbitrary size, theoretical work has been conducted in the search for analogous solutions for particles of other shapes. Due to the complexity of the problem, rigorous analytical formulas for solving Maxwell's equations for individual particles exist only in a few special cases: e.g., for spheres in the spherical coordinate system; for spheroids in the spheroid coordinate system [61]; and for rods of infinite length in several cylindrical coordinate systems [9]. For particles of other shapes, regular or irregular, two other approaches exist. One is to find approximate analytical solutions, and the other is to find ways to numerically compute the scattering intensity. In several instances, such as when the particles are either much smaller or much larger than the wavelength of light, theories that use approximations which yield results that are very close (or almost identical) to those from more rigorous computation have been well established and are widely used in many scientific fields (see the following subsections). Meanwhile, with ever-increasing computing power, new mathematical algorithms (and the associated software code for numerical computation) have been evolving rapidly, and in recent years the calculation of the scattering intensity from a particle, or even a distribution of particles, of arbitrary shape is becoming possible.

The analytical formulation of the scattering intensity from spheres of arbitrary size is now widely used in many light scattering technologies in which the assumption of spherical particles is always taken for granted. In the following, we introduce the rigorous solution for scattering from spheres, followed by three theories that are approximations of the scattering from particles either much smaller or much larger than the wavelength of light, and a summary of numerical computation approaches to the scattering of particles of other shapes.

### *The Rigorous Solution: Mie Theory*

The Mie theory is a rigorous solution for the scattering from a spherical, homogeneous, isotropic and non-magnetic particle of any diameter  $d$  in a non-absorbing medium. Although the theory generally called Mie theory or Lorenz-Mie theory, it was actually developed based on several independent theoretical works of many theoreticians including Lorenz and Mie (see p.55 of [9] for a historical postscript). The derivation of Mie theory can be found in several references and is beyond the scope of the present text [6,9]. The analytical formulas of Mie theory can be represented by the following matrix:

$$\begin{pmatrix} S_1 & S_4 \\ S_3 & S_2 \end{pmatrix} = \begin{pmatrix} \sum_{k=1} \frac{2k+1}{k^2+k} (a_k \pi_k + b_k \tau_k) & 0 \\ 0 & \sum_{k=1} \frac{2k+1}{k^2+k} (a_k \tau_k + b_k \pi_k) \end{pmatrix} \quad (2.8)$$

where  $a_k$  and  $b_k$  are functions of  $\alpha(= \pi d n_o / \lambda_o)$ ,  $\beta(= \pi d m_l / \lambda_o)$  and  $m(= m_l / n_o, m_l = n - ik$  is the complex refractive index of the particle) and  $\pi_k$  and  $\tau_k$  are functions of  $\cos(\theta)$ . The formulations for  $a_k$ ,  $b_k$ ,  $\tau_k$ , and  $\pi_k$  are listed in Appendix IV. Eq. 2.8 is a form of the spherical Bessel function that has the nature of oscillation.

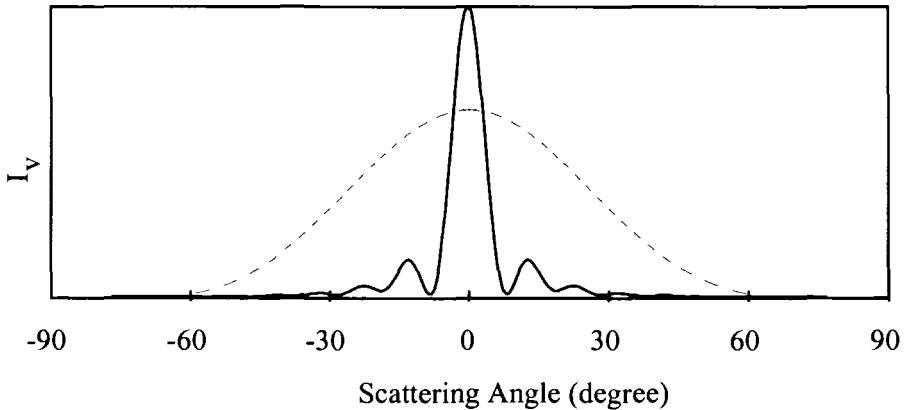


Figure 2.2. Schematics of scattering pattern for spheres.

For spheres, the scattering angular pattern is symmetric with respect to the axis of incident light, i.e., the scattering pattern is the same for the same absolute value of the scattering angle. In these patterns there are scattering minima and

maxima at different locations depending on the properties of particle. Figure 2.2 shows the scattering patterns from two spherical particles of different sizes.

As shown in Figure 2.2, the general characteristics of the scattering of spheres are that the location of the first intensity minimum is closer to the axis and the peak intensity is greater for a large particle (the solid line in Figure 2.2) as compared with that of a smaller particle (the dashed line in Figure 2.2). Because the scattering pattern is axially symmetric, i.e., the intensity curve at negative scattering angles is a mirror image of that at positive scattering angles in Figure 2.2. For the sake of convenience, we need only to focus our discussion using all positive angles. The intensity distribution of light scattered by a particle may also be displayed in a “radial graph” such as in Figure 2.3. In Figure 2.3, the particle is located at the center of the diagram. The bold trace is the intensity profile in which distance from the central point is proportional to the intensity at that angle.

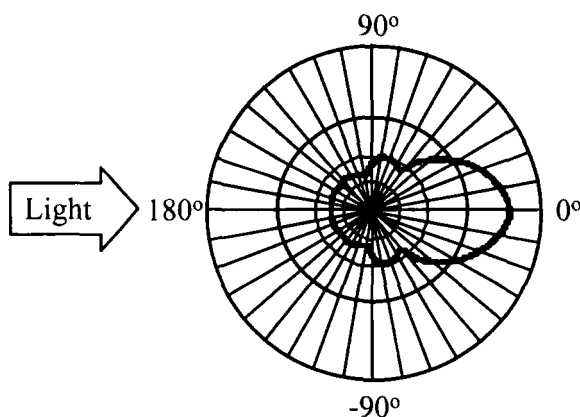


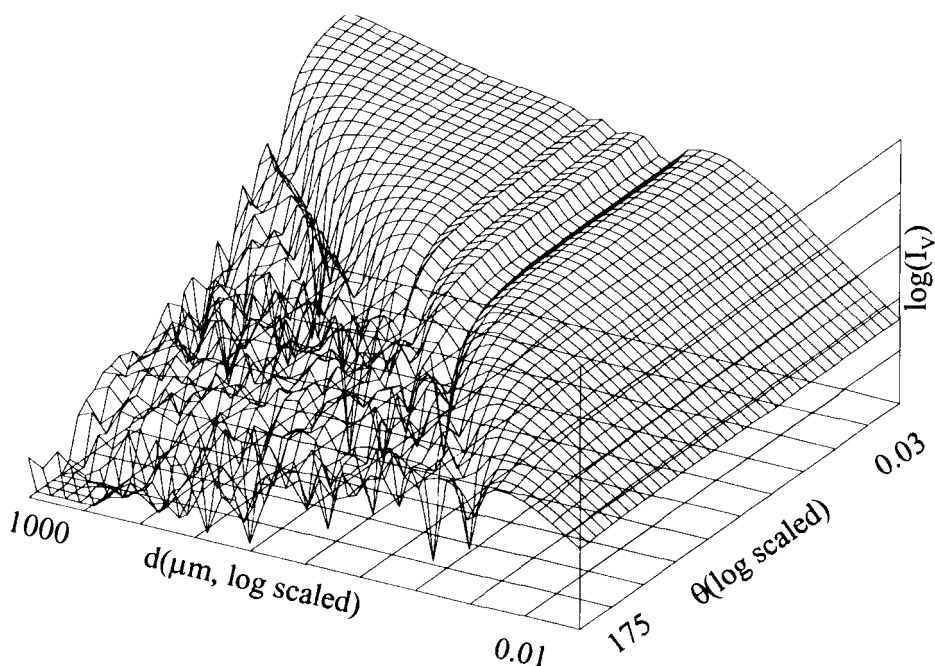
Figure 2.3. Radial graphic presentation of scattering intensity.

Figure 2.4 illustrates (in a three-dimensional fashion) the unit volume scattering intensity ( $I_v$ ) from polystyrene latex (PSL) spheres suspended in water and illuminated by a vertically polarized light  $I_{v,0}$  ( $\lambda_0 = 750$  nm). The intensity is plotted as a function of scattering angle and sphere diameter. Please note that all three axes are logarithmically scaled in order to capture the wide dynamic range and to reveal the details in the intensity variation. There are two general features in the figure:

1. The trend in scattering intensity variation: at small angles, the scattering intensity is stronger for large particles than that from small particles at the same scattering angle; scattering intensity diminishes as scattering angle increases for each particle. However, the angular dependence lessens as the size of sphere decreases. For spheres in the nanometer range, the intensity

profile becomes much less angularly dependent and reaches a flat line for those smaller than 50 nm.

2. Due to the oscillatory nature of Bessel function, there are many systematic ripples, peaks and valleys. Especially there are sharp intensity changes from the central peak values centered at zero degrees to the first minimum and to the subsequent minima and maxima. The pattern is characteristic for a given size particle. As shown in
3. Figure 2.4, if both scattering angle and diameter are spaced logarithmically, the first minimum displays a linear decrease in angle as particle size increases.



*Figure 2.4.* A 3-D plot of the Mie scattering intensity for spheres. All three axes are drawn in log scale [62] (by permission of Medpharm Scientific Publishers).

It is from these features that size information for spherical particles can be resolved through light scattering measurements. The shape of the 3-D map may vary depending on the values of relative refractive index and the incident wavelength, but these two general features always exist. Figure 2.5 shows

several scattering intensity curves for a 0.5  $\mu\text{m}$  PSL sphere suspended in water and illuminated by light of different wavelengths and polarizations.

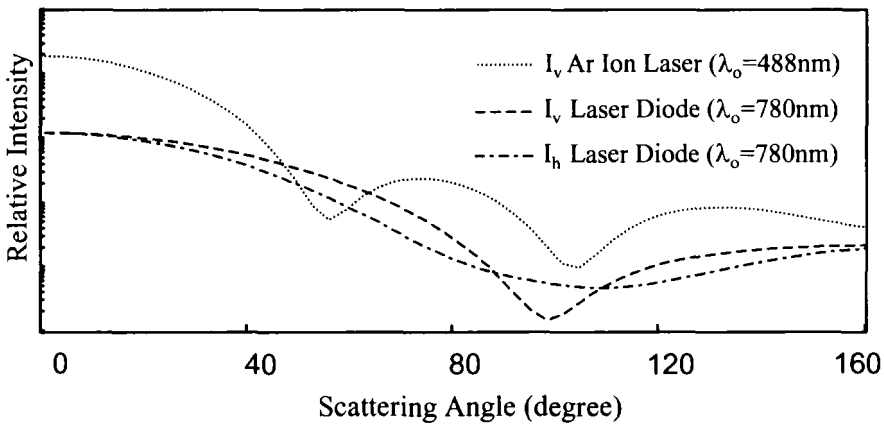


Figure 2.5. Wavelength and polarization variation of scattering intensity.

At small angles, typically less than 10 degrees, the scattering pattern for spheres is centrally symmetric in addition to being axially symmetric; i.e., it displays concentric rings in the direction of propagation of the incident light. In this range, the intensity will be the same for the same solid angle with respect to the incident light, and is not restricted to the angle  $\theta$  in the scattering plane relative to the tabletop as shown in Figure 2.1.

The computer source code for calculating scattering intensity according to the Mie theory is available in [12] and similar code can be downloaded from several web sites [63]. Variations of the Mie theory specific to different types of spheres, such as magnetic spheres [64], chiral spheres [65], and spheres having multiple layers with different optical properties at each layer, or even those having a radial refractive index gradient [66,67] have been developed. Their practicality in particle characterization technology presently is still very limited.

#### *The Zeroth-order Approximation: Rayleigh Scattering*

If a particle is much smaller than the wavelength of light, then each part of the particle will experience the same homogeneous electric field (uniform instantaneous phase) of the incident light and light scattered from the particle will be the same as if it was scattered from an oscillating dipole that radiates in all directions. This radiation is produced when a nonpolar particle (or molecule) is subjected to an electromagnetic wave; its electric charges are forced apart and an induced dipole moment is created, resulting in a polarized particle. This dipole is induced from penetration of the incident light into the particle due to the polarizability ( $\alpha$ ) of the particle in a time that is short when compared to the

period of light. The dipole moment oscillates synchronously with the field and the axis of the dipole moment aligns itself with the electric vector of the incident wave. This type of scattering is called Rayleigh scattering. To satisfy the above approximation, the following two conditions have to be met: 1)  $\text{size} \ll k_0^{-1}$ ; and 2)  $|\mathbf{m}| \cdot \text{size} \ll k_0^{-1}$ . Here, size is the longest dimension of the particle. In general,  $\alpha$  is a tensor; i.e., it has three components along three perpendicular directions. For most optically isotropic materials, all three components are the same. Scattering intensity is then only related to  $\alpha$  which is a function of the shape and volume of the particle. As long as the particle is isotropic, optically inactive, and the incident light is linearly polarized, all the scattered light is linearly polarized. Equal amounts of light are scattered into the forward and back hemispheres. The spatial pattern of scattering intensity has rotational symmetry about the dipole axis and a  $\cos^2\varphi$  dependence. At  $\varphi = 90^\circ$ , the scattering is almost zero since there is no scattering in the direction of dipole moment oscillation. A 3-D scattering intensity pattern of a dipole upon a polarized incident light is like a donut with an infinitely small hole in the center that is the dipole, as shown in Figure 2.6.

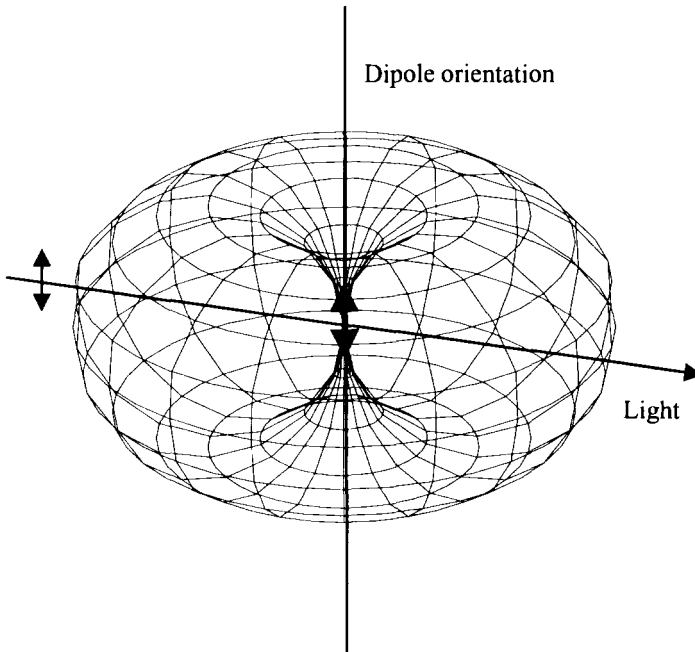


Figure 2.6. Scattering from a dipole.

The amplitude functions have the following values:



$$\begin{pmatrix} S_1 & S_4 \\ S_3 & S_2 \end{pmatrix} = ik_o^3 \alpha \begin{pmatrix} 1 & 0 \\ 0 & \cos \theta \end{pmatrix}. \quad (2.9)$$

Thus, for natural light, we have this well-known Rayleigh equation:

$$I = (1 + \cos^2 \theta) k_o^4 |\alpha|^2 I_o / 2r^2. \quad (2.10)$$

Since the probe length (the wavelength of light) is much larger than the particle no details, except the mass of the particle, can be found. The scattering intensity varies as the second power of the particle's mass (a sixth power dependence of the particle size). Although  $\alpha$  does depend on shape, all particles scatter light following Eq. 2.10; they are like structureless pieces of matter.

*The First-order Approximation: Rayleigh-Debye-Gans Scattering*

When the dimension of particle is larger than that which can be treated as a single dipole, the approach is to treat the particle as an assembly of many tiny and structureless scattering elements. Each of these scattering elements gives rise to Rayleigh scattering independent of other scattering elements in the particle. The phase shift corresponding to any element in the particle is negligible and the phase difference between different elements in the particle is determined only by their positions and is independent of the material properties of the particle. Scattering in a given direction from all these elements results in interference because of the different locations of these elements in the particle. To satisfy the above assumptions, the particle has to have a refractive index close to the medium ( $|m-1| \ll 1$ ), in addition to being small compared to the wavelength of light ( $|m-1| \cdot \text{size} \ll k_o^{-1}$ ). In the Rayleigh-Debye-Gans theory, the amplitude functions are summations of the scattering from all elements with a phase factor ( $\delta$ ) added to each element:

$$\begin{aligned} \begin{pmatrix} S_1 & S_4 \\ S_3 & S_2 \end{pmatrix} &= \frac{ik_o^3 (m-1)}{2\pi} \int e^{i\delta} dV \begin{pmatrix} 1 & 0 \\ 0 & \cos \theta \end{pmatrix} \\ &= \frac{ik_o^3 (m-1)V}{2\pi} \sqrt{P(x)} \begin{pmatrix} 1 & 0 \\ 0 & \cos \theta \end{pmatrix}. \end{aligned} \quad (2.11a)$$

$$P(x) = V^{-2} \left| \int e^{i\delta} dV \right|^2 = n^{-2} \sum_i \sum_j \sin Kr_{ij} / Kr_{ij}. \quad (2.11b)$$

In Eq. 2.11, we have taken the polarizability  $\alpha$  for a homogeneous particle when  $m$  is close to unity to be  $\alpha = (m^2 - 1)V/4\pi$ .  $P(x)$  is the scattering factor

determined by the shape of particle when  $m$  is real; i.e., there is no absorption.  $P(x)$  is derived from the consideration that a large particle has  $n$  active identical scattering centers, any two of which are separated by a spatial vector  $\mathbf{r}_{ij}$  of length  $r_{ij}$ . All possible pairwise combinations of these centers within the particle geometry form the basis of the scattering interference pattern. For many regular shapes, the scattering factors have been derived. An extensive collection of the published scattering factors for 27 different particle shapes is available [68]. Other scattering factors, including those for flat particles (rectangular, square, triangular and hexagonal), can also be found in the literature [69,70]. Appendix V lists a few scattering factors for randomly oriented isotropic regular particles. For most particles of regular shapes the scattering factors are a function of the product of their characteristic dimension and scattering vector. The symbol  $x$  is commonly used for this product (see the following for the definitions of  $x$  for particles of different shapes).  $P(x)$  can be generally formulated using a series expansion [10]:

$$P(x) = 1 - \frac{K^2 R_g^2}{3} + \dots \quad (2.12)$$

where  $R_g$  is the radius of gyration of a particle, which is the effective radius of a body as far as rotation is concerned, or the radius at which all mass is concentrated, defined by:

$$R_g^2 = \frac{\int \rho(r) r^2 dV}{\int \rho(r) dV} \quad (2.13)$$

where  $\rho(r)$  is the mass density at  $r$ . When  $x$  is less than 0.25, the third and higher terms in Eq. 2.12 can be dropped. The initial slope of  $P(x)$  versus  $K^2$  is then related to the radius of gyration of particle. The analytical formulas for scattering factors are thus much simpler than the rigorous solutions (if these solutions exist) for a particular shape. Scattering factors are monotonically decaying functions with increasing  $x$ . Figure 2.7 shows the scattering factors for several common shapes.

The scattering factors for optically anisotropic particles will have different forms depending on polarization of both the incident and scattered light. The greatest advantage in using scattering factors is that these functions are independent of the refractive index of the particle. Once the experimental setup is determined size and shape are the only variables. Thus, for small particles, once one knows the particle shape, size characterization is readily feasible provided that all particles have the same geometrical shape. For visible

light, the Rayleigh-Debye-Gans theory can be used for particles with sizes up to a few hundred nanometers. This theory has been widely used in the characterization of synthetic and natural macromolecules because most of these molecules that are in coil conformation in solution have sizes less than 100 nm. In principle, if the shape of particle is known, the angular scattering intensity measurement will yield information about size of the particle. In practice, due to limitations such as the polydispersity of shape for industrial particles and the weak angular intensity dependence for small particles, such applications are still limited to academic work where scattering factors are more often used in combination with PCS technology.

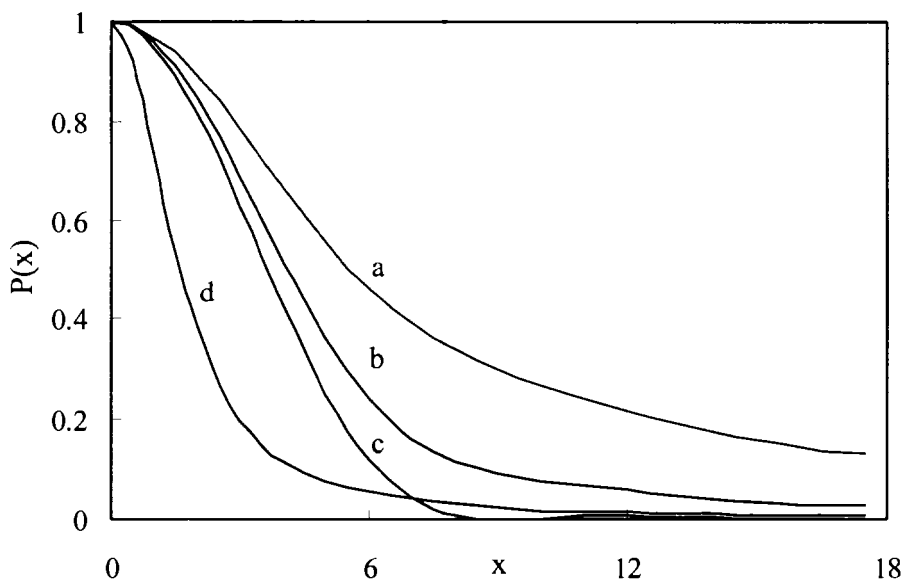


*Figure 2.7.* Scattering factors for common shapes. From the top down: a) randomly oriented circular rods with the length ( $L$ ) to diameter ( $d$ ) ratio  $L/d = 8$ , where  $x = 4\pi L \sin(\theta/2)/\lambda$ ; b) randomly oriented infinitely thin disks where  $x = 4\pi d \sin(\theta/2)/\lambda$  with  $d$  being the diameter; c) spheres where  $x = 4\pi d \sin(\theta/2)/\lambda$  with  $d$  being the diameter; and d) random coils where  $x = 4\pi R_g \sin(\theta/2)/\lambda$ , with  $R_g$  being the radius of gyration.

### *The Large-end Approximation: Fraunhofer Diffraction*

When the size of particle is much larger than the wavelength of light, the particle removes an amount of light energy proportional to twice its cross-sectional area. One areal cross-section is removed by the sum of reflection, refraction and absorption, and one areal cross-section via diffraction. For large particles, another quite different approach is used. When the particle dimension is much larger than the wavelength of light or the material is highly absorptive,

the edge effect of particle contributes much more to the total scattered intensity. The interference effect now arises mainly from particle's contour; i.e., diffraction produced by the bending of light at the particle boundary. In these instances, scattering from the inner part of the particle is less important and neglected as an approximation. For large particles, when only edge effects are considered, we can use various diffraction equations to describe the scattering patterns. The particle now behaves like a two-dimensional object instead of a three-dimensional particle. Only the projected area perpendicular to the light matters, not the volume of particle. Diffraction can be described by Huygen's principle: each point on a propagating wave front is an emitter of secondary wavelets. The locus of expanding wavelets forms the propagating wave. Interference between the secondary wavelets gives rise to a fringe pattern, which rapidly decreases in intensity with increasing angle from the initial direction of light propagation. Diffraction is an important physical effect inherent in all wave phenomena. There are two classes of diffraction, namely Fraunhofer and Fresnel diffraction. Fraunhofer diffraction (after Joseph von Fraunhofer in 1817 [71]) involves coherent plane waves incident upon an obstruction. Fresnel diffraction (after Augustin Fresnel in 1818) involves spherical waves incident upon an obstruction. Experimentally, Fresnel diffraction is produced from a point source and Fraunhofer diffraction from a parallel beam. Fraunhofer diffraction by an aperture is mathematically equivalent to the Fourier transform of the aperture shape. Because the integrals describing Fresnel diffraction are so intractable, Fresnel diffraction patterns have few analytical solutions, even in one dimension. In a light scattering measurement, because the light source is far away from scatterers and the optics are usually designed such that the incident beam is homogeneously collimated, only Fraunhofer diffraction will take place. In diffraction theory, both a black disk illuminated by light and a black screen that covers the entire wave front except for a hole will produce the same diffraction pattern since the edge effect dominates the diffraction pattern. In the diffraction region, the scattering amplitude functions  $S_3$  and  $S_4$  are both equal to zero, and  $S_1$  and  $S_2$  are equal to each other and can be computed by integration along the contour of the projected area of the particle in the light beam:

$$\begin{pmatrix} S_1 & S_4 \\ S_3 & S_2 \end{pmatrix} = \frac{k_o^2}{2\pi} \iint e^{-ik(x \cos \varphi + y \sin \varphi) \sin \theta} dx dy \begin{pmatrix} 1 & 0 \\ 0 & 1 \end{pmatrix}. \quad (2.14)$$

Amplitude functions for particles of any shape can be computed numerically or analytically using Eq. 2.14 [72,73,74,75]. Analytical solutions exist for several regular polygons. For example, the diffraction intensity pattern from a rectangle follows the equation:

$$S_1 = S_2 = \frac{2 \sin(ak_0 \cos \varphi \sin \theta) \sin(bk_0 \sin \varphi \sin \theta)}{\pi \cos \varphi \sin \theta \sin \varphi \sin \theta}, \quad (2.15)$$

where  $a$  and  $b$  are the half length and half height of the rectangle, respectively. From Eq. 2.14, it is obvious that diffraction intensity patterns have at least a two-fold symmetry:

$$I(\theta, \varphi) = I(\theta, \varphi + \pi). \quad (2.16)$$

For a regular polygon of  $n$ -fold symmetry, the diffraction intensity pattern has a  $n$ -fold symmetry when  $n$  is an even number and a  $2n$ -fold symmetry when  $n$  is an odd number. Thus, the diffraction intensity patterns of thin rods, triangles, rectangles, pentagons, and hexagons, if oriented perpendicular to the light, will have 2-fold, 6-fold, 4-fold, 10-fold, 6-fold symmetries, respectively. The symmetry will increase as the number of sides of the polygon increases. For a sphere, the symmetry of the diffraction intensity pattern is  $\infty$ -fold. The diffraction pattern for an elliptical object can also be expressed, with  $a$  and  $b$  being the half length of the long and short axes, respectively:

$$S_1 = S_2 = \frac{2\pi b J_1(z\pi\sqrt{\mu} 2a \sin \theta / \lambda)}{z\sqrt{\mu}\lambda \sin \theta}; z = \sqrt{\mu \cos^2 \varphi + \frac{1}{\mu} \sin^2 \varphi}; \mu = \frac{a}{b} \quad (2.17)$$

in which  $J_1$  is the Bessel function of the first kind of order unity:

$$J_1(x) = x \sum_{k=1}^{\infty} (-1)^{k+1} \frac{x^{2k-2}}{(k-1)! k! 2^{2k-1}}. \quad (2.18)$$

For spheres, Eq. 2.17 can be simplified by taking  $2b = 2a = d$  (diameter) and thus  $z = \mu = 1$ . This familiar Fraunhofer diffraction equation is a form of the rigorous Mie formulation at the limiting condition of  $d \gg \lambda$ :

$$\begin{pmatrix} S_1 & S_4 \\ S_3 & S_2 \end{pmatrix} = \frac{\pi d J_1(\pi d \sin \theta / \lambda)}{\lambda \sin \theta} \begin{pmatrix} 1 & 0 \\ 0 & 1 \end{pmatrix}. \quad (2.19)$$

Eq. 2.19 is derived assuming that a particle scatters as if it were an opaque circular disc of the same projected area positioned normally to the axis of the beam. Because of this assumption, in the Fraunhofer theory the refractive index of material is irrelevant. Fraunhofer diffraction applies to particles: 1) whose

longest dimension of the projected area is much larger than the wavelength of light (typically  $> 30 \mu\text{m}$ ) and non-transparent, i.e., the particles have different refractive indices than that of the medium (typically with the relative refractive index  $m$  being larger than 1.2); or, 2) that are highly absorptive (typically with absorption coefficient higher than 0.5). Because for large particles, where the Fraunhofer theory applies, the scattering intensity is concentrated in the forward direction - typically at angles smaller than 10 degrees, Fraunhofer diffraction is also known as forward scattering. In Fraunhofer diffraction by a sphere, the angle of the first minimum of scattering intensity is simply related to the object size by:

$$\sin \theta_{\text{1st.min.}} = \frac{1.22\lambda}{d} \quad (2.20)$$

and most of scattering intensity is concentrated in a very sharp central lobe as shown in Table 2.2.

Table 2.2. Intensity distribution of Fraunhofer diffraction from a sphere

Intensity Ring	Position ( $\theta$ )	Relative Intensity ( $I/I_0$ )	Intensity in Ring (%)
Central Maximum	0.0	1.0	83.8
First Minimum	$\sin^{-1}(1.22\lambda/d)$	0.0	
Second Maximum	$\sin^{-1}(1.64\lambda/d)$	0.0175	7.2
Second Minimum	$\sin^{-1}(2.23\lambda/d)$	0.0	
Third Maximum	$\sin^{-1}(2.68\lambda/d)$	0.0042	2.8
Third Minimum	$\sin^{-1}(3.24\lambda/d)$	0.0	
Fourth Maximum	$\sin^{-1}(3.70\lambda/d)$	0.0016	1.5
Fourth Minimum	$\sin^{-1}(4.24\lambda/d)$	0.0	

Figure 2.8 - Figure 2.11 show the diffraction intensity patterns of a square, a rectangle, an ellipse, and a circle, in which the symmetries are clearly shown.

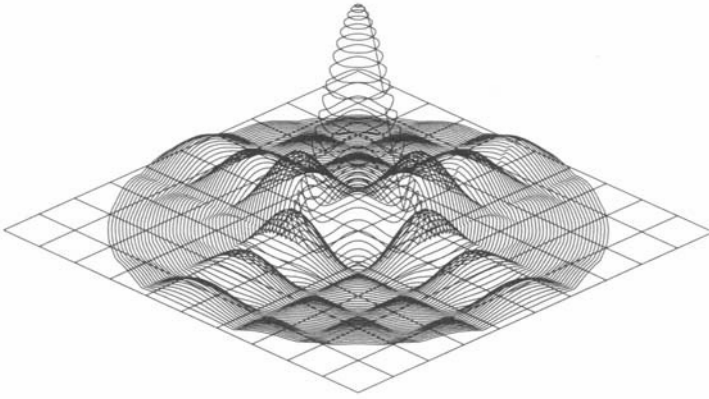


Figure 2.8. Diffraction pattern (absolute electromagnetic field distribution) of a square for the azimuthal angle  $\varphi$  from  $0^\circ$  to  $360^\circ$  and scattering angle  $\theta$  from  $0^\circ$  to  $7^\circ$  ( $ak_0 = 100$ ).

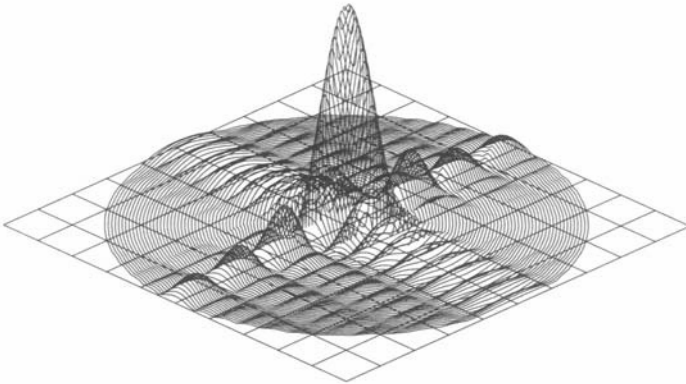
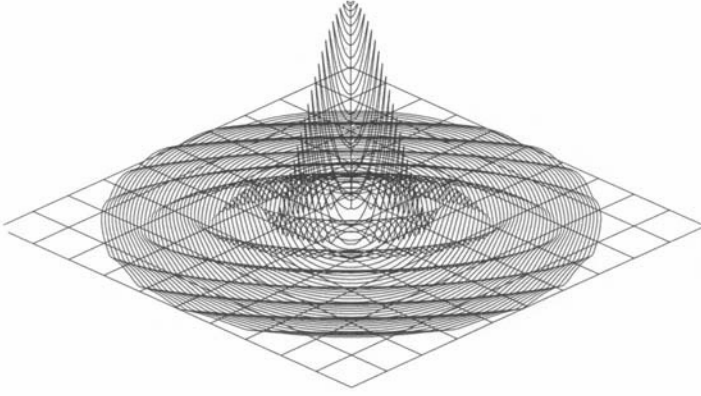
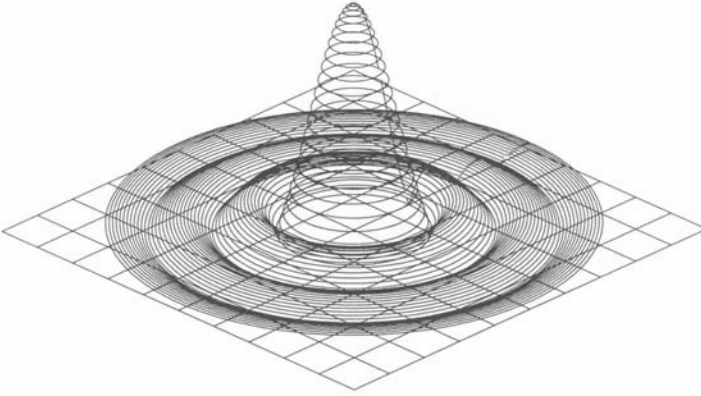


Figure 2.9. Diffraction pattern (absolute electromagnetic field distribution) of a rectangle for the azimuthal angle  $\varphi$  from  $0^\circ$  to  $360^\circ$  and scattering angle  $\theta$  from  $0^\circ$  to  $7^\circ$  ( $ak_0 = 100$ ,  $bk_0 = 250$ ).



*Figure 2.10.* Diffraction pattern (absolute electromagnetic field distribution) of an elliptical disk for the azimuthal angle  $\varphi$  from  $0^\circ$  to  $360^\circ$  and scattering angle  $\theta$  from  $0^\circ$  to  $3.5^\circ$  ( $ak_0 = 200$ ,  $bk_0 = 400$ ).



*Figure 2.11.* Diffraction pattern (absolute electromagnetic field distribution) of a circular disk for the azimuthal angle  $\varphi$  from  $0^\circ$  to  $360^\circ$  and scattering angle  $\theta$  from  $0^\circ$  to  $3.5^\circ$  ( $dk_0 = 400$ ).

Figure 2.12 is a photograph of the diffraction pattern of a  $500\ \mu\text{m}$  pinhole illuminated by a He-Ne laser.



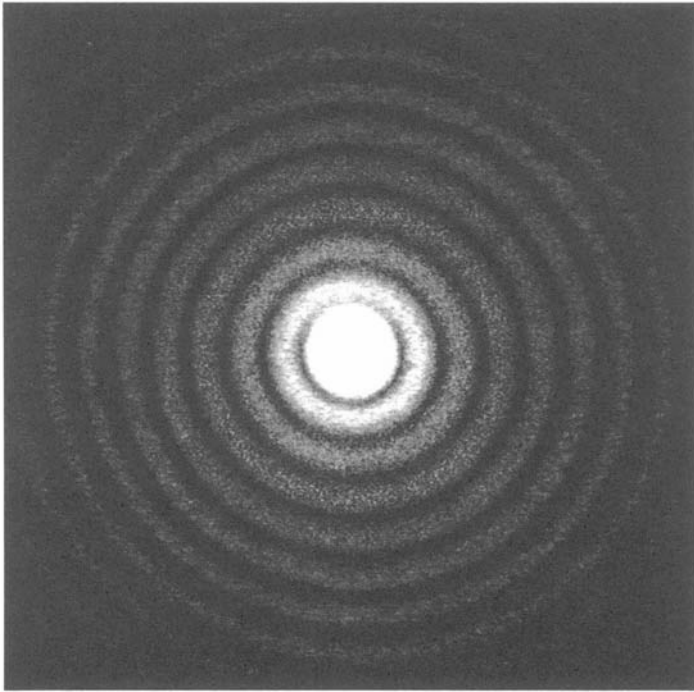


Figure 2.12. Diffraction pattern of a circular aperture.

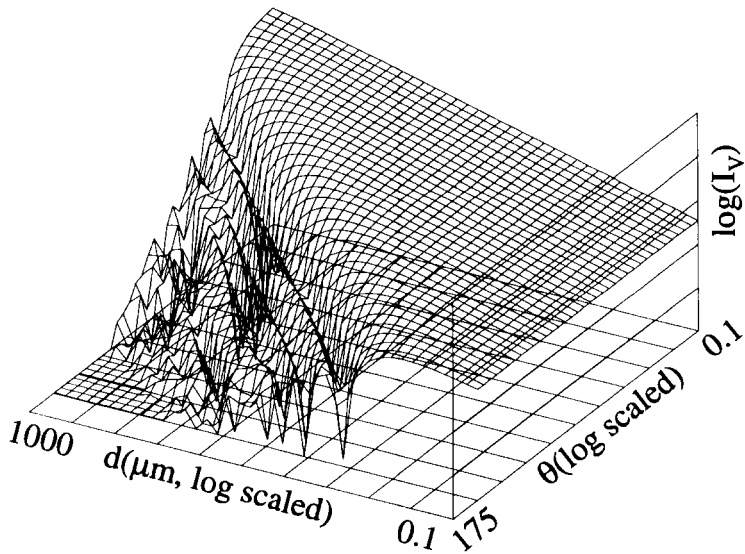


Figure 2.13. A 3-D display of Fraunhofer scattering intensity. All three axes are plotted in log scale [62] (by permission of Medpharm Scientific Publishers).

Since the diffraction pattern of a sphere has a central symmetry, we can take the intensity profile at any azimuthal angle and display a similar 3-D map of diffraction (scattering) intensity of unit volume as a function of sphere diameter and scattering angle  $\theta$  as that of Figure 2.4, but employing Eq. 2.19 instead of using Eq. 2.8. As expected, when particles are larger than about a few tens of microns, the Fraunhofer diffraction patterns of spheres at small angles are the same as those predicted by the Mie theory. The patterns predicted by these two theories diverge from each other more and more as either the scattering angle increases or particle size decreases.

For particles with small  $m$  values, even though their size may be large, Eq. 2.19 will no longer be valid because the effects of light transmitting or refracting through the particles also have to be taken into account. In this anomalous diffraction regime either a rigorous theory (such as the Mie theory for spheres) or some approximation has to be used [76]. There are several approximation algorithms in existence [77]. In one algorithm, another term  $f(m, \theta)$ , accounting for the refraction effect is added yielding [78]:

$$f(m, \theta) = 4 \left( \frac{m}{m^2 - 1} \right)^4 \frac{(m \cos(\theta/2) - 1)^3 (m - \cos(\theta/2))^3}{\cos(\theta/2) (m^2 + 1 - 2m \cos(\theta/2))^2} \left( 1 + \frac{1}{\cos^4(\theta/2)} \right), \quad (2.21)$$

$$I \propto 2 \left( \frac{\pi d J_1(\pi d \sin \theta / \lambda)}{\lambda \sin \theta} \right)^2 + \left( \frac{\pi d}{\lambda} \right)^2 f(m, \theta). \quad (2.22)$$

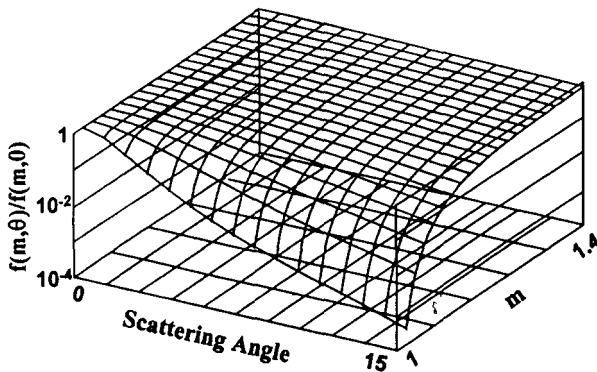


Figure 2.14. Anomalous diffraction function  $f(m, \theta)$ . (Reprinted from Ref. [79], pp.756 by courtesy of Marcel Dekker, Inc.)

In this case,  $f(m, \theta)$  has strong angular dependence which diminishes only when  $m$  is larger than approximately 1.2 as shown in Figure 2.14. For  $m > 1.2$ ,  $f(m, \theta)$  is a constant and the angular scattering pattern can be treated using the ordinary Fraunhofer theory.

### *Numerical Approaches*

For particles of arbitrary shape that are in a size range comparable with the wavelength of light, none of the above approximations can be used and analytical formulations are not possible. Thanks to the rapid advancement in modern microelectronics, numerical approaches to compute the scattering intensity of particles of complex shape have now become feasible and many source codes for such computations are available at several web sites, although there is still certainly some way to go before these methods can be applied to daily particle characterization practices. One recent review article concisely summarized up-to-date developments in computing elastic scattering intensity [80]. The numerical methods can be divided into surface-based methods and volume-based methods. In several surface-based methods, namely the point matching method, the T-matrix method and the generalized multipole technique, the scattered electric field is expanded into terms of spherical vector wave functions (or called multipoles) having their origin either at the center of the sphere, or somewhere in the sphere. The coefficients for the terms of expansion are obtained by satisfying the boundary conditions either at a number of discrete surface points (the point matching method) or by using surface integration over the particle's surface (the T-matrix method). One of the surface-based methods, the T-matrix method, has been applied to particles of sizes up to 30  $\mu\text{m}$  and many different shapes [81,82], and the source codes are available as a shareware.

In the volume-based methods, such as the finite different time domain method [83], the finite element method [84], or the discrete dipole approximation [85], the volume of particle is discretized into small elements, and the propagation of the incident light through the particle is computed stepwise using the elements. The electric field of each element is obtained from the contribution of its neighbor elements. Due to complexity in computation, the maximum size calculated using volume-based methods is still relatively small, up to a few microns in the visible light range.

In summary, the scattering intensity of a single particle, depending on the size and shape of particle and the relative refractive index, can be described by various theories. Figure 2.15 schematically shows the general relationships between particle properties and the applicable theories. The boundaries shown are only pictorial in nature since many additional factors determine the actual boundaries.

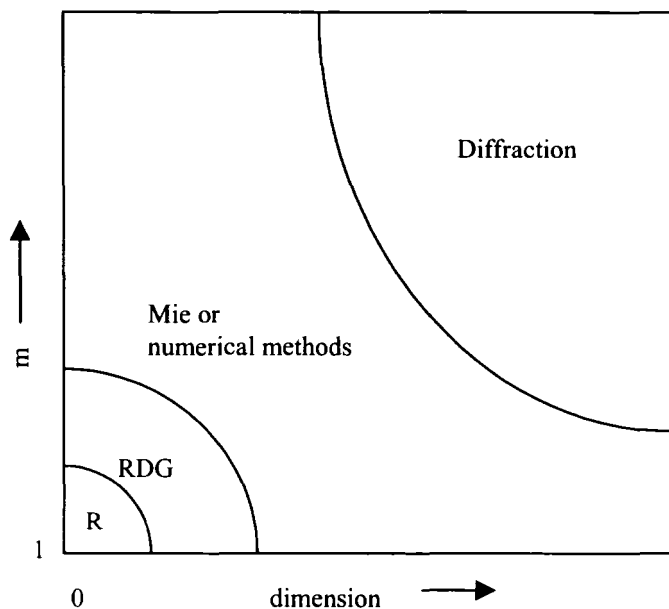


Figure 2.15. Application ranges for various theories (R: Rayleigh scattering; RDG: Rayleigh-Debye-Gans scattering).

### 2.2.3. TIME-AVERAGED SCATTERING INTENSITY OF PARTICLES

If there is more than one particle in the scattering volume, the total scattering intensity is the composite of the scattering from all particles in the scattering volume. Generally, there are two regions in between which the scattering contributions from each individual particle to the overall scattering pattern are different. In one region, when the number of particles is small and the distance between the particles is large, multiple scattering (as well as the influences arising from mutual light polarization between particles) can be neglected. Interactions of physical forces along with scattering interference between particles may be still present but have only a limited effect on the overall scattering pattern. In this region, the total scattering from particles in the scattering volume often can be treated as a simple summation of the scattering from each particle, although the actual scattering angle for each particle may be slightly different. One limiting case in this region exists when the number of particle is reduced to one. We now have only to consider the single particle scattering described in Section 2.2.2. In another region, the number density of particles is high enough so that these particles are in close proximity, and several phenomena may occur. The first one is known as multiple scattering. Here, some of the radiation scattered by a particular particle will be incident

upon a second particle, which then rescatters the radiation. Rescattering can happen multiple times. The rescattered light from the second particle becomes the incident light upon a third particle, which then rescatters; and so on. When particles are close enough to each other, e.g., less than a few diameters apart, several types of physical interactions between them will take place and scattering from any particle will again be affected by the existence of its neighbors. Thirdly, the light scattered from different particles will interfere in the detection plane. This is the region of high concentration. In this situation, multiple scattering, mutual polarization, and strong interference between particles exist, all of which are heavily dependent on the morphology, dimension and material nature of the particles. Therefore, information retrieval about the characteristics of the particles from a time-averaged intensity measurement is a very difficult task, although theoretical computation can be performed for some well-defined systems. In the Fraunhofer diffraction region, a general theory combining an empirical approach for retrieving a particle size distribution from concentrated suspensions that are not subjected to particle interaction but that involve multiple scattering has been proposed, and the results from several particulate systems have been published [86,87]. There is no clear borderline between these two regions since effects produced by an increase in concentration appear only gradually. In macromolecule studies, the concept of “overlap concentration”, when two chains start to overlap is often used to distinguish between the dilute and semi-dilute regions.

#### 2.2.4. SCATTERING INTENSITY FLUCTUATIONS OF PARTICLES

The theories described in Sections 2.2.2 and 2.2.3 are based on time-averaged scattering intensity with the assumptions that the scatterers are not moving and that the incident intensity is constant from a stable light source, and also that there is no relative movement between the components of experimental setup; i.e., everything is in some static condition. The term “static light scattering” is often used to describe these techniques. In reality, although the intensity of incident light ( $I_0$ ) can be maintained at a constant level and the instrument can be made rigid, particles in the scattering volume are in constant movement originating from various sources. The movement can arise from random thermal translational or rotational motions (Brownian motion), forced motion introduced by a flow or electric field, or even motion arising from bioactivity, such as the mobility of bacteria particles in water. Any motion of the particles will cause changes, fluctuations or jumps, in scattering intensity which may be fast or slow, depending on the nature of the motion and the type of particle. In any dynamic light scattering experiment, except photon migration spectroscopy, the intensity of the incident light is constant and the relative positions of the instrument components remain unchanged. The source of the intensity variation

is then purely from the movement of the particles, which causes changes in the relative positions between the particles, light source, and detector, and between the particles themselves (if there is more than one in the scattering volume). Thus, detecting intensity variations can provide information on the motions of particles, and the characteristics of particles can be revealed from a different aspect than from a time-averaged intensity measurement.

### *Doppler Shift*

Let us first imagine a situation where a person is standing on a platform next to a railroad track. He or she will hear the changing pitch of a train whistle as the train approaches and then recedes. This change in pitch arises from the relative motion of the source of the sound (the train) and the observer's ear. When the train is moving toward the person, the wave crests become closer together and the whistle's pitch sounds higher. As the train moves away from the person, the wave crests become farther apart and the whistle's pitch sounds lower. Generally speaking, whenever there is relative movement between the wave source and the receiver, the wave received by the receiver has a different frequency from the original one. This shift in frequency is called the Doppler shift after the Austrian physicist and mathematician Christian Doppler. A Doppler shift can occur in any type of waveform - light, x-ray, or sound. The relationship of the frequency shift  $\Delta\nu$  and the relative movement  $\Delta V$  between a wave source producing a wave of velocity  $V$  and the receiver is

$$\Delta\nu = \nu_0 \Delta V/V. \quad (2.23)$$

Now, let us look what happens in a light scattering experiment when the particles are moving. In this case, the particles act both as the receiver of the incident light and as the wave source of the scattered light. The detection of scattering is commonly performed by either a photomultiplier tube (PMT) or a photodiode (PD). Both type of detectors are square-law detectors; i.e., they detect light intensity in terms of the number of photoelectron pulses or by the photocurrent, which are proportional to square of the electric field falling onto the detector surface. In this scheme, the electric field arriving at the detector surface from  $N$  moving particles is:

$$\begin{aligned} E_s(t) &= \sum_{j=1}^N E_j(t) + E_m(t) = \sum_{j=1}^N A_j E_0 e^{-i(\omega_0 t - \mathbf{k}_0 \cdot \mathbf{r}_j(t) + \mathbf{k}_s \cdot \mathbf{r}_j(t))} + A_m E_0 e^{-i(\omega t - \phi_m)} \\ &= \sum_{j=1}^N A_j E_0 e^{-i(\omega_0 t - \mathbf{K} \cdot \mathbf{r}_j(t))} + A_m E_0 e^{-i(\omega t - \phi_m)} \end{aligned} \quad (2.24)$$

where  $\mathbf{r}_j(\mathbf{t})$  is the position of the center of mass of the  $j^{\text{th}}$  particle relative to a common reference point at time  $t$ . Because the particles are moving, the term  $\mathbf{K}\mathbf{r}_j(\mathbf{t})$  varies continuously; thus the frequency of scattered light shifts away from  $\omega_0$  (the incident light frequency) and a frequency distribution is produced. The last term accounts for the scattering from the molecules of the medium.  $A_j$  is the scattering amplitude from the  $j^{\text{th}}$  particle, which is governed by the scattering theory described in Section 2.2.2. Because the frequency shift produced by particle movement is less than a few hundred Hz, there is currently no detector that is able to register such a small shift in the range of visible light ( $10^{14}$  Hz). A secondary light source has to be mixed with the scattered light. These two beams will “beat” each other at the surface of photodetector and will enable a small frequency shift to be detected. This technique to measure small light frequency shifts is often called light-beating spectroscopy and can be demonstrated by comparing two sinusoidal functions with slightly different frequencies as is illustrated in Figure 2.16.

Although the difference in frequency is not very small in this example (10%), one can hardly discern the difference by looking at only the sinusoidal functions alone. But when these two functions are added, a beat frequency modulating the original frequency can be clearly seen. This beat frequency is half of the difference between the two original ones. In practice there are three experimental arrangements, shown in Figure 2.17.

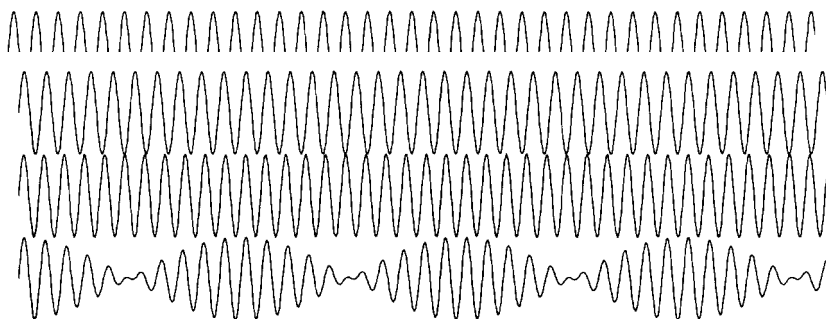


*Figure 2.16. Wave beating.*

The secondary light can be either the scattering from the particles themselves (Scheme A in Figure 2.17) or from a separate source. This additional light source, called a local oscillator, is often obtained by splitting the incident light. Part of the split beam, which may pass through a frequency shifter so its frequency is slightly altered (Scheme C in Figure 2.17), either illuminates the detector directly or illuminates some other fixed scattering object (such as a scratch on the sample cell) that scatters light onto the detector. There are two

sets of terminology used in the literature to describe these three schemes (Table 2.3). In the present book, we will adopt convention 1

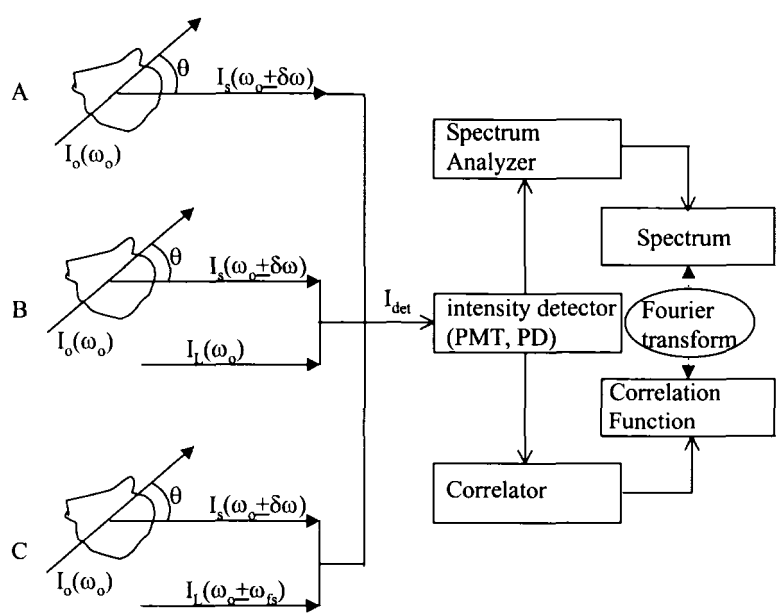


Figure 2.17. Dynamic light scattering schematics.

Table 2.3. Dynamic light scattering conventions

	Convention 1	Convention 2
Scheme A	Self-Beating	Homodyne
Scheme B	Homodyne	Heterodyne
Scheme C	Heterodyne	Heterodyne

*ACF and Power Spectrum*

As described in Figure 2.17, in scattering intensity fluctuation studies there are two major measurement schemes, correlation function measurement (either the autocorrelation function (ACF) or the cross-correlation function (CCF)), and spectrum analysis. These two types of measurement require the use of different hardware. Their results, the frequency spectrum and the correlation function, are related to each other. We will briefly discuss these two techniques and their relationship in certain experimental conditions. More details about the detection and interpretation of scattering fluctuations will be given in Chapter 5 and Chapter 6.

The time autocorrelation function of a variable  $x(t)$  is defined as



$$\text{ACF} = \langle x(t)x^*(t+\tau) \rangle = \lim_{T \rightarrow \infty} \frac{1}{2T} \int_0^{2T} x(t)x^*(t+\tau) dt \quad (2.25)$$

where the bracket indicates an ensemble average over the period of measurement ( $2T$ ). The symbol  $\tau$  is called the delay time and is the time difference between two measurements. The absolute time  $t$  can be any value within the period of the average. The physical meaning of the computation of the ACF is that, since the measurement at time  $(t+\tau)$  occurs right after the measurement at time  $t$ , the signal or information contained in the measured values of  $x(t)$  from these two measurements should be somehow related (correlated) if  $\tau$  is small. The larger the value of  $\tau$ , the further away the system at time  $(t+\tau)$  is from its original state at time  $t$ ; i.e., these two states become less and less correlated. When the delay time  $\tau$  goes to infinity, the two states become completely uncorrelated. In this case the average of the product  $x(t)$  and  $x(t+\tau)$  can be separated into the product of the averages of  $x(t)$  and  $x(t+\tau)$ :

$$\begin{aligned} \langle x(t)x^*(t+\tau) \rangle &\rightarrow \langle |x(t)|^2 \rangle & \tau \rightarrow 0 \\ &\rightarrow \langle x(t) \rangle^2 & \tau \rightarrow \infty. \end{aligned} \quad (2.26)$$

Since  $\langle |x(t)|^2 \rangle \geq \langle x(t) \rangle^2$ , the ACF has a maximum at  $\tau = 0$  and either remains constant or decays to the mean  $x(t)$  value squared at sufficiently large  $\tau$ . The form of decay depends on the nature of the variable  $x(t)$ . For time-invariant random processes,  $t$  in Eq. 2.25 can take any value. Thus, the following relation exists:

$$\langle x(t)x^*(t+\tau) \rangle = \langle x(0)x^*(\tau) \rangle. \quad (2.27)$$

In the digital form of the measurement, the time axis is divided into small discrete time intervals  $\Delta t$ . Thus  $T = N\Delta t$  and  $\tau_n = n\Delta t$ . The ACF then can be approximated when  $\Delta t \rightarrow 0$ :

$$\text{ACF} = \langle x(0)x^*(\tau_n) \rangle \cong \lim_{N \rightarrow \infty} \frac{1}{2N} \sum_{j=1}^{2N} x_j x_{j+n}^*. \quad (2.28)$$

According to the Wiener-Khintchine theorem [88], for random complex variables, the ACF is the inverse Fourier transform of the power spectral density  $S_x(\omega)$  and the power spectral density is the time Fourier transform of the ACF [38].

$$\langle x(t)x^*(t+\tau) \rangle = \int_{-\infty}^{\infty} S_x(\omega) e^{-i\omega\tau} d\omega, \quad (2.29a)$$

$$S_x(\omega) = \frac{1}{2\pi} \int_{-\infty}^{\infty} \langle x(t)x^*(t+\tau) \rangle e^{i\omega\tau} d\tau. \quad (2.29b)$$

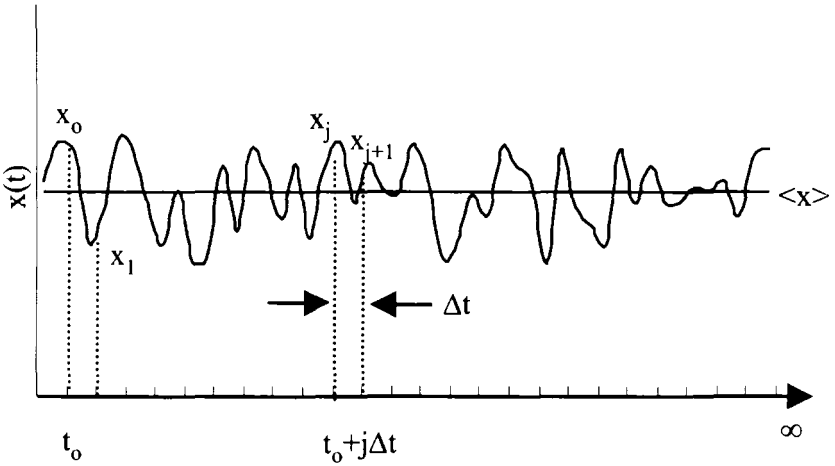


Figure 2.18. Scheme in the measurement of the ACF.

In light scattering, the variable in the ACF may be either the electric field or light intensity. The former is called the electric field-electric field ACF (or the first-order ACF,  $G^{(1)}(\tau)$ ) and the later is called the intensity-intensity ACF (or the second-order ACF,  $G^{(2)}(\tau)$ ). The symbols  $g^{(1)}(\tau)$  and  $g^{(2)}(\tau)$  are for the normalized  $G^{(1)}(\tau)$  and  $G^{(2)}(\tau)$ , respectively. For a mixture of scattering and reference light, the intensity-intensity ACF can be written as:

$$\begin{aligned} G_{\text{det}}^{(2)}(\tau) &= \\ &\langle [E_L^*(t) + E_s^*(t)][E_L(t) + E_s(t)][E_L^*(t+\tau) + E_s^*(t+\tau)][E_L(t+\tau) + E_s(t+\tau)] \rangle \\ &= I_L^2 + 2I_L \langle I_s \rangle + \langle E_s(t)E_s^*(t+\tau) \rangle \cos(\Delta\omega\tau) + \langle I_s(t)I_s(t+\tau) \rangle \end{aligned} \quad (2.30)$$

where  $\Delta\omega$  is the frequency difference between the main incident light and reference light (local oscillator). The second equality is obtained assuming the

local oscillator ( $E_L$ ) is not at all correlated with the scattering electric field and  $\langle e^{i\omega t} \rangle = 0$ . When  $I_L = 0$  (as in the case of Scheme A),

$$G_{\text{det}}^{(2)}(\tau) = G_s^{(2)}(\tau), \quad (2.31)$$

and when  $I_L \gg I_s$  (as in most homodyne and heterodyne experiments in Schemes B and C),

$$G_{\text{det}}^{(2)}(\tau) = I_L^2 + 2I_L \left| G_s^{(1)}(\tau) \right| \cos(\Delta\omega\tau). \quad (2.32)$$

In general,  $G^{(2)}(\tau)$  is not simply related to  $G^{(1)}(\tau)$ . However, in special cases when  $x(t)$  is a Gaussian random variable, such as the scattered electric field from particles undergoing Brownian motion, these two ACF's are related by the Siegert relation [89]:

$$G_s^{(2)}(\tau) = \langle I_s \rangle^2 + \left| G_s^{(1)}(\tau) \right|^2, \text{ or} \quad (2.33a)$$

$$g_s^{(2)}(\tau) = 1 + \left| g_s^{(1)}(\tau) \right|^2. \quad (2.33b)$$

Thus, in general, for a normalized ACF  $g_{\text{det}}^{(2)}(\tau)$  [90]:

$$g_{\text{det}}^{(2)}(\tau) = 1 + \frac{I_s^2}{(I_L + I_s)^2} \left| g_s^{(1)}(\tau) \right|^2 + \frac{2I_L I_s}{(I_L + I_s)^2} \left| g_s^{(1)}(\tau) \right| \cos(\Delta\omega\tau). \quad (2.34)$$

In practice, if the ACF is measured in the single photon counting mode as in most PCS experiments, strictly speaking the intensity  $I$  in the above equations is the number of photons  $n$ , although we use the symbol  $I$  throughout the present text.

### 2.3. Other Light Scattering Technologies

Several mature and popular light scattering technologies used in the field of particle characterization (namely laser diffraction, single particle optical counting, photon correlation spectroscopy, and electrophoretic light scattering) are discussed in detail in the following chapters. There are established international or national standards (Appendix II) and commercial instrument manufacturers (Appendix III) for these broadly employed technologies. In this section, several other light scattering technologies which are less widely used

are briefly described. Some of these technologies have been commercialized and have various research and practical applications. Major references are listed so readers can find more details or the latest developments regarding a particular technology.

### 2.3.1. STATIC LIGHT SCATTERING – ABSOLUTE SCATTERING INTENSITY MEASUREMENT

Any measurement of time-averaged scattering intensity falls into a category known as static light scattering (which includes laser diffraction, discussed in detail in Chapter 3). We limit the content of this subsection to the measurements of scattering intensity in order to determine absolute particle mass (molecular weight) and/or other parameters of very small and weak scatterers such as macromolecules and surfactants in solution in non-disturbed (still) solutions or suspensions.

Compared to solid particles, chain molecules have much smaller masses. For example, the mass of a 10 nm solid particle is 50 times larger than that of a straight chain of the same length. Most molecular chains are in the form of coils and so their sizes often are very small when compared with many industrial particles. For these two reasons, scattering from macromolecule solutions often falls into the Rayleigh-Debye-Gans scattering regime. Measurements are performed over a broad angular range using a photoelectron detector. The instrumentation, data collection, and interpretation used in applying the Rayleigh-Debye-Gans theory to macromolecule solutions have been extensively developed and there is an abundant amount of literature regarding various situations, from samples in dilute solution for chain characterization (including molecular weight, radius of gyration, virial coefficient and conformation), to samples in semi-dilute solutions in the study of chain interaction, as well as other topics [10,13]. Most of these studies were performed using a goniometer with a high power laser (a few hundred mW) in academia. Industrial applications and commercial instruments are more focused on the use of the technology as a detection setup connected to a separation devices such as in size exclusion chromatography or field-flow fractionation.

Figure 2.19 shows a schematic of instrumentation used for static light scattering. A static light scattering instrument differs from a laser diffraction instrument in that 1) the intensity is measured over a broader scattering angular range with less attention on extremely small angles; and, 2) the instrument is calibrated for absolute intensity determinations using substances of known scattering intensity.

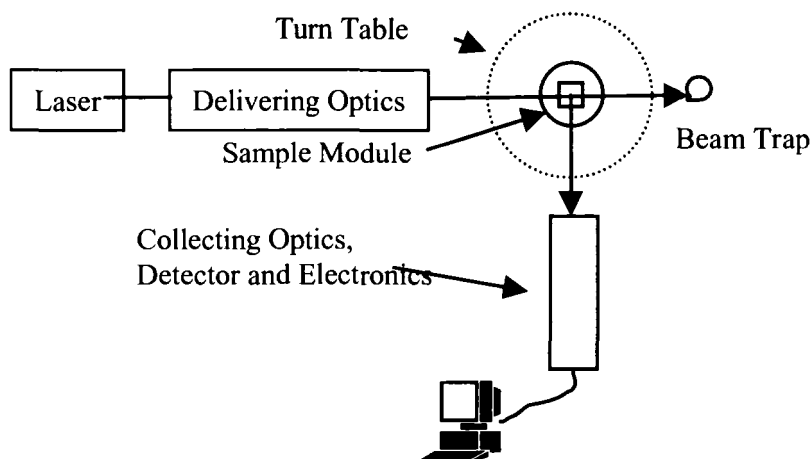


Figure 2.19. Schematic of a static light scattering instrument.

The Rayleigh-Debye-Gans model of scattering predicts that for  $N$  particles in a scattering volume  $V$ , each particle will occupy a volume  $V_p$ ; and the total scattered intensity  $I_s$  from a beam of vertically polarized incident light is the summation of the individual scattering intensities, modified by an additional term that contains a structure factor  $S'(r_{ij})$  that accounts for the inter-particle interaction as shown in Eq. 2.35.

In Eq. 2.35,  $M_i$ ,  $M_w$ ,  $N_A$ ,  $(\partial n/\partial C)_T$ , and  $C$  are the molecular weight of the  $i^{\text{th}}$  particle, the weight-averaged molecular weight of the sample, Avogadro's number, the refractive index increment of the solution due to presence of particles at a constant temperature, and the total particle concentration ( $\text{g}/\text{cm}^3$ ), respectively.  $H$  ( $\text{mole}\cdot\text{cm}^2/\text{g}^2$ ) is an optical constant defined as  $(2\pi n_0(\partial n/\partial C)_T)^2/(\lambda_0^4 N_A)$ .  $S'(r_{ij})$  is the structure factor for a pair of particles separated by a characteristic distance  $r_{ij}$ . Depending on the type of particles and their environment, there are different models of interparticle interaction and consequently different types of structure factors, such as the structure factors for hard spheres, sticky hard spheres, and etc. [68]. The summations apply to all particles separated by different distances in the scattering volume. The depolarized scattered intensity is assumed to be negligible for optically isotropic particles. For non-polarized light, a multiplier  $(1+\cos^2\theta)$  has to be added to the right side of Eq. 2.35.

$$\begin{aligned}
\frac{I_s - I_{\text{medium}}}{I_o V} &= \frac{k_o^4 (m-1)^2}{4\pi^2 V r^2} \left( \sum_{i=1}^N (V_{p,i}^2 P(x_i) + \sum_{j=1}^N V_{p,i} V_{p,j} S'(r_{ij})) \right) \\
&= \frac{4\pi^2 n_o^2 C^2}{\lambda_o^4 r^2 V} \left( \frac{\partial n}{\partial C} \right)_T^2 \left( \sum_{i=1}^N V_{p,i}^2 P(x_i) + \sum_{i=1}^N \sum_{j=1}^N V_{p,i} V_{p,j} S'(r_{ij}) \right) \\
&= \frac{HC}{r^2} \frac{\sum_{i=1}^N M_i^2 P(x_i) + \sum_{i=1}^N \sum_{j=1}^N M_i M_j S'(r_{ij})}{\sum_{i=1}^N M_i} \quad (2.35) \\
&= \frac{HC \bar{M}_w}{r^2} \cdot \frac{\sum_{i=1}^N M_i^2 P(x_i) + \sum_{i=1}^N \sum_{j=1}^N M_i M_j S'(r_{ij})}{\sum_{i=1}^N M_i^2}.
\end{aligned}$$

In studies of macromolecules or small particles in solution or suspension, the excess Rayleigh ratio is often used to characterize the absolute scattered intensity. The excess Rayleigh ratio is defined as:

$$\mathcal{R}_{\text{ex},p} = \frac{(I_s - I_{\text{medium}}) r^2}{I_o V}. \quad (2.36)$$

In an experiment, the excess Rayleigh ratio can be obtained by comparing the sample scattering intensity with the scattering of a substance of known Rayleigh ratio, such as cyclohexane, toluene or benzene [22]; e.g.,

$$\mathcal{R}_{\text{ex},p} = \frac{(I_s - I_{\text{medium}})}{I_{\text{cyclohexane}}} \mathcal{R}_{\text{ex,cyclohexane}}. \quad (2.37)$$

In experimental data analysis, the reciprocal of Eq. 2.35 is more often used:

$$\begin{aligned}
 \frac{HC}{\mathcal{R}_{ex,p}} &= \frac{1}{\bar{M}_w \bar{P}_z(x)} \left( 1 + \frac{\sum_{i=1}^N \sum_{j=1}^N M_i M_j S'(r_{ij})}{\bar{P}_z(x) \sum_{i=1}^N M_i^2} \right)^{-1} \\
 &= \frac{1}{\bar{M}_w} \left( 1 + \frac{K^2 \bar{R}_{gz}^2}{3} \right) - \frac{NS'(r)}{\bar{M}_w \bar{P}_z(x)} = \frac{1}{\bar{M}_w} \left( 1 + \frac{K^2 \bar{R}_{gz}^2}{3} \right) + 2A_2 C.
 \end{aligned}
 \tag{2.38}$$

The second equality in Eq. 2.38 is an approximation valid when both  $K^2 \bar{R}_{gz}^2$  and the term related to the structure factor are small and assuming  $S'(r_{ij})$  is invariant for different particles, both of which are true when dealing with small particles at small angles and in very dilute concentration. The third equality is obtained using the relation between the second virial coefficient  $A_2$  and the structure factor [36]. In the above equations  $\bar{M}_w$ ,  $\bar{R}_{gz}^2$  and  $\bar{P}_z$  are the weight-averaged molecular (particle) weight, the z-averaged square of the radius of gyration, and the z-averaged scattering factor, respectively. The number-averaged, weight-averaged, and z-averaged parameters are defined by Eq. 2.39 when  $k = 0, 1, 2$ , respectively. One should compare these definitions with the definitions in Section 1.3.3.

$$\bar{x}_k = \frac{\sum_{i=1}^N M_i^k x_i}{\sum_{i=1}^N M_i^k} = \frac{\sum_i n_i M_i^k x_i}{\sum_i n_i M_i^k}.
 \tag{2.39}$$

According to Eq. 2.38, through measurement of the scattering intensities at different concentrations and over different angles, the second virial coefficient and the z-averaged square of the radius of gyration can be obtained from the slopes of scattering intensity plotted as a function of concentration or scattering angle, respectively. The weight-averaged molecular weight can then be obtained from the common intercept of these plots.

For optically anisotropic but symmetric particles, Eq. 2.38 needs to be modified to take into account two of the principal scattering elements, polarizabilities  $\alpha$  and  $\beta$  [91]:

$$\frac{HC}{\mathcal{R}_{ex,p}} = \left(1 + \frac{4\delta^2}{5}\right)^{-2} \left\{ \frac{1}{\overline{M}_w} \left[ \left(1 + \frac{4\delta^2}{5}\right) + \frac{K^2 \overline{R}_{gz}^2}{3} \left(1 - \frac{4\delta}{5} + \frac{4\delta^2}{7}\right) \right] + 2A_2C \right\}. \quad (2.40)$$

In Eq. 2.40,  $\delta$  is the intrinsic anisotropy factor defined as  $\delta=(\alpha-\beta)/(\alpha+2\beta)$ . For random coils, the scattering factor has an asymptotic limit of  $P(x) = 2/x^2 - 2/x^4$  when  $x^2 (= (KR_g)^2 = MK^2 l_k^2 / (6m_o))$  is very large, ( $l_k$ ,  $M$ , and  $m_o$  being the segment length, molecular weight of coil and molecular weight of each segment, respectively). From the linear extrapolation to  $K \rightarrow 0$  of the plot of  $HC/\mathcal{R}_{ex,p}$  versus  $K^2$  at high  $K$  values, the number-averaged molecular weight and the number-averaged square of radius of gyration of the coils (polymer chains) can be obtained as shown by the following equation:

$$\begin{aligned} \frac{HC}{\mathcal{R}_{ex,p}} &= \frac{1}{\overline{M}_w \overline{P}_Z(x)} = \frac{\sum_{i=1}^N M_i}{\sum_{i=1}^N M_i^2 \left( \frac{2}{x_i^2} - \frac{2}{x_i^4} \right)} = \frac{\sum_{i=1}^N M_i}{\frac{12 m_o}{K^2 l_k^2} \left( \sum_{i=1}^N M_i - \sum_{i=1}^N \frac{6 m_o}{K^2 l_k^2} \right)} \\ &= \left( \frac{12 m_o}{K^2 l_k^2} \left[ 1 - \frac{6 m_o}{K^2 l_k^2 \overline{M}_n} \right] \right)^{-1} \cong \frac{K^2 l_k^2}{12 m_o} \left( 1 + \frac{6 m_o}{K^2 l_k^2 \overline{M}_n} \right) = \frac{K^2 l_k^2}{12 m_o} + \frac{1}{2 \overline{M}_n} \quad (2.41) \\ &= \frac{K^2 \overline{R}_{gn}^2}{12 \overline{M}_n} + \frac{1}{2 \overline{M}_n}. \end{aligned}$$

One well-known technique used in data reduction from the angular intensity measurements of solutions of different concentrations is the Zimm plot [92]. In the Zimm plot,  $HC/\mathcal{R}_{ex,p}$  (the left side of Eq. 2.38) is plotted against  $\sin^2(\theta/2) + K'C$ . The angular patterns of solutions of different concentrations are thus effectively spread out.  $K'$  is an arbitrary constant. Two systems of lines form a grid-like plot. One represents the angular dependence at constant concentration (the angular pattern for each sample.) The other is the concentration dependence at a given scattering angle. These systems of lines are extrapolated to zero angle or zero concentration, respectively. The individual points of the extrapolated dependence can be obtained according to Eq. 2.38. For example,  $HC/\mathcal{R}_{ex,p}(\theta_2)$  corresponding to the angle  $\theta_2$  and zero concentration has an abscissa of  $\sin^2(\theta_2/2)$ . Thus, on the extrapolated part of the concentration dependence of  $HC/\mathcal{R}_{ex,p}(\theta_2)$ , the point with the abscissa  $\sin^2(\theta_2/2)$  may be found (the symbol \* in Figure 2.20). After the same is done for all angles, these newly found points are connected and extrapolated to zero angle. The point at the



ordinate is the value  $HC/\mathcal{R}_{\text{ex,p}}(0)|_{c=0}$ . A similar process is done for the angular extrapolation. Another line connecting extrapolated zero-angle points at different concentrations forms another extrapolation to the ordinate, meeting at the same point  $HC/\mathcal{R}_{\text{ex,p}}(0)|_{c=0}$ . From the slopes and intercepts in the Zimm plot,  $\overline{M}_w$ ,  $R_{g,z}^2$ , and  $A_2$  of the sample can be obtained using Eq. 2.38.

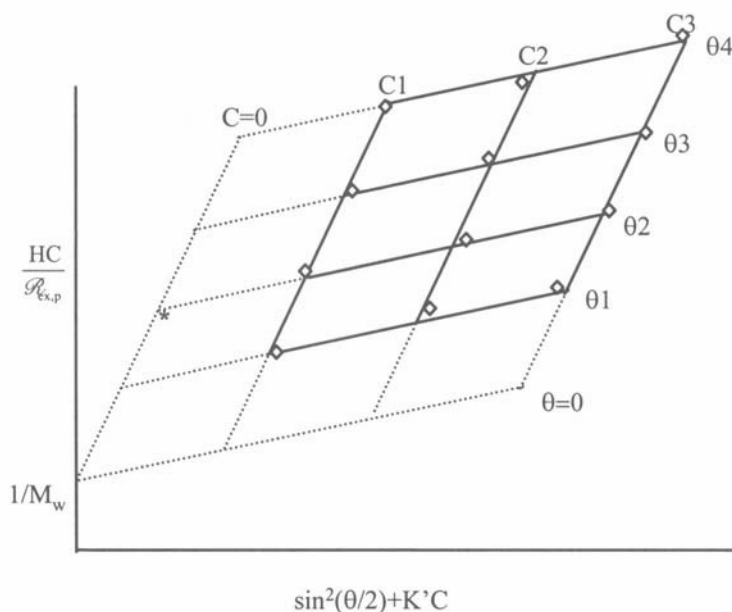


Figure 2.20. A typical Zimm plot.

### 2.3.2. FOCUSED BEAM REFLECTANCE

This is a single particle measurement technique. As shown in Figure 2.21, a laser beam is collimated and focused to a point. A mechanical device rotates the beam in a circular path. As the focal point intersects a particle, the particle scatters light back into a probe that transmits this back-scattering to a photodetector, generating a pulse. The duration and frequency of the pulse are indications of the length of particle intersecting the beam (called the cord length) and the number of particles. As long as the particle motion is significantly slower than the speed of beam rotation, the particles can be treated as if they were stationary. A circuit can be designed to reject or ignore the signals from particles that pass through the beam but do not exactly cross the focal point, and this circuit will count only the particles that intersect the focal point. From the rotational speed and the pulse width, a cord length can be

calculated from each pulse. Since the intersection of the beam with a particle can occur at any section on the particle, there are many possible traversing paths the beam may take. Cord lengths in most cases are not the same as the particle dimension. As an example, for a sphere, it is only when the beam crosses the particle center that the cord length will be equal to the diameter, assuming the beam rotating circle is much larger than the particle. All other paths will result in cord lengths smaller than the diameter. The cord length distribution obtained by this technique is related to the size distribution but is affected by many other factors. This may or may not represent the true size distribution, even for spherical particles. The technology is mainly used in on-line measurement for quality control purposes where the cord length distribution is used only to monitor changes for comparison with control materials. Still, the true size distribution may be correlated to the cord length distribution for a given sample [93,94,95].

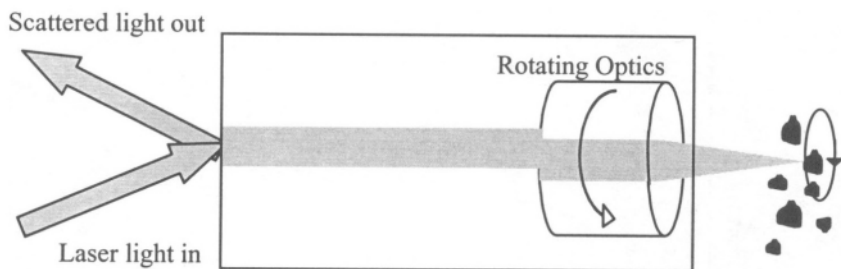


Figure 2.21. Schematic of Focused Beam Reflectance measurement.

### 2.3.3. TIME-OF-FLIGHT (TOF) MEASUREMENT

In particle size analyses using the TOF method, high-pressure air transports predispersed particles through a converging nozzle that is surrounded by sheath air. Particles are accelerated by the sheath flow to near supersonic speeds within a barrel shock envelope. Particles of different masses will be accelerated differently. Two laser beams separated by a known distance detect individual particles when the particles pass through the two beams consecutively. As particles pass through the beam they scatter light which is collected and converted to electrical signals by two photomultiplier tubes. One tube detects light as the particle passes through the first beam and the other tube detects light scattered as the particle passes through the second beam. Using the cross correlation technique the time difference between the light pulses detected at the two detectors indicates the time-of-flight, which is related to some particle dimension. The sampling rate can be as high as 100,000 particles per second. The individual sizing capability provides a high-resolution particle size

distribution of powders over a broad size range (0.2-700  $\mu\text{m}$ ). However, high counting efficiency can only be achieved for large particles (e.g., for particles larger than 7  $\mu\text{m}$ ) at low sampling rates ( $< 20,000$  particles/sec). For small particles at high sampling rates, non-linear response and low counting efficiency will produce erroneous particle counts and a distorted size distribution [96,97].

#### 2.3.4. TIME-OF-TRANSITION (TOT) MEASUREMENT

This technology is similar to *focused beam reflectance* in that it uses a rotating beam to scan a dilute air or liquid suspension in which particles are presented and intercepted by the beam as shown in Figure 2.22.



Figure 2.22. Schematic of TOT measurement.

Unlike focused beam reflectance, in which particles are detected through the reflection of the rotating beam by the sample, in this technology particles are detected by a large area photodiode through the change in transmission of the rotating beam. Optical pulse widths represent the cord lengths of particles intercepting the beam. When the beam spot size (typically a few  $\mu\text{m}$ ) is much smaller than the particle dimension and the beam rotational velocity is much faster than the motion of the particles, one can separate pulses that are produced when the beam's focal point transits across the centers of particles from pulses that are generated from particles that are intercepted either off-center or out of focus. This discrimination is achieved by distinguishing the shape and amplitude of pulses of different origins. After excluding these pulses not from particles transiting across their centers at the focus of beam, the pulse width distribution will be closely related to a true particle diameter distribution with the assumption that the particles are spherical in the size range from  $\sim 0.5 \mu\text{m}$  to  $\sim 1 \text{ mm}$ . Particle size distributions obtained using this method will exhibit high resolution because there are no multiple particle interactions. However, due to the high exclusion rate of pulses, the analysis is relatively slow in the case of samples having broad distributions [98].

### 2.3.5. TURBIDIMETRY

In a turbidity measurement a spectrophotometer is used to measure the attenuation of light as a function of wavelength as it passes through a sample. Conventional spectrophotometers use a single photo-detector to sequentially record light transmission at various wavelengths through either manual or automatic wavelength scans. The latest fiber-optic spectrophotometers use an optical fiber to carry the entire transmission spectrum to a miniaturized grating device, after which the spectrum is recorded by a photodetector array. All the recording components may be mounted on a single circuit board that can be installed inside a PC.

Variations in attenuation or transmission are the result of the scattering and absorption of the incident light at different wavelengths by particles. The turbidity  $\tau(\lambda)$  measured at a given wavelength  $\lambda$  for a number particle size distribution  $N(d)$  per unit volume is defined as the intensity attenuation after transmission of the incident beam through a known length of a suspension ( $l$ ) [8],

$$\tau(\lambda) = \frac{1}{l} \ln \left( \frac{I_o(\lambda)}{I(\lambda)} \right) = \left( \frac{\pi}{4} \right) \int_0^{\infty} Q_{ex}(\lambda, m, d) d^2 N(d) dd = \frac{2\lambda^2}{\pi} \int_0^{\infty} \text{Re}(S_1(0)) N(d) dd \quad (2.42)$$

where  $Q_{ex}(\lambda, m, d)$  is the extinction efficiency of particles of diameter  $d$ . The third equality is derived from Mie theory at  $\theta = 0$  where  $S_1(0) = S_2(0)$ . To resolve  $N(d)$ , algorithms similar to the ones described in Section 3.3.2, e.g., the assumed functional form [99], an iteration algorithm [100,101], or a matrix conversion algorithm [20] can be used, provided that  $m(\lambda)$  is known for the experimental wavelengths [102,103]. Turbidity measurements can also be used to determine sample concentration if mean particle size ( $\bar{D}_{3,2}$ ) is known.

In Eq. 2.43,  $\bar{Q}_{ex}$ ,  $C$ ,  $p$  are the mean extinction efficiency, the concentration in g/ml, and the particle density, respectively. The second equality is obtained according to the definitions of  $\bar{Q}_{ex}$ ,  $\bar{D}_{3,2}$  and  $C$ . If there is no absorption at a given wavelength  $\bar{Q}_{ex}$  is equal to  $\bar{Q}_{sca}$ .  $\bar{Q}_{sca} / \bar{D}_{3,2}$  is a function of  $\bar{D}_{3,2}$  which is independent of the form of the particle size distribution and this can be found in the literature [104]. Therefore,  $C$  can be derived from a measurement of  $\tau(\lambda)$ . In submicron region,  $\tau(\lambda)$  can be used sensitively to detect a trace amount of large particles in a majority of small particles [105].

$$\tau(\lambda) = \frac{\left(\frac{\pi}{4}\right) \int_0^{\infty} Q_{\text{ex}}(\lambda, m, d) d^2 N(d) dd \cdot \int_0^{\infty} d^2 N(d) dd}{\int_0^{\infty} d^2 N(d) dd \cdot \int_0^{\infty} d^3 N(d) dd} \cdot \int_0^{\infty} d^3 N(d) dd$$

$$= \left(\frac{\pi}{4}\right) \frac{\overline{Q}_{\text{ex}}(\lambda, m) 6C}{\overline{D}_{3,2} \rho \pi} = \frac{3\overline{Q}_{\text{ex}}(\lambda, m) C}{2\overline{D}_{3,2} \rho}.$$
(2.43)

In turbidity measurements, refractive index as a function of wavelength is the variable used in size analyses. Therefore, if the measurement is extended into the near UV region ( $\lambda < 400$  nm) both the real and imaginary refractive indices (as a function of wavelength) have to be known, even for colorless materials. Precise determination of  $m(\lambda)$  presents a real challenge and remains a barrier in the use of turbidity measurement for sizing many materials. Recently, in the effort to further extend the capability of turbidimetric measurement, spectra have been measured at other scattering angles in addition to the transmission path, e.g., measurements made in three dimensions covering both wavelength and scattering angle variation. The dynamic range that can be achieved by a change in the probe length  $K^{-1}$  (Eq. 2.4) from wavelength change is much smaller than that from scattering angle change. For example, in an angular measurement from  $\theta = 1^\circ$ - $90^\circ$ , the scattering vector  $K$  will change by a factor of eighty, while changing the wavelength from  $\lambda = 0.2$ - $1 \mu\text{m}$ ,  $K$  will change only by a factor of five. The combination of both wavelength and scattering angle variation can further extend the dynamic range of turbidity measurement and provides the possibility of obtaining more accurate sizing results in the submicron range [106].

### 2.3.6. BACK SCATTERING MEASUREMENT

Along with the ever increasing demand for on-line or in-line particle characterization in process control, requests for direct measurements of particles in pipelines or reactors are on the rise. In process control, any bias of the characterization method or precise physical meaning of the parameters determined are not of the utmost importance. Robustness, reliability, and precision of measurement are often the primary concerns. Besides focused beam reflectance and fiber optical PCS probe, back scattering intensity measurement is among the optical techniques preferred for in-process measurement due to the obvious reasons that when the concentration of a suspension is high, the

transmission or small angle scattering diminishes, so that only back scattering is accessible and setups for back scattering measurement are practically simple and easy.

Detection of back scattering can be accomplished either using a CCD camera to record back scattering images or by a PMT mounted on a translation stage to record angular scattering patterns, from which an intensity distribution (back scattering central lobe width) is analyzed [107]. Various fiber optic probes consisting of both illumination fibers and reception fibers are used to measure the scattering intensity at a particular angle (or over a narrow angular range) [108]. Light intensity back scattered from individual particles follows the same theories described previously when the scattering angle typically larger than  $165^\circ$ . However, when detecting scattering directly (i.e., without dilution) from samples in pipelines or reactors, particle concentration is usually much higher than what is required in single particle scattering. Multiple scattering is then always the dominant phenomenon, and particle interaction is also another prevailing factor. Therefore, to directly measure particle size is not a trivial task. In either setup (using a CCD camera or fiber probes), particle size information can only be obtained indirectly, and the apparent size values may have to be calibrated or correlated with the *real* values measured in dilute suspensions.

### 2.3.7 FREQUENCY DOMAIN PHOTON MIGRATION (FDPM)

In an FDPM measurement, a sinusoidally modulated light is launched into the scattering medium as a single point source and the multiply modulated and scattered light is detected at another point some distance away from the source. Due to scattering and absorption of the sample, the photon density wave is attenuated and phase-shifted relative to the incident light as it propagates through the scattering medium (Figure 2.23). The isotropic scattering coefficient  $\mu_s'$  can be fit from the phase shift  $\Delta\theta$  (and modulation  $M$ ) to the appropriate solution of optical diffusion approximation describing the transport of light in random media (Eq. 2.44) using different modulation of light at different wavelengths [51,109]:

$$\Delta\theta(\lambda) = -\frac{|l|}{\sqrt{c}} \sqrt{3(\mu_s'(\lambda) + \mu_a(\lambda)) \{(\mu_a(\lambda)c)^2 + \omega^2\}^{1/2}} \sin\left(\frac{1}{2} \tan^{-1}\left(\frac{\omega}{\mu_a(\lambda)c}\right)\right). \quad (2.44)$$

In Eq. 2.44,  $l$ ,  $\mu_a(\lambda)$ ,  $c$ ,  $\omega$  are the distances between the points of light source and detector, the absorption coefficient, the speed of light, and the modulation frequency, respectively. The particle size distribution  $q(d)$  and volume fraction  $(\phi)$  can then be determined using Eq. 2.45:

$$\mu'_s(\lambda) = \int_0^\infty \frac{3Q_{sca}(n, d, \lambda)}{2d} (1 - g(n, d, \lambda)) \phi q(d) dd \quad (2.45)$$

where  $Q_{sca}$  and  $g$  are scattering efficiency of a sphere and the average cosine of the scattering angle of radiation. Although this technique is still in its developmental stage, it has been demonstrated through using a number of model systems that it is a feasible alternative for on-line monitoring or controlling particle size distribution in concentrated suspensions.

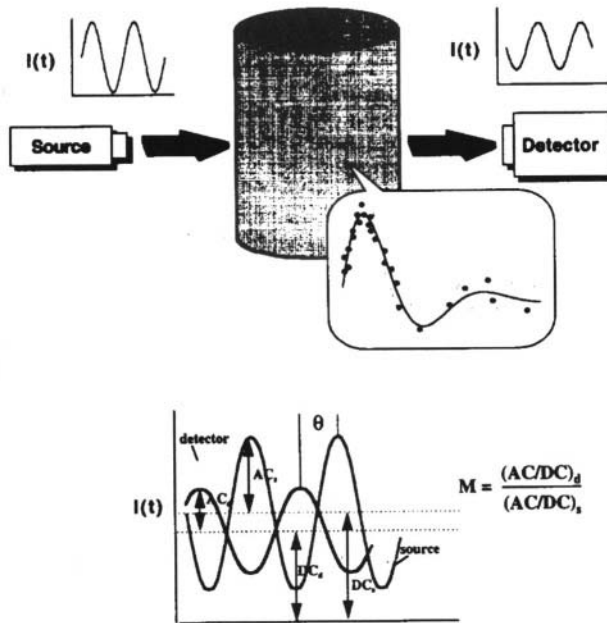


Figure 2.23. Schematic of FDPM measurements [51] (by permission of Wiley-VCH Verlag GmbH).

### 2.3.8. PHASE DOPPLER ANEMOMETRY (PDA)

Phase Doppler anemometry or phase Doppler analysis was proposed two decades ago, based on the then well-established flow measurement technology-laser Doppler velocimetry [110]. PDA is widely used in sizing spherical and homogeneous particles, such as liquid sprays, aerosols, air bubbles in liquid, or other spherical particles. When single particles move through the intersection of at least two focused laser beams, they scatter light from each beam with different individual Doppler frequency shifts. Multiple detectors are placed at

well-chosen locations. The superposition of the Doppler-shifted frequencies on any of the detectors yields a detectable Doppler burst whose frequency is linearly proportional to particle velocity. The phase delay between the Doppler signals from different detectors in a fixed instrument configuration is, for spheres, a direct measure of particle diameter. The technology simultaneously measures the diameter and flow velocity, as well as mass flux and concentration of moving individual particles without the need of calibration. A PDA measurement is not based on the scattered light intensity and thus is not subject to errors from beam alternation or deflection, which occur in dense particles and combustion environments. The sizing range can be adjusted depending on the optical configuration. A 50:1 dynamic range with sizing accuracy of 1% can be achieved for a chosen configuration. The overall sizing range of a commercial instrument can cover more than four orders of magnitude typically from 0.5 to 10,000  $\mu\text{m}$ .

In a PDA measurement, the relationship between the phase difference of the signals collected from different detectors and particle dimension is usually derived based on geometric ray tracing for smooth spheres with known refractive indices. As shown in Figure 2.24, the intensity of the incident light, upon encountering a sphere that has a different refractive index as that of the medium is partly reflected and partly refracted. Reflection and refraction, (collectively termed the scattering mode), can occur multiple times. The intensity ratios between multiple reflection and refraction depend on the incident angle, the polarization and the relative refractive index and are given by the Fresnel coefficients. Most of the intensity is contained in the first three scattering modes. The reflection and refraction angles are governed by Snell's law. Their relative phases are related to the optical pathlengths of the ray, which are related to the sphere diameter. Because there are many scattering modes, in order to establish a linear relationship between the measured phase difference and particle diameter, the detectors have to be such positioned so that only one scattering mode dominates. Otherwise the ambiguity in the phase-diameter relationship will be present due to simultaneous detection of different scattering modes of comparable intensity.



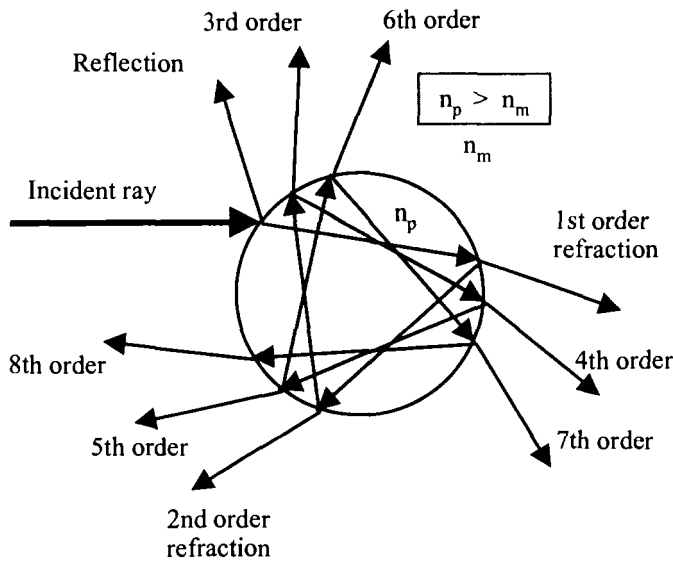


Figure 2.24. Scattering modes of a sphere.

At the present capacity PDA is mainly applied to smooth spheres that have a diameter much larger than the wavelength of light. Explorations into applying PDA to spheroids, rough surface particles, and submicron spheres can be found in the recent literature [111,112,113,114]. Current developments in PDA instrumentation include the placing of a pair of detectors at the scattering plane (the planar detectors), in addition to the off-axis detectors in the conventional PDA configuration [115]; replacing conventional photodetectors with a charge-coupled device (CCD) line scan sensor to improve temporal and spatial resolution [116]; and an innovative electronic design that involves signal burst detection, multi-bit sampling, frequency-band narrowing and phase signal validation [117]. Figure 2.25 shows a dual-mode PDA that minimizes or eliminates several unavoidable errors, such as errors due to trajectory and slit effects that commonly exist in the conventional PDA configuration, provides the ability to reject non-spherical particles, and produces high resolution and more accurate sizing results due to the addition of the planar detectors.

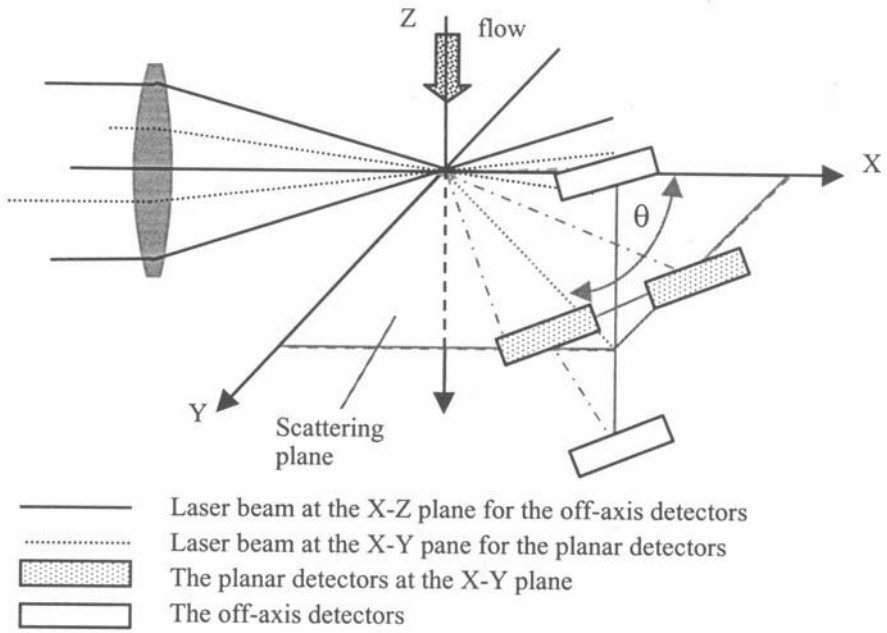


Figure 2.25. Schematic of the dual-mode PDA.

## REFERENCES

- 1 Wyatt, C. L., *Radiometric System Design*, MacMillan Publishing Co., New York, 1987.
- 2 Tyndall, J., On the Blue Colour of the Sky, the Polarization of the Skylight and on the Polarization of Light by Cloudy Matter Generally, *Phil. Mag.*, 1869, 37, 384-394.
- 3 Strutt, J. W. (Baron Rayleigh), On the Light from the Sky, its Polarization and Color, *Phil. Mag.*, 1871, 41, 107-120.
- 4 Lorenz, L. V., *Oeuvres Scientifiques de L. Lorenz. Revues et Annotées par H. Valentiner*, Lehmann & Stage, Copenhagen, 1898.
- 5 Mie, G., Contributions to the Optics of Turbid Media, Especially Colloidal Metal Suspensions, *Ann. Physik*, 1908, 25, 377-455.
- 6 Debye, P., *Ann. Physik*, 1909, 30, 755.
- 7 Einstein, A., Theory of the Opalescence of Homogeneous and of Mixed Liquids in the Neighborhood of the Critical Region, *Ann. Physik*, 1910, 33, 1275-1298.
- 8 Van de Hurst, H. C., *Light Scattering by Small Particles*, Dover Publications, New York, 1981.
- 9 Kerker, M., *The Scattering of Light and other electromagnetic radiation*. Academic Press, New York, 1969.
- 10 *Light Scattering from Polymer Solutions*, Ed. Huglin, M. B., Academic Press, New York, 1972.
- 11 *Light Scattering by Irregular Shaped Particles*, Ed. Shuerman, D. W., Plenum Press, New York, 1980.
- 12 Bohren, C., Huffman, D., *Absorption and Scattering of Light by Small Particles*, John Wiley & Sons, New York, 1983.
- 13 Kratochvil, P., *Classical Light Scattering from Polymer Solution*, Elsevier, Amsterdam, 1987.
- 14 *Single Particle Optical Counter: Principle and Application, Aerosol Generation, Measurement, Sampling, and Analysis*, Ed. Liu, B. Y. H., Academic Press, New York, 1976.
- 15 Monnier, O., Klein, J. P., Hoff, C., Ratsimba, B., Particle Size Determination by Laser Reflection, Methodology and Problems, *Part. Part. Syst. Charact.*, 1996, 13, 10-17.
- 16 Reichel, A., Gerber, M., Schwartz, F. H., Waggeling, R., A New System to Measure the Particle Size within Highly Concentrated Multiphase Medium: In-Line Visualization of Particular Changes, in *Proc. 7<sup>th</sup> European Symp. Part. Charact.*, Nürnberg, 1998, pp.1227-1236.
- 17 Weiner, B. B., Tscharnuter, W. W., Karasikov, N., Improvements in Accuracy and Speed Using the Time-of-Transition Method and Dynamic Image Analysis for Particle Sizing, in *Particle Size Distribution III*, Ed. Provder, T., ACS Symp. Series 693, American Chemical Society, Washington D.C., 1998, Chpt.8, pp.88-102.
- 18 Niven, R. W., Aerodynamic Particle Size Testing Using a Time-of-Flight Aerosol Beam Spectrometer, *Pharm. Tech.*, 1993, 17, 71-78.
- 19 Thorwirth, G., Optical Spatial Frequency Analysis Principle and Results, *Jena Review*, 1990, 2, 95-97.
- 20 Brandolin, A., Garcia-Rubio, L. H., Provder, T., Kohler, M., Kuo, C., Latex Size Distribution from Turbidimetry Using Inversion Techniques: Experimental Validation, in *Particle Size Distribution II*, Ed. Provder, T., ACS Symp. Series 472, American Chemical Society, Washington D.C., 1991, Chpt.2, pp. 15-30.
- 21 Jennings, B. R., Electric Field Light Scattering, in *Molecular Electro-Optics Vol. I*, Ed. O'Konski, C. T., Dekker, 1976, Chpt.8, pp.275-319.
- 22 Baloch, K. M., van de Ven, T. G. M., Transient Light Scattering of Suspensions of Charged Non-spherical Particles Subjected to an Electrical Field, *J. Colloid Interface Sci.*, 1989, 129, 90-104.

- 
- 23 Pohl, D. W., Schwaz, S. E., Irmiger, V., Forced Rayleigh Scattering, *Phys. Rev. Lett.*, 1973, 31, 32-35.
  - 24 Rossmanith, P., Köhler, W., Polymer Polydispersity Analysis by Thermal Diffusion Forced Rayleigh Scattering, *Macromolecules*, 1996, 29, 3203-3211.
  - 25 Pasternack, R. F., Collings, P., Resonance Light Scattering: a New Technique for Studying Chromophore Aggregation, *Science*, 1995, 269, 935-939.
  - 26 Van Dilla, M. A., Dean, P. N., Laerum, O. D., Melamed, M. R., *Flow Cytometry: Instrumentation and Data Analysis*, Academic Press, New York, 1985.
  - 27 Chernyshev, A. V., Prots, V. I., Doroshkin, A. A., Maltsev, V. P., Measurement of Scattering Properties of Individual Particles with a Scanning Flow Cytometer, *App. Opt.*, 1995, 34, 6301-6305.
  - 28 Salzman, G. C., Singham, S. B., Johnston, R. G., Bohren, C. F., Light Scattering and Cytometry, in *Flow Cytometry and Sorting*, Eds. Melamed, M. R. Lindmo, T., Mendelsohn, M. L., Wiley-Liss, New York, 1990, Chpt.5, pp.651-668.
  - 29 Hess, C. F., Characteristics of a Miniaturized Probe Employing the Pulse Displacement Technique, *Part. Part. Syst. Charact.*, 1997, 14, 129-137.
  - 30 Berne, B. J., Pecora, R., *Dynamic Light Scattering*, John Wiley & Sons, New York, 1976.
  - 31 *Photon Correlation and Light Beating Spectroscopy*, Eds. Cummins, H. Z., Pike, E. R., Plenum Press, New York, 1974.
  - 32 *Dynamic Light Scattering: Applications of Photon Correlation Spectroscopy*, Ed. Pecora, R., Plenum Press, New York, 1985.
  - 33 *Photon Correlation Spectroscopy and Velocimetry*, Eds. Cummins, H. Z., Pike, E. R., Plenum Press, New York, 1977.
  - 34 *Scattering Techniques Applied to Supramolecular Systems*, Eds. Chen, S.-H., Chu, B., Nossal, R., Plenum Press, New York, 1981.
  - 35 *Measurement of Suspended Particles by Quasi-elastic Light Scattering*, Ed. B. Dahneke, Wiley Interscience, New York, 1983.
  - 36 Schmitz, K., *An Introduction to Dynamic Light Scattering by Macromolecules*, Academic Press, New York, 1990.
  - 37 *Quasielastic Light Scattering by Macromolecular, Supramolecular, and Fluid Systems*, Ed. Chu, B., SPIE Milestone Series Vol. MS 12, SPIE Optical Engineering Press, Washington D. C., 1990.
  - 38 Chu, B., *Laser Light Scattering: Basic Principles and Practice*, 2nd Ed. Academic Press, New York, 1991.
  - 39 *Dynamic Light Scattering: the Method and Some Applications*, Ed. Brown, W., Oxford Science Publications, London, 1993.
  - 40 *Light Scattering and Photon Correlation Spectroscopy*, Eds. Pike, R., Abbiss, J. B., NATO ASI Ser. 3-40, Kluwer Academic Publishers, 1997.
  - 41 Ware, B. R., Haas, D. D., Electrophoretic Light Scattering, in *Fast Methods in Physical Biochemistry and Cell Biology*, Eds. Sha'afi, R. I., Fernandez, S. M., Elsevier, New York, 1983, Chpt.8, pp.173-220.
  - 42 Plantz, P. E., Ultrafine Particle Size Measurement in the Range 0.003 to 6.5 micrometers Using the Controlled Reference Method, in *Particle Size Distribution III*, Ed. Provder, T., ACS Symp. Series 693, American Chemical Society, Washington D.C., 1998, Chpt.9, pp.103-129.
  - 43 Durst, F., Zaré, M., Laser Doppler Measurements in Two-phase Flows, in *Proc. LDA Symp.*, Copenhagen, 1975, pp.403-429.
  - 44 Bachalo, W. D., Method for Measuring the Size and Velocity of Spheres by Dual-Beam Light-Scatter Interferometer, *Appl. Opt.*, 1980, 19, 363-370.

- 45 Bauckhage, K., Flögel, H. H., Simultaneous Measurement of Droplet Size and Velocity in Nozzle Sprays, in *Proc. 2<sup>nd</sup> Int. Symp. Application of Laser Anemometry to Fluid Mechanics*, Lisbon, 1984, pp.18.1.1-18.1.6.
- 46 Saffman, M., Buchhave, P., Tanger, H., Simultaneous Measurements of Size, Concentration and Velocity of Spherical Particles by a Laser Doppler Method, in *Laser Anemometry in Fluid Mechanics-II*, Eds. Adrian, R. J., et al., Ladoan, Lisbon, 1986, pp.85-104.
- 47 Bachalo, W. D., The Phase Method: Analysis and Application, in *Optical Sizing*, Eds. Gouesbet, G., Gréhan, G., Plenum Press, New York, 1988, pp.283-299.
- 48 Hirleman, E. D., History of Development of the Phase-Doppler Particle-sizing Velocimeter, *Part. Part. Syst. Charact.*, 1996, 13, 59-67.
- 49 Miller, J. F., Schätzel, K., Vincent, B., the Determination of Very Small Electrophoretic Mobilities in Polar and Nonpolar Colloidal Dispersions Using Phase Analysis Light Scattering, *J. Colloid Interface Sci.*, 1991, 143, 532-554.
- 50 Eppmann, P., Pruger, B., Gimsa, T., Particle Characterization by AC Electrokinetic Phenomena.2. Dielectrophoresis of Latex Particles Measured by Dielectrophoretic Phase Analysis Light Scattering (DPPALS), *Colloids Surf. A.*, 1999, 149, 443-449.
- 51 Richter, S. M., Shinde, R. R., Balgi, G. V., Sevick-Muraca, E. M., Particle Sizing Using Frequency Domain Photon Migration, *Part. Part. Syst. Charact.*, 1998, 15, 9-15.
- 52 Ho, K., Ooi, S., Nishi, N., Kimura, Y., Hayakawa, R., New Measurement Method of the Autocorrelation Function in the Quasi-elastic Light Scattering with the Sinusoidal Elastic Field, *J. Chem. Phys.*, 1994, 100, 6098-6100.
- 53 Dahneke, B. E., Huchins, D. K., Characterization of Particles by Modulated Dynamic Light Scattering. I. Theory, *J. Chem. Phys.*, 1994, 100, 7890-7902.
- 54 Huchins, D. K., Dahneke, B. E., Characterization of Particles by Modulated Dynamic Light Scattering. II. Experiment, *J. Chem. Phys.*, 1994, 100, 7903-7915.
- 55 Schrof, W., Klingler, J. F., Rozouvan, S., Horn, D., Raman Correlation Spectroscopy: a Method for Studying Chemical Composition and Dynamics of Disperse Systems, *Phys. Rev. E: Stat. Phys. Plasmas. Fluids, Relat. Interdiscip. Top.*, 1998, 57(3-A), R2523-2526.
- 56 Corbin, F., Gréhan, G., Gouesbet, G., Maheu, B., Interaction between a Sphere and a Gaussian Beam: Computations on a Micro-Computer, *Part. Part. Syst. Charact.*, 1988, 5, 103-108.
- 57 Gouesbet, G., Maheu, B., Gréhan, G., Light Scattering from a Sphere Arbitrarily Located in a Gaussian Beam Using Bromwich Formulation, *J. Opt. Soc. Am. A.* 1988, 5, 1427-1443.
- 58 Gouesbet, G., Generalized Lorenz-Mie Theory and Application, *Part. Part. Syst. Charact.*, 1994, 11,22-34.
- 59 Gouesbet, G., Mees, L., Gréhan, G., Ren, K. F., The Structure of Generalized Lorenz-Mie Theory for Elliptical Infinite Cylinders, *Part. Part. Syst. Charact.*, 1999, 16, 3-10.
- 60 Perrin, F., Polarization of Light Scattered by Isotropic Opalescent Media, *J. Chem. Phys.* 1942, 10, 415-427.
- 61 Asano, S., Light Scattering Properties of Spheroidal Particle, *Appl. Opt.*, 1979, 18, 712-722.
- 62 Xu, R., Improvements in Particle Size Analysis Using Light Scattering, in *Particle and Surface Characterisation Methods*, Eds. Müller, R. H., Mehnert, W., Medpharm Scientific Publishers, Stuttgart, 1997, Chpt.3, pp.27-56.
- 63 For example, <http://atol.ucsd.edu/~pflatau/scatlib/>.
- 64 Kerker, M., Wang, D. S., Giles, C. L., Electromagnetic Scattering by Magnetic Spheres, *J. Opt. Soc. Am.*, 1983, 73, 765-767.
- 65 Bohren, C. F., Light Scattering by an Optically Active Sphere, *Chem. Phys. Lett.*, 1974, 29, 458-462.
- 66 Kaiser, T., Schweiger, G., Stable Algorithm for the Computation of Mie Coefficients for Scattered and Transmitted Fields of a Coated Sphere, *Comput. Phys.*, 1993, 7, 682-686.

- 
- 67 Li, K., Massoli, P., Scattering of Electromagnetic Plane Waves by Radially Inhomogeneous Spheres: a Finely-Stratified Sphere Model, *Appl. Opt.*, 1994, 33, 501-511.
- 68 Pedersen, J. S., Analysis of Small-angle Scattering Data from Colloids and Polymer Solutions: Modeling and Least-squares Fitting, *Adv. Colloid Interface Sci.*, 1997, 70, 171-210.
- 69 Watson, R. M. J., Jennings, B. R., Large Particle Scattering Factor for Flat Particles, *J. Colloid Interface Sci.*, 1991, 142, 244-250.
- 70 Watson, R. M. J., Jennings, B. R., Electric Field Light Scattering: Scattering Factors for Orientated Tabular Particles, *J. Colloid Interface Sci.*, 1993, 157, 361-368.
- 71 Fraunhofer, J., Bestimmung des Brechungs und Farberstreuungsvermögens verschiedener Glasarten, *Gilberts Annalen der Physik*, 1817, 56, 193-226.
- 72 Heffels, C. M. G., On-line Particle Size and Shape Characterization by Narrow Angle Light Scattering, *Ph.D. Thesis*, Delft University of Technology, The Netherlands, 1995.
- 73 Komrska, J., Fraunhofer Diffraction at Apertures in the Form of Regular Polygons, *Optica Acta*, 1972, 19, 807-816.
- 74 Komrska, J., Fraunhofer Diffraction at Apertures in the Form of Regular Polygons II, *Optica Acta*, 1973, 20, 549-563.
- 75 Al-Chalabi, S. A. M., Jones, A. R., Development of a Mathematical Model for Light Scattering by Statistically Irregular Particles, *Part. Part. Syst. Charact.*, 1994, 11, 200-206.
- 76 Brown, D. J., Alexander, K., Cao, J., Anomalous Diffraction Effects in the Sizing of Solid Particles in Liquids, *Part. Part. Syst. Charact.*, 1991, 8, 175-178.
- 77 Sharma, S. K., On the Validity of the Anomalous Diffraction Approximation, *J. Mod. Opt.*, 1992, 39, 2355-2361.
- 78 Kusters, K. A., Wijers, J. G., Thoenes, D., Particle Sizing by Laser Diffraction Spectroscopy in the Anomalous Regime, *Appl. Opt.*, 1991, 30, 4839-4847.
- 79 Xu, R., Particle Size Distribution Analysis Using Light Scattering, in *Liquid and Surface-borne Particle Measurement Handbook*, Eds. Knapp, J. Z., Marber, T. A., Lieberman, A., Marcel Dekker, New York, 1996, Chpt.18, pp.745-777.
- 80 Wriedt, T., A Review of Elastic Light Scattering Theories, *Part. Part. Syst. Charact.*, 1998, 15, 67-74.
- 81 Doicu, A., Wriedt, T., Formulation of the Extended Boundary Condition Method for Three-dimensional Scattering Using the Method of Discrete Sources, *J. Mod. Opt.*, 1998, 45, 199-213.
- 82 Mishchenko, M. I., Travis, L. D., Mackowski, D. W., T-matrix Computations of Light Scattering by Nonspherical Particles: A Review, *J. Quant. Spectrosc. Radiat. Transfer*, 1996, 55, 535-575.
- 83 Taflove, A., *Computational Electrodynamics: the Finite Difference Time-domain Method*, Artech House, Boston, 1995.
- 84 Choi, M. K., Liebman, L. A., Brock, J. R., Finite Element Solution of the Maxwell Equations for a Absorption and Scattering of Electromagnetic Radiation by a Coated Dielectric Particle, *Chem. Eng. Comm.*, 1996, 151, 5-17.
- 85 Draine, B. T., Flatau, P. J., Discrete-dipole Approximation for Scattering Calculations, *J. Opt. Soc. Am. A*, 1994, 11, 1491-1499.
- 86 Hirleman, E. D., General Solution to the Inverse Near-forward-scattering Particle-sizing Problem in Multiple-scattering Environment: Theory, *App. Opt.*, 1991, 30, 4832-4838.
- 87 Harvill, T. L., Hoog, J. H., Holve, D. J., In-process Particle Size Distribution Measurements and Control, *Part. Part. Syst. Charact.*, 1995, 12, 309-313.
- 88 Khintchine, A., Korrelationstheorie der Stationären Stochastischen Prozesse, *Math. Ann.*, 1934, 109, 604-615.

- 89 Schulz-DuBois, E. O., High Resolution Intensity Interferometry by Photon Correlation, in *Photon Correlation Techniques in Fluid Mechanics*, Ed. E. O. Schultz-DuBois, Springer-Verlag, Berlin, 1983, Chpt.1, pp.6-27.
- 90 Saleh, B., *Photoelectron Statistics*, Springer-Verlag, New York, 1978.
- 91 Berry, G. C., Properties of an Optically Anisotropic Heterocyclic Ladder Polymer (BBL) in Dilute Solution, *J. Polym. Sci. Polym. Symp.*, 1978, 65, 143-172.
- 92 Zimm, B. H., Apparatus and Methods for Measurement and Interpretation of the Angular Variation of Light Scattering; Preliminary Results on Polystyrene Solutions, *J. Chem. Phys.*, 1948, 16, 1099-1116.
- 93 Tadayyon, A., Rohani, S., Determination of Particle Size Distribution by Par-Tec®100: Modeling and Experimental Results, *Part. Part. Syst. Charact.*, 1998, 15, 127-135.
- 94 Monnier, O., Klein, J., Hoff, C., Ratsimba, B., Particle Size Determination by Laser Reflection: Methodology and Problems, *Part. Part. Syst. Charact.*, 1996, 13, 10-17.
- 95 Reichel, A., Gerber, M., Schwartz, F. H., Wagdeling, R., In-situ Particle Measurements in High Concentrations, a Novel approach for Particle Size Measurement, in *Preprint of Partec 98. 7<sup>th</sup> European Symp. Part. Charact.*, Nünberg, 1998, pp.561-570.
- 96 Thornburg, J., Cooper, S. J., Leith, D., Counting Efficiency of the API Aerosizer, *J. Aerosol Sci.*, 1999, 30, 479-488.
- 97 Kinney, P. D., Pui, D. Y. H., Inlet Efficiency Study for the TSI Aerodynamic Particle Sizer, *Part. Part. Syst. Charact.*, 1995, 12, 188-193.
- 98 Aharonson, E. F., Karasikov, N., Roitberg, M., Shamir, J., Galai-CIS-1-A Novel Approach to Aerosol Particle Size Analysis, *J. Aerosol Sci.*, 1986, 17, 530-536.
- 99 Wallach, M. L., Heller, W., Stevenson, A. F., Theoretical Investigations on the Light Scattering of Colloidal Spheres XII. The Determination of Size Distribution Curves from Turbidity Spectra, *J. Chem. Phys.*, 1961, 34, 1796-1802.
- 100 Gulari, Es., Bazzi, G., Gulari, Er., Annapragada, A., Latex Particle Size Distribution from Multiwavelength Turbidity Spectra, *Part. Charact.*, 1987, 4, 96-100.
- 101 Ferri, F., Bassini, A., Paganini, E., Commercial Spectrophotometer for Particle Sizing, *Appl. Opt.*, 1997, 36, 885-891.
- 102 Wang, N., Wei, J., Hong, C., Zhang, H., Influence of Refractive Index on Particle Size Analysis Using the Turbidimetric Spectrum Method, *Part. Part. Syst. Charact.*, 1996, 13, 238-244.
- 103 Cai, X.-S., Gang, Z., Wang, N.-N., A New Dependent Model for Particle Sizing with Light Extinction, *J. Aerosol Sci.*, 1995, 26, 685-704.
- 104 Dobbins, R. A., Jizmagian, G. S., Optical Scattering Cross Sections for Polydispersions of Dielectric Spheres, *J. Opt. Soc. Am.*, 1966, 56, 1345-1350.
- 105 Cerni, T. A., Waisanen, S., Method and Apparatus for Measurement of Particle Size Distribution in Substantially Opaque Slurries, *US Patent (pending)*, filed 1998.
- 106 Bacon, C., Garcio-Rubio, L., Simultaneous Joint Particle Property Characterization Using the Multiangle-Multiwavelength (MAMW) Detection System, *Proc. Part. Technol. Forum*, American Institute of Chemical Engineers, Washington D. C., 1998, pp.717-723.
- 107 Dogariu, A., Uozumi, J., Asakura, T., Particle Size Effect on Optical Transport through Strongly Scattering Media, *Part. Part. Syst. Charact.*, 1994, 11, 250-257.
- 108 Etmüller, J., Eustachi, W., Hagenow, A., Polke, R., Schäfer, M., Rädle, M., Photometrische Messeinrichtung, *Eur. Pat. Appl. EP0472899B1*, 1991.
- 109 Fishkin, J., So, P. T. C., Cerussi, A. E., Fantini, S., M. A., Measuring Spectral Properties in Multiple-scattering Media: Methemoglobin Adsorption Spectrum in a Tissue-like Phantom, *Appl. Opt.*, 1995, 34, 1143-1155.
- 110 *Laser Doppler Velocimetry*, Ed. Adrian, R. J., SPIE Milestone Series Vol. MS 78, SPIE Optical Engineering Press, Bellingham, 1993.

- 
- 111 Naqwi, A. A., Innovative Phase Doppler Systems and Their Applications, *Part. Part. Syst. Charact.*, 1994, 11, 7-21.
  - 112 Buchhave, P., von Benzon, H., Exploring PDA Configurations, *Part. Part. Syst. Charact.*, 1996, 13, 68-78.
  - 113 Doicu, A., Schabel, S., Ebert, F., Generalized Lorenz-Mie Theory for Non-Spherical Particles with Applications to Phase-Doppler Anemometry, *Part. Part. Syst. Charact.*, 1996, 13, 79-88.
  - 114 Doicu, A., Wriedt, T., Bauckhage, K., Light Scattering by Homogeneous Axisymmetric Particles for PDA Calculations to Measure Both Axes of Spheroidal Particles, *Part. Part. Syst. Charact.*, 1997, 14, 3-11.
  - 115 Tropea, C., Xu, T.-H., Onofri, F., Gréhan, G., Haugen, P., Stieglmeier, M., Dual-mode Phase-Doppler Anemometer, *Part. Part. Syst. Charact.*, 1996, 13, 165-170.
  - 116 Rheims, J., Wriedt, T., Bauckhage, K., Working Principle and Experimental Results for a Differential Phase-Doppler Technique, *Part. Part. Syst. Charact.*, 1998, 15, 219-224.
  - 117 Evenstad, J., Naqwi, A. A., A Device for Phase Shift Measurement in an Advanced Phase Doppler Velocimeter, *Part. Part. Syst. Charact.*, 1998, 15, 75-80.



# LASER DIFFRACTION

## *Sizing from Nanometers to Millimeters*

### 3.1 Introduction

In laser diffraction measurements one obtains information about particle size distribution through measurements of scattering intensity as a function of the scattering angle and the wavelength of light based on applicable scattering models. This is an absolute method in the sense that once the experimental arrangement or instrument is correctly set up, calibration or scaling is not necessary. In the past two decades, laser diffraction has become a popular and important physical means for sizing industrial particles. Laser diffraction has to a large extent replaced conventional methods, such as sieving and sedimentation in the sizing of particles smaller than a few millimeters, and has taken the place of optical and electron microscopy for particles larger than some tens of nanometers. This is mainly due to the advantages of the technology: its ease of use and fast operation; its high reproducibility; and an extremely broad dynamic size range, spanning almost five orders of magnitude, from nanometers to millimeters.

Due to both the immaturity of the technology and limited computing power, at first particle sizing by laser diffraction was restricted to the use of only the Fraunhofer diffraction theory. Fraunhofer theory was used to calculate particle size even when particles were much smaller than some tens of a micrometer, far outside the applicable range of the theory. For this reason, this technology has historically, and is still to this day, widely known throughout industry as *laser diffraction*. However, the term *laser diffraction* no longer reflects the current state of the art because of advancements in the technology made over the past few years. Firstly, laser diffraction analyzers are no longer limited to just simple diffraction effects. More general approaches based on the Mie theory and the measurement of scattering intensity over a wide scattering angular range can be employed. The size range possible has also been extended into the submicron region. Secondly, some light source of continuous wavelength (white light) is often used to complement the main laser source in order to gain additional characteristic information about submicron-size particles based on wavelength and polarization dependencies of scattering intensity. In addition, through a new approach that uses the same technology for

shape characterization, diffraction itself may not be restricted to only spherical situations. *Angular light scattering* may be a more proper term for this technology; nevertheless the term *laser diffraction* has an advantage in that it distinguishes itself from all other scattering technologies (see Table 2.1) and has been accepted by national and international particle characterization communities.

Figure 3.1 shows the generic setup of a laser diffraction instrument and the major functions of each element along with the section number in this text where a more detailed description can be found.

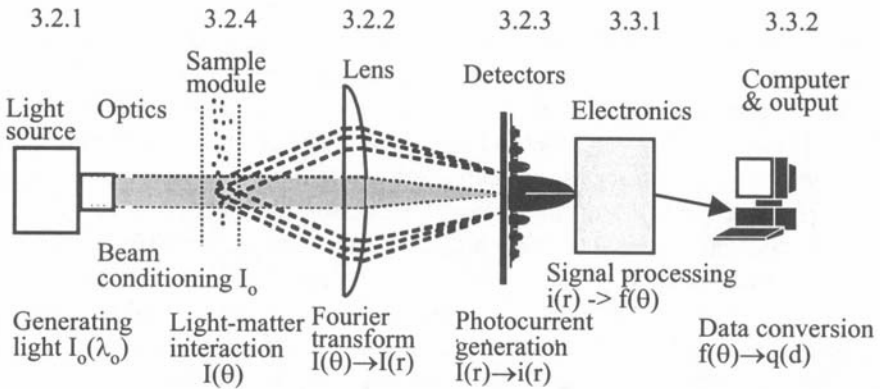


Figure 3.1. Schematic of a laser diffraction instrument.

The whole process starts with a light source that generates a monochromatic beam. After passing through several optical components, the raw beam is conditioned to create an expanded, collimated beam having a smooth (Gaussian) radial intensity distribution which illuminates the particles in the scattering volume. The particles scatter light, generating unique angular scattering patterns. These patterns ( $I(\theta)$ ) are then Fourier transformed into a spatial intensity pattern ( $I(r)$ ), which is detected by a multi-element photodetector array. The photocurrent from the detectors is subsequently processed and digitized creating an intensity flux pattern. Computer software utilizing appropriate scattering theories then converts the set of flux values into a particle size distribution.

As described in Chapter 2, in general the scattered light intensity of a particle detected at a fixed distance by a unit area of detection is a function of following variables: particle dimension and shape, the refractive index ratio between the particle and medium, the wavelength and polarization of light, and scattering angle. In addition to the above variables, scattering intensity from a particulate sample depends on particle concentration and particle-particle

interaction. Some of the variables are constants in any particular experimental setup, such as the detection distance, detector area, scattering volume, and light wavelength and polarization; and some of these variables are constant for a particular sample system, such as the refractive indexes. In characterizing particle size by laser diffraction, one optimizes the sample concentration so that the particles scatter with sufficient intensity to enable the measurement to be completed within a desired signal to noise ratio, but not so much as to saturate the detecting system. Sample concentration is also optimized for minimal particle-particle interaction and minimal multiple scattering (light scattered multiple times before it is detected) so that the measurement can be performed based on elastic single particle scattering. In addition, in a laser diffraction measurement one has to make an assumption that both the refractive index and the density of the particles in the sample are uniform, which is true in most cases. In this way the scattered light intensity is only a function of scattering angle, particle shape, and particle size. If one knows the relations between the scattering intensity, scattering angle, and particle size and shape, then through measurements of the angular scattering pattern the particle size and shape can be obtained, at least theoretically. Unfortunately, there are no easy interpretations of the scattering patterns of irregularly shaped particles. Even for regularly shaped particles, only a limited number of analytical formulas are available in the Rayleigh-Debye-Gans and Fraunhofer regions. In the regime where the dimension of the particles is comparable to the wavelength of light, the only practical formula available is for spheres (solid or concentric) as is described in Chapter 2.

Most industrial particles closely resemble spheres and the scattering effects from the corners and edges of these particles are smoothed out due to the tumbling and rotational motion in sample circulation during the measurement. Therefore, we can apply either Mie theory or Fraunhofer theory to most practical systems with one parameter: diameter. However, such treatment only yields apparent values. One should always keep in mind that the “size” obtained from most particle sizing technologies (no exception for laser diffraction), may differ from the real dimension. To date, the spherical modeling approach is the only feasible choice for a commercial instrument designed to be used for a broad range of samples, no matter what the real particle shapes.

As shown in Figure 2.4 and Figure 2.12, the location of the first intensity minima shifts towards smaller angles with increasing particle size; i.e., larger particles have a slimmer central scattering intensity peak. It is the rapid intensity change in this central lobe, along with fine structures of the angular pattern, that forms the foundation of this method of determining particle size from an angular intensity measurement. However, with decreasing particle size the fine structure in the scattering pattern diminishes and the scattering intensity change with respect to angle become very slow. When using a single

wavelength of light the practical upper limit depends on the smallest scattering angle that the instrument can access. Presently, this upper limit is about 8 mm, which covers a large portion of the classic dry sieve analysis of particles such as rice, peeled barley, glass beads, and even peas. Figure 3.2 shows a mixture of particles from 200  $\mu\text{m}$  to 8000  $\mu\text{m}$ . In this size range where the particle size is comparable to the beam diameter ( $< 4\text{ cm}$ ), the measurement is based on the scattering from a small number of particles.

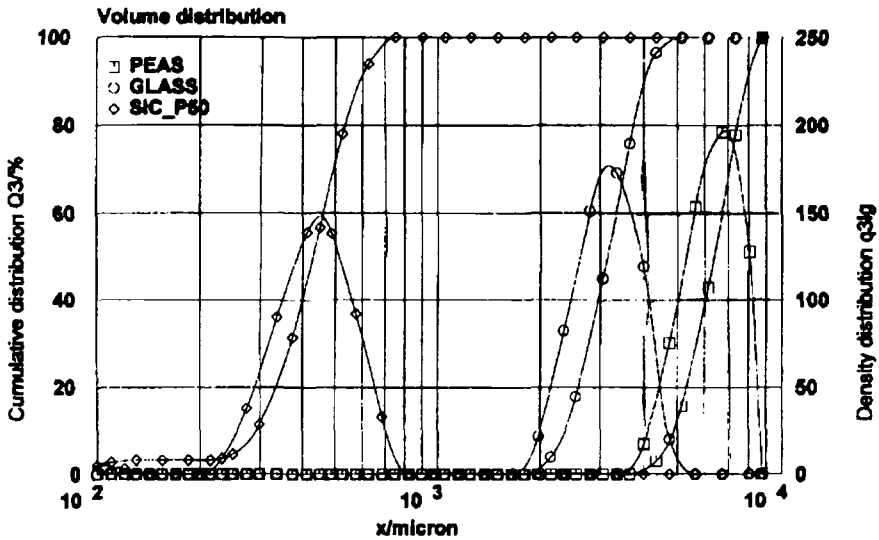


Figure 3.2. Laser diffraction result of a tri-modal mixture of large particles [1] (by permission of Wiley-VCH Verlag GmbH).

Applying Eq. 2.20, the first minimum in Fraunhofer theory for a sphere 8 mm in diameter is located at  $\theta = 0.005$  degrees. Thus in order to detect and fit the sharp intensity change within the central lobe, the smallest scattering angle accessible should be at least as small as that value. The higher the upper size limit desired becomes, the smaller the detection angle has to be. Using conventional optics, to achieve detection at very small angles without disturbance from the incident beam a very long optical bench is needed. The upper limit is also partially determined by practical necessity. For particles larger than a few millimeters other analytical methods such as sieving may be more suitable. When combining or comparing analyses results from two different technologies (such as sieving and laser diffraction), however, it should be noted that each technology has different weighting and sensitivity to constituents of the sample. Currently, laser diffraction technology is being applied in an ever-broadening variety of fields. Much effort has been spent to improve or optimize the optical

arrangement in order to increase the dynamic size range, in particular to extend the lower size limit of the technology. As particle size becomes smaller, the ratio of particle dimension to light wavelength ( $d/\lambda$ ) is reduced and the scattering pattern becomes smoother and less angularly dependent. In Figure 2.6 notice how smooth the scattering factors become when approaching small values of  $x$  ( $x < 1$ ). In this region, the relationship of particle size to scattering intensity pattern is greatly reduced, causing more and more difficulty in determining correct size values. To enhance sizing ability in this region, there are three approaches one may take. Combining these three approaches the theoretical and practical lower limit in particle sizing using laser diffraction can be extended.

The first approach to extend the lower sizing limit is by increasing the angular detecting range. For large particles, the characteristic patterns are mainly located at small angles. For smaller particles, the central lobe becomes flatter and broader and the angular pattern gets less characteristic. If we use the angular location of the first minimum in the scattering pattern as the criterion to correctly size a sphere we will find that in order to size a sphere having a diameter less than  $0.5\ \mu\text{m}$ , the maximum detection angle has to be greater than 90 degrees. Thus, in order to size a submicron particle, the detection angular range has to be designed to cover angles at least as large as 90 degrees; practically, the maximum detecting angle can be as large as  $175^\circ$  [2].

Scattering patterns are a function of light wavelength and particle size, and therefore their variations are related to the ratio between particle dimension and wavelength ( $d/\lambda$ ), which can be used as an indicator of the effectiveness in the use of the angular scattering pattern to size particles. Interference effects (which create the fine structure in a scattering profile) are greatly reduced when  $d/\lambda$  is less than 0.5. Obviously, if the wavelength of light is shorter the ratio will be greater and the lower sizing limit will be effectively extended. In other words, scattering patterns are compressed at shorter wavelengths and more information (structure) will be revealed over the same angular range as compared with what can be obtained using a longer wavelength. The shortest practical wavelength is about 350 nm because most materials exhibit strong absorption at wavelengths shorter than 300 nm. When using a wavelength shorter than 180 nm, the experiment has to be performed under vacuum. Using light of  $\lambda = 375\ \text{nm}$ , the lower sizing limit can be extended to half of that using light of  $\lambda = 750\ \text{nm}$ . For example, in Figure 2.5 for a  $0.5\ \mu\text{m}$  PSL sphere in water when light of  $\lambda = 488\ \text{nm}$  is used, the fine structure is more distinguishable when compared to a longer wavelength ( $\lambda = 780\ \text{nm}$ ).

These two approaches to increase the dynamic range can be quantitatively described by the magnitude of the momentum-transfer vector  $\mathbf{K}$ . For large particles, because the scattering intensity changes rapidly with scattering angle, the overall range of  $\mathbf{K}$  covered by the detectors should be small

in order to detect the details therefore achieving a high resolution. For small particles it is just the opposite, and the detectors should cover as wide a range of  $K$  as possible. For example, if one uses a laser with  $\lambda = 750 \text{ nm}$  to measure scattering up to 35 degrees,  $K_{\max} = 0.005 \text{ nm}^{-1}$ .  $K_{\max}$  will be increased by more than five fold to  $0.027 \text{ nm}^{-1}$  using light of  $\lambda = 450 \text{ nm}$  at an angle of 150 degrees.

Yet even when using both these two approaches, the lower size limit is still not low enough to meet the demands to size even smaller particles (tens of nanometers in diameter). For these smaller particles, any further increase in scattering angle will not yield any significant improvement due to the ever-slower angular variation. Figure 3.3 is a zoomed-in 3-D display from Figure 2.4 that illustrates the very slow angular variation for small particles.

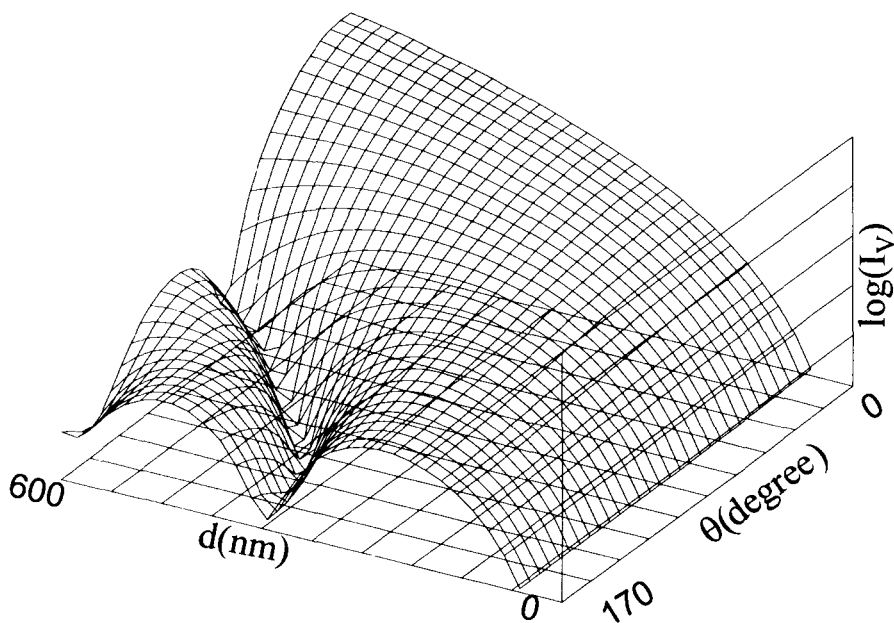


Figure 3.3. A 3-D display of Mie scattering intensity  $I_V$  from a unit volume of spheres with the relative refractive index  $m = 1.50 + 0i$  at  $\lambda = 750 \text{ nm}$  [3] (by permission of Medpharm Scientific Publishers).

Once particle size becomes smaller than approximately  $0.4 \text{ }\mu\text{m}$  not only does the intensity minimum disappear but also the maximum intensity contrast in the entire angular range becomes so small that it prevents the angular pattern to be used in obtaining size information. Figure 3.4 shows the maximum contrast in

the scattering intensity  $I_v$  at  $\lambda = 450$  nm from 0.5 degrees to 150 degrees for 100 nm spheres of different refractive indices. Figure 3.5 displays the maximum intensity contrast for submicron particles in the angular range from 0.5 degrees to 175 degrees at two different wavelengths. (Remember that for a particle of  $2000 \mu\text{m}$  in diameter, this contrast can be as large as  $10^7$ !)

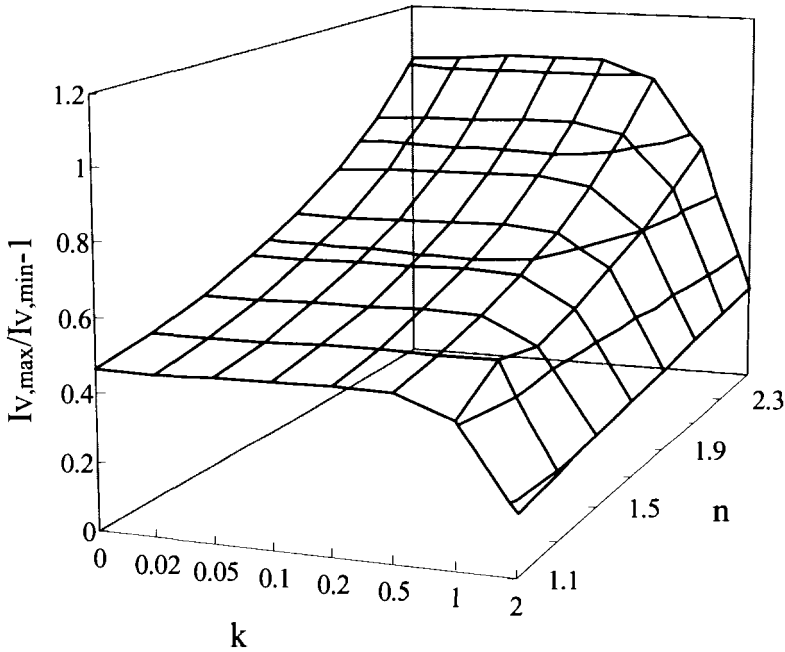


Figure 3.4. Maximum scattering intensity  $I_v$  contrast from  $\theta = 0.5^\circ$  to  $150^\circ$  for 100 nm spheres of different refractive indices at  $\lambda = 450$  nm.

As shown in Figure 3.5 at  $\lambda = 450$  nm particles less than 200 nm will create a maximum intensity contrast too small to effectively retrieve the correct particle size. This demonstrates that, for particles smaller than 200 nm, even by taking advantage of the above two approaches (i.e., using larger angles and shorter wavelengths), it is still difficult to obtain an accurate size. Of course, the actual boundary will change depending on the relative refractive index between the particle and medium.

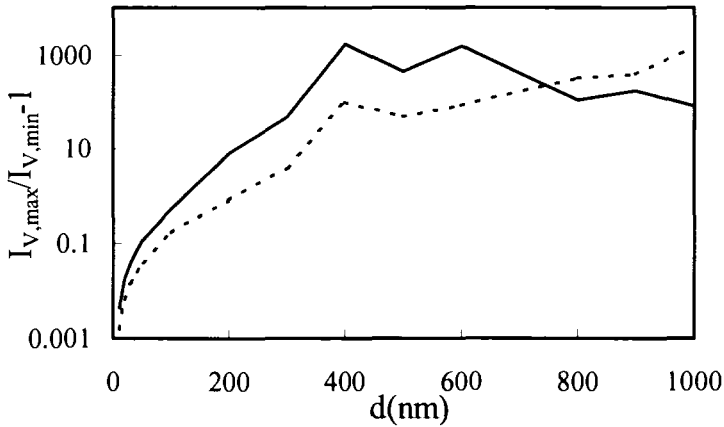


Figure 3.5. Maximum scattering intensity  $I_V$  contrast from  $\theta = 0.5^\circ$  to  $150^\circ$  for spheres ( $m = 1.5 - 0.02i$ ) in air at  $\lambda = 450$  nm (the solid line) and  $\lambda = 750$  nm (the dot line) [3] (by permission of Medpharm Scientific Publishers).

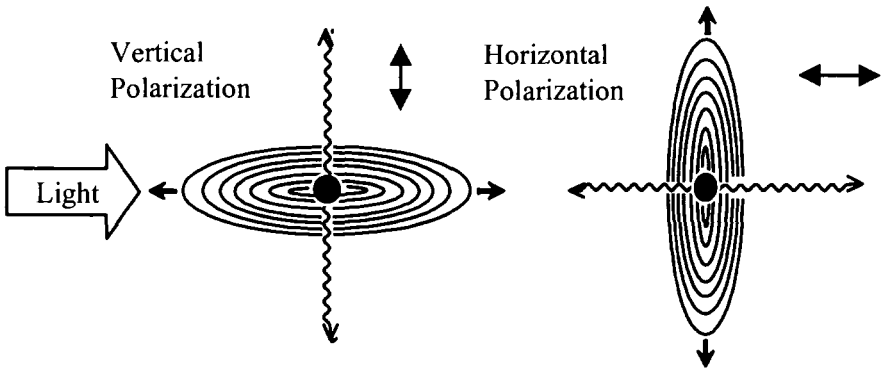


Figure 3.6. Scattering from different polarizations.

Generally, vertically polarized scattered light has different scattering patterns and fine structures from that of horizontally polarized light for small particles. The main characteristic of  $I_h$  for small particles is that there is a minimum around 90 degrees. This minimum shifts to larger angles for larger particles. Thus, although both  $I_v$  and  $I_h$  have only small contrast in the case of small particles, the difference between them can reveal a more distinguished fine structure, thereby making the sizing of small particles possible. Combining polarization effects with wavelength dependence at large angles, we can extend the lower sizing limit to as low as 50 nm, almost reaching the theoretical limit.



This combined approach is known as the *polarization intensity differential scattering* (PIDS) technique [4,5,6].

The origin of polarization effects can be understood in the following way. When a very tiny particle, much smaller than the light wavelength, is located in a light beam, the oscillating electric field of the light induces an oscillating dipole moment in the particle; i.e., the electrons in the atoms comprising the particle move back and forth relative to the stationary particle. The induced motion of the electrons will be in the direction of oscillation of the electric field, and therefore perpendicular to the direction of propagation of the light beam. As a result of the transverse nature of light, the oscillating dipole radiates light in all directions except in the direction of oscillation, as visualized in Figure 3.6. Thus, if the detector is facing the direction of oscillation it will receive no scattering from single dipoles. When the light beam is polarized in either the v direction or the h direction, the scattering intensity  $I_v$  and  $I_h$  for a given angle will be different. The difference between  $I_v$  and  $I_h$  ( $I_v - I_h$ ) is termed the PIDS signal. As particle size increases the intra-particle interference makes the particle's behavior deviate from that of a simple dipole and the scattering pattern will become more complex. For small particles the PIDS signal is roughly a quadratic curve centered at 90 degrees. For larger particles the pattern shifts to smaller angles and secondary peaks appear due to the scattering factor. Since the PIDS signal is dependent on particle size relative to light wavelength, valuable information about a particle size distribution can be obtained by measuring the PIDS signal at several wavelengths. In order to visualize the polarization effect in scattering intensity, let us look at the difference in  $I_v$  and  $I_h$  as a function of diameter and angle for particles of relative refractive index  $m = 1.20$  (polystyrene latex in water) at  $\lambda_o = 450$  nm, illustrated in Figure 3.7 and Figure 3.8.

The main difference between the plots in Figure 3.7 and in Figure 3.8 is that there is a minimum in the  $I_h$  scattering for particles smaller than 200 nm. Thus, the angular variation in scattering intensity for small particles can be enhanced if the differential intensity between  $I_v$  and  $I_h$  ( $I_v - I_h$ ) is used instead of only  $I_v$  (illustrated in Figure 3.9). Figure 3.10 displays a few lines of Figure 3.9 in a 2-D fashion in which the shift in the peak value and the change in contrast for particles of various diameters are clearly shown. In addition, because the PIDS signal varies at different wavelengths (it becomes flatter at longer light wavelengths), measurement of the PIDS signals at several wavelengths will provide additional scattering information that can be used to further refine the size retrieval process.

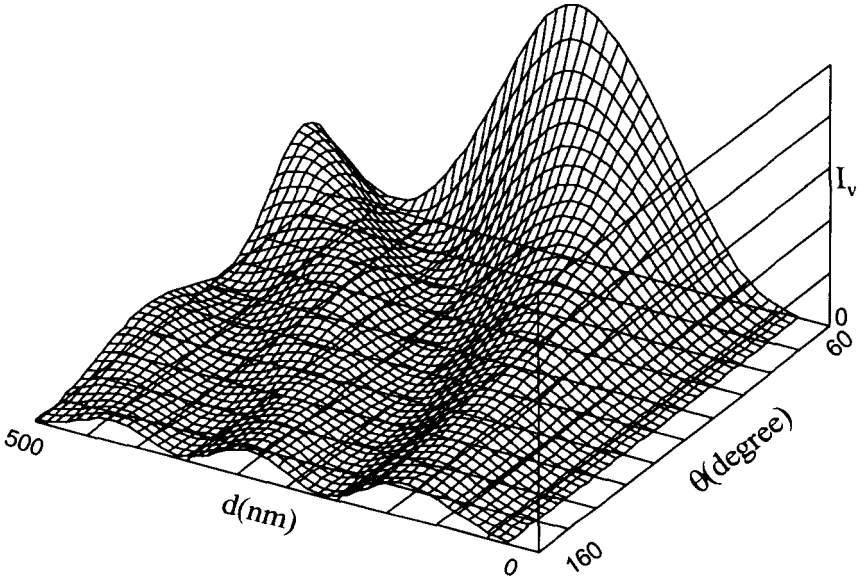


Figure 3.7. Unit volume scattering  $I_v$  of PSL in water ( $\lambda_o = 450$  nm).

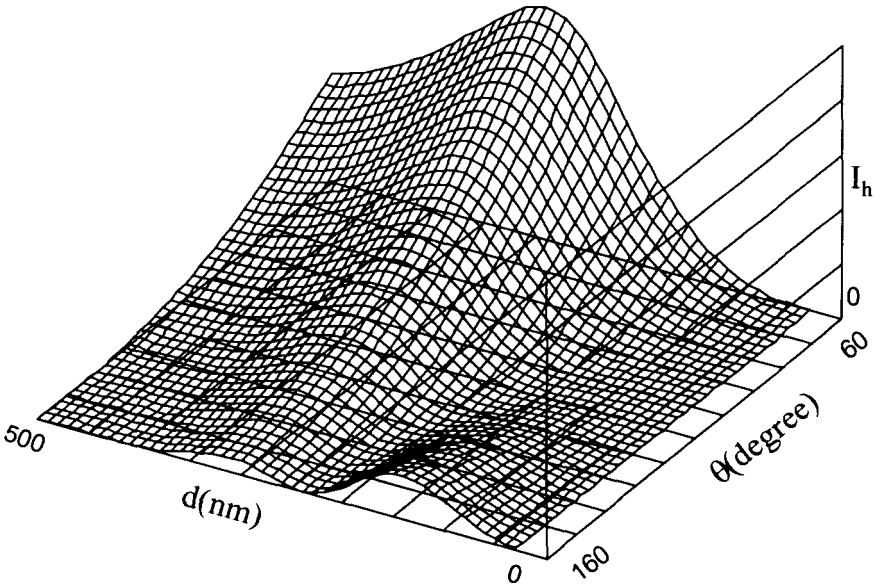


Figure 3.8. Unit volume scattering  $I_h$  of PSL in water ( $\lambda_o = 450$  nm).

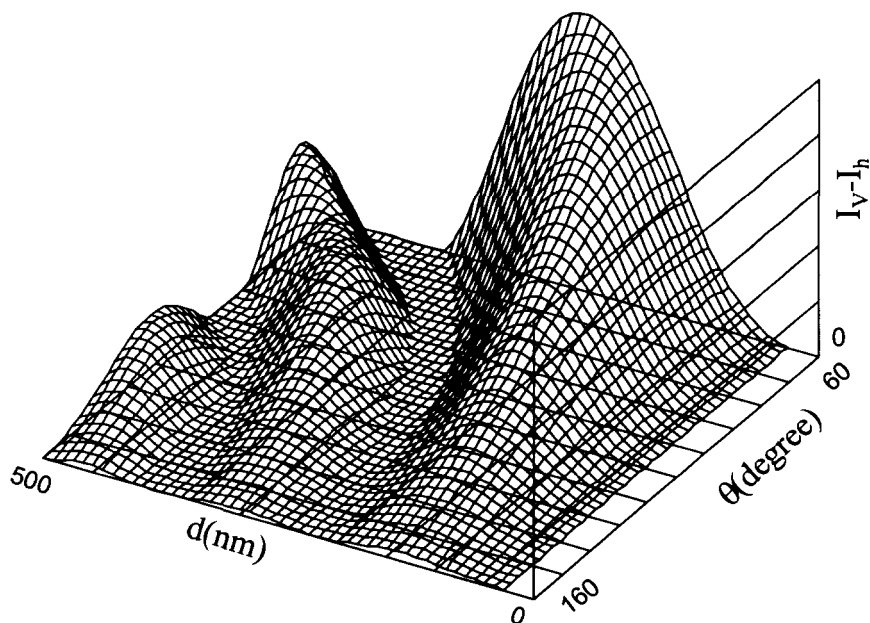


Figure 3.9. Unit volume scattering PIDS signal of PSL in water ( $\lambda_o = 450 \text{ nm}$ ).

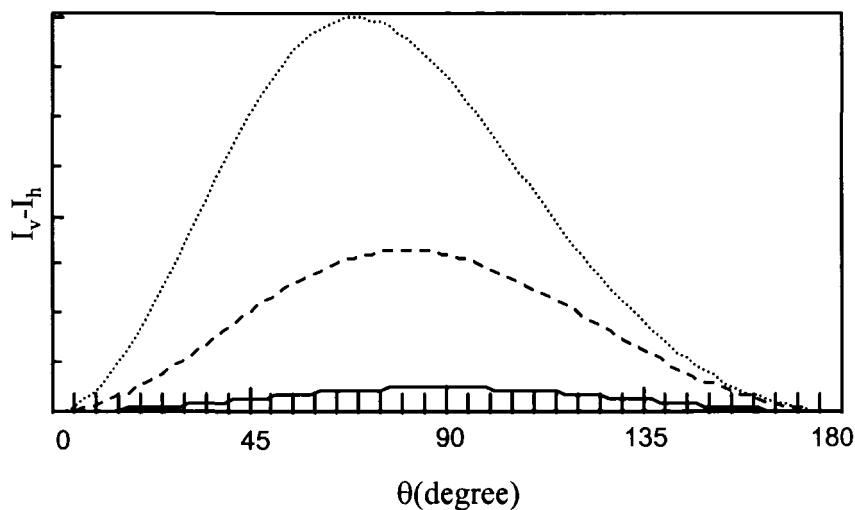


Figure 3.10.  $I_V - I_h$  of small PSL in water ( $\lambda_o = 450 \text{ nm}$ ). Dotted line:  $d = 150 \text{ nm}$ ; dashed line:  $d = 100 \text{ nm}$ ; and solid line:  $d = 50 \text{ nm}$ .

Figure 3.11 is a plot that displays the maximum PIDS contrast over the entire angular range from  $0^\circ$  to  $180^\circ$ . Comparing this plot with Figure 3.5, the signal

improvement for particles smaller than 200 nm is significant. From Figure 3.10, the angular patterns for 100 nm and even for 50 nm particles are recognizable, in addition to the shift in the axis of symmetry. It has been verified through both theoretical simulation and real experimentation that accurate sizing of particles smaller than approximately 200 nm by scattering intensity without the use of the PIDS technique is practically difficult and probably unrealistic. The combination of the three approaches (wider angular range, wavelength variation, and polarization effects) improves the accurate characterization of submicron particles using light scattering. An additional feature of the PIDS technique is that, because the technique measures the difference between two intensity measurements which are time-averaged and recorded by the same detector array, the noise (to the first order) is minimized. Another conclusion that can be drawn from Figure 3.11 is that for particles larger than one micron the PIDS data will have no effect at all since for these particles  $I_v$  and  $I_h$  are identical (see Eqs. 2.7 and 2.19.)

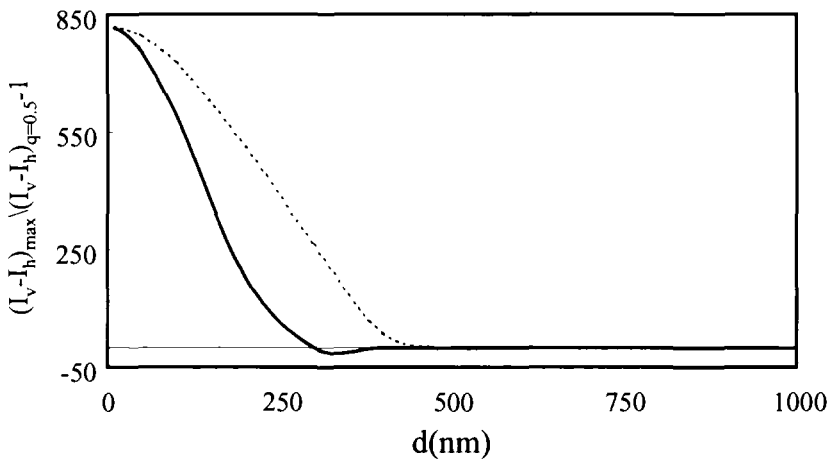
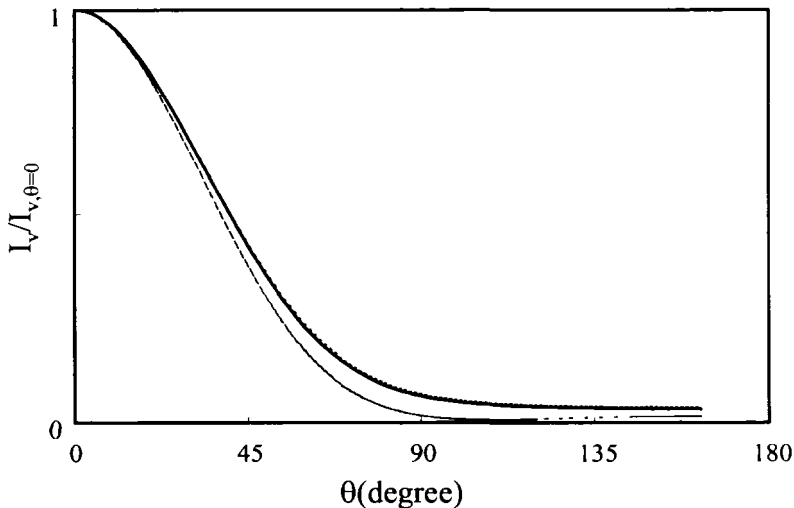


Figure 3.11. Maximum PIDS contrast in the PIDS angular pattern from  $0.5^\circ$  to  $150^\circ$  for spheres ( $m = 1.5 - 0.02i$ ) in air at the wavelengths of  $\lambda = 450$  nm (the solid line) and  $\lambda = 750$  nm (the dotted line) [3] (by permission of Medpharm Scientific Publishers).

We can do a signal analysis from a simulated trimodal distribution to see how the PIDS technique can resolve all three peaks while using only the shorter wavelengths and larger angles. Without utilizing the polarization effect the smallest size peak will be missed. In this example, we start with a log-normal distribution of PSL spheres in water (sample A). The distribution has a mean diameter of 460 nm and a variance of 0.01. Using Eq. 2.8 we calculate the  $I_v$  scattering angular pattern at  $\lambda \approx 563$  nm (the dashed line in Figure 3.12). We then mix a log-normal size distribution of PSL having a mean diameter of 240

nm and a variance of 0.01 with sample A at a ratio of 1:1 to form sample B. The corresponding  $I_v$  scattering pattern (the solid line in Figure 3.12) is now different from that of sample A alone. When we add a third component (a log-normal size distribution of PSL with a mean diameter of 64 nm and a variance of 0.01) to sample B at a ratio of 3:2 to create sample C, we do not see any appreciable change in the scattering pattern (the dotted line in Figure 3.12). The size retrieval process consists of a matrix inversion of the simulated scattering. In theory, one should be able to resolve the difference between sample A and sample B, separating the 240 nm peak from the 460 nm peak by a careful measurement using a sophisticated instrument. However, as there is only minimal change in the  $I_v$  pattern from sample B to sample C, one cannot expect to resolve the added small particles from the large particles within the experimental error limit, no matter how high the signal-to-noise ratio is or how sophisticated the inversion algorithm is.



*Figure 3.12.* Simulated normalized  $I_v$  pattern from mixtures of PSL spheres in water at  $\lambda_0 = 750$  nm. The sphere diameters of each component obey the log-normal distribution with a variance of 0.01. Dashed line: 460 nm spheres; solid line: 1:1 mixture of 240 nm and 460 nm spheres; dotted line: 3:1:1 mixture of 64 nm, 240 nm and 460 nm spheres [3] (by permission of Medpharm Scientific Publishers).

On the other hand, when we make the same simulation and comparison using the PIDS signals from the above three samples, not only do the PIDS patterns from sample A and sample B show a greater difference than the  $I_v$  pattern alone, but the PIDS pattern from sample C is also easily distinguishable from that of sample B (Figure 3.13). The differences between the PIDS patterns of samples B and C provide a foundation for resolving the 64 nm peak in sample C in a

laser diffraction measurement using the PIDS technique and this has been experimentally verified with a real trimodal sample.

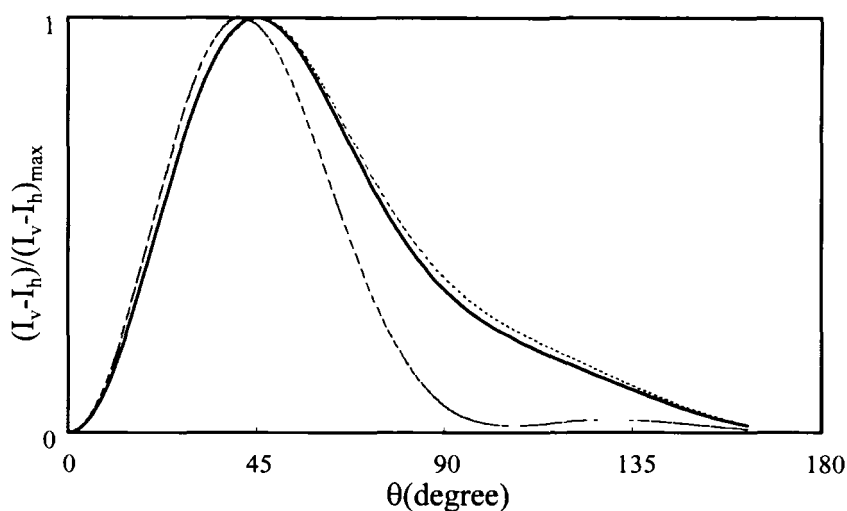


Figure 3.13. Simulated normalized PIDS patterns from the same mixtures of spheres as in Figure 3.12. The symbols are the same as those in Figure 3.12 [3] (by permission of Medpharm Scientific Publishers).

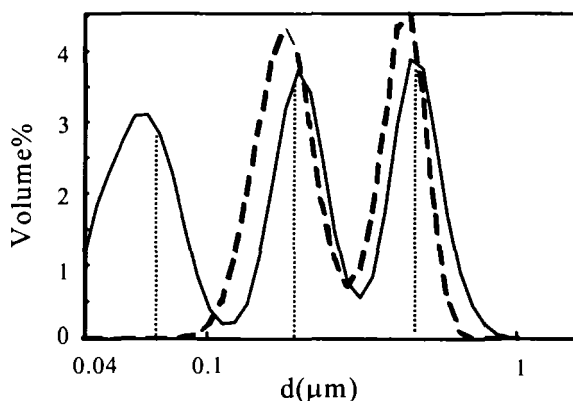
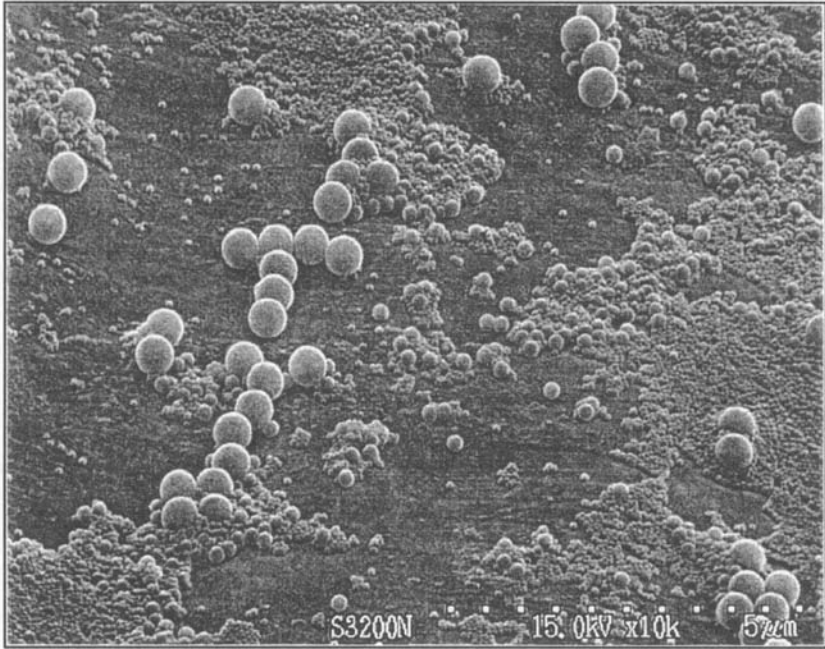


Figure 3.14. A trimodal mixture of PSL's (nominal diameters of 83 nm, 204 nm, and 503 nm with 1:1:1 volume ratio from Duke Scientific).

Figure 3.14 is a typical trimodal distribution retrieved in a laser diffraction experiment using the PIDS technique at multiple wavelengths ( $\lambda_0 = 450, 600, 750, \text{ and } 900 \text{ nm}$ ) and over a scattering angular range with angles up to 144 degrees, with (solid line) and without (dashed line) using the polarization effect.

The dotted lines represent the nominal diameter values of the latexes in the mixture as reported by the PSL vendor. Without the PIDS technique the smallest component is missed, even when using the information gathered at large scattering angles and short wavelengths. Figure 3.15 is a SEM image of the sample in Figure 3.14 in which three different sizes of particles can be seen.



*Figure 3.15. An electron microscopic image of the sample in Figure 3.14 [7] (by permission of Beckman Coulter KK).*

### **3.2. Instrumentation**

There are many different avenues to choose from in the design and construction of a laser diffraction analyzer. Depending on the desired specifications or applications, there are differences in how to design the electronics, optics, mechanics and the computer software used in the instrument. This is especially true in academic research situation where unique designs are created for specific research projects. It is neither the desire of the present text nor is it possible to provide a description that includes all practical designs. In this section only the typical and most commonly used designs are described, along with comments about their relative advantages and limitations.

### 3.2.1. LIGHT SOURCE

There are two types of light sources used in laser diffraction instruments. One is a white light source, typically a tungsten-halogen lamp, the other is a continuous laser light source. The former has random polarization and a broad spectral range with wavelengths typically ranging from 250 nm to 3000 nm and can be used when multi-wavelength measurements are required. By placing filters of different wavelength and polarizers in the beam path before the sample chamber, one can make diffraction measurements at selected wavelengths and different polarizations. Laser light has many advantages, especially valuable are the laser's high degree of stability, long lifetime, monochromatic illumination, and long spatial and temporal coherence. Thus although use of a laser as the light source is not essential, it provides definite benefits and is now almost always used in modern laser diffraction instrumentation as the main or sole light source. The following table lists the main characteristics of commonly used lasers.

Table 3.1. Common laser sources

Laser Type	Power(mW)	Wavelength(nm)	Features
Ar ion	30-2000	488, 514.5	Circularly collimated, water cooling needed for high power
He-Ne	1-50	543.5, 594.1, 612.0, 632.8	Circularly collimated
Diode Laser	0.1-200	405, 450, 635, 650, 670, 685, 750, 780	low cost, miniature and interfaceable with fiber optics, elliptical and very divergent output

The light beam from a He-Ne laser is circular with radial symmetry and is collimated with small divergence ( $< 2 \text{ mrad}$ ). A He-Ne laser produces stable monochromatic light and can have an expected life in excess of 20,000 hours. For these reasons and because of availability, He-Ne lasers ( $\lambda_0 = 632.8 \text{ nm}$ ) are commonly used in laser diffraction instruments. Recent advancements in semiconductors and fiber optics have allowed diode lasers to replace both gas and ion lasers more and more because of their low cost (often only one tenth of a gas laser), long lifetimes ( $> 50,000 \text{ hours}$ ), low operating voltage, and compactness (for example, a  $500 \text{ mm}^3$  package can house a 200 mW single-mode laser). However, opposed to a He-Ne laser or argon ion laser, the light from a diode laser is neither collimated nor radially symmetric, and it has severe astigmatism (the divergence of light at two perpendicular directions is different). A diode laser's monochromatic light must be conditioned. A set of optical components is needed to perform divergence correction, asymmetry correction and astigmatic correction in order to obtain a collimated circular beam. Lately, with advancements in micro-optics, such as gradient index



microlenses and optical fiber pig-tailing techniques, these tasks can be achieved in a compact manner and some of the optical components have been integrated in commercially available packaged diode lasers.

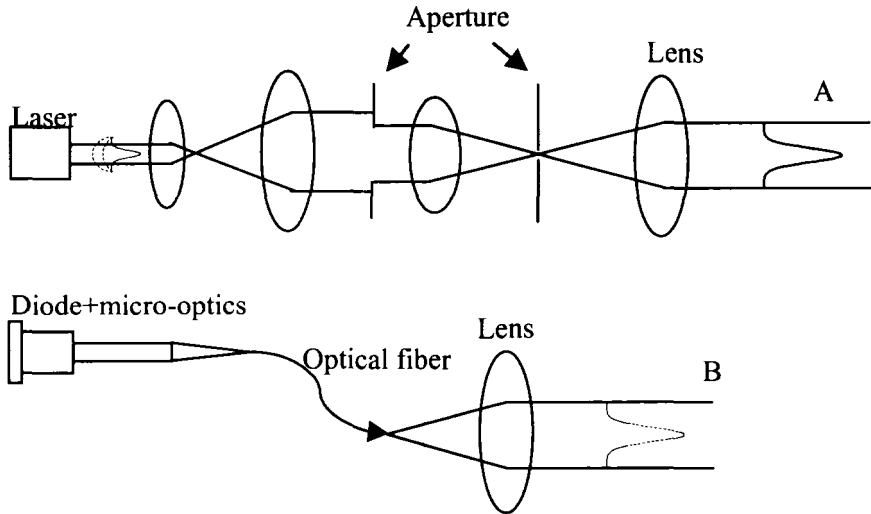


Figure 3.16. Spatial filtering using conventional optics (A) and fiber optics (B).

Even though light from gas lasers or from conditioned diode lasers is collimated with small divergence, imperfections in the optical surfaces and scattering caused by dust particles make the light beam “unclean,” and may affect diffraction measurements, especially at small angles. One device that is used to treat an illuminating source is known as a spatial filter. Spatial filtering can suppress beam background and maintain a very smooth beam irradiance distribution. A conventional spatial filter consists of a set of optical elements, such as lenses and apertures. Since all background light propagates in divergent directions from the main beam it is spatially separable at the lens’ focal plane. By centering a small aperture at the focal spot of the main beam most of the background light will be blocked, allowing only the main beam to pass. The result is a cone of light that has a very smooth irradiance distribution and can be expanded to form a collimated beam that is almost equally as smooth. Figure 3.16A is an illustration of spatial filtering using conventional optics. This type of spatial filter is not immune to mechanical movement and is large in volume and comes at a high cost. A novel and more rugged spatial filter design employs a length of monomode optic fiber coupled to a laser diode together with an optical system that uses micro-optics such as gradient index lenses (Figure 3.16B). Monomode fibers have very small diameters (typically measured in microns), and allow only the propagation of light waves along the fiber axis,

effectively filtering out all stray light by the spatial constraint. The small diameter of a monomode fiber creates a near-point source of light, which is superior in this application to conventional spatial filter designs. After leaving the fiber, the light is expanded by a lens system to a collimated circular beam with a diameter of around 10-20 mm which illuminates the sample in the sample chamber [8]. In both arrangements, the output diameter of the circular beam can be adjusted by adjusting the distance between the aperture and the lens (Figure 3.16A), or between the tip of fiber and the lens (Figure 3.16B).

### 3.2.2. COLLECTING OPTICS

Particles in the sample chamber scatter light out of the incident beam. Upon leaving the sample chamber the scattered light may be guided to the detector plane either by Fourier optics or by reverse Fourier optics. A typical schematic of these two optical configurations is shown in Figure 3.17.

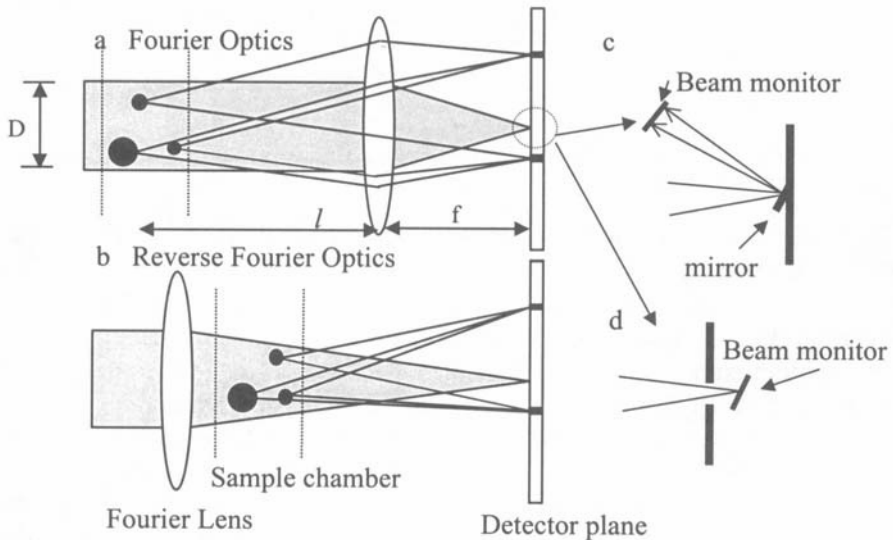


Figure 3.17. Fourier optics and reverse Fourier optics used in laser diffraction instrumentation.

In Fourier optics (Figure 3.17a), particles pass through an expanded and collimated laser beam at some fixed distance in front of a lens whose focal plane is positioned on a photosensitive detector array. The lens, which may be a single lens or a composite of several lenses, may be round or rectangular with a dimension typically around 50 mm. Together, the focal length or the effective focal length (in the case of a multi-lens arrangement), the detector array, and the laser wavelength determine the particle size range that can be analyzed. The

Fourier lens in Figure 3.17a serves two functions: it focuses the incident beam so it will not interfere with the scattered light, and it also transforms the angularly scattered light into a function of location on the detection plane. The incident beam is brought to focus onto the detection plane by the lens and is either reflected out by a mirror (Figure 3.17c), or passed through an aperture at the detector's center to a beam monitor (Figure 3.17d). The angular scattering pattern is recorded by the detector array. The most important feature of Fourier optics is that at a specific angle the scattered light will be refracted by the lens so as to fall onto a particular detector, regardless of the particle's position in the beam. Particles may flow or move through any part of the beam yet their diffraction pattern stays stationary and proportional in intensity to the total number of particles contributing to the scattering. In a polydisperse sample the angular pattern may change over time as the number distribution of particles in the scattering volume varies over time, with particles entering and leaving the beam. This temporal variation is usually integrated over time to give an average representation of the sample.

Design of the optics is guided by detector geometry and the intended sizing range for a given detector array dimension. For large particles, in order to detect central scattering lobes, the angle where the first is located has to be very small and the angular resolution needs to be high due to the rapid angular intensity fluctuations in the scattered light. On the other hand, to detect particles over a broad size range, a wide angular range (usually resulting in low resolution) has to be used in the same detector array. These two conflicting requirements have to be balanced if only one configuration of lenses and detector array is used. The maximum scattering angle,  $\theta_{\max}$ , at which the scattering intensity still can be collected by the lens is determined by the distance between the sample chamber and the lens ( $l$ , in Figure 3.17a), the lens size ( $d_L$ ), and the beam dimension ( $D$ ):

$$\theta_{\max} = \tan^{-1} \frac{d_L + D}{2l}. \quad (3.1)$$

For any given structure and dimension of a detector array, the angular range covered is inversely proportional to the focal length of the lens. For a short focal length (e.g.,  $f = 20$  mm),  $l$  will be small; the same detector array will cover a wider angular range. The fine structure at very small angle will then be lost because the first detector will correspond to a larger angle as compared to a configuration using a lens with a longer focal length (e.g.,  $f = 5000$  mm). The overall angular coverage now becomes smaller but the first detector will correspond to a much smaller angle and so the angular resolution is higher than in the short focal length setup. This, however, will result in a very long optical bench.

One way to design an optical setup having a wide dynamic size range is to use a set of lenses with different focal lengths to cover particles in different size ranges. Each lens covers a narrow size range. When particles out of the range are to be measured, a different lens replaces the present lens. From Eq. 3.1, in order to change the angular detection range, one can change either  $D$  or  $f$ , since there is little room to change  $d_L$ . One can use a short focal length to increase the angular detection range and use a long focal length to reduce the angular detection range. For example, in an optical design having a lens of focal length  $f = 50$  mm with a beam diameter of 2.2 mm, the sizing range is 0.18-87.5  $\mu\text{m}$ . When this lens is replaced with one of  $f = 5000$  mm and the beam diameter is increased to 39 mm, the sizing range is shifted to 45-8750  $\mu\text{m}$  [1].

The increase in beam diameter as the focal length is increased serves two purposes. First, when measuring large particles,  $D$  has to be at least larger than the largest particle to avoid statistical inaccuracy and illumination incompleteness. Also, a larger  $D$  becomes possible when  $f$  increases due to feasible lens structure. Secondly, the focal dot dimension at the focal plane is proportional to the ratio of focal length to beam diameter ( $f/D$ ). If  $f$  increases and  $D$  remains the same, the result is too large a focal dot and detection at small angles will become impossible. As an example, in order to detect the detail in the central lobes of a diffraction pattern, one wants the first detection angle at about one thirtieth of the first minimum location. This requires the beam width to be at least four times the largest particle diameter.

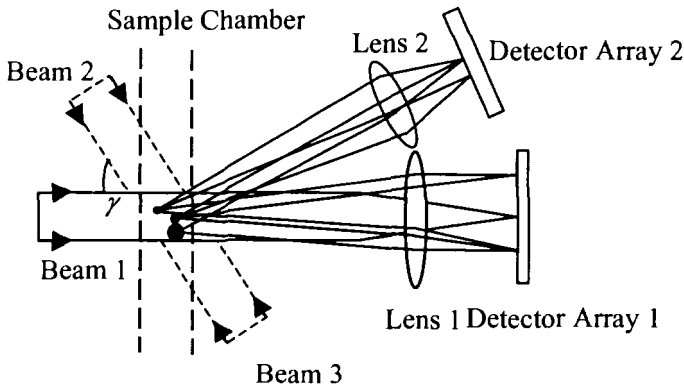


Figure 3.18. A double-lens, tri-laser optical system.

However, changing the lens can have adverse effects instrument ruggedness and integrity. The need for realignment each time a lens is changed or moved often prevents the results from being highly reproducible and also causes inconvenience in operation. A different way to achieve wide angular detection

while avoiding the changing or moving of lenses without compromising resolution is to use a second lens and a second detector array placed at a large angle. Such a design, as shown in Figure 3.18, also avoids the use of excessively large lenses. Besides the cost of large lenses, the quality of lens grinding and the associated aberrations that may affect large angle signals become more severe as the lens diameter increases.

The addition of a second lens and a second photodiode array can extend the detection angle to more than 35 degrees, effectively extending the lower sizing range to less than a few microns [9]. To detect scattering intensity over an even wider angular range, another alternative would be to use multiple lasers positioned in different directions so that the same detector array will receive scattering from the same particle but illuminated by the different lasers creating different effective scattering angles [10]. For example, in the system shown in Figure 3.18, if the two detectors cover an angular range from  $0^\circ$  to  $30^\circ$  using Beam 1, switching to Beam 2 the scattering angles will change to  $\gamma^\circ$  to  $(30+\gamma)^\circ$ . The angular scattering range will then be from  $(150-\gamma)^\circ$  to  $(180-\gamma)^\circ$  for Beam 3. In an optimal arrangement of both the three beams and the two detector arrays, a continuous angular intensity distribution from 0.02 to 165 degrees is possible. However, the alignment of multiple lasers (as a function of both intensity and position) is inherently complex and may be unstable. Non-synchronized intensity levels, polarization fluctuations and any drift in the three lasers will affect the uniformity of the angular pattern leading to possible additional measurement error because the angular pattern is created through three independent measurements. In addition, due to the nature of angular scattering patterns, detector dimension and spacing should be different when detecting scattered light at small angles or at large angles. In a tri-laser arrangement the same detector geometry has to be used for both small and large angles when switching between the lasers, and optimization of scattering detection can be difficult to accomplish. As stated in Section 3.1, simply increasing the detection angle only results in limited improvement. For any further increase in dynamic range, a different approach has to be used, such as the PIDS technique which utilizes both wavelength and polarization effects.

Another arrangement of the collecting optics, shown in Figure 3.17b, is known as reverse Fourier optics, in which the relative positions of sample chamber and Fourier lens are exchanged. In reverse Fourier optics, the particles are not illuminated by a collimated beam; instead, they are in a converging beam with the beam convergence determined by the focal length of the lens. Scattered light from particles is no longer collected by another lens; instead it is directly received by the detectors. The limitation on the size of the lens is therefore removed. In this arrangement, a lens with a long focal length can be used without increasing the length of the optical bench and a higher upper sizing limit is possible. If the detector dimensions are increased, detection of

scattering at large angles is also possible without the need for a second lens. But depending on the location of particles in the beam, in such an arrangement, scattered light from the same angle will not arrive at the same location in the detection plane. The same detector receives scattered light from different scattering angles depending on particle location in the converging beam. Figure 3.19 shows a geometrical analysis of the relation between particle position and scattering angle for the same point in the detection plane.

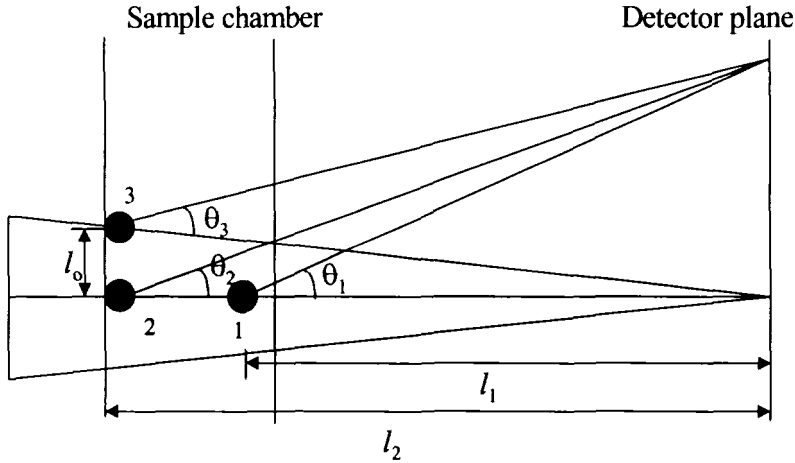


Figure 3.19. Geometrical analysis of particle scattering in reverse Fourier optics.

Based on simple geometry we can derive the following relations of the scattering angular range for each point on the detection plane due to the different locations of particles in the beam:

$$\frac{\theta_2 - \theta_3}{\theta_2} = \frac{1}{\theta_2} \cot^{-1} \left( \frac{l_0}{l_2 \sin^2(\theta_2)} + \frac{1}{\tan^3(\theta_2)} \right), \quad (3.2)$$

$$\frac{\theta_2 - \theta_1}{\theta_2} = \frac{1}{\theta_2} \cot^{-1} \left( \frac{2l_1}{(l_2 - l_1) \sin(2\theta_2)} + \tan(\theta_2) \right). \quad (3.3)$$

From Eq. 3.2, once  $l_0$  becomes much smaller than  $l_2$ , the error introduced can be negligible for particles having the same distance towards the detection plane but at different vertical positions (particles 2 and 3 in Figure 3.19). Because  $\Delta\theta$  is small it will have little effect on the deduced particle sizes.  $\Delta\theta$  at the same detector as detected from particles having different distances from the detection plane (particles 1 and 2 in Figure 3.19) is proportional to the relative distance

$((l_2-l_1)/l_1)$ . This will introduce a noticeable sizing error if the relative distance is not small. In practice, if the distance from the detection plane to the sample chamber is 20 cm and the chamber thickness is 5 mm, the maximum angular uncertainty would be 2.5%. Thus, when utilizing reverse Fourier optics, the sample chamber should be thin so that any sizing error may be minimized. The above two types of designs (Fourier optics and reverse Fourier optics) can also be mixed so the best features of both designs can be combined.

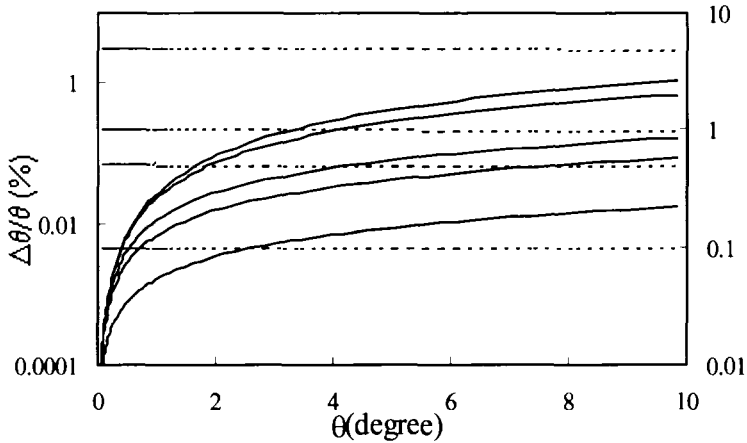


Figure 3.20. Angular uncertainty in reverse Fourier optics. The rising curves are calculated from Eq. 3.2 with  $l_0/l_2$  being 0.001, 0.005, 0.01, 0.05 and 0.1 for the curves from bottom to top respectively (left ordinate). The parallel dashed lines are calculated from Eq. 3.3 with  $(l_2-l_1)/l_1$  being 0.001, 0.005, 0.01 and 0.05 for the lines from bottom to top respectively (right ordinate).

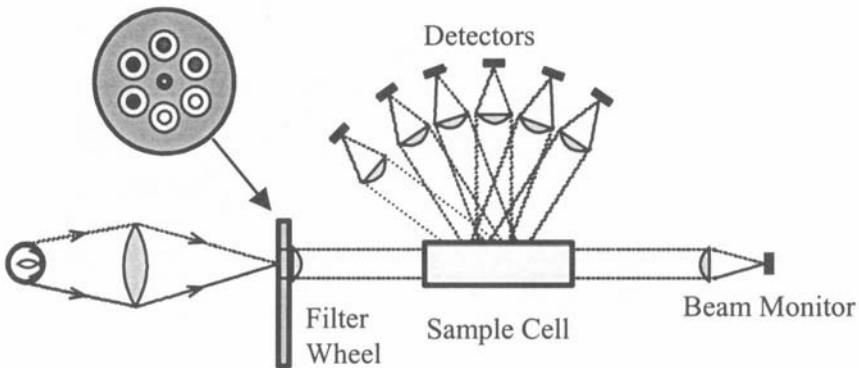


Figure 3.21. A typical PIDS system that utilizes wide angles, multiple wavelengths and polarizations to size submicron particles.

In a typical PIDS optical system (Figure 3.21), light from a white light source, for example, a tungsten-halogen lamp, is passed through filters of several wavelengths and at two polarizations. The collimated light illuminating the sample cell is recorded by a beam monitor. The differential intensity in the scattered light is recorded by detectors located through a wide angular range, typically from 60 degrees to 145 degrees. Measurements are made at each wavelength and polarization.

### 3.2.3. DETECTING SYSTEM

The detector array is perhaps the most sophisticated element in a laser diffraction instrument. Silicon detectors are commonly used as the detecting devices in laser diffraction analyzers because of their wide dynamic range (over seven decades of linear response), their high sensitivity ( $< 0.5$  A/W responsivity) and the long life of the silicon material. Lately, charge-coupled device (CCD) detectors have been tested in laser diffraction analyzers because they present an advantage in terms of their high resolution and two-dimensional geometry. However, the narrow dynamic range and low sensitivity of CCD detectors limit their application to a narrower size range when compared to the silicon detectors. For large particles in the Fraunhofer diffraction region, the diffraction pattern is the Fourier transform of the shape of the particle projection. If the particle images are acquired by a CCD the Fourier transform of the images, which are the diffraction patterns, can be computed and used in the data analysis. In this way, a long optical bench is not necessary when measuring large particles. In addition, the ability to measure the precise location of the incident beam on the CCD partially eliminates the need for fine mechanical alignment [11,12].

The geometry of a detector array depends on the desired angular range, sensitivity, angular resolution and other additional considerations. Ideally, the detector surface should have a reflectivity of zero. Since the central maximum intensity is so much stronger than that of the subsequent maxima (see Table 2.2), any reflection from the central peak can significantly affect detection of lower intensities at larger angles. As shown in Figure 2.4 and Figure 2.13, for large particles an important feature of the logarithmically measured scattering pattern is that the shape of scattering pattern remains the same only with its position on the log angle axis shifted, i.e., it is shift invariant. The locations of the first few maxima and minima of the scattering patterns at small scattering angles for different sizes change linearly if the detection angle is logarithmically scaled. Thus, a rational arrangement of elements in a detector has a logarithmic progression, each detector being larger than the preceding one by a constant multiple. The total area of each detector increases with increasing angle. The



angular progression or spacing between small angle detectors is much smaller than that between large angle detectors in order to keep similar resolution over the entire size range. For example, in the half-ring shaped detector shown in Figure 3.22 the area of the 20<sup>th</sup> ring is ~150 times larger than the area of the first ring (the innermost ring), and the total area of the 30<sup>th</sup> ring is ~1500 times larger than that of the first ring [13]. Such a design makes the size retrieval process (discussed in Section 3.3.2) most effective. In the forward scattering range there are only a few types of detector geometries presently in use: a simple linear pattern, a concentric half-ring pattern (Figure 3.22), an X pattern (Figure 3.23), and a fly-wing pattern (Figure 3.24).

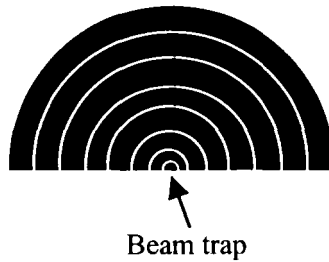


Figure 3.22. Schematic of the concentric half-ring pattern detector array (only a few half-rings are shown).

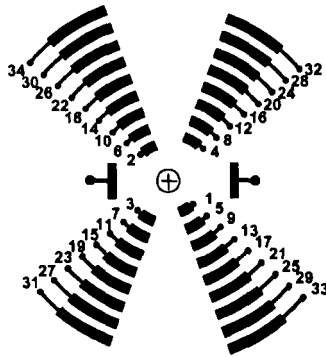


Figure 3.23. Schematic of the X pattern detector array.

The spacing and location of detector elements in these designs are tightly controlled, because even a small error in positioning can result in a substantial distortion in the particle size distribution. When comparing the two detector patterns in Figure 3.22 and Figure 3.23, major differences are that the elements in the half-ring pattern have larger detecting areas, which may result in high

capability sensitivity when scattering is weak but may be less sensitive to particle orientation for non-spherical particles. The X pattern allows for closer spacing of detector elements than in the half-ring design. Closer spacing at small angles enhances the angular resolution of the instrument resulting in higher resolution at the large end of the size range. The X pattern also provides possibilities for automatic instrument alignment and particle shape measurement.

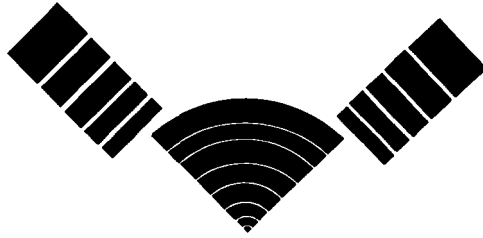


Figure 3.24. Schematic of the fly-wing pattern.

As mentioned earlier, in the center of detector array there is either a mirror or a hole which guides the unscattered beam to a beam monitor (Figure 3.17). The beam monitor serves several purposes:

- 1) Stray light "noise" is prevented from reaching the detectors;
- 2) The optimal amount of sample required for measurement can be determined from the attenuation of the incident light intensity ( $I/I_0$ ) as measured by the beam monitor. The proper range of attenuation, in which the least biased result can be obtained, depends on the instrument's hardware and software design and is often predetermined by the manufacturer in the case of commercial instruments;
- 3) Once the size distribution is obtained, from light attenuation the sample concentration, expressed as a volume percentage of particles can be estimated at least in the Fraunhofer diffraction regime:

$$C(v\%) = \frac{100 \ln\left(\frac{I}{I_0}\right)}{-3l \sum_i \frac{V_i(d)}{d_i}}. \quad (3.4)$$

In Eq. 3.4,  $l$ ,  $V_i$ , and  $d_i$  are the beam length across the sample (the sample chamber thickness), the volume, and the diameter of particle  $i$ , respectively. A correction factor can be added for non-spherical but regularly shaped particles [14]. Sample concentration can also be estimated because it is inversely

proportional to the transmitted intensity and to the square of the median diameter ( $d_{50}$ ) and is independent of particle shape [15], or it can be estimated using the more rigorous equation (Eq. 2.43) in Section 2.3.5.

Because scattering intensity changes rapidly with scattering angle, especially in the case of large particles, one determining factor in obtaining high resolution and correct size distribution is the number of detectors in the detector array. Even with the best data analysis algorithm, without enough detectors high resolution results are not achievable. One can never resolve more information from less information. Without inputting additional information or providing some restrictions or artifacts, the number of data points in the size distribution should be close to the number of detectors, i.e., the number of detectors determines the resolution of size distribution. In addition, due to the oscillatory nature of scattering pattern, if the number of detectors is too small the fine structure in the scattering pattern will be missed due to angular integration if each detector covers a large angular range and hence the ambiguity in computation will increase resulting in an incorrect size distribution. This is because the size retrieval process is based on reported discrete intensity that is integrated from the detector surface area, not the real continuous angular intensity. On the other hand, if the number of detectors over a given angular range is too large, each detector can only have a very small area and the signal-to-noise ratio may decrease significantly, making the detection more susceptible to particle orientation and experimental noise. As a consequence, the size retrieval process may then become unstable, resulting in poor reproducibility. Thus, the importance of optimization in detector design, taking into account considerations of resolution, sensitivity, and reproducibility can never be overestimated.

Figure 3.25 depicts the effects on resolution and accuracy using a scheme that depends only on the location of the first minimum position from a detector array with a large number of detectors as compared with a detector array having fewer detectors. In this example, in the array with a large number of detectors, one finds that the first minimum is located between 0.090 and 0.100 degrees, which corresponds to an angular width of one detector and represents the instrument resolution. If Eq. 2.20 is used with  $\lambda = 750 \text{ nm}$ , the corresponding size uncertainty will be  $58 \mu\text{m}$  (from 582 to 524  $\mu\text{m}$ ). The same calculation can be performed for the array with a smaller number of detectors. The minimum now falls between 0.085 and 0.105 degree. The size uncertainty is now  $118 \mu\text{m}$  (from 617 to 499  $\mu\text{m}$ , a much lower resolution. In Figure 3.26, a scattering curve from 500  $\mu\text{m}$  glass beads in water is recorded using two different detector arrays: one with 126 detectors (solid line), and the other with 42 detectors (solid line with beads). It is clear that the signal recorded using 42 detectors misses much of the fine structure when compared with that recorded using 126 detectors.

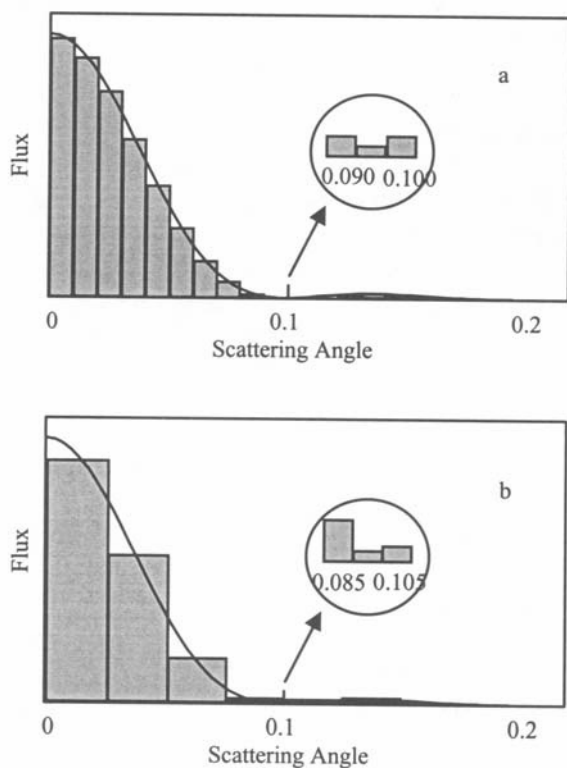


Figure 3.25. A demonstration of the effect of detector number in size resolution. The top graph shows a detector array with an angular resolution of 0.01 degree. The detector array in the bottom graph has an angular resolution of 0.02 degree [3] (by permission of Medpharm Scientific Publishers).

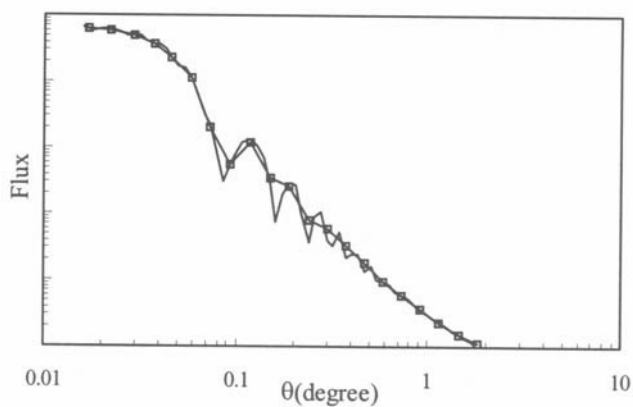


Figure 3.26. Detected signals from detector arrays of different detector numbers.

### 3.2.4. SAMPLE MODULE

The main function of a sample handling module is to expose particles to the light without discrimination to their size but also without introducing any undesirable effects such as air bubbles, thermal turbulence, attrition, or agglomeration. A typical sample module is composed of a sample chamber coupled to a dispersing and circulation system. There are three general categories of dispersing systems: those designed for dry powders, for liquid dispersions, and for aerosol sprays. Depending on the specific requirements of the instrument, it may be used to perform laboratory measurements, or for on-line (or in-line) tests. The specific sample processing modules will often be different. For aerosol sprays, an adapter is typically placed next to the beam so dry inhalers or liquid sprays (from propellant or pump sprays) can be measured at different distances from the spray nozzle. An actuator can be used to control the stroke length as well as spray velocity and acceleration. A vacuum extraction pipe with a filter is placed opposite to the particle flow so that the aerosols can be collected and properly disposed.

Particles in liquid media (dry powders and liquid-borne particles in liquid dispersion where the dispersing medium may be either an aqueous or an organic medium) may be pre-dispersed before being added to the sample module; or, alternatively, added directly into the liquid, often with some additives used to aid dispersion. The liquid suspension is continuously recirculated in a closed-loop circulating system so that each particle can enter the scattering volume more than once and its orientation in the beam will more likely be randomized. The dispersing and circulating part of the sample module may include certain mechanisms such as circulation pumps, heating coils, an ultrasonic probe, and stirring bars to better help disperse and circulate the particles. Figure 3.27 shows two typical sample circulation systems for particles in liquid.

Two types of circulating pumps can be used, centrifugal or peristaltic. A good circulation system should provide sample homogeneity, effective circulation and minimum attrition. The effectiveness of any circulating system can influence measurement results, sometime significantly. The necessary capacity of the sample module, which includes the overall volume of the sample reservoir, tubing, and sample chamber, is determined by the average particle size and the breadth of distribution of the samples to be analyzed. For a closed system, the minimum capacity needed to representatively measure a particulate sample is proportional to particle size and polydispersity. The larger the particle size and the broader the distribution, the greater the amount of sample (and thus also the more diluent) is required. A capacity of between 0.1-1 liter is often adequate. On the other hand, for precious samples or for very small particles,

sometimes only a small amount (e.g., 0.01 g) of specimen is available. The sample module then requires only a small capacity (< 50 ml, e.g., Figure 3.27b). Occasionally, to size samples having extremely broad distributions, a closed recirculation system having a liter or so of capacity is not enough. An open system (such as a flow-through system where all the particles are passed through the scattering volume only once and then flushed out) has to be adopted. For example, for dry river sediments which often consist of particles ranging from the submicrons up to millimeters in size, a few tens of grams of sample is required in order to achieve a good statistical representation of the specimen. More than 20 gallons of aqueous suspension is often needed for this amount of solids in a laser scattering measurement.

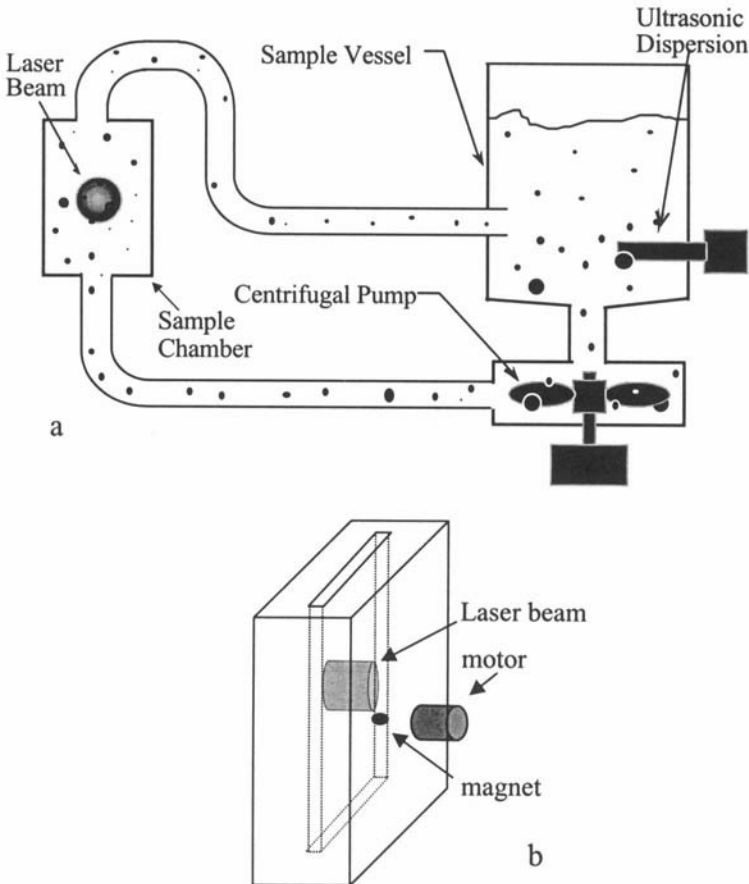


Figure 3.27. Typical sample circulation systems, a: for a large volume of liquid; b: for a small volume of liquid.

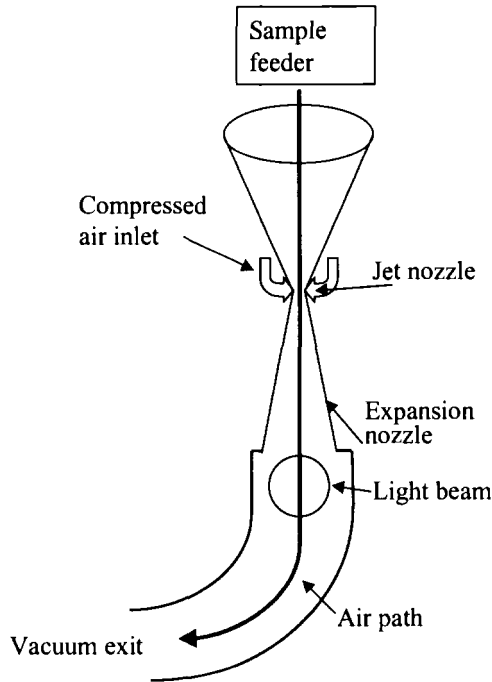


Figure 3.28. Schematic of a dry powder module.

For dry powders, the dispersing medium is usually air. Particles in a dry powder module are made to flow through the sample chamber by a driving force which results from the application of high pressure air and/or a vacuum force. On many occasions, complete dispersion of the particles is difficult to achieve without a proper balance of dispersing forces. Particles may be seen in the form of single particles, agglomerates, aggregates, or associations. This is especially true for particles smaller than  $5\text{ }\mu\text{m}$  because of their strong static charge or other cohesive forces. Dry powders can be predispersed using dry dispersants such as silica sols or carbon black. These dispersants are very small and so they will not change particle size after dispersing the particles by coating them. Dry powders can also be dispersed using mechanical means such as stirring or vibration combined with augering in a hopper or the rotational motion of a feeder, etc. For dry powders with particles larger than a few hundred microns, such as sands and gravels, the above dispersing means may not be needed. Gravitational dispersion in static air from the mouth of a falling shaft to the beam is usually sufficient. The design of the flow path and the ways high pressure and/or vacuum are used are the key issues in the effectiveness of a dry powder module with respect to sample dispersion [16,17]. Figure 3.28 shows a schematic for a module using both vacuum and adjustable air-jet forces. The sample feeder can

consist of a funnel, hopper, and vibratory chute along with several mechanical means to disperse the particles and to deliver a constant and homogeneous flow independent of the total load of the raw or predispersed particles. Dispersing particles as small as  $0.5\ \mu\text{m}$  is also possible by using air. On-line measurement of dry powders using laser diffraction can be easily accomplished after modification of a stand-alone module.

The sample chamber typically is comprised of an entrance, an exit, and a body with two to four windows arranged in a rectangular shape. If only forward scattering is to be measured, just the front and back windows are needed. A third window at one side may be needed for measurement at large angles, and the fourth one may be used for viewing purposes. The windows should not absorb or distort the incident beam. The thickness of the chamber (the distance between the front and back windows) should be thin in order to minimize the effects of multiple scattering or optical error in the case of reverse Fourier optics. For dry powder measurements, particles should flow through the middle of the chamber from the entrance to the exit without touching the windows so as to minimize possible window abrasion from hard particles. For particles in liquid suspension, the liquid flow should be designed so that any dead flow space is minimized and the distribution of particles of different sizes does not occur along the flow path. In all cases, and especially in an open flush system, a homogeneous non-size-discriminating flow in the sample module is very important. As shown in Figure 3.29, not all particles passing through the sample chamber are seen. This is itself a sampling process.

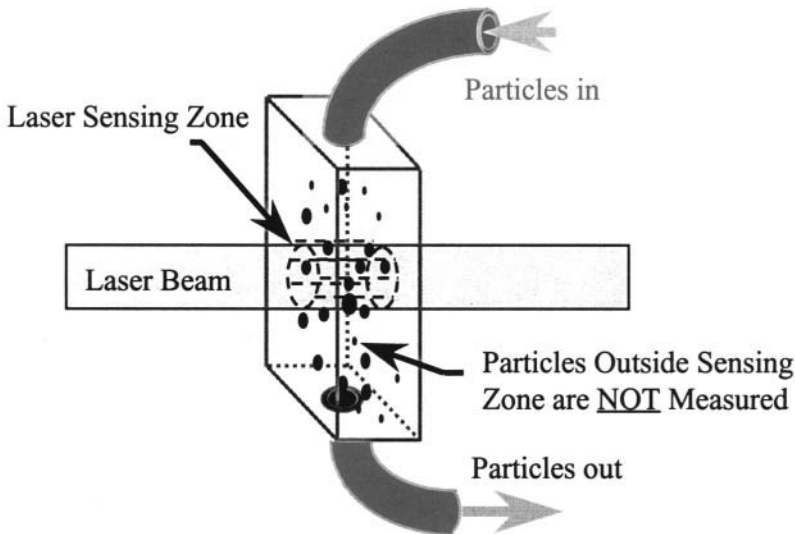


Figure 3.29. Particle sampling in sample chamber.



Autosamplers are now often used in laser scattering instruments to meet the demand for automation and quality control. A typical autosampler consists of a grid or carousel housing 20-40 sample tubes that in some instances may have bar-codes that uniquely identify each sample; a dispersing processor that can supply dispersant, means to apply sonication force, and in some instances an additional dispersing medium for each sample, and finally a sample dispensing device that sequentially dispenses sample materials to the sample handling module.

Laser diffraction technology is based on models of single particle scattering. The concentration of suspension thus has to be kept low to avoid multiple scattering. However in many instances dilution is not feasible and the sample has to be maintained in a concentrated suspension. For example, an emulsion may not be stable after being diluted; on-line measurement requires the sample to be analyzed unchanged. To address these situations while still using the laser diffraction principle the sample chamber has to be very thin. In the typical case there are only one or a few “layers” of particles in the beam. Light scattered from the particles exits the chamber without becoming the light incident upon any other particle. Thus, although the concentration is high, multiple scattering is kept to a minimum or altogether avoided. For particles of different sizes, the distance between the front and back windows may be adjustable from some few microns up to a few millimeters. Measurements of milk, paint, or latex suspensions have proven that once the transmittance of the incident light is higher than 30%, a correct size result can be obtained from concentrated suspensions using such a thin sample chamber [18].

### 3.2.5. INSTRUMENT CALIBRATION AND VERIFICATION

In the common understanding of calibration, the calibration procedure may involve the measurement of some reference material whose size has been carefully determined and verified by other reference techniques, and the instrument’s calibration constant will be adjusted to match the assayed value. However, since laser diffraction is an absolute measurement technology it is not required to use reference materials to calibrate the instrument, although one may use these materials to verify the validity and status of an instrument. For a laser diffraction analyzer, calibration is mainly related to the alignment of the optics (i.e., the laser and detectors). Since in most cases the detectors are etched onto a circuit board they are not individually mobile components. The task then is simply to align the laser, the focusing lens, and the detector array.

Precise alignment of the detector array is critical in order to obtain correct results, especially for large particles. Taking the derivative of Eq. 2.20,

the relative sizing error introduced due to error in the scattering angle is linearly proportional to sphere diameter in the Fraunhofer region ( $\lambda = 0.75 \mu\text{m}$ ):

$$\left| \frac{\Delta d}{d \Delta \theta} \right| \% = \frac{\pi}{180} \sqrt{\left( \frac{d}{1.22 \lambda} \right)^2 - 1} \cdot 100\% \approx \frac{d \pi}{180 \cdot 1.22 \lambda} \cdot 100\% = 1.9 d \%. \quad (3.5)$$

A 0.01 degree error in scattering angle will produce a 9.5% error in size for a  $500 \mu\text{m}$  particle, but will produce only a 0.095% error (which is negligible), for a  $5 \mu\text{m}$  particle. A detailed analysis of optical misalignment in instruments using the half-ring shaped detector indicates that in order to keep the sizing error due to any misalignment less than 0.5%, the transitional alignment (eccentricity) has to be better than 0.1 mm, and the angular alignment (inclination) has to be better than  $2.5^\circ$  when compared with ideally designed optics [19].

Figure 3.30 shows one alignment scheme in which the focusing lens is aligned using stepper motors so that the collimated beam is positioned at the center of the detector array.

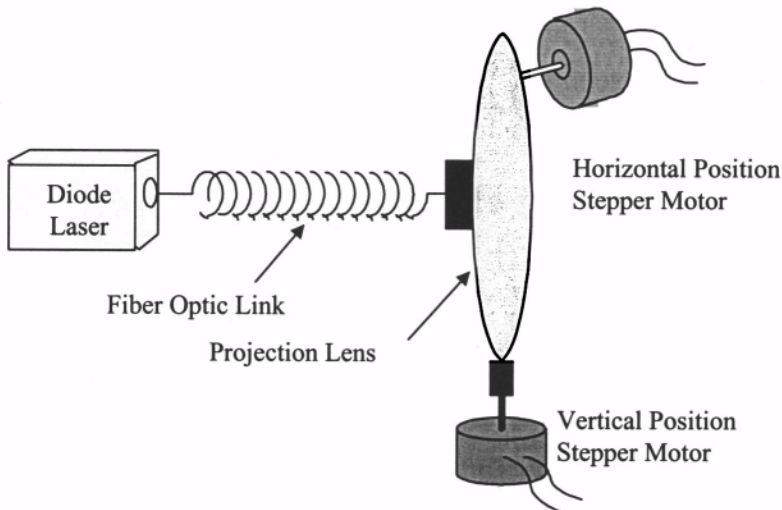


Figure 3.30. Alignment scheme for a laser diffraction instrument.

There are three common techniques used in instrument alignment. One is to use a spherical control or standard that is large and monodisperse in size (a few hundred microns). If an instrument is aligned the diffraction pattern will match the pattern predicted from theory. This scheme relies on an ideal sample that is often expensive to obtain. All operational factors have to be considered, such as

sample concentration, dispersion, circulation, etc.; and the control has to replace the sample in the sample chamber in order to perform the alignment. Thus, this scheme is often used only to validate and not to routinely align the instrument. The second technique is to use the forward incident beam as the alignment standard, as described in Figure 3.31.

Here three triangular detectors serve as the alignment targets. For a circular spot focused from the incident beam, perfect alignment will only be approached once all three detectors detect the same amount of intensity. This method is based on an assumption that the focal dot has a centrally symmetric intensity distribution and is perfectly circular. However, due to imperfections in the lenses and light sources asymmetry of the focal dot is unavoidable and is unique to each instrument since the optics in each instrument is different. Thus, although each instrument may achieve a certain degree of reproducibility and precision after compensating for any asymmetry, a sample measured using different instruments may yield different results because the optics in each instrument has its own characteristics. The typical instrument-to-instrument reproducibility is about a few percent from instruments that are aligned using this technique.

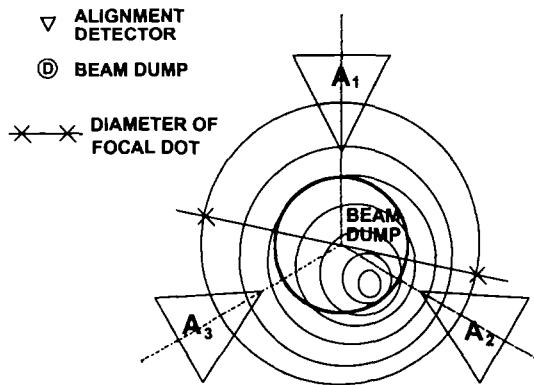


Figure 3.31. An optical alignment strategy.

The third method is to use a dark field reticle. A dark field reticle is either a single circular hole of a few hundred microns in diameter (or a set of holes) in a metal sheet or a set of black circular dots on a transparent sheet. Both transparent holes or black dots diffract light just the same as large spherical particles having the same size would. By inserting the reticle into the beam the scattering pattern from the hole(s) or dot(s) can be used to perform the alignment. If the beam is misplaced from the center then the intensities detected at the three detectors (Figure 3.31) or each quadrant of detectors (Figure 3.23) will be distorted differently. For the X-shaped detector arrangement, such

misalignment will produce a saw-tooth intensity pattern because of the unique detector sequence. When the beam is perfectly aligned the recorded intensity will be a smooth curve as shown in Figure 3.32. Thus, with the built-in reticle and the X pattern, alignment is easy, quick and can be fully automated under computer control without tedious manual loading and positioning. Instruments aligned with this method typically have a reproducibility of about  $\pm 1\%$ .

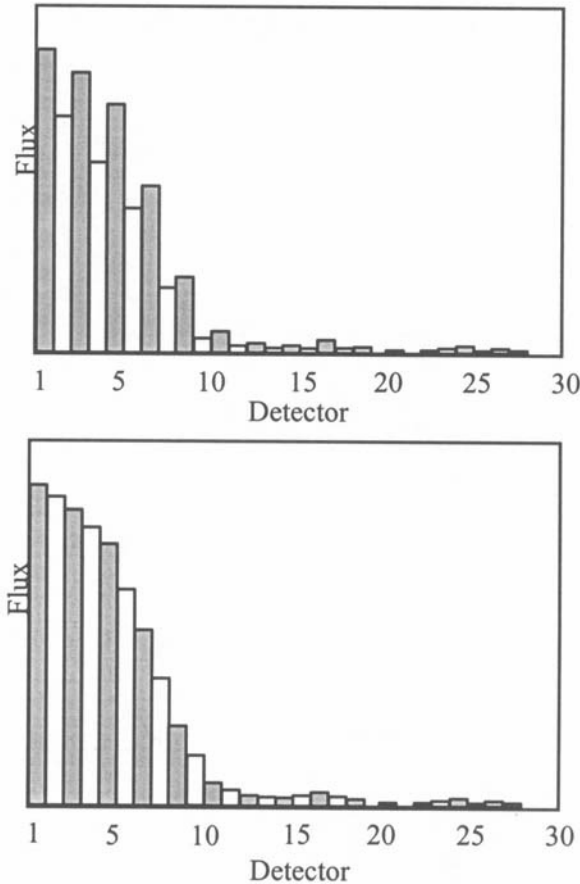


Figure 3.32. Alignment indication for the X-shaped detectors. Upper: misaligned; Lower: aligned.

There are two schemes in practice to verify and validate a laser diffraction instrument and its measurement. One is to use either reference materials (national standard or certified reference materials or secondary reference materials traceable to the national reference materials) or the instrument manufacturer's controls [20]. The average of the median size value ( $d_{50}$ ) from at least three independent measurements should agree with the certified value of

the reference material within 3%, and the average values at  $d_{10}$  and  $d_{90}$  should deviate by less than 5% from the certified values [21]. Several monodisperse spherical reference materials are available from various national agencies and more secondary reference materials are available from commercial vendors. For polydisperse standards, which can be used to test the linearity and sensitivity of an instrument over a broad dynamic range (spanning at least one decade of size), there are several non-spherical reference materials available worldwide, though these have not been proven to be appropriate candidates for laser diffraction instrumentation due to the poor precision caused by shape effects. There is an international effort to develop polydisperse spherical standardized reference materials. Presently, such materials, marketed as reference materials but not as certified reference materials, are available from several vendors [22]. Product samples that are of typical composition and particle size distribution for a specified class of product can also be used for instrument validation, provided that the particle size distribution has been proven to be stable over time. The results should comply with previously determined data, with the same precision and bias as that of the reference material.

**Table 3.2. Particle distribution used in the Malvern MSX62 reticle**

Diameter ( $\mu\text{m}$ )	Number of Particle
20.74	13
22.64	49
24.68	149
26.9	360
29.34	697
32	1076
34.9	1326
38.06	1304
41.5	1023
45.26	640
49.36	320
53.82	127
58.68	41
64	10

The second and less popular method is to use a reference reticle. A diffraction reference reticle is created to be a precision image of spherical particles on a polished optical flat. Ultra-thin chrome disks are placed on or in the flat using semiconductor mask making technology. Each reticle contains a set of circular disks that conform to some well-defined size distribution with a known statistical behavior, typically being constructed using discrete size classes from a log-normal volume particle distribution. These discrete size classes form a geometric progression that provides uniform size intervals on a log-size axis.

The number of particles in each size is taken from the defined size distribution and desired concentration. Images of disks can be measured with a calibrated graticule using a method traceable to a national standard. Table 3.2 lists the disks on the MSX62 reticle offered by Malvern Instruments [23]. In this reticle there are 7135 disks uniformly but randomly distributed over a 20 mm diameter circle yielding an effective projected area coverage of 2.5% and a predicted obscuration of 5%. It represents a discrete approximation to a log-normal volume distribution with a mean size of  $40\mu\text{m}$  and a width 1.2.

The diffraction reference reticle is a unique tool that can be applied invariantly to many instruments so that many operational factors which might introduce errors can be avoided provided the same reticle is used. However, a reticle has intrinsic limitations that prevent it from being used as a universal verification tool. The main limitation of the reticle arises from the fact that all the disks on the flat are static. They are not moving particles as would be the case in a real measurement. Their diffraction will thus produce a unique interference pattern which is different from the pattern that would be normally produced by truly randomly oriented and dynamic particles. The diffraction pattern from the reticle will not exactly match the theoretical prediction of either the Fraunhofer or Mie theories. Secondly, such a reticle has to be designed for instruments having specific beam characteristics. If the diameter of the illuminating beam is smaller than 20 mm, only part of the distribution will be measured. Even if the beam diameter is larger than 20 mm, the homogeneity or smoothness of the beam intensity distribution can affect the result. These effects, in addition to the accuracy of the sizes of the disks, limit the overall accuracy of a reticle measurement. For example, the accuracy of the  $d_{10}$  and  $d_{90}$  values (which 10% and 90% of the particles are smaller than the 100% value, respectively) of the MSX62 reticle is about  $\pm 5\%$ , which is much lower than what is possible in typical measurements using real spherical samples. A detailed analysis of this issue can be found elsewhere [24]. To overcome the first limitation, two approaches have been proposed based on a theoretical simulation. If the circular disks do not overlap as in the case of the present reticles, by defining and implementing a phase function in the data interpretation algorithm, the original size distribution can be retrieved with little distortion. Another approach is to distribute the disks on the reticle completely randomly without any restriction resulting in many disks overlapping each other. Except for a false small peak of larger particles, the retrieved size distribution otherwise agrees well with the original disk distribution on the reticle [25].

### 3.3. Data Acquisition and Analysis

### 3.3.1. DATA ACQUISITION

As sample is introduced to the sample chamber, it begins to scatter out light of its direct path along the optic axis, and the signal in the beam monitor decreases. When there is a sufficient amount of particles in the sample chamber to create a good signal at the photodetectors, but not so much as to cause multiple scattering, the conditions are optimized and measurement begins. During each “scan”, light intensity is converted to electric current by the photodetectors, and the signal from each detector is either processed by a dedicated amplification circuit or is connected to multiplexers and processed by a single amplification circuit that cycles through all detectors sequentially. The signals are then digitized and transferred to the computer. Each measurement consists of many scans that may take a fraction of one second or longer depending on the design of the electronics. Data from each scan are accumulated and written to a data file and saved or output when the measurement is completed. The values in this file typically include the scattering from the particles and the medium as well as any stray light from the optics. They may also include noise from the electronics. Thus, typically, two “calibration” measurements are needed. In the first one, sometimes called the dark current measurement, all illuminating lights are turned off. Any recorded signal then resulted purely from the electronics. Next, in the background measurement, the illuminating lights are on but the sample has not yet been introduced. The signal now received is the sum of the electronic noise plus any scattering from the medium and any stray light. The dark current and background at each detector have to be properly subtracted from the signal obtained from each detector during the sample measurement. Because of unavoidable inhomogeneity between individual detector surfaces and amplification circuits, the signal from each detector has to be scaled by some overall conversion or amplification factor for that detector, which is predetermined and further normalized by the detector area. Finally, a set of scattering flux  $f(\theta, \varphi)$  is obtained and ready for the size retrieval process.

#### *Instrument Alignment and Validation*

After switching the power on, the instrument should be given sufficient time for the light source to warm-up (typically 0.5-2 hrs) so that a stable light intensity can be delivered. This period also allows the instrument to reach an equilibrium state between the room temperature and the internal temperature of the optical bench. Without this, frequent alignments may have to be performed due to any temperature changes in the various optical parts. Before sample analysis, the instrument should be in a clean and neat condition, aligned, and validated by reference or control materials. If a change of lens or lens position is needed for the required measurement range, as is the case in several instrument designs,

more careful alignment is needed to ensure all optical parts are correctly positioned in order to achieve the specified precision and accuracy.

### *Sample Preparation and Introduction*

Ignoring the theoretical bias that may arise from applying incorrect refractive index and any departure of the particles from the theoretical constraints, in measurements performed by modern state-of-the-art commercial instruments, the major source of systematic errors is usually caused by improper sample preparation. Sources of improper sample preparation include 1) incorrect sampling in which case the specimen will lack a good statistical representation of the bulk material; 2) incomplete dispersion of the particles; and 3) particle comminution, dissolution, or evaporation. These possible error sources can be avoided through the use of a proper sample preparation procedure so that a stable suspension can be presented for measurement. The amount of sample delivered to the instrument should be monitored, usually via the light obscuration or transmission ratio. Most commercial instruments have a specified obscuration range that will produce the best results. For dry dispersions, since the particles pass through the scattering volume only once, a steady mass flow needs to be maintained. For liquid dispersions, avoiding or removing air bubbles is one of the most commonly overlooked steps in obtaining a good result.

### *Air Bubbles in Liquid Dispersion*

One of the subtle experimental error sources in measurements of liquid-borne particles is created by air bubbles. Since air bubbles have a large relative refractive index in aqueous suspensions, they scatter light just as would solid particles. Consequently, they will be sized and skew the true particle size distribution. If the non-removed air bubbles are stable throughout the measurement they will not, in most cases, affect the result since their influence can be compensated for by the background measured before sample is added. Often, when the sample size is not in the same region as the air bubbles, the user can just discard the air bubble peak. However, if air bubbles are present during the background measurement yet disappear over the course of the sample measurement due to their escape during circulation or for other reasons, negative data may be created in the sample flux pattern.

Most dissolved air bubbles have sizes ranging from 60-200  $\mu\text{m}$ , depending on the size, amount, and nature of the sample and also the water source. For example, air bubbles have a size range of 40-500  $\mu\text{m}$  in water, but 8-1000  $\mu\text{m}$  in highly viscous media. In some cases, air bubbles in excessive quantities may be visible, especially if the water pressure in the supply lines is high. This is due to the fact that a dissolved gas under high pressure will be released when the pressure is reduced; e.g., vented to atmospheric pressure. One



can inspect the sample chambers with a flashlight or check the sample entry port or surface of the diluent for bubbles. Large air bubbles can usually be removed by circulating the liquid through the sample module for a few minutes at lower pump speeds or by sonication. Table 3.3 summarizes the most common sources of gas (air) bubbles and ways to avoid them.

Table 3.3. Gas bubbles in liquid dispersion

Source of Gas Bubbles	Way of Avoiding Gas Bubbles
Dissolved gases (increase in temperature and/or decrease in pressure causes water to degas)	Use filtered, bottled water whenever possible. Tap water and deionized water have shown to be gaseous. If filtered, bottled water is not available, to allow the water to reach room temperature before measurement.
Excessive surfactant, dispersant, or residue cleaners	Reduce the dispersant amount whenever possible.
Viscosity of medium	Take extra care when handling viscous media (pour along side of vessel; pipette slowly, etc.); leave system for 1-2 hours (or overnight) with pump off to allow bubbles to rise to the surface or dissipate.
Holes or gaps in hoses or fittings	Check hoses for holes, creases, and tears and cell line fittings for tightness, rust, or particle buildup.

### 3.3.2. DATA ANALYSIS

For monodisperse particles, there is a one-to-one relationship between the scattering intensity and the scattering angle for a particular size. For polydisperse samples, each individual particle will contribute its own unique scattering signal to the composite angular pattern differentially. The intensity detected at a specific scattering angle is an integration of the scattering from all particles. Each detector has a finite dimension, covering some angular range  $\Delta\theta_i\Delta\phi_i$ . The values of  $\Delta\theta_i$  and  $\Delta\phi_i$  depend on the radial location of the detector. For detectors located at small angles,  $\Delta\theta_i$  and  $\Delta\phi_i$  are typically very small, usually on the order of  $10^{-3}$  degrees. For detectors at large angles, this range can be as large as some few tenths of a degree. Thus, integration over the detector area is needed:

$$a(\theta, \phi, d) = \int_{\theta_1}^{\theta_2} \int_{\phi_1}^{\phi_2} I(\theta, \phi, d) d\theta d\phi / \int_{\theta_1}^{\theta_2} \int_{\phi_1}^{\phi_2} d\theta d\phi. \quad (3.6)$$

In Eq. 3.6,  $\theta_u$ ,  $\theta_l$ ,  $\varphi_u$ , and  $\varphi_l$ , denote the lower and upper angular edges with respect to the angles  $\theta$  and  $\varphi$ . The term  $a(\theta, \varphi, d)$  is the unit volume scattering intensity from particles of diameter  $d$ , detected by a unit detector area at angles  $\theta$  and  $\varphi$  that are the average of  $\theta_u$  and  $\theta_l$ , and the average of  $\varphi_u$  and  $\varphi_l$ , respectively. The total scattering intensity detected at the average scattering angle  $\theta$  and  $\varphi$  from all particles in the scattering volume per unit detector area is:

$$f(\theta, \varphi) = \int_{d_{\min}}^{d_{\max}} a(\theta, \varphi, d) q(d) dd \quad (3.7)$$

This is the Fredholm integration of the first kind, with  $a(\theta, \varphi, d)$  termed the kernel function, the exact numerical solution of which is an ill-posed problem [26]. In practice, this continuous integration is often replaced by a discrete matrix format in order to resolve the size distribution  $q(d)$ :

$$\begin{bmatrix} f(\theta_1) \\ \dots \\ \dots \\ f(\theta_m) \end{bmatrix} = \begin{bmatrix} a(\theta_1, d_1) & \dots & \dots & a(\theta_1, d_n) \\ \dots & \dots & \dots & \dots \\ \dots & \dots & \dots & \dots \\ a(\theta_m, d_1) & \dots & \dots & a(\theta_m, d_n) \end{bmatrix} \begin{bmatrix} q(d_1) \\ \dots \\ \dots \\ q(d_n) \end{bmatrix}, \quad (3.8)$$

or

$$\mathbf{f} = \mathbf{a} \cdot \mathbf{q}. \quad (3.9)$$

If either Mie theory or Fraunhofer theory is used (as is the case in present practice), because of the symmetry of the scattering pattern the matrix is independent of  $\varphi$ . Thus, in Eq. 3.8 the variable  $\varphi$  has been removed. The left side of the matrix represents the detected intensity at scattering angles  $\theta_i$ , with  $i$  ranging from 1 to  $m$  for  $m$  detectors. The flux results from the scattering from all particles with diameters  $d_j$  that scatter  $a(\theta_i, d_j)$  amount of light per unit volume, with  $j$  ranging from 1 to  $n$  for  $n$  particles in the sample. For convenience, the particles are grouped. Although the distribution may be continuous, because of the countless number of particles, in a discrete matrix form only a fixed set of size classes is presumed. Particle having sizes between these chosen intervals will be represented by particles in the chosen size classes, with the number of such size classes being  $n$ , sometimes called the bin number. The matrix  $\mathbf{a}$  is called the scattering kernel, which can be computed according to the theories described in Chapter 2. Using a matrix inversion technique,  $q(d_i)$ , the particle size distribution can be resolved from the measured  $f(\theta_i)$  and the computed  $a(\theta_i, d_j)$ . Different instruments have a different specified size range

which is classified into some fixed number of size bins that have fixed locations and widths; and different instruments have unique detector arrays with fixed angular locations and angular coverage for each detector. Having defined both the detector geometry and the size classes, for a specific refractive index, a matrix **a** can be built for a particular instrument. This matrix is often referred to as an *optical model*.

There are many ways to resolve  $q(d)$  from  $f(\theta)$ . The simplest one is to assume an analytical distribution form incorporating a few adjustable parameters (typically two parameters - see Table 1.3 for some common forms). Calculation is made assuming the analytical form in combination with the optical model, with a guess about the adjustable parameters. The calculated flux pattern is then compared with the measured pattern iteratively by a least-squares method. Adjustments are made to the parameters to obtain a better fit between the calculated flux pattern and the measured one. This iteration goes on until a best fit is obtained. This scheme requires less computing power than other more complicated algorithms. However, it does assume some distribution form that may not be even close to the real distribution.

In the integral transform method  $q(d)$  is resolved from Eq. 3.7 based on a transformation function that provides an exact analytical solution from the scattering pattern in the Fraunhofer diffraction region. Here, the result is obtained without any *a priori* assumptions about, or modeling of, the distribution. The solution so derived is very stable, and no iterative linear algebra is involved [27,28,29,30,31]. The moments of  $q(d)$  can be obtained using the integral transform technique even without solving Eq. 3.7 [32]. Provided that the number concentration  $C_n$  is known, from the first three moments  $M_1$ ,  $M_2$  and  $M_3$ , the mean size,  $\bar{d}$ , the total surface area,  $S$ , and the total volume,  $V$ , of the particles in a unit volume suspension can be obtained.

$$M_1 = \frac{2}{k_o^3 \lambda} \lim_{\theta \rightarrow \infty} \theta^3 \frac{I(\theta)}{I_o} = \frac{\pi}{\lambda} C_n \bar{d}, \quad (3.10a)$$

$$M_2 = \frac{2}{k_o^3} \int_0^\infty \theta \frac{I(\theta)}{I_o} d\theta = \frac{S}{\pi}, \quad (3.10b)$$

$$M_3 = \frac{3\lambda}{4k_o^3} \int_0^\infty \frac{I(\theta)}{I_o} d\theta = \frac{6V}{\pi}. \quad (3.10c)$$

The latest (and most complex) method is to use a matrix inversion like the one given in Eq. 3.9 to obtain  $q(d)$ . There are many matrix inversion and data fitting techniques available [33,34,35], though the inversion algorithms used in

commercial instruments are almost always proprietary. Due to the oscillatory nature of the Bessel function (which is the mathematical foundation of both the Mie and Fraunhofer formulations) and because of measurement errors in the scattering pattern and the large number of matrix elements (for example in a detector array with 100 detectors and a range divided into 100 size class, there are 10,000 matrix elements and 100 equations), a direct inversion will often create an oscillating and physically unrealistic result, even with the incorporation of the non-negativity least-squares constraint. One way to overcome this is to use the Chahine scheme which uses an iterative correction to the size distribution until the residual approaches an asymptotic minimum [36]. Another common method to condition and suppress the oscillatory behavior of the process is the Phillips-Twomey method [37,38], in which a smoothing or covariance matrix  $\mathbf{H}$  is added. In this method, the solution to Eq. 3.9 is given by:

$$\mathbf{q}_{\text{smoothed}} = (\mathbf{a}^T \mathbf{a} + \gamma \mathbf{H})^{-1} (\mathbf{a}^T \mathbf{f} + \gamma \mathbf{p}) \quad (3.11)$$

where the superscript T denotes the transposition. Here  $\gamma$  is the regularization parameter that determines the degree of smoothing and  $\mathbf{H}$  contains smoothing instructions, which effectively link the elements of  $\mathbf{q}$  by their second-order differences or other constraints (separately or simultaneously) filtering both experimental and approximation errors;  $\mathbf{p}$  is a trial solution. The value of  $\gamma$  is typically in the range of 0.001 to 1 for any normalized  $\mathbf{a}$ . The optimal choice of  $\gamma$  can be determined by trial and error, or estimated using the generalized cross-validation technique [39]. The major advantages of the Phillips-Twomey method are its computational speed and its ability to handle many size classes stably. Its drawback is that the result is smoothed and thus resolution is sacrificed. A description of the Phillips-Twomey theory and examples of how to apply the theory when resolving particle size distributions from a laser diffraction experiment can be found in the literature [40]. Intensity fluctuations between scans during measurement can also be included in the matrix inversion procedure to refine the deconvolution process and to improve the sensitivity in detecting small amounts of large particles [41,42].

If one has some independent knowledge about the sample material, such as whether the size distribution is unimodal or multimodal, or narrow or broad, the incorporation of such knowledge into the matrix inversion procedure may help to obtain a better result, since the fitting procedure can then be finely tuned using these known conditions or criteria. For example, certain pre-tuned conditions can be used if the distribution's modality is known, or smoothing techniques can be used to create a more realistic distribution. The drawback of such "pre-choices" is that in most instances pre-fixing a distribution shape will

bias the end result towards the chosen distribution shape, and different choices may lead to different distributions, which is occasionally detrimental in obtaining the correct result. The following two figures display a typical scattering pattern and the corresponding size distribution obtained by using the matrix inversion method from a sample having an extremely broad size range ( $0.1\text{ }\mu\text{m}$  to  $1\text{ mm}$ ).

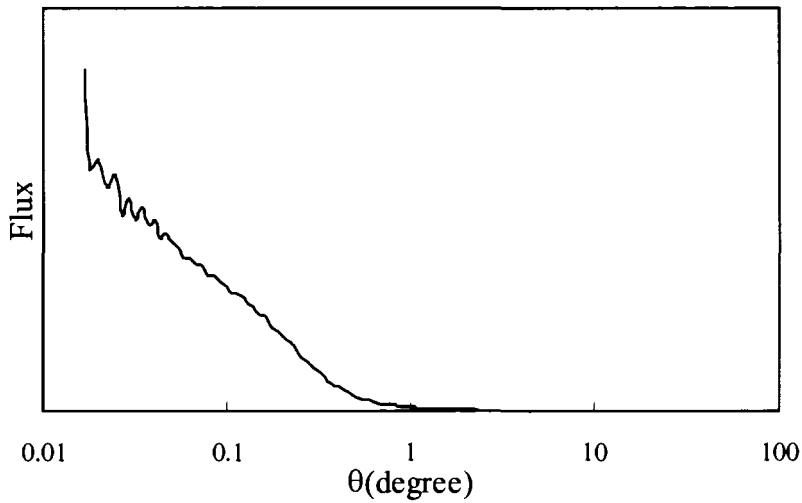


Figure 3.33. A typical scattering flux pattern.

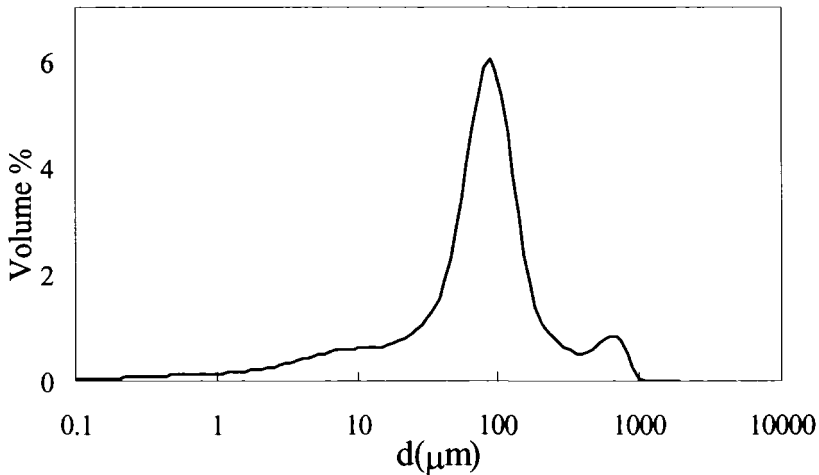


Figure 3.34. Particle size distribution resolved from the flux in Figure 3.33.

For small particles, the angular intensity pattern is much smoother and lacks any strong oscillation. Other inversion methods which do not use any matrix smoothing have been proposed. In one method - the maximum entropy method - the most probable solution for the distribution  $q(d)$  is the one that maximizes the Shannon-Jaynes-Skilling entropy function:

$$S = \sum_{j=1}^N (q(d_j) - q^o(d_j) - q(d_j) \ln(\frac{q(d_j)}{q^o(d_j)})) \quad (3.12)$$

where  $q^o(d_j)$  is an initial distribution that can be set flat for unknown distributions in which case,

$$q^o(d_j) = \frac{\sum_{k=1}^m f(\theta_k)}{\sum_{k=1}^m \sum_{j=1}^n a(\theta_k, d_j)}, \quad (3.13)$$

or it can be set according with the prior knowledge that the distribution goes to zero at the extremities of the chosen size range, and it varies quadratically. In this case,

$$q^o(d_j) = \frac{(d_1 d_n - (d_1 + d_n)d_j + d_j^2) \sum_{k=1}^m f(\theta_k)}{\sum_{k=1}^m \sum_{j=1}^n a(\theta_k, d_j) (d_1 d_n - (d_1 + d_n)d_j + d_j^2)}. \quad (3.14)$$

In another method - the constrained regularized method - the most probable distribution is obtained by minimizing the following expression through a least-squares algorithm with the constraints that the distribution is represented by non-negative numbers only and is also a smooth function that goes to zero at the extremities of the chosen size range:

$$(\mathbf{f} - \mathbf{a} \cdot \mathbf{q})^T \mathbf{w} (\mathbf{f} - \mathbf{a} \cdot \mathbf{q}) + \alpha (\mathbf{D} \cdot \mathbf{q})^T (\mathbf{D} \cdot \mathbf{q}). \quad (3.15)$$

In the above equation,  $\mathbf{w}$  is a diagonal  $m \times m$  matrix whose elements are inversely proportional to the variance of data points. The constraints are loaded

through the matrix operator  $\mathbf{D}$ , which is conditioned by the regularization parameter  $\alpha$ . The above two methods have been tested for multimodal and polydisperse submicron latex samples. The results are comparable to EM results and significantly better than those from photon correlation spectroscopy [43].

The data analysis procedure for scattering experiments that combine small angle scattering with the larger angle PIDS measurement is similar to the procedure described earlier. The matrix form is now extended to include both the forward scattering and the PIDS information since both the forward scattering and PIDS signals are mathematically based on the same theory and physically measured with the same material in the sample chamber. In Eq. 3.16,  $p(\theta_i, \lambda_j)$  is the PIDS signal measured at angle  $\theta_i$  ( $i = m+1$  to  $k$ ) and at wavelength  $\lambda_j$  ( $j = 1$  to  $h$ ). However, since the light sources and the detectors are different for the diffraction and PIDS measurements, their signals have to be weighted differently before they can be combined into a single matrix (Eq. 3.16). The weighting and scaling constants can be easily obtained using various photometric methods.

$$\begin{bmatrix} f(\theta_1) \\ \dots \\ f(\theta_m) \\ p(\theta_{m+1}, \lambda_1) \\ \dots \\ p(\theta_k, \lambda_h) \end{bmatrix} = \begin{bmatrix} a(\theta_1, d_1) & \dots & \dots & a(\theta_1, d_n) \\ \dots & \dots & \dots & \dots \\ a(\theta_m, d_1) & \dots & \dots & a(\theta_m, d_n) \\ a(\theta_{m+1}, \lambda_1, d_1) & \dots & \dots & a(\theta_{m+1}, \lambda_1, d_n) \\ \dots & \dots & \dots & \dots \\ a(\theta_k, \lambda_h, d_1) & \dots & \dots & a(\theta_k, \lambda_h, d_n) \end{bmatrix} \begin{bmatrix} q(d_1) \\ \dots \\ q(d_n) \end{bmatrix}. \quad (3.16)$$

One frequent mistake in a laser diffraction measurement arises not from the choice of sample module or the dispersion procedure but from the use of an inappropriate optical model in data analysis. This often produces an incorrect size distribution, even though the measurement was performed carefully and the instrument is functioning correctly. Typical errors that may occur when an inappropriate optical model is chosen (by using the Fraunhofer model for particles smaller than 2  $\mu\text{m}$ , for example) are: 1) multiple artificial peaks, 2) excessive peak broadening, and, 3) incorrect reporting of the mean size.

As discussed earlier, Fraunhofer theory is a special case of the more comprehensive Mie theory. For spherical opaque particles whose diameters are much larger than the wavelength of light, Mie theory can be simplified. This simplification gives rise to Fraunhofer approximation which involves only the diffraction of light at the edges of a particle. For particles that are larger than 100  $\mu\text{m}$  and are non-transparent, Fraunhofer theory is nearly identical to the Mie theory. When analyzing systems containing particles in the range of 10-100  $\mu\text{m}$ , Fraunhofer theory usually gives a fair approximation to Mie theory. For

particles smaller than 10  $\mu\text{m}$ , Fraunhofer theory will give a distorted result which may overemphasize or underemphasize certain portions of the distribution and therefore a Mie model using correct refractive index values should be used [44]. However, when there is no way of knowing or guessing the refractive index of the sample, the Fraunhofer approximation becomes the only alternative. The advantages of Fraunhofer theory are that there is no need to know the optical constants of the sample, particle shape has only a faint influence, and lastly, the matrix inversion may be greatly accelerated due to the simpler formulation. In using Mie theory, a unique matrix has to be generated for every material even if the optical constants are known, and non-sphericity may have a large effect on the solution. These are the main reasons that, even with today's computing power, which can both generate a  $100 \times 100$  matrix using Mie theory or perform the matrix inversion in only a few seconds, Fraunhofer theory still has a continuing position in laser diffraction technology.

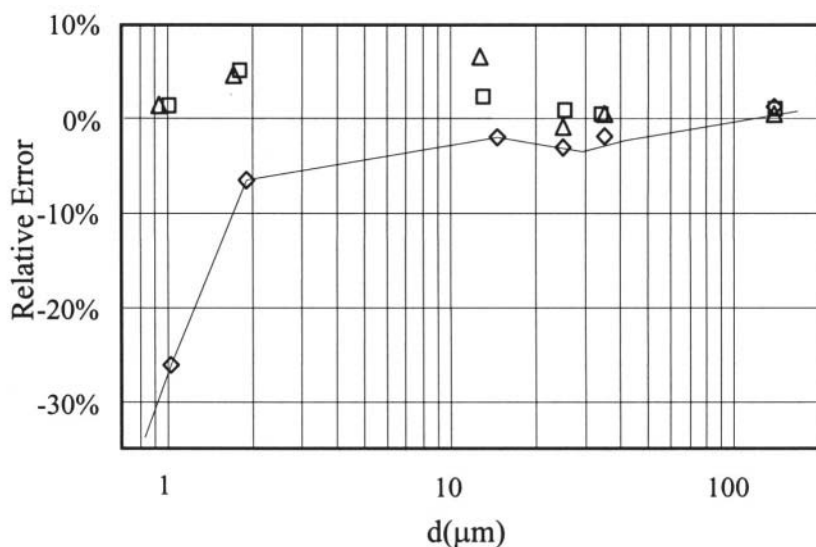


*Figure 3.35.* Comparison of particle sizes obtained from measurements of PSL's in aqueous suspensions using different refractive index values. The relative deviations are based on results from the correct  $m$  value ( $m = 1.20$ ) for polystyrene in water. Squares:  $m = 1.05$ ; Triangles:  $m = 2.25$ . Diamonds represent results of the Fraunhofer theory.

Figure 3.35 is from a series of laser diffraction measurements of monodisperse PSL's of various diameters suspended in water. Different sizes are obtained when using Fraunhofer theory and three Mie models generated with different relative refractive index values. When compared with the vendor's specified nominal values (which are determined by EM measurement) Fraunhofer theory



could only provide comparable results when  $d > 30 \mu\text{m}$ . For smaller particles, even if the refractive index value used in the Mie theory was incorrect, the sizes resolved were still much closer to the nominal size than those obtained using the Fraunhofer theory. However, caution has to be taken when generalizing this conclusion to other materials.

If a CCD detector is used to capture the images of large particles, then after the 2-D Fourier transformation, the diffraction pattern can be generated. This process is equivalent to one in which many elemental apertures located at the positions  $(s, t)$  relative to the optical axis with a varying transmission factor  $a(s, t)$  are illuminated by plane waves. The total field  $E$  at the image plane satisfies the following integral:

$$E(x, y) = \iint_{\text{beam}} a(s, t) \exp\left(\frac{-2\pi i}{\lambda f} [sx + ty]\right) ds dt \quad (3.17)$$

In Eq. 3.17,  $x$  and  $y$  are the coordinates at the image plane (the CCD surface) and  $f$  is the focal length of the Fourier lens. Once the scattering pattern is computed, it can be combined with the scattering pattern of small particles acquired using silicon detectors at large scattering angles to produce a particle size distribution over a broad size range.

For liquid sprays, the droplet size varies at different radial and axial directions from the nozzle. The time-averaged measurement and data analysis procedures described above cannot provide information about the local structure of the droplet size distribution. Several techniques have been developed to transform ordinary laser diffraction measurements into spatially resolved local measurements along the radial directions of the spray. The data from the measurements at different radial directions are then processed using either a deconvolution method with optical extinction and scattering coefficients [45] or a tomographical transformation method [46,47], yielding pointwise droplet size and liquid concentration distribution as well as all mean diameters of practical interest.

### 3.3.3. REFRACTIVE INDEX EFFECTS

One factor that will create different scattering patterns from two particles both having the same diameter is the particle's refractive index. The refractive index or, alternatively, the index of refraction, or refractivity, is the measure of the amount of refraction. It is a function of wavelength, temperature, and pressure. If the material is non-absorbing and non-magnetic at any wavelength, then the square of the refractive index is equal to the dielectric constant at that wavelength. For absorbing materials, the complex refractive index  $m = n - ik$  is

related to the absorptive index  $k$  where the real term describes the refraction and the imaginary term describes the absorption.

Because the angular scattering pattern depends on the ratio of the refractive indices between the medium and the particles, knowledge of the refractive indices of both is vital in characterizing particles in the size range where Mie theory has to be used. Fraunhofer theory is independent of refractive index as long as the relative refractive index does not approach unity; i.e., the material is not transparent. For transparent materials, and even for very large particles, anomalous diffraction prevents one from using Fraunhofer theory.

Refractive index values for suspending media (such as air, water, and organic solvents) can be found in various handbooks [48]. These values have often been determined using sodium light ( $\lambda_0 = 589.3 \text{ nm}$ ) and at one temperature since there is little dependence on either temperature or wavelength in the visible region for media's refractive indices. They are mostly non-absorbing and so their refractive index consists of a real part only. Appendix VI lists the refractive indices of common liquids along with their viscosity and dielectric constant values.

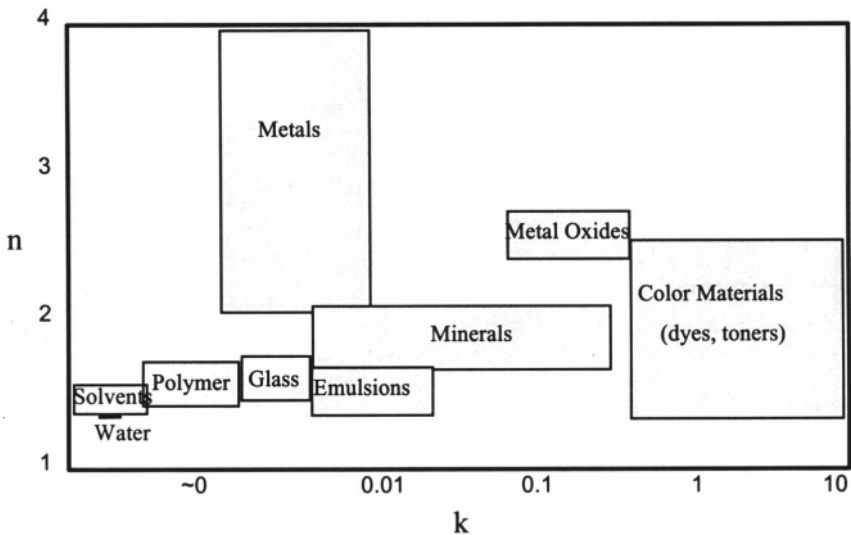


Figure 3.36. Chart of refractive indices.

The refractive indices of particulate materials depend on their electron structure. The following chart illustrates the approximate range of the complex refractive indices of common materials. Figure 3.36 is drawn in a lin-log form. The real part,  $n$ , is shown on the linear y-axis and the imaginary component (the absorption) on the logarithmic x-axis. Although some of these values measured

at one or two wavelengths can be found in the literature [49,50,51,52], others depend heavily on wavelength, especially for colored materials such as pigments or toners. Extrapolation, interpolation, or estimation from published values to the wavelengths used in a laser diffraction experiment is usually needed. The imaginary part of refractive index, however, can often be estimated from color of the material. As an example, one might expect a blue pigment to have high absorption at most wavelengths other than blue. Therefore, when estimating values for the imaginary portion, a value of zero should be a good approximation for a wavelength of 450 nm, and some value between 1 and 10 for wavelengths in the 600 nm to 900 nm range. A list of the refractive indices for many substances is contained in Appendix VII.

Determination of the refractive index of particulate materials can be accomplished by the index matching method. In this method, a set of index matching liquid with known refractive index is used. Particles are immersed into the liquids of different refractive indices and a light is used to illuminate the suspensions. The particles will be invisible in a liquid that has the same index of refraction. The refractive index of particles can thus be determined upon close examination using an amplifying lens or optical microscope. Particles' refractive index can also be determined from their angular scattering intensity pattern if the particle size is a few microns or smaller [53].

Bear in mind that in laser diffraction it is only the relative refractive index that is important. For example the same glass beads will create different scattering patterns when they are dispersed in air as opposed when they are dispersed in water. When choosing a refractive index, one also has to consider which form of the compound is being analyzed. For example, there are five forms of alumina listed in the CRC Handbook of Chemistry and Physics. Each has its own distinct molecular geometry and color and should be treated differently with regard to their real and imaginary refractive indices. The real part of refractive index is different for each of these five compounds ranging from 1.577 to 1.768.

In mixtures, if each component has a different refractive index, there is no ideal procedure to determine the refractive index value that should be used because the measurement is performed on all particles simultaneously. There is a particular instance where correct sizes of the mixture may be obtained - when the two components having substantially different sizes. For example if component A is much smaller than component B, one can then use the refractive index value of component B to compute the scattering kernel for small angles, and that of component A to compute the scattering kernel for large angles. Because large particles scatter less at large angles, most of their information can be retrieved from the scattering intensity at small angles where small particles contribute less to the overall intensity. (The converse is true for small particles at large angles.)

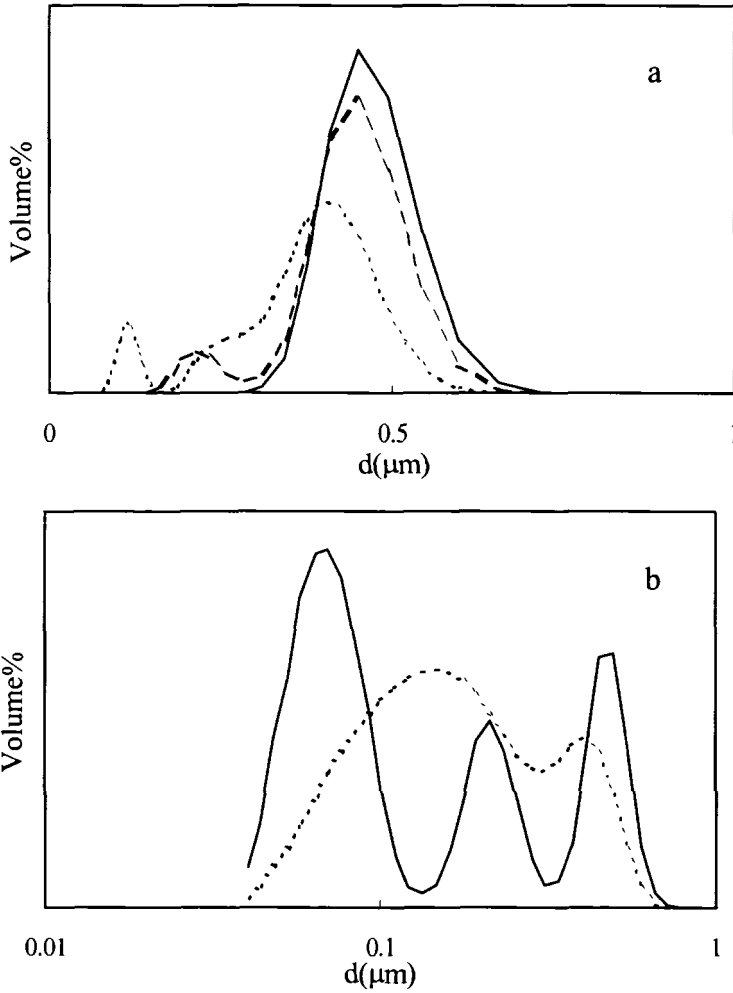


Figure 3.37. Effect of refractive index in particle sizing using laser diffraction.

Using the correct refractive index values is very important in retrieving an accurate particle size distribution when Mie theory is used in the matrix inversion. It is especially important when the relative refractive index approaches unity in which case even a minor error in the choice of a relative refractive index may lead to a significant variation in the result [54]. Figure 3.37 shows an example of the effect of refractive index in resolving particle size using laser diffraction. Correct results can only be obtained when correct values of the refractive index are used in the matrix inversion. Otherwise, an either

erroneous or low resolution distribution will be the result. In Figure 3.37a, a suspension of PSL's ( $d = 0.48 \mu\text{m}$ ) was measured and the correct value of  $0.48 \mu\text{m}$  was retrieved using the correct refractive index of 1.60 for PSL (solid line). However, when other refractive indices were used, both the distribution's shape and the mean value changed considerably. The dashed line results from applying a refractive index of 1.4, which produced a false peak with the overall mean shifted to  $0.42 \mu\text{m}$ . The dotted line is the result of applying a refractive index of 2.0, which also produced a false peak and a shoulder on the left with an overall mean of  $0.30 \mu\text{m}$ . Another example is shown in Figure 3.37b. In this case the sample is a tri-modal PSL mixture where the use of the wrong refractive index (1.4 instead of 1.6) produced a size distribution having a significantly lower resolution (the dotted line).

### 3.3.4. CONCENTRATION EFFECTS

In general, the particle concentration in dispersion should be above some minimum level, which for many instruments will correspond to a transmission level of about 95% in order to produce an acceptable signal-to-noise ratio at the detector. On the other hand, the concentration should be below some upper level in order to avoid multiple scattering. This upper concentration limit varies with particle size and instrument design. For many instruments, the upper concentration limit will correspond to about 85% of the initial transmission. Multiple scattering introduces sizing error once the transmission is below approximately 85% without correction. Such errors become unacceptably large for transmission levels below 60-70% if a multiple scattering correction is not incorporated in the deconvolution algorithm [18]. Since multiple scattering appears at larger scattering angles, without proper correction the amount of small particles calculated will exceed the true value. One multiple scattering correction scheme proposed by Hirleman is as follows [55,56,57].

Let us define  $\mathbf{I}_n(\theta)$  as the scattering for exactly  $n$  scattering events. The detected scattering  $\mathbf{I}(\theta)$  will have the form:

$$\mathbf{I}(\theta) = P_1 \mathbf{I}_1(\theta) + P_2 \mathbf{I}_2(\theta) + \dots P_\infty \mathbf{I}_\infty(\theta), \quad (3.18)$$

where  $P_i$  is the probability of the exact  $i$ -times multiple scattering event that is related to both suspension concentration and mean particle size and can be explicitly calculated in the Rayleigh scattering limits.  $P_n = (\bar{Q}_{\text{sca}} \tau l)^n e^{-\tau l} / n!$  where  $\bar{Q}_{\text{sca}}$ ,  $\tau$ , and  $l$  are the mean scattering efficiency, the turbidity, and the light path length (see Section 2.3.5), respectively. Let us further define  $\mathbf{H}$  as a redistribution matrix for one scattering event in which light that would be collected at angle  $\theta_i$  is redirected to angle  $\theta_j$ . Since the scattering of the  $n^{\text{th}}$  event

originates from the scattering of the  $(n-1)^{\text{th}}$  event modulated by the redistribution matrix:

$$\mathbf{I}_n(\theta) = \mathbf{H} \cdot \mathbf{I}_{n-1}(\theta). \quad (3.19)$$

Substituting Eq. 3.19 into Eq. 3.18, we have

$$\mathbf{I}(\theta) = (\mathbf{P}_1 + \mathbf{P}_2 \mathbf{H} + \mathbf{P}_3 \mathbf{H}^2 + \dots + \mathbf{P}_\infty \mathbf{H}^{\infty-1}) \mathbf{I}_1(\theta). \quad (3.20)$$

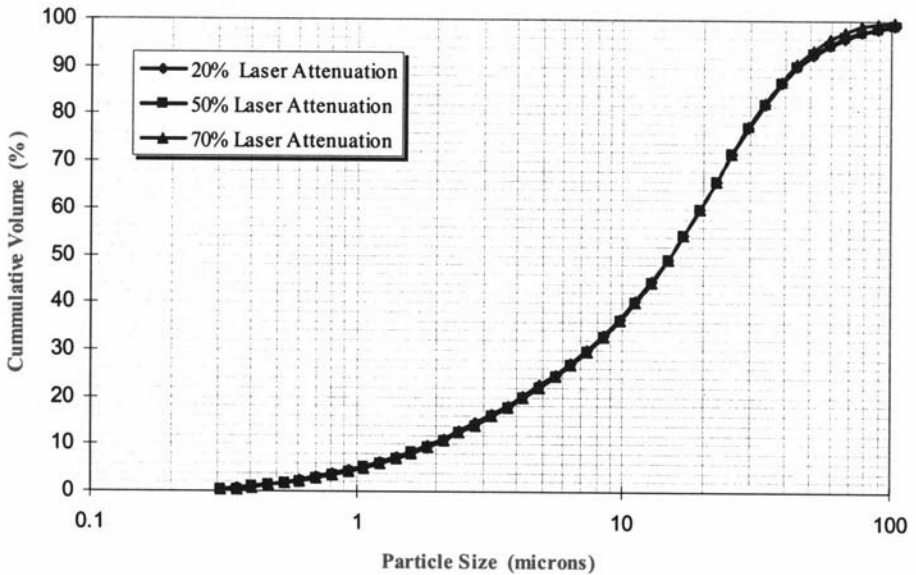


Figure 3.38. A comparison of Type 20 Cement particle size measurement at three different loading conditions [58] (by permission of Institution of Chemical Engineers).

The single event  $\mathbf{I}_1(\theta)$  can thus be resolved based on the measured signal  $\mathbf{I}(\theta)$  and  $\mathbf{H}$  which can be computed for a given instrument geometry. However,  $\mathbf{H}$  is also a function of  $\mathbf{I}_1$ . Solving Eq. 3.20 is not trivial in that it involves an iterative procedure. Although this model is based on Rayleigh scattering, its application has been extended to larger particles. As demonstrated by Figure 3.38, the same size distribution can be obtained from concentrated suspensions having low transmission (high attenuation) values [58]. Although this correction algorithm has been used to retrieve size distributions from concentrated powder streams having a light transmission value as low as a few percent [59,60], its validity for other materials needs to be tested and verified.

### 3.4. Accuracy of Laser Diffraction Technology

#### 3.4.1. RESOLUTION AND PRECISION

The technique of measuring the diffraction pattern created by a suspension rather than individual particles in order to determine particle size was first described almost three decades ago [61]. Since then, laser diffraction technology has grown out of its infancy and into maturity, now having several instrument manufacturers and a well established and growing commercial market. Because of the extremely wide dynamic range, short measurement times, and high reproducibility associated with this technology, laser diffraction has become one of the most popular methods in the sizing of particles from nanometers to millimeters - replacing several older technologies such as sieving, sedimentation and microscopy through a broad range of industrial fields. Combining multi-element detector arrays, efficient sample modules and a good data analysis procedure, the modal resolution of a laser diffraction instrument should be better than two, i.e., two samples having modal diameters with a ratio of two or even less than two can be resolved. Instrument resolution is affected by the design of the detector, the overall signal-to-noise ratio, the size range of the sample, the construction of any optical model, and the algorithm used in the deconvolution procedure. Due to the intricate nature of data retrieval process and the fact that both detector geometry and size bin locations are preset, the resolved size distribution is smoothed and therefore will be broader than the original distribution for narrow distributions. Figure 3.14 demonstrates the modal resolution and the broadening effect that arises from a mixture of monodisperse submicron spheres as compared to the electron microscopic image in Figure 3.15. Figure 3.39 demonstrates the same effects from a mixture of monodisperse submillimeter spheres as compared to the electron microscopic image in Figure 3.40. Although the spheres in the samples used in these experiments are quite uniform, the results from the laser diffraction measurements show broad peaks due to the present size bin location and spacing. Since the SD or the coefficient of variation for monodisperse samples will unavoidable be biased associated with the inherent resolution of the technology, when applying laser diffraction to monodisperse samples, one has to treat the reported SD or coefficient of variation from the measurement with caution. However, for most practical samples that have a distribution covering a size range broader than a few size bins, this problem is not significant.

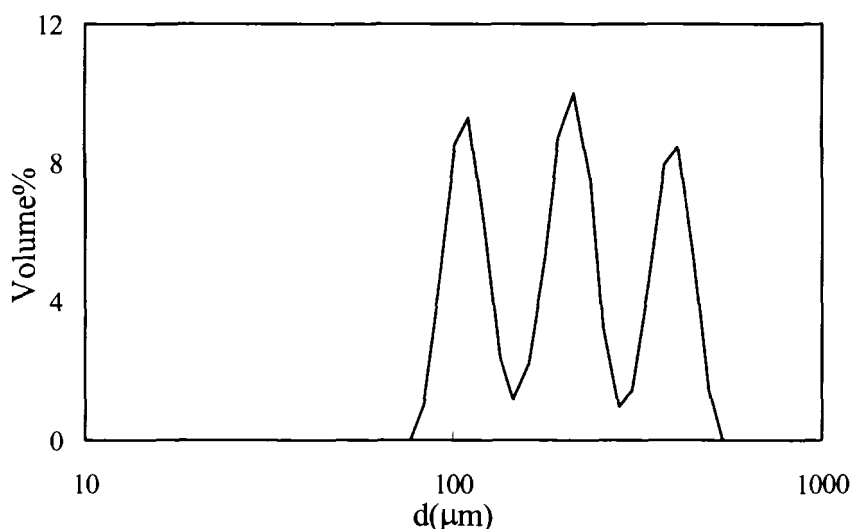


Figure 3.39. A trimodal mixture of monodisperse glass beads (nominal diameters of 115  $\mu\text{m}$ , 220  $\mu\text{m}$ , and 430  $\mu\text{m}$ ).

Advancements in laser diffraction technology have resulted in significant improvements in commercial instruments, such as greater precision, increased ease of use, more versatile sample handling, and the capability for on-line measurement. The popularity of this technique has led to several national and international collaborative studies focussing on the accuracy of the technology by comparison to other particle characterization methods. For spherical particles the results are very promising, in that the mean size and cumulative distributions from different models of laser diffraction instruments are close not only to each other but also to the values obtained by other methods and demonstrate excellent reproducibility. Even the first generation of commercial instruments introduced in the early 1980's demonstrated these advantages as shown by the results of some 18,000 measurements made over a three-year period [62]. For non-spherical particles, the results from the same instrument usually show only small standard deviations between repeat measurements of the same preparations, and between different preparations of the same sample. For particles larger than 10  $\mu\text{m}$ , a modern commercial instrument should easily achieve a relative standard deviation less than 3% for the median value in repeat measurements, and a relative standard deviation less than 5% at the extremes of the distribution (the  $d_{10}$  and  $d_{90}$  points). For smaller particles these values may be doubled [21].



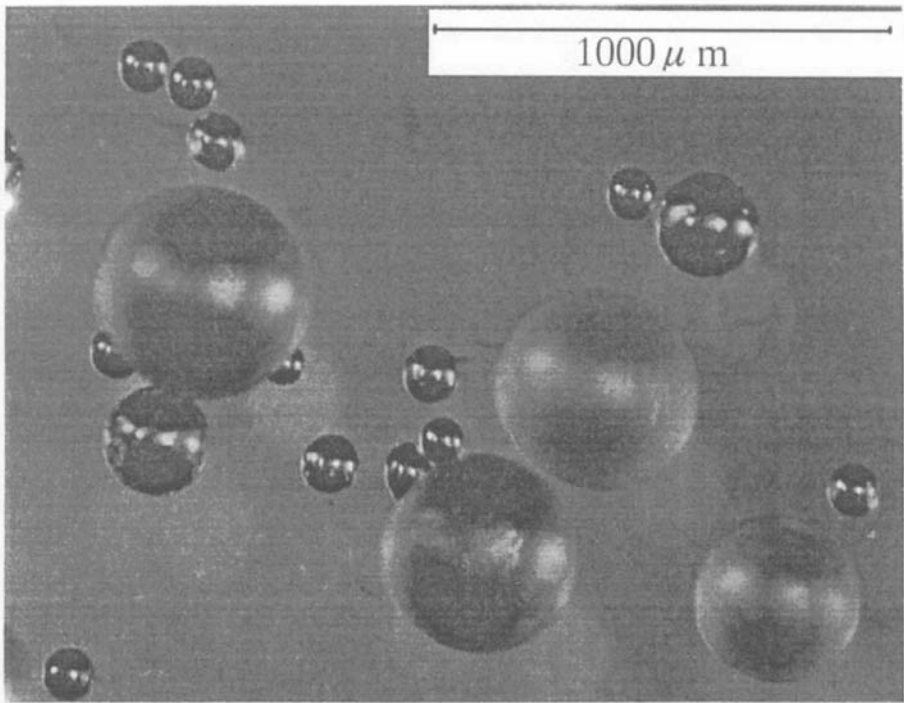


Figure 3.40. An electron microscopic image of the sample in Figure 3.39 [7] (by permission of Beckman Coulter KK).

In 10 repeat measurements using laser diffraction of a natural lacustrine sample with grains ranging from 1 to 100  $\mu\text{m}$ , the standard deviation of the mean size (8.59  $\mu\text{m}$ ) was only 0.03  $\mu\text{m}$ . A single measurement made on each of 10 subsamples split from the same bulk sample, the standard deviation of the mean size was only 0.09  $\mu\text{m}$ . Other statistical values from these two tests all had small deviations [63]. However, particle size results of non-spherical particles from different instruments are often less consistent with different degrees of deviation when compared to other methods and is often a function of sample polydispersity and particle shape.

An international collaborative study involving 24 laboratories using 21 laser diffraction instruments manufactured by six different manufacturers was performed in 1994. Sedimentation and the electrical sensing zone (ESZ) methods were used as reference methods in comparing results. Two irregularly shaped polydisperse quartz materials (BCR 67 and BCR 69, certified using the Andreasen pipette sedimentation method, obtained from the Community Bureau of Reference (BCR) of the Commission of the European Community) were used in the study [64]. In this investigation the standard deviations reported by each

participant showed comparable values using all three methods. However, the maximum spread of mean particle size from all participants using laser diffraction was much larger than that from either the ESZ or the sedimentation methods. Table 3.4 lists some of the values extracted from the study [64].

The poor repeatability in the laser diffraction results is possibly due to the fact that a) the randomness of particle orientation in scattering volume may be different when using different designs of sample modules to circulate the particles; b) different measurement sensitivities may exist for particles of various sizes due to differences in the optical design of the instruments; or c) the algorithms used in the size retrieval process and the approximations used in obtaining apparent values (equivalent spherical diameters) for non-spherical particles are different between manufacturers.

Table 3.4. Round-robin investigation using ESZ, sedimentation and laser diffraction

Material	$d_{50}$ (certified)	Sedimentation		ESZ		Laser Diffraction	
		SD	Spread	SD	Spread	SD	Spread
BCR67	10.4	2	1	0.3	1	0.5	~8
BCR69	37.9	0.3	10	1.5	10	3	~17

In Table 3.4, SD is the average standard deviation of  $d_{50}$  from individual participants; Spread is the maximum spreading of  $d_{50}$  among all participants. All numbers are in  $\mu\text{m}$ . The values for  $d_{50}(\text{certified})$  is extracted from the BCR certificate.

### 3.4.2. BIAS AND SHAPE EFFECTS

Most of the particles in nature, such as atmospheric dusts, soils, sands and mineral powders are irregularly shaped and can have either a smooth or a rough surface. For a single irregularly shaped particle an angular scattering pattern may be calculated using the methods mentioned in Section 2.2.2 provided the irregularity and size of particle are known. To reveal the dimension and a “brief” description of the shape of an irregularly shaped particle from its scattering pattern however is very difficult, if not impossible. For an ensemble of particles of arbitrary shapes, the definition of “size” and the scattering model needed will vary for each particle. Thus, to obtain a “real size distribution” from an intensity measurement is often impossible and hence senseless. Generally, in the measurement of randomly oriented particles there are three schemes that can be used to fit the results of a diffraction experiment.

The first one is to use a spherical approximation and treat every particle as a sphere regardless of the real shape. This is the analysis strategy that all commercial instruments employ. This method produces a size distribution with one variable, diameter, which is easily traceable and comparable to the results

obtained from other technologies. This method also often works well for many irregularly shaped particles. Because the finite detector area integrates and smoothes out the intensity fluctuation caused by any surface roughness, and additionally because there is a smoothing effect from the rotation of the particles, the scattering patterns approximate those created by spheres [65]. A theoretical study has shown that the forward peak of a diffraction pattern is not sensitive to particle shape, though particle irregularity may lead to an over-sized result. Although the second maximum, as well as the rest of scattering pattern, is sensitive to the shape of irregularly shaped particles, these maxima are less influential in the data fitting procedure [66]. However, for many particles, because of their deviation from perfect sphericity, the size distribution obtained is only apparent or nominal, and will be biased. In certain extreme cases the results of using a spherical model on non-spherical particles will be very different than from the truth. For example, when monodisperse or polydisperse (but unimodal) square tablets or cuboids were measured using laser diffraction and analyzed using a spherical model, multiple peaks resulted, with the mean value of each peak moving away from the true dimension [67]. Similar phenomena were observed for elliptical particles. This type of systematic bias often shows up when comparing laser diffraction results with those obtained from other methods [68].

For non-solid particles (for example particles that are porous), the systematic deviation in particle size analysis using different methods is much larger. In a multinational study of several silicas having different porosity using seven different models of laser diffraction instruments and eight different ESZ counters, the repeatability between the laser diffraction instruments was much worse than the repeatability between the different ESZ counters. The mean sizes reported by the laser diffraction method deviated increasingly from that obtained using the ESZ method with increasing particle pore volumes [69]. This is mainly due to the nature of the ESZ method, in which only the medium volume actually replaced by solid mass is detected. For porous materials, even though particles have much larger contour dimensions as measured by laser diffraction, owing to pore filling by the medium, ESZ will always undersize them. Figure 3.41 shows an extreme example of particle size distributions from a sponge-plate-like material using both the ESZ method and laser diffraction. The mean values from these two methods differ by as much as 6.7 times!

There have been many comparative studies to compare the mean size and distribution obtained using commercial laser diffraction instruments that apply a spherical assumption to other methods. In one such study, several oxide and non-oxide ceramic powders were measured using laser diffraction instruments from eight manufacturers, photo-sedimentation instruments from four manufacturers, ESZ counters from three manufacturers, and X-ray sedimentation instruments. For all powders, the instrument-to-instrument

repeatability of laser diffraction was close to that of photo-sedimentation but much worse than that of the X-ray sedimentation and ESZ methods. The mean values obtained using different technologies showed various deviations. A summary of this study is given in Table 3.5 [70,71].

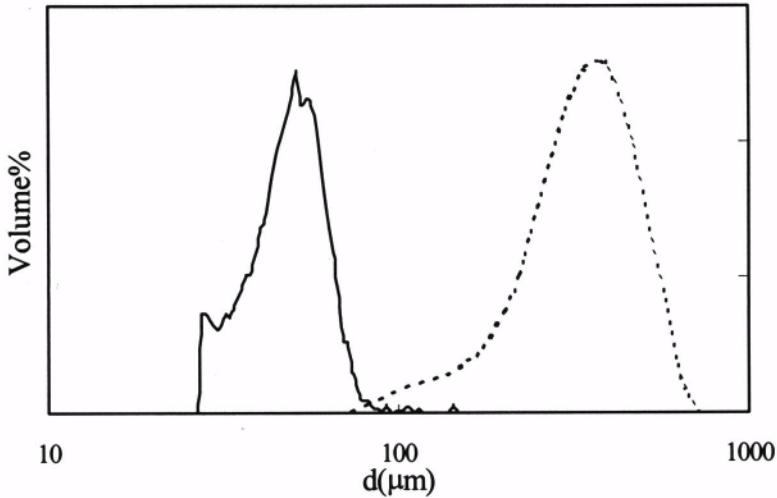


Figure 3.41. Particle size distribution of hyaluronic acid by ESZ method (solid line) and laser diffraction (dashed line) [72].

Table 3.5. Comparative study of particle sizing technologies (all values are for  $d_{50} \pm SD$  ( $\mu m$ ), except those in the second column)

Materials	Size Range (Photo Sed.) ( $d_{10}$ - $d_{90}$ )( $\mu m$ )	Laser Diffraction	Photo Sedimen.	x-ray Sedimen.	ESZ
Alumina	0.9-4.1	$2.1 \pm 0.3$	$1.7 \pm 0.2$	$1.9 \pm 0.1$	$2.2 \pm 0.2$
Barium Titarate	0.9-2.5	$1.7 \pm 0.2$	$1.5 \pm 0.2$	$1.7 \pm 0.1$	$1.6 \pm 0.1$
Zirconia	0.2-11	$5.8 \pm 2.6$	$1.2 \pm 0.8$	$0.33 \pm 0.04$	
Silicon Carbide	0.16-1.5	$0.61 \pm 0.10$	$0.45 \pm 0.18$	$0.46 \pm 0.10$	
Silicon Nitride	0.3-2.9	$1.0 \pm 0.1$	$0.63 \pm 0.11$	$0.56 \pm 0.04$	
Boron Nitride	2.1-15	$8.8 \pm 1.3$	$4.9 \pm 1.2$		$6.7 \pm 0.8$

Table 3.6 summarizes many other recent studies in the comparison of laser diffraction results to those of other technologies. Although the comparative ratios of the mean size for particles with different shapes cluster around some central value (the fourth column), laser diffraction always yields a larger apparent diameter than that obtained from other methods except the methods in [75] and [82]. The corresponding biases in the size distributions can be found in the original references. However, it seems there is a lack of a clear trend or

relationship between the size ratio and particle shape. In Table 3.6, for material type (1) the size indicates the overall range for the mean sizes of several monodisperse samples; for material type (2), the size indicates the overall range for the median sizes of several polydisperse samples.  $d_{50}$  is the median size; and other  $d$  values are the mean sizes.  $d_{sed}$  is the Stokes diameter obtained from Eq. 1.1.  $d_{ESZ}$  is the volume equivalent sphere diameter. Microscopic diameters are defined differently in different references. In [74],  $d_{SEM}$  was calculated assuming a sphere formed by a rotating circular disk. In [75],  $d_{SEM}$  of mica was the projected circular disk diameter and that of the fiber was the rod diameter. In [77] and [80],  $d_{OM}$  and  $d_{SEM}$  were the projected circular disk diameters.

Table 3.6. Comparison of results of laser diffraction with that of other sizing technologies

Technique	Material Type	Size ( $\mu\text{m}$ )	Comparison	Ref.
ESZ	Porous silica (irregular) (pore volume 0.4 mL/g)	$d_{50,ESZ} = 4.2$	$d_{50,id}/d_{50,ESZ} \sim 1.1$	69
ESZ	Porous silica (irregular) (pore volume 0.85 mL/g)	$d_{50,ESZ} = 28$	$d_{50,id}/d_{50,ESZ} \sim 1.2$	69
ESZ	Porous silica (irregular) (pore volume 1.8 mL/g)	$d_{50,ESZ} = 4$	$d_{50,id}/d_{50,ESZ} \sim 1.7$	69
ESZ	Cracking catalyst (spheres)	$d_{50,ESZ} = 56.7$	$d_{50,id}/d_{50,ESZ} = 1.14$	73
Sieve	Cracking catalyst (spheres)	$d_{50,sieve} = 64.3$	$d_{50,id}/d_{50,sieve} = 1.00$	73
ESZ	Hyaluronic acid (porous plates)	$d_{ESZ} = 47.51$	$d_{id}/d_{ESZ} = 6.7$	72
ESZ	Latex (spheres)	$d_{ESZ} = 20.11$	$d_{id}/d_{ESZ} = 1.0$	72
ESZ	Boron carbide (plates)	$d_{ESZ} = 19.45$	$d_{id}/d_{ESZ} = 1.5$	72
ESZ	Difloxacin HCl (rods)	$d_{ESZ} = 6.57$	$d_{id}/d_{ESZ} = 1.4$	72
SEM	Alumina (plates)	$d_{50,SEM} = 6.8$ $t_{SEM} = 0.6$	$d_{50,id}/d_{50,SEM} = 1.1$	74
SEM	Mica (plates) (1)	$d_{SEM} = 100-226$ $t_{SEM} = 6-17$	$d_{id}/d_{SEM} \sim 1$	75
Sedimen.	Mica (plates) (1)	$d_{SEM} = 100-226$ $t_{SEM} = 6-17$	$d_{id}/d_{sed} \sim 3$	75
SEM	Carbon fiber (rods) (1)	$d_{SEM} = 21-26$ $l_{SEM} = 100$	$d_{id}/d_{SEM} \sim 0.5$	75
Sedimen.	Carbon fiber (rods) (1)	$d_{SEM} = 21-26$ $l_{SEM} = 100$	$d_{id}/d_{sed} \sim 1$	75
Sedimen.	Glass beads (spheres) (1)	$d_{sed} = 10-50$	$d_{id}/d_{sed} \sim 1$	76
Sedimen.	Kaolin (plates)	$d_{sed} = 0.8$	$d_{id}/d_{sed} \sim 3$	76
OM	PMMA latex (spheres) (2)	$d_{50,OM} = 10-61$	$d_{50,id}/d_{50,OM} \sim 0.9-1.1$	77
ESZ	PMMA latex (spheres) (2)	$d_{50,ESZ} = 13-60$	$d_{50,id}/d_{50,ESZ} \sim 0.9-1.0$	77
OM	NaCl (cubes) (2)	$d_{50,OM} = 35-134$	$d_{50,id}/d_{50,OM} \sim 1.2-1.5$	77
ESZ	NaCl (cubes) (2)	$d_{50,ESZ} = 41-144$	$d_{50,id}/d_{50,ESZ} \sim 1.1-1.4$	77
OM	Mica (plates) (2)	$d_{50,OM} = 79-158$	$d_{50,id}/d_{50,OM} \sim 1.0$	77
ESZ	Mica (plates) (2)	$d_{50,OM} = 59-89$	$d_{50,id}/d_{50,ESZ} \sim 1.3-1.6$	77

Sedimen.	Kaolin(plates)	$d_{50, \text{sed}} = 2.4$	$d_{50, \text{ld}}/d_{50, \text{sed}} \sim 2.5$	78
ESZ	Kaolin(plates)	$d_{50, \text{ESZ}} = 4.0$	$d_{50, \text{ld}}/d_{50, \text{ESZ}} \sim 1.5$	78
Sedimen.	Kaolin (plates)(delaminated)	$d_{50, \text{sed}} = 0.6$	$d_{50, \text{ld}}/d_{50, \text{sed}} \sim 3$	78
ESZ	Kaolin (plates)(delaminated)	$d_{50, \text{ESZ}} = 1.2$	$d_{\text{ld}}/d_{\text{ESZ}} \sim 1.5$	78
Sedimen.	Talc (plates)	$d_{50, \text{sed}} = 9.3$	$d_{50, \text{ld}}/d_{50, \text{sed}} \sim 1.4$	78
ESZ	Talc (plates)	$d_{50, \text{ESZ}} = 11.2$	$d_{50, \text{ld}}/d_{50, \text{ESZ}} \sim 1.2$	78
Sedimen.	Talc (plates) (delaminated)	$d_{50, \text{sed}} = 1.5$	$d_{50, \text{ld}}/d_{50, \text{sed}} \sim 5.3$	78
ESZ	Talc (plates) (delaminated)	$d_{50, \text{ESZ}} = 4.6$	$d_{50, \text{ld}}/d_{50, \text{ESZ}} \sim 1.7$	78
Sieve	Hard wheat flour (irregular) (2)	$d_{50, \text{ld}} = 10\text{-}300$	$V\%_{d < 45 \mu\text{m}, \text{ld}}/$ $V\%_{d < 45 \mu\text{m}, \text{sieve}} \sim 1$	79
Sieve	Soft wheat flour (irregular) (2)	$d_{50, \text{ld}} = 10\text{-}300$	$V\%_{d < 45 \mu\text{m}, \text{ld}}/$ $V\%_{d < 45 \mu\text{m}, \text{sieve}} \sim 1.5\text{-}2$	79
SEM	Zirconium oxide compound (~spherical)	$d_{50, \text{SEM}} = 51$	$d_{50, \text{ld}}/d_{50, \text{SEM}} \sim 1.0\text{-}$ $1.2$	80
ESZ	PDVS latex (spheres)	$d_{\text{ESZ}} = 10.37$	$d_{\text{ld}}/d_{\text{ESZ}} = 1.02$	81
ESZ	Glass bead (spheres)	$d_{\text{ESZ}} = 49.61$	$d_{\text{ld}}/d_{\text{ESZ}} = 1.06$	81
ESZ	9 types of talc (plates)	$d_{\text{ESZ}} = 4.67$	$d_{\text{ld}}/d_{\text{ESZ}} = 2.43$	81
ESZ	Mica powder (plates)	$d_{\text{ESZ}} = 3.09$	$d_{\text{ld}}/d_{\text{ESZ}} = 2.05$	81
ESZ	Potassium titanate (rods)	$d_{\text{ESZ}} = 1.59$	$d_{\text{ld}}/d_{\text{ESZ}} = 3.88$	81
ESZ	Sapphire powders (rods)	$d_{\text{ESZ}} = 6.87$	$d_{\text{ld}}/d_{\text{ESZ}} = 2.72$	81
Sedimen.	BCR 130	$d_{\text{sed}} = 132.8$	$d_{\text{ld}}/d_{\text{sed}} = 0.91$	82

Since any bias is different for each technology if a spherical approximation is used for non-spherical particles, the variations in the size results of laser diffraction compared with that of sedimentation, for example, will be different than those obtained in a comparison with the ESZ method. Practically, when comparing results from laser diffraction to results from another technology, some scaling or weighting factors for size and/or density distributions are often employed to artificially shift or reweigh one of the instrument's results. In some cases, a correlation study may be needed to find the factors and their variations as a function of particle sizes.

An alternative route is to use the available formulas for oriented or randomly oriented non-spherical particles in the Rayleigh-Debye-Gans region, or in the Fraunhofer region for materials that are more-or-less regularly shaped. In these applications there are often two parameters. Typically, one parameter is fixed and the ratio of the two parameters is fitted out. For example, for randomly oriented ellipsoids (oblate having semi-axes of (a,a,b) or prolate having semi-axes of (a,b,b)) the following equations can be used to relate a shape coefficient  $\beta$  to the distribution of one axial length from the diameter distribution ( $d_{\text{ld}}$ ) measured by laser diffraction if the other axial length is fixed, under the approximation that the square root of the mean scattered light intensity is proportional to the equivalent diameter determined from the average cross-sectional area [75].

$$\frac{d_{ld}}{c} = \beta_{oblate} = \left(1 + \frac{\ln(\sqrt{\xi^2 - 1} + \xi)}{\xi\sqrt{\xi^2 - 1}}\right)^{1/2}, \quad (3.21)$$

$$\xi = \frac{a}{b} \quad \begin{array}{ll} \xi = 1, & \beta = \sqrt{2} \\ \xi = \infty, & \beta = 1 \end{array} ;$$

$$\frac{d_{ld}}{c} = \beta_{prolate} = \frac{1}{\zeta} \left(1 + \frac{\zeta^2 \sin^{-1}(\frac{\sqrt{\zeta^2 - 1}}{\zeta})}{\sqrt{\zeta^2 - 1}}\right)^{1/2}, \quad (3.22)$$

$$\zeta = \frac{a}{b} \quad \begin{array}{ll} \zeta = 1, & \beta = \sqrt{2} \\ \zeta = \infty, & \beta = 0 \end{array} .$$

In Eqs. 3.21 and 3.22,  $c$  is a proportional constant. A three-dimensional size distribution plot can be generated if one other independent measurement can be accomplished. Applications of these theories, however, are still largely based on individual cases and limited to academic research.

The last route is to try to solve the scattering problem directly for particles having irregular shapes and possessing no symmetry. Irregular shapes produce strong polarization effects, and edges and asperity of the surface cause smoothing effects in the scattering pattern. In many cases, spherical approximations will completely neglect to account for the polarization effects arising from non-spherical particles and hence underestimate scattering cross sections. Two alternative approaches have been investigated. One is to calculate the statistically averaged scattering behavior from individual scattering patterns followed by the summation of these patterns from all particles. The other is to calculate the averaged scattering intensity from the whole particle ensemble directly. Many semi-empirical methods have been explored in both approaches [83,84]. Some of these can successfully predict angular scattering patterns that agree well with experimental results. For example, Pollack and Cuzzi used a global analysis technique that combines the Mie theory (in the small particle regime) with Fraunhofer diffraction using a scaled equivalent sphere, light reflection from the Fresnel coefficient averaged polarization, and the transmitted intensity using an empirical logarithm formula (in the large particle regime). The predicted angular scattering patterns for polydisperse samples of cubes, platelets, octahedral particles and convex or concave particles generated by this technique agreed very well with experimental data [85]. However, in practice, calculating a scattering pattern to fit experimental data of known particles is not sufficient. There is still a need for further theoretical

development if one wants to reveal size information of irregular shaped particles from the measurement of randomly oriented particles.

One other use of laser diffraction in measurements of irregular particles is in the fractal dimension determination of irregular clusters formed by the agglomeration of small particles, though such clusters often lack self-similarity and are usually polydisperse. When the scattering vector  $K$  is much larger than  $1/R_g$  but much smaller than  $1/d_o$  (where  $R_g$  and  $d_o$  are the radius of gyration of the aggregates and the primary particle size respectively), there exists a simple relation between the fractal dimension  $d_f$  and the scattering angular pattern:

$$I(K) \propto K^{-d_f}. \quad (3.23)$$

Thus the fractal dimension of aggregates can be easily measured at small scattering angles using a laser diffraction instrument [86].

Measurement of some finite number of particles, from one particle to less than one hundred particles, leads to another way of shape determination for regularly shaped particles, because for any non-spherical particle there is a non-uniformity of scattered intensity with azimuthal angle ( $\phi$  in Figure 2.1). The non-uniformity is clearly shown in Figures 2.8 and 2.9 for rectangular particles. For a cylinder, scattering would be very strong in the plane orthogonal to its axis. Thus, by measuring the azimuthal distribution of scattering from one or a few particles, shape information can be obtained. In one such application, a custom multi-element photodiode detector array (Figure 3.42a) was used in combination with a neural-network pattern recognition system to monitor shape variation [87]. In this case, airborne mineral fibers were distinguished from non-fibrous materials using the azimuthal scattering pattern [88,89]. In another instrument, eight azimuthal angles at a constant side scattering angle of  $55^\circ$  were used to detect the signals from a steadily flowing particle stream passing through the beam inside a spherical measuring chamber. For non-spherical particles, the signals detected at the eight detectors would be different. A "spherical index", calculated from the standard deviation of the eight signals per particle was defined. The spherical index is unity for spheres and deviate from unity as the non-sphericity of particle increases [90].



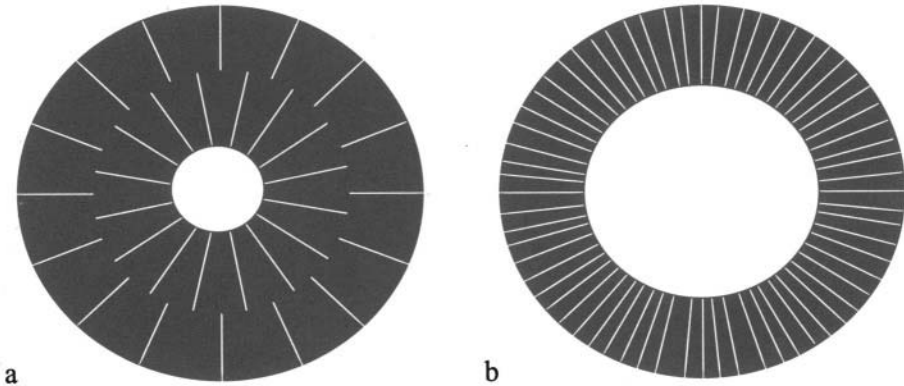


Figure 3.42. Custom photodiode detector arrays for shape recognition.

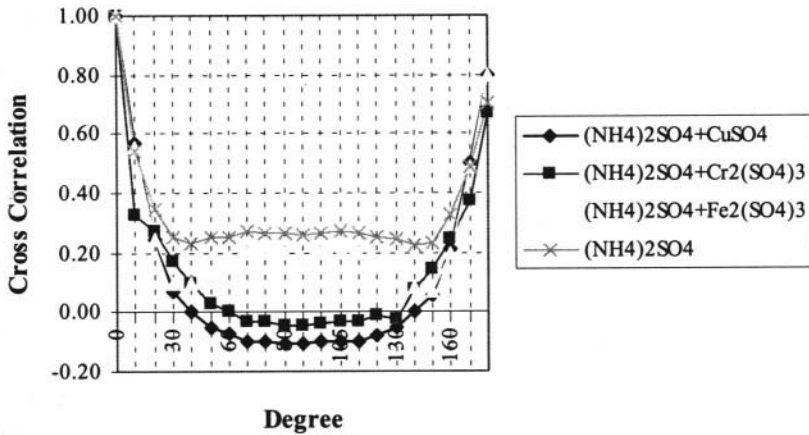
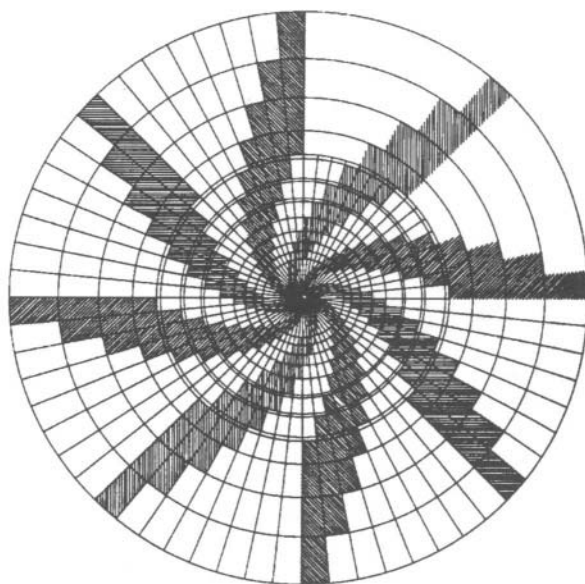


Figure 3.43. Shape correlation graphs of crystals of  $(\text{NH}_4)_2\text{SO}_4$  with additives [92] (by permission of Institution of Chemical Engineers).

Using a segmented ring photodetector array such as the one that shown in Figure 3.42b, the azimuthal intensity distribution is detected from a limited number of particles in the scattering volume. Particle shape is characterized by the correlation coefficient across azimuthal angles computed from intensity-intensity correlation around each azimuthal angle. For spheres, because of their uniform intensity distribution at all azimuthal angles, the correlation coefficient is a constant. For other regularly shaped particles, each shape will have a unique correlation graph for correlation angles from  $0^\circ$  to  $180^\circ$ . As an example, there will be three maxima at  $0^\circ$ ,  $90^\circ$ , and  $180^\circ$ , and two minima around  $45^\circ$  and  $135^\circ$

in the correlation graph of a square. (One may get an idea of the correlation graph from Figure 2.8). For an ellipse, there will be two maxima at  $0^\circ$  and  $180^\circ$ , and one minimum at  $90^\circ$  (Figure 2.10). Experimental verification has been performed using glass beads, hair fibers, beach sands, and crystals [91]. Shape change can thus be monitored by this technique as shown in Figure 3.43, where crystals of  $(\text{NH}_4)_2\text{SO}_4$  change shape as additional ions are added [92]. This method can be used in characterization of particles having distinguished regular shapes or to monitor shape changes. However, any measurement has to be limited to a finite number of particles without a complete randomization of particle orientation. Otherwise, the correlation coefficient will be reduced and shape characteristics will disappear. In such a design, the size of the detecting ring must be adjusted for particle size and the effective focal length of the optics. For a rigid instrument, a more complicated detector array is required such as the one shown in Figure 3.44.



*Figure 3.44.* An advanced detector pattern for laser diffraction shape measurement [93] (by permission of Wiley-VCH Verlag GmbH).

## REFERENCES

- 1 Witt, W., Röthele, S., Laser Diffraction-Unlimited? *Part. Part. Syst. Charact.*, 1996, 13, 280-286.
- 2 Igushi, T., Togawa, Y., Apparatus for Simultaneously Measuring Large and Small Particle Size Distribution, *US Patent 5,185,641*, 1993.
- 3 Xu, R., Improvement in Particle Size Analysis Using Light Scattering, in *Particle and Surface Characterization Methods*, Eds. Müller, R. H., Mehnert, W., Medpharm Scientific Publishers, Stuttgart, 1997, Chpt.3, pp.27-56.
- 4 Bott, S. E., Hart, W. H., Extremely Wide Dynamic Range, High-Resolution Particle Sizing by Light Scattering, in *Particle Size Distribution II*, Ed. Provder, T., ACS Symp. Series 472, American Chemical Society, Washington D. C., 1991, Chpt.7, pp.106-122.
- 5 Bott, S. E., Hart, W. H., Particle Size Analysis Utilizing Polarization Intensity Differential Scattering, *US Patent 4,953,978*, 1990.
- 6 Bott, S. E., Hart, W. H., Particle Size Analysis Utilizing Polarization Intensity Differential Scattering, *US Patent 5,104,221*, 1992.
- 7 Toyoda, M., Laser Diffraction Particle Size Distribution Measurement Instrument: Coulter LS and Its Application to Pigment Particles, *The Industrial Coating (Japan)*, 1998, 151, 30-34.
- 8 Schmitz, B., Bott, S. E., Hart, W. H., Laser Diffraction Particle Sizing Method Using a Monomode Optical Fiber, *US Patent 5,610,712*, 1997.
- 9 Bott, S. E., Hart, W. H., Method and Apparatus for Particle Size Analysis, *US Patent 5,056,918*, 1991.
- 10 Trainer, M. N., Methods and Apparatus for Determining Small Particle Size Distribution Utilizing Multiple Light Beams, *US Patent 5,416,580*, 1995.
- 11 Conklin, W. B., Olivier, J. P., Strickland, M. L., Capturing Static Light Scattering Data Using a High Resolution Charge-Coupled Device Detector, in *Particle Size Distribution III*, Ed. Provder, T., ACS Symp. Series 693, American Chemical Society, Washington D. C., 1998, Chpt.2, pp. 14-22.
- 12 Szychter, H., Cilas Particle Size Analyzer 1180: How to Measure Coarse and Fine Particles at the Same Time with a Video Camera and a Short Bench, *Powder Handling and Processing*, 1998, 10, 412-413.
- 13 De Boer, G. B. J., de Weerd, C., Thoenes, D., Goossens, H. W. J., Laser Diffraction Spectrometry: Fraunhofer Diffraction Versus Mie Scattering, *Part. Charact.*, 1987, 4, 14-19.
- 14 Brown, D. J., Felton, P. G., Direct Measurement of Concentration and Size for Particles of Different Shapes using Laser Light Diffraction, *Ghent. Eng. Res. Des.*, 1985, 63, 125-132.
- 15 Inaba, K., Matsumoto, K., the Measurement of Particle Concentration using a Laser Diffraction Particle Size Analyzer, *J. Soc. Powder Technol. Japan*, 1997, 34, 490-498.
- 16 Baker, J. P., Mott, S. C., Wright, C. A., Method and Apparatus for Dry Particle Analysis, *US Patent 5,359,907*, 1994.
- 17 Leschonski, K., Röthele, S., Menzel, U., A Special Feeder for Diffraction Pattern Analysis of Dry Powders, *Part. Charact.*, 1984, 1, 161-166.
- 18 Lehner, D., Kellner, G., Schnablegger, H., Clatter, O., Static Light Scattering on Dense Colloidal Systems: New Instrumentation and Experimental Results, *J. Colloid Interface Sci.*, 1998, 201, 34-47.
- 19 Wang, N., Shen, J., A Study of the Influence of Misalignment on Measuring Results for Laser Particle Analyzers, *Part. Part. Syst. Charact.*, 1998, 3, 122-126.
- 20 Xu, R., Reference Materials in Particle Measurement, in *Liquid and Surface-Borne Particle Measurement Handbook*, Eds. Knapp, J. Z., Barber, T. A., Lieberman, A., Marcel Dekker, New York, 1996, Chpt.16, pp.709-720.

- 
- 21 *ISO 13320-1 Particle Size Analysis-Laser Diffraction Methods. Part I: General Principle*, International Organization of Standardization, Genève, 1999.
  - 22 For example, Duke Scientific, Palo Alto, CA.
  - 23 *Product Specification, Diffraction Reference Reticle*, Malvern Instrument, Malvern, 1993.
  - 24 Cao, J., Watson, D., Diffraction Patterns of Static Particles on a 2-D Surface, *Part. Part. Syst. Charact.*, 1994,11,235-240.
  - 25 Mühlenweg, H., Hirleman, E. D., Reticles as Standards in Laser Diffraction Spectroscopy, *Part. Part. Syst. Charact.*, 1999, 16, 47-53.
  - 26 Tikhonov, A. N., Arsenin, V. Y., *Solution of Ill-posed Problems*, Winston, Washington D.C., 1977.
  - 27 Chin, J. H., Spliepevich, C. M., Tribus, M., Particle Size Distribution from Angular Variation of Intensity of Forward-scattering Light, *J. Phys. Chem.*, 1955, 59, 841-844.
  - 28 Koo, J. H., Particle Size Analysis Using Integral Transform Techniques on Fraunhofer Diffraction Pattern, *D. Sci. Dissertation*, George Washington Uni., Washington D. C., 1987.
  - 29 Shifrin, K. S., Perelman, A. Ya., The Determination of the Spectrum of Particles in Dispersed System from Data on Its Transparency, *Opt. Spectrosc.* (USSR), 1963, 15, 285-289.
  - 30 Kouzelis, D., Candel, S. M., Esposito, E., Zikikout, S., Particle Sizing by Laser Light Diffraction: Improvements in Optics and Algorithms, *Part. Charact.*, 1987, 4, 151-156.
  - 31 Bayvel, L. P., Knight, J., Roberston, G., Alternative Model-Independent Inversion Programme for Malvern Particle Sizer, *Part. Charact.*, 1987, 4, 49-53.
  - 32 Mroczka, J., Method of Moments in Light Scattering Data Inversion in the Particle Size Distribution Function, *Optics Comm.*, 1993, 99, 147-151.
  - 33 Hirleman, E. D., Optimal Scaling of the Inverse Fraunhofer Diffraction Particle Sizing Problem: the Linear System Produced by Quadrature, *Part. Part. Syst. Charact.*, 1987, 4, 128-133.
  - 34 Mühlenweg, H., Weichert, R., Optical Particle Sizer: A New Development with Mathematical Correlation of Spread Measurement Data, *Part. Part. Syst. Charact.*, 1997, 14, 205-210.
  - 35 Agrawal, Y. C., Pottsmith, H. C., Optimizing the Kernel for Laser Diffraction Particle Sizing, *App. Opt.*, 1993,32,4285-4286.
  - 36 Bassini, A., Musazzi, S., Paganini, E., Perini, U. U., Ferri, F., Giglio, M., Optical Particle Sizer Based on the Chahine Inversion Scheme, *Opt. Eng.*, 1992, 31,1112-1117.
  - 37 Phillips, B. L., A Technique for the Numerical Solution of Certain Integral Equations of the First Kind, *J. Assoc. Comput. Mach.*, 1962, 9, 84-97.
  - 38 Twomey, S., On the Numerical Solution of Fredholm Integral Equations of the First Kind by the Inversion of Linear System Produced by Quadrature, *J. Assoc. Comput. Mach.*, 1963, 10, 97-101.
  - 39 Tarantola, A., *Inverse Problem Theory*, Elsevier, Amsterdam, 1987.
  - 40 Heuer, M., Leschonski, K., Results Obtained with a New Instrument for the Measurement of Particle Size Distributions from Diffraction Patterns, *Part. Charact.*, 1985, 2, 7-13.
  - 41 Boxman, A., Merkus, H. G., Verheijen, J. T., Scarlett, B., Deconvolution of Light-Scattering Pattern by Observing Intensity Fluctuations, *App. Opt.*, 1991, 30, 4818-4823.
  - 42 Ma, Z., Merkus, H. G., de Smet, J. G. A. E., Verheijen, P. J. T., Scarlett, B., Improving the Sensitivity of Forward Light Scattering Technique to Large Particles, *Part. Part. Syst. Charact.*, 1999, 16,71-76.
  - 43 Finsy, R., Deriemaeker, L., Gelade, E., Joosten, J., Inversion of Static Light Scattering Measurements for Particle Size Distribution, *J. Colloid Interface Sci.*, 1992, 153, 337-354.
  - 44 Tüzün, U., Farhadpour, F. A., Dynamic Particle Size Analysis with Light Scattering Technique, *Part. Charact.*, 1986, 3, 151-157.

- 
- 45 Hammond, D. C., Deconvolution Technique for Line-of-Sight Optical Scattering Measurements in Axisymmetric Sprays, *Appl. Opt.*, 1981, 20,493-499.
  - 46 Yule, A. J., Ahseng, C., Felton, P. G., Ungut, A., Chigier, N. A., A Laser Tomographic Investigation of Liquid Fuel Sprays, *Proc. 18<sup>th</sup> Symp. Combustion*, 1981, pp.1501-1510.
  - 47 Li. X., Rensizbulut, M., Further Development and Application of a Tomographical Data Processing Method for Laser Diffraction Measurements in Sprays, *Part. Part. Syst. Charact.*, 1999, 16,212-219.
  - 48 *Handbook of Chemistry and Physics*, 75<sup>th</sup> Ed., CRC Press, Boca Raton, 1995.
  - 49 *Handbook of Optical Constants of Solids*, Ed. Palik, E. D., Academic Press, New York, 1997.
  - 50 Fanderlik, I., *Optical Properties of Glass*, Elsevier, New York, 1983.
  - 51 *Pigment Handbook*, Ed. Lewis, P. A., John Wiley & Sons, New York, 1988
  - 52 *Polymer Handbook*, Eds. Brandrup, J., Immergut, E. H., Grulke, E. A., 4<sup>th</sup> Ed., Wiley-Interscience, New York, 1999.
  - 53 Schnablegger, H., Glatter, O., Simultaneous Determination of Size Distribution and Refractive Index of Colloidal Particle from Static Light Scattering Experiments, *J. Colloid Interface Sci.*, 1993,158, 228-242.
  - 54 Hitchen, C. J., The Effect of Suspension Medium Refractive Index on the Particle Size Analysis of Quartz by Laser Diffraction, *Part. Part. Syst. Charact.*, 1992, 9, 171-175.
  - 55 Hirleman, E. D., Modeling of Multiple Scattering Effects in Fraunhofer Diffraction Particle Size Analysis, *Part. Part. Syst. Charact.*, 1988, 5, 57-65.
  - 56 Hirleman, E. D., General Solution to the Inverse Near-forward-scattering Particle-sizing Problem in Multiple-scattering Environment: Theory, *App. Opt.*, 1991, 30, 4832-4838.
  - 57 Hirleman, E. D., A General Solution to Fraunhofer Diffraction Particle Sizing in Multiple Scattering Environment: Theory, in *Proc. 2<sup>nd</sup> Int. Congress Opt. Part. Sizing*, Tempe, 1990.
  - 58 Wedd, M. W., Holve, D. J., On-line Control of Powder Milling Using Laser Diffraction, in *Proc. World Congress Part. Technol. 3*, Brighton, 1998, (ICHEME), Paper No.45.
  - 59 Ward-Smith, S., Jones, R., Wedd, M., Determination of Continuous Particle Size Distribution of Concentrated Sprays, *Am. Lab.*, 1999, January, pp. 17-21.
  - 60 Harvill, T. L., Hoog, J. H., Holve, D. J., In-process Particle Size Distribution Measurements and Control, *Part. Part. Syst. Charact.*, 1995, 12, 309-313.
  - 61 Cornillault, J., Particle Size Analyzer, *Appl. Opt.*, 1972, 11, 262-268.
  - 62 Bürkholz, A., Polke, R., Laser Diffraction Spectrometers/Experience in Particle Size Analysis, *Part. Charact.*, 1984, 1, 153-160.
  - 63 Loizeau, J. —L., Arbouille, D., Santiago, S., Vernet, J. —P., Evaluation of a Wide Range Laser Diffraction Grain Size Analyzer for Use with Sediments, *Sedimentology*, 1994, 41, 353-361.
  - 64 Merkus, H. G., Bischof, O., Drescher, S., Scarlett, B., Precision and Accuracy in Particle Sizing, Round-robin Results from Sedimentation, Laser Diffraction and Electrical Sensing Zone Using BCR 67 and BCR 69, in *Prep. 6<sup>th</sup> European Symp. Part. Charact.*, Nürnberg, 1995, pp.427-436.
  - 65 Mühlenweg, H., Hirleman, E. D., Laser Diffraction Spectroscopy: Influence of Particle Shape and a Shape Adaptation Technique, *Part. Part. Syst. Charact.*, 1998, 15, 163-169.
  - 66 Jones, A. R., Fraunhofer Diffraction by Random Irregular Particles, *Part. Part. Syst. Charact.*, 1987, 4, 123-127.
  - 67 Heffels, C. M. G., Verheijen, P. J. T., Heitzmann, D., Scarlett, B., Correction of the Effect of Particle Shape on the Size Distribution Measured with a Laser Diffraction Instrument, *Part. Part. Syst. Charact.* 1996, 13, 271-279.
  - 68 Barreiros, F. M., Ferreira, P. J., Figueiredo, M. M. Calculating Shape Factors from Particle Sizing Data, *Part. Part. Syst. Charact.*, 1996, 13, 368-373.

- 
- 69 Michoel, A., De Jaeger, N., Sneyers, R., De Wispelaere, W., Geladé, E., Kern, J., van Amserdam, P., Den Tandt, Y., Houtmeyers, E., van Cotthem, L., Influence of Porosity on the Electrical Sensing Zone and Laser Diffraction Sizing of Silicas. A Collaborative Study, *Part. Part. Syst. Charact.* 1994, 11, 391-397.
  - 70 Hayakawa, O., Nakahira, K., Tsubaki, J., Comparison of Particle Size Analysis and Evaluation of Its Measuring Technique with Fine Ceramics Powders, Part 1, *J. Cera. Soc. Japan*, 1995, 103, 392-397.
  - 71 Hayakawa, O., Nakahira, K., Tsubaki, J., Comparison of Particle Size Analysis and Evaluation of Its Measuring Technique with Fine Ceramics Powders, Part 2, *J. Cera. Soc. Japan*, 1995, 103, 500-505.
  - 72 Palmer, A. T., Logiudice, P. J., Cowley, J., Comparison of Sizing Results Obtained with Electrolyte Volume Displacement and Laser Light Scattering Instrumentation, *Am. Lab.*, 1994, November, pp. 15-19.
  - 73 Flank, W. H., Comparison of ASTM Round-Robin Data on Particle Size Using Three Different Methods, *Ind. Eng. Chem. Res.*, 1987, 26, 1750-1753.
  - 74 Bowen, P., Humphy-Baker, R., Herard, C., Particle Size Distribution Measurement of Regular Anisotropic Particles - Cylinders and Platelets, in *Proc. World Congress Part. Technol.* 3, Brighton, 1998, Paper No.29.
  - 75 Endoh, S., Kuga, Y., Ohya, H., Ikeda, C., Iwata, H., Shape Estimation of Anisometric Particles Using Sizing Measurement Techniques, *Part. Part. Syst. Charact.*, 1998, 15, 145-149.
  - 76 Umhauer, H., Bottlingor, M., Effect of Particle Shape and Structure on the Results of Single-Particle Light Scattering Size Analysis, *Appl. Opt.*, 1991, 30, 4980-4986.
  - 77 Inaba, K., Matsumoto, K., Effect of Particle Shape on Particle Size Analysis Using the Electric Sensing Zone Method and Laser Diffraction Method, *J. Soc. Powder Technol. Japan*, 1995, 32, 722-730.
  - 78 Baudet, G., Bizi, M., Rona, J. P., Estimation of the Average Aspect Ratio of Lamellae-Shaped Particles by Laser Diffractometry, *Part. Sci. Tech.*, 1993, 11, 73-96.
  - 79 Hareland, G. A., Evaluation of Flour Particle Size Distribution by Laser Diffraction, Sieve Analysis and Near-infrared Reflectance Spectroscopy, *J. Cereal Sci.*, 1994, 21, 183-190.
  - 80 Pei, P., Kelly, J., Malghan, S., Dapkunas, S., Analysis of Zirconia Powder for Thermal Spray: Reference Material for Particle Size Distribution Measurement, in *Thermal Spray: Practical Solution for Engineering Problem*, Ed. Berndt, C. C., ASM International, Newbury, 1996, pp.263-273.
  - 81 Yang, I., Hideaki, I., Measuring Techniques for Particle Size Distribution, *Coating Technology (Japan)*, 1992, 7, 83-87.
  - 82 Hubner, T., Will, S., Leipertz, A., Determination of Particle Size Distribution and Particle Density Based on a Combination of Photosedimentation and Laser Diffraction, in *Preprints of Partec 98, 7<sup>th</sup> European Symp. Part. Charact.*, Nürnberg, 1998, pp.743-752.
  - 83 *Light Scattering by Irregularly Shaped Particles*, Ed. Schuerman, D. W., Plenum Press, New York, 1980.
  - 84 Al-Chalabi, S. A. M., Jones, A. R., Light Scattering by Irregular Particles in the Rayleigh-Gans-Debye Approximation, *J. Phys. D*, 1995, 28, 1304-1308.
  - 85 Pollack, J. B., Cuzzi, J. N., in *Light Scattering by Irregular Shaped Particles*, Ed. Schuerman, D.W., Plenum Press, New York, 1980, pp.113-125.
  - 86 Bushell, G. C., Amal, R., Raper, J. A., The Effect of Polydispersity in Primary Particle Size on Measurement of the Fractal Dimension of Aggregates, *Part. Part. Syst. Charact.*, 1998, 15, 3-8.
  - 87 Kaye, P., Hirst, E., Wang-Thomas, Z., Neural-network-based Spatial Light-Scattering Instrument for Hazardous Airborne Fiber Detection, *App. Opt.*, 1997, 36, 6149-6156.

- 
- 88 Barthel, H., Sachweh, B., Ebert, F., Measurement of Airborne Mineral Fibres Using a New Differential Light Scattering Device, *Meas. Sci. Technol.*, 1998, 9, 206-216.
  - 89 List, J., Weichert, R., Detection of Fibers by Light Diffraction, in *Preprints of Partec 98, 7<sup>th</sup> European Symp. Part. Charact.*, Nürnberg, 1998, pp.705-714.
  - 90 Dick, W. D., McMurry, P. H., Sachweh, B., Distinguishing Between Spherical and Non-spherical Particles by Measuring the Variability in Azimuthal Light Scattering, *Aerosol Sci. Tech.*, 1995,23,373-391.
  - 91 Heffels, C. M. G., Heitzmann, D., Hirleman, E. D., Scarlett, B., The Use of Azimuthal Intensity Variation in Diffraction Patterns for Particle Shape Characterization, *Part. Part. Syst. Charact.*, 1994, 11, 194-199.
  - 92 de Smet, J. G. A. E., Heffels, C. M. G., Szychter, H. S., Merkus, H., Scarlett, B., Measurement of Particle Size and Shape by Forward Light Scattering, in *Proc. World Congress Part. Technol. 3*, Brighton, 1998, (IChemE), Paper No.48.
  - 93 Heffels, C. M. G., Polke, R., Rädle, M., Sachweh, B., Schäfer, M., Scholz, N., Control of Particulate Processes by Optical Measurement Techniques, *Part. Part. Syst. Charact.*, 1998, 15,211-218.

# OPTICAL PARTICLE COUNTING

## *Counting and Sizing*

### 4.1. Introduction

Single optical particle counting (OPC) is one of the main technologies employed in environmental monitoring and in the control of many particulate materials. Because of its ability to make in-situ measurements, OPC is widely used in contamination analyses (e.g., water, clean rooms, hydraulic fluids) and in atmospheric analyses of liquid-borne or air-borne particles. In these situations particulate content is typically no more than a gram per cubic meter in ambient atmospheres, less than 10 to  $10^5$  particles larger than  $0.1\text{ }\mu\text{m}$  per cubic meter in a clean room environment, and less than 10 particles larger than 50 nm per liter of the deionized water used in the semiconductor industry. In many cases these particles are all “unwanted” substances. Here, the differential size distribution is less important than the cumulative number concentration at sizes above some benchmark size threshold. In many industries that require tight control of particulate matter in a specific size range, OPC has been indispensable in the verification and control of product quality. OPC is perhaps the only on-line technology that can be used to obtain information on whether or not all the particles in the material being measured fall within the required size limits. Simultaneous counting, sizing, as well as in-situ material identification of individual particles in the sample, is one of the present developmental activities in OPC [1].

The measurement of individual particles through their interaction with light has been in common usage for many years. The development of optical particle counting began more than seventy years ago [2]. The first modern light scattering optical particle counter appeared in the late 1940's and was used in the detection of air-borne chemical warfare agents [3]. Light extinction OPC was subsequently developed during 1960's. Present-day OPC technology makes use of the light scattering from single particles in order to both count and size small particles (sometimes as small as 50 nm), and of the light extinction caused by the particles' presence in the light beam in order to count and size large particles (as large as 1 mm). The particles may be in the form of aerosols, dry powders, or liquid suspensions. All particles are individually introduced into the sensing zone by means of pressure, vacuum, or sheath or natural flow. OPC is



different from laser diffraction, which resolves the particle size distribution from an ensemble measurement of the angular scattering intensity pattern. OPC counts and sizes particles using the signals generated by individual particles. In sufficiently dilute liquid or gas suspensions these particles flow one at a time through a small sensing zone of uniform illumination produced either by a laser or an incandescent light. Passage of the particle through the sensing zone gives rise to a detectable pulse, the magnitude of which depends on the dimension and optical properties of the particle, and the physical principle used for detection (light scattering or light extinction). Electric pulses generated at the photodetector from the light signals are sorted and recorded. Particle count and size are then resolved according to a calibration curve which is obtained from a known size standard or control. This is a non-ensemble measurement technology. Since the scattering is from a single particle, the theories described in Chapter 2 can be directly applied without having to consider the complexity of multiple scattering and the exceedingly difficult deconvolution of the signals from an ensemble of particles that may differ in size and shape as seen in laser diffraction. After calibration, a one-to-one correspondence between the pulse amplitude and particle size exists. Compared to many characteristics of an ensemble measurement, such as its broad dynamic range, high statistical accuracy, and relatively low resolution, OPC is a high resolution technology but one with a relatively narrow dynamic range and low statistical accuracy.

Section 4.2 describes the instrumentation of OPC including the optics, electronics, and sample handling systems. Data analysis scheme and analyses of the resolution and accuracy of both sizing and counting functions are presented in Section 4.3.

## **4.2. Instrumentation**

As described in detail in Chapter 2, the scattered light from a single particle is a function of the illuminating wavelength and intensity, the configuration of the illuminating and collecting optics, the physical properties of particle and medium, as well as particle orientation. For the same type of particle, the scattering flux is a power function of size ranging from the sixth power for small particles to the second power for large particles. Therefore, although the overall sizing range of OPC technology may extend from 50 nm to 1 mm, as shown in Table 4.1, because of the limitation in the linearity of electronic data processing systems, each optical configuration typically covers a range of 4:1 to 100:1. In Table 4.1 the size range shown is that of particles passing through the sensing zone, which does not necessarily represent the original particle size. In using a condensation nucleus counter (CNC) (an optical particle counter preceded by nucleus condensation), the original particle sizes before vapor condensation may be as small as a few nanometers [4]. OPC instrumentation

has evolved from equipment weighing 200 kg in 1954 [5] to a battery operated and hand-held counters weighing only 1 kg today. There are many designs which vary in their different components in order to be applied to particles in specific size or concentration ranges. There is no intention to describe all possible or marketed configurations in this text. Only typical ones are described in schematic form. All optical designs include a light source, a set of optic components to condition the light and to define the sensing zone (also called the viewing volume), the collecting optics, and the photodetectors. Depending on particle size range, either light scattering OPC or light extinction OPC can be used. The former is more suitable for small particles and the latter for larger particles. Since most aerosol particles in an ambient or industrial environment are small in size, the light extinction technique is rarely used for aerosols, and only occasionally used for dry powders, but it is frequently used in the characterization of particles in liquid.

Table 4.1. OPC size and sample flow range

Medium	Liquid-Borne			Air-Borne
Detection Means	In-Situ		Volumetric	Volumetric
	Spectrometer	Monitor		
Light Scattering Size Range	0.05-5 $\mu\text{m}$			0.05-20 $\mu\text{m}$
Light Extinction Size Range	1-1000 $\mu\text{m}$			> 25 $\mu\text{m}$
Sample Flow Rate Range	0.002-8 ml/s			0.1-500 ml/s

In air-borne (and most liquid-borne) OPC measurements, the dimension of the particle stream is smaller than the beam dimension so that the sample passing through the sensing zone is uniformly illuminated and will be completely sampled. All particles in the sample with sizes slightly above the threshold will be counted and sized: these are called volumetric designs. In liquid measurement, there is another class of instruments, in which only a fraction of the flow (typically a few percent) is illuminated. Such devices are very useful in applications in which the liquid cannot be efficiently pumped at high velocity and focused into a stream smaller than the beam size. Such instruments are called “in-situ” devices, meaning that the process of measurement is not designed to feed the complete sample into the instrument, instead it is to probe particles in-situ. In-situ OPC is suitable for very clean media where a large flow is needed in order to measure a sufficiently large number of particles, and where episodic events (short term, out of spec fluctuations) are present. Since aerosol fluids can always be plumbed and focused dynamically into well-controlled particle streams which pass through the beam in constrained paths it is not necessary for in-situ aerosol OPC instruments. There are two types of optical designs for liquid in-situ OPC. One is the spectrometer design, in which only the particles passing through a well-defined sensing zone where the beam

intensity is uniform are then counted and sized. Therefore, the particle size distribution obtained would be very close to that from a volumetric optical particle counter. Another type of design widely used in liquid contamination monitoring (called monitor) does not provide uniform sample volume illumination and has poor resolution but provides high sensitivity, high sample flow rates and is less expensive [6].

#### 4.2.1. LIGHT SOURCE

There are three types of light sources used in OPC - incandescent filament lamps ( $\lambda = 200\text{-}3000\text{ nm}$ ), gas lasers (He-Ne or Ar ion) and diode lasers. The advantages of lasers are their high power, stable intensity, and well-defined beam characteristics, which produces better measurement reproducibility. High intensity enables small particles ( $< 0.1\text{ }\mu\text{m}$ ) to be measured, and so most designs use a laser as the light source. Despite all the disadvantages of incandescent light (as compared to laser light) the multi-wavelength nature of an incandescent source provides a unique advantage when measuring particles at small angles over a specific size range where there is a polytonic response of the scattered light as a function of particle size at some single wavelength. In many instances, polychromatic light “smoothes” the scattering curve and thus provides a more desirable, nearly monotonic response. More discussion is provided in the next section.

To measure very small aerosol particles ( $< 0.1\text{ }\mu\text{m}$ ), specially designed counters have been developed in which particles are injected into the radiation field of an open cavity He-Ne laser. Normally, in order to reach a high lasing efficiency there is only 1% of the resonance energy inside the cavity is emitted. The resonance power inside the laser cavity of a 1 mW laser can be as high as 1 W. Therefore, access to this very intense energy density can provide a counter a very powerful light source without the use of a high power laser which often involves high cost and a large footprint. Such access is achieved through the use of a Brewster’s window to seal one end of the laser. The sensing zone is then set between the Brewster’s window and the reflective mirror of the laser (Figure 4.1). Particles are illuminated from both directions, increasing the collectable scattered light. A further enhancement in light power can be made by replacing the left mirror in Figure 4.1 with another plasma tube also with a Brewster’s window. Such an instrument can size particles from  $0.05\text{-}5\text{ }\mu\text{m}$  [7,8]. Recently, a chromium-doped lithium strontium aluminum fluoride crystal pumped by a red diode laser combined with a high reflective mirror has been used as the intra-cavity device for sizing and counting small aerosols [9].

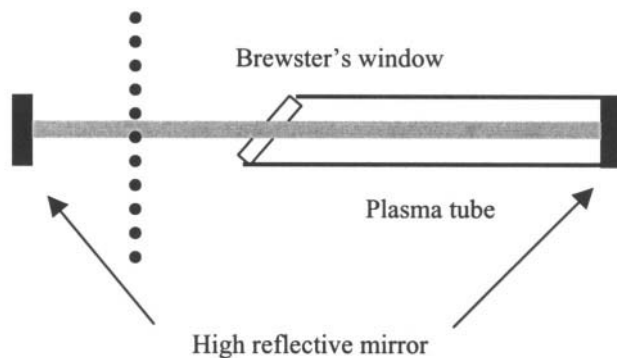


Figure 4.1. Schematic of OPC utilizing laser cavity.

#### 4.2.2. OPTICS OF THE VOLUMETRIC INSTRUMENT

##### *Light Scattering OPC*

Depending on the particle size range of interest, the optics will be designed to collect light scattered at either very large or very small scattering angles. All designs collect the scattered light over an integrated solid angular range, which is different than the scheme used in laser diffraction instruments in which the scattering pattern is collected at discrete angles. Figure 4.2 and Figure 4.3 show two such designs. In the right-angle light scattering optical systems, Mangin mirrors (a concave spherical mirror) are often used to collect scattered light over a solid angular range of either  $90^\circ \pm 45^\circ$  or  $60^\circ \pm 45^\circ$ . The design can be used to count and size particles as small as 50 nm. On the other hand, collecting scattered intensity at small angles with the lower end of the solid angular range varying from about  $4^\circ$  to  $15^\circ$  enables an instrument to measure larger particles ( $0.5\text{--}20\text{ }\mu\text{m}$ ). In co-axial optics, the scattered light is collected by a lens (as shown in Figure 4.3) or by parabolic mirrors in various arrangements (Figure 4.4 shows one such setup). In the former case the collecting system is like a dark field microscope in which the unscattered light is directed into a beam trap and the scattered light is collected by a lens and focused onto a detector. There are four angles which describe the light interaction in the sensing zone: the half angle of the illumination cone  $\gamma$  (typically ranging from  $5\text{--}15^\circ$ ), the beam trap half angle  $\alpha$ , the collecting aperture half angle  $\beta$  (typically ranging from  $10\text{--}45^\circ$ ), and  $\Psi$ , the inclination angle between the illuminating and collecting cone axes. The scattering collection angular range is determined by these four angles. For example, for the right-angle optical system in Figure 4.2 the angular scattering collection ranges from  $\gamma + \beta + \Psi$  to  $\Psi - \beta - \gamma$ ; and for the co-axis optical system (Figure 4.3) the angular scattering range is from  $\gamma + \beta$  to  $\alpha - \gamma$ .

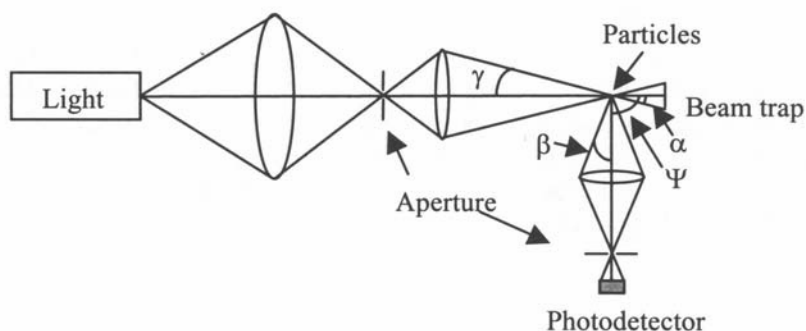


Figure 4.2. Light scattering OPC at high scattering angle (off-axis) collection.

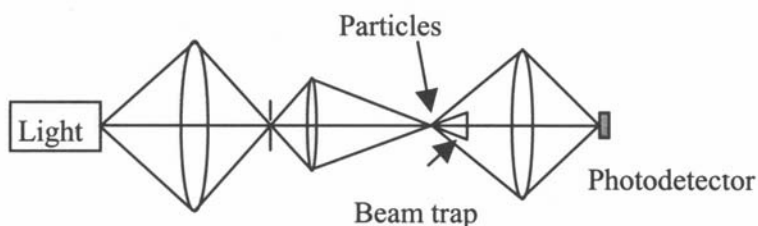


Figure 4.3. Light scattering OPC at low scattering angle (co-axis) collection.

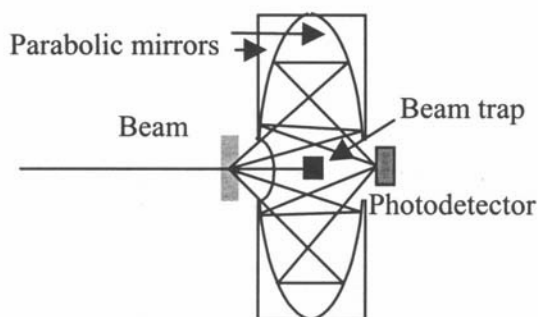


Figure 4.4. Light scattering OPC using parabolic mirrors.

### Light Extinction OPC

The light extinction method (also called the light blockage or obscuration method) is mainly used for counting and sizing particles larger than a few microns, mostly in liquid suspensions, although occasionally dry powders are also counted and sized. As shown in Figure 4.5, light from some type of light source is conditioned to create a totally parallel and uniform beam that illuminates a small volume of the fluid carrying the particles. The sensing zone

is defined by the flow boundaries and the beam dimensions. The light transmission, as detected by the photodetector facing the beam, is constant if there are no particles present. Each time a particle traverses the beam, some part of the incident beam is lost, or blocked either due to the light scattered out of or absorbed by the particle. The light flux detected by the photodetector is then reduced and a negative signal pulse is produced. The amplitude of the pulse is directly related to the particle size.

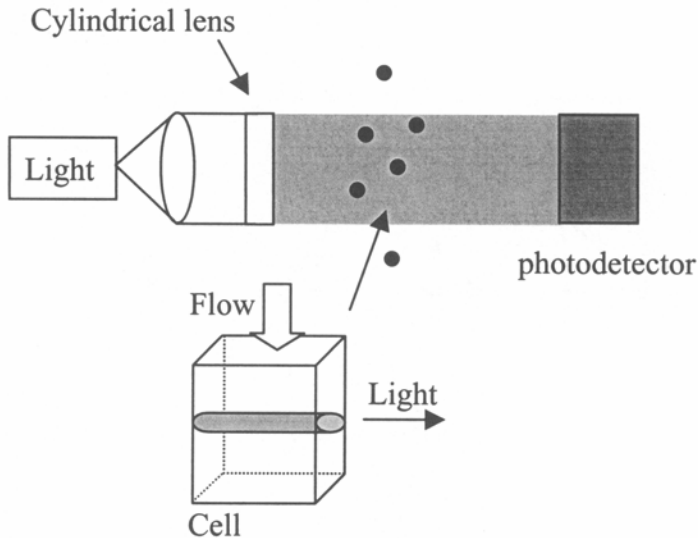


Figure 4.5. Light extinction optics.

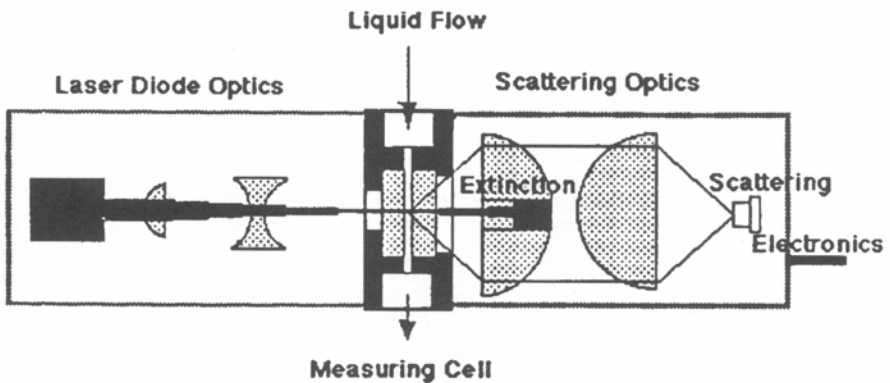


Figure 4.6. Optics of an optical particle counter combining both scattering and extinction measurement [10] (by permission of the author).

### Combined Optics

Since the light scattering method has the advantage of being able to detect small particles and the light extinction method is more suitable in detecting large particles, a combination of these two techniques can increase the dynamic range of a single instrument. Small particles can be counted and sized using a scattering detector and large particles can be measured using an extinction detector. One such design is shown in Figure 4.6. The instrument automatically combines the signals from both detectors to extend the size range from submicron to submillimeter. Figure 4.7 shows calibration curves from a commercial counter that employs a scattering detector to cover the size range from 0.5-1.63  $\mu\text{m}$ , and an extinction detector to cover the size range from 1.53-350  $\mu\text{m}$ .

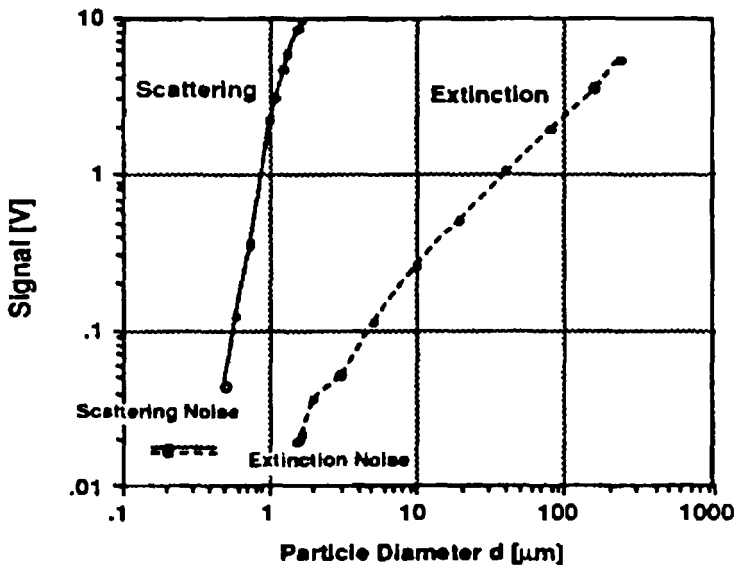


Figure 4.7. Calibration curves of a combined scattering-extinction optical particle counter [10] (by permission of the author).

### 4.2.3. OPTICS OF THE IN-SITU SPECTROMETER

In an in-situ optical particle counter, the laser beam passes through a large volume of liquid. The collecting optics are typically oriented at  $90^\circ$  to avoid viewing directly the illuminated interfaces at the entrance and exit windows, thus avoiding much of the stray light from the interfaces. The sensitivity can therefore approach the limit imposed by the noise created by scattering from the medium. Since particles are not constrained mechanically to intersect the beam in any special manner, the beam diameter can be made very small to maximize

sensitivity. To achieve sizing accuracy and resolution, the optics have to be designed so that only particles that pass through locations where the beam intensity is uniform are counted and sized. Signals from particles passing through the edges or only partially entering the beam are discarded [11]. Although the liquid is not mechanically forced to enter the uniformly illuminated region, the final result of such a design is comparable to the volumetric OPC, since only particles in the uniformly illuminated region are counted. A scheme using a simultaneous two-detector measurement to “pick” particles in the region of uniform intensity is depicted in Figure 4.8.

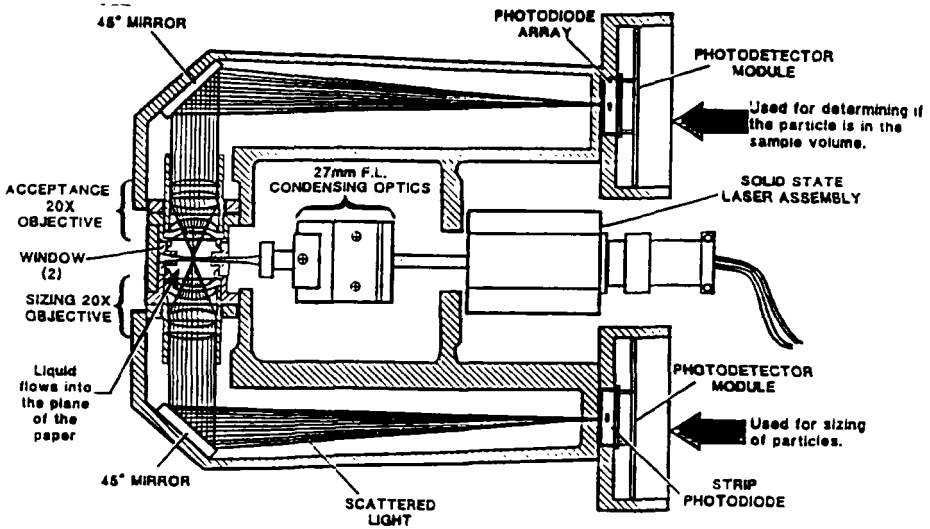


Figure 4.8. Optical system for in-situ OPC [6] (©Institute of Environmental Sciences and Technology, (847)-255-1561).

In Figure 4.8, the laser beam is focused on the sensing zone using stigmatic condensing optics, which generate a beam with an elliptical cross section. The waist of each ellipsis' axis is co-located at the center of the sensing zone. Wide angle collecting optics are used to produce high sensitivity and to obtain a monotonic calibration curve (see Section 4.3). The objectives in both arms sense the same particle and the signal is fed into two different detectors. The “sizing” module contains a strip photodiode and the “acceptance” module has a linear photodiode array. Both detectors “see” the same sensing zone, which is defined by the beam profile and the object plane of the imaging system. If a particle is outside of the region, the energy received by the apertured array detector is substantially reduced because of a shift in image position and an increase in image size related to depth-of-field position. Pulse comparison circuitry is used to simultaneously compare the amplitudes generated by the two



detectors. When the total signal amplitude summed over all elements in the array detector is equal to or larger than that of the strip detector, the particle is judged to be in the preferred region of uniform intensity and the pulse is then accepted. When the amplitude produced by the array detector is less than that observed from the strip detector, the pulse is rejected. Individual signals from the elements on the array detector are compared (via parallel processing) to a common threshold so as to determine particle validity. This type of dual detecting scheme can easily reject random noise and achieve high resolution in in-situ measurements [12]. At a flow rate of 100 ml/min (300 ml/min), in which the sampled volume flow rate is 0.1 ml/min (1 ml/min), the in-situ instrument can detect particles in the size range of 50-200 nm (100-1000 nm) with a sizing error of less than 10 nm [6].

#### 4.2.4. SAMPLE HANDLING

##### *Sample Acquisition*

Besides the discussion in Chapter 1, in order to ensure particles measured are statistically representative of the material, the following is especially important in environmental sampling. When sampling from a static fluid, it is necessary to make sure that particles in the fluid are homogeneously well dispersed which can be achieved by carefully agitating or mixing without introducing air bubbles. For liquid samples the use of sample vessels with a round bottom is suggested. For still air sampling, a moving vertical thin-walled sample probe with an upward-facing inlet may be used to sample particles with small relative settling velocity (the ratio of particle settling velocity in still air to sample probe inlet velocity) and small ratio of the stopping distance of a particle to the diameter of the sample probe inlet [13]. When sampling from a flowing fluid stream, isokinetic sampling (when the stream velocity is the same as the sampled fluid velocity entering the sample probe inlet) is often the key of correct sampling. In isokinetic sampling, the probe inlet should face into the fluid stream flow and should be parallel to that flow. Otherwise, sudden velocity changes in the fluid or centrifugal forces produced by excessive curvature of the sample flowpath will redistribute particles in the stream and change particle trajectories causing sampling errors as large as 5%, especially for large particles. The sampling tubing should be short, with no sudden dimension change, sharp bends, and with minimum electrostatic charge, and inert to materials passing through. For gas samples, the gas volume from which the sampled particles are acquired becomes difficult to evaluate if a velocity change exists.

After sampling from an environment, the sample has to be transferred through a transit line into the instrument. Depending on the nature of the fluid (liquid or gas) and the size and density of the material, particles may be lost if

handled incorrectly. Keeping the sampling lines vertical, minimizing residence time in the line, and avoiding abrupt changes in the line dimension and configuration are important to minimize particle loss during sample transport.

For dry powders, particles must be suspended in a gaseous medium which forms a relatively quiescent cloud in the case of small particles or a powder stream of constant velocity by means of a vibratory inclined trough feeder for large particles. Dry powders can also be suspended in a liquid medium forming liquid suspension. When using an optical particle counter to measure dry powders concentration information is usually not needed and generally cannot be developed.

All fluids should be kept within specified temperature and pressure range. Otherwise, problems associated with liquid condensation (too low temperature), bubble formation (too low pressure) and unsafe operation (too high gas pressure) will have to be overcome.

#### *Sample Delivering in Volumetric Measurement*

In optical particle counting, it often is the absolute concentration or count per unit volume fluid that needs to be determined. Therefore, volumetric metering or fluid control is an important part of OPC. Particles are introduced into the sensing zone of the instrument either through a known volume of fluid that is moved across the sensing zone using vacuum aspiration or pressure (ranging from near ambient to about 500 kPa when the concentration is defined per unit fluid volume) or by a fluid flow over a given time period using vacuum aspiration or pressure (ranging from ambient to about 1 kPa). Figure 4.9 shows a liquid sample feeder that uses aspiration, in which two adjustable meniscus detectors are used to measure the liquid volume that has moved through the sensing volume [14]. Figure 4.10 shows a closed-loop liquid system that delivers sample using syringe pressure. In some instances, only one type can be used. For example, if the sample is to be removed from a large container and it is difficult to transfer the liquid, aspiration may be the only available sample acquisition method. On the other hand, liquids containing gas will change viscosity, boil, or vaporize under reduced pressure, as occurs during aspiration. In these situations, aspiration should be avoided, since it will produce gas or vapor bubbles, thus yielding erroneous counting and sizing results; the measurement has to be performed using pressure. For concentrated liquid suspensions an auto dilution device may be installed at some point upstream of the sensing zone so that the instrument can perform automatic and off-line measurements [15]. For liquid samples, a flow meter or a volumetric sample container downstream of the sensing volume and a timer (e.g., a stopwatch) may be used in volumetric measurements.



If the sample contains dense particles, it may have to be stirred to keep the particles suspended. Otherwise, particles will stratify in the container. The stirring speed should be below that where a vortex can form since air drawn into a vortex will form bubbles that will be erroneously counted.

The major difference between the sample delivery system for liquid-borne particles and the sample delivery system for air-borne particles is that the former requires enclosure of the liquid stream; and thus windows for the liquid stream at the point of measurement are needed. There are two ways to further define the sensing zone. One way is to use the container volume that intersects the beam as the sensing zone to produce complete sampling of all particles passing through the beam. Figure 4.11 and Figure 4.12 show a rectangular liquid sample cell and a capillary liquid sample cell. However, in such designs the interface between the cell wall and liquid is illuminated. Stray light will be produced from reflection and refraction, as well as from any surface contamination at the flow tube inner surface due to refractive index differences at the interface. The noise generated from stray light limits sizing to particles larger than 0.1  $\mu\text{m}$ . When measuring smaller particles, higher sensitivity can be achieved using hydro-focusing to direct the liquid stream into an optically defined sensing zone so that every particle can be sensed with minimal noise [16].

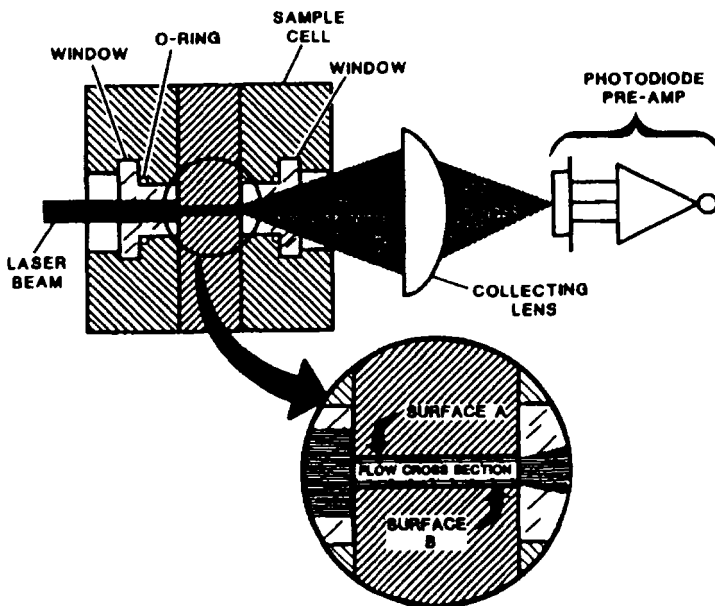


Figure 4.11. A square sample cell for liquid volumetric OPC [6] (©Institute of Environmental Sciences and Technology, (847)-255-1561).

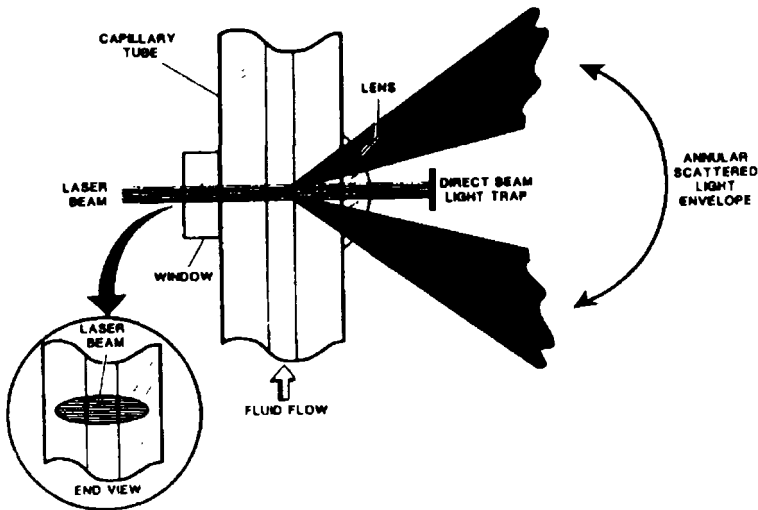


Figure 4.12. A capillary cell for liquid volumetric OPC [6] (©Institute of Environmental Sciences and Technology, (847)-255-1561).

One way to achieve liquid hydrodynamic focusing is shown in Figure 4.13. In this design, the dispersion flow passes through the capillary (a) with a tapered tip of 0.2 mm diameter. The particle stream undergoes an initial focusing (creating a factor of 11.4 in reduction of the stream diameter) when it enters a faster flowing inner water stream. When both streams are forced to converge in the upper conical nozzle (e), a further reduction (by a factor of 6.6) of the dispersion stream results in a very narrow stream ( $\sim 3 \mu\text{m}$  in diameter), in which the particles are entirely concentrated in the center. The stream expands between the exit of the upper nozzle and the entrance to the lower nozzle. The stream width in the sensing zone is about  $6 \mu\text{m}$ , which is much smaller than the beam width, ensuring that the particles are illuminated in the uniform region of the beam. After passing through the sensing zone, the dispersion enters the lower nozzle, which stabilizes the particle stream spatially, and leaves the cell. The outer water flow serves to prevent contamination of the cell windows, which are far enough away from the sensing zone so interference from the glass in the detected signal can be avoided [17].

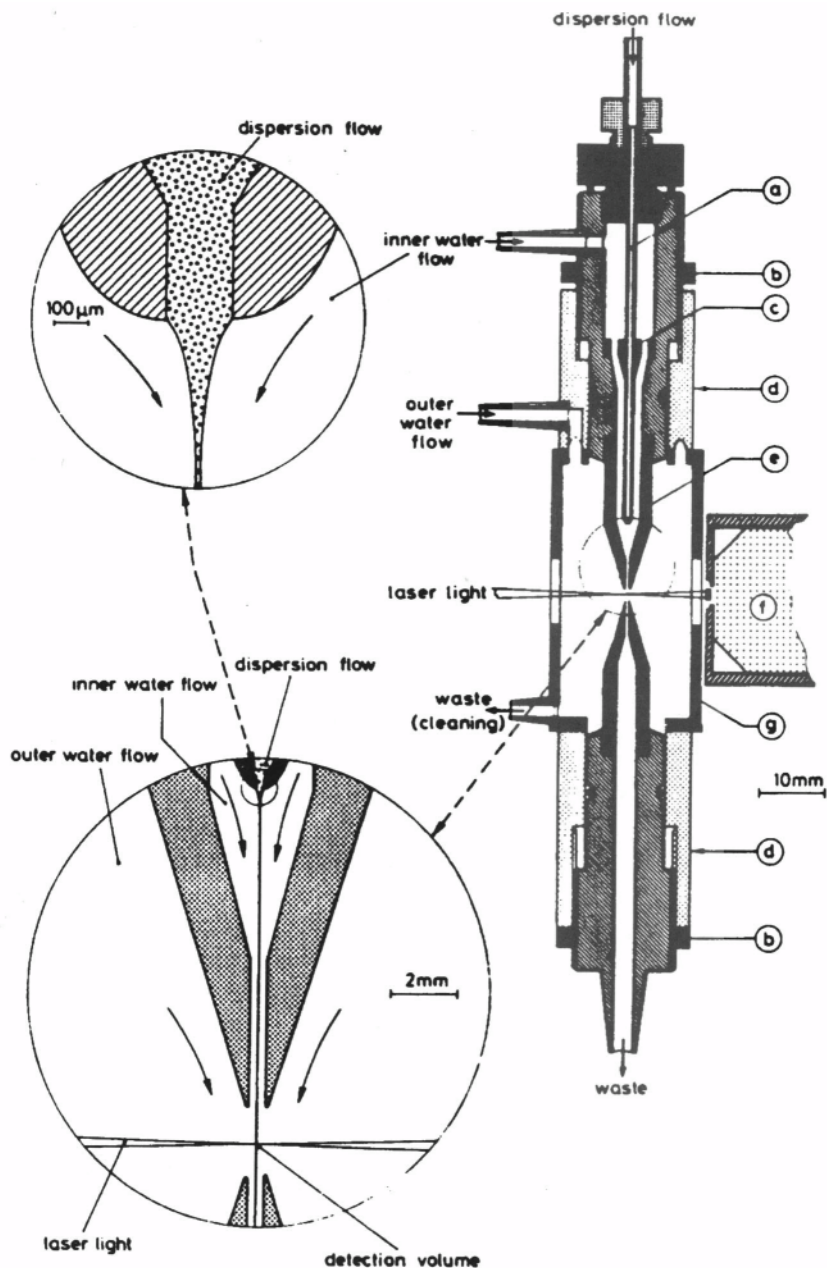


Figure 4.13. A hydrodynamic focusing flow cell. (a) capillary, (b) nut-locks, (c) capillary support, (d) cell support, (e) upper nozzle, (f) microscope objective, and (g) cell wall. Two inserts show details of hydrodynamic focusing [17] (by permission of Academic Press).

For gas samples at low flow rates, the flow is usually established by an internal pump aspirated at more than 10 times the sample flow rate. The excess flow is filtered and recirculated to provide a clean gas sheath flow around the sample in order to maintain a uniform stream. Particles in the central core of the clean-gas sheath flow pass directly through the illuminated sensing zone. This reduces counting errors arising from particles passing through the edges of the sensing zone. The sheath flow also prevents any recirculation of the particles into the sensing zone and improves the signal-to-noise ratio by focusing the particle stream into the area of the sensing zone which has a uniform intensity. Figure 4.14 is an example of a gas flow control system using sheath airflow [8].

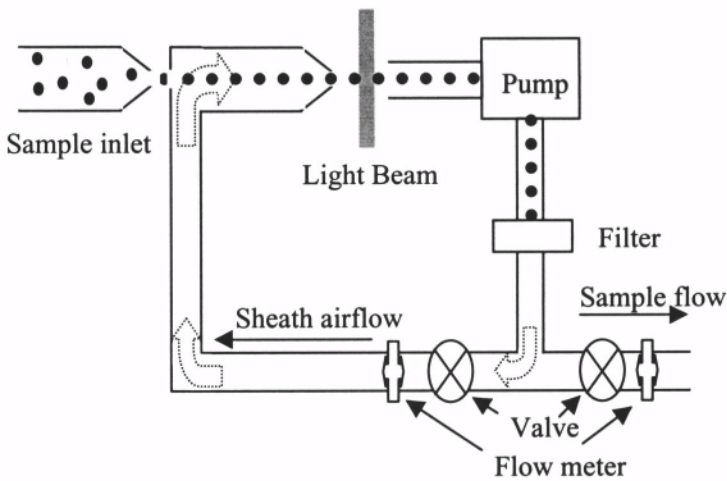


Figure 4.14. Flow control for sheathed airflow system.

For gas samples with high flow rates, an external pumping system may have to be used. The sample stream is emitted from a nozzle passed through the sensing zone and removed through an exhaust nozzle connected to the pump. Another line that delivers a purge flow is often used to eliminate deposited particles on the nozzles. Figure 4.15 shows such a system.

Since a change in flow rate will change the pulse duration and amplitude, the sampling flow rate must be kept the same as that at which the instrument was calibrated. This can be achieved by facing one end of the sample inlet into the airflow path and using isokinetic sampling to control the velocity at the inlet. If the counter is not located directly in the sampled air flow, a probe may be located at the end of a sample transport tube with residence time in the tube kept as short as possible to avoid particle loss. In most gas flow control systems the volumetric gas flow rate is defined at ambient pressure and

temperature. If the flow is measured and controlled by a mass flow meter, some correction to the reported sample volume to ambient condition is required.

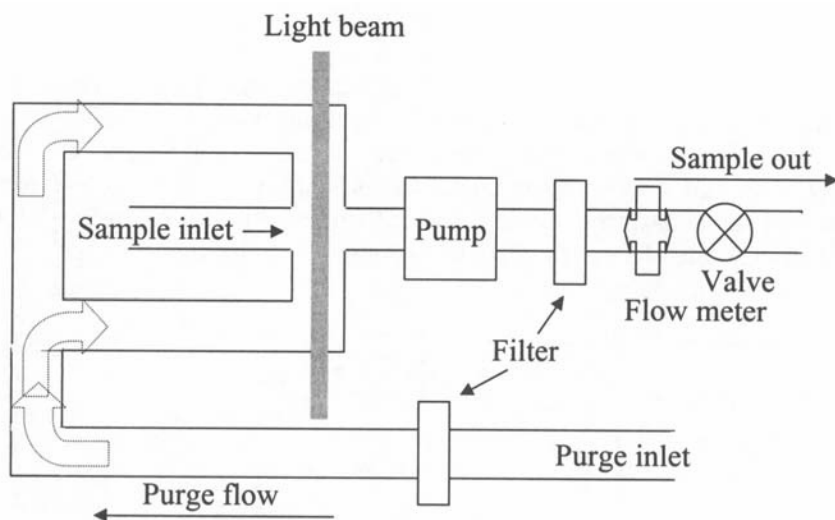


Figure 4.15. Flow control for unsheathed airflow system.

#### 4.2.5. ELECTRONIC SYSTEMS

The main functions of any electronic system are to convert light intensity pulses to electronic pulses, count the individual pulses, and sort them according to their amplitude into predefined channels. Each channel stores the counts from pulses that have amplitudes between the upper and lower boundaries of the channel, which corresponds to a “size” as determined by the instrument’s specifications and its calibration. A multichannel analyzer (MCA) is often used to accomplish this task; usually combined with a pulse stretcher, a comparator, or other pulse processing means. Recently, high density charge-coupled devices (CCD) have also been used for submicron particle detection, in which charge storage is utilized to buffer each data frame transferred from the CCD. Multiple serial outputs are processed by a parallel processor that incorporates threshold detection and analog-to-digital conversion circuitry [18]. The electronics should have minimum noise and adequate bandwidth to be able to count the smallest particles specified at a defined flow rate. As a rule of thumb, the root mean square background noise amplitude from the electronics should not reach the level of the signal from the smallest particles to be measured. The amount of electronic noise can be measured by how many pulses are detected when using a particle-free fluid, which has been filtered using a filter with a pore size not more than half the size of the smallest measurable particle, for a period up to



two hours for two or three repeat measurements. The pulse counting system should be capable of counting at a rate about ten times greater than the rate anticipated for particles at the maximum average concentration, since the particles may not be homogeneously suspended in the diluent. At some point there may be a burst of particles with a much higher concentration presented to the sensing zone. The amplitude of the largest noise pulse generated at a rate of 10% of the anticipated counting rate should be less than half of the amplitude of the average size pulse from the smallest particles to be measured.

### 4.3. Data Analysis

#### 4.3.1. OPTICAL RESPONSE

For linearly polarized light irradiating from one direction, the optical response (pulse amplitude) for scattered light collected over a solid angular range for a particle obeying the Mie scattering theory can be generally stated by:

$$R(m, d) = c \int_{\lambda_{\min}}^{\lambda_{\max}} \frac{\lambda^2}{4\pi^2} I_o(\lambda) \iint_{\Omega} (|S_1|^2 G_1(\theta, \varphi) + |S_2|^2 G_2(\theta, \varphi)) d\theta d\varphi d\lambda. \quad (4.1)$$

In Eq. 4.1,  $c$  is an instrument-related proportionality constant;  $I_o(\lambda)$  is the illumination intensity function of the incident light;  $G_1(\theta, \varphi)$  and  $G_2(\theta, \varphi)$  are geometrical terms specific to the optical design. The integration is done over the entire solid angular collecting range. Light scattered over a small solid angle often shows a polytonic response as a function of particle size for a given relative refractive index. Any minor change in the relative refractive index will change the scattering pattern significantly. Figure 4.16 and Figure 4.17 show several scattering intensity vs. size patterns in two different angular ranges. As shown in these two figures, for particles smaller than about  $0.7 \mu\text{m}$  the monotonic dependence of the scattering intensity as a function of size makes precise determination of particle size through intensity measurement possible. However, for monochromatic light the polytonic response of the scattering intensity versus particle size for particles larger than a few microns may inhibit these particles from being accurately sized [19]. For example, in Figure 4.18 the minimum channel width (resolution) will be  $w_1$  and  $w_2$  in the chosen polytonic regions.

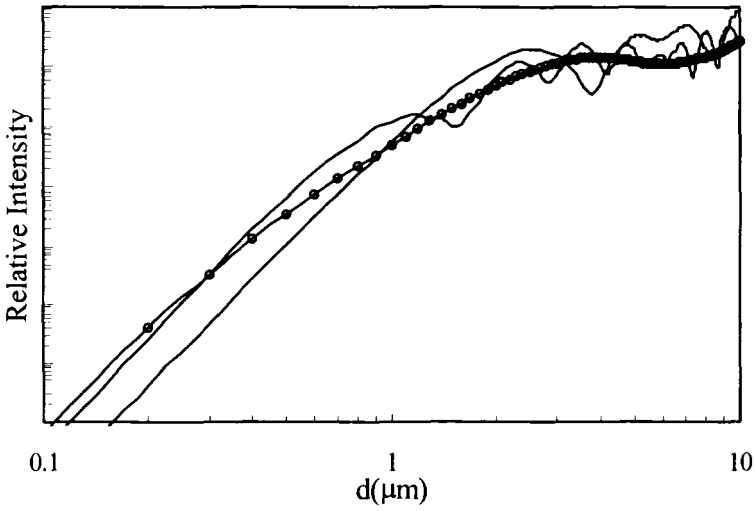


Figure 4.16. Relative particle scattering intensity over the solid angular range  $5^\circ$ - $10^\circ$  at  $\lambda = 650$  nm and  $n_0 = 1.0$ . Bottom solid curve:  $m = 1.2-0i$ ; top solid curve:  $m = 1.5-0i$ ; and solid curve with beads:  $m = 1.5-0.5i$ .

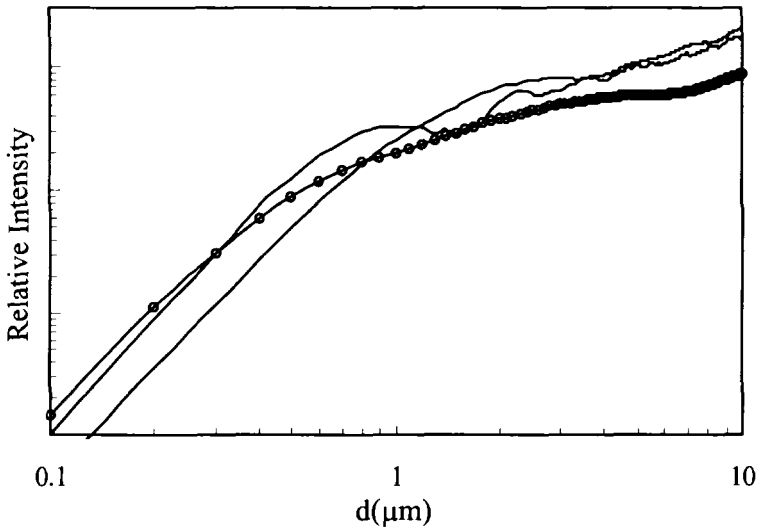


Figure 4.17. Relative particle scattering intensity over a solid angular range of  $5^\circ$  to  $38^\circ$  at  $\lambda = 650$  nm and  $n_0 = 1.0$ . Bottom solid curve:  $m = 1.2-0i$ ; top solid curve:  $m = 1.5-0i$ ; and solid curve with beads:  $m = 1.5-0.5i$ .

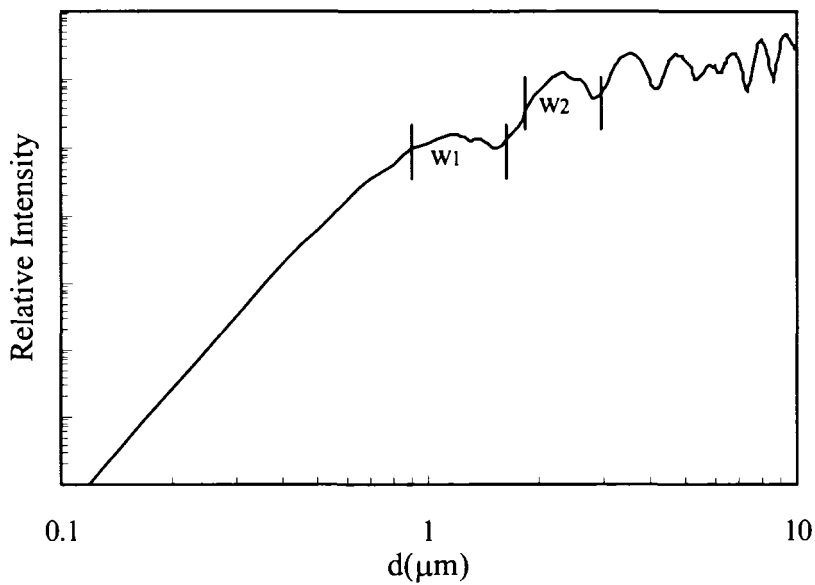


Figure 4.18. Size resolution limited by the polytonic nature of the intensity pattern.

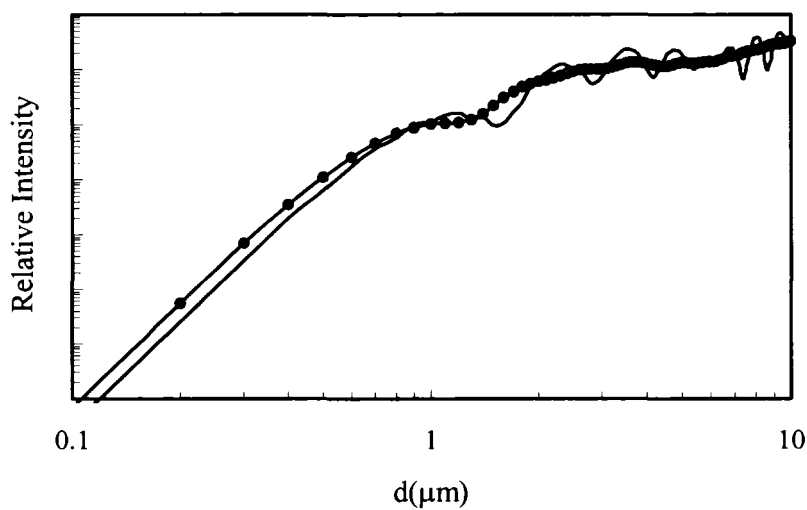


Figure 4.19. Relative particle scattering intensity over the solid angular range  $5^\circ$ - $10^\circ$  for a particle of  $m = 1.5 - 0i$  and  $n_0 = 1.0$ . The oscillating curve:  $\lambda = 650$  nm; the smooth curve with beads:  $\lambda = 450$ - $750$  nm.

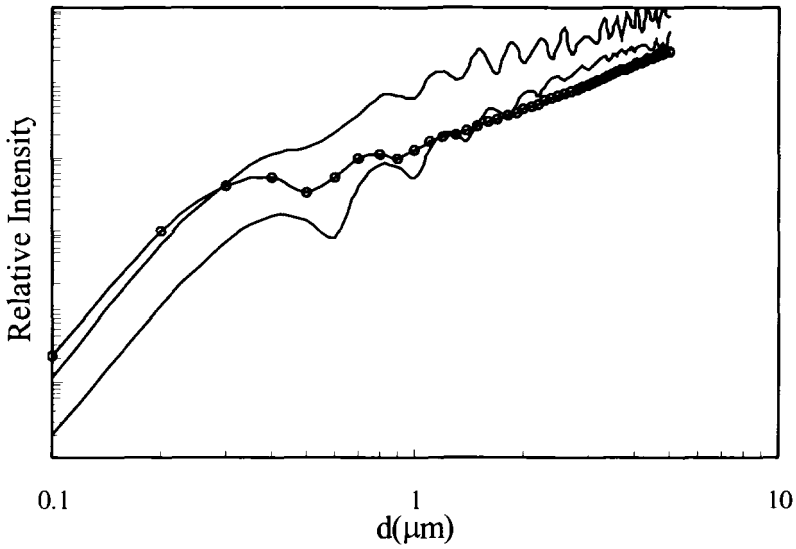


Figure 4.20. Relative particle scattering intensity over the scattering angular range  $85^\circ$ - $95^\circ$  at  $\lambda = 650$  nm and  $n_0 = 1.0$ . Bottom solid curve:  $m = 1.2-0i$ ; top solid curve:  $m = 1.5-0i$ ; and solid curve with beads:  $m = 1.5-0.5i$ .

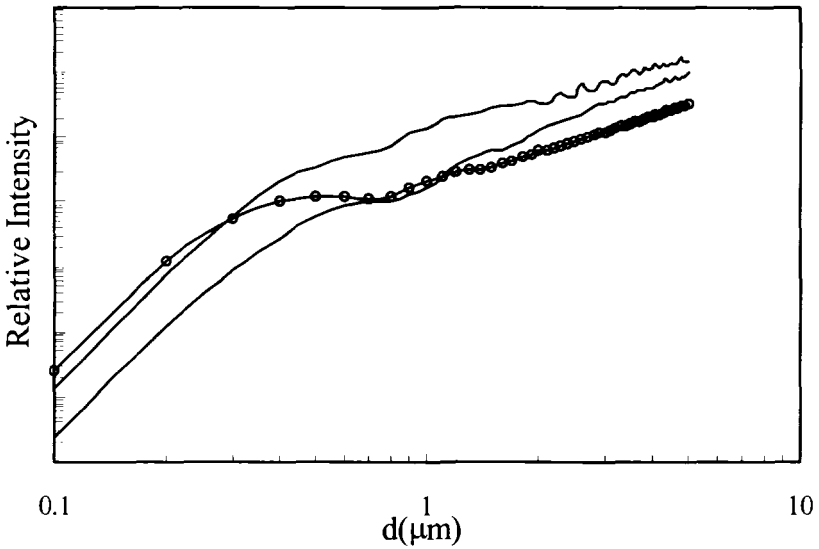


Figure 4.21. Relative particle scattering intensity over the scattering angular range  $45^\circ$ - $135^\circ$  at  $\lambda = 650$  nm and  $n_0 = 1.0$ . Bottom solid curve:  $m = 1.2-0i$ ; top solid curve:  $m = 1.5-0i$ ; and solid curve with beads:  $m = 1.5-0.5i$ .

Numerical simulations have shown that when using a model size distribution as an input to a simulated particle counter, the oscillations in the polytonic scattering curve may cause unrealistic maxima and minima in the output size distribution. This behavior has raised doubts about several published results using OPC and the accompanying discussions [20]. This polytonic behavior can be smoothed out in one or more of the following conditions: (1) highly absorptive particles (the curves with beads in Figure 4.16, Figure 4.17, Figure 4.20, and Figure 4.21); (2) wide collection angles (compare Figure 4.16 with Figure 4.17 and Figure 4.20 with Figure 4.21); or (3) a light source of continuous wavelength such as an incandescent lamp (Figure 4.19). Wide collection angles can also be accomplished using a combination of two solid angular ranges (e.g., 10-30° and 150-170° [21,22]) in which a weighted superposition of light flux from the two angular ranges results in monotonically increasing response characteristics versus particle size.

Although in the optical design, the illuminating intensity in the sensing zone is made as uniform as possible, there is always a distribution in intensity within the sensing zone. In situations where a focused or sheathed flow cannot be used, such as in in-situ measurements or in high vacuum measurements, not all particles passing through the sensing zone follow the same trajectory. A numerical inversion scheme to unfold the dependence of the scattering signals on particle trajectory through the measurement volume has to be used to correct sizing bias caused by the trajectory variation [23]. In this method, all particles are assumed to have an equal probability of passing through any element of the sensing zone, and to have the same mean velocity,  $u$ . A set of equations relating the experimental pulse height analyzer data  $C(A_i)$ , the cross-sectional area of the measurement volume normal to the flow direction  $\Delta S_{ij}$ , which yield a normalized signal peak amplitude  $A_i$  for particles of size  $d_j$ , and the number distribution function  $N(d)$  can be written in the matrix form:

$$\begin{pmatrix} C(A_1) \\ \vdots \\ C(A_i) \\ \vdots \\ C(A_m) \end{pmatrix} = u \begin{pmatrix} \Delta S_{11} & \dots & \Delta S_{1i} & \dots & \Delta S_{1m} \\ \vdots & \ddots & \vdots & \ddots & \vdots \\ \Delta S_{i1} & \dots & \Delta S_{ii} & \dots & \Delta S_{im} \\ \vdots & \ddots & \vdots & \ddots & \vdots \\ \Delta S_{m1} & \dots & \Delta S_{mi} & \dots & \Delta S_{mm} \end{pmatrix} \begin{pmatrix} N(d_1) \\ \vdots \\ N(d_i) \\ \vdots \\ N(d_m) \end{pmatrix}. \quad (4.2)$$

The matrix  $\Delta S$  can be obtained using a few monodisperse samples of known diameter and concentration. The samples pass through the measurement volume at a known mean velocity.  $N(d)$  can then be obtained using any matrix inversion scheme, such as Phillips-Twomey regularization [24], or a non-negative least-

squares technique [25], to solve Eq. 4.2. Another way to resolve  $\Delta S$  is to assume a characteristic curve for  $\Delta S$ , by which calibration can be accomplished using a polydisperse sample with a known particle size distribution. One such characteristic form is the log-normal distribution:

$$\Delta S(A, d) = \frac{1}{Abd\sqrt{2\pi}} \exp \left( - \frac{\left( \ln \frac{A}{A_{50}} \right)^2}{2b^2 d^2} \right). \quad (4.3)$$

In this formula, there are two variables,  $A_{50}$  and  $b$ . If the response from the mean value of the calibration sample is taken as  $A_{50}$ , there is only one parameter ( $b$ ) to be determined by calibration. After a sample with a known particle size distribution is measured using an optical particle counter and its signal amplitude distribution is recorded, a minimization is carried out by comparing the measured data to theoretical data calculated using different values for  $b$ . This procedure should be performed a few times to obtain a representative result. Figure 4.22 shows the OPC result of a 500 nm polymer particle sample with and without correction for inhomogeneous illumination [26].

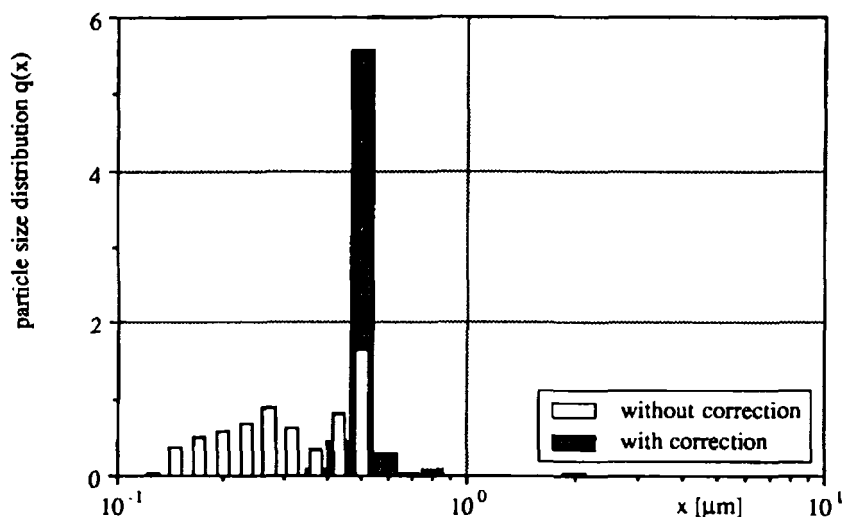


Figure 4.22. Particle size distribution from OPC measurement with and without correction (by permission of Wiley-VCH Verlag GmbH).

Another error similar to the one caused by inhomogeneous illumination is the border zone error. This error occurs when a particle passes through the sensing zone at the edges resulting in light pulse smaller than that which occurs when it passes through the center. The border zone error can be corrected using either a second photodetector that detects the scattering from a second zone overlapping the first one [27] or by a specially shaped (T-shaped) sensing zone [28].

The light extinction created by the presence of particles in the beam is due to the scattering and absorption from the particles. If the particles do not absorb light at the wavelength, then the extinction arises solely from scattering. For a single particle, the fraction of the incident light intensity lost due to the presence of the particle according to the Mie theory is termed the extinction coefficient  $\gamma$ , given by

$$\gamma = \frac{\lambda^2}{2} \sum_{k=1}^{\infty} (2k+1) \{ \text{Re}(a_k + b_k) \} = \frac{\pi d^2}{4} Q_{\text{ext}}. \quad (4.4)$$

In Eq. 4.4,  $a_k$  and  $b_k$  are the same functions as those in Eq. 2.8.  $Q_{\text{ext}}$  is termed the extinction efficiency, which is the particle intersection area normalized extinction.  $\gamma$  is independent of the state of polarization of the incident light. Figure 4.23 - Figure 4.25 show extinction efficiency as functions of particle size and relative refractive index.

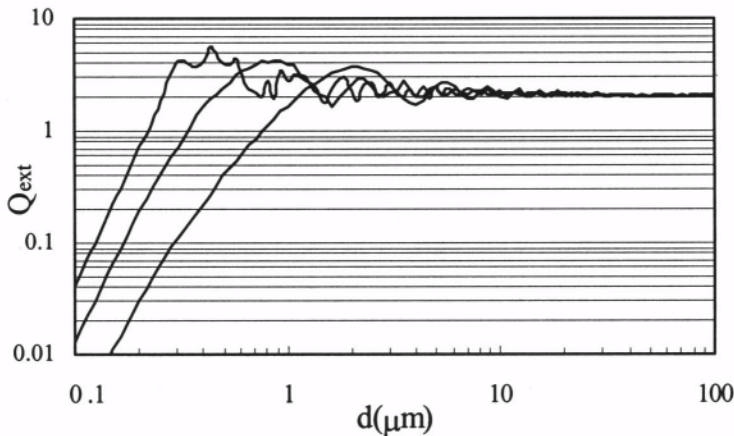


**Figure 4.23.** Extinction efficiencies for spheres with different relative refractive indices  $m$  in air at  $\lambda = 650$  nm. Top curve:  $m = 2.0-0i$ ; middle curve:  $m = 1.5-0i$ ; bottom curve:  $m = 1.2-0i$ .

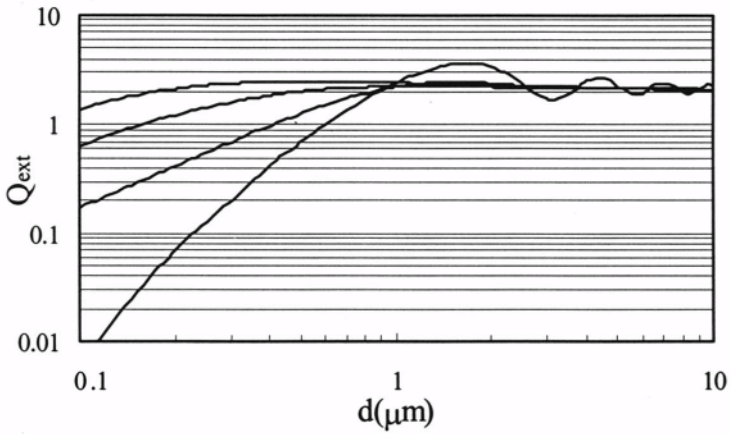


Figure 4.24. Extinction efficiencies for spheres with different relative refractive indices  $m$  in water ( $n_o = 1.33$ ) at  $\lambda_o = 650$  nm. Curves from the top down:  $m = 1.19 - 0.8i$ ;  $m = 1.19 - 0.38i$ ;  $m = 1.19 - 0.1i$ ;  $m = 1.19 - 0i$ .

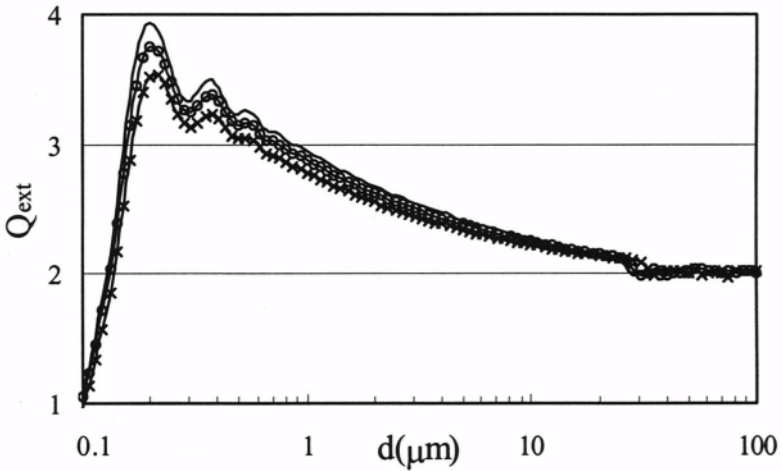


Figure 4.25. Extinction efficiencies of spheres with different relative refractive indices  $m$  in air for  $\lambda = 650$  nm. Solid curve:  $m = 1.2 - 3.0i$ ; solid curve with beads:  $m = 1.5 - 3.0i$ ; solid curve with crosses:  $m = 2.0 - 3.0i$ .

As shown in these figures, the extinction efficiency for large or highly absorptive particles approaches the value of 2. This is the Fraunhofer regime, where the total extinction is due to the redistribution of the incident light because of diffraction about the edge of the sphere, specular reflection at the



surface, and any refraction into the sphere. In absorptive materials the refracted light will be attenuated and lost inside the sphere. In the region where  $d > 10 \mu\text{m}$ , the extinction efficiency is almost independent of the relative refractive index. For highly absorptive materials, even at smaller sizes ( $d > 1 \mu\text{m}$ ), the variation in the extinction efficiencies for particles of different refractive indices versus particle size are similar (Figure 4.25). Therefore, the pulse amplitude varies directly as the second power of the particle size. For small or non-absorptive particles, the extinction efficiency oscillates as a function of particle size and varies widely with the refractive index of the particle. It is these oscillations that prevent the precise sizing of small particles using light extinction OPC unless the counter has been calibrated with particles of the same refractive index as that of the sample. Different results may also be expected when making measurements using devices of different designs.

#### 4.3.2. LOWER SIZING LIMIT

The ability to detect small particles by optical particle counters is determined by the difference between the light scattered by the particles compared with the stray light and scattering from the molecules in the media. Stray light is created by optical elements such as lenses, beam traps and other interfaces in the light path. In a well-designed optical system, the stray light should be negligible when compared to the scattering of the medium's molecules. The molecules of the medium, whether liquid molecules or gas molecules, all scattered light and contribute to the background scattering intensity. Their scattering intensity is the product of their number density, the mean illumination intensity, the scattering cross-section of any single molecule, and the sensing zone volume. In order to reduce the background scattering one can reduce the sensing zone dimensions by focusing the beam, or in the case of air reduce the number density of the medium molecules by reducing the air pressure, or if it is feasible to change the medium to one with molecules having a smaller scattering cross-section (switching from air to helium in aerosol measurement or from water to solvent in liquid suspension measurement, for example).

Reducing the sensing zone volume can be achieved through the use of lenses with short focal lengths. The lower practical limit of the sensing zone volume is about  $1 \mu\text{m}^3$ . In an ideal situation at standard temperature and pressure, a 1 W He-Ne laser will cause air molecules in a sensing zone volume of  $1 \mu\text{m}^3$  to scatter similarly to a 7 nm latex bead. Taking into account intensity collection efficiency and detection time, the realistic lower sizing limit, if the scattering pulse from a particle is to be reliably detected and classified, is around 30 nm using a 1 W laser for aerosol particles. This is the main reason that the resonant cavity laser can be effectively used to size aerosol particles as small as 50 nm because of the laser's high power (often in excess of 5000

W/cm<sup>2</sup> in some commercial instruments). The lower sizing limit shifts upward for larger sensing zones. For example, a sensing zone of  $10^7 \mu\text{m}^3$  will have a lower sizing limit of about 65 nm [8]. For measurement made in liquids, because of the much stronger scattering from liquid molecules than from air molecules due to their larger scattering cross-sections, inhomogeneity in medium's refractive index caused by any type of fluctuations, and smaller relative refractive index between the particles and the medium, the detection of small particles is more difficult and requires a higher power laser and smaller sensing zone. Lately, developments in high power laser diodes and advanced optical designs have made the task of detecting particles as small as 50 nm in liquid possible.

### 4.3.3. ACCURACY IN PARTICLE SIZING

#### *Calibration Particles*

In order to measure particle size distributions, the relationship between scattering intensity and particle size must be known. Therefore, any optical particle counter has to be calibrated [29]. There are two types of calibration particles used in OPC. One is monodisperse spheres of known refractive index and size, such as polystyrene latex (PSL) and dioctylphthalate (DOP). Each sample has a narrow and well-calibrated size distribution with a known small standard deviation produced by reputable sources. For liquid measurements, the latex suspension can be used directly if a proper concentration is chosen. For aerosol measurements, the latex suspension needs to be nebulized, dried, and then diluted with particle-free gas to the proper concentration. Monodisperse submicron aerosol particles of various materials having different sizes can be generated using a vibrating orifice aerosol generator which allows generation of aerosols of predetermined size with an accuracy of  $\sim 1\%$  and with a coefficient of variation of 1% [30]. Micron-sized aerosols of different materials can also be generated using an aerosol generator [31]. In an aerosol generator, a stream of monodisperse droplets is generated and passed through a charge neutralizer which is used to reduce the particle electrostatic charge. Monodisperse aerosols up to a few microns can also be generated using an electrostatic classifier, in which a solution of aerosol material is sprayed through a compressed air atomizer. The atomized droplets are then dried and passed through a charge neutralizer where charges are equilibrated with the bipolar ions generated by a radioactive source. The aerosols are then sent through a differential mobility analyzer (Section 1.2.6) and classified into monodisperse aerosols. An electrostatic classifier can generate aerosols with sizes accurate to  $\sim 2\%$  and with a 4% relative standard deviation [32].

During calibration, The calibrated sizes are recorded, along with the standard deviations, and this data is used to generate a calibration plot of pulse

amplitude as a function of particle size. Instrument calibrations using standards having a size within the polytonic response range should be avoided. The median value of the reported particle size distribution from OPC should not vary from the specified value of the calibrated particles by more than 5%. Excellent agreement between the size distribution determined by OPC and that from other methods can be obtained. In Figure 4.26 a comparison of size distributions of latex particles obtained using both a COULTER COUNTER<sup>®</sup> and an optical particle counter is shown.

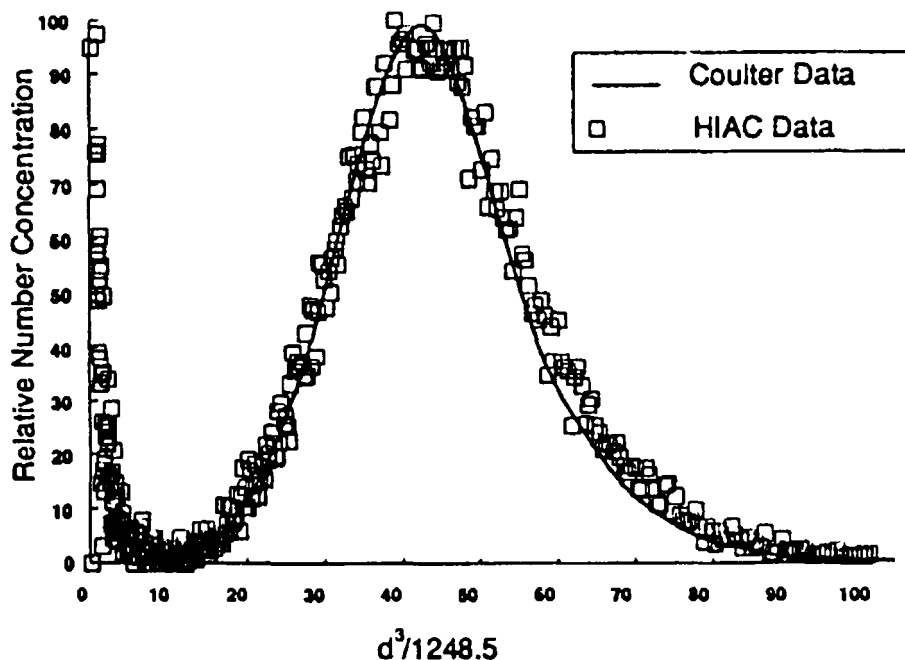


Figure 4.26. Comparison of latex size distributions using a modified HIAC optical particle counter and a Coulter Counter<sup>®</sup> [33] (reproduced by permission of The Royal Society of Chemistry).

The second type of calibration standard is a batch of polydisperse particles with a known size distribution and a carefully determined concentration. For these polydisperse standards, the cumulative concentration at any selected size should not differ from the specified value by more than 10%, except for a certain population of particles that has only a few particles. This type of calibration can be carried out by incorporating data from another particle characterization technology. For example, by comparing the pulse-height distribution from an optical particle counter with the size distribution obtained using an aerodynamic

particle sizer, a calibration curve can be obtained for both spherical and non-spherical particles [34].

### *Sample Particles*

The calibration curve obtained using the calibrating particles is only correct for the optical properties of the calibration particles. Calibration particles of the same size but having different optical properties will generate different calibration curves. For many samples, such as natural aerosols, particles may have different refractive indices and the refractive index may change, for example, depending on the quantity of water the sample contains. Rarely will a real sample have the same optical properties as those of the calibration particles. For particles suspended in liquid, the relative refractive index may change if the refractive index of the liquid changes. As an example, in the semiconductor manufacturing process, liquids can have refractive indices that vary from 1.29 (for hydrofluoric acid) to 1.5 (for xylene) depending on the location and time of particle sampling. The same particle may produce different responses because of a change in liquid refractive index. One study showed that the same latex particle will appear 37% smaller when the medium is changed from trichloroethane to water [35]. Therefore, the particle size distribution obtained using a calibration curve from calibration particles with certain optical properties yields only an *optically equivalent* diameter distribution relative to the calibration particles, even when both the calibration particles and the sample particles are spheres! Such a size may then be called an “equivalent latex sphere diameter” or an “equivalent glass bead diameter,” depending on the type of calibration particle used. This optically equivalent size may be very different from the particle’s true geometric dimension. To overcome this bias, calibration particles that have the same or similar optical properties to that of the sample particles should be used. The closer the optical properties of the sample and the calibrator, the closer the reported size will be to the true particle dimension. Mainly because of the polytonic behavior of the scattering pattern, different OPC designs will generate different “equivalent” size distributions from the same calibration material, depending on the angular collecting range and the wavelength of light used in the counter. Therefore, if the calibration material has different optical properties from that of the sample material, significant variation in results can be expected from different instruments.

Even this “equivalent” size distribution may be biased due to sampling efficiency as a function of particle size. Let us assume a calibration curve obtained using five monodisperse latex samples. In the measurement of a real sample of polydisperse latex particles, even though each pulse will correspond to the right size, the number of pulses in each size segment will be distorted due to non-constant sampling efficiency; therefore the particle size distribution will

also be distorted. For instance, a commercial counter's sampling efficiency can vary from 0.9 for 5  $\mu\text{m}$  particles to 0.45 for 30  $\mu\text{m}$  particles [36].

There are a few ways to reconcile the discrepancies between the real diameter (for spheres) and the "equivalent" diameter in cases in which there is a good agreement between the theoretical prediction and experimental calibration when using spherical particles [37]. One method is to match the results from the calibration particles to the real sample after establishing the calibration curve for a given refractive index experimentally. Theoretical response curves for this refractive index and that of the sample may be drawn according to the experimental scaling factor of the instrument in the monotonic range. The theoretical curve for the sample's refractive index may then be used as the calibration curve. Another way to correct for the effects caused by the difference between the refractive index of the calibration particles and the sample particles is to use a scaling factor which is the ratio of the sample's particle size to that of some calibration particle that generates the same output voltage from the counter in order to determine how to shift the reported particle size distribution [38].

For non-spherical particles, a study using six different types of counters has shown that when particle size is smaller than the light wavelength, the reported diameter of a non-spherical particle closely approaches to its volume-equivalent diameter. For irregularly shaped particles that are larger than the light wavelength, anything better than conditions which will yield a "projected area" response cannot be achieved [39].

#### 4.3.4. PARTICLE SIZE RESOLUTION

In particle size analysis the term "resolution" as used is defined how well an instrument is able to differentiate populations of particles of similar size. One acceptable criterion states that an optical particle counter should be able to detect the difference between particles that vary in median size by 5% or more. This capability depends on the uniformity of the light intensity in the sensing zone, the uniformity of sensitivity of the photodetector, and on the electronic and optical noise. The resolution is commonly judged by the increase in the standard deviation or coefficient of variation of the size distribution reported for a monodisperse standard which has a mean size larger than twice that of the instrument's lower sizing limit, when compared with a previously determined standard deviation. The accepted standard is that an increase in the reported standard deviation for monodisperse particles does not exceed 10% of the previously determined value. Size resolution can also be increased by increasing the dimensions of sensing zone in the direction parallel to the flowpath so that the particle's resident time in the sensing zone becomes longer and the pulse width increases resulting in more accurate sizing. However, precautions have to

be taken to ensure that the same signal will be created by the same particle located in different portions of the sensing zone. Size resolution is closely associated with counting and sizing accuracy. For example, if size resolution is  $0.1\text{ }\mu\text{m}$ , then particles of size  $0.3\text{ }\mu\text{m}$  and  $0.35\text{ }\mu\text{m}$  would be sized and counted as the same. Therefore, both correct counting and sizing are compromised.

A typical instrument may have between 15 and 64 size channels depending on the dynamic range of the instrument. For instruments that use a MCA of 1024 channels, the apparent resolution is usually much higher than the intrinsic instrumental resolution, although such excessive resolution, (often termed “empty” resolution by microscopists) may afford some computational statistics [6]. For instruments used to measure extremely dilute samples, such as in clean room air or in clean water analyses, because the passage of a particle constitutes a “rare event,” a large volume of sample and thus a high flow rate is needed to provide adequate statistical confidence. A large sensing zone increases non-uniformity of beam and thus reduces size resolution. Such instruments typically have fewer channels (4-8) and much lower resolution.

In a light extinction measurement of non-spherical particles the reported size is influenced by particle shape since the projected area of the particle measured depends on its orientation in the sensing zone. Repeat measurements of the same particle will yield a range of different projected areas according to the orientation of the particle. The result of this is a broadened particle size distribution, even for monodisperse particles. This limitation can be overcome if a transformation matrix that describes the signal height spectrum for a particular material of known size can be obtained by calibration. Through deconvolution of the orientation effects in the measured data (similar to that given in Eq. 4.2) it is possible to determine the loss in resolution caused by the influences of shape and structure, and to eliminate these effects from the experimentally determined size distribution [40]. Simultaneous measurement of the projected area of the particle from different directions (e.g., from three mutually orthogonal directions using three pairs of light sources and photodetectors) can serve to smooth out any shape effects when the sizes reported by the three sub-optical systems are averaged. Figure 4.27 shows the results from an OPC measurement of two narrow and closely spaced limestone particle fractions using a normal optical system and from an instrument having three simultaneous optical measuring systems. The result from the latter demonstrates an increase in resolution and a reduction in distribution broadening due to the smoothing of shape effect [41].

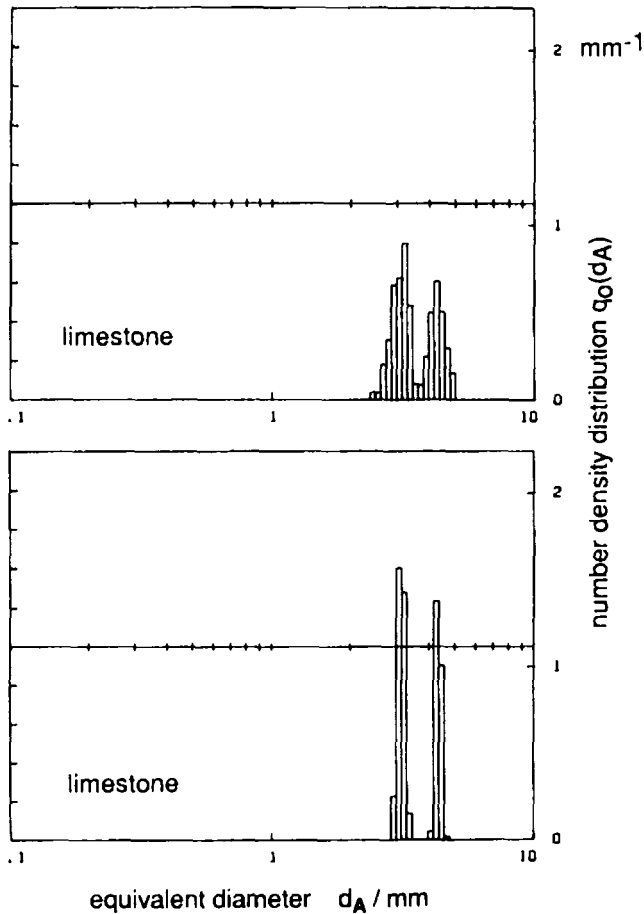


Figure 4.27. Results of OPC measurements of limestone particle fractions. Top: from one optical system; Bottom: from three simultaneous optical systems [42] (reproduced by permission of The Royal Society of Chemistry). (The unit of the diameter should be  $\mu\text{m}$  instead of mm).

#### 4.3.5. PARTICLE COUNTING EFFICIENCY AND ACCURACY

When an optical particle counter operates correctly, all particles having sizes falling between the upper and lower boundaries of a size channel will produce the number of counts in that channel. Ideally, the instrument should be able to count particles accurately over the entire operational size range. The reproducibility in concentration measurements between instruments should be better than 20%. The counting efficiency and accuracy can be affected by one or more of the following factors:

- a. The zero count rate is high. The zero count rate is the background count created by the optics and electronics and is measured using particle-free fluid during a specified time. To ensure the instrument can correctly measure the smallest particles as specified, the zero count should not exceed 5% of the anticipated count for the smallest particles in the sample.
- b. The optical system is misaligned making the calibration being distorted.
- c. The sample stream is partly lost in the inlet, or the stream bypasses the sensing zone so that many particles are not counted. The inlet tube should be short and without bends in order to reduce probable sample loss especially for particles larger than 5  $\mu\text{m}$  in an aerosol measurement.
- d. Flow eddies exist and recirculation of the sample through the sensing zone produces a higher count.
- e. In liquid measurements, air bubbles are not removed either through sonication or by vacuum and these bubbles are then counted as particles.
- f. Incorrect metering of fluid flowing through the sensing zone creates an erroneous concentration measurement. (Especially true for gas-borne particle systems, where particle concentration is reported in terms of particle per unit volume of gas at ambient pressure and temperature rather than at standard conditions. Therefore, a measurement performed at a sea level will be different from that made in a mountain area.) Correct calibration and a constant flow rate are the keys to retrieve the correct concentration. Otherwise, even if the particle count is correct the concentration may be wrong.
- g. Too low a particle concentration or particle number which will reduce the statistical validity of the reported counting and sizing results. If the statistical probability of obtaining a correct count obeys the Poisson distribution, then the relative standard deviation is inversely proportional to the square root of the total count. A count of 100 particles will then have a relative standard deviation of 10%, and a count of 10000 particles will have a relative standard deviation of 1%, and so on. The lower concentration limit should be determined to ensure that there are enough particles counted in the measurement period not longer than 15 minutes.
- h. Too high a particle concentration will greatly affect both counting and sizing accuracy through two effects. One is particle coincidence which arises from the presence of more than one particle in the sensing zone at any one time. The coincident particles are reported as a single particle with a size equivalent to the summed size of the individual particles simultaneously present in the sensing zone, resulting in under-reporting



of particle number and incorrect particle size. The reported particle concentration will be less than the true value and the reported distribution will be shifted to larger sizes. The second effect is electronic saturation, which is the inability of the electronics to detect and sort individual pulses that are too closely spaced in time. When the particle concentration increases, physical coincidence occurs first, followed by electronic saturation. When pulses start to overlap each other, they extend over a longer time period as the particles move through the sensing zone. The continuous electronic saturation inhibits the electronics to reset and detect separate pulses. Eventually, the instrument will report a zero count since the sensing zone is continuously occupied, and the scattering intensity never decreases to the point where a single "pulse" can be count. For small particles with dimensions much smaller than that of the sensing zone, if the product of the number concentration (the number of particles per unit volume) and the volume of the sensing zone is smaller than 0.1, the deviation of the measured distribution from the true distribution will be relatively small and can often be neglected when compared to other unavoidable errors. If this product is smaller than 0.3, a complete coincidence correction is possible using one of the various schemes for coincidence correction [43]. In one scheme [36] the ratio of the reported count ( $N_r$ ) and the true count ( $N_t$ ) per unit volume is related to the product of the true count and the sensing zone volume ( $V$ ) by

$$\frac{N_r}{N_t} = e^{-N_t V} \quad (4.5)$$

One way to check the influence of coincidence is to perform a second measurement at a more dilute concentration. If the particle concentration ratio of the two measurements differs from the known dilution ratio of the two samples, some effects of coincidence in the first measurement are probable and the result should be discarded and a new dilution prepared to test the second sample. Progressive measurements should be made until the reported concentration ratio between two consecutive samples agrees with the known dilution ratio. The highest concentration at which this occurs is then accepted as the uppermost concentration limit for the instrument used in measuring this material. No specific concentration limit can be specified since this will depend on the particle size distribution, instrument design, and the flow rate. The overall maximum concentration may range from a few particles to a few thousand particles per ml.

Another source of erroneous particle counts originates from a high concentration of small particles that fall outside the specified sizing range.

Although individually such small particles will not produce any detectable scattering intensity above the background noise, if random batches of such small particles collectively enter the sensing zone the particle count corresponding to the scattering intensity from all these small particles will be reported and can lead to an erroneous result.

Since the electronic counting circuitry cannot respond to the presence of a particle entering the sensing zone until the signal from a previous particle has decreased to the system reset level, the presence of large particles whose sizes are significant relative to the sensing zone volume results in an effective increase in the sensing zone volume [44], as shown in Figure 4.28. This increase in the effective beam dimension reaches the high concentration limit more quickly than expected from a calculation of the probability of coincident small particles.

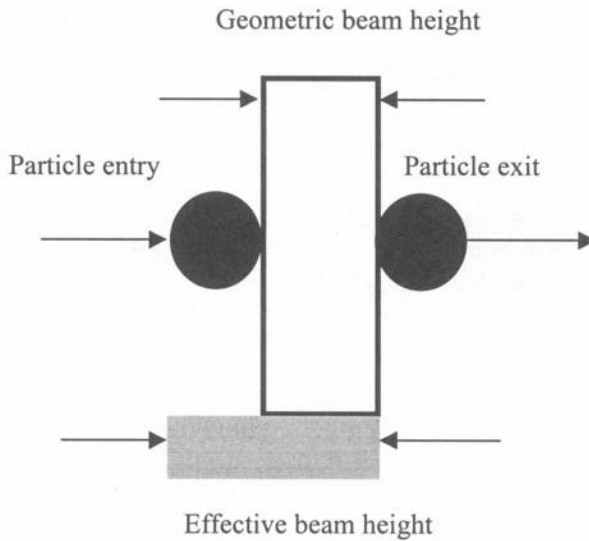


Figure 4.28. Large particle effect on the effective dimension of the sensing zone [44].

Although there are a few vendors who provide count standards of different sizes, there is no acceptable national or international count standard with a specified accuracy available at present. The best way to judge the counting efficiency of an optical particle counter of either gas-borne or liquid-borne particles is to compare the counting result of a monodisperse sample to a “standard” instrument that has been verified to have near 100% counting efficiency using several direct or indirect methods. The ratio of the count obtained from the same sample when analyzed on the testing unit and the “standard” unit is termed the counting efficiency of the unit. The acceptable

counting efficiency for OPC is  $50\% \pm 20\%$  at the minimum detection size (the threshold) and  $100\% \pm 10\%$  for particles  $\geq 1.5$  times the minimum size. Studies have shown that instrument counting efficiencies, especially for small particles, vary not only between instrument types, but also among instruments of the same type. While the cumulative number distribution may provide acceptable agreement, the differential distribution often shows much larger discrepancies between instruments. This is the reason why a 50% counting efficiency is usually chosen as the threshold, since 50% is the value that reflects the size value corresponding to the mode of a normal distribution (for most standard samples). If for example, a 90% counting efficiency is used, large variations in instrument calibration will be produced among instruments of different resolutions. As shown in Figure 4.29, a choice of 50% counting efficiency results in the same threshold setting for counters of different size resolution but a large shift in the threshold when choosing a 90% counting efficiency. Counting efficiency is also affected by flow velocity and sample inlet and pipe shape. Generally, counting efficiency decreases with decreasing particle size and increases with reduced flow velocity. Therefore, each instrument has to be quantified individually as to its counting efficiency. This quantification has to be performed periodically to ensure no changes have occurred [45,46,47,48].

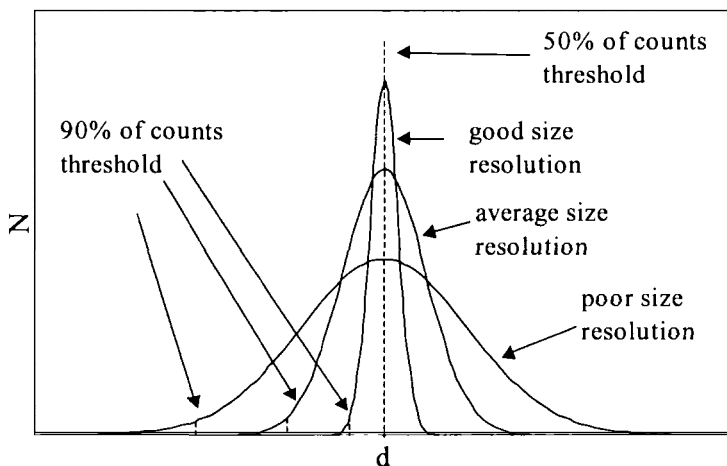


Figure 4.29. Effects of OPC size resolution on threshold settings.

#### 4.3.6. DATA ANALYSIS OF LIQUID MONITOR [6]

In many applications, such as in the analysis of clean water, the main task in particle detection is not to obtain a differential particle size distribution, but to detect how many unwanted particles larger than a certain threshold are present.

A high resolution and expensive volumetric or in-situ counter is often over-qualified for this purpose. A simple particle monitor can do the job just as well. A “monitor” is an in-situ counter that has no restriction as to where particles traverse the beam. Any particle in the beam, regardless of whether the particle’s trajectory takes it fully or only partially through the sensing zone will be both counted and sized, as long as the signal generated is above some threshold. In such an environment, a single particle passing through different portions of the beam will generate a range of scattering amplitudes due to non-uniformity of beam intensity which ranges from a maximum at the beam’s center to a minimum at the beam’s edges. Two consequences result from this non-uniformity in the beam intensity. The first is an obvious loss in size resolution. Each size value will be broadened to a distribution that corresponds to the beam profile. The apparent size distribution will be a convolution of the beam profile and the true size distribution. The second is the variation in the sensing zone volume as a function of particle size. This effect can be described by the following simple example: suppose that the beam profile is Gaussian with a maximum scattering intensity  $I$  and the threshold for the measurement is  $10^{-5}I$ . For a large particle that is at the upper sizing limit, the signal will be detected and counted anywhere in the beam as long as the scattering intensity is higher than  $10^{-5}I$ , which corresponds to a beam diameter  $d = 9.6\sigma$ . The sensing zone will be a cylinder of diameter  $9.6\sigma$  intersected by the detecting cone. For a small particle in the center of the beam, the scattering intensity is  $10^{-3}$  of that of the large particle. The locations where its scattering will be detected can only be those where the scattering intensity is at least  $10^{-5}I$ , which corresponds to a beam diameter of only  $d = 6.1\sigma$ . Therefore, the sensing zone volume for the smaller particle is about 2.5 times smaller than that for the larger particle. Larger particles will thus be over-sampled and smaller particles will be under-sampled.

Because of these limitations, a monitor-type counter intrinsically has very poor size resolution, with only a few size channels in the size range covered. However, despite their inferior resolution, monitors provide both high sensitivity and sample rates and have excellent reliability and repeatability from unit to unit, and they generally yield cumulative distributions that match very well with those obtained using a high resolution counter. Figure 4.30 shows comparative cumulative size distributions of DI water from different monitors (size range 50-200 nm) and from a high resolution counter (size range 100-800 nm).

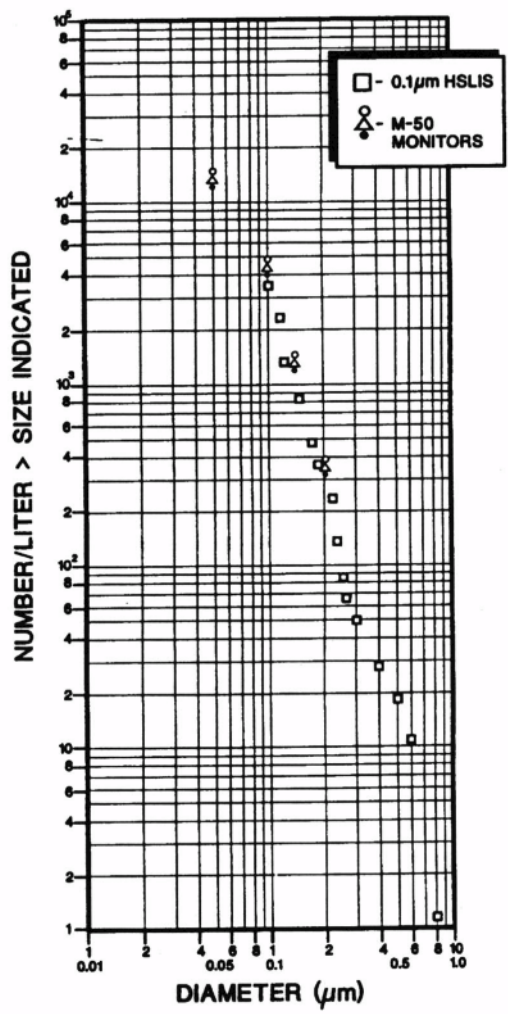


Figure 4.30. Comparative results of particles in DI water from monitor-type and regular counters [6]. (©Institute of Environmental Sciences and Technology, (847)-255-1561)

## REFERENCES

- 1 Artaxo, P., The Microanalysis of Individual Atmospheric Aerosol Particles by Electron, Proton and Laser Microprobe, in *Proc. 2<sup>nd</sup> World Congress Part. Technol.*, Kyoto, 1990, pp.421-426.
- 2 Whytlaw-Gray, R., Patterson, H. S., The Scattering of Light by Individual Particles in Smoke, *Proc. Roy. Soc. London Ser. A.*, 1926, 113, 302-322.
- 3 Gucker, F. T. Jr., O'Konski, C. T., Pickard, H. B., Pitts, J. N., Jr., A Photoelectronic Counter for Colloidal Particles, *J. Am. Chem. Soc.*, 1947, 69, 2422-2431.
- 4 Koropchak, J. A., Sadain, S., Yang, X., Magnusson, L., Heybroek, M., Anisimov, M., Kaufman, S. L., Nanoparticle Detection Technology for Chemical Analysis, *Ana. Chem.*, 1999, 71, 386A-393A.
- 5 Fisher, M. A., Katz, S., Lieberman, A., Alexander, N. E., The Aerosoloscope: an Instrument for the Automatic Counting and Sizing of Aerosol Particles, in *Proc. 3<sup>rd</sup> National Air Pollution Symp.*, Pasadena, CA 1955.
- 6 Knollenberg, R. G., Veal, D. L., Optical Particle Monitors, Counters and Spectrometers: Performance Characterization, Comparison and Use, in *Proc. Inst. Environ. Sci. Technol.*, San Diego, CA, 1991, pp751-771.
- 7 Schuster, B. G., Knollenberg, R., Detecting and Sizing of Small Particles in an Open Cavity Gas Laser, *Appl. Opt.*, 1972, 11, 1515-1520.
- 8 Knollenberg, R. G., The Measurement of Particle Sizes below 0.1 Micrometers, *J. Environ. Sci.*, 1985, 28, 32-47.
- 9 DeFreez, R., Girvin, K. L., A Solid-state Laser Single-particle Sensor for Gas Borne and Vacuum Counting and Sizing Applications, in *Proc. 5<sup>th</sup> Int. Congress Opt. Part. Sizing*, University of Minnesota, Minneapolis, 1998, pp.57-59.
- 10 Sommer, H. T., Harrison, C. F., Montague, C. E., Particle Size Distribution from Light Scattering, in Particle Size Analysis, Eds. Stanley-Wood, N. G., Lines, R. W., The Royal Society of Chemistry, Cambridge, 1992.
- 11 Knollenberg, S. C., Knollenberg, R. G., Nonintrusive Modular Particle Detecting Device, *US Patent 5,459,569*, 1995.
- 12 Knollenberg, R. G., "In Situ" Optical Particle Size Measurements in Liquid Media, in *Proc. Pure Water Conf.*, Palo Alto, CA, 1983.
- 13 Agarwal, J. K., Liu, B. Y. H., A Criterion for Sampling in Still Air, *Amer. Ind. Hyg. Assoc. J.*, 1980, 41, 191-197.
- 14 Lieberman, A., Parameters Controlling Counting Efficiency for Optical Liquid-borne Particle Counters in Semiconductor Fabrication: Technology and Metrology, *ASTM STP 990*, Ed. Gupta, D. C., American Society for Testing and Materials, West Conshohocken, 1989.
- 15 Nicoli, D. F., filings, U. B., Automatic Dilution System, *US Patent 4,794,806*, 1989.
- 16 Ovod, V. I., Hydrodynamic Focusing of Particle Trajectories in Light-Scattering Counters and Phase-Doppler Analysis, *Part. Part. Syst. Charact.*, 1995, 12, 207-211.
- 17 Pelssers, E. G. M., Cohen Stuart, M. A., Fleer, G. J., Single Particle Optical Sizing (SPOS), *J. Colloid Interface Sci.*, 1990, 137, 350-361.
- 18 Knollenberg, R. G., Submicron Diameter Particle Detection Utilizing High Density Array, *US Patent 5,282,151*, 1994.
- 19 Szymanski, W. W., Liu, B. Y. H., On the Sizing Accuracy of Laser Optical Particle Counter, *Part. Charact.*, 1986,3, 1-7.
- 20 Jaenicke, R., Hanusch, T., Simulation of the Optical Particle Counter Forward Scattering Spectrometer Probe 100 (FSSP-100), *Aero. Sci. Tech.*, 1993, 18, 309-322.
- 21 Szymanski, W. W., New Frontiers of Elastic Light Scattering in Aerosols, in *Proc. SPIE Vol. 3573: 5<sup>th</sup> Congress on Modern Optics*, 1998, pp 184-191.

- 
- 22 Szymanski, W. W., Ciach, T., Podgorski, A., Gradon, L., Optimized Response Characteristics of an Optical Particle Spectrometer for Size Measurement of Aerosols, *J. Quant. Spectrosc. Radiat. Transfer* 2000, 1999, 64, 75-86.
  - 23 Holve, D., Self, S. A., An Optical Particle-sizing Counter for In-situ Measurement, *Technical Report for Project SQUID, subcontract 8960-7*, December 1977.
  - 24 Twomey, S., *Introduction to the Mathematics of Inversion in Remote Sensing and Indirect Measurements*, Elsevier, Amsterdam, 1977.
  - 25 Lawson, C. L., Hanson, R. J., *Solving Least Squares Problems*, Prentice-Hall, Englewood Cliffs, 1974.
  - 26 Mühlenweg, H., Weichert, R., Optical Particle Sizer: A New Development with Mathematical Correction of Spread Measurement Data, *Part. Part. Syst. Charact.*, 1997, 14, 205-210.
  - 27 Umhauer, H., Particle Size Distribution Analysis by Scattered Light Measurements Using an Optically Defined Measuring Volume, *J. Aerosol Sci.*, 1983, 14, 765-770.
  - 28 Lindenthal, G., Mölter, L., New White-Light Single Particle Counter-Border Zone Error Nearly Eliminated, in *Preprints of Partec 98, 7<sup>th</sup> European Symp., Part. Charact.*, Nürnberg, 1998, pp.581-590.
  - 29 Heidenreich, S., Friehmelt, R., Büttner, H., Ebert, F., Methods to Calibrate Optical Particle Counters, in *Preprints of Partec 98, 7<sup>th</sup> European Symp. Part. Charact.*, Nürnberg, 1998, pp.723-732.
  - 30 Berglund, R. N., Liu, B. Y. H., Generation of Monodisperse Aerosol Standard, *Environ. Sci. Technol.*, 1973, 7, 147-153.
  - 31 Chein, H., Chou, C. C. K., A Modified High-output, Size-selective Aerosol Generator, *Part. Part. Syst. Charact.*, 1997, 14, 290-294.
  - 32 Liu, B. Y. H., Pui, D. Y. H., A Submicron Aerosol Standard and the Primary Absolute Calibration of the Condensation Nuclei Counter, *J. Colloid Interface Sci.*, 1974, 47, 155-171.
  - 33 Akers, R. J., Rushton, A. G., Sinclair, I., Stenhouse, J. I. T., The Particle Size Analysis of Flocs Using the Light Obscuration Principle, in *Particle Size Analysis*, Eds. Stanley-Wood, N. G., Lines, R. W., The Royal Society of Chemistry, Cambridge, 1992, pp 246-255.
  - 34 Heidenreich, S., Büttner, H., Ebert, F., Investigations on the Behavior of an Aerodynamic Particle Sizer and Its Applicability to Calibrate an Optical Particle Counter, *Part. Part. Syst. Charact.*, 1995, 12, 304-308.
  - 35 Knollenberg, R. G., The Importance of Media Refractive Index in Estimating Liquid and Surface Microcontamination Measurements, *J. Environ. Sci.*, 1987, 30, 50-58.
  - 36 Willeke, K., Liu, B. Y. H., Single Particle Optical Counter: Principle and Application, in *Aerosol Generation, Measurement, Sampling, and Analysis*, Ed. Liu, B. Y. H., Academic Press, New York, 1976, pp.697-729.
  - 37 Lee, H. S., Chae, S. K., Liu, B. Y. H., Size Characterization of Liquid-borne Particles by Light Scattering Counters, *Part. Part. Syst. Charact.*, 1989, 6, 93-99.
  - 38 Whitby, K. T., Vomela, R. A., Response of Single Particle Optical Counters to Non-ideal Particles, *Environ. Sci. Technol.*, 1967, 1, 801-814.
  - 39 Gebhart, J., Response of Single-Particle Optical Counters to Particles of Irregular Shape, *Part. Part. Syst. Charact.*, 1991, 8, 40-47.
  - 40 Bottlinger, M., Umhauer, H., Single Particle Light Scattering Size Analysis: Quantification and Elimination of the Effect of Particle Shape and Structure, *Part. Part. Syst. Charact.*, 1989, 6, 100-109.
  - 41 Umhauer, H., Bottlinger, M., Effect of Particle Shape and Structure on the Results of Single Particle Light Scattering Size Analysis, *App. Opt.*, 1991, 30, 4980-4986.

- 
- 42 Umhauer, H., A New Device for Particle Characterization by Single Particle Light Extinction Measurements, in *Particle Size Analysis*, Eds. Stanley-Wood, N. G., Lines, R. W., The Royal Society of Chemistry, Cambridge, 1992.
  - 43 Raasch, J., Umhauer, H., Errors in the Determination of Particle Size Distributions Caused by Coincidences in Optical Particle Counters, *Part. Charact.*, 1984, 1, 53-58.
  - 44 Knapp, J. Z., Abramson, L. R., Validation of Counting Accuracy in Single-Particle Counters: Application of a New Coincidence Model, in *Liquid and Surface-Borne Particle Measurement Handbook*, Eds. Knapp, J. Z., Barber, T. A., Lieberman, A., Marcel Dekker, New York, 1996, Chpt.10, pp.451-568.
  - 45 Peacock, S. L., Accomazzo, M. A., Grant, D. C., Quantitative Count Calibration of Light Scattering Particle Counters, *J. Environ. Sci.*, 1986, 29, 23-27.
  - 46 Wen, H. Y., Kasper, G., Counting Efficiencies of Six Commercial Particle Counters, *J. Aerosol Sci.*, 1986, 17, 947-961.
  - 47 Peters, C., Gebhart, J., Roth, C., Sehrt, S., Test of High Sensitive Laser Particle Counters with PSL-Aerosols and a CNC Reference, *J. Aerosol Sci.*, 1991, 22, 5363-5366.
  - 48 Liu, B. Y. H., Szymanski, W. W., Ahn, K. H., On Aerosol Size Distribution Measurement by Laser and White Light Optical Particle Counters, *J. Environ. Sci.*, 1985, 28, 19-24.



## PHOTON CORRELATION SPECTROSCOPY

### *Submicron Particle Characterization*

#### 5.1. Introduction

Photon correlation spectroscopy (PCS) has become a mature and popular technology for probing the diffusion of particulate materials either in solution or in suspension. By determining the rate of diffusion (the diffusion coefficient), information regarding the size of particles, the conformation of macromolecular chains, various interactions among the constituents in the solution or suspension, and even the kinetics of the scatterers can be obtained without the need for calibration. Commercial PCS instruments have evolved from heavy and bulky optical setups with furniture-sized electronics and correlators, to miniature setups utilizing fiber optics and chip correlators that use digital signal processing. The advantages of PCS, which include the fact that it is a non-invasive absolute technique requiring only a small amount of sample, and does not require extensive sample preparation, have made this technology the method of choice for sizing submicron particles and it is increasingly used as a means to certify particle size standards and controls. Several new innovations in PCS have emerged, such as cross correlation function measurement and diffusing-wave scattering, created by the demand for a fast and non-invasive on-line or in-line way to characterize particles or to monitor or control product quality in manufacturing processes (see [40] of Chapter 2). An international standard covering the use of PCS to obtain mean particle size in a dilute suspension has been established [1].

Photon correlation spectroscopy is a technology for measuring the dynamic light scattering (sometimes called quasi-elastic light scattering) of small scatterers in a suspension. PCS, which was developed originally as a research tool for probing the dynamics of macromolecules in solution and for studying critical phenomena and the statistical nature of light [2,3], has been employed in many different disciplines of science, from polymer science, colloid chemistry, physical chemistry, to material science. There are excellent monographs and proceedings covering PCS applications in macromolecule solution. In the present chapter, only the topics relevant to particle size and shape characterization are discussed. Readers are urged to consult the references

[26-40] in Chapter 2 and the extensive literature contained in those publications for a more complete explication of PCS technology and its applications.

In a PCS experiment the fluctuations (temporal variation, typically in a  $\mu\text{s}$  to  $\text{ms}$  time scale) of the scattered light from scatterers in a medium are recorded and analyzed in correlation delay time domain. The scatterers can be anything that has a different refractive index than that of the medium and are stable throughout the duration of the measurement. Although there have been a few reports of the application of PCS in submicron aerosol analyses [4], in which the measurement of particle diffusivity will reveal the aerosol size after some empirical corrections, the vast majority of applications involve particles in liquid media. In the typical situation the scatterers are solid particles (such as metal oxides, mineral debris, and latex particles) or soft particles (such as vesicles and micelles) in suspension, or macromolecular chains (such as synthetic polymers and biomaterials) in solution. The common property of these particles probed in a PCS measurement is their movement. This movement arises from the random thermal motion of the medium's molecules (this motion, first observed by the English botanist Robert Brown while using an optical microscope to observe flower pollens in water, is known as *Brownian motion*), and is free from external forces such as turbulence or the gravitational force. The detected scattering may be from individual particles (single scattering), or from the multiple scattering in a concentrated solution or suspension. Fluctuations in the scattering intensity at a given scattering angle arise because the phase and polarization of the light scattered by each particle changes with time and the particles continuously rearrange their configuration in the scattering volume due to Brownian motion. The relative positions of the particles in the scattering volume at any instant determine the magnitude of constructive or destructive interference of the scattered light at some fixed point in space. In practice, that point is where the detector is located. Since the diffusion rate of particles is determined by their sizes in a given environment, information about their size is contained in the rate of fluctuation of the scattered light [5].

Generally speaking, the lower size limit of this type of measurement is determined by the detectable scattering fluctuations of particles versus the experimental noise. The measured scattering fluctuations must be greater than the experimental noise created by various sources, including environment disturbances, temperature fluctuations, and the inherent electronic noise, in order to obtain an unbiased result. The upper size limit of these measurements is determined primarily by the sedimentation limit. Particles that are being analyzed must be stably suspended. Sedimenting particles leave the scattering volume and undergo directed motion that complicates the information in the scattering fluctuations. Practically, the upper size limit in a PCS experiment is about a few microns depending on material density and medium viscosity, and

the lower size limit is about a few nanometers depending on the refractive index difference between the particles and the medium.

## 5.2. Instrumentation

During the past twenty years, PCS instrumentation has gone through big changes mainly because of the advancements in both lasers and microelectronics. Single PC card or even software correlators have replaced the old furniture-sized correlators. Fiber optics is used more and more in later models of commercial instruments. PCS measurements of concentrated suspensions have become viable. Through all that, PCS has now truly become a workhorse for daily and routine particle characterization in many applications.

Figure 5.1 shows the schematic of a multi-angle PCS instrument. (The probe-type PCS device will be described separately.) It is neither necessary nor is it the desire of the present text to list all possible optical arrangements of PCS instrumentation. Only a few typical setups will be addressed; other types of optical configurations may be found in [38] in Chapter 2.

A typical PCS instrument consists of following components: a light source, a set of optical elements to condition and transmit the beam, a sample module, second set of optical elements to collect the scattered light, a detection system, a correlator, and a computer for experiment control, data analysis, and result output [6].

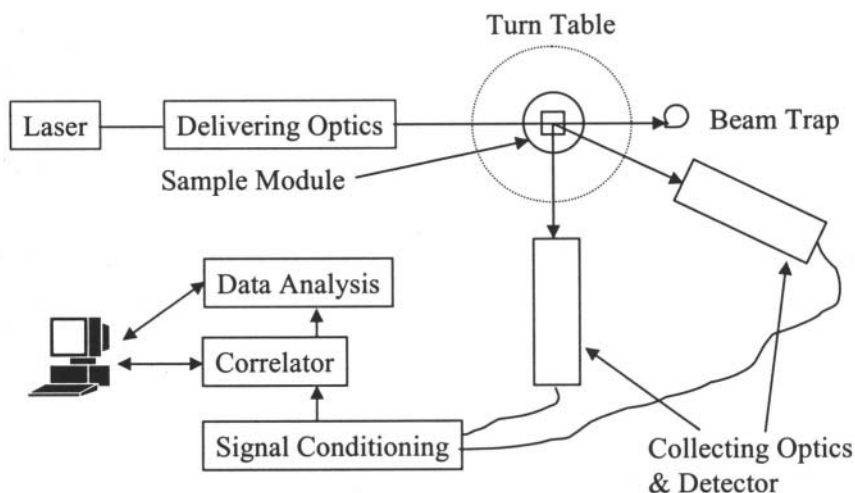


Figure 5.1. Schematic of a PCS instrument.

### 5.2.1. LIGHT SOURCE

In a PCS experiment, because the correlation of scattered photons needs to be calculated based on interferometric measurement of the scattering intensity fluctuations created by an ensemble of particles, the illuminating source has to be coherent. Coherence is a term describing light waves that are in phase in both time and space. Monochromaticity and low divergence are two properties of coherent light. A high degree of coherence means that there is a constant phase difference between any two points in a series of equal-amplitude wavefronts (spatial coherence) and a correlation in time between the same points on different wavefronts (temporal coherence). The coherence length is equal to the coherence time multiplied by the speed of light. In a PCS experiment, the incident radiation (photons) needs to be in phase and have the same wavefront so that one can gain information on the particle movement by measuring the coherence loss amongst the scattered photons. If the incident photons are not coherent, the relationship between the scattering and particle movement cannot be established. Ordinary light sources emit random, non-polarized, non-coherent light which cannot be used in a PCS measurement. Coherence time of radiation (the duration of an uninterrupted wavetrain) from these light sources is about  $10^{-13}$  s, or 30  $\mu\text{m}$  in coherence length. In other words, there will be no phase correlation between photons emitted from two scatterers 30  $\mu\text{m}$  apart. On the other hand, light emitted from a laser has a much greater degree of coherence due to the fact that the lasing process stimulates identical photons. Depending upon the type and structure of the laser, the coherence length varies. The following table lists typical values for the coherence length and coherence time for various light sources.

Table 5.1. Typical coherence lengths and polarization ratios of various light sources

Light Source	Coherence		Polarization
	Length	Time	
Light emitting diode	$3 \times 10^{-5}$ m	$10^{-13}$ s	Random
Index-gained diode laser	0.03 m	$10^{-10}$ s	> 100:1
Long coherence diode laser	3 m	$10^{-8}$ s	> 50:1
He-Ne laser	3 m	$10^{-8}$ s	> 500:1
External cavity diode laser	300 m	$10^{-6}$ s	> 100:1
Frequency stabilized He-Ne laser [7]	$10^8$ m	0.3 s	> 500:1

For non-spherical or optically anisotropic particles, the scattering field is not orientation invariant; i.e., the complex amplitude functions  $S_3$  and  $S_4$  are not equal to zero (see Chapter 2). Thus the interference fluctuation will be affected by rotational motion as well as translational motion and some degree of depolarization of the original light may result. In order to simplify theoretical

analysis of the scattering intensity correlation measurement and to resolve different types of particle motions, a further requirement for the light source used in PCS instruments is that it is linearly polarized.

Due to all the above reasons and because of its high stability, laser light is exclusively used in PCS instrumentation. Within the available variety of lasers, the argon ion laser and the He-Ne laser are the most popular, especially the latter, because of their high degree of coherence, excellent beam collimation, and commercial availability. However, diode lasers have lately become a new comer in PCS instrumentation due to its low cost, small footage, robustness and connectability to fiber optics as described in Chapter 3.2.1. Diode lasers with emitting power as high as 100 mW in the visible light region are available. Efforts have been made to improve the coherence length and optical characteristics of diode lasers so they can be better used in interferometric measurements.

### 5.2.2. DELIVERING OPTICS

The delivering optics transmits and delivers light from the light source to the scattering volume, which is defined by the cross section of the incident beam and the collecting cone. In homodyne and heterodyne experiments, light from the light source may also have to be directly delivered to the detector in order to be mixed with the scattered light. Light from most types of lasers is collimated with the polarization orientation well defined (usually polarized vertically) with a circular beam having a diameter about one millimeter. Nowadays, commercially available laser diodes emit light with the above characteristics since the micro-optics needed to correct astigmatism and divergence of raw light from a laser diode has been included as part of the device. To achieve high correlation efficiencies, the laser beam often has to be further focused down to a smaller dimension since the scattered photons need to come essentially from the same wavefront. Coherence will completely vanish when the relative phases of the wavefronts reaching the observer from any two points of the extended source change by  $\pm\pi$ . If we assume that the incident beam is circular (with a diameter  $D_w$  at the waist), to maintain a relative phase of the wavefront that is less than  $\pm\pi$  between any two points in the scattering volume, the scattering volume has to be compromised according to the scattering angular range being measured, satisfying the following relation [8]:

$$\Delta\theta\Delta\phi = \frac{\lambda^2 \sin^2 \theta}{4D_w (D_A + D_w \cos \theta)}. \quad (5.1)$$

In Eq. 5.1,  $D_A$  is the diameter of the collecting optics cone at the intersection of the incident beam, and  $\Delta\theta$  and  $\Delta\phi$  define the angular range of the collecting optics for scattering angle  $\theta$  and azimuthal angle  $\phi$ , respectively.

Eq. 5.1 has to be considered in terms of the specific samples. If the scattering volume is too small, the scattering may be too weak, resulting in a poor signal-to-noise ratio, and number of particles may not be enough to satisfy statistics in normal PCS measurements in which the number fluctuation is supposedly negligible in order for Eq. 2.34 to be valid. On the other hand, if the scattering volume is too large, scattering from different parts of the scattering volume may not be correlated. Thus, depending on the targeted particulate system, i.e., particle size, concentration, and motion to be measured, a proper scattering volume has to be chosen that compromises both scattering intensity and signal correlation. One of the dimensions in determining the scattering volume is the focused beam diameter. According to basic optics, the waist of a focused beam is related to the beam diameter  $D$  and the focal length  $f$  of the focusing lens:

$$D_w \cong 2.44\lambda f / D. \quad (5.2)$$

Near the focal point, the beam dimension  $D_{l_w}$  at a distance  $l_w$  from the focal point can be calculated:

$$D_{l_w} = D_w \sqrt{1 + \left( \frac{4\lambda l_w}{\pi D_w^2} \right)^2}. \quad (5.3)$$

For example, the distance  $l_w$  in Figure 5.2, at which the diameter of the beam increases 5%, can be calculated according to  $l_w = (\pi D_w^2)/(12\lambda)$ .

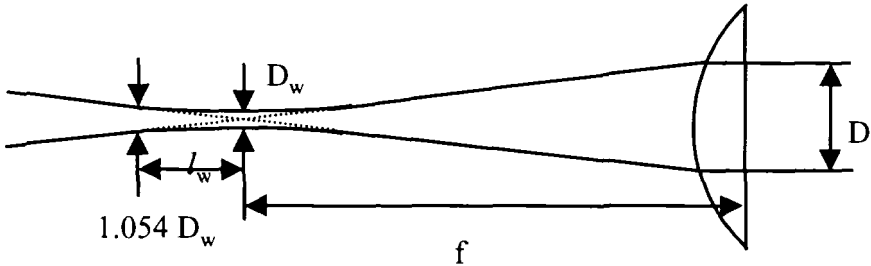


Figure 5.2. Collimated beam focused by a lens.

Thus, in order to achieve a certain beam diameter in the focused area, besides choosing a lens of proper focal length, the beam from the light source may have to be expanded before it is focused down. In addition, a spatial filter to clean up the beam as well as a polarizer to further increase polarization ratio of the beam may be inserted. Depending on the instrument geometry, the light may have to be guided through reflection mirrors, prisms, apertures and lenses. Optical fiber can also be used in guiding light to illuminate sample, especially in instrument designed for measuring concentrated suspensions. Monomode optical fiber can also naturally serve as a spatial filter that saves space and cost of additional parts needed as that in the conventional spatial filter (see Section 3.2.1).

### 5.2.3. SAMPLE MODULE

The sample module is usually comprised of a sample cell and a sample cell holder which provides both mechanical and temperature stability. Depending on the desired measurement temperature, temperature control with the resolution of up to  $0.1^{\circ}\text{C}$  can be achieved by circulation of a fluid such as water or oil, in a circulation jacket [9] or simply by use of a Peltier device. Sample cells can take different shapes. Square and round cuvettes are the most common ones. Low cost plastic and high optical quality glass or quartz cuvettes are commercially available. The advantage of the round design is that there is no refraction when light scatters across the cell and so the actual scattering angle is the same as the geometrical angle between the detector and the incident light as shown by Figure 5.3a. For square cells, except for right angle ( $90^{\circ}$  degrees), the relation is more complicated. If the detecting system is aligned towards the cell's center, the actual scattering angle will not agree with the apparent angle and the scattering volume will not remain at the cell's center. Both the scattering angle and the scattering volume location depend on the refractive index of the suspension medium (Figure 5.3b). If one wants to keep the scattering volume near the cell's center (since that is where the light has been focused), the detection system has to be aligned differently as shown in Figure 5.3c. But then when another medium with a different refractive index is used, the scattering center will be shifted away from the cell center. Sophisticated cells of other shapes or with special features can be found in the literature. For example, in studying polymer chain dynamics, a cell of a wall thickness of  $0.01\text{ mm}$  has been used in order to achieve fast solution temperature equilibrium [10]. Yet another cell design eliminates the need to know the refractive index of the medium [11]. Usually, the sample volume is a few milliliters or less, and for a flow cell connected to a separation device such as an SEC column, the sample volume has to be very small, typically in the microliter range [12].

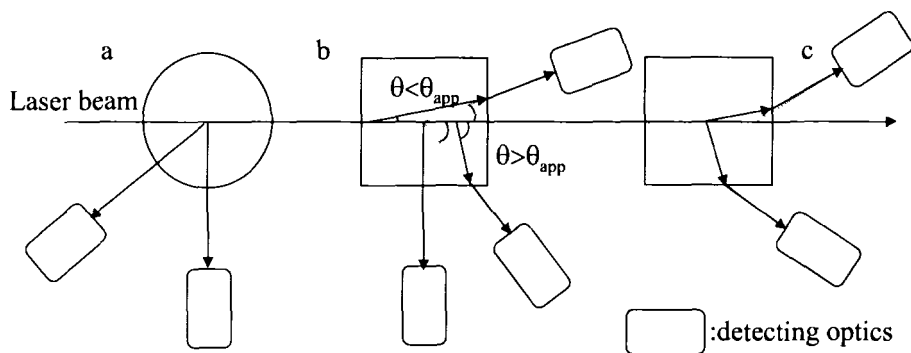


Figure 5.3. Refraction created by different cells assuming the detector only collects the scattered light perpendicular to it.

#### 5.2.4. COLLECTING OPTICS

The collecting optics of a typical PCS instrument consists of a set of apertures and lenses that collect the scattered light from a defined volume in the sample cell at a specified scattering angle (or an angular range). Although there are many designs, most of them can be classified into two types, as shown in Figure 5.4 (A) and (B).

In the optics in Figure 5.4 (A), the distance between the lens and the scattering volume (the gray parallelogram) is longer than  $2f$  ( $f$  is the focal length of the lens), and the aperture, P2, is set at the focal point of the lens. In this configuration, the dimension of the scattering volume is controlled by the aperture P1 and the scattering angular ranges  $\Delta\theta$  and  $\Delta\phi$  are controlled by P2. The aperture can be in the form of a circular pinhole or a rectangular slit. The size of the aperture may be fixed, adjustable, or selectable if using a multi-aperture turret. For the optics in (B), the distance between the lens and the scattering volume ranges from  $f$  to  $2f$ . In this setup, the scattering volume (gray circle) is mainly controlled by P4 and the distances between the scattering volume, the lens and P4. The scattering angular ranges  $\Delta\theta$  and  $\Delta\phi$  are mainly controlled by P3. Although both setups work well, the first setup (A) is commonly used. Especially when using fiber optics, this provides more flexibility and adaptability. The optics in (C) is a simplified version of (A) in which only two small apertures are used that combinatorily define the scattering volume and angular uncertainty. A polarizer can be placed in the collecting optics. If the direction of polarization is the same as that of the incident light (commonly vertical),  $I_{vv}$  is collected. Otherwise, when these two directions are perpendicular to each other (called the depolarization scattering),  $I_{vh}$  is measured. One criterion in choosing the proper apertures is that any signal



detected by the detector should emanate from one or maximum a few coherent areas which satisfies Eq. 5.1 to maximize the signal-to-noise ratio.

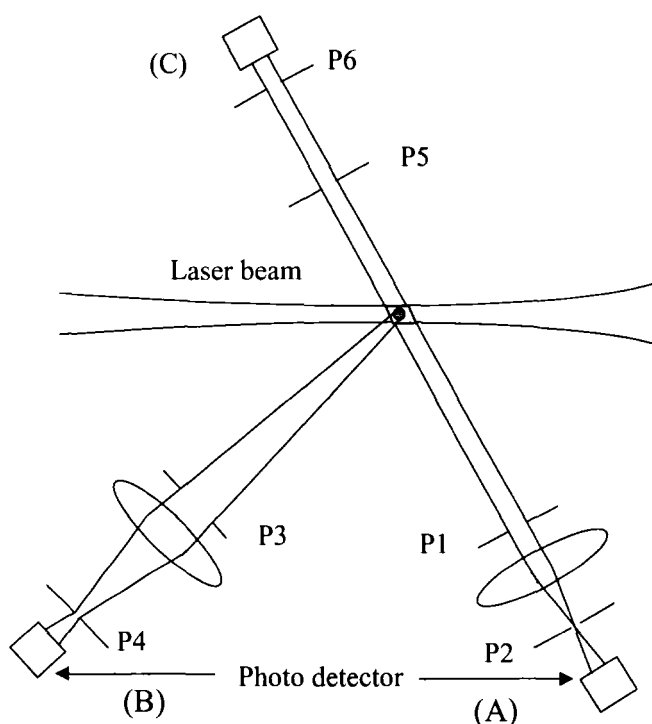


Figure 5.4. Schematics of PCS collecting optics.

The collecting optics is set at a scattering angle at which the PCS measurement is to be made. If measurements at more than one scattering angle need to be performed, then either a precision goniometer or multiple sets of optics placed at different angles have to be used. In a goniometer, either the light source or the collecting optics revolves around the sample cell to make measurements at different scattering angles. The angular precision in either setup needs to be better than  $0.1^\circ$ . In the former case, both the cell holder and the cell are coaxial with the goniometer's axis. In the latter case, fiber optics is often used and optical fibers (with or without micro lenses) are placed at preset angles. Measurement can be performed simultaneously if each fiber is connected to a dedicated photodetector and the subsequent electronics, or sequentially if only one photodetector is used. For example, in a fiber-optic based light scattering instrument shown in Figure 5.5, nine sets of optic fiber-PMT's at fixed scattering angles are used for a simultaneous static (at nine angles) and dynamic light scattering measurement (at six angles using six correlators). By changing

the direction of the incident beam (moving the mirror M2), the optics can cover a continuous scattering angular range, in this case from  $3.6^\circ$  to  $144.1^\circ$  [13].

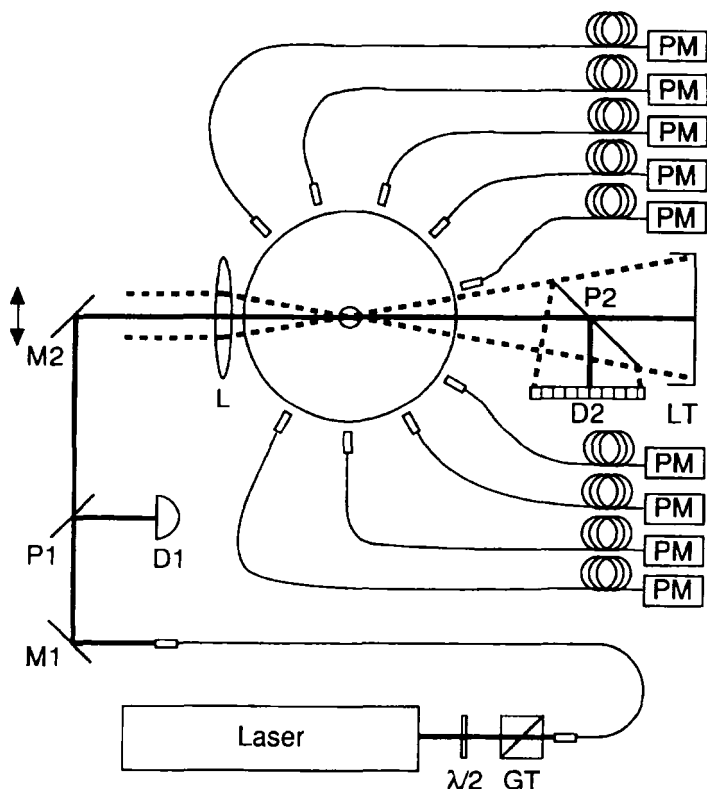


Figure 5.5. A multiangle PCS instrument. (Reprinted with permission from Egelhaaf, S. U., Schurtenberger, P., A Fiber-Optics-Based Light Scattering Instrument for Time-Resolved Simultaneous Static and Dynamic Measurements, *Rev. Sci. Instrum.*, 1996, 67, 540-545. Copyright 1996, American Institute of Physics.)

Fibers used in PCS collecting optics can be either multimode or monomode. Although the former is less efficient because of coherence loss and the polarization of the light is not preserved, these fibers collect more light due to larger fiber diameter (some tens of microns) compared with that of monomode fibers with diameters of only a few microns. The latter has superior noise statistics due to the stripping of the higher order modes. A comparison involving pinhole receivers, monomode fiber receivers, few-mode fiber receivers, and multimode fiber receivers in PCS experiment has been published. It concluded that for a miniature PCS setup, a few-mode fiber receiver is the

best option since it optimizes both detection efficiency and instrument alignment [14].

In measurements other than self-beating autocorrelation spectroscopy, two light beams, a reference beam in addition to the scattered light, need to be delivered to the detector. The reference beam, which is frequency-stationary, then *beats* at the detector surface with scattered light from the sample. There are several ways to create a reference beam. One simple way is to make a scratch on the wall of the sample cell. When light illuminates the cell, the scratch results in a stationary scattering center. For this reason, the reference beam is also called the local oscillator. Another way is to split the incident beam so that a small portion of it can be delivered directly to the detector.

#### 5.2.5. DETECTOR

A photodetector is used to convert photons collected by the collecting optics to either electron pulses or current. Two types of photoelectron detectors are commonly used in PCS analyzers: photomultiplier tubes (PMT) or photodiodes (PD).

A PMT consists of a series of metallic dynodes that are held at progressively higher electric potentials. An incident photon strikes the photocathode thereby releasing a photoelectron. This electron accelerates to the first dynode under the influence of a volt potential striking the first dynode with fairly high kinetic energy breaking loose many new electrons in a process known as secondary emission, each which will in turn accelerate to the next dynode in the chain. Such a chain of dynode collisions ultimately results in a large pulse with perhaps one million electrons reaching the anode. PMT's provide high sensitivity (current amplification of  $10^6$  or higher), low noise (typically a dark count of less than one hundred per second or a dark current on the order of nanoamperes. For some PMT's operating at reduced temperatures, the dark count can be as low as a few per second), broad dynamic range (a linear response range of  $10^6$  or greater), and fast response (in the range of nanoseconds or sub-nanoseconds with a pulse width of a few tens of nanoseconds). The sensitive wavelength zone of the photocathode material must match the wavelength of light used in the experiment to achieve a high yield. Lately compact PMT's that have a footprint of only  $1\text{ cm}^3$  with a weight of 5 g have been developed. Due to the sensitivity and linear response range of PMT's, excessive light illumination must be avoided. Otherwise the relationship of photon counts to electron pulses may not be linear and, in the case of extremely strong illumination in just a very short time a PMT may be damaged.

An important requirement of a PMT is that it should produce a minimal amount of afterpulses. An afterpulse is a secondary pulse generated after a pulse created by the incoming photons. Since this second pulse is correlated with the

first pulse and produces a peak in the ACF at short time intervals, its existence at low count rate will distort the ACF. PMT's may be operated in either a pulse-counting mode in which a single photon event is effectively amplified into a measurable pulse of electrons and each pulse of electrons is registered as "an event," or in a current mode where the current at the output electronics is proportional to the intensity of the incident photons. In a PCS experiment either mode can be used. When the light intensity is low, electron pulses produced by the PMT can be separately registered. The pulse-counting mode is more efficient and thus preferred [15]. When the light intensity is high, photoelectron pulses tend to overlap and the pulses from the electrons become continuous. The current mode has to be used. Different electronics have to be used for the two modes.

Photodiodes work by a different principle. In a simple diode structure, if a photon is absorbed in the depletion region an electron-hole pair is generated. This electron-hole pair is then swept out of the depletion region between two differently doped semiconductor regions and a photocurrent is produced. Since not all of the light incident on the device will be absorbed, a low internal quantum efficiency is the result. A P-I-N diode improves the quantum efficiency of the device by replacing the depletion region with an intrinsic undoped layer of semiconductor sandwiched between the P- and N-sides of the diode. These photodiodes do not provide any internal gain. They require electronic amplification to increase the level of the signal. To further increase the sensitivity, avalanche photodiodes (APD) have been developed. An APD is the semiconductor equivalent of a PMT. In an APD, photo-excited carriers accelerate in a strong electric field. Their kinetic energy is then used to excite secondary carriers through the avalanche effect. An avalanche occurs when the velocity of a carrier becomes so great that when it collides with a lattice site it may strip an electron from the valence band, creating a new electron-hole pair. In an APD, the pair excited by a single photo-absorption event is multiplied by the avalanche effect and so many carriers are collected. The latest APD's combine the optical absorption properties of InGaAs and the avalanche multiplication properties of silicon by using the wafer fusion technique to integrate the two materials, despite their lattice mismatch. Although APD's generally have a less-favored specification than that of PMT's in a PCS experiment, the latest development has made it possible for the performance of APD's to approach that of PMT's in most PCS applications [12]. In addition to its advantages of being low-cost, compact, and robust, large-area APD's with an internal gain as large as 300x and quantum efficiencies of up to 90% are available in the marketplace. This is an order of magnitude better than the ones used when the pioneering work in applying APD's in PCS instruments was performed, and higher than that of PMT's at long wavelengths ( $> 650 \text{ nm}$ ) [16].

### 5.2.6. ELECTRONICS

Since photodetectors usually have high output impedance, which is a characteristic of a current source, they are most efficient when driving a low impedance input. Therefore, a transimpedance amplifier usually follows the detector in the receiver subsystem. This transimpedance amplifier is often considered part of the receiver circuit. The desired characteristics of a transimpedance amplifier are high gain ( $> 100$ ), low noise, low input impedance, and output impedance matching the next stage, which often is a pulse discriminator held at a constant bias in order to discriminate the valid pulses from the noise. After being de-randomized using a high speed clock the pulses arrive more equally spaced and no pulses are lost due to dead time associated with the electronics. After passing through a scalar timer, (a counter that continuously samples the pulses), the train of pulses is then delivered to the correlator. Both the amplifier and discriminator should have a bandwidth broad enough to accommodate the detected signals that may have a fast rising time or a small dead time ( $< 50$  ns). Otherwise the ACF will be distorted producing spurious correlation or anti-correlation at high count rates.

Although the photon-counting mode is preferred for PCS measurements, at high intensity or for motions with long characteristic times, the current mode is more appropriate. In the current mode, the current is proportional to the incident photon flux. A load resistor combined with a stray shunt capacitor can be used to convert photocurrent into voltage. The voltage fluctuation can then be fed into a spectrum analyzer for power spectral analysis, or in the present state of PCS experiments converted back to digital form. The conversion can be done using a single voltage-to-frequency converter to change the output voltage to frequency, followed by digitization to number of counts; or by using a fast A/D converter and digitizing the voltage first then using a rate multiplier with a short pulse sampled at a fixed sampling speed (e.g.  $1\ \mu\text{s}$ ) [17].

### 5.2.7. CORRELATOR

After the electronics described above, a train of digitized numbers (counts) is fed into the correlator. This train of number  $n(t)$ ,  $n(t+\Delta t)$ ,  $n(t+2\Delta t)$ , ..... is created by counting the number of photon events occurring in a defined time interval (sample time),  $\Delta t$  in the photon-counting mode, or from the digitized event frequency at the fixed sample time when in the current mode. These counts are stored and the correlator then performs the operation defined by Eq. 2.25; i.e., multiplying every pair of numbers that are separated by a delay time  $j\Delta t$  and averaging them over the measurement time ( $N_s\Delta t$ ) to form one data point in the ACF. The entire ACF is computed by varying the value of  $j$  in the

following equation until  $j$  is large enough that any correlation between events  $n(t_i)$  and  $n(t_i+j\Delta t)$  vanishes:

$$G^{(2)}(\tau_j = j\Delta t) = \sum_{i=1}^N n(t_i)n(t_i + j\Delta t), \quad N = N_s - j. \quad (5.4)$$

Many schemes can be used to perform the multiplication and addition that use either specially designed or off-the-shelf hardware or software using an ordinary PC. One scheme often used is the register-shifting procedure. In this procedure, a train of  $L$  number  $n(t_i-\Delta t)$ ,  $n(t_i-2\Delta t)$ , .....  $n(t_i-L\Delta t)$  is stored in shift registers. Any number in the train is then multiplied by the next number  $n(t_i)$ , yielding  $n(t_i)n(t_i-\Delta t)$ ,  $n(t_i)n(t_i-2\Delta t)$ , .....  $n(t_i)n(t_i-L\Delta t)$  as the product. These products are stored in  $L$  separate storage counters. Meanwhile, all numbers in the shift registers are shifted one position over to take in the number  $n(t_i)$ . Now, the numbers contained in  $L$  registers become  $n(t_i)$ ,  $n(t_i-\Delta t)$ , .....  $n(t_i-(L-1)\Delta t)$ , and the subsequent products of the multiplication become  $n(t_i+\Delta t)n(t_i)$ ,  $n(t_i+\Delta t)n(t_i-\Delta t)$ , .....  $n(t_i+\Delta t)n(t_i-(L-1)\Delta t)$ , which are added to the previous set in the storage counters. Thus, each counter in the storage counters accumulates the product of two numbers separated by a fixed delay time  $j\Delta t$  throughout the entire measurement time to produce the desired ACF. In this scheme, the delay time  $j\Delta t$  has linearly spaced increments. The bandwidth (dynamic range) of the correlator is from  $\Delta t$  to  $L\Delta t$ . Information about motion faster than  $\Delta t$  will be completely lost and motions slower than  $L\Delta t$  will only be partially captured and so the results may be biased. Particulate systems often have a broad distribution in terms of size and motion, (e.g., rotational and translational, which often have different time scales). A linear correlator may lack the necessary dynamic range to uncover all the pertinent information, even if it has a few hundred channels. Most commercial correlators use a multiple delay time arrangement. A fixed finite number of channels (commonly from 64 to 1024) is divided into several groups. Within each group the increments in the delay time are linear. The increment between the groups is set at some fixed ratio or it may be set by the user at arbitrary ratios. Thus, depending on the application, the same number of channels can be used to analyze different dynamic ranges. Fast particle motion will be covered by the densely spaced initial channels and slower motion will be more completely covered by the long delay time of the later channels. The ratio between the two subsequent groups may be as large as  $2^7$ ; i.e., one group may have a delay time increment 128 times longer than that of the previous group. For example, if 16 channels are divided into 4 groups then each group will have 4 channels. The following table

shows the delay time  $\tau$  (in unit of  $\Delta t$ ) for each channel at different settings of the increment ratio as compared with the first group.

Table 5.2. Examples of correlator delay times

Ratio	C1	C2	C3	C4	C5	C6	C7	C8	C9	C10	C11	C12	C13	C14	C15	C16
1:1:1:1	1	2	3	4	5	6	7	8	9	10	11	12	13	14	15	16
1:2:4:8	1	3	5	7	11	15	19	23	31	39	47	55	71	87	103	119
1:4:8:32	1	2	3	4	8	12	16	20	28	36	44	52	84	116	148	180

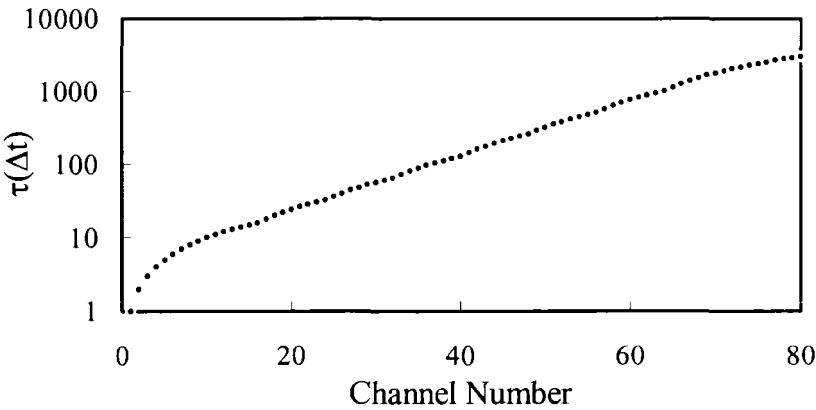


Figure 5.6. Arrangement of correlator channels in a non-linear correlator.

A correlator with non-linearly spaced correlation channels has a much wider dynamic range than that of a linear correlator with the same number of channels. For example, in the Coulter® N4 Plus™ multi-angle PCS instrument, 80 correlator channels are divided into eight groups. Channels within each group are spaced linearly while the delay times between the groups are incremented according to a set ratio. By such an arrangement, the 80 real channels span a delay time scale equivalent to 3072 linearly spaced channels resulting in a better statistical accuracy. Figure 5.6 shows the correlator channel arrangement for the correlator employed in the Coulter® N4 Plus™. If the channels are spaced appropriately, for a given sample, there is no advantage in having a large number of channels. Five channels may be all that are needed for a two-component sample [18]. However, since the correlation channels in a correlator are arranged at discrete values of  $\tau$ , the choice of sample time ( $\Delta t$ ) and delay time ( $\tau$ ) for each channel that represent the ACF for some range in between  $G^{(2)}(\tau_{i-1})$  and  $G^{(2)}(\tau_{i+1})$  are not trivial in a non-linear correlator and need to be considered carefully [19].

The range of sample times ( $\Delta t$ ) in a correlator is typically from 50-100 ns to a few seconds that is sufficient in most applications. In faster ACF measurements used in the study of extremely small particles at large angles, a time-of-arrival correlator that measures the arrival times of photons having a delay time as short as 2.5 ns has to be used

During the measurement of the ACF in the photon counting mode, the number of counts per sample time ( $\Delta t$ ) is taken by a single-byte register. For low bit registers, the maximum number of counts is very limited. For example, a 4-bit correlator can only take 16 counts per  $\Delta t$ , otherwise the register will become saturated and overflow. Thus, if the scattering intensity is high or  $\Delta t$  is long, an overflow is often unavoidable. To overcome this problem, many correlators use a scaling technique that counts photon events once every few pulses instead of every pulse. For example, if the scaling factor is 4, the correlator will count only one pulse in every four pulses. For Gaussian signals the statistical accuracy of ACF is essentially unaffected when the scaling factor is small. The accuracy is only affected when the scaling factor becomes too big [21]. This problem is almost non-existent when using present-day 32-bit microelectronics, in which any prescaling becomes unnecessary most of the times. Another alternative to avoid overflow without using scaling is to separate sampling and sample times, i.e., sampling (counting) does not take place over the whole sample time interval  $\Delta t$ .

New developments in correlators have always been catalyzed by advancements in microelectronics and computer technology. Present-day computer technology has made many earlier attempts in designing a correlator, such as the clipped correlator or the add-subtract correlator either irrelevant or obsolete. Utilizing 32-bit digital signal processing (DSP) with speeds faster than a few hundred MHz, the modern correlator can be the size of a PC card or even just a single chip, and can easily accomplish an ACF measurement suitable for most particle characterization needs. An ordinary PC can be used to host and control as many as eight correlators simultaneously with the delay time as short as 25 ns and as long as a thousand seconds or more representing a time span of ten decades! Because of the continuing increases in both memory and storage capacity of ordinary PC's, software correlators that uses software to computer the ACF from a prerecorded train of numbers is more feasible and compatible with the specifications and features of hardware correlators. A software correlator can be hybridized with a hardware correlator to further extend the dynamic range, in which the first part of the ACF which needs fast processing is computed by the hardware correlator and the second part of the ACF is accomplished by software computation. The compactness and low-cost of correlators may allow simultaneous multi-angle measurement that employs multiple correlators to become more accessible.



After completion of the ACF computation,  $G^{(2)}_{\text{det}}(\tau)$ , which is the primary data in a PCS experiment, and the average intensity (photon count) over the total measurement time, are ready to be fed into the data analysis process. There are two ways to obtain the average count: one is obtained from the baseline channels, which are additional channels that have delay times much longer than the last channel of the ACF. The average intensity of the baseline channels is the measured baseline, which ideally is equal to  $N_s \langle n(t) \rangle^2$  with  $N_s$  being the number of sampling. The other one is obtained by the addition of all counts during the measurement and is computed using  $A = N_s \langle n(t) \rangle^2$ , termed the calculated baseline. Theoretically, these two baseline values should be identical. In reality, in a good measurement, their difference is often less than a few tenths of one percent. This difference can be used to judge the quality of ACF.

## 5.2.8. EXPERIMENTAL CONSIDERATIONS

In any PCS experiment, the key to success is to obtain a good quality ACF. Otherwise, no matter how sophisticated the data analysis is, a correct result is hard to obtain. To get an ACF of good quality, two factors need to be addressed: 1) reduction of any experimental noise, and 2) choosing the correct delay time range, covering all detectable delay characteristics as much as possible. The following is a partial list (in a chronological order) as to the attention that has to be paid during an experiment.

### *Sample Quality*

A good sample preparation procedure will ensure that particles are properly dispersed and stable, no foreign particles are present, the suspension is homogenous, and the temperature is equilibrated. Since PCS measures submicron particles which often scatter very weakly, the scattering may easily be overshadowed by the presence of a few large dust particles. In addition, these dust particles, because often there are only a few, will create sudden and great intensity fluctuations as they move into or out of the scattering volume through Brownian motion. Thus, it is very important that the diluent or solvent used in sample preparation is contaminant-free, which can be achieved through the use of a proper filter. The filter should be suitable for the medium and have a pore size smaller than that of the particles to be measured. Currently, disposable filters with a pore size of 25 nm (or even smaller) are commercially available for various media. A good filtering technique is also important, especially when dealing with polar media which attract dust particles from air very easily. Another issue often neglected by many practitioners is that the medium used to prepare the sample should not alter the physical properties of the particles; this is especially important when measuring particles in an aqueous medium.

Cleanliness of the sample cell is another issue that should not be overlooked. The sample cell should be clean and have minimum surface reflection; otherwise the results may be greatly affected [22]. Any dirt or scratch (e.g. a fingerprint) on the cell walls may behave like a local oscillator if it just happens to be illuminated by the incident beam. Thus, in a self-beating experiment (Scheme A, Figure 2.17),  $I_L$  will not be zero and the interpretation of the ACF using Eq. 2.34 will lead to unpredictable result. A useful check for the cleanliness of the medium and sample cell is to perform a quick PCS measurement of the medium only (better if made at a small scattering angle); this should produce a flat ACF with a very low count rate.

### *Particle Concentration*

Sample concentration should be adjusted so that the scattering from the particles is much stronger than the scattering from the medium's molecules but not so strong to saturate the PMT or overflow the correlator channels. Typically, the count rate should be between  $10^4$ - $10^6$  s<sup>-1</sup>. If the suspension is milky white then it is obviously too concentrated. Using a laser beam (e.g., from a laser pointer) to illuminate the suspension, if the beam does not appear as a line but instead as a spreading halo, then the concentration is too high. Too high a concentration will cause multiple scattering and particle-particle interactions that complicate the data analysis process. These effects are discussed later in this chapter. If the concentration cannot be further reduced yet the scattering is still too strong, some instrument adjustment, such as the use of a smaller aperture or a lower laser power, has to be made. If needed, any dilution should be carried in a clean vial and not in the sample cell. On the other hand, too low a concentration will cause particle number fluctuations which invalidates the standard ACF theory, produce too weak scattering, and reduce the signal-to-noise ratio and measurement efficiency. In Eq. 2.33,  $G_s^{(2)}(\tau)$  is the ACF of scattering from particles and the medium's molecules. If we further separate these two terms, Eq. 2.33 becomes:

$$\begin{aligned}
 G_s^{(2)}(\tau) &= \langle I_p + I_m \rangle^2 + \left| (A_p E_p(t) + A_m E_m(t))(A_p E_p^*(t + \tau) + A_m E_m^*(t + \tau)) \right|^2 \\
 &= \langle I_p + I_m \rangle^2 + \left| (A_p^2 E_p(t) E_p^*(t + \tau)) \right|^2 \quad \text{or} \\
 g_s^{(2)}(\tau) &= 1 + \frac{I_p^2}{I^2} \left| g^{(1)}(\tau) \right|^2.
 \end{aligned} \tag{5.5}$$

In Eq. 5.5, the correlation of medium's molecules is assumed to occur in a time scale much faster than that of the particles so their correlation is neglected. The measured ACF amplitude depends upon the total scattering from particles over

and above the scattering of the medium. For an acceptable amplitude value, one should observe a sample count rate at least 2.5 times higher than that of the medium.

### *Instrument Condition*

Any instrument should be carefully checked for mechanical stability and electrical noise. Because PCS is a time correlation measurement, any mechanical instability, such as table and/or building vibrations, and electrical noise, such as power line noise or interference caused by other appliances (such as motors, fans, etc.), should be avoided. Additionally, the instrument should be turned on for some period of time prior to use to stabilize the laser source so that no light intensity drift occurs during the measurement, and a stable temperature gradient is established between instrument and room temperature. The sample should be placed in the sample holder long enough to reach the desired temperature.

### *ACF Delay Time*

A proper delay time range, sample time and the ratio of the delay time increment between groups of channel should be chosen according to the correlator specifications. The range should be able to measure the slowest motion but yet not miss the fastest motion to be detected. Many commercial instruments provide an algorithm which automatically determines the proper delay time. For a simple particulate system, such as spherical particles, the proper delay range can be estimated by satisfying  $\tau_{\max} = 2.5/\bar{\Gamma}$  where  $\bar{\Gamma}$  is the mean decay rate of the ACF. (See the next section for a more detailed discussion). For systems involving many kinds of motions, a more sophisticated estimation, or trial-and-error have to be used to find the best sample time, number of delay channel groups, and delay time ratios between the groups. The correctness of the delay time range can be judged by the limiting values of the normalized ACF:  $|g^{(1)}(\tau_1)|^2 \geq 0.998$  and  $|g^{(1)}(\tau_{\max})|^2 \leq 0.005$  usually indicating that all motions detectable have been covered.

### *Scattering Angle*

The choice of a proper scattering angle or angular range is based on the particle size, size distribution, and sample concentration in order to maximize the information obtained and also to increase the signal-to-noise ratio. More discussion about the angle selection and about multiangle measurements is given in the last subsection of this chapter.

### *Measurement Time*

To increase the signal-to-noise ratio and the statistical accuracy, the measurement time should be long enough to produce a smooth ACF. The actual

duration depends on many factors, such as scattering intensity, scattering angle and delay time. Typically, for strong scatterers a minimum time of a few minutes is needed. A much longer time is needed for weak scatterers. To achieve better result, many short measurements should be made instead of making a very long measurement, each of which is normalized and then added together as proposed by Chu ([38] of Chapter 2).

#### *ACF Quality*

The quality of the ACF can be judged by the difference between the measured and calculated baselines, which should be less than a few tenths of one percent. A large baseline difference often indicates too short a measurement time, inhomogeneity in the sample, particle number fluctuations in the scattering volume, or a sudden scattering intensity change caused by dust particles, temperature fluctuation, or changes in the sample. A large baseline difference is often associated with channel overflow in low-bit correlators using prescaling. A good measurement should have no overflow channels.

#### 5.2.9. MULTIANGLE MEASUREMENT

In PCS measurements of monodisperse samples, or samples having narrow size distributions, if motions other than those arising from translation are discounted, there is only one characteristic motion and the scattering from particles will not be detected discriminatorily. Once an appropriate delay time range is chosen for the ACF for a given scattering angle, size information can be retrieved with little bias. Thus, many PCS instruments only employ single angle detection, usually  $90^\circ$ , and consequently experiments are performed only at that angle. However, to obtain an unbiased result for the mean size or size distribution of a polydisperse sample is not an easy task. Measurements at one scattering angle are often inadequate because particles of different sizes have different scattering intensities and different velocities at the given scattering angle. Measurements made at more than one angle (multiangle measurements) provide several advantages and are often necessary in order to obtain a correct result.

The biggest difficulty in using PCS to characterize polydisperse samples arises from the fact that the angular scattering intensity patterns per unit volume for particles of different size (mass) are quite different. This is described in Chapter 2 and shown in Figures 2.4, and 2.7 - 2.11. In the submicron-to-micron size range the larger the particles are the larger the absolute scattering intensity per unit volume will be at small scattering angles. As a first order approximation, the scattering per unit volume is proportional to the mass of the particle at small scattering angles. The shape of the angular pattern becomes smoother and less angle-dependent as particles get smaller. Because the particles in the sample have different scattering intensities per unit

volume for a given scattering angle, the signal detected is weighted by the scattering intensity of the sample constituents and not by the volume or weight percentage of these constituents.

In general, a measurement performed at small scattering angles will be heavily weighted by any scattering from larger particles in the sample; and a measurement performed at large scattering angles will be weighted more by the scattering from smaller particles in the sample. In many cases, because of the angular scattering pattern, there may be not enough scattering from particles of a particular size at the measurement angle. This is especially true for particles larger than the wavelength of light in the medium. Figure 5.7 displays the scattering from a unit volume of particles of different sizes at three scattering angles, and Figure 5.8 displays the scattering from a unit volume of particles of three sizes made at different scattering angles.

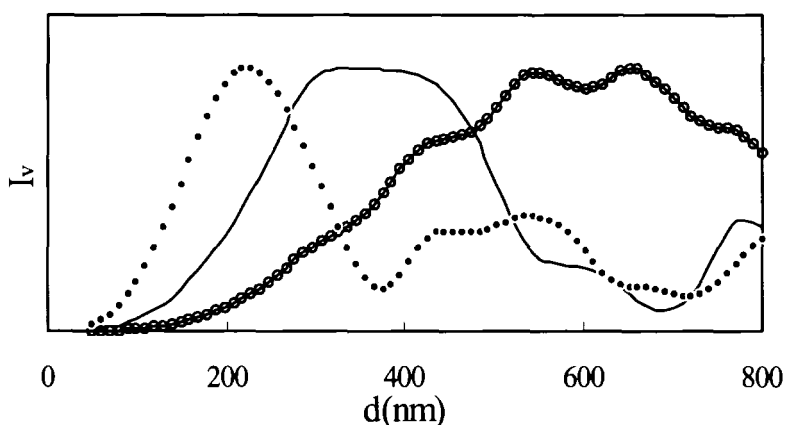


Figure 5.7. Unit volume scattering from glass beads in water at scattering angles of 15 degrees (solid line with hollow spheres), 45 degrees (solid line), and 90 degrees (dots) for  $\lambda_0 = 633$  nm. Each curve is differently scaled.

In a sample that contains a mixture of equal volumes of 600 nm and 100 nm glass beads, there will be little signal from the 100 nm particles ( $\sim 1\%$ ) if the measurement is performed at 15 degrees. Obviously, the resolved size distribution will be distorted. Thus, although bias due to the different scattering intensities from particles of different sizes may be corrected by changing the weighting of the retrieved size distribution from one that is intensity-weighted to one that is volume-weighted by using a proper model (e.g., Mie theory can be used for solid spheres, and various form factors can be used for submicron particles of other shapes), such correction will not be effective, or will introduce large uncertainties, if in the first place information is missed due to the

extremely weak scattering from certain components at the measurement angle. Therefore, if the measurement is only performed at one angle, even if the distribution is reweighed, the result may be still incorrect. A multiangle measurement is necessary in these cases to eliminate the blind spot effect and to confirm and verify the size distribution.

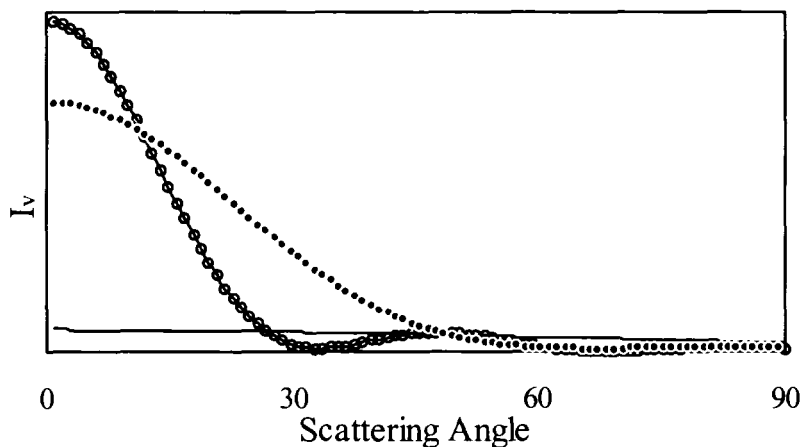


Figure 5.8. Unit volume scattering patterns for glass particles in water ( $d = 800$  nm (solid line with hollow spheres), 500 nm (dotted line) and 200 nm (solid line)) at  $\lambda_o = 633$  nm.

Depending upon their size distribution range, for many samples there is an optimal angular range over which the least biased size distribution can be obtained. For example, it is clear from the scattering patterns in Figure 5.8 that for a mixture of equal volumes of 200 nm and 800 nm glass particles the best angular range would be from about 40 to 55 degrees. At scattering angles smaller than 15 degrees, the scattering from the 800 nm particles will overshadow the scattering from the 200 nm particles even when using a delay time suitable for the 200 nm particles; and vice versa for the 800 nm particles at scattering angles greater than 60 degrees. In fact, there is a blind spot at around 30 degrees for the 800 nm particles in this particular case. In another application, a multiangle analyzer may be used to choose a specific angle in order not to “see” certain constituents as opposed to optimize signals from all constituents as described above. Examples of such applications are in the measurement of the main component in contaminated samples; or detecting trace amounts of small particles in samples that are mainly composed of large particles, etc.

Scattering intensity per unit volume is proportional to the mass of the particle. For spherical scatterers, the mass of solid particles varies as the cube of

their diameter, and the mass of macromolecular chains varies only approximately as the square (or at times less) of their hydrodynamic diameter. Thus, for the same size range, the scattering intensity dilemma in angle selection is less pronounced for macromolecule chains than that for solid particles.

The second difficulty in a PCS measurement of polydisperse samples is that each moving particle has its own distinctive velocity, or rate of diffusion, covering a wide dynamic range. Conventional correlators with delay time arranged linearly will not perform satisfactorily. With a finite number of delay channels (typically between 64 channels to 1024 channels), the measurement of a wide range of velocities cannot be accomplished. If the delay time is too short, the slow motion from large particles may not be fully covered. If the delay time is too long, the details of the fast motion from small particles will be missed. In either case, some bias in the size information obtained will be unavoidable. To make a more complete analysis of all kind of motions, one has either to make a few measurements using different delay times at the same scattering angle, or make a multiangle measurement. The benefit of a multiangle measurement rests on the fact that the same motion viewed at different angles is different. If a person stands on a road and watches a car driving away, he or she will perceive a much slower speed of the car compared with that when he or she stands on the side of the road and experiences the car passing by him or her. Similarly, when measuring the rate of particle diffusion, the choice of delay time and thus the dynamic range are closely dependent on the detecting angle. A PCS measurement can be thought of as a measure of time that it takes for a particle to diffuse a distance  $K^{-1}$ . This time is proportional to  $K^{-2}$ . Thus, for example, the time for the diffusion process viewed at 15 degrees is 29 times longer than that for the same process measured at 90 degrees. In other words, a measurement at a small angle effectively slows down the diffusion process of fast moving particles as viewed by the detector. Consequently the delay time used for the experiment can be increased by the same factor. For example, in cases when measurement is performed at 90 degrees, even using the shortest delay time of the correlator, particle motion still cannot be recorded because it is too fast; using a smaller angle (e.g., 15 degrees) may allow one to collect an ACF containing the necessary information.

The third advantage of multiangle PCS measurements is related to sample concentration. Ideally the sample concentration for PCS measurements must be dilute enough so that multiple scattering and particle interactions can be avoided and the scattering will not saturate the detection device. The sample concentration also cannot be so dilute that the scattering intensity is not intense enough to produce a good signal-to-noise ratio, and satisfy the statistics for photon correlation. However, there are many instances where sample concentration cannot be adjusted to fit the experimental parameters. Several

examples are: a) when the concentration is already very low, as in many biological samples; b) if the original concentration is high, but the scattering is still weak, as in many surfactants and synthetic polymer samples; and, c) the concentration is too high causing detector saturation yet the sample cannot be diluted otherwise the particles will change. In these examples, one needs to adjust experimental conditions so that a proper measurement can be made. Changing the scattering angle is the most feasible and convenient approach.

The amount of light scattered onto the detector is directly proportional to the scattering volume. In the collecting optics, such as the ones described in Figure 5.4, the scattering volume at a scattering angle  $\theta$  is greater than that at 90 degrees by at least a factor of  $(\sin\theta)^{-1}$ . By this relation, for example, about 3.9 times as much light is collected at 15 degrees as compared to that at 90 degrees. Since the signal-to-noise ratio is proportional to the square of the light intensity, the signal is improved by a factor of 15 over that for the 90 degrees scattering angle. For over-diluted or weakly scattering samples, performing the measurement at small angles is equivalent to using a more powerful laser. On the other hand, for samples that scatter too much light, measurement at large angles will effectively reduce the scattering intensity reaching the photodetector, thus avoiding possible detector saturation.

An additional concentration effect in multiangle measurements is related to the detection time scale. Because at smaller scattering angles longer delay times have to be used, more light can be collected, permitting measurement of weakly scattering samples. Conversely, performing measurements at large angles will effectively speed up the diffusion process, enabling measurement of strongly scattering samples by using a short delay time. Thus, by changing the scattering angle, one effectively changes the scattering volume and the time scale for the diffusion process, which is equivalent to manipulating sample concentration without actually changing the sample.

Finally, the necessity of multiangle measurement lies on the fact that except for spheres, the measured ACF includes coupled signals from both translational and rotational motions. Without decoupling the two types of motions, further characterization of particle shape and size is impossible. In many cases, this type of data interpretation can only be accomplished by combining the ACF from several angles. A further explanation of this issue is provided in the next section.

### 5.3. Data Analysis

In this section, we will limit our discussion to the most common PCS application - the scattering from particles in dilute suspensions or solutions, in which particles move and scatter independently without influence from other



particles and without the use of a reference beam (Scheme A, Figure 2.17). Here,  $I_L$  is equal to zero and Eq. 5.5 is the “master” equation. Eq. 5.5 describes an ideal situation in which all incident photons are completely coherent and photon beating at detector surface is also perfectly synchronous. In any real experiment, due to various reasons such as a finite scattering volume, electronic and optical noises, etc., the photon mixing efficiency is always less than unity. Therefore an instrument efficiency coefficient  $\beta$  is introduced to account for these factors,  $\beta$  is always less than one. The value of  $\beta$  often is an indication of the overall efficiency of the PCS instrument, especially the optical part. Eq. 5.5 is now written as:

$$|g^{(1)}(\tau, K)| = \sqrt{\frac{G^{(2)}(\tau, K) - A}{A\beta'}} = \sqrt{\frac{g^{(2)}(\tau, K) - 1}{\beta'}}. \quad (5.6)$$

The variable  $K$  is added indicating that the ACF is also a function of the scattering angle  $\theta$  when  $\lambda$  is fixed and the subscript  $s$  in  $G_s^{(2)}$  and  $g_s^{(2)}$  is dropped for the sake of clarification.  $\beta' (= I_p^2\beta/I^2)$  is the measurement efficiency coefficient.  $\langle I_p + I_m \rangle^2$  is replaced by the conventional notation  $A$  which is the baseline in the ACF.

### 5.3.1. ANALYSIS OF CHARACTERISTIC DECAY CONSTANT

For a polydisperse particulate system in dilute suspension or solution, the electric field ACF,  $g^{(1)}(\tau, K)$ , is a summation of the exponential decay functions, each with a characteristic decay constant  $\Gamma$  which is the reciprocal of the time scale for the corresponding particle diffusion:

$$|g^{(1)}(\tau, K)| = \sum q(\Gamma_i) \exp(-\Gamma_i \tau) = \int_0^\infty q(\Gamma) \exp(-\Gamma \tau) d\Gamma \quad (5.7)$$

Figure 5.9 is an example of an ACF showing characteristic exponential decay. In Eq. 5.7,  $i$  represents a group of particles with population  $q(\Gamma_i)$  that has the same characteristic decay constant  $\Gamma_i$ .  $q(\Gamma_i)$  and  $q(\Gamma)$  are the intensity-weighted discrete and continuous distributions of the decay rates, respectively. The parameter  $\Gamma$  is related to the translational and rotational motions of particles in a given medium. For a macromolecular chain,  $\Gamma$  is mainly determined by its chain length and conformation in the medium. For a soft particle,  $\Gamma$  relates to the softness, flexibility, dimension and shape of the particle. For a solid particle,  $\Gamma$  is characteristic of its shape and dimension. It should be noted that, except for

limited types of particles (such as solid spheres), each particle may have more than one decay constant. For example, a rod-shaped particle will have at least one decay constant related to its translational motion and another one for its rotational motion; if both these motions can be detected. For this reason, generally speaking, neither  $q(\Gamma_i)$  nor  $q(\Gamma)$  is necessarily related to a particle size distribution in a straightforward manner.

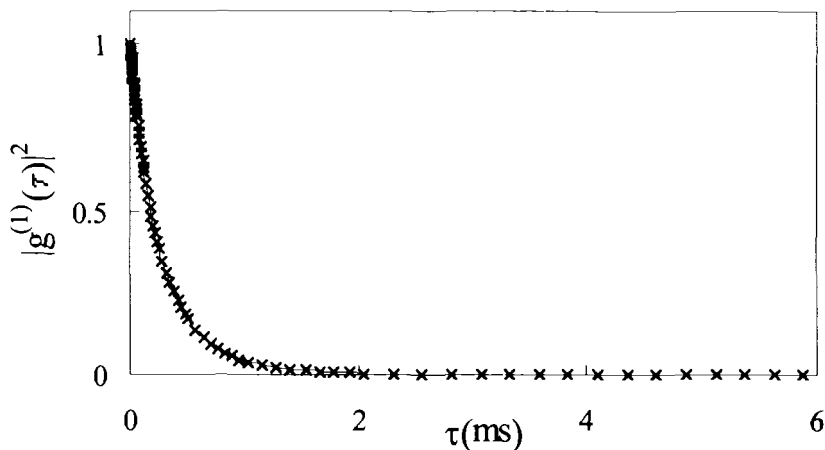


Figure 5.9. A typical ACF.

Once  $q(\Gamma)$  is obtained, one is able to obtain some dimension of the particles, which often is the primary interest in particle characterization using PCS experiment, when combined with other known information of the sample. Thus, resolving  $q(\Gamma)$  in Eq. 5.7 from the measured  $g^{(1)}(\tau, K)$  is the key step in the data retrieval process.

There are three common routes one can take to obtain the decay characteristics of the particles' motions from the ACF. The first is to calculate the mean value and other moments ignoring the details of  $q(\Gamma)$ . The second is to use an assumed or known analytical distribution form. In this case, the task is simply to adjust the variables of the analytical form so a best fit to the experimental data can be found. The third route is to resolve the complete distribution by performing an inversion of the Laplace integral equation (Eq. 5.7). Detailed mathematical derivations of these methods can be found in the literature, but are beyond the scope of present text. The important aspect for most readers is to understand the nature, jargon (technical terms), the application range, and the most appropriate use of each method. A detailed discussion of PCS data analysis methods can be found elsewhere [23].

*Cumulants Method [24,25]*

The cumulants method is a moment expansion method. It compresses the entire multi-exponential decay distribution into the exponent and then expands the exponent  $\Gamma$  to a polynomial expression of the cumulants (the moments) and is:

$$\begin{aligned} |g^{(1)}(\tau, K)| &= \exp\left[\sum_{m=1} C_m (-\tau)^m / m!\right] \\ &= \exp\left[-\bar{\Gamma}\tau + \frac{1}{2!}\mu_2\tau^2 - \frac{1}{3!}\mu_3\tau^3 + \frac{1}{4!}(\mu_4 - 3\mu_2^2)\tau^4 - \dots\right], \end{aligned} \quad (5.8)$$

in which  $C_m$  is the  $m^{\text{th}}$  cumulant,  $\bar{\Gamma}$  is the mean decay constant, defined as

$$\bar{\Gamma} = \int_0^{\infty} \Gamma q(\Gamma) d\Gamma \quad (5.9)$$

and the central moments  $\mu_i$  are

$$\mu_i = \int_0^{\infty} (\Gamma - \bar{\Gamma})^i q(\Gamma) d\Gamma. \quad (5.10)$$

Here, the standard deviation is the square root of the second moment. The third moment describes the extent of the distribution's asymmetry. The ratio of the second moment  $\mu_2$  and the square of the mean value represent a measure of distribution breadth, defined as the polydispersity index (P.I.):

$$\text{P.I.} = \frac{\mu_2}{\bar{\Gamma}^2} = \frac{1}{\bar{\Gamma}^2} \int_0^{\infty} (\Gamma - \bar{\Gamma})^2 q(\Gamma) d\Gamma. \quad (5.11)$$

Because the ACF is a function of the scattering vector  $K$ , all cumulants are also a function of  $K$ . At small delay times, for particulate systems that have size distributions which are not very broad ( $\text{P.I.} < 0.3$ ), the cumulants method has been proven to be able to provide fairly good mean values of  $\Gamma$  over a broad range of practice although it will not accurately recover more than the first three cumulants. Although  $\bar{\Gamma}$  obtained using the cumulants method is not very sensitive to experimental noise, the P.I. is. It has been concluded that the baseline value must be correctly established better than 0.1% otherwise

surprisingly large error occurs in the P.I. value [26]. The current ISO standard recommends only the cumulants method in PCS particle sizing.

Obtaining  $\bar{\Gamma}$  and P.I. from the ACF using the cumulants method can be accomplished by a non-linear least-squares fitting of the ACF  $(\beta^{1/2}|g^{(1)}(\tau, K)|)$  by using the gradient method, the Gauss-Newton method, or the Levenberg-Marquadt method. In the Levenberg-Marquadt method, the set of fitting parameters is found through an iterative procedure that minimizes  $\chi^2$ , the sum of the squares of the difference between the experimental data and calculated data using specified parameters. In the  $(N+1)^{\text{th}}$  step of the iteration, the parameter vector  $\mathbf{P}$  ( $P_1 = \beta'$ ,  $P_2 = \bar{\Gamma}$ ,  $P_{i,i \geq 2} = C_{i-1}/(i-1)!$ ) is calculated by

$$\mathbf{P}^{(N+1)} = \mathbf{P}^{(N)} - [\lambda^{(N)} \mathbf{I} + \mathbf{J}^T \mathbf{J}]^{-1} \mathbf{J}^T \mathbf{R}^{(N)} \quad (5.12)$$

where  $\lambda^{(N)}$  is a scalar quantity, called the Marquardt parameter (which may change with each iteration);  $\mathbf{I}$  is the identity matrix with  $I_{ij} = \delta_{ij}$ ;  $\mathbf{J}$  is the Jacobian matrix whose elements are given by  $J_{ij} = \partial R_i^{(N)} / \partial P_j^{(N)}$ ; and  $\mathbf{R}^{(N)}$  is the residual vector at the  $N^{\text{th}}$  estimation with  $R_i^{(N)}$  being the difference between the experimental data and the calculated data using the parameter  $\mathbf{P}^{(N)}$ . The notation  $\mathbf{J}^T$  indicates the transpose of the matrix  $\mathbf{J}$ ; i.e.,  $J_{ij}^T = J_{ji}$ . After  $\mathbf{P}^{(N+1)}$  is obtained,  $\chi^2$  is calculated. If  $\chi^2$  is decreased, a new iteration starts with a smaller  $\lambda^{(N+1)}$ ; otherwise, a larger  $\lambda^{(N+1)}$  is used until the change of  $\chi^2$  is flat or smaller than a fixed amount. In Eq. 5.12, if  $\lambda^{(N)} = 0$ , the algorithm reduces to the Gauss-Newton method, and if  $\lambda^{(N)} \rightarrow \infty$ , the algorithm approaches the gradient method. Detailed discussions of these methods can be found elsewhere [27]. One procedure using the Levenberg-Marquardt method in fitting the cumulants has been described by Chu [28].  $\bar{\Gamma}$  and P.I. can also be obtained by a linear least-squares fit to the logarithm of the ACF with proper statistical weighting for each data point, since the operation of taking the logarithm of the data affects the weighting of the data points. The data points now are not equally significant, although the error associated with counting statistics may not be significantly different between channels. The mean value and polydispersity obtained from the cumulants method are scattering intensity weighted. To convert these values into a volume or number weighted result, one has to assume a form of distribution and use an empirical heuristic correction factor in the Rayleigh scattering regime; the procedure is not easy in practice [29].

### Functional Fitting

The second route to obtain the  $\Gamma$  distribution is by inserting a known analytical function with a few variables into Eq. 5.7. Such a function usually has two parameters, one is related to the mean value and the other to the distribution broadness. These two variables are fitted out through the regression of Eq. 5.7.

Commonly used functions are listed in Table 1.3. In the integral form, the functional fitting involves extensive numerical integration techniques. With the development of the Laplace inversion technique, because of the arbitrariness in choosing a proper function, functional forms are used primarily for theoretical modeling and simulation.

#### *Inversion of Laplace Integral Equation*

Eq. 5.7 is a Laplace transform relation that is a special case of the general class of linear Fredholm integral equations of the first kind since it has a general kernel of  $e^{-\Gamma t}$ . The Laplace integral equation is a mature, accepted technique in mathematics. However, there are two limitations that arise in a PCS experiment that make the transform ill-posed. One is that there are all kinds of noise that do not exhibit the nature of exponential decay but are often random, and several types of distortions in the ACF due to non-ideal experimental conditions, such as non-uniform laser beam profile, insufficient bit resolution in signal quantization, and baseline errors [30]. The second one is that no matter what kind of correlator is used, the bandwidth (the range of delay times) is always limited, i.e., the summation or integration limits in Eq. 5.7 are from  $\Gamma_{\min}$  to  $\Gamma_{\max}$  instead of from 0 to  $\infty$ . Here,  $\Gamma_{\min}$  and  $\Gamma_{\max}$  are not the actual limiting decay characteristics of the sample but the detectable range based on the experimental settings. To resolve  $q(\Gamma)$  from the Laplace inversion of Eq. 5.7 in ill-posed conditions is much harder than that in a perfect condition. In fact, this stands as one of the most severe inversion problems in applied mathematics. Because the problem is ill-conditioned, the amount of information that can be retrieved is quite limited. Much information that otherwise might be recovered is lost in the noise. Any attempt to recover too much information is senseless and often results in physically unreasonable solutions. The exact solution to the problem may not exist, or may be very different from the real distribution of the sample. On the other hand, there will be many sets of approximate solutions that may satisfy certain mathematical criteria through the inversion of Eq. 5.7 or that may fit experimental data equally well. Many of them may have no physical significance. Even very small differences in the ACF may result in quite different distributions after inversion [31]. Generally speaking, experimental error and the structure of the correlator define the class of distributions which all may be candidates for the solution. The better the data, the smaller the number of distributions that will fall within that class, thereby leaving fewer alternatives for the algorithm used in solving the problem. To further reduce the number of possible solutions, the number of the degrees of freedom needs to be reduced. One constraint widely used in many algorithms is that all amplitude values in the solution have to be positive. Since a distribution can never be negative, no matter whether it is a distribution of particle size, diffusion coefficient, or other physical properties, the constraint, i.e., non-negative

solution is always valid and its use is always justified. Addition of this constraint to a well-formed algorithm dramatically reduces the class of possible solutions. However, the number of the remaining solutions that can fit experimental data well may be still too many and one cannot pick one of them at random and assume that it accurately represents the actual distribution. Different algorithms or inversion strategies having further constraints are then developed out of the necessity to find the best solution which is most likely to be the true distribution.

In many inversion methods, a set of  $N$  discrete numbers  $q(\Gamma_i)$  that represent the continuous distribution  $q(\Gamma)$ , spaced in a particular pattern, (commonly linearly or logarithmically), over a chosen range of  $\Gamma$ , results in the following set of equations:

$$g^{(1)}(\tau_j, K) = \sum_{i=1}^N q(\Gamma_i) \exp(-\Gamma_i \tau_j) + \varepsilon_j \quad (j=1,2,3,...M). \quad (5.13)$$

In these equations, the set of  $\Gamma_i$  is fixed. The task of the inversion algorithm is to find the best, physically meaningful  $q(\Gamma_i)$  values that will produce the best fit to the ACF.  $\varepsilon_j$  is the measurement error of each ACF channel that can be estimated according to a theoretical model [32].

Through intensive research and development of information retrieval procedures to obtain  $q(\Gamma)$  from PCS measurements, both in mathematical formulation and in practical verification, several feasible and reliable algorithms have emerged [33]: namely, a histogram that uses a relatively small number of intervals with specified boundaries approximating the distribution [34], multiexponential eigenvalue decomposition [35]; singular value decomposition using the decay rate of the singular numbers to find a stable and reliable solution without an *a priori* parameter setting [36,37,38]; exponential sampling that specifies the distribution as a small number of *a priori* spaced delta functions [39]; the maximum entropy method [40,41]; and the regularized non-negative least-squares method [42, 43]. We will only discuss the last two methods, which are the most widely used.

*Maximum Entropy Method (MEM).* MEM is based on information theory that the information content of a physical system is related to its entropy in a logarithmic formalism. The induced probability distribution of the system is the only one having the maximum entropy and corresponds to that with the minimum assumption about the system. In a PCS application, reconstruction of  $q(\Gamma)$  is based on the Shannon-Jaynes entropy model. The most probable solution of  $q(\Gamma)$  or  $q(\Gamma_i)$  will be the one that will maximize the entropy function. In its discrete form, the function is

$$S = - \sum_{i=1}^N \left( q(\Gamma_i) \ln \left( \frac{q(\Gamma_i)}{A_o} \right) - q(\Gamma_i) \right). \quad (5.14)$$

$A_o$  is a prior uniform probability assignment (which can be set to  $\sqrt{\beta'}/N$ ) and  $q(\Gamma_i)$  is the discrete amplitude of the distribution over logarithmically spaced  $\Gamma$ ; i.e., the x-axis is equally spaced as  $\ln \Gamma$ . If  $\Gamma$  is linearly spaced for narrow distributions,  $A_o$  will not be a constant for all  $q(\Gamma_i)$  but proportional to  $\Gamma_i^{-1}$ , and the algorithm is not very effective. The maximization of  $S$  in Eq. 5.14 is also subject to the minimization of the residual  $\chi^2$ .

There are many ways to solve this nonlinear equality-constrained optimization problem. One method is the quadratic model approximation [44]. The maximum entropy method can provide the least biased estimates on the basis of available information about the problems. The proven objectivity of the method relies on the fact that the solution is dictated purely by the experimental data and the nature of the problem, not by an arbitrarily introduced differential operator such as the ones may be found in the regularization method.

*Regularized Non-Negative Least-Squares Method.* This method uses the corresponding system of normal equations to find the unknown coefficient. In order to further reduce the class of possible solutions, a regularizer ( $\mathbf{G}$ ) is introduced in a quadratic form when solving the weighted least-squares problem. During the fitting process, instead of minimizing the residue between experimental data and calculated values from the fitted parameters, the algorithm minimizes the regularized residua:

$$\chi^2(\alpha) = \left\| \frac{\mathbf{g} - \mathbf{A}\mathbf{q}}{\boldsymbol{\sigma}} \right\|^2 + \alpha^2 \|\mathbf{G}\mathbf{q}\|^2. \quad (5.15)$$

In Eq. 5.15,  $\mathbf{A}$ ,  $\mathbf{q}$ ,  $\mathbf{g}$  and  $\boldsymbol{\sigma}$  are the  $m \times n$  kernel matrix, the distribution vector, the ACF vector, and the error vector, respectively. The regularizer  $\mathbf{G}$  is a linear constraint operator that defines the additional constraint to the process. The best possible fit is sacrificed in order to find a reasonable and stable solution.  $\mathbf{G}$  can be set in various values: the identity matrix, the first derivative operator, or the second derivative operator. The coefficient  $\alpha$ , called the regularization parameter, allows the process to define the strength of the constraint in the solution. A value of zero leads the algorithm back to a normal non-negative least-squares result. A small value does not introduce any effective constraint and so the result may be unstable and may have little relation to the actual solution. Values that are too large are insensitive to the measured data, resulting

in a solution that is smooth (and “nice”) but underfits the data and hence extracts only part of the information available [45].

Regularized non-negative least-squares is the most widely applied Laplace integral transform algorithm. In particular, the well-documented computation routine known as CONTIN created by Provencher utilizes regularized non-negative least-squares technique combined with eigenfunction analysis. It has won wide acceptance and has been implemented as the main data retrieval algorithm for PCS in many research laboratories throughout the world and in several commercial instruments. CONTIN uses a non-linear statistical technique to smooth the solution and reduce the number of degrees of freedom to an acceptable level. Prior knowledge of the expected distribution is needed since users need to specify the distribution range, the number of data points and other constraints. The regularization parameter can be automatically chosen on the basis of an F-test and confidence levels. CONTIN takes into account the weighting of the distribution due to the use of discrete data points in the continuous distribution and then calculates different moments of the computed distribution [46]. CONTIN is often used as the reference point when evaluating performance of other algorithms.

With careful sample preparation, temperature stabilization, and extended data acquisition time, information in the ACF can be retrieved well using the Laplace inversion technique. However, due to the nature of the technology, the resolution of the distributions retrieved from PCS measurements is low. Generally speaking, a peak resolution of no less than two in the  $\Gamma$  distribution can be achieved for ideal samples such as mixtures of monodisperse spheres. In other words, if two subpopulations in the sample have a peak ratio  $\Gamma_{\text{peak1}}/\Gamma_{\text{peak2}} \geq 2$ , these two subpopulations can be resolved. Of course, the above statement is subject to the width and distribution shape of each subpopulation. Practically, a peak resolution of three is not difficult to achieve. There are many examples in the literature regarding the effectiveness of the Laplace inversion in retrieving a multimodal distribution over a broad  $\Gamma$  range (typically 2 to 3 decades) by either computer simulated or real experimental ACFs [47]. Due to the nature of the exponentially decaying ACF, most inversion techniques work in a logarithmically scaled space. The output from such inversions are also logarithmically spaced where the discrete fractional distribution  $q(\Gamma_i)$  can be equalized to the continuous distribution  $q(\Gamma)$  after each point in  $q(\Gamma_i)$  is multiplied by a factor  $\Gamma_i^{-1}$  [39]. Consequently, an equal resolution throughout the distribution is only true for  $\log(\Gamma_i)$ , and not for  $\Gamma_i$ .

*Parameter Selection for the Inversion Process.* There are many parameters that need to be set (and can be adjusted) in the Laplace inversion algorithm. Although each algorithm has different parameters and the importance and



sensitivity of these parameters may vary, there are several parameters whose effects are worthwhile to discuss here to provide some general guidelines:

- a) **The Range of Corrector Channels in the Inversion Process.** This is particularly important when it is known in advance that some of the channels contain incorrect or biased information which will distort the result. This often happens in channels at the beginning or at the end of the ACF. When the delay time is very short, in some correlators, the first channel is often affected by noise from electronics and appears as a very fast decay. When the delay time is very long, channels at the end of the ACF are more susceptible to environmental disturbances such as table vibration. Thus, one may want to exclude certain channels in order to get a better result.
- b) **The Number of Discrete Intervals in the Computed Distribution.** The number of size bins in a distribution is primarily determined by the information content of the ACF, the goodness of the fitting algorithm and historically, computing power. The information content of the ACF is dependent upon noise, correlator structure and the distribution itself. Choosing too large a number of bins (e.g., larger than 50) will produce a non-stabilized and thus distorted solution since the information to be sorted is more than the ACF contains. Too small a number of bins (e.g., smaller than 15) will cause reduced resolution and the distribution will not have enough detail to provide a good fit to the experimental data and again a distorted solution will be produced. Any practical setting for bin numbers has to be based on experience, trial and error, and prior knowledge. The intervals between bins can usually be set either linearly or logarithmically. The latter is preferred for broad distributions. Data points in the distribution obtained in the unequally spaced discrete intervals have to be properly reweighed if they are to be presented in equally spaced intervals. Otherwise, the continuous distribution represented by these discrete points will be biased.
- c) **The Distribution Range (the Upper and Lower Limits).** These parameters define the range over which the distribution is computed. This range should be set to include the slowest and fastest exponential components detected during the ACF measurement that can be recovered. If the range is too wide the actual distribution may have too few bins, resulting in low resolution. On the other hand, if the range is too narrow part of the actual distribution may fall outside the range, but the fitting process will still try to find the best solution within this narrow range. The result of this misfitting is often non-predicable. In many inversion algorithms the best resolution and information retrieval occur in the middle of the distribution range. Therefore, it is always advisable to use a wider range than that of the actual distribution.

- d) The Baseline Value. As discussed earlier, there are two baseline values in an ACF measurement: the measured baseline and the calculated baseline. Ideally these two values should be the same. In reality, there is always a difference between the two values. The larger this difference, the worse the measurement. Since the Laplace inversion process is performed to the first order ACF  $g^{(1)}(\tau, K)$ , the baseline value (the normalization factor  $A$  in Eq. 5.6) is vital in converting  $G^{(2)}(\tau, K)$  to  $g^{(1)}(\tau, K)$ . Any uncertainty in  $A$  will introduce a systematic error in  $g^{(1)}(\tau, K)$ . Because all data points are divided by the same  $A$  value, the normalization errors increase as the values of  $g^{(1)}(\tau, K)$  decrease, which can be approximated by

$$\frac{\Delta g^{(1)}(\tau, K)}{g^{(1)}(\tau, K)} = -\frac{1}{2} \left( \frac{1}{(g^{(1)}(\tau, K))^2} + 1 \right) \frac{\Delta A}{A}. \quad (5.16)$$

A 0.25% variation in the baseline value may produce a completely different solution [48,49]. Since random noise always exists no matter how good the data is, at the end of ACF,  $G^{(2)}(\tau, K)$  may be smaller than  $A$  (see Eq. 5.6). The expression under the square root sign may be negative. Thus, in converting  $G^{(2)}(\tau, K)$  to  $g^{(1)}(\tau, K)$  the square root of a negative number may have to be taken. Several “tricks” are used for channels where  $(G^{(2)}(\tau, K) - A)$  is smaller than zero: 1) the channels are discarded; 2)  $g^{(1)}(\tau, K)$  is set to zero; 3)  $G^{(1)}(\tau, K)$  is estimated as  $-(G^{(2)}(\tau, K) - A)^{1/2}$ . All three approaches will increase random error and may even introduce systematic error. The third “trick” is used most often, although it is odd from a purely mathematical point of view. Thus, question of whether the measured baseline, or the calculated baseline, or a value somewhere in between should be used in the inversion process should be left open. Judgement should be made based on the fitting result. An alternative to avoid such error is to compute the distribution in two stages. In the first stage, the inversion is based on  $(g^{(2)}(\tau, K) - 1)$  to calculate  $q(\Gamma) \cdot q(\Gamma)$ . The smoothed estimation of  $g^{(2)}(\tau, K)$  is then computed and used to compute  $g^{(1)}(\tau, K)$ .  $q(\Gamma)$  is finally fitted out from the newly computed  $g^{(1)}(\tau, K)$  [50].

#### *Judgment of the Computed Distribution*

If one knows how many peaks the distribution should have and where these peaks are located, one should have no difficulty in judging whether the result from the inversion process is reasonable or not. The more knowledge about the sample one has, the better one can justify the result. Since we are dealing with an unstable and ill-posed mathematical problem, the solution is not unique and generally is not the one that provides the best fit to the experimental data.

Instead, the solution should be the one that provides a reasonable fit but is stable enough. “Stable enough” means that the solution will not change drastically with small changes in any parameter or in the experimental data. For example, one would expect to obtain similar distributions from several measurements made on the same sample, although the data will differ slightly due to the inevitable experimental noise. Another indication is that the result doesn’t change drastically when the distribution fitting range or the number of bins are varied slightly. One judgement from a mathematical point of view is the residual error distribution for each channel. A reasonable and stable fit should have a random distribution of the residual values in all channels.

### *Data Analysis of Multiangle Measurement*

There are two data analysis schemes in a multiangle PCS measurement. The simpler one is the analysis of the ACF measured at some single angle using one of the algorithms described above. This type of analysis is useful in finding the best angle at which the least biased result can be obtained.

In addition to the theoretical reasons explained earlier, there are several experimental error sources that can cause discrepancies in results at different angles. Avoiding and correcting these sources of error are vital in obtaining a correct size distribution. Some common error sources are:

- a) incorrect angular values resulting from instrument misalignment;
- b) a scratch or spot on the sample cell surface producing a strong local oscillator which changes the experiment from one that is self-beating to one that is homodyne;
- c) incorrect delay time;
- d) a few foreign particles drifting in and out of the scattering volume causing fluctuations in particle number and baseline error;
- e) a dynamic sample that changes with time.

One big disadvantage of separately analyzing the ACF from individual angles in a multiangle measurement is that when the results from different angles are different, even after a proper conversion to present the distributions in volume percentage, one is often puzzled as to which is the correct answer. In these cases, knowledge of the sample and of the scattering technology is needed to correctly interpret the results. In certain instances, a global analysis that incorporates the ACF as well as the scattering intensities (measured using a calibrated instrument) from different angles into the inversion process may present a better approach [51, 52, 53, 54, 55].

In a global analysis, both the ACF’s and the scattering intensities measured at several angles are used in the fitting process simultaneously. For that purpose, the instrument has to be calibrated using intensity measurements in order to account for intensity variations at each angle. For spherical particles, we have the following formula at each angle:

$$\begin{bmatrix} g^{(1)}(\tau_1, K_1) \\ \dots \\ g^{(1)}(\tau_m, K_1) \end{bmatrix} = \begin{bmatrix} e^{-\Gamma_1(K_1)\tau_1} & \dots & e^{-\Gamma_j(K_1)\tau_1} \\ \dots & \dots & \dots \\ e^{-\Gamma_1(K_1)\tau_m} & \dots & e^{-\Gamma_j(K_1)\tau_m} \end{bmatrix} \begin{bmatrix} s(d_1, K_1) & 0 & 0 \\ 0 & \dots & 0 \\ 0 & 0 & s(d_j, K_1) \end{bmatrix} \begin{bmatrix} q(d_1) \\ \dots \\ q(d_j) \end{bmatrix} \quad (5.17)$$

in which  $\mathbf{q}$  is the volume-weighted size distribution, and  $\mathbf{s}(K_i)$  is a  $j \times j$  diagonal matrix whose diagonal components  $s(d_j, K_i)$  are the volume-to-intensity conversion factors. The combination of several ACF's will produce several matrices (the number of the matrix is equal to the number of correlator channel), each of which will have the format:

$$\begin{bmatrix} \langle I(K_1) \rangle^2 g^{(1)}(\tau_m, K_1) \\ \dots \\ \langle I(K_n) \rangle^2 g^{(1)}(\tau_m, K_n) \end{bmatrix} = \begin{bmatrix} \mathbf{K}(K_1) \mathbf{s}(K_1) \\ \dots \\ \mathbf{K}(K_n) \mathbf{s}(K_n) \end{bmatrix} \begin{bmatrix} q(d_1) \\ \dots \\ q(d_j) \end{bmatrix} \quad (5.18)$$

where  $\mathbf{K}(K_i)$  is a  $1 \times j$  matrix whose elements are the kernel of the transform ( $\exp(-\Gamma_j(K_i)\tau_m)$ ) and  $I(K_n)$  is the calibrated intensity at the  $n^{\text{th}}$  scattering angle. A global fitting procedure using all the matrices will yield one size distribution result. Several algorithms have been used in multiangle inversions, for example, the singular value analysis [52,56], the multiangle version of CONTIN [52,53], and the non-negative least-squares technique [54,57]. These methods perform a simultaneous global analysis of several data sets that differ from each other in the scattering intensity and in the values of  $\tau$ . When compared with single angle analysis, the global analysis using one of the above three algorithms for both simulated data and ideal systems such as spherical polystyrene latex has shown improved accuracy (recovering the correct mean values), resolution (resolving individual population from bimodal distribution), sensitivity (detecting minor components in the sample), and reproducibility (repeatable results from multiple measurements) for broad distributions. The result can be further improved if multiangle PCS analysis is combined with multiangle static light scattering experiment [54,57]. These approaches, however, require specific knowledge of the sample material, such as the refractive index, the particle shape, and the angular dependence of scattering intensity, in order to choose proper conversion factors (the matrix  $\mathbf{s}$ ). These approaches work well with spherical particles. There is no conclusive report regarding multiangle analysis for particles of other shapes or with imprecisely known refractive index. In these instances, good results should not be expected.

### 5.3.2. ANALYSIS OF DIFFUSION COEFFICIENT

The characteristic decay constant ( $\Gamma$ ) distribution obtained from the ACF through the algorithms discussed above originates from the motion of the particles. There are several types of motions for a particle of arbitrary shape and internal structure, including those arising from translational diffusion, rotational diffusion, and bending or stretching motions. Other types of motion (such as vibrational motion) exist but are mostly out of the detectable range in a PCS experiment, and so they are not discussed here. For solid particles, the types of motion of interest are limited to translational and rotational motion. For flexible particles, such as liposomes and polymer chains, bending, stretching and contracting are also motions of interest although they are much more difficult to study in a conventional PCS experiment [58].

Diffusion is characterized by the diffusion coefficient, which is the rate of diffusion. The translational diffusion coefficient  $D_T$  is defined by Fick's first law, which states that in the process of translational diffusion the amount of material crossing a plane of unit area per unit time is proportional to the concentration gradient through the diffusion coefficient  $D_T$ .  $D_T$  is expressed in units of area per unit time ( $\text{cm}^2/\text{s}$ ).  $D_R$  is the rate of diffusional rotation along a given axis, and has units of  $\text{s}^{-1}$ . Both  $D_T$  and  $D_R$  vary with suspension temperature and particle concentration. For a particle of arbitrary shape, there will be one translational diffusion coefficient for each direction of translational motion and one rotational diffusion coefficient for each axis of rotation if the motions are anisotropic. However, because PCS is an ensemble technology, the received signal is from particles that are both randomly oriented and moving in all directions, unless oriented by a foreign field. Theoretically, at least for regularly shaped particles the diffusion coefficients for each direction or axis are measurable [59]. In practice, retrieving more than one translational diffusion coefficient and one rotational diffusion coefficient from a PCS measurement is extremely difficult, since all motions are coupled and contribute to the detected signal in a complex manner [60,61]. In the following paragraphs, we discuss the situations in which only one translational diffusion coefficient ( $D_T$ ) and one rotational diffusion coefficient ( $D_R$ ) exist. For spheres or coiled polymer chains, only  $D_T$  is detectable since their rotations are indistinguishable.

We will only discuss polarized ACF measurement, in which the incident light and scattered light have the same polarization, and leave out depolarized ACF measurement. In depolarized ACF experiments, the incident light is perpendicularly polarized as that of the scattered light. Extremely careful measurement is required to collect the signals from the very weak depolarized scattering, which is difficult to perform in ordinary laboratory conditions without a high quality instrument. Interested readers can find discussions of depolarization PCS in [30-40] of Chapter 2.

For a symmetrically shaped particle in the Rayleigh-Debye-Gans scattering regime,

$$g^{(1)}(\tau, K) = \sum_{n=0, \text{even}} P_n(x) \exp[(-D_T K^2 - n(n+1)D_R)\tau]. \quad (5.19)$$

$P_n(x)$  is the  $n^{\text{th}}$  component of the particle scattering factor  $P(x) (= \sum P_n(x))$ , see Appendix V) which can be calculated theoretically. The formulas of  $P_n(x)$  for several particle shapes such as thin rods and thin disks have been derived [62]. From Eq. 5.19, it is obvious that at an arbitrary scattering angle, even for one non-spherical particle, there will be a few components in the  $\Gamma$  distribution representing different couplings between  $D_T$  and  $D_R$ . For a polydisperse system,  $q(\Gamma)$  is a collection of the contributions from different particles of different couplings of  $D_T$  and  $D_R$ . Spheres and random coils of polymer chains will be exceptions. For spheres and random coils all  $P_n(x) = 0$ , except in the case that  $n = 0$ . Therefore,  $q(\Gamma)$  for spheres or coils is proportional to a distribution of  $D_T$ , with each component weighted by the scattering factor  $P(x)$ . For other shapes, the extraction of  $D_T$  and  $D_R$  from  $\Gamma$  is much more difficult. Even for monodisperse samples, since  $P_n(x)$  is a function of  $x$  ( $= KL$  with  $L$  being the particle dimension) and  $P_n(x)$  for different values of  $n$  is different for a given  $x$ , one has to use an iterating method to find the correct particle dimension that best fits the values of  $D_T$ ,  $D_R$  and  $P_n(x)$  for each term. For example in a monodisperse sample of thin rods, the  $\Gamma$  distribution will have the following pairs of numbers:

$\Gamma$	$q(\Gamma)$
$D_T K^2$	$P_0(x)/P(x)$
$D_T K^2 + 6D_R$	$P_2(x)/P(x)$
$D_T K^2 + 20D_R$	$P_4(x)/P(x)$

The mean  $\Gamma$  value is

$$\bar{\Gamma} = D_T K^2 + D_R \sum_{n=\text{even}} n(n+1) P_n(x) / P(x). \quad (5.20)$$

If  $D_T$ ,  $D_R$ , and  $P_n(x)$  as a function of rod length  $L$  are all known,  $L$  can be retrieved, at least theoretically. For real polydisperse samples the task involves substantial data treatment and assumptions [61], if it is possible at all. For several regular shapes such as thin rods and thin disks, when  $x$  is small (typically less than 5)  $P_0(x)$  is the dominant term in  $P(x)$  and all other term are negligible. With increasing  $x$ ,  $P_0(x)$  monotonically decreases to zero and the

higher order terms increasingly affect  $P(x)$  in a progression order as shown in Figure 5.10 [63].

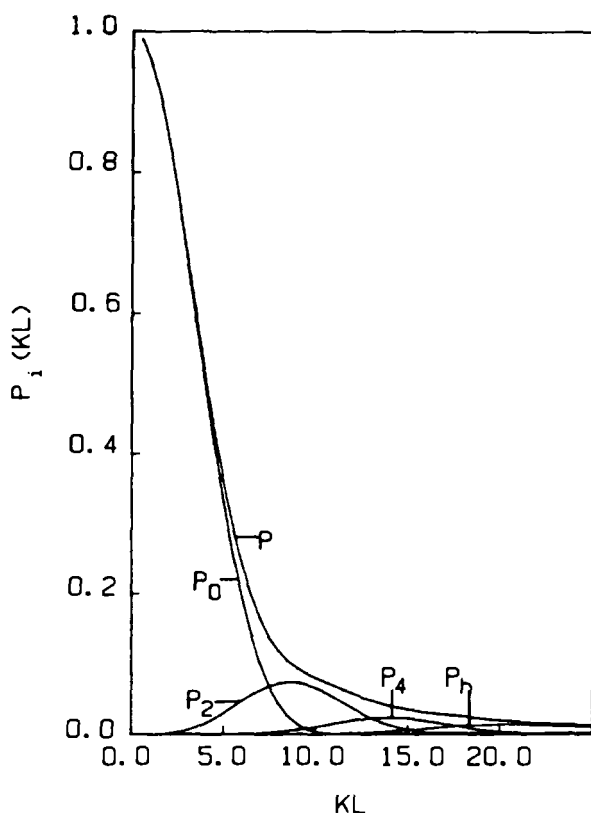


Figure 5.10. Scattering factor of thin disks.  $P_h$  represents the remaining higher order terms. (Reprinted with permission from Xu, R.; Ford, J. R.; Chu, B. In *Particle Size Distribution I*, Provder, T., ed.; ACS Symposium Series 332, American Chemical Society: Washington, DC, 1987; pp115-132. Copyright 1987, American Chemical Society.)

Taking advantage of the fact that  $P(x)|_{x \rightarrow 0} = P_0(x)$  the decay will be related only to  $D_T$  at sufficiently small scattering angles for small particles. Using a dimensionless number  $f$  (which depends on particle structure and other factors), the characteristic decay constant can generally be written as [64]:

$$\Gamma(K) = D_T K^2 (1 + f \langle R_g^2 \rangle K^2). \quad (5.21)$$

Thus the  $D_T$  distribution  $q(D_T)$  of non-spherical particles can be obtained either through a small angle measurement or by extrapolating several  $q(\Gamma)$  functions from multiangle measurements to a zero angle. This extrapolation can be performed based on the mean  $\Gamma$  value or the entire  $q(\Gamma)$  from each angle.

### 5.3.3. ANALYSIS OF PARTICLE SIZE

#### *Concentration Effect*

For a given temperature and viscosity the translational diffusion of the suspended particles is a function of their shape, size and concentration.  $D_T$  is influenced by either too high and too low a concentrations. If the concentration is too high, two effects occur: multiple scattering from overlapping scatterers and a scattering structure factor from particle-particle interactions. Multiple scattering occurs when the light scattered at an angle  $\theta_1$  by an initial particle is then scattered a second time at an angle  $\theta_2$  by another particle. Since  $\theta_1$  and  $\theta_2$  can have any value, the relationship between the desired scattering angle and the real scattering angle becomes ambiguous and the signal actually may come from a broad range of real scattering angles. For example, in Figure 5.11 the detector is located at a scattering angle of 90 degrees. However, besides receiving scattered light from particles 1, 2, and 3 at 90 degrees, the detector also receives secondary scattering from particle 1 by particle 2 and particle 3 at scattering angles  $\theta_1$  and  $\theta_2$ , respectively. Both  $\theta_1$  and  $\theta_2$  are smaller than 90 degrees. In Figure 5.11 the secondary scattering from particles 2 and 3 are not shown. In addition, because the ACF now is computed based on multiple scattered (or “multiply fluctuated”) light, the diffusion coefficient will be apparently larger than that obtained from single scattering, and consequently a smaller particle size will be obtained for spherical particles (Eq. 5.24) [65].

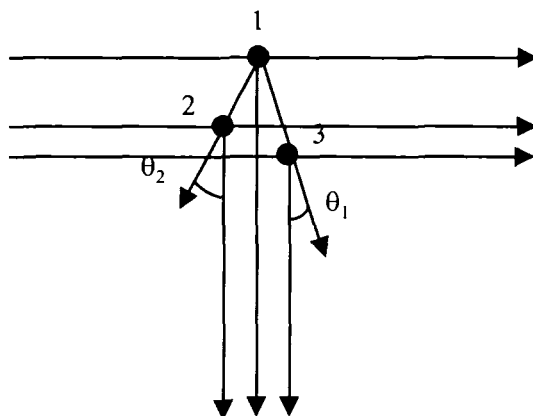


Figure 5.11. Description of multiple scattering.



Particle interactions affect the determination of the diffusion coefficient from the particle's motion [66]. One assumption in PCS measurement of a dilute colloidal suspension is that particles move freely, the only restriction arising from the medium's molecules. When the distance between particles becomes too small, the driving force in diffusion, which is the thermal kinetic energy of a single particle, is altered by particle interaction and the opposing friction force from neighboring particles starts to influence the interaction. Depending on which type of force is dominant (repulsive electrostatic and steric interaction, or attractive van der Waals force) the diffusion coefficient will either increase with increasing concentration (repulsive interaction) or decrease with increasing concentration (attractive interaction). The diffusion coefficient at concentrated samples can be completely different when compared to that of a single particle [67].

The above two effects often coexist. In the case of large particles ( $d$  larger than a few hundred nanometers) the scattering intensity is very strong, multiple scattering can occur even at moderate concentrations. For a fixed volume fraction, the average interparticle distance decreases with particle size. Hence the effect of interaction will be less pronounced. For smaller particles, which scatter much less light even at very high concentrations (e.g., 0.01%), the effect of multiple scattering may not impact the result. Here particle interaction will be the dominant effect. In order to discount the concentration effect so that the size retrieved is closer to the actual dimension, PCS measurements need to be performed in suspensions of very low concentration. Typically the mean distance between particles should be at least 20-40 times of their diameters.

In principle, one should measure the ACF from a suspension as dilute as possible, as long as there is enough scattering. However at too low a concentration the problem of number fluctuation arises. In the derivation of PCS equation Eq. 2.30, it is assumed that the scattered intensity is from a fixed number of particles. If the total number of particles is too small, particles moving in and out of the scattering volume will actually change the total number of particles to a degree that causes significant scattering intensity fluctuation. When this happens, the equations concerning the ACF listed so far would have to be modified. If the same set of equation was to be used, the number fluctuations will cause an extra slow decay in the ACF. This will cause either a large baseline error or a smaller apparent  $D_T$  and consequently a larger apparent size (Eq. 5.24). An example of this was shown in a multi-laboratory round-robin comparison of analysis of a monodisperse latex sample ( $d_{TEM} = 804$  nm). At a volume fraction of  $2 \times 10^{-4}$ , the PCS-determined diameter varied from 1082 nm to 1372 nm [68]. Practically, as suggested by Finsy, the additional intensity fluctuation from number fluctuation can be avoided if the total number of particles in the scattering volume is larger than 1000 [5]. At a typical

scattering volume of  $10^{-3} \text{ mm}^3$ , this criterion is easy to fulfill for particles smaller than 500 nm if the suspension concentration is in the range of  $10^{-4}$  to  $10^{-5}$  volume fraction. For large particles it is not always possible to find a proper concentration that is not so low as to cause number fluctuation and not so high as to create multiple scattering, especially for particles  $1 \text{ }\mu\text{m}$  and larger. Making measurements at small scattering angles with a large scattering volume effectively increases the number of particles, and may partially reduce the number fluctuation. In many instances, however, dilution is not feasible for weak scatterers or flexible chains; in this case extrapolation of the measured  $D_T$  in finite concentrations to the optimal dilution has to be made. As a first order approximation, the concentration dependence of the diffusion coefficient can be written as:

$$D_T = D_T^0(1 + k_d C) \quad (5.22)$$

where  $k_d$  is a system specific second virial coefficient which takes into account all effects related to particle-particle interactions and multiple scattering in finite concentration.

Since for spherical particles there is no detectable rotational motion,  $\Gamma$  is only related to  $D_T$  at any angle, which in turn is directly related to the hydrodynamic diameter  $d_h$  through the well-known Stokes-Einstein equation at some infinite dilution:

$$\Gamma = K^2 D_T, \quad (5.23)$$

$$D_T^0 = \frac{k_B T}{3\pi\eta_0 d_h} \quad (5.24)$$

with  $k_B$ ,  $T$ , and  $\eta_0$  being the Boltzmann constant, the absolute temperature, and the solvent viscosity, respectively.

#### *Absorption Effect*

Absorption of the incident light by the scatterers will lead to local heating of the scattering medium as well as the scatterers. Particles will move faster because of the increase in temperature and the decrease in medium viscosity. In a first order approximation, the measured diffusion coefficient  $D_T'$  is linearly related to the diffusion coefficient without absorption by:

$$D_T' = D_T \left(1 + \frac{\mu_a}{k_T} c I_0\right) \quad (5.25)$$

where  $\mu_a$ ,  $k_T$ ,  $c$  and  $I_0$  are the absorption coefficient, the thermal conductivity, a proportionality constant, and the incident light intensity, respectively. In practice, a linear extrapolation of  $D_T'$  as a function of  $I_0$  to  $I_0 \rightarrow 0$  will yield the correct  $D_T$  [69].

### Hydrodynamic Effect

The fact that the hydrodynamic diameter  $d_h$  obtained from a PCS measurement is not necessarily the dimension of the particle has been neglected by many practitioners for some time. Though it has long been noticed that the  $d_h$  values obtained from PCS measurement even for solid spheres are often larger than the diameters obtained from TEM measurements and change with the suspension condition, such values were used non-discriminatorily as the particle dimension for both research and quality control purposes. Such discrepancies can be as large as 20%. There are several theories regarding the origin of this discrepancy. One popular model attributes the larger apparent size to a hairy layer formed by surface molecular chains [70].

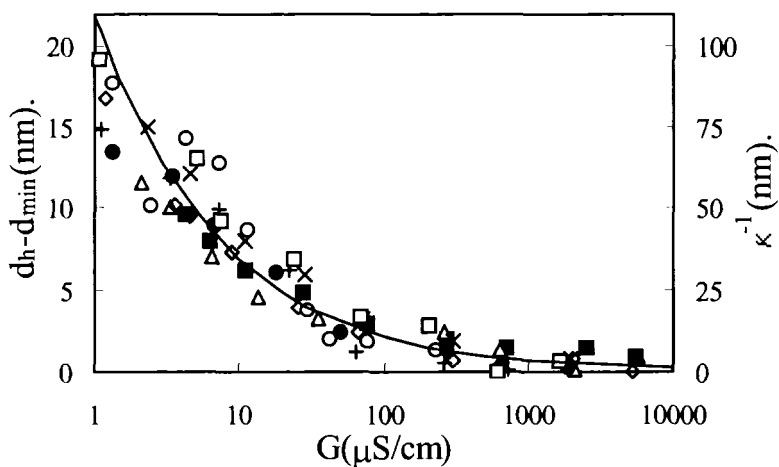


Figure 5.12. Increment of  $d_h$  as a function of suspension conductivity. For each sample, the  $d_h$  at high conductivity, which is very close to the dry value from TEM measurement, is used as the reference point ( $d_{min}$ ). Filled squares: 50 nm PSL; hollow triangles: 83 nm PSL; crosses: 155 nm PSL; hollow diamonds: 304 nm PSL; hollow squares: 120 nm PSL; hollow circles: 300 nm PSL; pluses: 199 nm PSL; filled circles: 100 nm silica. The solid line is the estimated double layer characteristic thickness (the right ordinate). (Reprinted with permission from *Langmuir* 1998, 14, 2593-2597. Copyright 1998 American Chemical Society.)

Recently, in a systematic PCS study several different types of monodisperse spheres (smoothed gold or silica spheres and hairy PSL spheres) were used in order to study the relationship between  $d_h$  and the suspension condition. The diameters of the spheres ranged from 20 nm to 300 nm. In this study, the effects of particle scattering factors, structure factors, and particle interaction were carefully avoided and the suspension conductivity was precisely controlled. It was found that  $d_h$  monotonically increases as the suspension conductivity reduces, as shown in Figure 5.12. This mainly originates from the fact that when suspended particles undergo Brownian motion, they don't move alone. A layer of the surrounding medium which is a part of the electric double layer moves with the particle, leading to a larger  $d_h$  than would be predicted from the solid dimension. The incremental change in  $d_h$  did not show a dependence to the particle surface potential, surface morphology, or particle size. Such an electric double layer could be suppressed by increasing the ionic strength of the suspension. The result suggested that in order to obtain a particle diameter close to its solid dimension, the PCS measurement has to be performed at high ionic strengths, preferably at a conductivity greater than 1 mS/cm, by using a univalent salt. However, the sample stability during the addition of ions has to be monitored closely when making such a measurement [71].

Once  $q(\Gamma)$  is obtained through one of the inversion algorithms and the hydrodynamic and concentration effects have been properly taken care of, the particle size distribution  $q(d)$  for spheres can be obtained through converting  $q(\Gamma)$ . After having determined the range in the  $d$  space required to adequately cover the size distribution, the range can be linearly spaced or logarithmically spaced and the corresponding  $\Gamma_i$  values are calculated according to Eqs. 5.23 and 5.24. By taking into account the Jacobian of transformation and the scattering intensity weighting (e.g., the scattering factor  $P(x)$  in the Rayleigh-Debye-Gans scattering), the ordinate can be converted:

$$q(d) = \Gamma^2 q(\Gamma) / P(x) . \quad (5.26)$$

The weighting factor correction can also be made using other models, such as Mie theory. The mean size obtained from  $\bar{\Gamma}$  through the cumulants fitting method is represented by Eq. 5.27, where  $I_i$  is the scattering intensity from a particle of diameter  $d_i$ .

$$\bar{\Gamma}^{-1} \propto \left( \bar{d}^{-1} \right)^{-1} = \frac{\sum_{i=1}^N I_i}{\sum_{i=1}^N \left( \frac{I_i}{d_i} \right)} \quad (5.27)$$

For particles smaller than the wavelength of light, the scattering intensity is proportional to the volume squared or the sixth power of the particle dimension (Eq. 2.11). Thus, following the convention in Chapter 1 (Eq. 1.14):

$$\left(\overline{d^{-1}}\right)^{-1} = \overline{D}_{6,5} = \frac{\sum_{i=1}^N d_i^6}{\sum_{i=1}^N d_i^5}, \quad (5.28)$$

in which  $\left(\overline{d^{-1}}\right)^{-1}$  is larger than  $\overline{D}_{4,3}$  (the weight average). For larger particles,  $\left(\overline{d^{-1}}\right)^{-1}$  is usually smaller than  $\overline{D}_{6,5}$  and even smaller than  $\overline{D}_{4,3}$  [72].

#### *Multiangle Analysis - Fingerprint*

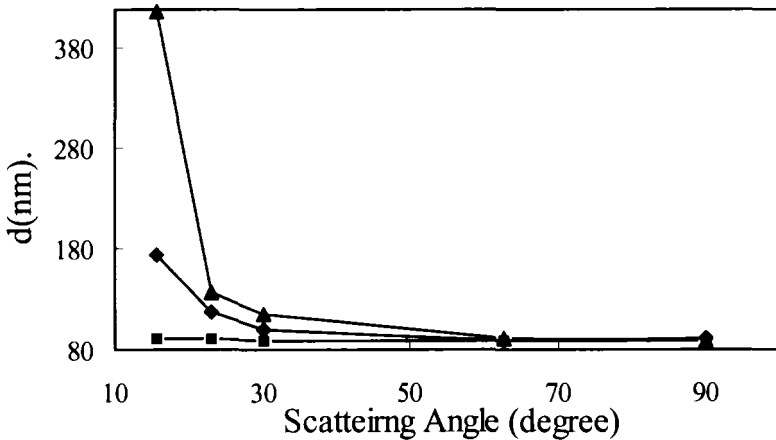


*Figure 5.13.* Fingerprint of multiangle PCS measurements of mixtures of 91 nm and 503 nm PSL particles at different mixing volume ratios ( $C_{91}:C_{503}$ ): Squares (1:0); Diamonds (1:0.0001); and Triangles (1:0.0008).

In practice, one of the best ways to use multiangle measurement in quality control or for trace amount detection is the *Fingerprint Method* [73]. In this method the cumulants analysis is performed on the ACF's at several angles separately; the mean size are then plotted versus the scattering angle. Based on the fact that larger particles scatter more strongly in the forward direction and

smaller particles exhibit a more isotropic pattern, if a sample is polydisperse or multimodal, the mean size value will monotonically decrease as scattering angle increases. If the sample is from a production line and the measurement is for quality control, then the mean size value versus scattering angle, “the fingerprint”, can be used to monitor the sample quality. Other applications of the fingerprint method include colloid stability studies, aggregation or flocculation studies, and adsorption studies. Figure 5.13 shows fingerprints obtained from mixing 503 nm PSL particles into suspension of 91 nm PSL particles at different mixing ratios. Each mixture exhibits a characteristic fingerprint. These fingerprints can be used as an alternative method for sample characterization in lieu of a size distribution, especially in detecting a trace amount of aggregates.

### *Particle Shape Effect*

For non-spherical but symmetrical particles, there are two translational diffusion coefficients; one parallel and one perpendicular to the symmetric axis. However, only the average can be retrieved in most situations. This average translational diffusion coefficient  $D_T$  is related to both dimensions of the particle. It can generally be written in the same formula as the Stokes-Einstein equation:

$$D_T^o = \frac{k_B T}{3\pi\eta_o} A, \quad (5.29)$$

$A$  is a reciprocal of the equivalent hydrodynamic diameter of a sphere. Table 5.3 lists  $A$  values for several common shapes, where  $x = 2b/L$ , with  $b$  and  $L$  being the half-length of the short axis and the length of the long axis, respectively. If one knows or assumes the axial ratio or one of the axis lengths for all particles, then the distribution  $q(L)$  can be obtained from  $q(D_T)$ . This is relatively easy for thin rods or disks. For many products the rod or disk thickness is either a constant or much smaller than the corresponding rod length or disk diameter.

A similar formula (Eq. 5.30) as that given in Eq. 5.29 exists for the rotational diffusion coefficient. In Eq. 5.30,  $B$  is a reciprocal of the equivalent hydrodynamic diameter of a sphere and is listed in Table 5.3 for several common shapes. The mean value for the rotational diffusion coefficient  $D_R^o$  can be obtained from the angular dependence of the mean characteristic decay  $\bar{\Gamma}$  in a multiangle PCS experiment following Eqs. 5.19 and 5.20. If another independent experiment, such as depolarized PCS or transient electric birefringence can be performed to determine  $D_R$ , a combination of  $D_T$  and  $D_R$

can be used to retrieve the dimension of both axes or may even be able to retrieve the distributions of the axial dimensions [61,74].

$$D_R^0 = \frac{k_B T}{3\pi\eta_0} B. \quad (5.30)$$

Table 5.3. Coefficients A and B of non-spherical symmetrical particles

Shape	A	B
Prolate ellipsoid [75] (cigar-shaped, axes = 2b, 2b, L)	$\frac{\ln(x^{-1} + \sqrt{x^{-2} - 1})}{L\sqrt{1 - x^{-2}}}$	$\frac{9\left((2 - x^2)\ln(x^{-1} + \sqrt{x^{-2} - 1}) - \sqrt{1 - x^{-2}}\right)}{2L^3\sqrt{1 - x^{-2}}(1 - x^4)}$
Oblate ellipsoid [75] (disk-shaped, axes = 2b, L, L)	$\frac{\tan^{-1}\sqrt{x^{-2} - 1}}{2b\sqrt{x^{-2} - 1}}$	$\frac{9\left((2 - x^{-2})\tan^{-1}(\sqrt{x^{-2} - 1}) - \sqrt{x^{-2} - 1}\right)}{16b^3\sqrt{x^{-2} - 1}(1 - x^{-4})}$
Infinite thin disks [75]	$\pi/2L$	$9\pi/4L^3$
Thin rod [76]	$\frac{1}{L}\left(6.02 - 4.15\left(\ln\frac{2}{x}\right)^{-1} + 5.8\left(\ln\frac{2}{x}\right)^{-2}\right)$	$\frac{9}{L^3}\left(\ln\frac{2}{x} - 0.9 - 4.05\left(\ln\frac{2}{x}\right)^{-1} + 7.5\left(\ln\frac{2}{x}\right)^{-2}\right)$

### *Distribution Type*

In discussion above, the distributions of  $\Gamma$ ,  $D_T$  and  $d$  obtained from the ACF are primarily intensity-weighted. For example, in the  $\Gamma$  distribution, the amplitude  $q(\Gamma_i)$  represents the fraction of total scattered intensity having the decay constant  $\Gamma_i$ . This intensity-weighted result often is not what one needs. It may have to be converted to weight (or volume)-weighted or number-weighted distributions in practical applications. If one knows the scattering power for particles of a given size, by weighing the original amplitudes of the distribution by the scattering power per particle or per volume, both the number distribution and volume distribution can be obtained. According to the theories introduced in Chapter 2, we can use Rayleigh scattering or Rayleigh-Debye-Gans scattering for small particles. In Rayleigh scattering, the weighting factor will be  $d_i^3$  and  $d_i^6$  for weight distribution and number distribution, respectively. In Rayleigh-Debye-Gans scattering the respective weighting factors will be  $d_i^3P(x_i)$  and  $d_i^6P(x_i)$ . For large spherical particles, Mie theory has to be used, which requires the refractive index of particles to be precisely known [77]. However this type of transformation amplifies the uncertainty or error in the intensity-weighted distribution (see the discussion in Section 1.3.5), especially for broad distributions. Thus, the number distribution obtained from a PCS

experiment is seldom correct and PCS should not be used as a means to obtain particle number distributions.

### 5.3.4. ANALYSIS OF MOLECULAR WEIGHT

For a given type of particle or macromolecular chain in a given environment (diluent, solvent, temperature, etc.), there is an empirical scaling relation between the translational motion and the weight of the particle:

$$D_T = k_D M^{-\alpha_D} \quad (5.31)$$

with  $k_D$  and  $\alpha_D$  being two scaling constants related to the characteristics of particle shape, chain conformation and the environment.  $k_D$  and  $\alpha_D$  can be experimentally determined by measuring values of  $D_T$  from several narrow distribution samples of known  $M$ . A plot of  $\log(D_T)$  versus  $\log(M)$  will yield an intercept of  $\log(k_D)$  and a slope of  $(-\alpha_D)$ . The  $k_D$  and  $\alpha_D$  values for many polymers have been reported and collectively published [78].

Once  $k_D$  and  $\alpha_D$  are known,  $q(\Gamma)$ , if it is related only to the translational motion, can be readily converted to  $q(M)$  by converting the abscissa using Eq. 5.31, and the ordinate by using  $q(M) = q(\Gamma)\Gamma/M$ . The weight-averaged molecular weight ( $\bar{M}_w$ ) and number-averaged molecular weight ( $\bar{M}_n$ ) can be computed accordingly [79]:

$$\bar{M}_w = (K^2 k_D)^{1/\alpha_D} \frac{\sum q(\Gamma_i) \Gamma_i}{\sum q(\Gamma_i) \Gamma_i^{(1/\alpha_D + 1)}}, \quad (5.32)$$

$$\bar{M}_n = (K^2 k_D)^{1/\alpha_D} \frac{\sum q(\Gamma_i) \Gamma_i^{(1/\alpha_D + 1)}}{\sum q(\Gamma_i) \Gamma_i^{(2/\alpha_D + 1)}}. \quad (5.33)$$

### 5.3.5. ACCURACY AND RESOLUTION

Figure 5.14 is a flowchart summarizing the data analysis process from an ACF measurement to obtain particle size or weight as outlined in the present section. PCS is intrinsically a low-resolution technology when compared with many other particle sizing technologies and other light scattering methods. As stated earlier, due to the nature of the ill-posed problem, the distribution retrieved typically is smoothed and contains little detail. The peak resolution is no better than two with three to one by diameter probably being the practical boundary.



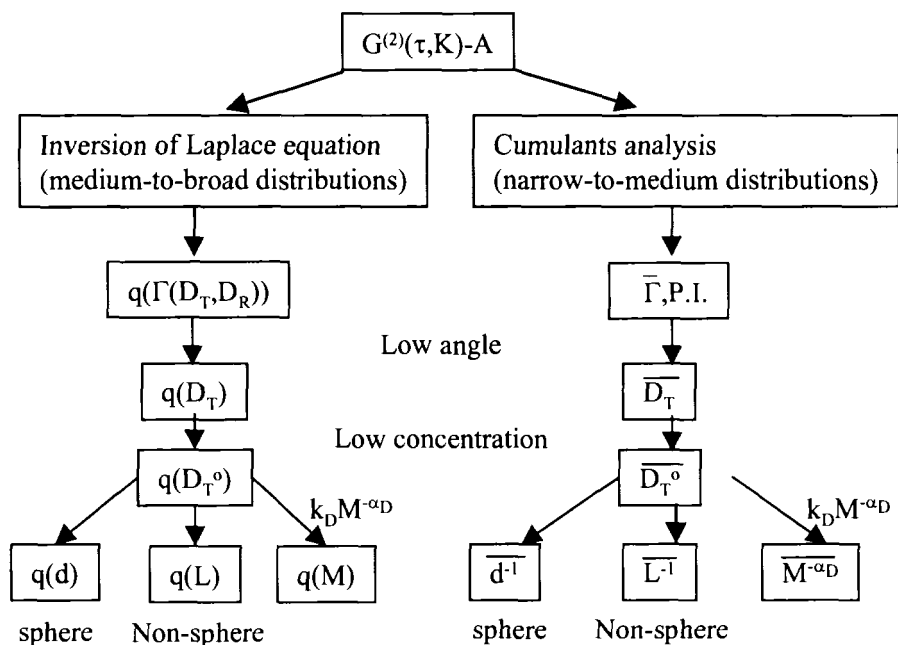


Figure 5.14. Flowchart of data analysis in a PCS experiment.

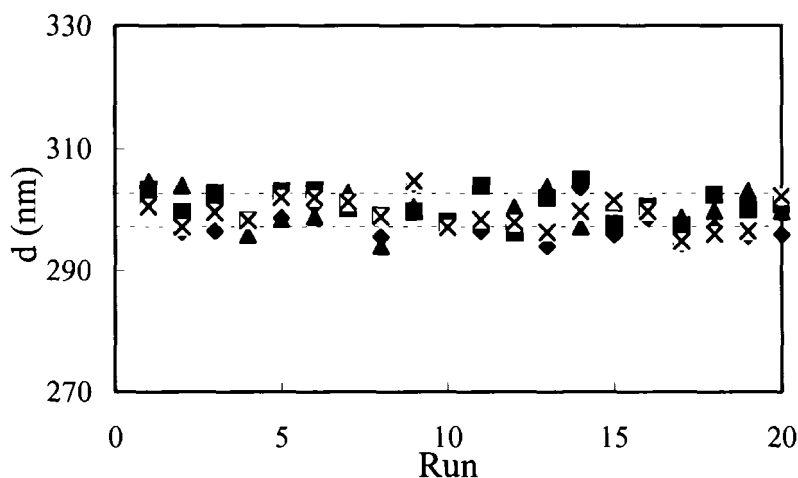


Figure 5.15. Mean diameter of a PSL sample in n-butanol recovered from PCS measurements using four Coulter<sup>®</sup>N4 Plus<sup>™</sup> instruments, represented by four different symbols, at a scattering angle of 90 degrees. The dotted lines are the overall standard deviation [80](by permission of Medpharm Scientific Publishers).

For monodisperse samples, the reproducibility using the cumulants method to retrieve a mean value and polydispersity index is however relatively good. It can easily achieve a reproducibility of 2-3% for the mean size. Figure 5.15 illustrates repeat PCS measurements of a monodisperse polystyrene latex sample of nominal 300 nm diameter dispersed in n-butanol (the sample had been kept in a sealed cell for seven years.) The measurements were performed using four PCS instruments with 20 repeat measurements on each instrument. The overall standard deviation is just 0.9%.

For polydisperse samples, even in a mixture of two monodisperse spheres, the result however may still be far from satisfactory. In a round-robin study performed by eight laboratories a mixture of 400 nm and 1000 nm monodisperse latexes was measured using different PCS instruments and the data were processed using different inversion algorithms. The modality, mean diameter, and percentages of each population retrieved from the eight laboratories varied widely [81, 82].

#### 5.4. PCS Measurement in Concentrated Suspensions

The theory and practice discussed so far are mainly for diluted or semi-diluted suspensions in which single scattering is the main phenomenon. Although initial multiple scattering and certain degrees of particle interaction exist, they often can be corrected in a first order approximation by performing concentration and scattering angle extrapolations as has been discussed earlier. With increasing demand for in-line or on-line quality control and particle characterization, PCS experiments more and more have to be executed in highly concentrated and opaque suspensions, sometimes in concentrations as high as 10-30% solids content [83]. At such high concentrations, multiple scattering becomes the main event and particle interaction further constrains the particles' motions. Different approaches have to be used to obtain useful information about the particle characteristics from PCS measurements. Three types of techniques are currently in use and will be discussed in this section. Two of them (fiber-optic PCS and two-color cross correlation spectroscopy) measure single scattering events by avoiding or suppressing multiple scattering; and the third one (diffusing-wave spectroscopy) utilizes the property of multiple scattering in a concentrated suspension. In all three approaches however, the measured diffusion coefficient is not  $D_T^0$  and cannot be related to actual particle dimension as described earlier.  $D_T$  is the result of particle movement that is constrained by particle-particle interactions and spatial effects. In dilute suspensions, the motions of different particles are uncorrelated and the ACF is a measurement of "free" particles. In highly concentrated suspensions, motions of different particles become correlated and scattering amplitude and particle positions become correlated

with each other.  $D_T$  is no longer only a function of particle size. Theoretical studies in deducing particle size from a characteristic decay  $\Gamma$  in concentrated suspensions have been conducted. The analytical form is only available for identical particles [66]. Numerical results in a certain conditions have been reported [84]. These results are not readily applicable in daily operation.

#### 5.4.1. FIBER OPTIC PCS

Fiber optics has been used in PCS instrumentation since early 1980s [85]. The pioneering work of Brown [16,86] has proven that combining diode lasers with avalanche photodiodes and fiber optics makes miniaturization of PCS instruments possible. Fiber optics also has the advantages of being less prone to damage, less expensive and allowing for remote access in transmitting and collecting light. Lately, the incorporation of fiber optics in PCS technology is more focused on back-scattering measurements of concentrated samples. In a concentrated opaque suspension, the intensity of the incident light diminishes rapidly when it passes through the scattering volume due to strong multiple scattering. Scattered light diffuses in random directions due to the same causes that create multiple scattering. In these situations, measuring the light scattering from a thin layer of a sample becomes the best choice in order to avoid strong multiple scattering. Without special effort involved in making an extra thin cell, the back-scattering measurement from a few layers of particles near the incident light using an optode (an optical fiber probe) accomplishes a task that is almost impossible using conventional optics. In a fiber optic optode, an optical fiber is used to deliver the incident light to illuminate particles near the optode and to detect any back-scattering from these particles. When the back-scattering is from particles within a few layers from the optode, the dominant signal detected is from single scattering of particles, provided that the core size of the fiber is smaller than the scattering mean free path in the suspension [87]. Furthermore, in a back-scattering measurement, the decay rates of doubly or singly scattered light for small, non-interacting particles are equal [88]. Thus a small amount of double scattering will not alter the ACF or affect the result. The angular range ( $\Delta\theta$ ) in which scattering can be collected depends both on the distance and location of the particles from the optode and the design of the optode. If a fiber is used directly to collect the scattered light without additional optical elements at the end of the optode, then  $\Delta\theta$  will depend on the maximum angle of light acceptance of the optode. The acceptance cone can be defined by the angle illustrated in Figure 5.16, which is related mainly to the refractive index difference between the core and the cladding of the fiber. This angle is typically around  $4.7^\circ$  for monomode fibers and larger than  $9^\circ$  for multimode fibers. Since at large scattering angles, a change of few degrees in the scattering angle will not cause significant change in  $K$  (the amplitude of the scattering vector), the

error or smearing effect introduced by such angular uncertainty is not large. For example, at  $180^\circ$  a  $\pm 5^\circ$  change in the scattering angle will cause a variation of only 0.2% in  $K$ , while the same uncertainty in  $K$  at a  $15^\circ$  scattering angle corresponds to only a  $0.02^\circ$  angular tolerance.

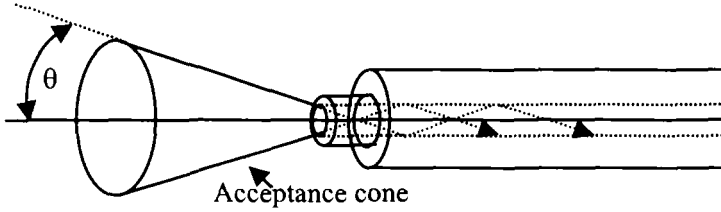


Figure 5.16. Acceptance cone of an optical fiber.

Most designs employ the optical schematics A or B in Figure 5.17. In design A, one fiber is used to both transmit the incident light and detect the scattered light downstream from a 3-port directional coupler that merges two fibers for the incoming light as well as for the outgoing signal. In design B, these two tasks are carried out by two fibers separately. The scattering angle in design B is related to the slant angle ( $\alpha$ ) of the two fibers, which either varies in different designs or can be adjusted [89]:

$$\theta = \pi - 2 \sin^{-1} \left( \frac{n_{\text{core}}}{n_{\text{medium}}} \sin \left( \frac{\alpha}{2} \right) \right). \quad (5.34)$$

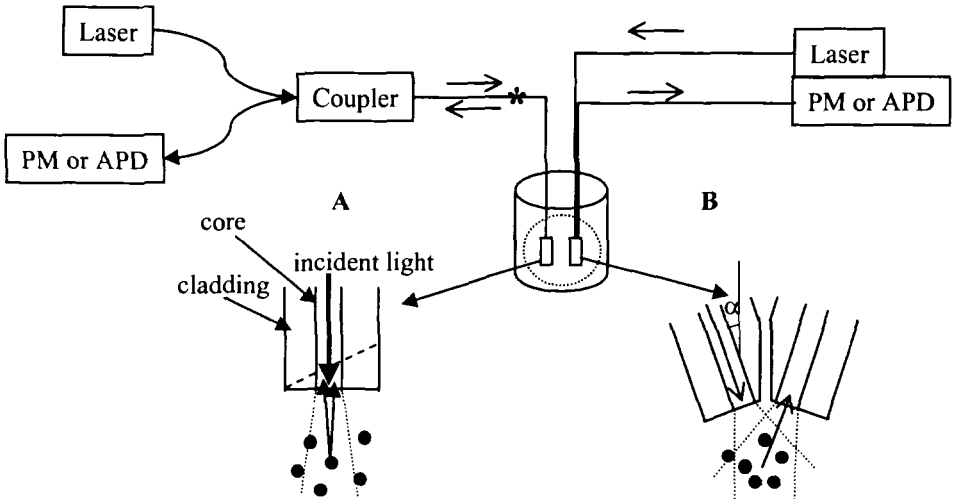


Figure 5.17. Fiber optic PCS setup.

Other designs using a bundled optical fiber array as the probe have been described [90,91]. Many optode designs have demonstrated that in a back scattering measurement using an optode multiple scattering is minimized and particle characterization can be carried out with various degrees of concentration, typically between 0.01% to 50% subject to the existence of any particle interactions. A common problem for all fiber optic optodes is that the fiber collects not only the scattered light from the dispersed particles but also the incident light reflected by the optode tip, which functions as a local oscillator. Thus, the experiment becomes homodyne with an ambiguous  $I_L$  to  $I_s$  ratio. Two solutions to this problem have been proposed. One is to use a carefully cleaned and slanted tip (the dashed line in the fiber tip shown in Figure 5.17A) to avoid  $I_L$  so the experiment can be treated as self-beating PCS. Using ray optics it is easy to show that by grinding a monomode fiber at an angle  $> 2^\circ$ , back-scattered light from the end face will be lost in the fiber cladding. At a  $10^\circ$  slant angle, the reflection can be reduced by at least 30 dB, which then can be neglected for samples with concentrations higher than 1% [92]. However, for less concentrated samples, since scattering  $I_s$  is weak this approach will still produce a residue of back reflection comparable to  $I_s$  and the measurement again becomes a homodyne experiment with an unknown  $I_L/I_s$  ratio. Another type of approaches is to make  $I_L$  as strong as possible so that data can be analyzed using Eq. 2.32. One such approach is to introduce an extra oscillator by inserting a fiber-fiber adapter in the \* location in Figure 5.17; i.e., cutting that section of fiber into two pieces thereby introducing two scattering surfaces [93].

Practically, a measurement may be neither self-beating nor homodyne. A careful judgement is then needed to apply the correct equations to resolve the dynamic information from the ACF. If the instrument efficiency coefficient ( $\beta$ ) is known, Eq. 5.35 can be used to extract the field ACF  $g^{(1)}(\tau)$  from a scattering signal with an arbitrary  $I_L/I_s$  ratio, where  $a$  is the intercept of the normalized intensity ACF, i.e.,  $G^{(2)}_{\text{det}}(0)/A = 1+a$  [94].

$$\left| g^{(1)}(\tau) \right| = \frac{\left( 1 - \frac{a}{\beta} + \frac{G^{(2)}_{\text{det}}(\tau) - A}{A\beta} \right)^{1/2} - \left( 1 - \frac{a}{\beta} \right)^{1/2}}{1 - \left( 1 - \frac{a}{\beta} \right)^{1/2}} \quad (5.35)$$

## 5.4.2. CROSS CORRELATION FUNCTION MEASUREMENT

The second approach to suppress multiple scattering during the measurement of particles' diffusive motion in a concentrated suspension is to perform a cross correlation function (CCF) measurement. In a CCF measurement, two incident beams illuminate the same scattering volume and two detectors are used. The scattered light collected from each detector then is cross-correlated using

$$G_{\text{det}}^{(2)}(\tau) = \langle I^1(0)I^2(\tau) \rangle. \quad (5.36)$$

Although multiple scattering cannot be completely removed in the CCF method, its contribution is significantly suppressed. In multiple scattering, double scattering is the main component. The double scattering contribution in the CCF is less than its contribution to the ACF by a factor of  $(n/N)^2$  with  $n$  being the number of particles interacting with a given particle and  $N$  being the total number of particles in the scattering volume. This reduction of double scattering in the CCF permits PCS measurements in more concentrated samples if both the incident and scattered beams are plane waves and the two scattering vectors can be matched to within  $\lambda/10$  over the scattering volume. The optics is constructed so that the two beam-detector pairs have an identical scattering vector of amplitude  $K$ . This can be achieved by using counter-propagating laser beams of the same wavelength with detectors set at  $90^\circ$  on either side of the laser beam (Figure 5.18), as used by Phillies when the idea of CCF was originally proposed [95].

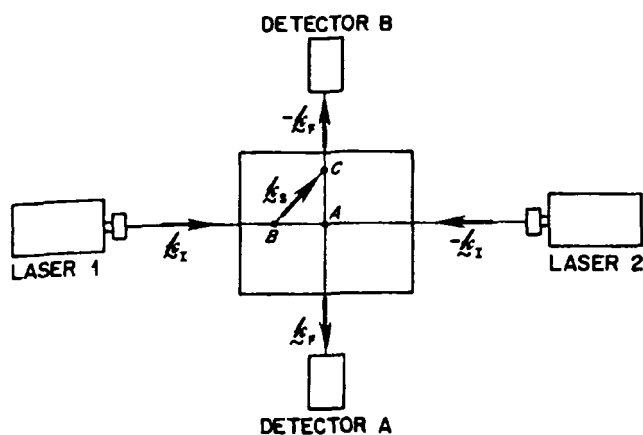


Figure 5.18. A CCF measurement setup. (Reprinted with permission from Phillies, G. D., Suppression of Multiple Scattering Effects in Quasielastic Light Scattering by Homodyne Cross-correlation Techniques, *J. Chem. Phys.*, 1981, 74, 260-262. Copyright 1981, American Institute of Physics.)

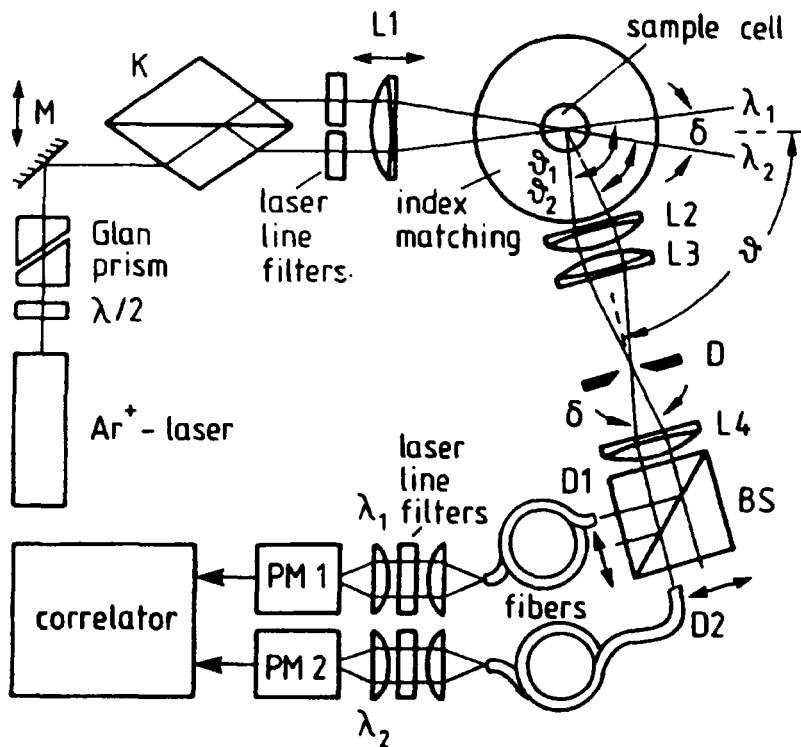
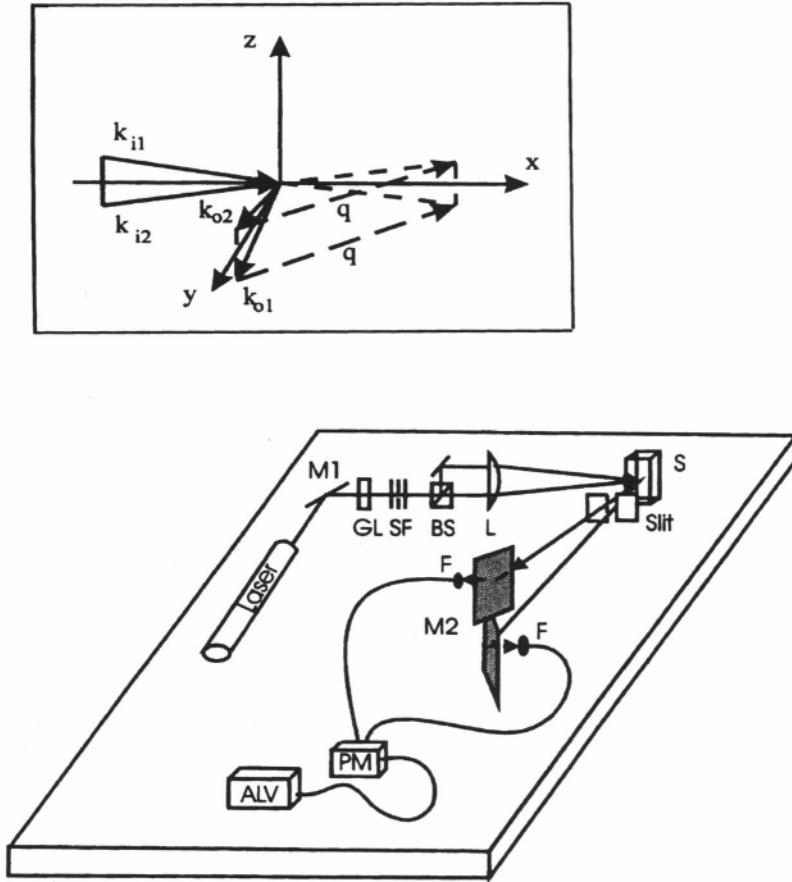


Figure 5.19. A two-color PCS instrument. M: mirror; K: double Koesters prism; L1-L3: lenses;  $\theta_1$  and  $\theta_2$ : scattering angles;  $\delta = (\theta_1 - \theta_2)/2$ ;  $\theta = (\theta_1 + \theta_2)/2$ ;  $\lambda$ : wavelength; D: diaphragm; D1 and D2: fiber apertures; PM1 and PM2: photomultiplier tubes. (by permission of Optical Society of America).

The scattering vector match can also be achieved using laser beams of two different wavelengths. Figure 5.19 shows a two-color spectrometer in a CCF measurement. After attenuation by a  $\lambda/2$ -waveplate-Glan-prism combination, the lights with  $\lambda_o = 488$  nm and  $\lambda_o = 514.5$  nm from an argon ion laser are split by a double Koesters prism into two parallel beams. The beams are then fed symmetrically through the transmitting achromatic lens L1 and cross at the cell center. The measurement volume is imaged onto a pinhole (D) of diameter 0.2 mm by the achromatic lens system L2-L3. The Fourier lens (L4) provides transformation of angular to lateral separations in the far field behind a cube beam splitter. Detection is achieved through multimode optical fibers, which are positioned so that their angular separation  $\delta$  fits that of the coherence angle. The two angles are chosen in such a way that the scattering vectors for both beams coincide and can be adjusted through translation of one of the optical parts M, L1, or D1 and D2 [96]. This approach is more versatile since the scattering

angle can easily be varied over a wide range. However, its optical alignment is affected by the dispersion of the medium refractive index at varying temperatures.



**Figure 5.20.** Optic setup for a 3-D CCF experiment. The upper frame shows the scattering geometry and the two identical scattering vectors ( $q$  in this figure) (by permission of Steinkopff Verlag GmbH & Co.KG).

The third way to suppress multiple scattering effects is an even simpler 3-D arrangement, in which the CCF can be measured at arbitrary angles, as in conventional goniometry. The 3-D setup has a much higher signal-to-noise ratio as compared to the two-color setup [97]. Figure 5.20 shows such a setup at  $90^\circ$ . The laser light is split into two parallel beams by a beam splitter (BS) after the polarizer (GL) and a spatial filter (SF), and focused by the lens (L) into the sample (S) from different azimuthal angles. The detection arm is positioned at



the scattering angle  $\theta$ . The scattered light, constrained by the slit from each of the given scattering planes, is detected by the detecting optics at the plane (the mirror (M) with the optic fiber (F) guiding light into a PMT). The signals from the two PMTs are then fed into the two inputs of the cross-correlator (ALV) [98].

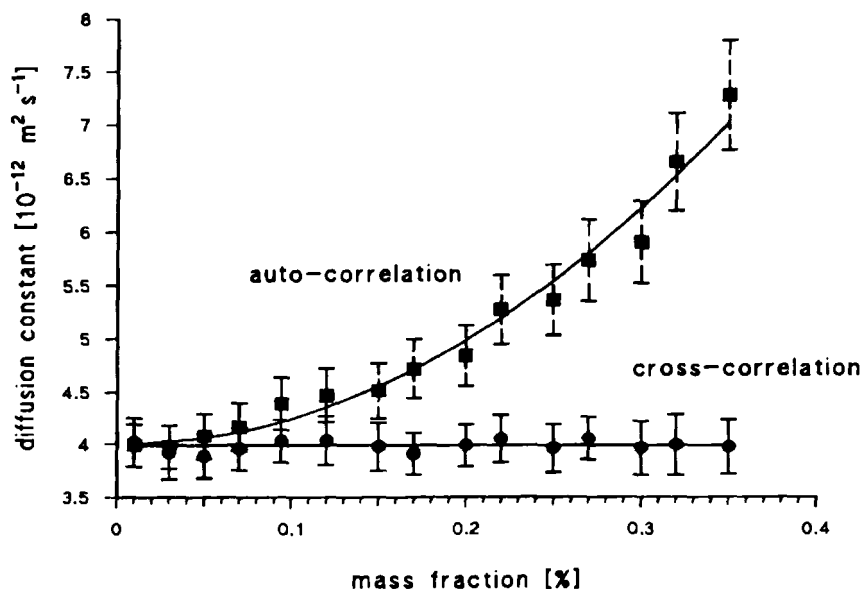


Figure 5.21. ACF and CCF characterization of latex particles (diameter 109 nm) at 21°C in suspension [98] (by permission of Steinkopff Verlag GmbH & Co. KG).

In all three schemes, the experimental challenge is to assure that the signals detected at two detectors are from the same scattering volume and identical scattering vectors, which often requires delicate alignment. For single scattering, since each detector has the same “view” of the particle’s motion in the suspension, there exists a cross correlation between the light collected from the two detectors and so the CCF is identical to the ACF from a conventional PCS experiment. For multiple scattering, cross correlation does not exist. As a consequence, the CCF method acts as a filter for multiple scattering. The time-dependent part of the CCF reflects only single scattering, and multiple scattering contributes only to the time-independent baseline. Assuming that the average intensity  $\langle I \rangle$  from the two detectors are the same,

$$\langle I^1(0)I^2(\tau) \rangle \cong 4 \langle I \rangle^2 (1 + \beta_c |g^{(1)}(\tau, K)|^2). \quad (5.37)$$

$\beta_c$  is an efficiency coefficient that ranges ideally from 0.5 to 1 depending on the setup. Figure 5.21 shows the suppression of multiple scattering from the CCF measurements of a 109 nm latex suspension at different concentrations as compared to that from an ACF measurement in which multiple scattering causes apparently faster motions and thus smaller particle size. As shown in Figure 5.20, the CCF measurement suffers from the drawback that it requires a complex light scattering apparatus and it can only be effectively applied to suspensions of about 1% solid content [99]. Otherwise, even though multiple scattering may be suppressed, the single scattering event will be extremely weak, yielding poor results.

#### 5.4.3. DIFFUSING-WAVE SPECTROSCOPY (DWS)

Differing from the two approaches above in which multiple scattering is avoided or suppressed as much as possible, the DWS technology approaches the problem from an entirely different direction by utilizing multiple scattering. DWS is applied only in cases of very strong multiple scattering and in which single scattering is negligible in order to characterize particles and their motions in concentrated suspensions [100]. In DWS, the propagation of light in the medium is scattered a very large number of times and random scattering events result in a diffusion process of photons. This process can be described by the diffusion approximation that neglects any interference effects of the light and assumes that the light intensity diffuses. Another approximation assumes that the details of individual scattering events play a less critical role. Because of these fundamental approximations, DWS can only be applied to samples with very strong scattering with no absorption. Otherwise, any detected single or double scattering events will invalidate the basic equations.

Experimentally, DWS can use the same instrument as in a conventional PCS experiment to measure the ACF, except that a much stronger laser with a long coherence length is needed because of the diffusing light over a much longer path length. The light path in the medium has to be arranged such that only completely randomized diffusing light is detected. Since the diffusing light leaves the sample with nearly uniform intensity in all directions, the angle of detection is not critical. Back-scattering and transmission ( $180^\circ$  or  $0^\circ$  scattering angles) are two convenient setups for a DWS experiment that both have simple theoretical formulations. The ACF's for these two arrangements are:

$$\text{Back scattering:} \quad g^{(1)}(\tau) = \exp(-\gamma\sqrt{6D_T k_o^2 \tau}). \quad (5.38)$$

Transmission:

$$g^{(1)}(\tau) = \frac{\left(\frac{l}{l^*} + \frac{4}{3}\right)\sqrt{6D_T k_o^2 \tau}}{\left(1 + \frac{8D_T k_o^2 \tau}{3}\right) \sinh\left(\frac{l}{l^*} \sqrt{6D_T k_o^2 \tau}\right) + \frac{4}{3} \sqrt{6D_T k_o^2 \tau} \cosh\left(\frac{l}{l^*} \sqrt{6D_T k_o^2 \tau}\right)}, \quad (5.39)$$

In the above equations,  $\gamma$  is a variable related to the transport mean free path  $l^*$ , which is the length that a photon must travel before its direction is completely randomized, and  $l$  is the sample thickness. Eq. 5.39 has a characteristic decay time  $\tau(l^*/l)^2$ . In neither setup, can  $D_T$  be resolved directly unless  $l^*$  is known. Although in principle this can be done by comparing a static transmission measurement to a sample of known  $l^*$  in the exactly same optical arrangement, it is not an easy task. In the back-scattering setup,  $\gamma$  can be approximated in a narrow range of particle size as a constant ( $\cong 2.1$ ; accurate to about 20 percent). However, in back-scattering, there are unavoidable strong single and double scattering events from the first few layers of particles, in which the diffusion approximation does not apply. In addition, for polydisperse samples the best result from a DWS experiment that one can get is an ill-defined mean value of  $D_T$ ; no information about the size distribution can be extracted. Thus, although the principle of DWS was proposed a decade ago [101] and much theoretical work has been conducted, DWS has to date found very limited use in particle characterization with few reported applications, the most notable being the dynamic characterization of air bubbles in liquid (foams) [102] and the monitoring of cluster growth in a suspension [103]. Although there is a potential for DWS to be applied in on-line particle characterization, where often only specific changes in the particles' characteristics are to be monitored thus making the separation of  $l^*$  from  $D_T$  less important, considerable development is needed before this technology can match the widespread utility of conventional PCS technology.

In summary, PCS technology has become a mature tool in particle size characterization in both industrial applications and academic research. Although the size distributions obtained from PCS measurements are of low resolution and often have distorted shapes due to the nature of information content in the ACF, it is still one of the best non-invasive submicron sizing methods available for measuring particulates in liquid media. Multiangle measurements using a digital correlator having logarithmically spaced delay times can extend the dynamic size range of the measurement and obtain more representative results by avoiding intensity blind spots in the scattering pattern and by optimizing the concentration effect. Global analyses combining both dynamic and static light scattering data present a challenge in the further advancement of data analysis.

Great potential exists, but much more work needs to be done before measurements of concentrated samples becomes a powerful tool to not only monitor changes but also to characterize a variety of particulate materials.

## REFERENCES

- 1 ISO 13321 Particle Size Analysis-Photon Correlation Spectroscopy, International Organization for Standardization (ISO), Genève, 1996.
- 2 Pecora, R., Doppler Shifts in Light Scattering from Pure Liquid and Polymer Solutions, *J. Chem. Phys.*, 1964, 40, 1604-1614.
- 3 Cummins, H. Z., Knable, N., Yeh, Y., Observation of Diffusion Broadening of Rayleigh Scattered Light, *Phys. Rev. Lett.*, 1964, 12, 150-153.
- 4 Krahn, W., Luckas, M., Lucas, K., Determination of Particle Size Distribution in Fluids using Photon Correlation Spectroscopy, *Part. Part. Syst. Charact.*, 1988, 5, 72-76.
- 5 Finsy, R., Particle Sizing by Quasi-elastic Light Scattering, *Adv. Coll. Inter. Sci.*, 1994, 52, 79-143.
- 6 Chu, B., Xu, R., A Prism-Cell Laser Light-Scattering Spectrometer, in *OSA Proc. Photon Correlation Techniques and Applications, Vol. 1*, Optical Society of America, Washington D.C., 1989, pp.137-146.
- 7 OSHA Directives, PUB 8-1.7 - Guidelines for Laser Safety and Hazard Assessment, U.S. Department of Labor, Occupational Safety & Health Administration, Washington, D.C., 1991.
- 8 Dhadwal, H. S., Chu, B., A Fiber-optic Light-scattering Spectrometer, *Rev. Sci. Instrum.*, 1989, 60, 845-853.
- 9 Chu, B., Wu, C., Buck, W., Light Scattering Characterization of Polytetrafluoroethylene, *Macromolecules*, 1988, 21, 397-402.
- 10 Chu, B., Ying, Q., Grosberg, A. Y., Two-stage Kinetics of Single-chain Collapse. Polystyrene in Cyclohexane, *Macromolecules*, 1995, 28, 180-189.
- 11 Will, S., Leipertz, A., Dynamic Light Scattering System with a Novel Scattering Cell for the Measurement of Particle Diffusion Coefficients, *Rev. Sci. Instrum.*, 1996, 67, 3164-3169.
- 12 Ford, N., Havard T., Wallas, P., Analysis of Macromolecules Using Low and Right Angle Laser Light Scattering and Photon Correlation Spectroscopy, in *Particle Size Distribution III*, Ed. Provder, T., ACS Symp. Series 693, American Chemical Society, Washington D. C., 1998, Chpt.5, pp.39-51.
- 13 Egelhaaf, S. U., Schurtenberger, P., A Fiber-Optics-Based Light Scattering Instrument for Time-Resolved Simultaneous Static and Dynamic Measurements, *Rev. Sci. Instrum.*, 1996, 67, 540-545.
- 14 Vanhoudt, J., Clauwaert, J., Experimental Comparison of Fiber Receivers and a Pinhole Receiver for Dynamic Light Scattering, *Langmuir*, 1999, 15, 44-57.
- 15 Jones, R., Oliver, C. J., Pike, E. R., Experimental and Theoretical Comparison of Photon-counting and Current Measurements of Light Intensity, *Appl. Opt.* 1971, 10, 1673-1680.
- 16 Brown, R. G. W., Dynamic Light Scattering Using Monomode Optical Fibres, *Appl. Opt.*, 1987, 26, 4846-4851.
- 17 Terui, G., Kohno, T., Fukino, Y., Ohbayashi, K., Circuit to Use a Photon Correlator as a Fast Analog Correlator, *Jap. J. Appl. Phys.*, 1986, 25, 1243-1246.
- 18 Bertero, M., Boccacci, P., Pike, E. R., On the Recovery and Resolution of Exponential Relaxation Rates from Experimental Data II. The Optimum Choice of the Sampling Points, *Proc. Royal. Soc. Land.*, 1984, A393, 51-65.
- 19 Phillies, G. D., On the Temporal Resolution of Multi-tau Digital Correlator, *Rev. Sci. Instrum.*, 1996, 67, 3423-3427.
- 20 Dhadwal, H. S., Chu, B., Xu, R., Time-of-Arrival Photoelectron Correlator, *Rev. Sci. Instrum.*, 1987, 58, 1445-1449.
- 21 Jakeman, E., Oliver, C. J., Pike, E. R., Pusey, P. N., Correlation of Scaled Photon-counting Fluctuations, *Phys. A. Gen. Phys.*, 1972, 5, L93-L96.

- 
- 22 Van der Meeren, P., Vanderdeelen, J., Baert, L., Relevance of Reflection in Static and Dynamic Light Scattering Experiments, *Part. Part. Syst. Charact.*, 1994, 11, 320-326.
  - 23 Štěpánek, P., Data Analysis in Dynamic Light Scattering, in *Dynamic Light Scattering*, Ed. Brown, W., Oxford Science Publication, Oxford, 1993, Chpt.4, pp. 177-241.
  - 24 Koppel, D. E., Analysis of Macromolecular Polydispersity in Intensity Correlation Spectroscopy: the Method of Cumulants, *J. Chem. Phys.* 1972, 57, 4814-4820.
  - 25 Isenberg, I., Dyson, R. D., Hanson, R., Studies on the Analysis of Fluorescence Decay Data by the Method of Moments, *Biophys. J.*, 1973, 13, 1090-1115.
  - 26 Weiner, B. B., Tscharnuter, W. W., Uses and Abuses of Photon Correlation Spectroscopy, in *Particle Size Distribution I*, Ed. Provder, T., ACS Symp. Series 332, American Chemical Society, Washington, D. C., 1987, Chpt.3, pp.48-61.
  - 27 Bevington, P. R., *Data Reduction and Error Analysis for the Physical Sciences*, McGraw-Hill, New York, 1969.
  - 28 Chu, B., Ford, J. R., Dhadwal, H. S., Correlation Function Profile Analysis of Polydisperse Macromolecular Solutions and Colloidal Suspensions, in *Methods in Enzymology Vol. 117*, Academic Press, New York, 1985, Chpt. 15, pp.256-297.
  - 29 Hanus, L. H., Ploehn, H. J., Correction of Intensity-Averaged Photon Correlation Spectroscopy Measurements to Number-Averaged Particle Size Distributions. 1. Theoretical Development, *Langmuir*, 1999, 15, 3091-3100.
  - 30 Ross, D. A., Dimas, N., Particle Sizing by Dynamic Light Scattering: Nose and Distortion in Correlation Data, *Part. Part. Syst. Charact.*, 1993, 10, 62-69.
  - 31 Ruf, H., Data Accuracy and Resolution in Particle Sizing by Dynamic Light Scattering, *Adv. Coll. Inter. Sci.*, 1993, 46, 333-342.
  - 32 Schätzel, K., Noise on Photon Correlation Data: I. Autocorrelation Functions, *Quantum Opt.*, 1990, 2, 287-306.
  - 33 Clatter, O., Sieberer, J., Schnablegger, H., A Comparative Study on Different Scattering Techniques and Data Evaluation Methods for Sizing of Colloidal Systems Using Light Scattering, *Part. Part. Syst. Charact.*, 1991, 8, 274-281.
  - 34 Gulari, Es., Qulari, Er., Tsunasima, Y., Chu, B., Photon Correlation Spectroscopy of Particle Distribution, *J. Chem. Phys.*, 1979, 70, 3965-3972.
  - 35 Pike, E. R., Watson, D., McNeil Watson, F., Analysis of Polydisperse Scattering Data II, in *Measurement of Suspended Particles by Quasi-elastic Light Scattering*, Ed. Dahneke, B. E., John Wiley & Sons, New York, 1983, Chpt.4, pp.107-128.
  - 36 Bertero, M., Boccacci, P., Pike, E. R., On the Recovery and Resolution of Exponential Relaxation Rates from Experimental Data: A Singular-value Analysis of the Laplace Transform Inversion in the Presence of Noise, *Proc. R. Soc. London, Ser. A.*, 1982, 383, 15-29.
  - 37 Bertero, M., Boccacci, P., Pike, E. R., On the Recovery and Resolution of Exponential Relaxation Rates from Experimental Data: III. The Effect of Sampling and Truncation of Data on the Laplace Transform Inversion, *Proc. R. Soc. London, Ser. A.*, 1985, 398, 23-30.
  - 38 Finsy, R., de Groen, P., Deriemaeker, L., van Laethem, M., Singular Value Analysis and Reconstruction of Photon Correlation Data Equidistant in Time, *J. Chem. Phys.*, 1989, 91, 7374-7383.
  - 39 McWhirter, J. G., Pike, E. R., On the Numerical Inversion of the Laplace Transform and Similar Fredholm Integral Equations of the First Kind, *J. Phys. A. Math. Gen.*, 1978, 11, 1729-1745.
  - 40 Livesey, A. K., Licinio, P., Delaye, M., Maximum Entropy Analysis of Quasielastic Light Scattering from Colloidal Dispersions, *J. Chem. Phys.*, 1986, 84, 5102-5107.
  - 41 Nyeo, S.-L., Chu, B., Maximum Entropy Analysis of Photon Correlation Spectroscopy Data, *Macromolecules*, 1989, 22, 3998-4009.

- 
- 42 Provencher, S. W., A Constrained Regularization Method for Inverting Data Represented by Linear Algebraic Integral Equations, *Comput. Phys. Commun.*, 1982, 27, 213-227.
- 43 Ross, D. A., Dhadwal, H. S., Regularized Inversion of the Laplace Transform: Accuracy of Analytical and Discrete Inversion, *Part. Part. Syst. Charact.*, 1991, 8, 282-286.
- 44 Stalling, J., Gull, S. F., in *Maximum-entropy and Bayesian Methods in Inverse Problems*, Eds. Smith, C. R., Grandy, W. T. Jr., D. Reidel, Dordrecht, 1985.
- 45 Ross, D. A., Nguyen, T. H., Spectral Properties of the Regularized Inversion of the Laplace Transform, *Part. Part. Syst., Charact.*, 1990, 7, 80-86.
- 46 Provencher, S. W., CONTIN: A General Purpose Constrained Regularization Program for Inverting Noisy Linear Algebraic Integral Equations, *Computer Phys. Comm.*, 1982, 27, 229-242.
- 47 Chu, B., Xu, R., Nyeo, S., Applications of Prism-cell Light-scattering Spectrometer to Particle Sizing in Polymer Solutions, *Part. Part. Syst. Charact.*, 1989, 6, 34-38.
- 48 Ruf, H., Effects of Normalization Errors on Size Distribution Obtained from Dynamic Light Scattering, *Biophys. J.*, 1989, 56, 67-78.
- 49 Ruf, H., Grell, E., Stelzer, E., Size Distribution of Submicron Particles by Dynamic Light Scattering Measurement: Analyses Considering Normalization Errors, *Eur. Biophys. J.*, 1992, 21, 21-28.
- 50 Goldlin, A. A., *Opt. Spectrosc.*, 1991, 71, 485-489.
- 51 Bott, S. E., in *Particle Size Analysis*, Ed. P. J. Lloyd, Wiley, London, 1988, pp.77-88.
- 52 Finsy, R., de Groen, P., Deriemaeker, L., Geladé, E., Joosten, J., Data Analysis of Multi-Angle Photon Correlation Measurements without and with Prior Knowledge, *Part. Part. Syst. Charact.*, 1992, 9, 237-251.
- 53 Provencher, S. W., Štěpánek, P., Global Analysis of Dynamic Light Scattering Autocorrelation Function, *Part. Part. Syst. Charact.*, 1996, 13, 291-294.
- 54 Bryant, G., Thomas, J. C., Improved Particle Size Distribution Measurements Using Multiangle Dynamic Light Scattering, *Langmuir*, 1995, 11, 2480-2485.
- 55 Wu, C., Unterforsthuber, K., Lilge, D., Lüddecke, E., Horn, D., Determination of Particle Size Distribution by the Analysis of Intensity-constrained Multi-angle Photon Correlation Spectroscopic Data, *Part. Part. Syst. Charact.*, 1994, 11, 145-149.
- 56 De Vos, C., Deriemaeker, L., Finsy, R., Quantitative Assessment of the Conditioning of the Inversion of Quasi-elastic and Static Light Scattering Data for Particle Size Distribution, *Langmuir*, 1996, 12, 2630-2636.
- 57 Bryant, G., Abeynayake, C., Thomas, J., Improved Particle Size Distribution Measurements Using Multiangle Dynamic Light Scattering. 2. Refinements and Applications, *Langmuir*, 1996, 12, 6224-6228.
- 58 Burchard, W., Quasi-elastic Light Scattering: Separability of Effects of Polydispersity and Internal Nodes of Motion, *Polymer*, 1979, 20, 577-581.
- 59 Fujime, S., Kubota, K., Dynamic Light Scattering from Dilute Suspensions of Thin Disks and Thin Rods as Limiting Forms of Cylinders, Ellipsoid, and Ellipsoidal Shell of Revolution, *Biophys. Chem.*, 1985, 23, 1-13.
- 60 Kubota, K., Tominaga, Y., Fujime, S., Otomo, J., Ikegami, A., Dynamic Light Scattering Study of Suspensions of Purple Membrane, *Biophys. Chem.*, 1985, 23, 15-29.
- 61 Xu, R., Chu, B., Dynamic Light Scattering of Thin Disks: Coupling of Diffusive Motion, *J. Colloid Interface Sci.*, 1987, 117, 22-30.
- 62 Aragon, S. R., Pecora, R., Theory of Dynamic Light Scattering from Large Anisotropic Particles, *J. Chem. Phys.*, 1977, 66, 2506-2516.
- 63 Xu, R., Ford, J. R., Chu, B., Photon Correlation Spectroscopy, Transient Electric Birefringence and Characterization of Particle Size Distribution in Colloidal Suspensions, in

- 
- Particle Size Distribution I*, Ed. Provder, T., ACS Symposium Series 332, American Chemical Society, Washington, D. C., 1987, Chpt.8, pp.115-132.
- 64 Stockmayer, W. H., Schmidt, M., Effects of Polydispersity, Branching & Chain Stiffness on Quasielastic Light Scattering, *Pure & Appl. Chem.*, 1982, 54, 407-414.
- 65 Phillies, G. D., Experiment Demonstration of Multiple-scattering Suppression in Quasielastic-light-scattering Spectroscopy by Homodyne Coincidence Techniques, *Phys. Rev. A.*, 1981, 24, 1939-1942.
- 66 Pusey, P., Tough, R., Particle Interaction, in *Dynamic Light Scattering*, Ed. Pecora, R., Plenum, New York, 1985, Chpt.4, pp.85-180.
- 67 Finsy, R., Use of One-parameter Models for the Assessment of Particle Interaction by Photon Correlation Spectroscopy, *Part. Part. Syst. Character.*, 1990, 7, 74-79.
- 68 De Jaeger, N., Demeyere, H., Finsy, R., Sneyers, R., Vanderdeelen, J., Van der Meeren, P., Van Laethem, M., Particle Sizing by Photon Correlation Spectroscopy. Part I. Monodisperse Latices: Influence of Scattering Angle and Concentration of Dispersed Material, *Part. Part. Syst. Character.*, 1991, 8, 179-186.
- 69 Hall, R. S., Oh, Y. S., Johnson, C. S. Jr., Photon Correlation Spectroscopy in Strongly Absorbing and Concentrated Samples with Applications to Unliganded Hemoglobin, *J. Phys. Chem.*, 1980, 84, 756-767.
- 70 Seebergh, J. E., Berg, J. C., Evidence of a Hairy Layer at the Surface of Polystyrene Latex Particles, *Colloids Surf.* 1995, 100, 139.
- 71 Xu, R., Shear Plane and Hydrodynamic Diameter of Microspheres in Suspension, *Langmuir*, 1998, 14, 2593-2597.
- 72 Finsy, R., De Jaeger, N., Particle Sizing by Photon Correlation Spectroscopy Part II: Average Values, *Part. Part. Syst. Character.*, 1991, 8, 187-193.
- 73 Hildebrand, H., Row, G., Detecting Trace Contamination Using a Multiangle PCS Particle Sizer, *Am. Lab. News*, 1995, 2, 6.
- 74 Chu, B., Xu, R., DiNapoli, A., Light Scattering Studies of a Colloidal Suspension of Iron Oxide Particles, *J. Colloid Interface Sci.*, 1987, 116, 182-195.
- 75 Chu, B., *Laser Light Scattering*, Academic Press, New York, 1974.
- 76 Newman, J., Swinney, H. L., Hydrodynamic Properties and Structure of fd Virus, *J. Mol. Biol.*, 1977, 116, 593-603.
- 77 Van der Meeren, P., Bogaert, H., Vanderdeelen, J., Baert, L., Relevance of Light Scattering Theory in Photon Correlation Spectroscopic Experiments, *Part. Part. Syst. Character.*, 1992, 9, 138-143.
- 78 *Polymer Handbook*, 4<sup>th</sup> Ed., Eds. Brandrup, J., Immergut, E. H., Grulke, E. A., Abe, A., John Wiley & Sons, New York, 1999.
- 79 Xu, R., Light Scattering and Transient Electric Birefringence of Polydiacetylene (P4BCMU) in Dilute Solution, *Ph.D. Thesis*, State University of New York at Stony Brook, Stony Brook, 1988.
- 80 Xu, R., Multiangle Photon Correlation Spectroscopy in Particle Characterization, in *Particle and Surface Characterisation Methods*, Eds. Müller, R. H., Mehnert, W., Medpharm Scientific Publishers, Stuttgart, 1997, Chpt.1, pp.1-17.
- 81 Finsy, R., De Jaeger, N., Sneyers, R., Geladé, E., Particle Sizing by Photon Correlation Spectroscopy. Part III: Mono and Bimodal Distributions and Data Analysis, *Part. Part. Syst. Character.*, 1992, 9, 125-137.
- 82 Finsy, R., Deriemaeker, L., De Jaeger, N., Sneyers, R., Van der Deelen, J., Van der Meeren, P., Demeyere, H., Stone-Masui, J., Haestier, A., Clauwaert, J., De Wispelaere, W., Gillioen, P., Steyfkens, S., Gelade, E., Particle Sizing by Photon Correlation Spectroscopy. Part IV: Resolution of Bimodals and Comparison with Other Particle Sizing Methods, *Part. Part. Syst. Character.*, 1993, 19, 118-128.



- 
- 83 Ansari, R. R., Suh, K., Dynamic Light Scattering Particle Size Measurements in Turbid Media, *Proc. SPIE-Int. Soc. Opt. Eng.* 1998, 3251, 146-156.
  - 84 Beenakker, C. W. J., Mazur, P., Diffusion of Spheres in a Concentrated Suspension II, *Physica A*, 1984, 126, 349-370.
  - 85 Auweter, H., Horn, D. F., Fibre-optical Quasi-elastic Light Scattering of Concentrated Dispersion, *J. Colloid Interface Sci.*, 1985, 105, 399-409.
  - 86 Brown, R. G. W., Burnett, J. G., Chow, K., Rarity, J. G., Miniature Light Scattering System for On-line Process Particle Size and Velocity Measurement, in *SPIE Vol. 102: In-Process Optical Measurements*, 1988, pp. 144-149.
  - 87 Van Keuren, E. R., Wiese, H., Horn, D. F., Fiber-optic Quasielastic Light Scattering in Concentrated Latex Dispersions: Angular Dependent Measurements of Singly Scattered Light, *Langmuir*, 1993, 9, 2883-2887.
  - 88 Dhont, J. K. G., de Kruif, C. G., Vrij, A., Light Scattering in Colloidal Dispersions: Effects of Multiple Scattering, *J. Colloid Interface Sci.*, 1985, 105, 539-551.
  - 89 Dhadwal, H. S., Ansari, R. R., Meyer, W. V., A Fiber-optic Probe for Particle Sizing in Concentrated Suspensions, *Rev. Sci. Instrum.*, 1991, 62, 2963-2968.
  - 90 Brenci, M., Mencaglia, A., Mignani, A. G., Pieraccini, M., Circular-array Optical-fiber Probe for Backscattering Photon Correlation Spectroscopy Measurements, *Appl. Opt.*, 1996, 35, 6775-6780.
  - 91 Horn, D., Particle Size Measurement in Concentrated Latex Suspensions Using Fiber-Optic Photon Correlation Spectroscopy, *J. Phys. D: Appl. Phys.*, 1989, 22, 1257-1265.
  - 92 Horn, D., Single-mode Fibers in Fiber-optic Quasielastic Light Scattering: A Study of the Dynamics of Concentration Latex Dispersions, *J. Chem. Phys.*, 1991, 94, 6429-6443.
  - 93 Willemse, A. W., Merkus, H. G., Scarlett, B., Development of On-line Measurement and Control Techniques for Fine Grinding and Dispersion Process, in *Proc. World Congress Part. Technol. 3*, Brighton, 1998, Paper No.2.
  - 94 Bremer, L. G. B., Deriemaeker, L., Finsy, R., Geladé, E., Joosten, J. G. H., Fiber Optic Dynamic Light Scattering, neither Homodyne nor Heterodyne, *Langmuir*, 1993, 9, 2008-2014.
  - 95 Phillies, G. D., Suppression of Multiple Scattering Effects in Quasielastic Light Scattering by Homodyne Cross-correlation Techniques, *J. Chem. Phys.*, 1981, 74, 260-262.
  - 96 Drewel, M., Ahrens, J., Podschus, U., Decorrelation of Multiple Scattering for Arbitrary Scattering Angle, *J. Opt. Soc. Am.*, 1990, 7, 206-210.
  - 97 Sinn, C., Niehuser, R., Overbeck, E., Palberg, T., Dynamic Light Scattering by Preserved Skimmed Cow Milk. A Comparison of Two-color and Three-dimensional Cross-correlation Experiments, *Prog. Coll. Polym. Sci.*, 1998, 110, 8-11.
  - 98 Aberle, L. B., Wiegard, S., Schröer, W., Staude, W., Suppression of Multiple Scattered Light by Photon Cross-Correlation in a 3D Experiment, *Progr. Coll. Polym. Sci.*, 1997, 104, 121-125.
  - 99 Sinn, C., Niehüser, R., Overbeck, E., Palberg, T., Particle Characterization Using Multiple Scattering Decorrelation Methods, Part 1, Standard Latex Particles, *Part. Part. Syst. Charact.*, 1999, 16, 95-101.
  - 100 Weitz, D. A., Pine, D. J., Diffusing-wave Spectroscopy, in *Dynamic Light Scattering*, Ed. Brown, W., Oxford Science Publications, Oxford, 1993, Chpt. 16, pp.652-720.
  - 101 Pine, D. J., Weitz, D. A., Chaikin, P. M., Herbolzheimer, E., Diffusing-wave Spectroscopy, *Phys. Rev. Lett.*, 1988, 60, 1134-1137.
  - 102 Durian, D. J., Weitz, D. A., Pine, D. J., Multiple Light Scattering Probes of Foam and Dynamics, *Science*, 1991, 252, 686-690.

- 
- 103 Ishii, K., Iwai, T., Monitoring of the Cluster Growth in the Colloidal Suspension Using a Diffusive-Wave Spectroscopic Technique, *Proc. SPIE-Int. Soc. Opt. Eng.*, 1999, 3599, 76-85.

# ELECTROPHORETIC LIGHT SCATTERING

## *Zeta Potential Measurement*

### 6.1. Introduction

This chapter deals with a different topic in particle characterization. Instead of particle size analysis, the technology of electrophoretic light scattering (ELS) is primarily used to characterize the surface charges of colloidal particles (a collective term for micrometer to nanometer-sized particles) in liquid media. One distinctive property of colloidal particles, as compared with large particles or bulk materials, is that because of their small dimension, colloidal particles have extremely large specific surface areas (surface area per unit weight). For example, a sphere of 1 mm in diameter with a density of 2 g/ml has a specific surface area of 30 cm<sup>2</sup>/g; but if the dimension of the sphere is reduced to 10 nm, the specific surface area will become 3×10<sup>6</sup> cm<sup>2</sup>/g. The large specific surface area of colloidal particles means that the particle-liquid interface can strongly affect many of the physical properties of colloidal dispersions, such as dispersibility and stability. Behavior of colloidal dispersions is intimately related to surface structure and interfacial phenomenon. Thus, characterization of surface structure is always one of the focal points in colloid science. For charged particles in liquid suspension, besides surface chemical composition, surface charge and surface morphology (especially the former) are the two most important surface characteristics of a particle. One parameter that is common to both phenomena and is often used to characterize a particle's surface is *zeta potential*. Zeta potential is a key factor used in the preparation or destruction of colloidal dispersions and in manufacturing processes, and it is also widely employed across a broad spectrum of industrial and academic sectors to monitor and tune the behavior of colloidal systems. For example, the pigments in paints must be well dispersed in order for the paint to perform successfully. If the pigments agglomerate, then the paint will seem to have larger pigment particles and may fail color quality tests. Gloss and texture are also affected by the degree of dispersion between the particles in the paint. These phenomena can all be controlled and tuned by monitoring and adjusting the zeta potential of pigments. Many other examples from other fields can be given. A brief synopsis of a long list of zeta potential applications includes:

Adsorption	Biomedical technology	Clay technology
Detergency	Emulsions	Flocculation
Genetic Studies	Mineral and ore floatation	Oil well technology
Paints	Paper-making	Pharmaceuticals
Rheological Studies	Soil Mechanics	Waste treatment

The present chapter is dedicated to how the zeta potential of microparticles is characterized. It is divided into five sections as follows: Section 6.2 defines and describes zeta potential and introduces the most popular way to measure zeta potential, i.e., the electrophoretic mobility measurement. Section 6.3 describes the modern technology used to measure electrophoretic mobility - electrophoretic light scattering (ELS), including the optics and the sample cell; followed by the data analysis of ELS experiment in Section 6.4. Section 6.5 introduces a new technique in ELS, known as phase analysis light scattering (PALS) that can be used to measure extremely small mobilities in non-polar media.

## 6.2. Zeta Potential and Electrophoretic Mobility

### 6.2.1. ZETA POTENTIAL

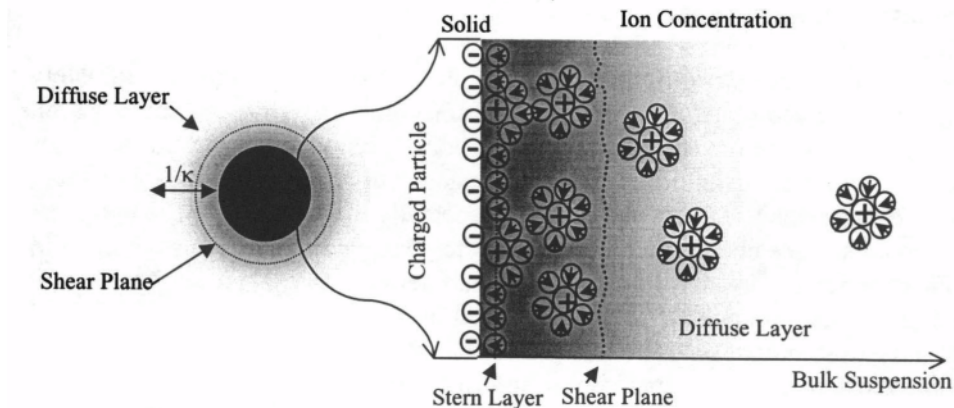


Figure 6.1. Electrical double layer structure according to the Gouy-Chapman-Stern-Grahame model.

When a colloidal particle carrying surface charge is dispersed in a liquid, ions of opposite charge (called counter-ions) in the suspension are attracted to the particle forming a firmly attached layer around the surface called the Stern layer. Additional counter-ions are still attracted by the particle, but now they are repelled by the Stern layer as well as by each other. This dynamic equilibrium

results in formation of a diffuse layer of counter-ions in order to neutralize the charged particle. There is a high concentration of counter-ions near the surface, which gradually decreases with distance, until it reaches equilibrium with the counter-ions concentration in the bulk. Meanwhile, co-ion concentration gradually increases as the distance from the particle surface increases until it reaches the concentration in the bulk at a large distance. Most of the surface charge is neutralized by the tightly bound counter-ions in the Stern layer; the remaining charge is balanced by the diffuse layer of counter-ions extending far outside to the bulk phase. Such a diffuse layer can be visualized as a charged atmosphere surrounding the particle (Figure 6.1).

For originally non-charged particles dispersed in polar media, the surface preferential adsorption of ions, surface molecular group dissociation, isomorphic substitution, adsorption of polyelectrolytes, and even surface polarization will make them behave similarly to charged particles. The Stern layer and diffuse layer comprise what is commonly known as the electrical double layer, the thickness of which depends on the type and concentration of the ions in the suspension as well as on the particle surface. A parameter, called the Debye-Hückel parameter  $\kappa$ , is used to characterize electrical double layer thickness.  $\kappa$  has the dimension of reciprocal length. For smooth surfaces in simple electrolytes,

$$\kappa = \left( \frac{e^2 \sum n_i^0 z_i^2}{\epsilon k_B T} \right)^{1/2} = 3.288 \sqrt{\frac{1}{2} \sum C_i z_i^2} \text{ (nm}^{-1}\text{)}. \quad (6.1)$$

In Eq. 6.1,  $e$ ,  $n_i^0$ ,  $\epsilon$ ,  $k_B$ ,  $T$ ,  $C_i$  and  $z_i$  are the elementary charge, the number of ions of type  $i$  per unit volume in the bulk, the permittivity of the medium ( $= \epsilon_0 D$  with  $\epsilon_0$  being the permittivity in *vacuo* and  $D$ , the dielectric constant), the Boltzmann constant, the absolute temperature, the concentration in units of M (mol/l), and the valence of the ion  $i$ , respectively. The second equality is for aqueous suspensions at 25°C. Due to charge separation on the surface of a particle there is an electro-kinetic potential between the surface of particle and any point in the bulk which is called the surface potential with the voltage amplitude being in the order of millivolts. Surface potential drops off roughly linearly in the Stern layer and then exponentially throughout the diffuse layer because of the gradual change of counter-ion concentration. Surface potential approaches zero at the boundary of the double layer. Since the whole suspension is neutral, the potential in the bulk has to be zero.

It is not easy to directly measure the surface potential of small particles. Even if it was possible, because of statistical reasons the measurement cannot be made on only one particle. One way to measure surface potential of small

particles macroscopically, though indirectly, is to apply an electric field to the colloidal suspension and measure the velocity of the moving particles. This moving velocity of the particles is related to the electric field strength and to the particle's electric potential at the boundary between the moving particle and liquid. A particle never moves alone; it always moves carrying a certain amount of the surrounding molecules and ions in the medium because of the attraction force and the friction force between the particle's solid boundary and the molecules and ions (or other species) in the medium. Fluid very close to the particle moves with a velocity similar to that of the particle. Further away from the surface, because of the shear force and viscosity of the medium, fluid moves slower and its velocity decreases as the distance to particle surface increases until at some distance away the medium is static and not moving. Since the actual velocity profile of the surrounding liquid as a function of distance to the surface is affected by many factors, there is no simple model available to describe such velocity profiles. One approach widely used in colloid science is to define an imaginary plane called the shear plane. Liquid as well as all species between the shear plane and particle surface presumably moves along with the particle at the same velocity when the particle moves. Beyond the shear plane liquid and other species will not move at all when the particle moves. Obviously, in this simplified model of a moving velocity profile the location of shear plane is ill-defined, and in most cases is difficult to pin-point. In general, the shear plane is located between the Stern layer and the outer boundary of the diffuse layer (Figure 6.1). This simplified definition provides a great practical feasibility in the measurement of surface potential of micro-particles as will be described throughout the rest of this chapter.

The electric potential of a particle varies gradually from the value of the surface potential ( $\psi_0$ ) to zero. For the majority of particles without a complex surface structure, the variation is monotonic. Thus, electric potential at the shear plane is in between  $\psi_0$  and zero (Figure 6.2). This potential is called the *zeta potential* ( $\zeta$  potential). Zeta potential is different from surface potential  $\psi_0$  but is a measurable amount. Since the shear plane is located at the "frontier" of the particle surface, any interfacial interaction of particle with other species (ions, neighboring particles, etc.) in medium will be encountered at the shear plane. Zeta potential actually has more direct influence compared with surface potential. Zeta potential is determined by many factors, mainly 1) surface potential, 2) potential curve, which is determined by the concentrations and valences of the co- and counter ions in the system and the dielectric constant of the continuous phase, and 3) location of the shear plane. There is no definite relationship between surface potential and zeta potential. For example, in different environments and particle surface conditions, the same zeta potential may correspond to different surface potentials and the same surface potential may result in different zeta potentials. Figure 6.2 describes the relation between

these conditions and zeta potential. These hypothetical potential curves are from three possible situations, such as the different media's ionic strengths (Curves a and b), and the surface adsorption of ionic species (Curve c). Potential curves a and b have the same  $\psi_0$  but their potential variation as a function of distance to the surface are different resulting in different zeta potentials. Curve c has a different  $\psi_0$  from curve a, but these two curves have the same zeta potential. If for some reason the shear plane location is shifted (moved to Shear plane 2 in Figure 6.2, one such way to shift the shear plane is by adsorbing polymer chains onto the surface) then Curves a and c may no longer have the same zeta potential. Zeta potential is a "representation" of particle surface charge. In reality, its measurement only gives an indication as to what the surface charge and potential might be, although that is adequate in many cases.

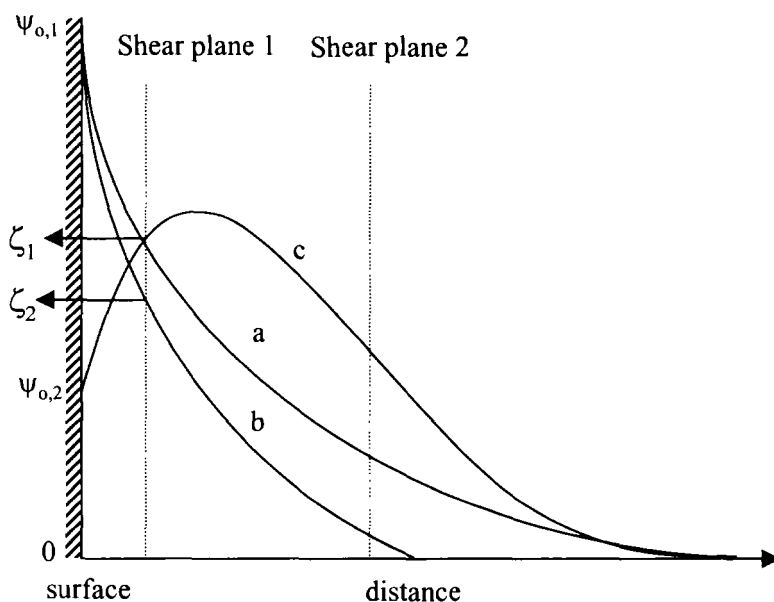


Figure 6.2. Electric potentials of a charged surface.

Zeta potential is related to electrostatic repulsion when two colloids approach each other and their double layers begin to interfere. An electrostatic repulsion curve is used to indicate the energy that must be overcome if the particles are to be forced together. It has a maximum value when the particles are almost touching and decreases to zero outside the double layer. In the meantime there are the van der Waals attraction forces between the individual molecules in any colloid that pulls colloids together. These two opposite types of forces determine whether colloids agglomerate or remain dispersed. If the net energy

is attractive, the particles agglomerate. If the net energy is repulsive, then the point of maximum repulsive energy is called the energy barrier. The height of the barrier indicates how stable the system is. In order for agglomeration to occur, two particles on a collision course must have sufficient kinetic energy due to their velocity and mass to jump over this barrier. Therefore, zeta potential is closely related to stability of colloidal systems. Quantitatively, since zeta potential varies depending on many factors such as the steric effect between particle surfaces and the concentration and type of ions in solution, there is no single guideline to what absolute value the zeta potential should be in order to create a stable colloidal dispersion. Commonly, 30 mV is accepted as the threshold for stability in many colloidal systems. For oil/water emulsions, the threshold is 5 mV, and for metal sols, 70 mV. When the zeta potential is higher than the threshold strong electric repulsive forces will prevent the particles from getting too close thus increasing its stability. The higher the zeta potential is, the more stable the system will be. Below the threshold, electric static repulsive force may not be strong enough to overcome the attractive van der Waals force between particles and so particles may agglomerate causing destruction of the colloidal stability. In the neighborhood of the isoelectric point (where the zeta potential is zero) aggregation is most likely to occur.

There are two different definitions of the zero point regarding to the charges on colloidal particles in different suspension conditions. The suspension pH is the variable most commonly used. Other variables such as total ionic strength or the concentration of some specific ion are also sometimes used. The *point of zero charge* (PZC) is the point at which the particle surface charge is zero. This usually occurs at the pH when adsorption of the  $H^+$  ions is equal to that of the  $OH^-$  ions. The PZC can be determined by a potentiometer or by conductometric titration. The *isoelectric point* (IEP) is the point at which the zeta potential is zero and is determined by electrophoresis measurement. The IEP varies significantly between different materials. For example, silica ( $SiO_2$ ) has an IEP at  $pH = 2$  while magnesia's IEP is at  $pH = 12$ . In the absence of specific adsorption,  $IEP = PZC$ . Specific adsorption causes the IEP and the PZC to separate apart along the pH scale in opposite directions and may have very different values than that of particles with a "clean" surface.

The information on colloidal surface and zeta potential introduced above is given only for the purpose of providing some background knowledge that is needed to understand ELS technology, and is by no means meant to lecture the reader beyond the ABCs of colloid science. Interested readers are suggested to consult monographs of colloid science, especially those dealing with zeta potential for more detailed discussion [1,2,3].



### 6.2.2. ELECTROPHORETIC MOBILITY

The most popular and straightforward way to determine zeta potential is to apply an electric field to a colloidal suspension. In the case of neutral particles nothing happens, while particles carrying surface charges will have an oriented motion dependent on the direction of the electric field. Several phenomena (collectively known as electrokinetic effects) are observed; i.e., electrophoresis, electroosmosis, streaming potential, and sedimentation potential. In this chapter we will discuss the first two effects.

Electrophoresis is the motion of a liquid-borne particle in an applied electric field. Electroosmosis is the motion of a liquid relative to a fixed charged interfacial surface in an applied electric field. The applied field acts on the ions in the liquid which during their movement in the field move the liquid along with them. If surface morphology and any polarization change induced by the field and shape effect are discounted, as a first-order approximation particle moving velocity in low field will be proportional to the field strength and particle surface charge density. Electrophoretic mobility is defined as the electrophoretic velocity ( $u$ ) per unit electric field:

$$\mu = u/E. \quad (6.2)$$

The unit for  $\mu$  in SI nomenclature is  $m^2/V \cdot s$ . A more convenient unit having the same order of magnitude as that of most colloidal particles is  $\mu m \cdot cm/V \cdot s$ . Because there are molecules of the medium as well as ions surrounding the particles, and because many of them move with the particles, the relationship between the particle surface condition and mobility is not simple. For nonconducting spheres, Henry derived the following relation (Eq. 6.3) between zeta potential and electrophoretic mobility almost seventy years ago [4] under the assumptions:

- a) the total electric field a particle experiences is a superposition of the applied field and the field due to the charge on the particle;
- b) the distortion of the field induced by the movement of the particle (i.e., the relaxation effect) can be ignored;
- c) the inertial terms in the hydrodynamic equation are negligible;
- d)  $e\psi/k_B T \ll 1$ .

$$\mu = \frac{2\zeta\epsilon}{3\eta} f(\kappa r), \quad (6.3)$$

$$f(\kappa r) = 1 + \frac{(\kappa r)^2}{16} - \frac{5(\kappa r)^3}{48} - \frac{(\kappa r)^4}{96} + \frac{(\kappa r)^5}{96} - \left( \frac{(\kappa r)^4}{8} - \frac{(\kappa r)^6}{96} \right) e^{\kappa r} \int_{\infty}^{\kappa r} \frac{e^{-t}}{t} dt \quad (6.4)$$

$$\approx \frac{3}{2} - \frac{9}{2\kappa r} + \frac{75}{2(\kappa r)^2} - \frac{330}{(\kappa r)^3}$$

where  $\eta$  and  $r$  are the medium's viscosity and the sphere radius, respectively. When  $\kappa r > 25$ , the value for  $f(\kappa r)$  can be approximated (the second line in Eq. 6.4) which is accurate to three significant figures. The function  $f(\kappa r)$  is a monotonic function of  $\kappa r$  varying from  $f(\kappa r)_{\kappa r \rightarrow 0} = 1$  to  $f(\kappa r)_{\kappa r \rightarrow \infty} = 3/2$ . There are many refined or more rigorous models between  $\mu$  and  $\zeta$  without having to impose above restrictions [5,6,7]. However the calculation of zeta potential from electrophoretic mobility using these procedures requires tedious computation and prior knowledge of some parameters related to the sample, whose values are often unknown or difficult to obtain. When  $\kappa r < 0.01$  or  $> 200$ , the zeta potential calculated from the Henry equation and from the more rigorous models is virtually the same. In the range of  $\kappa r$  between 1 and 10, there is no unique assignment of  $\zeta$  to a particular mobility  $\mu$  according to these rigorous models. If one uses the Henry equation the error in the zeta potential computed due to the neglect of the relaxation effect is a function of  $\mu$  and  $\kappa r$ . This error increases monotonically with increasing  $\mu$  and reaches a maximum when  $\kappa r$  approaches around 4 [5].

Table 6.1. Theoretical models for electrophoretic mobility of regularly shaped particles

Particle Shape	Characteristic	Reference
Sphere	Uniform	[4,5,6,7]
	In weak electrolyte	[8]
	Non-uniformly charged	[9]
	Porous	[10]
	Hairy	[11]
Rod	Randomly oriented	[4,12,13]
	Polarized double layer	[14,15,16]
Spheroid	Low potential	[17]
	Thin double layer	[18]
	Non-uniformly charged	[19]

Relationships between electrophoretic mobility and zeta potential for other types of particles in dilute suspensions can be found in the literature and are summarized in Table 6.1. To date, these rigorous or approximate models have only academic significance as evidenced in many research publications of electrophoretic mobility determination of various model systems. Their

applications in the real world are fairly limited. Since in most experiments, a distribution of particles having different sizes and so different  $\kappa r$  values are measured, it is impractical to apply complex and different conversions for each component in the distribution in order to obtain the complete zeta potential distribution.

Eq. 6.3 with  $f(\kappa r)$  taking the value of either  $3/2$  for large particles when  $\kappa r > 200$ , called the Smoluchowski equation, which was derived even earlier than Henry's function [20], or  $1$  for small particles when  $\kappa r < 0.01$ , called the Hückel equation, is still the most popular way to convert a mobility distribution to a zeta potential distribution. Electrophoretic mobility can also be presented by particle's surface charge density  $s$  [21]

$$\mu = \frac{ze f(\kappa r)}{6\pi\eta r(1 + \kappa r)} = \frac{2rf(\kappa r)s}{3\eta(1 + \kappa r)} = \left( \frac{s}{\eta\kappa} \right)_{\kappa r > 200} \quad (6.5)$$

In practice,  $1/\kappa$  is generally of the order of a few nm, and so the limit of small particles is rarely achieved and the limit of large particles is quite common in which  $\mu$  is independent of particle size and determined directly by the surface charge density.

Microelectrophoresis measurement is the conventional and direct way to determine electrophoretic mobility. It can be traced back to two centuries ago when Reuss performed the first electrophoresis experiment on clay particles as shown in Figure 6.3 [22].

In a microelectrophoresis experiment, the suspension is injected into a capillary with a pair of electrodes located at the ends of capillary. Eyes (often with the help of an optical microscope) or other optical elements are used to directly observe the movement of the particles in suspension. The application of an electric field causes the attraction of charged particles towards the electrode of opposite charge. Particles accelerate during a short time ( $< 10^{-5}$  s) until the friction force of viscous drag due to their translation through the stationary solution matches the attractive force of the field. The time an individual particle will move a given distance between two well-defined points is determined by the operator. From the time and the distance, the particle velocity is calculated. From the current, conductivity of the solution, and the cross-sectional area of the cell, the electric field strength is determined. The electrophoretic mobility is thus calculated. This microscopic method suffers from many serious disadvantages:

- 1) It is very slow, tedious, and time-consuming;
- 2) Only a few particles can be followed and timed;
- 3) It yields results of low statistical significance;
- 4) It is confined to particles visible under the microscope;

- 5) It cannot be used to determine mobility distribution;
- 6) There is a bias toward more easily visible particles;
- 7) Eyestrain becomes unbearable after a short while.

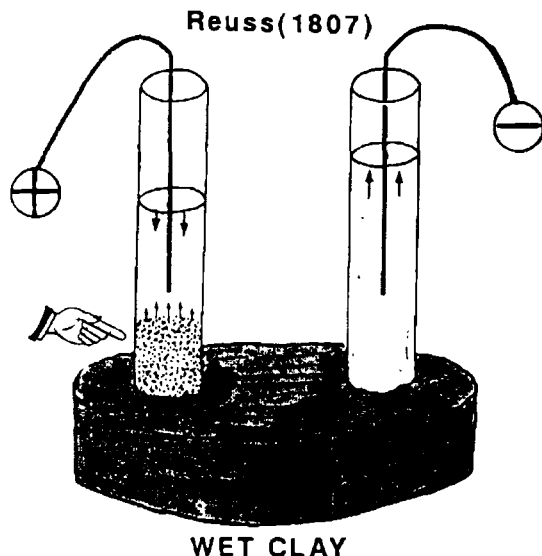


Figure 6.3. Reuss' electrophoresis experiment setup [23] (by permission of Japanese Electrophoresis Society).

Lately, computer-controlled experiments combining image recording facilities with image analysis software have greatly increased measurement accuracy and speed, and released the operator from labor-intensive operation. However, some limitations still remain. This method is based on the measurement of individual particles and may offer high resolution but with very low statistical accuracy, especially for samples that have polydisperse electrophoretic mobility. In order to record an accurate moving distance, prolonged application of an electric field may have to be used, and that may introduce some adverse effects. In addition a very low particle concentration is needed in order to track individual particles. For submicroscopic particles, moving-boundary electrophoresis, in which a sharp boundary formed between a solution containing particles and a buffer solution is monitored as an electric field is applied, was used in earlier days for the analysis and separation of plasma proteins, leading to a Nobel prize for the inventor Tiselius in 1948 [24,25]. The moving-boundary method is rarely used today because it is slow and the concentration gradients and boundaries can lead to anomalies and difficulties in interpretation. There are other ways to measure electrophoretic mobility and zeta potential, including the acoustic method and the electroacoustic method which are briefly described in Chapter 1.

### 6.2.3. ELECTROPHORETIC LIGHT SCATTERING

ELS is a technology for rapid measurement of electrophoretic mobility via the Doppler shifts in the scattered light. The methodology is loosely analogous to the determination of the speed of a moving object by radar, where the velocity is obtained by measuring the Doppler shift of microwave radiation reflected by the object. In an ELS experiment, a coherent incident light illuminates dispersed particles in a diluent that is subject to an applied electric field. Charged particles move toward either the anode or the cathode, depending on the sign of their net charge. Because of the motion, the frequency of scattered light from particles will be different from that of the incident light due to the Doppler effect. From the frequency shift and frequency shift distribution, the velocity of particles traveling through the diluent can be determined, and consequently the electrophoretic mobility (or zeta potential) and particle diffusion coefficient can be measured simultaneously. Compared to microelectrophoresis, ELS is an indirect ensemble method that provides rapid, accurate, automatic, highly reproducible electrophoretograms of complex particulate samples suspended in both aqueous and non-aqueous media without the need for calibration. Since its inception in 1971 [26,27], ELS has become the most popular method to measure electrophoretic mobility (or the zeta potential) of biological particles ranging from small proteins to large living cells, and colloidal particles from gold sols to multiple component drilling mud. The application of ELS has proved ever more useful in both industrial and academic laboratories for both diagnostic and predictive measurements [28].

### 6.3. Instrumentation

ELS is a measurement of scattering intensity fluctuations from suspended particles under influence of an applied electric field. It measures the ACF or power spectrum of interferential light intensity using the heterodyne arrangement (Scheme C, Figure 2.17); i.e., light of different frequency is mixed with the scattered light. ELS instrumentation is very similar to that of PCS since they operate under the same principles and detect similar signals. In fact, when the electric field is turned off an ELS instrument can perform a PCS experiment and measure particle size distribution in the heterodyne mode; and when the reference light is also blocked, an ELS instrument is no different from a PCS instrument. Many designs combine the measurement of particle size and zeta potential in the same instrument, making it is more versatile. As shown in Figure 6.4, an ELS instrument consists of a coherent light source, delivering optics, a sample module, collecting optics, detectors, and correlators or spectrum analyzers, and a computer to control the experiment, analyze data and

report results. We have discussed each of the elements in a PCS instrument in Chapter 5 and will not repeat those that are either identical or very similar to those in ELS instrumentation. Only the ones that are unique to ELS are discussed here. These include the ways that the frequency-shifted reference light is produced (the frequency shifter), and how it is mixed with the scattered light; the cell design; the electric field; and the data collection scheme. Data analysis in ELS is discussed in the next section.

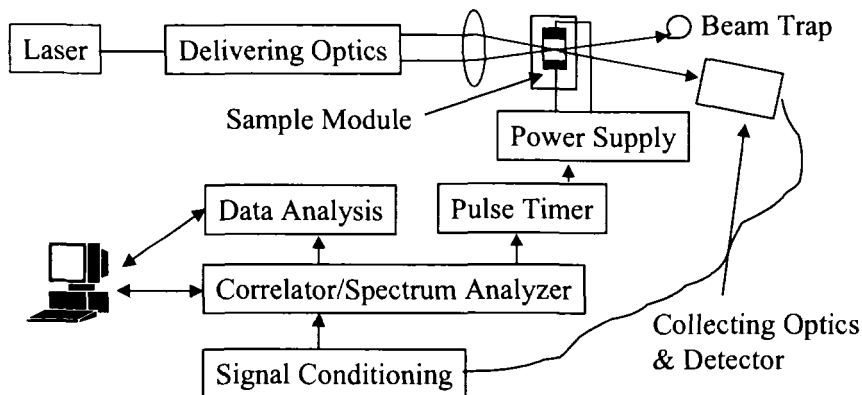


Figure 6.4. Schematic of ELS instrumentation.

### 6.3.1. HETERODYNE MEASUREMENT

In PCS experiments, the measurement is commonly performed in the self-beating mode, in which all non-particle-scattered light is avoided during detection, and the particle size distribution is produced by analyzing the ACF. Although spectral analyses of power spectra, which consists of Fourier transform of the ACF can also be used in PCS experiment, it is much less common for both practical and theoretical reasons. In ELS, the primary goal is to measure oriented motion that is proportional to the frequency shift of scattered light. Analysis of the power spectrum often provides an easy and direct means to obtain mobility information, although the ACF can also provide the same information. There are two ways to obtain a power spectrum. One is to use a spectrum analyzer to analyze the photocurrent directly; the second one is to acquire the ACF first and then to obtain the spectrum by Fourier transformation.

In ideal situations, there are two types of motion for particles in an electric field: the jostling motion of random Brownian diffusion and an oriented electrophoretic motion. In the power spectrum, the Brownian motion is characterized by a Lorentzian peak centered about the frequency shift produced by electrophoretic motion. Analogously, in the ACF, electrophoretic motion is a

cosine factor in the exponential decay produced by Brownian motion. In order to distinguish the shifted frequency of scattered light, usually in the range of zero to a few hundred Hz from the incident light frequency ( $\sim 10^{14}$  Hz), the light beating technique has to be used in which a portion of the incident light is mixed with the scattered light (Figure 2.16). The interference between these two beams results in a “beating” frequency that is the product of the frequency shift due to particle velocity. In this homodyne arrangement, the frequency shift of the scattered light will start from 0 Hz when the field is off and move to the frequency corresponding to the electrophoretic motion as the field is applied. Some significant problems are encountered when using the homodyne method. Because the beating frequency is located near 0 Hz, environmental disturbances, such as building and table vibration or electrical noise, are often problems during measurement. In addition, the desirable AC coupling of the signal causes the low-frequency content to be lost. Finally, because the method uses a frequency measurement centered at 0 Hz, the direction of particle movement, which corresponds to the sign of the charge on the particles and the electric field polarity, is difficult to determine, since light beating only detects the frequency difference and not the sign of the difference. To overcome this ambiguity, in practice all ELS experiments adopt a heterodyne arrangement, in which a coherent reference light of different frequency is mixed with the scattered light. In this arrangement, even for stationary particles, there is a fixed frequency difference between the scattered light and the reference light, typically between 50 Hz to 500 Hz, which effectively moves the frequency reference point from zero to the preset frequency. When the particles move, depending on the direction of their movement, the Doppler shift of the scattered light will either increase or decrease the net frequency difference between the scattered light and reference light, and thus the charge sign of the particles can be distinguished from the known polarity of the applied electric field. In addition, since the starting point is now not at 0 Hz, the measurement is more immune to environmental disturbance.

As shown in Figure 6.5, the reference beam is split from the main beam and so they have the same characteristics. One of the beams, either the main beam or the reference beam is then frequency-shifted before it is delivered to the sample cell. The photodetector detects both the directly incident reference beam and the scattered light from particles in the cell illuminated by the main beam. Typically, the intensity of the reference beam is such adjusted so that its intensity is at least a few times stronger than that of the scattered light so that the condition of  $I_L \gg I_s$  can be satisfied. Because the scattered light in a small angular cone for most colloidal particles is typically only  $10^{-4}$  of the illuminating intensity, the intensity ratio of the main beam to the reference beam is typically larger than 100. Thus, in Figure 6.5, even though the reference beam also illuminates the cell and particle scattering will be produced and collected at

zero angle scattering, its contribution is negligible when compared to the scattering from the main beam. To completely avoid scattering from the reference beam, the reference beam can be guided using mirrors to bypass the cell and enter the detector directly (illustrated by the dotted line, instead of the dashed line, in Figure 6.5). Multiple reference beams can be produced and used simultaneously with corresponding detectors to make simultaneous multiangle measurements.

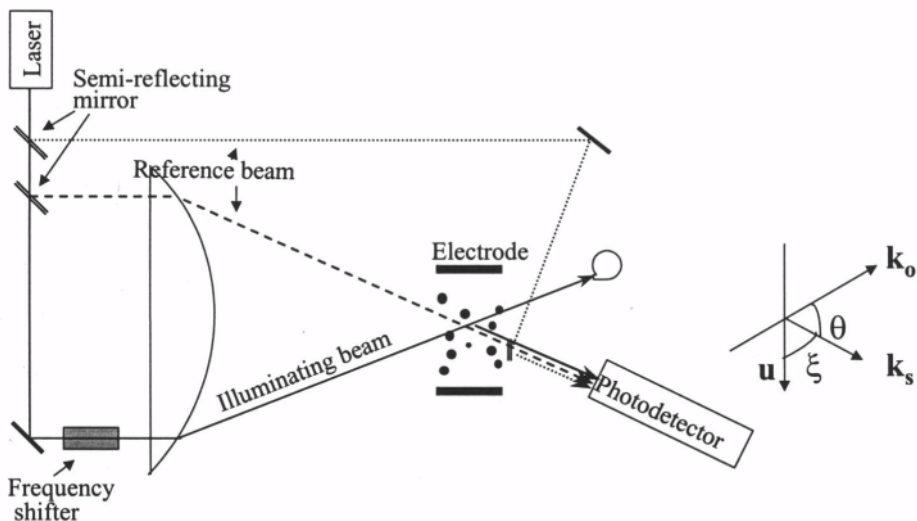


Figure 6.5. Reference beam optics in electrophoretic light scattering.

As shown in Figure 6.5, the illuminating beam and the scattered light have wave vectors  $\mathbf{k}_o$  and  $\mathbf{k}_s$  and particles move with a velocity  $\mathbf{u}$ . The angles between  $\mathbf{k}_o$  and  $\mathbf{u}$  and between  $\mathbf{k}_s$  and  $\mathbf{u}$  are  $(\theta + \xi)$  and  $\xi$ , respectively. If we treat a particle that receives a non-moving incident light and scatters light that will be detected by a stationary detector as a moving transmitter, there are actually two Doppler shifts. According to Eq. 2.23, the Doppler shift for the light frequency is

$$\Delta\nu = \frac{v_o}{c} u. \quad (6.6)$$

Here  $u$  is the component of  $\mathbf{u}$  in the direction of light. Motion with respect to the incident light causes a shift:

$$\Delta\nu_1 = -\frac{v_o}{c} \mathbf{u} \cdot \frac{\lambda}{2\pi} \mathbf{k}_o = \frac{-\mathbf{u} \cdot \mathbf{k}_o}{2\pi}. \quad (6.7)$$



Similarly, motion with respect to the stationary detector causes a second Doppler shift:

$$\Delta v_2 = \frac{v_o}{c} \mathbf{u} \cdot \frac{\lambda}{2\pi} \mathbf{k}_s = \frac{\mathbf{u} \cdot \mathbf{k}_s}{2\pi}. \quad (6.8)$$

The total frequency shift of the scattered light when compared with the illuminating beam, excluding the Brownian motion, is then:

$$\begin{aligned} \omega_s - \omega_o &= 2\pi(\Delta v_1 + \Delta v_2) = \mathbf{u}(\mathbf{k}_s - \mathbf{k}_o) = \mathbf{u} \cdot \mathbf{K} \\ &= \frac{2\pi n u}{\lambda_o} (\cos \xi - \cos(\theta + \xi)) = \frac{4\pi n u}{\lambda_o} \sin\left(\frac{\theta}{2}\right) \sin\left(\frac{\theta}{2} + \xi\right) \\ &= \frac{4\pi n u}{\lambda_o} \sin\left(\frac{\theta}{2}\right). \end{aligned} \quad (6.9)$$

The last equality exists if  $(\theta/2 + \xi) = \pi/2$  (i.e.,  $\mathbf{K}$  and  $\mathbf{u}$  are parallel), which is often adopted in practical instrumentation, where the Doppler shift will be maximized. When  $\xi = \pi/2$ ,  $\omega_s - \omega_o = 2\pi n u \sin \theta / \lambda_o$ . If the mobile direction is changed, the frequency difference will have the same amplitude but an opposite sign. The frequency difference between the scattered light and frequency-preshifted reference beam ( $\omega_L = \omega_o + \omega_{ps}$ ) now becomes:

$$\omega_s - \omega_L = \frac{4\pi n u}{\lambda_o} \sin\left(\frac{\theta}{2}\right) \sin\left(\frac{\theta}{2} + \xi\right) - \omega_{ps}. \quad (6.10)$$

According to Eq. 6.9, the Doppler shift will vanish at the limit of the zero degree scattering angle, since at the forward scattering direction the Doppler shifts with respect to the laser and the detector cancel each other exactly ( $\Delta v_1 = -\Delta v_2$ ). This is another reason that even though the reference beam passes through the cell, its zero degree scattering will not affect the observed mobility.

Another less common optical arrangement used to measure electrophoretic motion is the crossbeam method as shown in Figure 6.6. In the crossbeam method, the main beam is split into two beams of equal intensity, one beam's frequency being preshifted (e.g.,  $\omega_{o1} = \omega_o + \omega_{ps}$ ). The detector is located in between the two beams. The scattering from each particle is a product of its illumination of both beams yet at different scattering angles. Another way to view the arrangement is to understand that since the two beams are coherent, they form an interference pattern in the cell. The detection of electrophoretic motion is through particle's movement in the strip-like pattern with the fringe

spacing  $\Delta x = \lambda_o/2n\sin\theta$ . The frequency shift now results from two scattered beams, and is independent of either scattering angle and only depends on the crossbeam angle  $\theta'$ :

$$\begin{aligned} & (\omega_{s1} - \omega_{o1}) - (\omega_{s2} - \omega_{o2}) \\ &= \mathbf{u}(\mathbf{k}_s - \mathbf{k}_{o1}) - \mathbf{u}(\mathbf{k}_s - \mathbf{k}_{o2}) - \omega_{ps} = \frac{4\pi n u}{\lambda_o} \sin \theta' - \omega_{ps}. \end{aligned} \quad (6.11)$$

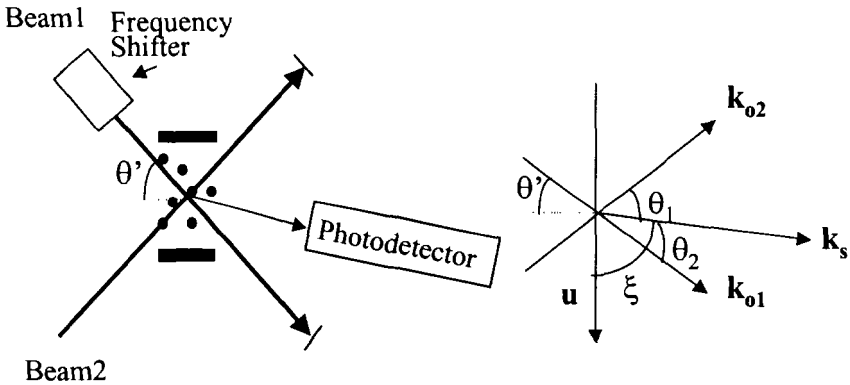


Figure 6.6. Crossbeam optics in electrophoretic light scattering.

A broad scattering volume is important for reducing transit-time broadening of the spectrum, which results from particles passing through the scattering volume in less time than the duration of data collection. To avoid transit-time broadening, the laser beam is focused into a long, thin shape at the scattering region. Another reason to create a broad scattering volume is for statistical purpose. For large particles in dilute suspension, the number of particles in the scattering volume can be few, and become the limiting aspect of spectral quality. The scattering volume should also be constructed to avoid the cell windows, and the regions very near the windows. The positioning of the beam cross point and selection of their relative intensities to satisfy  $I_L \gg I_s$  are critical to the optimization of signal quality.

### 6.3.2. FREQUENCY SHIFTER

In order to shift the frequency of one of the two beams, a device called frequency shifter is needed. A frequency shifter shifts the light frequency without changing its intensity. There are several ways that can be used to shift the frequency of light, which are commonly used in laser Doppler velocimetry

[29]. The most common way is to change the pathlength at a constant rate during light transmission. The phase part of an electromagnetic wave is  $2\pi\nu(t+x/c)$  with  $c$  being the speed of light. If the transmission pathlength remains invariant,  $x/c$  is a constant and the light frequency is also a constant ( $=\nu$ ) at the detector surface. If the light pathlength changes at a constant rate, i.e.,  $x = x_0 + \alpha t$ , the phase of the electromagnetic wave becomes

$$2\pi\nu\left(t + \frac{x_0 + \alpha t}{c}\right) = 2\pi\nu\left(1 + \frac{\alpha}{c}\right)\left(t + \frac{x_0}{\alpha + c}\right) = 2\pi\nu'\left(t + \frac{x_0}{\alpha + c}\right). \quad (6.12)$$

The light frequency is now changed. The frequency change ( $\Delta\nu$ ) is equal to  $\alpha/\lambda$ . For a 500 Hz frequency shift in the light from a He-Ne laser ( $\lambda_0 = 632.8$  nm), the rate of pathlength change is about 0.3 mm/s.

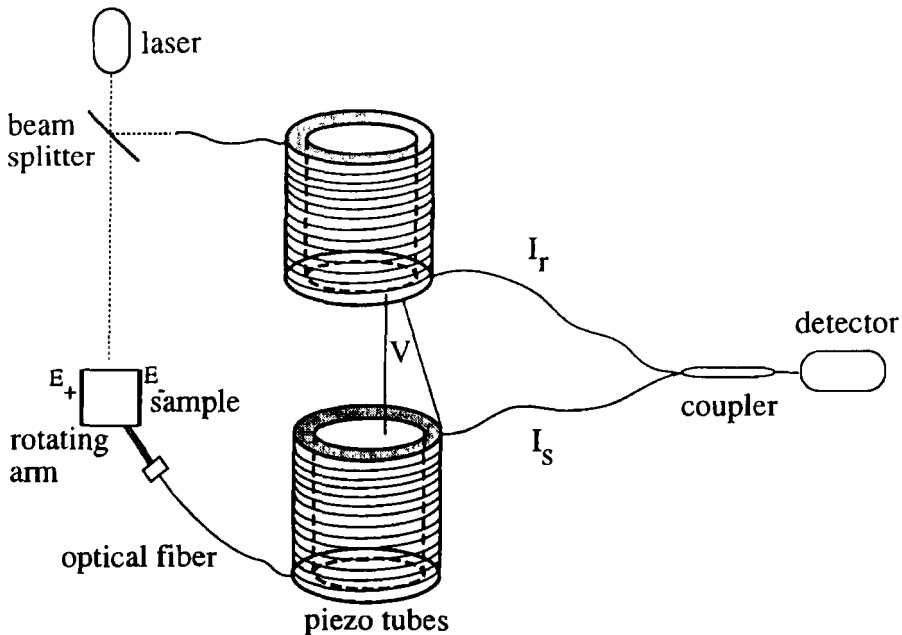


Figure 6.7. Schematic of a fiber optic frequency shifter. (Reprinted with permission from Xu, R., Schmitz, B., Lynch, M., A Fiber Optic Frequency Shifter, *Rev. Sci. Instrum.*, 1997, 68, 1952-1961. Copyright 1997, American Institute of Physics.)

The conventional way to change the pathlength is to insert two mirrors in the light's path. The light reflected by the first mirror is directed to the second mirror, upon which it is further reflected and directed into the sample cell. The distance between the two mirrors can be changed by moving one or both of the

mirrors at a constant rate which will effectively shift the light frequency. Frequency shifters using moving mirror systems have many disadvantages. They require high-precision mechanical components and are also very sensitive to any external vibration. They often have a large footprint and are expensive to manufacture.

An alternative way to produce a frequency shift by the same means (varying light pathlength) is to utilize the flexibility and light guiding properties of optical fiber. In a novel design of a fiber optic frequency shifter (Figure 6.7), the frequency shift is accomplished by stretching and contracting a length of optical fiber that is wound around two piezoelectric ceramic tubes. The diameters of the piezoelectric ceramic tubes are linearly changed when an electric field controlled by a closed loop servo is applied. A frequency shift of up to 300 Hz with duration of up to 2.5 s with a linewidth of less than 1 Hz can be achieved. The use of this type of fiber optic interferometer to produce a heterodyne of two beams can make an ELS instrument smaller, less expensive and more robust [30].

Acousto-optic modulation (commonly called the Bragg cell) which is based on the Debye-Sears effect can also be used to change the frequency of light [31]. When a light beam of frequency  $\omega_o$  is passed through a medium through which an acoustic signal is also propagating at a frequency  $\omega_b$  in a direction not parallel to the light beam, the light that diffracts from the acoustic wave will produce many diffraction lines in addition to the main transmission pattern. The two first-order diffracted beams have frequencies equal to  $\omega_o \pm \omega_b$ . Most of the incident beam power can be concentrated into one of the first-order beams through proper alignment, as shown in Figure 6.8.

However the typical acoustic frequencies required to produce good first-order diffraction are between 50-100 MHz, which is much too high for that needed in ELS experiments (usually between 25-500 Hz). Therefore, two Bragg cells with stable, but adjustable acoustic frequencies accurate to some tens of Hz (which can be realized using a single sideband modulator) are needed, one at each beam. One Bragg cell has the first order diffraction frequency of  $\omega_o + \omega_b$  and the other has a frequency of  $\omega_o + \omega_b + \omega_{ps}$ . Thus, the net difference in frequency of the two beams (one reference beam and one main beam in the reference beam optics and two cross beams in the crossbeam optics) is  $\omega_{ps}$  [32]. Because the difference in the adjustable acoustic frequency between two Bragg cells ( $\omega_{ps}$ ) are extremely small when compared with  $\omega_b$ , the spectral purity and uncertainty often cannot satisfy the requirement in an ELS experiment. In addition, amplitude modulation and cross talk between the two cells further deteriorates the beam quality. Therefore, using either the Bragg cell or by using a rotating grating in which two sidebands are produced due to the first-order diffraction effects with the frequencies being  $\pm 2\pi/a$  ( $a$  is the grating constant)

[33] to introduce frequency shift are not as effective as changing the light pathlength.

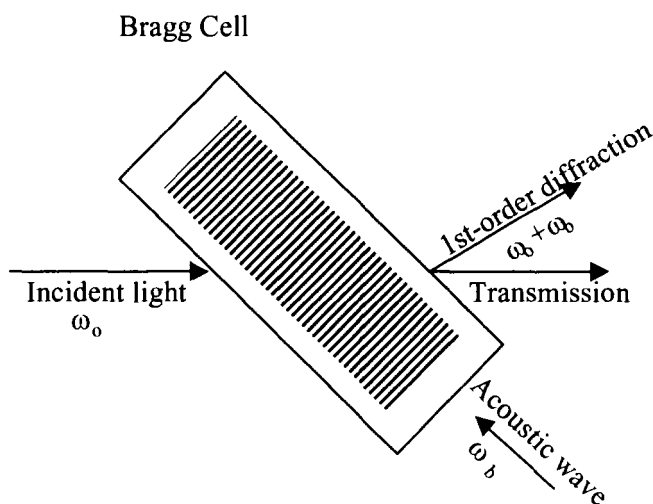


Figure 6.8. Schematic of the Debye-Sears effect using a Bragg cell.

### 6.3.3. SAMPLE CELL

The sample cell in ELS is used to hold the suspension sample, and to allow entering of the incident beam and exit of the scattered light, and to provide for an electric field. The electric field should be homogenous, stable, and cause the least disturbance to the sample, and not to obscure the optical measurement. Temperature control and stabilization are also important. Efficient heat transfer is required to minimize the rise in suspension temperature due to Joule heating during the application of an electric field. The material from which the cell is made must be chemically compatible with the samples to be studied, and the cell should be easy to clean. Two fundamentally different configurations of ELS cells have been proposed and are currently in use. One type is a cell in which the field is applied through a capillary. The development of this type of cell was created originally for microelectrophoresis experiments, evolving from the single flat tube cell [34], the double-tube cylindrical cell [35], the double-tube rectangular cell [36,37], the open-end capillary cell [38], to the current design. The other type of cell use an ordinary square cuvette in which the electric field is applied across a thin layer of sample in between two parallel electrodes. Each design has its own advantages and disadvantages. We will briefly describe these two types of cells along with their major features and drawbacks.

### Capillary ELS Cells [39]

In the capillary cell, a capillary (a few mm to a few cm long with the intersection dimension being a few mm) with the intersection being either circular or rectangular is used to hold the sample. Two electrodes are located at the ends of the capillary. The scattering volume is at the center of the capillary. Electrodes may have different forms. For rectangular capillary, different shapes have been adopted for various situations such as for suspensions of high concentration or high conductivity and for precipitating particles [40]. The following figures show a circular capillary cell with two probe-type electrodes (Figure 6.9), a rectangular capillary cell with two electrodes having hemispherical cavities (Figure 6.10), and a rectangular cell with membranes (Figure 6.11).

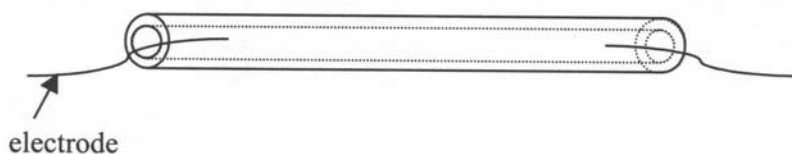


Figure 6.9. A simple capillary ELS cell.

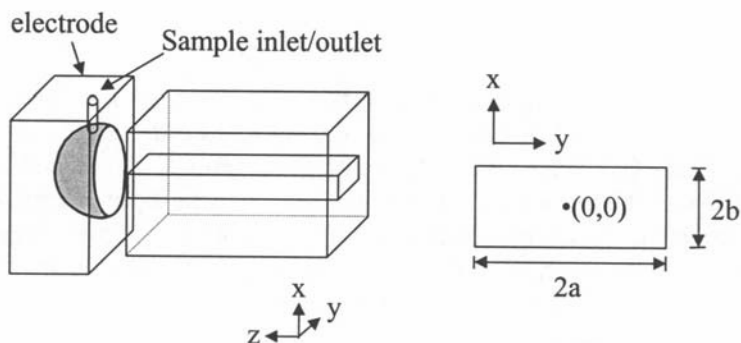


Figure 6.10. A capillary cell with electrodes having hemispherical cavities (only one electrode is shown).

The capillary provides a confined space for the electric field. At the center of the capillary, where scattering is detected, the electric field is parallel and homogenous. In addition, since the electrodes are at a distance away from the scattering volume, any possible disturbance produced from electrode surface (such as air bubbles, surface reaction, or Joule heating of the sample in the scattering volume) is minimized and the cell has a small thermal time constant

on the order of ten seconds [28]. For the electrodes in Figure 6.10, the surface in contact with the liquid is more than fifty times larger than the capillary intersection. Thus, the electric field is effectively “diluted” at the electrode surface, as shown in Figure 6.12 where the isopotential lines are vertical in the gap and become arcs of circles concentric with the electrodes in the cavities. In this instance, a high electric field can be obtained at the scattering volume while the field strength at the electrode surface is still relatively low to prevent the above adverse effects, which can be quite substantial when measuring suspensions of high conductivity such as seawater, from occurring. The ability of the instrument to apply a high electric field is very important for low mobility samples since the frequency shift produced by the Doppler effect is proportional to the field strength. Large volume metal electrodes can also easily dissipate the heat generated by the electric current. The narrow gap between the glass spacers also serves to inhibit convection in the scattering region. Although the solution outside the narrow channel that is housed by the curved walls exhibits convection that allows rapid heat transfer from the gap to the thermostatic large metal electrodes, convection is inhibited in the channel due to the stabilizing effect of the closely spaced horizontal surfaces. Another advantage of the capillary design is that the scattering angular range can be quite large, typically larger than 30 degrees, since the electrodes do not block the scattering path. Spectra obtained at widely differing angles allow qualitative determinations to be made about the particles size distribution and permit certain diagnostic determinations, such as whether peaks are due to noise or actual sample mobility.

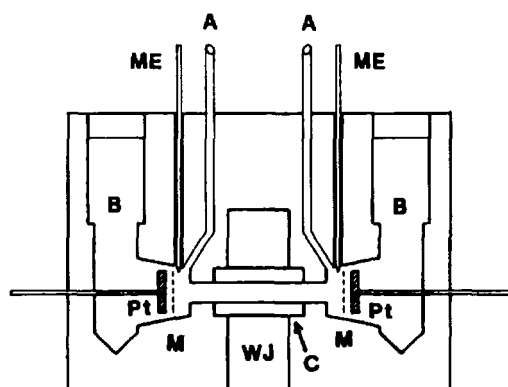


Figure 6.11. A capillary cell with membranes. C, quartz rectangular cell; Pt, electrode; M, semipermeable membrane; WJ, constant temperature block; B, electrode chamber; A, sample inlet/outlet; ME, monitor electrode [23] (by permission of Japanese Electrophoresis Society).

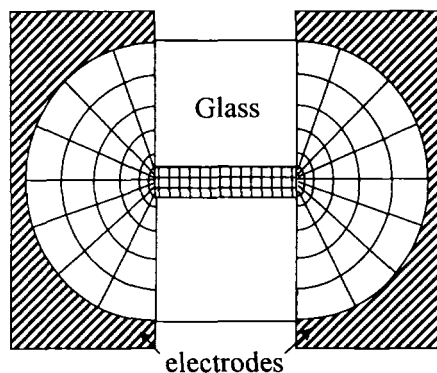


Figure 6.12. Electric field map for hemispherical electrodes separated by a dielectric insert.

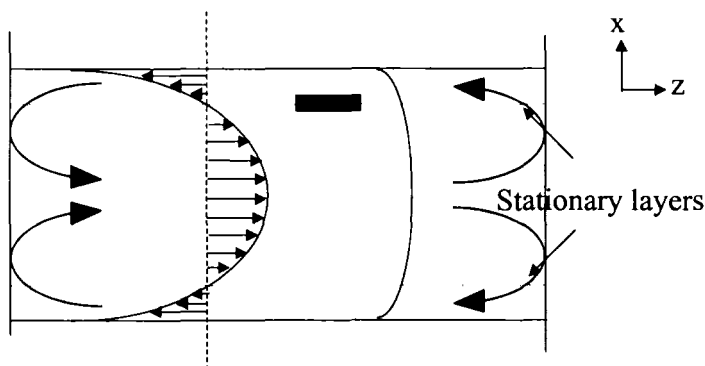


Figure 6.13. Liquid flow profile in a capillary. The coordinates are the same as the ones in Figure 6.10.

One major disadvantage of capillary ELS cells is created by the effects of liquid electroosmosis, which is the motion of liquid relative to a fixed, charged interfacial surface. Electroosmosis arises from the fact that most materials which capillaries are made of, such as borosilicate glass or silica quartz, carry charges in polar media. These charges mainly are the products of silanol groups whose concentration varies with both glass type and cell history [41]. When an electric field is applied the liquid near the surface moves along the applied field because of the diffuse double-layer charges in the fluid layer adjacent to the charged capillary surface. However, since the entire capillary is a closed system, the moving liquid near the wall has to reverse its motion at the end of the capillary and thus pushes the liquid in the central part of the capillary in the other direction forming a parabolic liquid flow profile as illustrated in Figure 6.13 in a 2-D view. For a given capillary shape and dimension, the profile can be theoretically predicted if all walls have the same surface charge condition.



For cylindrical capillaries the electroosmotic fluid mobility profile is

$$\mu_{eo}(r) = \mu_{0,eo} \left( \frac{2r^2}{R^2} - 1 \right), \quad (6.13)$$

where  $\mu_{0,eo}$ ,  $r$ , and  $R$  are the electroosmotic fluid mobility at the slip plane of the wall, the distance from the axis, and the capillary radius, respectively. For rectangular capillaries, theoretical models have been proposed with different boundary conditions at the cell walls: different upper and lower walls conditions [42]; side wall velocities being different than that of the upper and lower walls [43]. The following equations describe the liquid flow profile using the coordinates in Figure 6.10 for the common situation in which the four walls of a rectangular capillary have the same condition [44]:

$$\mu_{eo}(x, y) = \mu_{0,eo} \left( 1 + \frac{24ab}{6K + 16ab^3} (x^2 - b^2 - \chi) \right)$$

$$K = \frac{512b^4}{\pi^5} \sum_{n=0}^{\infty} \frac{(-1)^{n+1}}{(2n+1)^5} \tanh\left(\frac{(2n+1)\pi}{2b} a\right)$$

$$\chi = \frac{32b^2}{\pi^3} \sum_{n=0}^{\infty} \frac{(-1)^{n+1}}{(2n+1)^3} \cosh\left(\frac{(2n+1)\pi}{2b} y\right) \cos\left(\frac{(2n+1)\pi}{2b} x\right) \operatorname{sech}\left(\frac{(2n+1)\pi}{2b} a\right). \quad (6.14)$$

The shape of the parabolic flow profile varies with  $\mu_{0,eo}$  which changes depending on surface condition [45]. Because of the effect on liquid motion from electroosmosis, the observed particle motion under an electric field is no longer purely electrophoretic motion, but the net result of particle electrophoresis and liquid electroosmosis. In order to correctly access the electrophoretic mobility of the particles, the measurement has to be performed at the locations where liquid has no movement, i.e.,  $\mu_{eo}(r)$  or  $\mu_{eo}(x, y) = 0$ . These locations are called the stationary layer. For circular capillaries this layer is a circle with  $r = 0.707R$ . For rectangular capillaries, the stationary layer is a rectangle (Figure 6.14) with the locations (the distance from the walls) dependent on the width to height ratio of the capillary. For large ratios of  $a/b$ , the zero velocity at  $y = 0$  can be found by

$$x_{\mu_{eo}=0} = \pm b \sqrt{\frac{1}{3} + \frac{128b}{\pi^5 a}}. \quad (6.15)$$

For a width to height ratio of 3, the upper and lower stationary layers near the center of the channel are located at 84% and 16% of the capillary height ( $l$  in Figure 6.14). Using the coordinates in Figure 6.10, if  $a/b = 3$  and  $b = 0.5$  mm, the two horizontal stationary layers are located at  $x = \pm 0.34$  mm with the  $y$  values in the proximity of the channel center ( $y = 0$ ). The value of the coordinate  $z$  is irrelevant.

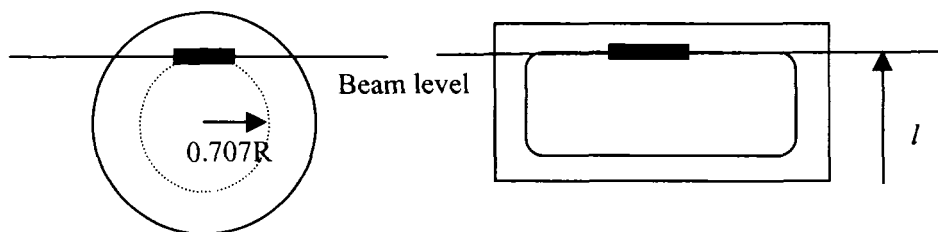


Figure 6.14. Stationary layers and scattering volume locations in capillary ELS cells (viewed at the cross section of the capillary).

In practice, when the incident beam is placed at a level as that indicated in Figure 6.14, the effect of liquid electroosmosis could be mostly eliminated. In Figure 6.13 and Figure 6.14, the thick bars indicate the preferred scattering volume location (the cross section of the incident beam and the detection cone). Obviously, since the incident beam has a certain thickness, particles actually are located adjacent to the stationary layer. For the rectangular capillary, it can be expected that liquid above and below the stationary layer experiencing only a small amount of electroosmosis in opposite directions will have net zero electroosmotic velocity. For circular capillaries, since the stationary layer is not a plane, a deviation from zero liquid velocity may result even when the beam center is located exactly at the stationary layer.

If the capillary is in a good condition, the electrophoretic mobility obtained at the stationary layer is electroosmosis-free. In fact, the electrophoretic mobility value of the electrophoretic mobility standard reference material (SRM) from NIST (the National Institute of Standards and Technology, Gaithersburg, MD) is determined by ELS using capillary cells measured at the stationary layers. However, if the surface charge (which is also affected by adsorption of ions and other species from the sample and air or gas bubbles) between the upper and lower inner surfaces of a rectangular capillary or at different locations in a circular capillary is inhomogeneous, an asymmetric liquid profile will be produced and errors of different significance will be

introduced [46]. Therefore, it is very important to make sure a symmetric profile exists so that true stationary layer locations can be maintained. One way to check this is to take measurements at different locations across the capillary height so that apparent electrophoretic mobility can be plotted as a function of beam location. Figure 6.15 shows apparent electrophoretic mobility values obtained at different cell positions in a rectangular capillary cell. The squares are from a PSL sample ( $d = 310$  nm) with a mobility of  $-4.20 \mu\text{m}\cdot\text{cm}/\text{V}\cdot\text{s}$ . The triangles are from a PSL sample ( $d = 90$  nm) with positive dodecyltrimethylammonium ions adsorbed in a 1 mM solution of NaBr. The symmetric shape of the profiles indicates that the upper cell surface and lower cell surface have the same surface condition. Two arrows indicate the two stationary layers where electroosmotic flow is null and true electrophoretic mobility can be obtained. More experimental results of electroosmotic flow profiles from various cells can be found elsewhere in the literature [40,47].

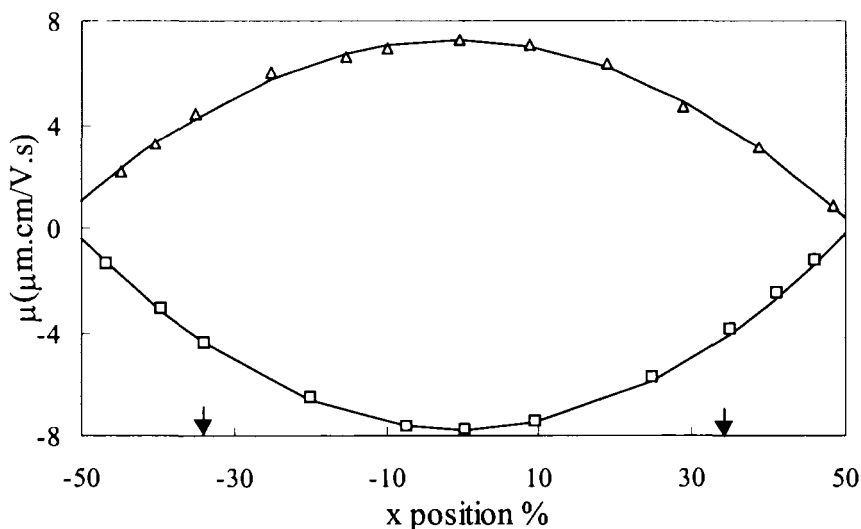


Figure 6.15. Apparent electrophoretic mobility values obtained at different cell positions.

Another effect of electroosmosis is the broadening in the reported mobility distribution. Any light beam has a finite thickness. In ELS instrumentation the illuminating beam typically has a beam thickness of  $50 \mu\text{m}$ . When the beam center is located at the stationary layer (the thick bar in Figure 6.13), part of the beam illuminates the liquid flowing toward the right-side and part of the beam illuminates the liquid flowing toward the left-side. Even for particles having ideally monodisperse mobility, the reported mobility will be a distribution instead of a single value although the mean may still be correct. At the capillary

center where the flow profile has a much flatter slope, liquid and particles will experience similar flow. Thus distribution broadening is minimal. Therefore, one way to obtain the right distribution in the presence of electroosmosis is to make two measurements, one at the capillary center and one at one of the stationary layers. Mobility distribution obtained at the center will have the correct shape but a shifted absolute value, which can then be corrected by the mean value obtained at the stationary layer [48].

Since capillary cells have many advantages, different approaches have been used to avoid or minimize the effects caused by electroosmosis. One way to reduce electroosmosis is by coating the internal surface of the capillary by a material that will reduce contact of silanol groups with the medium. There are various recipes available for coating ELS cells [49,50]. In particular, poly(ethylene glycol)-poly(ethylene imine) (PEG-PEI) coating or grafting significantly reduce electroosmosis and positively control adsorption and wetting in the glass surface over a wide range of pH and ionic strength. The coating stability and ease of application in using these recipes need to be further improved. The reduction in electroosmosis (shown in Figure 6.13, right curve) greatly increases measurement accuracy and resolution since the exact location is less critical due to a much smaller flow profile slope near the stationary layers [46].

Another method to avoid liquid electroosmosis is to use a DC field with a changing polarity of high frequency ( $> 10$  Hz). The main idea is that it will take a much longer time for the liquid to reach the terminal velocity than that of the particles. The acceleration time for non-moving particles to reach their electrophoretic velocity is in the range of nanoseconds to microseconds but for liquids is in the range of sub-seconds. Therefore, if the electric field polarity changes rapidly, the liquid will be static and electroosmosis is eliminated [51,52]. In a constant DC field ELS measurements at the center of capillary ((0,0) in Figure 6.10) from a few monodisperse spherical particulate samples showed that the measured electrophoretic mobility is monotonically reduced from high values when the frequency of DC polarity change increases. When this frequency is increased to  $\sim 10$  Hz, there is no difference between mobility obtained at the capillary center and at the stationary layer. Therefore, measurements can be performed at any location in the capillary if the scheme to acquire the ACF or to perform direct spectrum analysis can accompany rapid changing field polarity. However, when using a high frequency field, spectrum resolution is inevitably reduced and harmonic sidebands will be produced due to field modulation and this will complicate the spectrum, especially for materials of polydisperse mobility (see Figure 6.17 at the end of this subsection) [53].

*Parallel-Plate ELS Cells [53,54]*

Another type of ELS cell is square cuvettes, made of plastic or quartz. Two plate electrodes are inserted parallelly into the cuvette. An electric field is formed in the suspension between the electrodes with a gap typically of 1-4 mm. This type of cell is easy to use since there is no complicated cell assembly and it is completely free from electroosmosis. In order to produce a parallel and homogeneous electric field (otherwise electrophoretic motion will not be well directed), the two electrodes must have a certain size and cannot be separated too far. Otherwise, the field uniformity, edge effects, and any lack of parallelism of the electrodes may introduce errors. Field uniformity can only be achieved at the center of the gap between the electrodes. If the scattering volume is located off-center, large errors up to 100% can be produced. Figure 6.16 shows the electrophoretic mobility of a PSL sample ( $d = 305 \text{ nm}$ ) in 1 mM NaCl solution measured using the phase analysis light scattering technique (see the last section of this chapter) as a function of position in a cell 4 mm long and a cell 10 mm long with the gap between electrodes being 4 mm [55]. In this case, a correct  $\mu$  value can only be obtained in the proximity of the cell center ( $\pm 1 \text{ mm}$ ).

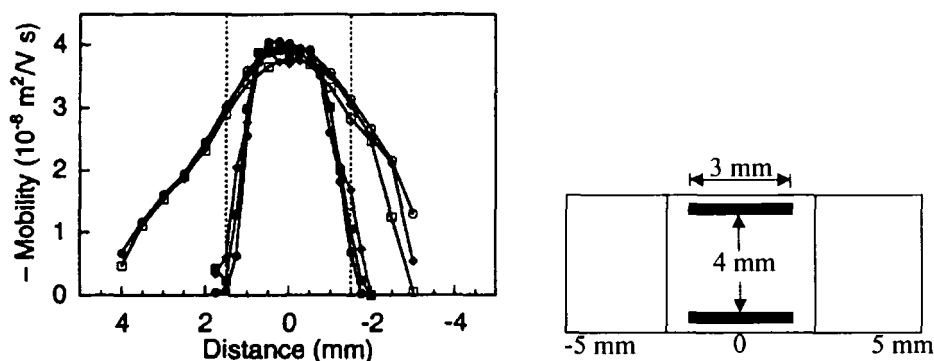


Figure 6.16. Electrophoretic mobility of a PSL sample in 1 mM NaCl solution as a function of position in a 4 mm long cell (solid symbols) and a 10 mm long cell (open symbols). The gap between the electrodes is 4 mm. Circles, squares and diamonds correspond to electric field frequencies of 5, 30, 100 Hz, respectively. Dotted lines denote the front and back edges of the electrodes [55]. (by permission of Academic Press). The right drawing shows the 4 mm cell (two inside lines) and the 10 mm cell.

Because of the narrow gap and small volume between the electrodes, heat dissipation is efficient and the temperature gradient between the gap is low. However, it is not easy to maintain the fluid being still in between the electrodes and sample integrity without interference from Joule heating, thermal convection (there is no vertical boundary), or surface reactions from the nearby

electrodes, especially for high conductivity samples. Because at the surface of an electrode, for a given diluent, there is a current density limit beyond which surface reactions will begin to take place, causing oxidation of electrodes, bubble formation, and contamination. These phenomena render measurements less accurate. Not like a capillary cell where there is a big ratio between the electrode surface area and the channel cross-section, in a parallel-plate cell the cross-sectional area of the scattering volume is the same as that of the electrodes, meaning that the current density in the scattering volume is limited to that present at the electrodes. Consequently, the electric field that can be applied is much smaller than that in a capillary cell at the same solution conductivity. In this type of cell, the liquid between the electrodes will be at a higher temperature than the liquid behind the electrodes, causing an upward convectional flow between the electrodes. Once there is thermal convection, electrophoretic motion of particles is nearly impossible to measure because of the superimposed swirling motion. Temperature differences will also cause inhomogeneity in refractive index and contribute to measurement noise. Reproducibility may be poor in these instances. In practice, during each sampling period a square-wave field with a frequency around 10 Hz is used to minimize local conductance change, electrode reaction, and net particle displacement but this procedure introduces a complication into the ELS spectrum. With each polarity reversal the phase change of the Doppler signal is reversed. The result is a set of modulation sidebands at multiples of the switching frequency in the spectrum and a coherence echo in the ACF. Figure 6.17 shows the electrophoretic mobility obtained at different field frequencies. In these spectra, when the frequency is higher than 5 Hz, not only are sidebands produced, but the main peak is also shifted. Therefore, a wrong conclusion is unavoidable [55].

The intensity envelope of the sideband peaks is determined by the mobility profile of the spectrum. Different formulas have been derived to interpret the spectra having imbedded sideband [53,54]. These sidebands carry no useful information but will overlap and mess up the whole spectrum for multiple-mobility samples. A number of techniques may be used to reduce the sidebands but even these will not completely eliminate them [54]. Since the gap between the electrodes is narrow and long, the accessible scattering angles (scattering from angles larger than 15 degrees may be blocked by the electrodes) as well as the size of scattering volume are limited. Table 6.2 summarizes the features of both types of cells.

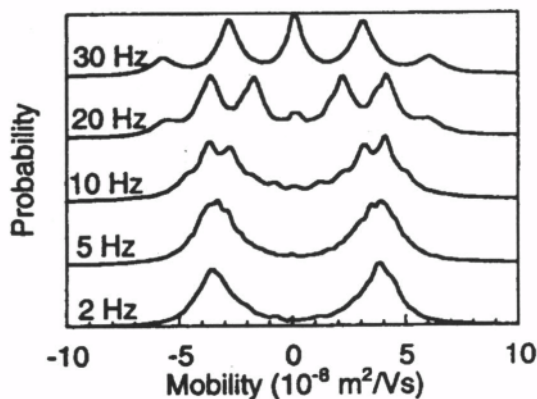


Figure 6.17. Electrophoretic mobility spectra for a PSL sample in 1 mM NaCl at various electric field frequencies [55]. (by permission of Academic Press).

Table 6.2. Comparison of capillary and parallel-plate cells

Capillary Cells	Parallel-plate Cells
Broad dynamic range of electric field and sample conductivity	Limited range of electric field and sample conductivity
High resolution due to less heat generated from low surface current density	Resolution and reproducibility are affected by heat convection
Broad scattering angular range and width of scattering volume	Limited scattering angular range and width of scattering volume
Measurement has to be performed at stationary layers	Cell position and optical focus are not critical
Special procedure needed to minimize electroosmosis	No electroosmotic liquid flow at the cell center
Less convenient to operate and clean	Simple assembly, easy to use and clean, or disposable
Homogeneous electric field in the detection area	Fast alternating field polarity produces sidebands
High sensitivity for samples of low mobility	Efficient Heat Dissipation

#### 6.3.4. ELECTRIC FIELD

Electrophoretic mobility is measured in a DC field. The power supply should be able to provide a well-regulated low-noise pulse at either constant voltage (typically 0-300 V) or constant current (0-10 mA). Excessively high field strength should be avoided as it will cause irregular motion of the particles and the velocity will no longer be proportional to the field strength. In addition, a phenomenon known as dielectrophoresis can occur at high field strength when there is a large difference in dielectric constant between particles and medium [56].

Since a typical measurement takes between half a minute to a few minutes to obtain an electrophoretogram of good quality, the field polarity needs to be altered periodically during the measurement. Otherwise, sample and electrode polarization and particle accumulation on one side of the cell may occur due to long-time electrophoresis. In order to permit Joule heating to dissipate there should be a field-off period in between two field-on periods. Duration of the field-on period should be as long as the minimum required time specified by the sampling theorem (see the next section); e.g., for a spectral resolution of 0.5 Hz a 2 second field-on data collection time is minimally required. The field-off time, typically a few seconds, depends on the thermal time constant of the cell (the heat dissipation rate) and the heat generated during the field-on period. A timing device is needed to turn the field on and off, to alternate its polarity, and to synchronize the pulse sequence with data collection. The time sequence for the applied field is shown in Figure 6.18.

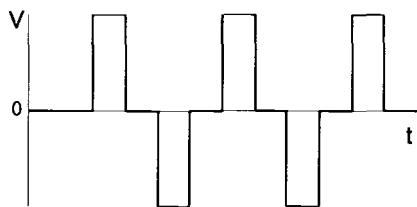


*Figure 6.18.* Time sequence of the electric field in ELS measurement.

The field polarity alters once every few seconds (or shorter if electroosmosis is to be avoided). For highly conductive samples, such as particles in biological buffers or species in seawater, even a very short application of a low intensity field (e.g., 10 V for 1 s) will produce enough Joule heat to result in heating of the liquid. Heating of the liquid produces four effects: a) solution viscosity decreases which increases both the particle's Brownian motion and electrophoretic motion; b) solution conductivity increases; c) depending on cell design, temperature inside the cell may become inhomogeneous; d) convection may be produced if enough heat is generated. The increase in temperature in the scattering volume due to Joule heating changes the suspension conductivity of aqueous suspensions by about two percent per degree of temperature change. The change in conductivity of a liquid is primarily due to the change in viscosity - that is, the conductivity is altered by the change in drag on the current-carrying ions. Electrophoretic mobility of a particle depends inversely on the viscosity of the suspending liquid. In these cases a constant current field instead of constant voltage field is often more appropriate. According to Ohm's law, the electric field is proportional to the ionic electric current  $i$ :



$$E = i/GA \quad (6.16)$$

where  $G$  (Siemens/cm) and  $A$  are the solution conductivity and the cross-sectional area between the electrodes, respectively. The passage of any current through a solution produces heat. The power dissipated per unit volume of solution is

$$P = i^2/A^2G. \quad (6.17)$$

The maximum possible temperature rise can be estimated by assuming that none of the heat is removed from the sample. For an aqueous solution, the temperature rise after a pulse of duration of  $t$  seconds is [49]:

$$\Delta T(^{\circ}\text{C}) = \frac{0.24i^2t}{A^2G}. \quad (6.18)$$

By maintaining a constant current, the increasing conductivity creates a decreasing electric field strength in the solution which compensates for the change in liquid viscosity with temperature since they are in the same proportion. Thus, the electrophoretic mobility of the particles (to a first-order approximation) fortuitously remains constant even though the temperature in the cell is changing. For low conductivity liquids Joule heating is rarely a problem and the electronic circuitry usually can maintain a constant current in the cell more consistently than when the instrument is operated in constant voltage mode. When the liquid conductivity is extremely low, such as in pure deionized water or organic solvents, the current will be too low to be controlled accurately (e.g.,  $1\ \mu\text{A}$ ) and the conductivity cannot be measured accurately, resulting in a large uncertainty in the calculation of the electric field using Eq. 6.16. The constant voltage mode then becomes the preferred choice. The choices for the material of the electrodes are numerous. Any metal or metal alloy that has surface stability, such as silver, gold, palladium, platinum, platinum black, can be used and produce good result. Cost and availability are often the main issue in choosing the material.

### 6.3.5. MULTIANGLE MEASUREMENT

For particles of polydisperse size, the angular scattering intensity patterns vary according to particle size. The same argument we have made in Section 5.2, regard the necessity of multiangle measurement in a PCS experiment is completely valid in an ELS experiment. If these particles have different

mobilities, in order to get a complete view of particles of different sizes, a multiangle measurement is necessary. For example, if a sample has two populations of particles, with particles in one group that are large in size and in the other group that are small in size, and each group has a distinguishable electrophoretic mobility, measurements performed at different angles will yield distributions of the two different populations. The measurement made at a small angle will have a high intensity population for the group of large particles and the distribution obtained at a large angle will have a high intensity population for the group of small particles. Of course, these intensity-weighted distributions can be converted to volume-weighted distribution using the same procedure discussed in Section 5.3 if a proper model can be used.

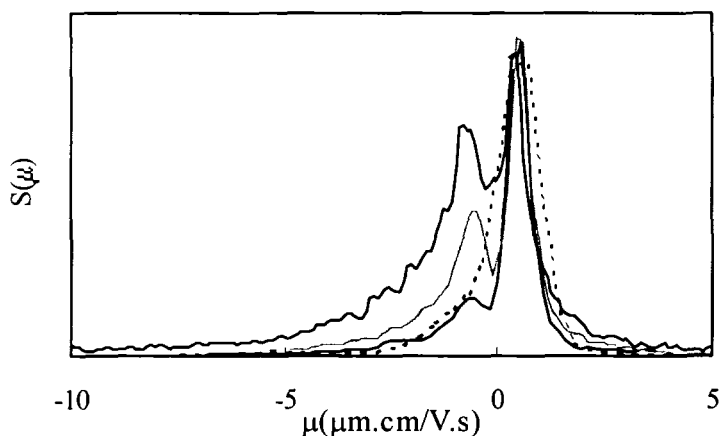


Figure 6.19. Bimodal mobility distributions of a drug carrier suspension. Measurement angles: dotted line, 8.6°; lower solid line, 17.1°; middle solid line, 25.6°; and upper solid line, 34.2°.

Figure 6.19 shows a bimodal mobility distribution from a suspension of drug vesicles that has a group of small particles that are negatively charged and a group of large particles that are positively charged. The measurement was made at four scattering angles simultaneously using a Coulter® Delsa 440SX instrument. The curve from the largest scattering angle (34.2°) is the one with the highest amplitude for the negative peak and the one from the smallest scattering angle (8.6°) is the one with the lowest amplitude (just barely a shoulder) for the negative peak. The other two curves in the middle are from two intermediate angles (17.1° and 25.6°). Since in this case each curve is normalized by the positive peak, the decreasing amplitudes in the negative peak from the largest angle to the smallest angle indicate this peak corresponds to small particles relative to the large particles having positive mobility. If the

system is dynamic, then the multiangle measurement needs to be performed simultaneously. Otherwise, exclusion of the possibility of sample changes occurring during the measurement and correct analysis can hardly be expected. Other advantages of multiangle measurement will be discussed in the next section.

#### 6.3.6. SIGNAL PROCESSING

The entire data collection process may be controlled by a PC using a timer that turns on the field, triggers the data recording sequence, turns off the field and stops the data collection. The process is repeated a number of times (each time is called a scan) and the successive spectral signal are averaged to improve the signal-to-noise ratio for weak scatterers and the statistics for larger but fewer particles. ELS is a low-frequency heterodyne measurement. To maintain a high  $I_L/I_s$  ratio, the signal level is usually high and the typical photon flux per measurement time is far exceeds the threshold of the photon counting mode of a PMT. If one wants to employ photon counting, it will generally be necessary to attenuate the laser by a large factor in order to achieve at a count rate that is within the linear response range of the PMT. The result will be a lower signal-to-noise ratio and a longer time to achieve a satisfactory spectrum. Therefore, photon counting is not an attractive option.

There are several ways to process signals received by the photodetector in order to resolve the electrophoretogram. A Fourier-transform spectrum analyzer can be directly connected to the output of the photodetector after a proper loading match. The spectrum analyzer must be real-time efficient, have a good baseline flatness specification, be capable of signal averaging, and be able to be operated in the transient capture mode with an external trigger in order to collect a single spectrum so that it can be synchronized with the electric field sequence. Commercially available spectrum analyzers provide good results but are often costly. An alternative approach would be to record digitized signal by a computer and perform a Fourier transform to the signal as it is collected. Yet another alternative is to use a correlator to record the ACF of the digitized signal from the analog photocurrent that has been amplified by a low gain amplifier with variable high and low-frequency cutoffs chosen according to the specific spectral frequency region of interest and then Fourier transform the ACF to a power spectrum.

#### 6.3.7. EXPERIMENTAL CONSIDERATIONS

Since an ELS experiment in its nature is a PCS measurement, the same considerations that are discussed in Section 5.2.8 need to be considered along with the additional ones detailed in the following paragraphs.

### *Sample Preparation*

Since the zeta potential and thus the electrophoretic mobility of suspended particles is a function of pH, the type and concentration of counter-ions and co-ions, when the original sample has to be diluted in order to perform an ELS experiment, (which most samples require), it is better to dilute in the same buffer conditions as the original one. Otherwise, the result may not reflect the particles in the original condition. Of course, since the particle concentration changes, if there is any particle-particle interaction, the zeta potential may be different between the concentrated and diluted suspensions anyway. However, at least when the medium condition remains the same, the result is closer to the truth.

### *Particle Size and Concentration Limits*

For the ELS experiments employing the heterodyne mode with a strong reference beam in photocurrent mode as opposed to the photon counting mode, the suspension concentration has to meet a different requirement than that in a PCS experiment. For large particles, the upper concentration limit is due to multiple scattering and saturation of the photodetector, which can be overcome by dilution, or using a smaller scattering volume, or reducing incident light intensity. The lower concentration limitation is not due to insufficient scattering intensity, but from a poor statistical representation of the sample caused by a finite number of particles in the scattering volume, which typically can be overcome by repeated scans over a long time. For heavy or large particles, sedimentation is sometimes unavoidable. Since the vertical motion of sedimentation will not alter the Doppler frequency shift that is derived from horizontal movement, correct mobility values can still be obtained if there are enough particles in the scattering volume. To prevent particles from completely disappearing in the scattering volume, a tall channel is needed in the capillary cell. When the scattering volume is located near the bottom of the capillary, sedimenting particles ensure that there are always particles being measured throughout entire measurement. Of course for polydisperse samples, sampling errors will be unavoidable. For small particles, although there can be no absolute lower limit specified for molecular weight, ELS experiments for particles with masses below  $10^5$  g/mol are challenging and below  $10^4$  g/mol are very difficult. Using ELS to measure the electrophoretic mobility of particles as small as surfactant micelles has been reported [47,57,58]. A practical index proposed by Ware for the lower concentration limit can be obtained from the product of the molecular weight (g/mol) times the weight concentration (g/l) times the refractive index increment  $dn/dc$  (l/g, typically in the order of  $10^{-4}$ ). If this product does not exceed unity, measurement is probably practically

impossible. If the product exceeds 100, the measurement should be straightforward.

### *Experimental Noises*

There are two major sources of experimental noise in measurement in the frequency domain. One is electromagnetic interference that will present as spectral peaks at the power-line frequency and its harmonics. Noise of this origin can be identified by its presence even when all light is blocked. Electromagnetic interference can be reduced to an acceptable level by proper shielding and grounding of the electronic components of the instrument. Vibration of optical components will introduce spurious sharp peaks into the spectrum. These peaks can be distinguished by the fact that they are not affected by changing electric field strength. Vibration noise can be eliminated by isolating the instrument from the sources of vibration and by mounting optical components rigidly with respect to each other.

### *Mobility Controls*

Although ELS is an absolute measurement technology (in the sense that calibration is not needed in order to obtain the electrophoretic mobility of particles), a standard or control material is always useful in verifying the status of instrument and confirming the measurement result. There is an electrophoretic mobility standard from NIST that is an acicular goethite particle suspension ( $\alpha$ -FeOOH) in a buffer at a pH of 2.5. The certified mobility is  $2.53 \pm 0.12 \text{ } \mu\text{m}\cdot\text{cm}/\text{V}\cdot\text{s}$ . Several ELS instrument manufacturers and other vendors have their own mobility controls; most of them are uniform, charge-stabilized polymer microspheres that have negative mobility values and long stability. An extensive collaborative study performed in Japan to establish a mobility standard found that polymer microspheres have the best reproducibility using a variety of different methods and instruments [40,59]. Some proteins and polyelectrolytes whose electrophoretic mobility has been well established using other methods (e.g., the microelectrophoresis method) can also be used as mobility controls.

## **6.4. Data Analysis**

### **6.4.1. ACF AND POWER SPECTRUM**

In an ELS experiment, there are two types of motions that produce light intensity fluctuations and frequency shifts in the scattered light; i.e., the random Brownian motion and the oriented electrophoretic motion of suspended particles, if the scattering from medium is discounted. The effect of Brownian motion is characterized by a Lorentzian peak in the power spectrum (frequency

domain) or an exponential decay in the ACF (time domain), which has been extensively discussed in Chapter 5. Electrophoretic motion is characterized by a drift of frequency in the power spectrum or a sinusoidal oscillation in the ACF. The measured signal is a sum of these two types of motion from all particles in the scattering volume. Electrophoretic motion is only present when the applied field is turned on. Therefore, in ELS the ACF is a damped cosine function with the frequency related to the electrophoretic drift velocity of the particles and the damping constant related to their diffusion coefficient. The power spectrum is a Lorentzian peak with the width related to the diffusion coefficient of the particles and the location related to their electrophoretic drift velocity. Figure 6.20 - Figure 6.22 show signals from a monodisperse system obtained from ELS, but recorded in different domains with both electric field and frequency shifter turned off (Figure 6.20); with negligible Brownian motion (Figure 6.21); and in a normal situation (Figure 6.22). Under the condition  $I_L \gg I_s$ , the following formulas represent the ACF and power spectrum from a polydisperse system in the above situations (Eqs. 6.19 - 6.20, both electric field and frequency shifter are off; Eqs. 6.21 - 6.22, negligible Brownian motion; Eqs. 6.23 - 6.24, normal situation, respectively). The shot noise, which is related to the autocorrelation of pulsed photocurrent in a very short delay time, has been omitted from these equations.

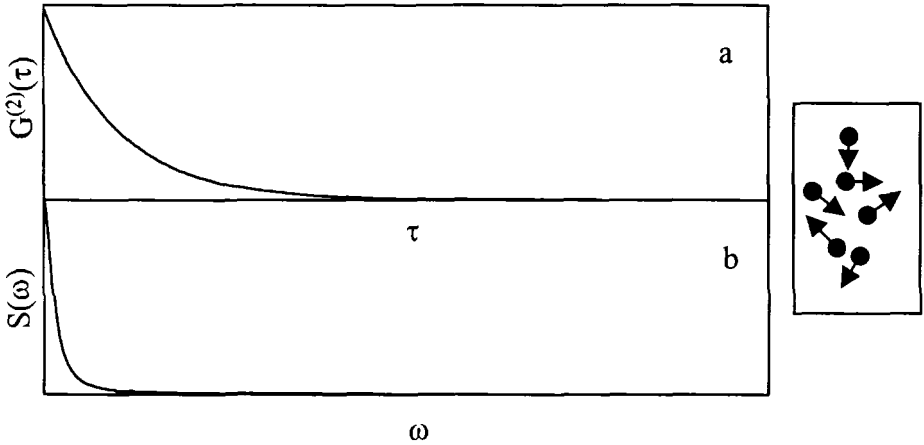


Figure 6.20. Signals from ELS with both electric field and frequency shifter turned off in different domains, a) the ACF; b) the power spectrum.

$$G_{\substack{E=0 \\ \omega_{ps}=0}}^{(2)}(\tau) = I_L^2 + 2I_L \sum_{i=d_{\min}}^{d_{\max}} I_{s,i} e^{-\Gamma_i |\tau|}, \quad (6.19)$$

$$S_{E=0}(\omega) = 2\pi I_L^2 \delta(\omega) + 2I_L \sum_{i=d_{\min}}^{d_{\max}} \frac{I_{s,i} \Gamma_i}{\omega^2 + \Gamma_i^2}, \quad (6.20)$$

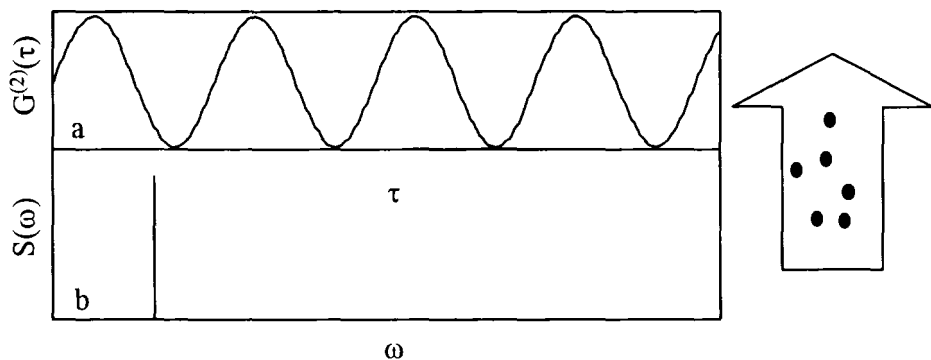


Figure 6.21. Signals from ELS with negligible Brownian motion in different domains, a) the ACF; b) the power spectrum.

$$G_{\Gamma \rightarrow 0}^{(2)}(\tau) = I_L^2 + 2I_L \sum_{j=\Delta v_{s,\min}}^{\Delta v_{s,\max}} I_{s,j} \cos((\omega_{ps} + 2\pi \Delta v_{s,j})\tau), \quad (6.21)$$

$$S_{\Gamma \rightarrow 0}(\omega) = 2\pi I_L^2 \delta(\omega) + 2I_L \sum_{j=\Delta v_{s,\min}}^{\Delta v_{s,\max}} I_{s,j} \delta(\mp(\omega_{ps} + 2\pi \Delta v_{s,j})), \quad (6.22)$$

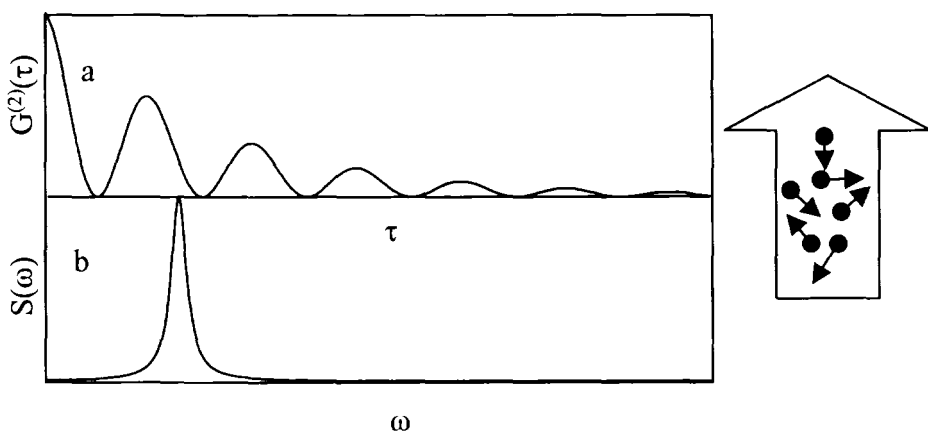


Figure 6.22. Signals from ELS in different domains, a) the ACF; b) the power spectrum.

$$G^{(2)}(\tau) = I_L^2 + 2I_L \sum_{i=d_{\min}}^{d_{\max}} \sum_{j=\Delta v_{s,\min}}^{\Delta v_{s,\max}} I_{s,ij} e^{-\Gamma_i |\tau|} \cos(\omega_{ps} + 2\pi \Delta v_{s,ij}) \tau, \quad (6.23)$$

$$S(\omega) = 2\pi I_L^2 \delta(\omega) + 2I_L \sum_{i=d_{\min}}^{d_{\max}} \sum_{j=\Delta v_{s,\min}}^{\Delta v_{s,\max}} \frac{I_{s,ij} \Gamma_i}{(\omega \mp (\omega_{ps} + 2\pi \Delta v_{s,ij}))^2 + \Gamma_i^2}. \quad (6.24)$$

In the above equations,  $I_{s,ij}$  is the scattered intensity from particles of  $i^{\text{th}}$  size and  $j^{\text{th}}$  mobility;  $\Gamma_i$  is the characteristic Lorentzian half linewidth at half height from particles of the  $i^{\text{th}}$  size, which for spherical particles is related to particle dimension through Eqs. 5.23 and 5.24.  $\Delta v_{ij}$  is the frequency shift caused by the electrophoretic motion of particles with  $i^{\text{th}}$  size and  $j^{\text{th}}$  mobility. In Eqs. 6.22 and 6.24, the symbol  $\mp$  in the denominator denotes that there are two peaks in the spectrum. One is located in the negative frequency region that cannot be observed and the other in the visible positive frequency region. For the sake of clarity, we assume that the summation  $(\omega_{ps} + 2\pi \Delta v_{ij})$  is always positive so that a negative sign can be used instead of using  $\mp$ . In practice, this condition can always be satisfied by choosing a large preshifted frequency for the reference beam. Eqs. 6.19 and 6.23 are the Fourier transforms of Eqs. 6.20 and 6.24, respectively. For both the ACF and the power spectrum, the absolute amplitude scale is immaterial in the determination of either  $\mu$  or  $\Gamma$ . If  $\Delta v_{s,ij}$  can be resolved from the above equations, then depending on the optical arrangement, using Eq. 6.10 or Eq. 6.11 and Eq. 6.2, the electrophoretic mobility  $\mu_{ij}$  can be obtained. In the reference beam setup,

$$\mu = \frac{\Delta \omega \lambda_o}{4\pi n E \sin(\theta/2) \sin(\theta/2 + \xi)}, \quad (6.25)$$

and the zeta potential can be further resolved according to Eq. 6.3. For large particles where the effects of Brownian motion are negligible, the spectrum can be interpreted as a velocity histogram with each particle in the histogram being weighted in proportion to its light scattering cross-section at the scattering angle.

Since in general  $\Delta v_{ij}$  is a function of both size and zeta potential, the number distribution of a particulate sample must be seen in a 3D fashion; i.e.,  $N(\mu, d)$ . As discussed in Chapters 2-5 in general  $I(\mu, d) \neq N(\mu, d)$ , but since  $I(\mu, d)$  can be converted to  $N(\mu, d)$  by one of the theories outlined earlier, we only address  $I(\mu, d)$  here. There are three categories of  $I(\mu, d)$  distributions:



- a) Monodisperse or polydisperse size with monodisperse mobility.  $G_{E=0}^{(2)}(\tau)$  and  $G^{(2)}(\tau)$  have different single sinusoidal frequencies. The difference in the sinusoidal frequency is the unsealed mobility and the mean damping constant (the exponential decay constant) is proportional to the mean diffusion coefficient.  $S(\omega)$  and  $S_{E=0}(\omega)$  have the same shape but different peak locations. The difference in the modes of the two spectra is the unsealed mobility and the half-width at half maximum is the mean decay constant  $\Gamma$ .
- b) Monodisperse size with polydisperse mobility. Eqs. 6.19, 6.20, 6.23, 6.24 can now be written:

$$G_{E=0, \omega_{ps}=0}^{(2)}(\tau) = I_L^2 + 2I_L e^{-\Gamma|\tau|}, \quad (6.26)$$

$$S_{E=0, \omega_{ps}=0}(\omega) = 2\pi I_L^2 \delta(\omega) + 2I_L \frac{I_s \Gamma}{\omega^2 + \Gamma^2}, \quad (6.27)$$

$$G^{(2)}(\tau) = I_L^2 + 2I_L \sum_{j=\Delta v_{s,\min}}^{\Delta v_{s,\max}} I_{s,j} e^{-\Gamma|\tau|} \cos((\omega_{ps} + 2\pi\Delta v_{s,j})\tau), \quad (6.28)$$

$$S(\omega) = 2\pi I_L^2 \delta(\omega) + 2I_L \sum_{j=\Delta v_{s,\min}}^{\Delta v_{s,\max}} \frac{I_{s,j} \Gamma}{(\omega \mp (\omega_{ps} + 2\pi\Delta v_{s,j}))^2 + \Gamma^2}. \quad (6.29)$$

Once  $\Gamma$  is found from either  $G_{E=0, \omega_{ps}=0}^{(2)}(\tau)$  or  $S_{E=0, \omega_{ps}=0}(\omega)$ ,  $I_{s,j}$  can be fitted using

the normalized  $G^{(2)}(\tau)$  or  $S(\omega)$  by applying the nonnegative least-squares (NNLS) or other fitting algorithms to the matrix forms of the above equations:

$$\begin{pmatrix} a_1 \\ a_2 \\ \vdots \\ a_k \end{pmatrix} = \begin{pmatrix} b_{11} & b_{22} & \cdot & \cdot & b_{1j} \\ b_{21} & \cdot & \cdot & \cdot & \cdot \\ \cdot & \cdot & \cdot & \cdot & \cdot \\ \cdot & \cdot & \cdot & \cdot & \cdot \\ \cdot & \cdot & \cdot & \cdot & b_{kj} \end{pmatrix} \begin{pmatrix} I_{s,1} \\ I_{s,2} \\ \cdot \\ \cdot \\ I_{s,j} \end{pmatrix} \quad (6.30)$$

where  $a_k$  is either  $G^{(2)}(\tau_k)$  or  $S(\omega_k)$  and  $b_{kj}$  are the transform elements  $\exp(-\Gamma|\tau_k|\cos((\omega_{ps}+2\pi\Delta v_{s,j})\tau_k))$  for  $G^{(2)}(\tau_k)$  or  $\Gamma/((\omega_k-(\omega_{ps}+2\pi\Delta v_{s,j}))^2+\Gamma^2)$  for  $S(\omega_k)$  in a selected range of  $\Delta v_{s,j}$ , respectively,

- c) Polydisperse size and polydisperse mobility, which is the general situation. The 3D mapping for the two distributions requires more than two independent physical measurements. There are only two independent measurements in an ELS experiment; i.e., measurements made with and without the applied electric field. Therefore, one can obtain only an approximate projection of the 3D mapping in either the mobility distribution plane or the size distribution plane.

There is virtually no analytical solution to resolve a complete 3D mapping (of both mobility and size distributions) for systems in category c if one does not presume a functional form and some relation between the two distributions, even when one of the distributions is functionally known. In spectral analysis, without deconvolving the Brownian motion from the electrophoretogram, the distribution is broadened from the true mobility distribution by Brownian motion. The degree of broadening depends on particle size. The smaller the average particle size is, the more severe the peak broadening is. Using Eqs. 5.23 and 5.24 we can estimate that for a 3  $\mu\text{m}$  particle and a 30 nm particle the  $\Gamma$  values at a 15 degrees scattering angle are respectively 1.7  $\text{s}^{-1}$  and 170  $\text{s}^{-1}$ . Thus for micron-sized particles the broadening may be negligible, and the spectrum can be directly regarded as the mobility distribution; but for nanometer-sized particles, the broadening will severely impair the resolution and accuracy of the mobility determination. In most applications, since the Brownian motion symmetrically broadens the spectrum, one still can obtain a correct mean mobility. However, mobility distribution information may be completely lost since the peak width may arise mostly from the Brownian motion and the abscissa of the spectrum cannot be labeled in terms of electrophoretic mobility. For multimodal distributions, peaks are smeared together due to the Lorentzian shape of each individual peak. Most ELS instruments commercially available display apparent mobility distributions with the Brownian motion imbedded.

For unimodal spectra, one way to give a quick estimation of whether the peak broadening is due mainly to Brownian motion or due to mobility inhomogeneity is through a plot of the angular dependence of spectral linewidth (peak width). The Brownian motion increases the spectral linewidth by the square of  $K$  (Eq. 5.23) compared to the linear increase in the spectral linewidth from the electrophoretic mobility distribution (Eq. 6.9). A plot of the linewidth versus the scattering vector  $K$  will be quadratic if the primary source of broadening is the Brownian motion or linear if mobility inhomogeneity is the main source of the broadening (Figure 6.23). Without this, a measurement of electrophoretic mobility made at a single angle provides information only about

the mean value. The shape of the peak, which is influenced by either of the two effects, cannot be interpreted based on any one single measurement. Multiangle measurement thus provides another advantage in that it allows peak shapes to be interpreted even in spectra containing several peaks.

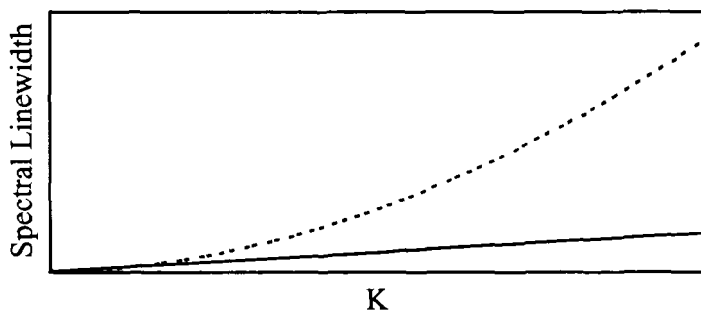


Figure 6.23. A plot of spectral linewidth versus  $K$ . Solid line is from electrophoretic mobility broadening. Dotted line is due to diffusion broadening.

Another method, known as the “peeling method”, has been proposed to minimize the effect of Brownian motion in the electrophoretogram regardless of the shape of the particle size or mobility distributions. In this method, a spectrum obtained without the application of the electric field (thus representing only the Brownian motion of the particles) after having been scaled properly and shifted by a proper frequency is iteratively subtracted (peeled off) from the spectrum measured under the field. The amplitude of each “peeling” corresponds to the amplitude of the mobility distribution at a shifted frequency that is proportional to the mobility. This method can effectively remove the Brownian motion broadening from the spectrum without assumptions about the forms of both the diffusion coefficient distribution or the mobility distribution [60]. Figure 6.24 shows an ELS power spectrum obtained from a mixture of 300 nm PSL and 890 nm PSL acquired at  $\theta = 34.2^\circ$  under a constant current of 0.15 mA ( $E \approx 20.3$  V/cm) as measured at the stationary layer using a Coulter<sup>®</sup> Delsa 440SX instrument (the left solid curve). The solid curve at the right was from the field-off measurement and whose width is due to Brownian motion. The dashed line with symbols represents the result of the peeling procedure. The two mobility peaks of the two PSL’s are revealed only after the removal of the Brownian motion broadening of the spectrum, and which would otherwise show up as a single broad peak.

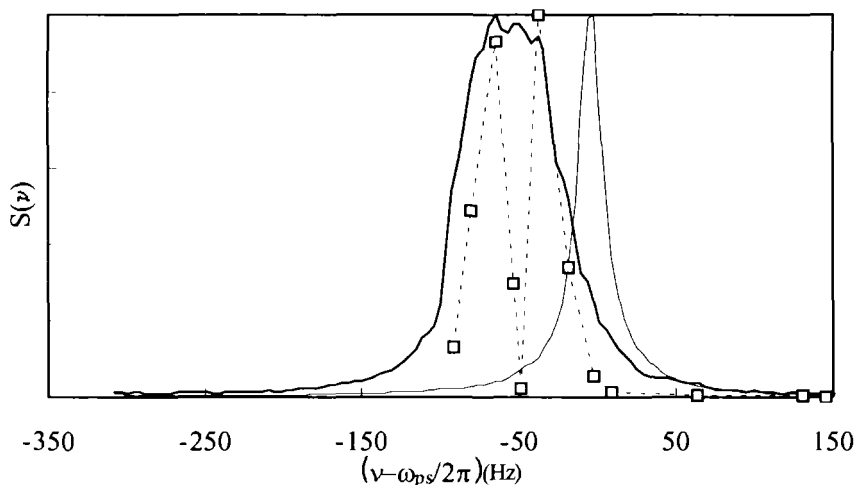


Figure 6.24. The peeling method applied to the spectrum from a bimodal mixture of PSL's.

#### 6.4.2. SPECTRUM RANGE AND RESOLUTION

The frequency range and resolution of the power spectrum is governed by how the scattered intensity is recorded. The highest frequency is determined by the sampling rate of data points according to the Nyquist sampling theorem, which posits that at least two data points be obtained during each cycle of the highest frequency of the spectrum [61]. If even higher frequencies are actually present in the original signal, those frequencies must be filtered out to prevent “aliasing” of their amplitude into the measured spectrum. Thus, if the highest frequency of the spectrum is 250 Hz, at least 500 data points per second are needed. On the other hand, since the spectrum is a Fourier transform of the measured signal or the ACF, the smallest separation between points in the frequency spectrum is equal to the reciprocal of the longest time separation between any two data points acquired. This requirement sets a lower limit on the length of time that the electric field must be applied for a single scan. If a resolution of 0.5 Hz is desired for the spectrum, the scattered intensity from the particles must be recorded for at least 2 seconds and the minimum field-on time has to be 2 seconds. Therefore, the field-on time and the frequency of data sampling are fully determined by the desired spectrum dynamic range and resolution.

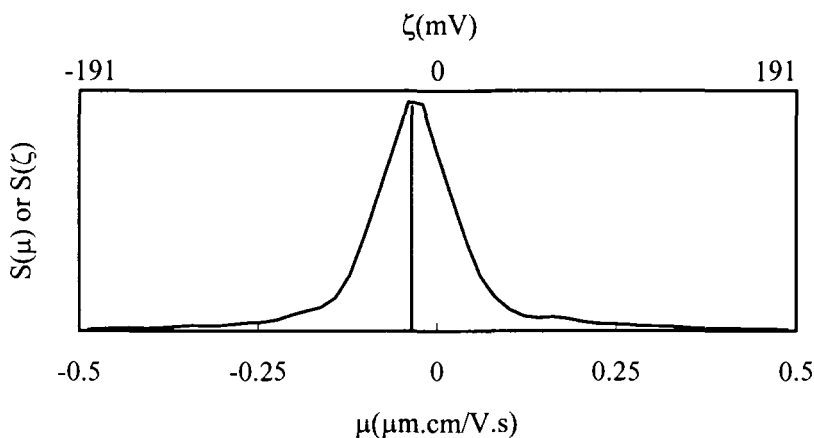


Figure 6.25. Carbon black in kerosene with a mean mobility of  $-0.035 \mu\text{m}\cdot\text{cm}/\text{V}\cdot\text{s}$ , corresponding to a mean zeta potential of  $-13.2 \text{ mV}$ .

A variable frequency range can optimize the resolution and dynamic range of an ELS measurement. If a sample contains only low-mobility material, particularly if the material is multimodal or in non-polar media in which mobility is typically very small due to a low dielectric constant even at moderate zeta potential, a small frequency range, and therefore a high resolution measurement, can provide information that otherwise would be lost when using a wide frequency range. Using a 50 Hz preshifted frequency a 200 data point spectrum acquired using a 2 second scan will have a resolution of 0.5 Hz, compared with a 500 Hz preshifted frequency that will provide a much lower resolution of 5 Hz. Figure 6.25 shows an electrophoretogram (with the effects of Brownian motion imbedded) of carbon black in kerosene (dielectric constant of 4). The measurement was performed using a reference beam with a preshifted frequency of 125 Hz at  $25^\circ\text{C}$ . The electric field of 78 V/cm was applied with constant voltage in a sequence of 2 seconds on and 0.5 second off-times. Electrophoretic mobilities as small as  $0.0025 \mu\text{m}\cdot\text{cm}/\text{V}\cdot\text{s}$  for particles in dodecane has been reported [62].

At the other extreme, using a broad frequency range may provide prevention against false peak for high mobility samples. For a sample having a large negative mobility that produces a frequency shift of  $-280 \text{ Hz}$  at the chosen electric field, if the frequency shifter produces a  $500 \text{ Hz}$  frequency shift ( $\omega_{\text{ps}}/2\pi = 500 \text{ Hz}$ ), a peak at  $-280 \text{ Hz}$  will indicate the right result. However, if  $\omega_{\text{ps}}/2\pi = 250 \text{ Hz}$ , an interesting phenomenon will occur: the peak that is  $30 \text{ Hz}$  out of the range (below zero in the undetectable region) will appear at  $-220 \text{ Hz}$ ;

i.e., it bounces back from the zero axis (Figure 6.26) and a false result is obtained.

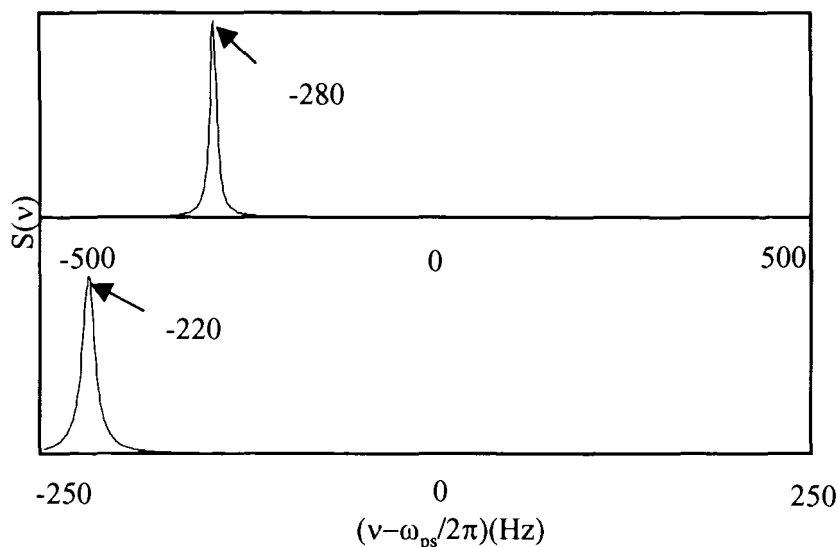


Figure 6.26. False mobility peak due to too narrow spectral range.

For the Brownian motion imbedded ELS spectrum, Ware and Flygare [26] defined the analytical resolution (not the spectral resolution discussed earlier) in terms of the ratio of the Doppler shift to the diffusion broadened half-width:

$$\text{resolution} = \frac{\mathbf{K} \cdot \mathbf{u}}{D_T K^2} = \frac{\mu E \lambda_0}{D_T 4\pi n \sin(\theta/2)}. \quad (6.31)$$

The second equality describes a setup where  $\mathbf{K}$  and  $\mathbf{u}$  are parallel. Eq. 6.31 shows that the analytical resolution can be improved either by increasing the electric field strength or by decreasing the scattering angle. Increasing  $E$  to increase resolution is obvious from Eq. 6.31. Decreasing the scattering angle increases the resolution by reducing the diffusion broadening, but has two negative effects: 1) the Doppler shift actually decreases (Eq. 6.9), rendering it more difficult to measure; 2) the relative angular uncertainty for a fixed detection aperture increases so that high precision in the scattering angle is required. Figure 6.27 shows four Brownian motion imbedded spectra obtained at different scattering angles.

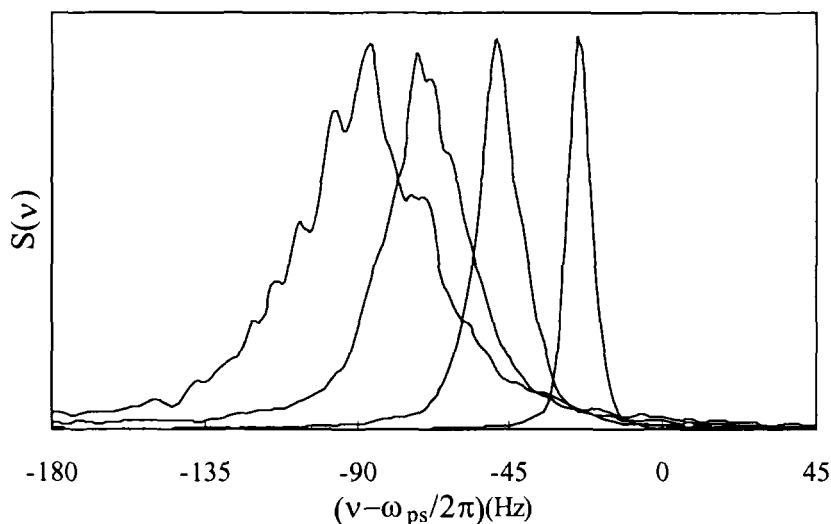


Figure 6.27. ELS spectra of a PSL sample measured at four different scattering angles, from left to right:  $34.2^\circ$ ,  $25.6^\circ$ ,  $17.1^\circ$ ,  $8.6^\circ$ .

For small particles, if the Brownian broadening is not removed using the peeling method, it is essential to work at low scattering angles. The limitations depend on how low an angle one could select and on how small a frequency shift one can detect with the required precision and accuracy at the electric field amplitude and duration that is accessible but that will not produce adverse effects such as excessive heat and sample reaction. In most cases, solution ionic strength is the constraining factor since to obtain high resolution at low frequency, a long field-on time is needed. This limits the field strength and/or the solution ionic strength. For large particles, analytical resolution is less affected by the Brownian broadening.

Figure 6.28 shows the Brownian broadening from small particles ( $d = 20$  nm) as compared to that from large particles ( $d = 1$   $\mu\text{m}$ ). For monodisperse particles of a few hundred nanometers or larger in diameter, the analytical resolution better than  $0.5$   $\mu\text{m}\cdot\text{cm}/\text{V}\cdot\text{s}$  is achievable. However, if other broadening factors such as transient time and field inhomogeneity exist, optimization of the scattering angle is still needed [63]. For example, in a study of a PSL mixture of five different latexes the mobility values resolved from the mixture were very close to that from the individual samples (Table 6.3).

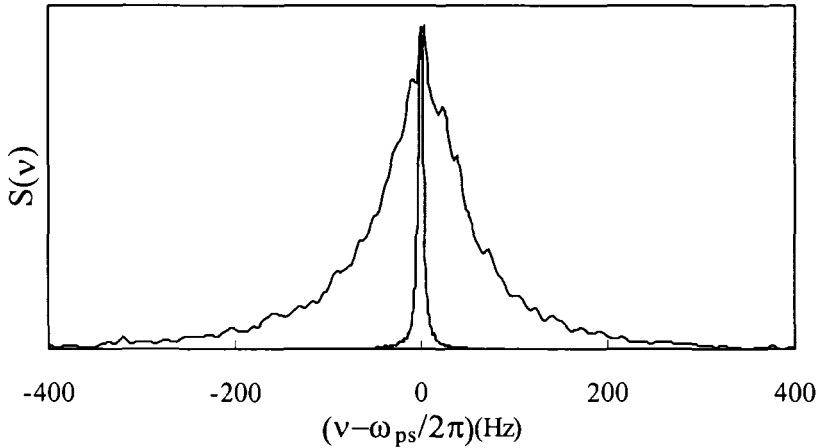


Figure 6.28. Spectra of a 1  $\mu\text{m}$  PSL sample (the narrow peak) and a 20 nm PSL sample (the broad peak) at zero field measured at the same scattering angle.

Table 6.3. Mobility of latexes obtained from spectra [40]

$d_h(\text{nm})$	Mobility( $\mu\text{m}\cdot\text{cm}/\text{V}\cdot\text{s}$ )	
	Single-comp.	Mixture
137	-4.84	-4.86
212	-5.21	-5.40
394	-6.45	-6.58
605	-3.56	-3.34
1000	-8.22	-8.27

#### 6.4.3. ACCURACY OF ELECTROPHORETIC MOBILITY MEASUREMENT

The accuracy of mobility measurement (bias and reproducibility) is mainly determined by all external effects on the stillness of the liquid. Electroosmosis is obviously one factor that affects the accuracy of peak location. Any other distortions, such as heat convection, surface reaction, etc., that cause bulk liquid flow will also reduce the accuracy. A zero field spectrum should be checked at the beginning and end of each measurement to ensure that no bulk flow is present. In the absence of an applied electric field, the spectrum should consist of a single peak centered at zero frequency. Any shift to a positive or negative frequency indicates liquid motion that should be corrected. Field heterogeneity that causes particles to move in a different direction from the direction they should move electrophoretically according to the design of instrument will also affect the accuracy by peak shifting and broadening.



The accuracy is also related to spectral resolution. For a 50 Hz Doppler shift, if the accuracy is deemed to be 1%, the spectral resolution needs to be better than 0.5 Hz. To achieve that a 2-second scan is minimally required whether using a spectrum analyzer or a correlator.

Another effect that limits accuracy is that when the mobility is low the particle displacement produced in a given time is very small. If the displacement is less than  $K^{-1}$ , the signal will not complete a cycle of  $2\pi$  and cannot be accurately measured using either spectral analysis or ACF measurement. Assuming a 10 V/cm field is applied for 2 seconds, the minimum  $\mu$  that will produce a displacement larger than  $K^{-1}$  is  $0.02 \mu\text{m}\cdot\text{cm}/\text{V}\cdot\text{s}$  for a measurement at a  $10^\circ$  scattering angle, and  $0.007 \mu\text{m}\cdot\text{cm}/\text{V}\cdot\text{s}$  for a measurement at a  $30^\circ$  scattering angle using a He-Ne light source in aqueous suspensions.

Once the magnitude of the Doppler shift has been determined, there are seven other parameters required to calculate electrophoretic mobility according to Eqs. 6.10 and 6.16; i.e.,  $\lambda_0$ ,  $n$ ,  $A$ ,  $G$ ,  $i$ ,  $\theta$ , and  $\xi$ .  $\lambda_0$  and  $n$  are usually known accurately ( $< 0.1\%$ ). The current ( $i$ ) can be held constant and measured accurately ( $< 0.1\%$ ). In instruments with fixed optical parts  $\theta$  and  $\xi$  can be set and determined geometrically with an accuracy better than  $0.1\%$ . If the scattering angle is set using moving optical parts, the accuracy may not be easily achieved to better than  $0.1\%$  at small angles. The area  $A$  is easily measured in capillary type cells since it is often fixed. For parallel-plate cells, the area  $A$  is more difficult to measure, kept constant and uniform, making it more difficult to be employed with equivalent accuracy. Fringe field effects must be considered when calculating field strength between electrodes [54]. The solution conductivity can be measured precisely, but the accuracy can hardly be better than  $0.1\%$ . In summary, considering all the factors that contribute to the measurement and calculation of electrophoretic mobility, the overall accuracy can only be estimated to be about 1 % or larger.

There are two more parameters in the calculation of zeta potential - the viscosity and dielectric constant of the medium. The accuracy of zeta potential is very difficult to estimate since it is not an experimentally determined quantity. Its accuracy depends heavily on the suitability of the model used in the calculation and the biases of the model as it relates to real particles. Because the interpretation of zeta potential is not accurate to the same level as the present experimental accuracy, any motivation to further improve experimental accuracy is not great if the ultimate parameter one wants to obtain is zeta potential.

#### 6.4.4. APPLICATIONS

Since the first successful electrophoretic light scattering experiment in 1971 [26], ELS has been applied in a very broad range of scientific and industrial

fields. A few excellent articles published in the early 1980s summarized the applications up to then [28,53,54]. As of today, there has not been an extensive review of advancements in this field. This technology initially started with applications in the biological sciences to characterize species such as living cells (blood cells and lymphocytes) and other biological particles and biomacromolecules. In the late 1980 and early 1990 its development and application then shifted to particles and materials having industrial significance. During the past few years, along with the growth in the biotechnology industry and education about this technology aimed at scientists outside the field of physical chemistry, ELS has been employed more and more in pharmaceutical development and in biomedical applications. The following brief and incomplete list of biomedical applications of ELS serves as a closing remark for this section:

Blood cells:

- differences between blood cells
- concentration dependence of aldehyde
- normal and inverted red cell membrane vesicles
- endocytosis and exocytosis of living cells

Lymphocytes:

- normal, preoperative cancer, and tuberculosis

T and B cells of animals

- reaction with antigens

Liposomes (as drug delivery carriers)

Colloids, antigen and antibody

Proteins (ASTM Standard)

Serums

Parenteral fluid

Dental materials

Paramagnetic particles

DNA Studies

- counter-ion condensation
- conformation

Immunoassays

- antigen-antibody reaction
- hepatitis, rheumatoid arthritis

Human platelets and lipoprotein

Kidney stone studies: calcium oxalate stones

## 6.5. Phase Analysis Light Scattering (PALS)

As opposed to frequency analysis, phase analysis light scattering (PALS) analyzes particle's mobility from the phase variation of scattered light as first proposed in 1990 [64,65].

If a particle  $j$  at a position  $x_j(0)$  at  $t = 0$  moves, the phase change of the scattered light ( $\phi_j(t) - \phi_j(0)$ ) at a time  $t$  is directly related to the new position of the particle. If there is only directed motion caused by an applied electric field (the electrophoretic motion), the distance that the particle moved can be related to the phase change, and for a given instrumental setup (direction of the incident light, the scattered light and the electric field), the electrophoretic mobility can be revealed. Brownian motion contributes to the phase change in a random fashion. Thus, if the phase change is monitored over a period of many identical cycles of a high frequency electric field, the mean phase change with time should yield information about the electrophoretic motion and the mean squared phase change could contain information of diffusion contribution. Of course, any disturbance, such as experimental noise, which causes the particles to move will also produce a phase change. For an ensemble of polydisperse particles, phase analysis of the scattered light is more complicated. To find some parameter that links measurable quantities to the electrophoretic motion of the particles, the amplitude-weighted phase difference (AWPD)  $Q(t)$  is defined, which is the product of the phase change  $\delta\phi$  with the instantaneous amplitude  $A$ . Using an approximation that assumes that the contributions of Brownian motion and electrophoretic motion for any polydisperse system are completely separable and statistically independent, which practically removes the contribution of the Brownian motion from the experimentally measured AWPD, and that the measured amplitude and phase change are an average value for the whole sample, which reduces the number of polydisperse mobility values to one non-defined mean value  $\bar{\mu}$ , the temporally averaged AWPD over many identical cycles of the applied field  $E(t)$  is:

$$\langle Q(t) - Q(0) \rangle = \bar{A}K\bar{\mu} \int_0^t E(t') dt'. \quad (6.32)$$

Eq. 6.32 is derived for crossbeam optics (Figure 6.6). If using reference beam optics (Figure 6.5), a cosine term containing the angle between the scattering vector and the electric field has to be multiplied, reflecting the component of electrophoretic motion at the direction of scattering vector (Eq. 6.9). In reality, other collective motions may also be present, for example, those due to thermal convection or sedimentation or creaming. If we assume that these collective motions can be represented by a constant velocity term  $V_c$ , which is not related

to the amplitude of the electric field and does not change during the entire measurement duration, then the AWPDP in Eq. 6.32 for a square field (Eq. 6.33) and for a sinusoidal field ( $E(t) = E_0 \sin(\omega t + \phi)$ , Eq. 6.34) are, respectively,

$$\langle Q(t) - Q(0) \rangle = \bar{A}K(\bar{\mu}E(t) + V_c t), \quad (6.33)$$

$$\langle Q(t) - Q(0) \rangle = \bar{A}K(\bar{\mu}E_0(\cos \phi - \cos(\omega t + \phi)) / \omega + V_c t). \quad (6.34)$$

The experimental setup of PALS is very similar to that of an ELS instrument. The main differences lie in the frequency of the applied electric field, signal detection, and data analysis. In order to measure the averaged AWPDP over many cycles of the applied field, the frequency of field is usually higher than that used in ELS, typically 5-200 Hz. The reference beam is phase modulated to a certain frequency. The deviation in the scattered light frequency is measured by performing a phase comparison of the detected signal to that of the imposed modulator frequency. Any shift in the otherwise constant relative phase detected by a phase comparator indicates non-zero particle mobility. This comparison can be carried out using either an analog lock-in amplifier or through digital signal processing. According to Eqs. 6.33 and 6.34, AWPDP has the same oscillation, and is synchronous with the applied field (square or sinusoidal), plus a shift due to other collective motion. Therefore high quality data can be obtained by averaging over many applications of the field. Figure 6.29 and Figure 6.30 show AWPDP's measured using a sinusoidal field with little influence from  $V_c$  and a square field with  $V_c$  in different frequency ranges, respectively.

If the measurement time is not very long and the term  $V_c$  is truly held as a constant, the PALS technique is immune to any thermal convection and other experimental noises which may produce collective motions other than electrophoretic motion since such collective motion is directly measured and separated from the electrophoretic motion. Typically, in a 20-second measurement, 30 separate phase spectra can be collected and averaged. Because of these advantages, PALS is very appropriate when measuring particles of small mobility in a nonpolar solvent, or particles in suspensions of high viscosity or high ionic strength. If the phase demodulation frequency can be adjusted, taking into account of the  $V_c$  term which may be obtained using spectral analysis, any substantial thermal or other drift to particle can be further removed or compressed. Extremely small electrophoretic mobility determination now becomes possible. An electrophoretic mobility value as small as  $0.0002 \mu\text{m}\cdot\text{cm}/\text{V}\cdot\text{s}$  was determined using PALS for particles of calcium high base-number sulphonate (CaHBNS) in hydrocarbon oil of high viscosity [66]. This value is about 100 times smaller than that which can be measured

using regular ELS. PALS can also be used to estimate the mean particle size by the continuous averaging over all times of the mean squared phase change, although the type of mean is not defined for a polydisperse system.

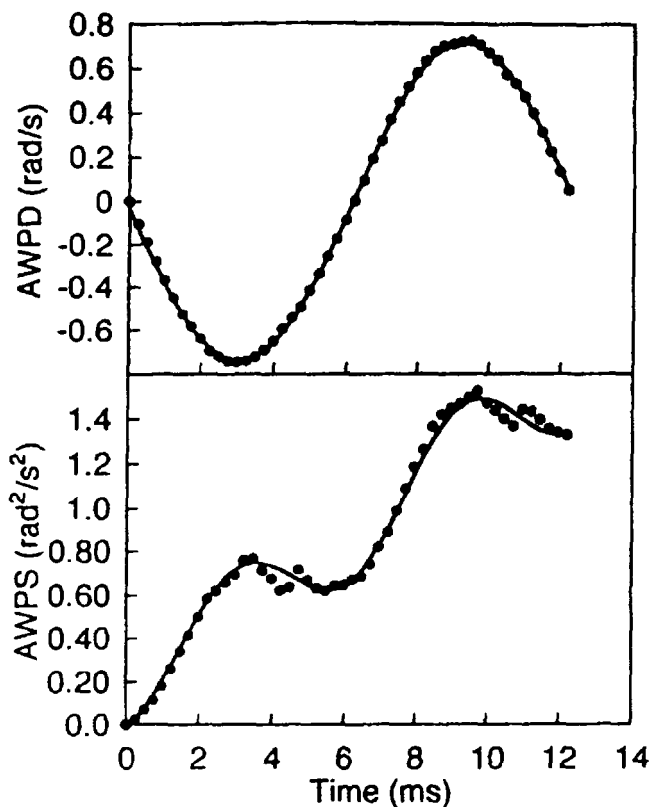


Figure 6.29. AWP and amplitude-weighted square phase difference (AWPS) of a PSL sample in distilled water. Circle, experimental data point; solid lines, the best fit according to the theory (by permission of Academic Press) [55].

The major limitation of PALS is that no mobility distribution information can be obtained and the type of mean is not defined. In addition, the accuracy of the measured electrophoretic mobility depends on the accuracy of the scattering vector  $K$ , which can be determined quite accurately based on instrument setup, and the accuracy of  $\bar{A}$ , which is often affected by experimental noise and is difficult to ascertain. Other factors, such as electroosmosis, electronic artifact and the choice of a correct field frequency can also affect the measurement accuracy, as demonstrated in Figure 6.31, in which correct electrophoretic mobility value using PALS can only be obtained at electric field frequencies between 30-200 Hz.

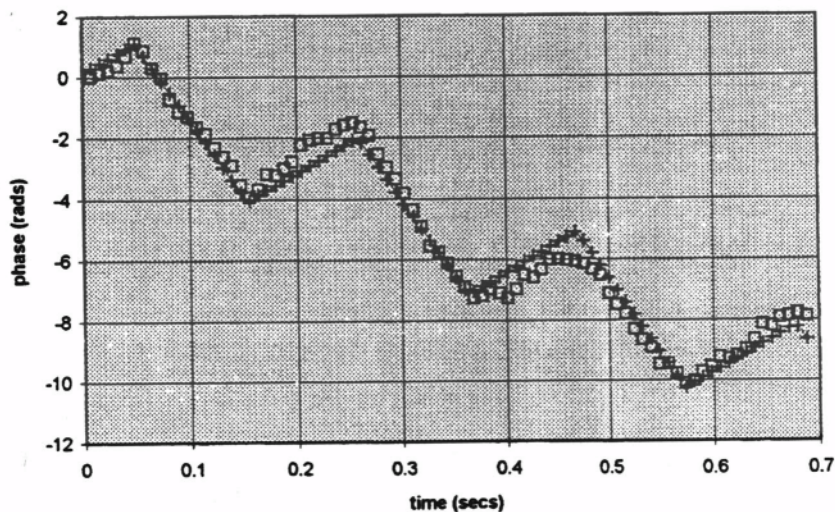


Figure 6.30. AWPD for 49 nm PSL in 1 mM KCl under a 5 Hz square field of 8.33 V/cm. Squares: experimental data; Crossed line: fitted curve for  $\mu = -2.685 \mu\text{m}\cdot\text{cm}/\text{V}\cdot\text{s}$  [67].

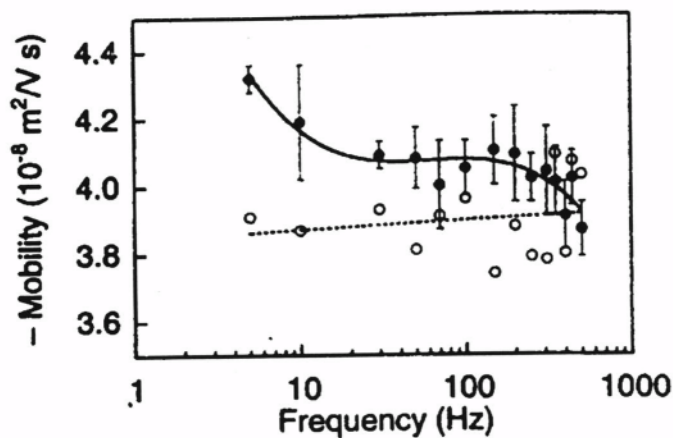


Figure 6.31. Electrophoretic mobility of a PSL ( $d = 305 \text{ nm}$ ) sample in 1 mM NaCl solution as a function of electric field frequency obtained using PALS. Solid symbols, experimental data points; open symbols, simulated values assuming a mobility of  $-4 \mu\text{m}\cdot\text{cm}/\text{V}\cdot\text{s}$  (by permission of Academic Press) [55].

## REFERENCES

- 1 Hunter, R., *Zeta Potential in Colloid Science*, Academic Press, New York, 1981
- 2 Hunter, R., *Foundations of Colloid Sciences*, Oxford Science Publications, London, 1987
- 3 *Surfactant Science Series 76: Electrical Phenomena at Interfaces*, Eds. Ohshima, H., Furusawa, K., Marcel Dekker, New York, 1998.
- 4 Henry, D. C., The Cataphoresis of Suspended Particles. Part I. The Equation of Cataphoresis, *Proc. R. Soc. London*, 1931, A133, 106-129.
- 5 Wiersema, P. H., Loeb, A. L., Overbeek, J. Th. G., Calculation of the Electrophoretic Mobility of a Spherical Colloid Particle, *J. Colloid Interface Sci.*, 1966, 22, 78-99.
- 6 O'Brian, R. W., White, L. R., Electrophoretic Mobility of a Spherical Colloidal Particle, *J. Chem. Soc. Faraday Trans. 2*, 1978, 74, 1607-1626.
- 7 Deggelmann, M., Palberg, T., Hagenbuchle, M., Maire, E., Krause, R., Graf, C., Weber, R., Electrokinetic Properties of Aqueous Suspensions of Polystyrene Spheres in the Gas and Liquid-like Phase, *J. Colloid Interface Sci.*, 1991, 143, 318-326.
- 8 Grosse, C., Shilov, V. N., Electrophoretic Mobility of Colloidal Particles in Weak Electrolyte Solutions, *J. Colloid Interface Sci.*, 1999, 211, 160-170.
- 9 Solomentsev, Y. E., Pawar, Y., Anderson, J., Electrophoretic Mobility of Non-uniformly Charged Spherical Particles with Polarization of the Double Layer, *J. Colloid Interface Sci.*, 1993, 158, 1-9.
- 10 O'Brien, R. W., The Dynamic Mobility of a Porous Particle, *J. Colloid Interface Sci.*, 1995, 171, 495-504.
- 11 Ohshima, H., Electrophoretic Mobility of a Polyelectrolyte Adsorbed Particle: Effect of Segment Density Distribution, *J. Colloid Interface Sci.*, 1997, 185, 269-273.
- 12 Ohshima, H., Dynamic Electrophoretic Mobility of a Cylindrical Colloidal Particle, *J. Colloid Interface Sci.*, 1997, 185, 131-139.
- 13 De Keizer, A., van der Drift, W. P. J. T., Overbeek, J. Th. G., Electrophoresis of Randomly Oriented Cylindrical Particles, *Biophys. Chem.*, 1975, 3, 107-108.
- 14 Stigter, D., Electrophoresis of Highly Charged Colloidal Cylinders in Univalent Salt Solutions. 1. Mobility in Transverse Field, *J. Phys. Chem.*, 1978, 82, 1417-1423.
- 15 Morrison, F. A., Transient Electrophoresis of an Arbitrarily Oriented Cylinder, *J. Colloid Interface Sci.*, 1971, 36, 139-145.
- 16 Keh, H. J., Chen, S. B., Diffusiophoresis and Electrophoresis of Colloidal Cylinders, *Langmuir*, 1993, 9, 1142-1148.
- 17 Yoon, B. J., Kirn, S., Electrophoresis of Spheroidal Particles, *J. Colloid Interface Sci.*, 1989, 128, 275-288.
- 18 O'Brien, R. W., Ward, D. N., Electrophoresis of A Spheroid with a Thin Double Layer, *J. Colloid Interface Sci.*, 1988, 121, 402-413.
- 19 Fair, M. C., Anderson, J. L., Electrophoresis of Non-uniformly Charged Ellipsoidal Particles, *J. Colloid Interface Sci.*, 1988, 127, 388-395.
- 20 Smoluchowski, M. v., Versuch einer mathematischen Theorie der Koagulationskinetik kolloider Lösungen, *Z. Physik. Chem.*, 1918, 92, 129-168.
- 21 Tanford, C., *Physical Chemistry of Macromolecules*, Wiley, New York, 1961.
- 22 Reuss, A., *Mem. Soc. Imp. D. Moscow*, 1807, t11, 327.
- 23 Takagi, T., Electrophoretic Light Scattering-a new apparatus applicable to proteins to cells, *Japanese J. Electrophoresis*, 1992, 36, 21-31.
- 24 Tiselius, A., A New Apparatus for Electrophoretic Analysis of Colloidal Mixture, *Trans. Faraday Soc.*, 1937, 33, 524-531.
- 25 Alberty, R. A., An Introduction to Electrophoresis, *J. Chem. Educ.*, 1948, 25, 426-433, 619-629.

- 
- 26 Ware, B. R., Flygare, W. H., The Simultaneous Measurement of the Electrophoretic Mobility and Diffusion Coefficient in Bovine Serum Albumin Solutions by Light Scattering, *Chem. Phys. Lett.*, 1971, 12, 81-85.
  - 27 Uzgiris, E. E., Measurement of Electrophoresis by Laser Light Scattering, *Biophys. J.*, 1972, 12, 1439.
  - 28 Ware, B. R., Haas, D. D., Electrophoretic Light Scattering, in *Fast Methods in Physical Biochemistry and Cell Biology*, Eds. Sha'afi, R. I., Fernandez, S. M., Elsevier, New York, 1983, Chpt.8, p173-220.
  - 29 Durst, F., Melling, A., Whitelaw, J. H., *Principles and Practices of Laser-Doppler Anemometry*, 2<sup>nd</sup> Ed., Academic Press, London, 1981.
  - 30 Xu, R., Schmitz, B., Lynch, M., A Fiber Optic Frequency Shifter, *Rev. Sci. Instrum.*, 1997, 68, 1952-1961.
  - 31 Debye, P., Sears, F. W., *Proc. Natl. Acad. Sci. USA*, 1932, 18, 409.
  - 32 Mazumder, M. K., Laser Doppler Velocity Measurement without Directional Ambiguity by Using Frequency Shifted Incident Beams, *App. Phys. Lett.*, 1970, 16, 462-464.
  - 33 Suzuki, T., Hioki, R., Translation of Light Frequency by a Moving Grating, *J. Opt. Soc. Am.*, 1967, 57, 1551-1551.
  - 34 Abramson, H. A., Microscopic Method of Electrophoresis, *J. Phys. Chem.*, 1932, 36, 1454.
  - 35 Smith, M. E., Lisse, M. W., A New Electrophoresis Cell for Microscopic Observations, *J. Phys. Chem.*, 1936, 40, 399-412.
  - 36 Beniams, H., Gustavson, R. G., The Theory and Application of a Two-path Rectangular Microelectrophoresis Cell, *J. Phys. Chem.*, 1942, 46, 1015-1023.
  - 37 Hamilton, J. D., Stevens, T. J., A Double-tube Flat Microelectrophoresis Cell, *J. Colloid Interface Sci.*, 1967, 25, 519-525.
  - 38 Rutgers, A. J., Facq, L., van der Minne, J. L., A Microscopic Electrophoresis Cell, *Nature*, 1950, 166, 100-102.
  - 39 Haas, D. D., Ware, B. R., Design and Construction of a New Electrophoretic Light-scattering Chamber and Application to Solutions of Hemoglobin, *Anal. Biochem.*, 1976, 74, 175-188.
  - 40 Oka, K., Furusawa, K., Electrophoresis, in *Surfactant Science Series 76: Electrical Phenomena at Interfaces*, Eds. Ohshima, H., Furusawa, K., Marcel Dekker, New York, 1998, Chpt.8, p.151-224.
  - 41 Emoto, K., Harris, J. M., Van Alstine, J. M., Grafting Poly(ethylene glycol) Epoxide to Amino-derivatized Quartz: Effect of Temperature and pH on Grafting Density, *Anal. Chem.* 1996, 68, 3751-3757.
  - 42 White, P., Theory of Electroosmotic Circulation in Closed Vessels, *Phil. Mag.*, 1937, 23, 811-823.
  - 43 Komagata, S., *Researches of the Electrotechnical Laboratory*, Ministry of Communications, Tokyo, 1933, March, p.348.
  - 44 Burns, N. L., Surface Characterization Through Measurement of Electroosmosis at Flat Plates, *J. Colloid Interface Sci.*, 1996, 183, 249-259.
  - 45 Oka, K., Otani, W., Kameyama, K., Kidai, M., Takagi, T., Development of a High-performance Electrophoretic Light Scattering Apparatus for Mobility Determination of Particles with Their Stokes' Radii of Several Nanometers, *Appl. Theoretical Electrophoresis*, 1990, 1, 273-278.
  - 46 Knox, R. J., Burns, N. L., Van Alstine, J. M., Harris, J. M., Seaman, G. V. F., Automated Particle Electrophoresis: Modeling and Control of Adverse Chamber Surface Properties, *Anal. Chem.*, 1998, 70, 2268-2279.
  - 47 Xu, R., Smart, G., Electrophoretic Mobility Study of Dodecyltrimethylammonium Bromide in Aqueous Solution and Adsorption on Microspheres, *Langmuir*, 1996, 12, 4125-4133.



- 
- 48 Finsy, R., Xu, R., Deriemaeker, L., Effect of Laser Beam Dimension on Electrophoretic Mobility Measurements, *Part. Part. Syst. Charact.*, 1994, 11, 375-378.
  - 49 Smith, B. A., Ware, B. R., Apparatus and Methods for Laser Doppler Electrophoresis, in *Contemporary Topics in Analytical and Clinical Chemistry v.2*, Eds. Hercules, D., Hieftje, M., Snyder, L. R., Evenson, M. A., Plenum, New York, 1978, Chpt. 2, p29-54.
  - 50 Hjertén, S., High-performance Electrophoresis: Elimination of Electroendosmosis and Solute Adsorption, *J. Chromatogr.*, 1985, 347, 191-198.
  - 51 Schatzel, K., Weise, W., Sobotta, A., Drewel, M., Electroosmosis in an Oscillating Field: Avoiding Distortions in Measured Electrophoretic Mobilities. *J. Colloid Interface Sci.*, 1991, 143, 287-293.
  - 52 Minor, M., van der Linde, A. J., van Leeuwen, H. P., Lyklema, J., Dynamic Aspects of Electrophoresis and Electroosmosis: a New Fast Method for Measuring Particle Mobility, *J. Colloid Interface Sci.*, 1997, 189, 370-375.
  - 53 Uzgiris, E. E., Laser Doppler Spectroscopy: Applications to Cell and Particle Electrophoresis, *Adv. Coll. Inter. Sci.*, 1981, 14, 75-171.
  - 54 Uzgiris, E. E., Laser Doppler Methods in Electrophoresis, *Prog. Surface Sci.*, 1981, 10, 53-164.
  - 55 Miller, J., Velev, O., Wu, S. C. C., Ploehn, H. J., A Combined Instrument for Phase Analysis Light Scattering and Dielectric Spectroscopy, *J. Colloid Interface Sci.*, 1995, 174, 490-499.
  - 56 Pohl, H. A., *Dielectrophoresis*, Cambridge University Press, Cambridge, 1978.
  - 57 Kameyama, K., Takagi, T., Measurement of Electrophoretic Mobility of SDS Simple Micelles and mixed Micelles with a Non-ionic Surfactant, Octaethylene Glycol Dodecyl Ether, by Electrophoretic Light Scattering with the Correction for Electroosmotic Flow, *J. Colloid Interface Sci.*, 1990, 140, 517-524.
  - 58 Imae, T., Otani, W., Oka, K., Electrophoretic Light Scattering of Surfactant Micelle Colloids, *J. Phys. Chem.*, 1990, 94, 853-855.
  - 59 Seaman, G. V. F., Knox, R. J., Microparticles for Standardization of Electrophoretic Devices and Process Control, *J. Dispersion Sci. Tech.*, 1998, 19, 915-936.
  - 60 Xu, R., Methods to Resolve Mobility from Electrophoretic Laser Light Scattering Measurement, *Langmuir*, 1993, 9, 2955-2962.
  - 61 Davenport Jr., W. B., Root, W. L., *Random Signals and Noise*, McGraw-Hill, New York, 1958.
  - 62 Kornbrekke, R. E., Morrison, I. D., Oja, T., Electrophoretic Mobility Measurements in Low Conductivity Media, *Langmuir*, 1992, 8, 1211-1217.
  - 63 Uzgiris, E. E., in *Cell Electrophoresis*, Eds. Preece, A., Sabolovic, D., Elsevier, Amsterdam, 1978, pp381.
  - 64 Miller, J. F., The Determination of Very Small Electrophoretic Mobilities of Dispersions in Non-Polar Media Using Phase Analysis Light Scattering, *Ph.D. Thesis*, University of Bristol, Bristol, 1990.
  - 65 Miller, J. F., Schatzal, K., Vincent, B., The Determination of Very Small Electrophoretic Mobilities in Polar and Nonpolar Colloidal Dispersions Using Phase Analysis Light Scattering, *J. Colloid Interface Sci.*, 1991, 143, 532-553.
  - 66 Miller, J. F., Clifton, B. J., Benneyworth, P. R., Vincent, B., MacDonald, I. P., Marsh, J. F., Electrophoretic Studies of Calcium Carbonate Particles Dispersed in Various Hydrocarbon Liquids, *Coll. Surf.*, 1992, 66, 197-202.
  - 67 Tscharnuter, W. W., The Measurement of Zeta Potential, in *Course Notes, Particle Characterization '97*, Sydney, 1997.

## APPENDIX I: SYMBOLS AND ABBREVIATIONS

### 1. Symbols

$\alpha$	Polarizability
	Angle
$\alpha_D$	Scaling parameter relating $D_T$ and molecular weight
$\beta$	Polarizability
	Angle
	PCS instrument efficiency coefficient
$\delta$	Phase factor
	Intrinsic anisotropic factor
$\epsilon$	Permittivity
$\phi$	Volume fraction
$\gamma$	Extinction coefficient
	Angle
$\eta$	Viscosity
$\varphi$	Scattering azimuthal angle
	Phase
$\kappa$	Debye-Hlickel parameter
$\lambda$	Wavelength
$\mu$	Electrophoretic mobility
$\mu_a$	Absorption coefficient
$\mu_{eo}$	Electroosmotic mobility
$\mu_d$	Dynamic mobility
$\mu_i$	$i^{\text{th}}$ central moment of a distribution
$\mu_s$	Scattering coefficient
$\nu$	Frequency
$\theta$	Scattering angle
$\rho$	Density
	Electrolyte resistivity
$\sigma$	Surface area covered by one molecule
	Standard deviation
$\sigma^2$	Variance
$\tau$	Delay time
	Turbidity

$\omega$	Angular frequency
$\xi$	Angle between scattered light and particle moving direction
$\psi$	Electric potential
$\zeta$	Zeta potential
$B(m,n)$	Beta function
$\Gamma$	Correlation function decay constant, spectrum linewidth
$\Gamma(n)$	Gamma function
$a(\theta,\varphi,d)$	Scattering kernel function
$a$	Half length of long axis
$b$	Half length of short axis
$c$	Constant
	Speed of light
$d$	Diameter
$e$	Elementary charge
$f$	Focal length
	Shape factor
$f(m,\theta)$	Anomalous diffraction function
$f(\theta)$	Scattering angular pattern
$f(\kappa r)$	Henry's function
$g$	Acceleration
$g_1$	Skewness
$g_2$	Kurtosis
$g^{(1)}(\tau)$	Normalized first-order correlation function
$g^{(2)}(\tau)$	Normalized second-order correlation function
$h$	Height
$i$	Current
$\mathbf{k}$	Wave vector
$k$	Imaginary refractive index
$k_B$	Boltzmann constant
$k_d$	Diffusional second virial coefficient
$k_D$	Scaling parameter relating $D_T$ and molecular weight
$k_T$	Thermal conductivity
$l$	Length
	Distance
	Thickness
$m$	Relative complex refractive index
$m_i$	Complex refractive index of component $i$
$n$	Amount adsorbed
	Number
	Real refractive index
$q(x)$	Differential distribution function

$q(x_i)$	Discrete fractional distribution
$r$	Distance
	Radius
$s$	Surface charge density
$t$	Time
	Temperature
$u$	Particle velocity
$x$	General variable
$\bar{x}$	Mean value of $x$
$z$	Ion valence
$A$	Amplitude
	Baseline of correlation function
	Area
$A_2$	Second virial coefficient
$C$	concentration
$C_i$	$i^{\text{th}}$ cumulant
$D$	Diameter
	Dielectric constant
$D_R$	Rotational diffusion coefficient
$D_T$	Translational diffusion coefficient
$\bar{D}_{p,q}$	Mean value in the moment-ratio notation
$E$	Electric field of light
	Electric field
$G$	Geometric term in OPC
	Conductivity
$G^{(1)}(\tau)$	First-order correlation function
$G^{(2)}(\tau)$	Second-order correlation function
$H$	Optical constant in static light scattering
$I$	Light intensity
$J_1$	Bessel function of the first kind of order unity
$\mathbf{K}$	Scattering vector
$L$	Length of long axis
$M$	Molecular weight
	Moment of a distribution
$M_{k,r}$	$k^{\text{th}}$ moment in the moment notation
$N(d)$	Number distribution
$N$	Number
$N_A$	Avogadro's number
$P$	Pressure
	Probability
	Power
$P(x)$	Scattering factor

$Q(x)$	Cumulative distribution
$Q_{ex}$	Particle extinction efficiency
$Q_{sc}$	Particle scattering efficiency
$R$	Radius
	Optical response in OPC
$\mathcal{R}_{ex}$	Excess Rayleigh ratio
$R_g$	Radius of gyration
$S$	Surface area
	Power spectrum
	Entropy function
$S'$	Structure factor
$S_{i,i=1 \text{ to } 4}$	Scattering amplitude function
$T$	Absolute temperature
$U$	Pulse amplitude
	Stokes parameter
$V$	Velocity
	Volume
	Stokes parameter

## 2. Abbreviations

ACF	Autocorrelation function
AFM	Atomic force microscopy
APD	Avalanche photodiode
ASTM	American Society for Testing and Materials
AWPD	Amplitude-weighted phase difference
AWPS	Amplitude-weighted square phase difference
BCR	Community Bureau of Reference
BET	Brunauer-Emmett-Teller
BJH	Barrett-Joyner-Halenda
CCD	Charge-coupled device
CCF	Cross-correlation function
CLSM	Confocal laser scanning microscopy
CNC	Condensation nucleus counter
DICM	Differential interference contrast microscopy
DOP	Diocetylphthalate
DWS	Diffusing-wave spectroscopy
ELS	Elastic light scattering
ELS	Electrophoretic light scattering
EM	Electron microscopy
ESA	Electrokinetic sonic amplitude effect
ESZ	Electrical sensing zone

FFF	Field flow fractionation
GPC	Gel permeation chromatography
HDC	Hydrodynamic chromatography
IELS	Inelastic light scattering
IEP	Isoelectric point
ISO	International organization of standardization
LS	Light scattering
MCA	Multichannel analyzer
NIST	The National Institute of Standards and Technology
NNLS	Non-negative least-squares
NSOM	Near-field scanning optical microscopy
OM	Optical microscopy
OPC	Optical particle counting
PALS	Phase analysis light scattering
PCS	Photon correlation spectroscopy
PD	Photodiode
PIDS	Polarization intensity differential scattering
PMT	Photomultiplier tube
PSL	Polystyrene latex
PZC	Point of zero charge
QELS	Quasi-elastic light scattering
RCS	Raman correlation spectroscopy
RDG	Rayleigh-Debye-Gans
SEC	Size exclusion chromatography
SEM	Scanning electron microscopy
SRM	Standard reference material
STEM	Scanning transmission electron microscopy
STM	Scanning tunneling microscopy
TEM	Transmission electron microscopy

## **APPENDIX II: ISO AND ASTM STANDARDS**

### **1. Data Presentation**

ISO 9276-1:1998 Representation of Results of Particle Size Analysis – Part 1: Graphical Representation

ISO/DIS 9276-2 Representation of Results of Particle Size Analysis – Part 2: Calculation of Average Particle Sizes/Diameters and Moments from Particle Size Distributions

ISO/DIS 9276-4 Representation of Results of Particle Size Analysis – Part 4: Characterization of a Classification Process

ASTM E1919-97 Standard Guide for Worldwide Published Standards Relating to Particle and Spray Characterization

ASTM E177-90a Standard Practice for Use of the Terms Precision and Bias in ASTM Test Methods

ASTM E1617-97 Standard Practice for Reporting Particle Size Characterization Data

ASTM F1877-98 Standard Practice for Characterization of Particles

### **2. Laser Diffraction**

ISO/FDIS 13320-1 Particle Size Analysis – Laser Diffraction Methods – Part 1: General Principles

ASTM B822-92 Standard Test Method for Particle Size Distribution of Metal Powders and Related Compound by Light Scattering

ASTM C1070-86e1 Standard Test Method for Determining Particle Size Distribution of Alumina or Quartz by Laser Light Scattering

ASTM D4464-85 Standard Test Method for Particle Size Distribution of Catalytic Material by Laser Light Scattering

ASTM E1458-92 Standard Test Method for Calibration Verification of Laser Diffraction Particle Sizing Instruments Using Photomask Reticles

ASTM E1260-95 Standard Test Method for Determining Liquid Drop Size Characteristics in a Spray Using Optical Nonimaging Light-Scattering Instruments

### 3. Optical Particle Counting

ISO/DIS 4548-12 Methods of Test for Full-Flow Lubricating Oil Filters for Internal Combustion Engines – Part 12: Particle Retention Ability and Contaminant Holding Capacity Using Particle Counting

ISO/DIS 11171 Hydraulic Fluid Power – Calibration of Liquid Automatic Particle Counters

ISO 11500:1997 Hydraulic Fluid Power – Determination of Panicle Contamination by Automatic Counting Using the Light Extinction Principle

ISO/DIS 11943 Hydraulic Fluid Power – On-line Liquid Automatic Particle-Counting Systems – Methods of Calibration and Validation

ISO/DIS 13323-1 Determination of Particle Size Distribution – Single Particle Light Interaction Methods – Part I: Light Interaction Considerations

ASTM F25-68(1995)el Standard Test Method for Sizing and Counting Airborne Panicle Contamination in Clean Rooms and Other Dust-Controlled Areas Designed for Electronic and Similar Applications

ASTM F50-92(1996) Standard Practice for Continuous Sizing and Counting of Airborne Particles in Dust-Controlled Areas and Clean Rooms Using Instruments Capable of Detecting Single Sub-Micrometer and Larger Particles

ASTM F1226-89(1994)el Standard Test Method for Calibration of Liquid-Borne Particle Counters for Submicrometer Particle Sizing

ASTM F660-83(1993) Standard Practice for Comparing Particle Size in the Use of Alternative Types of Particle Counters

ASTM F328-98 Standard Practice for Calibration of an Airborne Particle Counter Using Monodisperse Spherical Particles

ASTM F658-87(1992) Standard Practice for Defining Size Calibration, Resolution, and Counting Accuracy of a Liquid-Borne Particle Counter Using Near-Monodisperse Spherical Particulate Material

ASTM F649-80(1992) Standard Practice for Secondary Calibration of Airborne Particle Counter Using Comparison Procedures

ASTM F662-86(1992)el Standard Test Method for Measurement of Particle Count and Size Distribution in Batch Samples for Filter Evaluation Using an Electrical Resistance Particle Counter

ASTM F661-92 Standard Practice for Particle Count and Size Distribution Measurement in Batch Samples for Filter Evaluation Using an Optical Particle Counter

ASTM F327-78(1989)el Standard Practice for Sampling Gas Blow Down Systems and Components for Particulate Contamination by Automatic Particle Monitor Method

ASTM F795-88(1993) Standard Practice for Determining the Performance of a Filter Medium Employing a Single-Pass, Constant-Rate, Liquid Test



**4. Photon Correlation Spectroscopy**

ISO 13321:1996 Particle Size Analysis – Photon Correlation Spectroscopy

**5. Electrophoretic Light Scattering**

ASTM 1470-92(1998) Standard Test Method For Characterization of Protein by Electrophoretic Mobility

### APPENDIX III: INSTRUMENT MANUFACTURERS

Manufacturer	LS	OPC	PCS	ELS
ALV-Laser Vertriebsgesellschaft m.b.H. (Langen, Germany)			✓	
Beckman Coulter Inc. (Miami, FL, USA)	✓		✓	✓
Brookhaven Instruments Corp. (Holtsville, NY, USA)			✓	✓
Chevalier Photonics NV (Merelbeke, Belgium)		✓		
Cilas (Marcoussis, France)	✓			
Fritsch GmbH (Idar-Oberstein, Germany)	✓			
Honeywell Inc. (Phoenix, AZ, USA)	✓		✓	
Horiba, Ltd. (Kyoto, Japan)	✓		✓	
Malvern Instruments Ltd. (Malvern, Worcs., UK)	✓	✓	✓	✓
Omec Instruments Co., Ltd. (Zhuhai, Guangdong, China)	✓			
Otsuka Electronics Co., Ltd. (Osaka, Japan)			✓	✓
Pacific Scientific Instruments (Grants Pass, OR, USA)		✓		
Particle Measuring Systems Inc. (Boulder, CO, USA)		✓		
Particle Sizing Systems (Santa Barbara, CA, USA)		✓	✓	✓
Pen Kem, Inc. (Bedford Hills, NY, USA)				✓
Phoenix Instruments, Inc. (Sunderland, MA, USA)			✓	
Precision Detectors, Inc. (Franklin, MA, USA)			✓	
Protein Solutions, Inc. (Charlottesville, VA, USA)			✓	
Seishin Enterprise Co., Ltd. (Tokyo, Japan)	✓			
Sematech (Nice, France)			✓	
Spectrex Corp. (Redwood City, CA, USA)		✓		
Shimadzu Corp. (Tokyo, Japan)	✓			
Sympatec GmbH (Clausthal-Zellerfeld, Germany)	✓			

\*: The listing is based on the best of the author's knowledge and does not mean the endorsement to the manufacturers listed.

## APPENDIX IV: SCATTERING FUNCTIONS OF A SPHERE

$$S_1 = \sum_{k=1} \frac{2k+1}{k^2+k} (a_k \pi_k(\cos \theta) + b_k \tau_k(\cos \theta)) \quad (\text{A4.1})$$

$$S_2 = \sum_{k=1} \frac{2k+1}{k^2+k} (a_k \tau_k(\cos \theta) + b_k \pi_k(\cos \theta)) \quad (\text{A4.2})$$

where

$$\pi_k(\cos \theta) = \frac{2k-1}{k-1} \cos \theta \cdot \pi_{k-1}(\cos \theta) - \frac{k}{k-1} \pi_{k-2}(\cos \theta) \quad (\text{A4.3})$$

$$\pi_0(\cos \theta) = 0; \quad \pi_1(\cos \theta) = 1 \quad (\text{A4.4})$$

$$\tau_k(\cos \theta) = \pi_k(\cos \theta) \cos \theta - (1 - \cos^2 \theta) \pi'_k(\cos \theta) \quad (\text{A4.5})$$

$$\tau_1(\cos \theta) = \cos \theta \quad (\text{A4.6})$$

$$\pi'_k(\cos \theta) = (2k-1) \pi_{k-1}(\cos \theta) + \pi'_{k-2}(\cos \theta) \quad (\text{A4.7})$$

$$\pi'_0(\cos \theta) = 0; \quad \pi'_1(\cos \theta) = 0 \quad (\text{A4.8})$$

$$a_k = \frac{\Psi_k(\alpha)(\eta_k^{(1)}(\beta) - m\eta_k^{(1)}(\alpha))}{\zeta_k(\alpha)(\eta_k^{(1)}(\beta) - m\eta_k^{(3)}(\alpha))} \quad (\text{A4.9})$$

$$b_k = \frac{\Psi_k(\alpha)(\eta_k^{(1)}(\alpha) - m\eta_k^{(1)}(\beta))}{\zeta_k(\alpha)(\eta_k^{(3)}(\alpha) - m\eta_k^{(1)}(\beta))} \quad (\text{A4.10})$$

$$\Psi_k(\alpha) = \frac{2k-1}{\alpha} \Psi_{k-1}(\alpha) - \Psi_{k-2}(\alpha) \quad (\text{A4.11})$$

$$\Psi_0(\alpha) = \sin \alpha \quad \Psi_1(\alpha) = \frac{\sin \alpha}{\alpha} - \cos \alpha \quad (\text{A4.12})$$

$$\eta_k^{(1)}(y) = \frac{y^2 + ky\eta_{k-1}^{(1)}(y) - k^2}{ky - y^2\eta_{k-1}^{(1)}(y)} \quad (\text{A4.13})$$

$$\eta_0^{(1)}(y) = \cot y; \quad y = \alpha, \beta \quad (\text{A4.14})$$

$$\varsigma_k(\alpha) = \frac{2k-1}{\alpha} \varsigma_{k-1}(\alpha) - \varsigma_{k-2}(\alpha) \quad (\text{A4.15})$$

$$\varsigma_0(\alpha) = \sin \alpha + i \cos \alpha; \quad \varsigma_1(\alpha) = \frac{\sin \alpha}{\alpha} - \cos \alpha + i\left(\frac{\cos \alpha}{\alpha} + \sin \alpha\right) \quad (\text{A4.16})$$

$$\eta_k^3(\alpha) = \frac{\varsigma_{k-1}(\alpha)}{\varsigma_k(\alpha)} - \frac{k}{\alpha} \quad (\text{A4.17})$$

$$\alpha = \pi d n_0 / \lambda_0; \quad \beta = \pi d m / \lambda_0 \quad (\text{A4.18})$$

# APPENDIX V: SCATTERING FACTORS FOR RANDOMLY ORIENTED PARTICLES\*

Shape	Scattering Factor P(x)	$R_g^2$
Sphere	$\left[ \frac{3(\sin x - x \cos x)}{x^3} \right]^2$	$3d^2/20$
	$x = Kd/2$ , $d$ = diameter.	
Thin disk	$\frac{2}{x^2} \left( 1 - \frac{1}{x} J_1(2x) \right)$	$d^2/8$
	$x = Kd/2$ , $d$ = diameter.	
Thin rod	$\int_0^{2x} \frac{\sin t}{t} dt - \frac{\sin^2 x}{x^2}$	$l^2/12$
	$x = Kl/2$ , $l$ = length.	
Random coil	$\frac{2}{x^4} (e^{-x^2} + x^2 - 1)$	$n_s L_k^2/6$ or $l_e^2/6$
	$x = KR_g$ , $n_s$ : number of segment, $L_k$ : segment length (Kuhn length), $l_e$ : end-to-end distance of the chain.	
Concentric spheres (core shell)	$\left[ \frac{3(\sin x - x \cos x)}{x^3} + \frac{m_i - m_o}{m_o - 1} \left( \frac{d_i}{d_o} \right)^3 \left( \frac{3(\sin y - y \cos y)}{y^3} \right) \right]^2$	Same as spheres if the shell and core have the same density
	$x = Kd_o/2$ , $y = Kd_i/2$ , $d$ = diameter, $m = R.I.$ , $o$ = shell, $i$ = core.	
Circular rod	$\int_0^{\pi/2} \frac{\pi}{2y \cos \beta} \left[ J_{0.5}(y \cos \beta) \cdot \frac{2J_1(x \sin \beta)}{x \sin \beta} \right]^2 \sin \beta d\beta$	$3l^2/20$
	$y = Kl/2$ , $l$ = length, $x = Kd/2$ , $d$ = diameter, $\beta$ is angle between axis of rod and bisectrix.	
Ellipsoid of revolution	$\int_0^{\pi/2} \left[ \frac{3(\sin x - x \cos x)}{x^3} \right]^2 \cos \beta d\beta$	$(a^2 + 2b^2)/5$
	$x = Ka \sqrt{\left( \cos^2 \beta + \left( \frac{b}{a} \sin \beta \right)^2 \right)}$ , $a, b$ = semiaxes, $\beta$ is angle between figure axis and bisectrix.	

\*: A more extensive list of scattering factors can be found in [68] of Chapter 2.

## APPENDIX VI: PHYSICAL CONSTANTS OF COMMON LIQUIDS

### 1. Water

#### 1.1. REFRACTIVE INDEX

Refractive index is the ratio of the wavelength or phase velocity of an electromagnetic wave in a vacuum to that in the substance. It is a function of wavelength, temperature, and pressure. If the material is non-absorbing and non-magnetic at any wavelength, then the square of refractive index is equal to the dielectric constant at that wavelength. For absorbing materials, the complex refractive index  $m = n - ik$  is related to the absorptive index  $k$  where the real term describes the refraction and the imaginary term describes the absorption. The following empirical equation, from *International Critical Tables Of Numerical Data, Physics, Chemistry And Technology*, National Research Council (U.S.), McGraw-Hill, New York, 1926-30, describes the refractive index of water as a function of wavelength ( $\lambda$ ) in microns and temperature. In the temperature range from 0 °C to 50 °C and wavelength range from 0.4  $\mu\text{m}$  to 0.7  $\mu\text{m}$ , the values computed from the formula are accurate up to five significant figures as compared with the numerical values in the *CRC Handbook of Chemistry and Physics*, CRC Press, Boca Raton, 1999.

$$n(\lambda, t) = \left( 1.75648 - 0.013414\lambda^2 + \frac{0.0065438}{\lambda^2 - 0.11512^2} \right)^{0.5} + 0.00204976 - 10^{-5} \left( 0.124(t - 20) + 0.1993(t^2 - 20^2) - 0.000005(t^4 - 20^4) \right) \quad (\text{A6.1})$$

#### 1.2. VISCOSITY

Viscosity is a measure of a fluid's resistance to flow. It describes the internal friction of a moving fluid. Viscosity is expressed in dyne-seconds per  $\text{cm}^2$  or poises ( $\text{g}/\text{cm}\cdot\text{s}$ ). The common unit for viscosity is centipoise (cp), which is equal to 0.01 poise. Kinematic viscosity is the ratio of viscosity to density in stokes ( $\text{cm}^2/\text{s}$ ). The following empirical equations are for the viscosity of water in centipoises at different temperatures. Eq. A6.2 is for the temperature range from 0 °C to 20 °C, from Hardy, R. C., Cottington, R. L., *J. Res. NBS*, 1949, 42,

573; and Eq. A6.3 is for the temperature range from 20 °C to 100 °C, from Swindells, J. F., NBS. The viscosity at 20 °C is 1.002 cp.

$$\log_{10} \eta_t = \frac{1301}{998.333 + 8.1855(t - 20) + 0.00585(t - 20)^2} - 1.30233 \quad (\text{A6.2})$$

$$\log_{10} \frac{\eta_t}{\eta_{20}} = \frac{1.3272(20 - t) - 0.001053(t - 20)^2}{t + 105} \quad (\text{A6.3})$$

### 1.3. DIELECTRIC CONSTANT

Dielectric constant is a measure of the amount of electrical charge a given substance can withstand at a given electric field as compared to air. The following empirical equation is from Maryott and Smith, *NBS Cir.* 514, 1951. In the temperature range from 0 °C to 60 °C, the values computed from the formula are accurate up to four significant figures as compared with the numerical values in the *CRC Handbook of Chemistry and Physics*, CRC Press, BocaRaton, 1999.

$$D = 78.30 \left( 1 - 4.579 \cdot 10^{-3}(t - 25) + 1.19 \cdot 10^{-5}(t - 25)^2 - 2.8 \cdot 10^{-8}(t - 25)^3 \right) \quad (\text{A6.4})$$

Liquid	t(°C)	η(cp)	R.I.	Dielectric Constant
1,1,2,2-Tetrabromoethane	25	9.00	1.6380	7.0
1,1,2,2-Tetrachloroethane	15	1.844	1.4944	7
1,2-Dichloroethane	25/50	.464/.362	1.4443	9.3
1,2-Propanediol	25	40.4	1.4324	32
1-Octanol	25/50	7.288/3.232	1.4293	10
1-Propyl Alcohol	20/30	2.23/1.72	1.3854	20
2,2,4-Trimethylpentane	20	.5	1.3916	1.94
2-Ethoxyethanol	20	1.72	1.402	16.9
2-Propyl Alcohol	15/30	2.86/1.77	1.377	18
Acetaldehyde	10/20	.255/.22	1.3316	22
Acetic Acid	18/25	1.30/1.16	1.3718	6.15
Acetic Anhydride	18/50	.90/.62	1.3904	20
Acetone	20/25	.326/.316	1.3589	20.7
Acetonitrile	20/25	.360/.345	1.3460	37.5
Acetophenone	20/25	1.8/1.62	1.5342	17.4
Allyl Alcohol	20/30	1.363/1.07	1.4135	22
Amyl Acetate(iso)	20	.867	1.4012	7.252
Aniline	20/50	4.40/1.85	1.5863	6.89

Anisole	20	1.32	1.5179	4.3
Benzaldehyde	20/25	1.6/1.35	1.5463	17.8
Benzene	20/50	.652/.436	1.5011	2.28
Benzyl Alcohol	20/50	5.8/2.57	1.5396	13.1
Benzylamine	20	1.59	1.5401	4.6
Bromobenzene	15/30	1.196/.985	1.5602	5.5
Bromoform	15/25	2.15/1.89	1.5980	4.4
Carbon Disulfide	20/40	.363/.330	1.6280	2.64
Carbon Tetrachloride	20/50	.969/.654	1.4630	2.24
Castor oil	25	600	1.47	4.0
Chlorobenzene	20/50	.799/.58	1.5248	2.71
Chloroform	20/25	.580/.542	1.4464	4.81
Cyclohexane	17/20	1.02/.696	1.4264	2.02
Cyclohexanol	25/50	47.5/12.3	1.4655	15
Cyclohexanone	15/30	2.453/1.803	1.451	18.3
Cyclohexene	20/50	.696/.456	1.4451	2.02
Cyclopentane	20	.44	1.406	1.97
Delphi Liquid	20		1.2718	
Dibutyl Phthalate	25/50	16.6/6.47	1.4900	~ 8
Dichloromethane	15/30	.449/.393	1.4244	9.09
Diethylamine	25	.346	1.3864	3.7
Dimethyl Sulfate	15/30	2.0/1.57	1.3874	55
Dimethyl Sulfoxide	25	2.0	1.47	4.7
Dimethylaniline	20/50	1.41/.9	1.5582	4.4
Dimethylformamide	25	.802	1.42	36.7
Dioxane	15/25	1.44/1.177	1.4175	2.2
Ether (Di-Ethyl)	20/25	.233/.222	1.3497	4.3
Ethyl Acetate	20/25	.455/.441	1.3722	6.0
Ethyl Alcohol	20/30	1.2/1.003	1.3611	25
Ethyl Benzene	17/25	.691/.640	1.49	2.5
Ethyl Bromide	20/25	.402/.374	1.4239	4.9
Ethylene Bromide	20	1.721	1.5379	
Ethylene Glycol (10%)	20/30	0.812/0.699	1.4627	
Ethylene Glycol (20%)	20/30	1.835/1.494	1.4627	
Ethylene Glycol (50%)	20/30	4.2/3.11	1.4627	
Ethylene Glycol (70%)	20/30	7.11/5.04	1.4627	
Ethylene Glycol (100%)	20/30	19.9/12.2	1.4627	38.7
Formamide	20/25	3.76/3.30	1.4453	84
Formic Acid	20/50	1.80/1.03	1.3714	58
Freon (11 and 113)	25	.415	1.36	3.1
Furfural	20/25	1.63/1.49	1.5261	42
Glycerin (10wt%)	20/25	1.311/1.153	1.3448	
Glycerin (20wt%)	20/25	1.769/1.542	1.3575	
Glycerin (40wt%)	20/25	3.750/3.181	1.3841	
Glycerin (100wt%)	20/25	1499/945	1.4729	42.5
Heptane	20/25	.409/.386	1.3876	1.92
Hexane	20/25	.326/.294	1.3754	1.89



Iodoethane	25/50	.556/.444	1.5168	7.4
Isobutyl Alcohol	15/20	4.703/3.9	1.3968	15.8
Isopar G	20/40	1.49/1.12	1.4186	2.0
Isopar M	37.8	34-36.5	1.4362	
Isopentane	20	.223	1.3550	
Isopropyl Alcohol	15/30	2.86/1.77	1.377	18
Isopropyl Ether	25/50	.396/.304	1.3680	3.85
Iso-Propylacetate	20	.525	1.377	
m-Bromoaniline	20	6.81	1.6260	13
Methanol	20/25	.597/.547	1.3312	33.6
Methyl Acetate	20/40	.381/.320	1.3614	7
Methyl Cyclohexane	25/50	.679/.501	1.4253	2
Methyl Ethyl Ketone	20/50	.42/.31	1.38	19
Methyl Iodide	20	.500	1.5293	7.0
Methyl Isobutyl Ketone	20/50	.579/.542	1.396	18
Methylacetate	20/50	.381/.286	1.3594	6.7
Methylene Chloride	15/30	.449/.393	1.4237	9.08
m-Toluidine	20	.81	1.5711	6.0
m-Xylene	15/20	.650/.620	1.4972	2.37
n-Amyl Alcohol	15/30	4.65/2.99	1.4099	13.9
n-Butyl Acetate	20	.73	1.3951	5.0
n-Butyl Alcohol	20/50	2.948/1.42	1.3993	17.8
n-Decane	20/50	.92/.615	1.4120	2.0
Nitrobenzene	20/50	2.0/1.24	1.5529	35
Nitromethane	20/25	.66/.620	1.3818	39.4
n-Nonane	20/50	.711/.492	1.4054	1.972
n-Octane	20/50	.542/.389	1.3975	2.0
n-Pentane	0/20	.277/.240	1.3570	1.84
n-Propylacetate	20/50	.537/.39	1.384	6.3
o-Dichlorobenzene	25	1.32	1.5515	99
o-Nitrotoluene	20/40	2.37/1.63	1.5474	27.4
o-Toluidine	20	.39	1.5728	6.34
o-Xylene	16/20	.876/.810	1.5055	2.568
Propyl Bromide	20	.524	1.4341	7.2
Propylene Glycol (10%)	20/30	1.5/1.2	1.344	
Propylene Glycol (20%)	20/30	2.18/1.59	1.355	
Propylene Glycol (30%)	20/30	3.0/2.1	1.367	
Propylene Glycol (100%)	20/40	56/18	1.433	
p-Toluidine	20	.80	1.5532	6.0
p-Xylene	16/20	.696/.648	1.4958	2.27
Pyridine	20	.95	1.5102	12.5
Sec-Butyl Alcohol	25/50	3.096/1.332	1.3954	15.8
Styrene (Vinyl Benzene)	20/50	.749/.502	1.55	2.4
Sulphuric Acid	20	.254	1.8340	84
Tert-Butyl Alcohol	25/50	4.312/1.421	1.3847	11.5
Tetrachloroethylene	15	.93	1.5044	2.5
Tetradecane	20/50	2.31/1.32	1.429	
Tetrahydrofuran	20/30	.575/.525	1.40	7.6

Toluene	20/30	.590/.526	1.4969	2.4
Trichloroethane	20	.2	1.4377	7.5
Trichloroethylene	20	.57	1.4784	3.4
Triethylamine	25/50	.347/.273	1.4003	2.4
Water	20/25	1.002/.8904	1.3330	80.2

Note:

- a) Liquid viscosity values in the third column are at the corresponding temperatures in the second column. Refractive indices are at the sodium yellow line ( $\lambda = 589.3$  nm) at 20 °C. Dielectric constants are at 20 °C. The values are from *CRC Handbook of Physics and Chemistry*, CRC Press, Boca Raton, and other sources.
- b) The content of this appendix is adopted from “*Some Physical Constants Used in Particle Characterization*” by Particle Characterization, Beckman Coulter, Inc., Miami, by permission.

## APPENDIX VII: REFRACTIVE INDEX OF SUBSTANCES

Name	Composition	R.I.		$\lambda(\text{nm})$
		Real	Imagi.	
Acetic Anhydride		1.390		
Acetylene Soot		1.56-1.99	0.3-0.5	633
Actinolite		1.618-1.641		
Adularia (moonstone)		1.525		
Adventurine (feldspar)		1.532-1.542		
Adventurine (quartz)		1.544-1.553		
Agalmatoite		1.55		
Agate	$\text{SiO}_2$	1.544-1.553		
Ailicate	$\text{Al}_2\text{O}_3 \cdot \text{SiO}_2$	1.66		
Alabandite	$\text{MnS}$	2.70		
Albite (feldspar)	$\text{NaAlSi}_3\text{O}_8$	1.525-1.536		
Albite (moonstone)	$\text{NaAlSi}_3\text{O}_8$	1.535		
Alexandrite	$\text{BeAl}_2\text{O}_4$	1.744-1.755		
Alginic acid, sodium salt		1.334		
Almandite		1.790		
Alumina ( $\alpha$ )	$\text{Al}_2\text{O}_3$	1.765		
Alumina ( $\gamma$ )	$\text{Al}_2\text{O}_3$	1.7		
Aluminite	$\text{Al}_2(\text{SO}_4)(\text{OH})_4 \cdot 7\text{H}_2\text{O}$	1.46-1.47		
Aluminum	$\text{Al}$	1.48	3.9	657
Aluminum	$\text{Al}$	2.143		729
Aluminum	$\text{Al}$	0.598		443
Aluminum	$\text{Al}$	1.304		620
Aluminum	$\text{Al}$	2.237		886
Aluminum chloride	$\text{AlCl}_3 \cdot 6\text{H}_2\text{O}$ or $\text{Al}_2\text{Cl}_6$	1.56		
Aluminum nitrate	$\text{Al}(\text{NO}_3)_3 \cdot 9\text{H}_2\text{O}$	1.54		
Aluminum oxide	$\text{Al}_2\text{O}_3$	1.768		
Aluminum oxide	$\text{Al}_2\text{O}_3 \cdot \text{H}_2\text{O}$	1.624		
Alunite	$(\text{K} \cdot \text{Na})\text{Al}_3(\text{SO}_4)_2(\text{OH})_6$	1.57-1.59		
Amazonite (feldspar)		1.525		
Amber		1.54		
Amblygonite		1.611-1.637		
Amethyst	$\text{SiO}_2 \cdot n\text{H}_2\text{O}$	1.533-1.553		
Ammonium aluminum sulfate	$\text{NH}_4\text{Al}(\text{SO}_4)_2 \cdot 12\text{H}_2\text{O}$	1.459		
Ammonium calcium phosphate	$\text{NH}_4\text{CaPO}_4 \cdot 7\text{H}_2\text{O}$	1.561		
Ammonium chloride	$\text{NH}_4\text{Cl}$	1.642		
Ammonium ditartrate	$(\text{NH}_4)_2\text{C}_4\text{H}_4\text{O}_6$	1.55-1.58		
Ammonium hydrocarbonate	$\text{NH}_4\text{HCO}_3$	1.423		
Ammonium hydroditartrate	$\text{NH}_4\text{HC}_4\text{H}_4\text{O}_6$	1.561		
Ammonium hydrosulfate	$\text{NH}_4\text{H}_2\text{SO}_4$	1.473		

Ammonium hydrosulfide	$\text{NH}_4\text{HS}$	1.74		
Ammonium nitrate	$\text{NH}_4\text{NO}_3$	1.41		
Ammonium perchlorate	$\text{NH}_4\text{ClO}_4$	1.482		
Ammonium sulfite	$(\text{NH}_3)_2\text{SO}_3 \cdot \text{H}_2\text{O}$	1.515		
Ammonium zinc sulfate	$(\text{NH}_4)_2\text{SO}_4 \cdot \text{ZnSO}_4 \cdot 6\text{H}_2\text{O}$	1.493		
Analcite	$\text{NaAlSi}_2\text{O}_6 \cdot \text{H}_2\text{O}$	1.48-1.49		
Anatase	$\text{TiO}_2$	2.49-2.56		
Andalusite	$\text{Al}_2\text{OSiO}_4$	1.63-1.65		
Anglesite	$\text{PbSO}_4$	1.87		
Anhydrite	$\text{CaSO}_4$	1.57-1.61		
Anorthite	$\text{CaAl}_2\text{Si}_2\text{O}_3$ (or) $\text{CaAl}_2\text{O}_3 \cdot 2\text{SiO}_3$	1.583		
Anorthoclase	$(\text{Na},\text{K})\text{AlSi}_3\text{O}_8$	1.52-1.53		
Antimony bromide	$\text{SbBr}_3$	1.74		
Antimony pentachloride	$\text{SbCl}_5$	1.601		
Antimony tetraoxide	$\text{Sb}_2\text{O}_4$ (or) $\text{Sb}_2\text{O}_3 \cdot \text{Sb}_2\text{O}_5$	2.00		
Antimony trioxide	$\text{Sb}_2\text{O}_3$ (or) $\text{Sb}_4\text{O}_4$	2.087-2.18		
Antimony trisulfide	$\text{Sb}_2\text{S}_3$	4.064		
Apatite	$\text{CaS}(\text{PO}_4)_2(\text{OH},\text{F},\text{Cl})$	1.63-1.67		
Apophyllite		1.536		
Aquamarine		1.577-1.583		
Aragonite		1.53-1.69		
Arsenic triiodide	$\text{AsI}_3$	2.23-2.59		
Arsenic trioxide	$\text{As}_2\text{O}_3$ (or) $\text{As}_4\text{O}_6$	1.76-1.9		
Arsenic trisulfide	$\text{As}_2\text{S}_3$	2.5976	0.42	644
Arsenic trisulfide	$\text{As}_2\text{S}_3$	2.5586	0.13	701
Artinite	$\text{MgCO}_3 \cdot \text{Mg}(\text{OH})_2 \cdot 3\text{H}_2\text{O}$	1.489		
Augelite		1.574-1.588		
Azurite	$2\text{CuCO}_3 \cdot \text{Cu}(\text{OH})_2$	1.730		
Baddeleyite	$\text{ZrO}_2$	2.17		
Barite	$\text{BaSO}_4$	1.64-1.65		
Barium acetate	$\text{Ba}(\text{C}_2\text{H}_3\text{O}_2)_2 \cdot \text{H}_2\text{O}$	1.52		
Barium chloride ( $\alpha$ )	$\text{BaCl}_2$	1.73		
Barium dithionate	$\text{Ba}(\text{SO}_3)_2 \cdot 2\text{H}_2\text{O}$	1.58		
Barium fluoride	$\text{BaF}_2$	1.484		404
Barium fluoride	$\text{BaF}_2$	1.476		546
Barium fluoride	$\text{BaF}_2$	1.474		589
Barium fluoride	$\text{BaF}_2$	1.473		656
Barium fluoride	$\text{BaF}_2$	1.472		706
Barium fluoride	$\text{BaF}_2$	1.469		894
Barium formate	$\text{Ba}(\text{CHO}_2)_2$	1.59		
Barium hydroxide	$\text{Ba}(\text{OH})_2 \cdot 8\text{H}_2\text{O}$	1.47		
Barium oxide	$\text{BaO}$	1.9		
Barium selenide	$\text{BaSe}$	2.26		
Barium sulfide	$\text{BaS}$	2.15		
Barium titanate	$\text{BaTiO}_3$	2.4		
Barium yellow	$\text{BaCrO}_4$	1.94-1.98		
Basic artinite	$\text{MgCO}_3 \cdot \text{Mg}(\text{OH})_2 \cdot 3\text{H}_2\text{O}$	1.534		
Bastnaesite	$\text{CeFCO}_3$	1.717		

Bauxite	$\text{AlO}(\text{OH})$	1.56-1.75		
Bayerite	$\text{Al}_2\text{O}_3 \cdot 3\text{H}_2\text{O}$	1.583		
Beeswax (white)		1.45-1.47		
Beryl		1.577-1.583		
Beryl (white, colorless)		1.577-1.583		
Beryllium aluminate		1.75		
Beryllium aluminum silicate	$\text{Be}_3\text{Al}_2(\text{SiO}_3)_6$	1.580		
Beryllonite		1.553-1.562		
Bieberite	$\text{CoSO}_4 \cdot 7\text{H}_2\text{O}$	1.47		
Bischofite	$\text{MgCl}_2 \cdot 6\text{H}_2\text{O}$	1.495		
Bismuth trioxide	$\text{Bi}_2\text{O}_3$	1.9		
Bisphenol-A polycarbonate		1.586		
BK7 Schott glass		1.523		480
BK7 Schott glass		1.519		546
BK7 Schott glass		1.517		589
BK7 Schott glass		1.515		644
BK7 Schott glass		1.513		707
BK7 Schott glass		1.510		852
Bloedite	$\text{Na}_2\text{SO}_4 \cdot \text{MgSO}_4 \cdot 4\text{H}_2\text{O}$	1.486		
Boehmite	$\text{AlO}(\text{OH})$	1.64-1.67		
Bone Ash		1.60-1.66		
Boracio acid	$\text{H}_3\text{BO}_3$	1.337-1.462		
Borax	$\text{Na}_2\text{B}_4\text{O}_7 \cdot 10\text{H}_2\text{O}$	1.45-1.47		
Boric acid	$\text{HBO}_2$	1.62		
Boron oxide	$\text{B}_2\text{O}_3$	1.63		
Brazilianite		1.603-1.623		
Brochantite	$\text{CuSO}_4 \cdot 3\text{Cu}(\text{OH})_2$	1.771		
Bromellite	$\text{BeO}$	1.720-1.735		
Bromyrite	$\text{AgBr}$	2.253		
Brookite	$\text{TiO}_2$	2.58-2.70		
Brownite		1.567-1.576		
Brucite	$\text{Mg}(\text{OH})_2$	1.56-1.60		
Brushite	$\text{CaHPO}_4 \cdot 2\text{H}_2\text{O}$	1.557		
Bunsenite	$\text{NiO}$	2.182		
Butyl rubber (unvulcanized)		1.508		
Butylphenol formaldehyde resin		1.66		
Cadmium	$\text{Cd}$	1.13		
Cadmium fluoride	$\text{CdF}_2$	1.56		
Cadmium metasilicate	$\text{CdSiO}_3$	1.739		
Cadmium oxide	$\text{CdO}$	2.49		
Cadmium sulfate	$3\text{CdSO}_4 \cdot 8\text{H}_2\text{O}$	1.565		
Cadmium yellow	$\text{CdS}$	2.35-2.53		589/625
Calcite	$\text{CaCO}_3$	1.49-1.66		589/643
Calcium acetate	$\text{Ca}(\text{C}_2\text{H}_3\text{O}_2)_2$	1.55		
Calcium aluminate	$\text{CaAl}_2\text{O}_4$ or $\text{CaO} \cdot \text{Al}_2\text{O}_3$	1.643		
Calcium aluminosilicate	$2\text{CaAl}_2\text{O}_3 \cdot \text{SiO}_2$	1.669		
Calcium carbide	$\text{CaC}_2$	1.75		
Calcium carbonate	$\text{CaCO}_3$	1.486-1.681		
Calcium chloride	$\text{CaCl}_2$	1.52		

Calcium chloride	$\text{CaCl}_2 \cdot 6\text{H}_2\text{O}$	1.417		
Calcium fluoride	$\text{CaF}_2$	1.437		486
Calcium fluoride	$\text{CaF}_2$	1.436		500
Calcium fluoride	$\text{CaF}_2$	1.434		587
Calcium fluoride	$\text{CaF}_2$	1.432		656
Calcium fluoride	$\text{CaF}_2$	1.431		728
Calcium fluoride	$\text{CaF}_2$	1.430		884
Calcium hydroxide	$\text{Ca}(\text{OH})_2$	1.574		
Calcium hypochlorite	$\text{Ca}(\text{ClO})_2$	1.545-1.69		
Calcium magnesium carbonate	$\text{CaCO}_3 \cdot \text{MgCO}_3$	1.681		
Calcium magnesium metasilicate	$\text{CaO} \cdot \text{MgO} \cdot 2\text{SiO}_2$	1.665		
Calcium metaborate	$\text{Ca}(\text{BO}_3)_2$	1.550-1.660		
Calcium metaphosphate	$\text{Ca}(\text{PO}_3)_2$	1.588		
Calcium orthophosphate	$\text{Ca}_3(\text{PO}_4)_2$	1.629		
Calcium peroxide		1.895		
Calcium phosphate	$\text{Ca}(\text{H}_2\text{PO}_4)_2$	1.529		
Calcium phosphate	$\text{Ca}(\text{H}_2\text{PO}_4)_2 \cdot 2\text{H}_2\text{O}$	1.439		
Calcium phosphate	$\text{Ca}_3(\text{PO}_4)_2$	1.60-1.66		
Calcium pyrophosphate	$\text{Ca}_2(\text{P}_2\text{O}_7)$	1.585		
Calcium stearate	$\text{Ca}(\text{C}_{18}\text{H}_{35}\text{O}_2)_2$	1.46		
Calcium sulfate	$\text{CaSO}_4 \cdot 2\text{H}_2\text{O}$	1.521		
Calcium sulfate (anhydrite)	$\text{CaSO}_4$	1.569		
Calcium trialuminate	$\text{Ca}_3\text{Al}_2\text{O}_6 \cdot 3\text{CaO} \cdot \text{Al}_2\text{O}_3$	1.710		
Camauba wax		1.47		
Cancrinite		1.491-1.524		
Carbon black	C	1.6-2.0	0.3-0.8i	633
Celestite	$\text{SrSO}_4$	1.622-1.631		
Celite		1.98		
Cellulose		1.54		
Cellulose acetate		1.475		
Cellulose acetate butyrate		1.475		
Cellulose nitrate		1.51		
Ceragyrite	$\text{AgCl}$	2.071		
Cerium fluoride	$\text{CeF}_4 \cdot 2\text{H}_2\text{O}$	1.614		
Cerium molybdate	$\text{Ce}_2(\text{MoO}_4)_3$	2.019		
Ceruseite	$\text{PbCO}_3$	2.076		
Cesium aluminum sulfate	$\text{CsAl}(\text{SO}_4)_2 \cdot 12\text{H}_2\text{O}$	1.45		
Cesium borohydride	$\text{CsBH}_4$	1.49		
Cesium bromide	$\text{CsBr}$	1.69		
Cesium bromide	$\text{CsBr}$	1.709		500
Cesium chloride	$\text{CsCl}$	1.69		
Cesium iodide	$\text{CsI}$	1.806		500
Cesium iron sulfate	$\text{Cs}_2\text{SO}_4 \cdot \text{FeSO}_4 \cdot 6\text{H}_2\text{O}$	1.56		
Cesium selenate	$\text{Cs}_2\text{SeO}_4$	1.59		
Cesium sulfate	$\text{Cs}_2\text{SO}_4$	1.56		
Chalcedony	$\text{SiO}_2$	1.53-1.54		
Chalcedony		1.535-1.539		
Chalk	$\text{CaCO}_3$	1.51-1.65		
Chlorocalcite	$\text{KCl} \cdot \text{CaCl}$	1.52		

Chloromanganokalite	$4\text{KCl}\cdot\text{MnCl}_2$	1.50		
Chromium	Cr	1.800		443
Chromium	Cr	3.480		620
Chromium	Cr	3.840		701
Chromium	Cr	4.420		912
Chromium orthophosphate	$\text{CrPO}_4\cdot 6\text{H}_2\text{O}$	1.56		
Chromium oxide	$\text{Cr}_2\text{O}_3$	2.55		
Chromium sulfate	$\text{Cr}_2(\text{SO}_4)_3\cdot 8\text{H}_2\text{O}$	1.56		
Chrysoberyl		1.746-1.755		
Chrysocolla		1.5		
Chrysoprase		1.534		
Citrine		1.55		
Cobalt acetate	$\text{Co}(\text{C}_2\text{H}_3\text{O}_2)_4\cdot 4\text{H}_2\text{O}$	1.54		
Cobalt ammonium cobaltate tetranitrodiamine	$\text{NH}_4[\text{Co}(\text{NH}_3)_2(\text{NO}_2)_4]$	1.7		
Cobalt chloride	$\text{CoCl}_2\cdot \text{H}_2\text{O}$	1.6		
Cobalt nitrate	$\text{Co}(\text{NO}_3)_2\cdot 6\text{H}_2\text{O}$	1.55		
Cobalt selenate		1.52		
Cobalt (single crystal E I c)	Co	1.720		442
Cobalt (single crystal E I c)	Co	2.130		590
Cobalt (single crystal E I c)	Co	2.830		729
Cobalt (single crystal E I c)	Co	3.550		886
Cobalt (single crystal E II c)	Co	1.660		443
Cobalt (single crystal E II c)	Co	2.130		590
Cobalt (single crystal E II c)	Co	2.660		701
Cobalt (single crystal E II c)	Co	3.370		886
Colemanite		1.586-1.614		
Common salt (halite)	NaCl	1.544		
Copper	Cu	1.170		443
Copper	Cu	0.470		590
Copper	Cu	0.220		729
Copper	Cu	0.260		827
Copper carbonate	$\text{CuCO}_3$	1.655		
Copper chloride(ous)	$\text{CuCl}$ (or) $\text{Cu}_2\text{Cl}_2$	1.495		
Copper perchlorate	$\text{Cu}(\text{ClO}_4)_2$	1.495		
Copper sulfate	$\text{Cu}_2\text{SO}_4$	1.724		
Copper sulfate	$\text{CuSO}_4$	1.733		
Coral		1.486-1.658		
Cordierite		1.54		
Corning Pyrex cylinder		1.470		633
Corundum	$\text{Al}_2\text{O}_3$	1.76-1.77		589/668
Cotunite	$\text{PbCl}_2$	2.199		
Covellite	CuS	1.45		
Cristobalite	$\text{SiO}_2$	1.48		
Cuprite	$\text{Cu}_2\text{O}$	2.705		
Cussiterite	$\text{SnO}_2$	1.997		
Danburite		1.633		
Diamond	C	2.41-2.42		589/644
Diaspore	$\text{AlO}(\text{OH})$	1.68-1.75		

Diopside	$\text{CaCO}_3 \cdot \text{MgCO}_3$	1.817		
Dolomite	$\text{CaMg}(\text{CO}_3)_2$	1.50-1.68		
Ekanite		1.6		
Elaeolite		1.532-1.549		
Emerald	$\text{Be}_3\text{Al}_2\text{Si}_6\text{O}_{18}$	1.56-1.60		
Enstatite		1.663-1.673		
Epsomite	$\text{MgSO}_4 \cdot 7\text{H}_2\text{O}$	1.433		
Eriochaleite	$\text{CuCl}_2 \cdot 2\text{H}_2\text{O}$	1.644		
Ethyl cellulose		1.479		
Ethylene/methacrylic acid ionomer, sodium ion		1.51		
Ethylene/vinyl acetate copolymer-28% vinyl acetate		1.485		
Ethylene/vinyl acetate copolymer-33% vinyl acetate		1.482		
Ethylene/vinyl acetate copolymer-40% vinyl acetate		1.476		
Euclase		1.652-1.672		
Eulytite	$2\text{Bi}_2\text{O}_3 \cdot 3\text{SiO}_2$	2.05		
Feldspar	$\text{KAlSi}_3\text{O}_8$ (or) $\text{K}_2\text{O} \cdot \text{Al}_2\text{O}_3 \cdot 6\text{SiO}_2$	1.525		
Ferberite	$\text{FeWO}_4$	2.40		
Fibrolite		1.659-1.68		
Fluorite	$\text{CaF}_2$	1.43-1.44		589/644
Formazine		1.85		
GaAs		4.3		
Galena	$\text{PbS}$	3.921		
Gallium oxide	$\text{Ga}_2\text{O}_3$	1.92		
Garnet		1.71-1.89		
Gaylussite		1.517		
Germanium oxide	$\text{GeO}$	1.650		
Germanium tetrabromide	$\text{GeBr}_4$	1.626		
Gibbsite	$\text{Al}_2\text{O}_3 \cdot 3\text{H}_2\text{O}$	1.577		
Gibbsite	$\text{Al}(\text{OH})_3$	1.56-1.60		
Glass		1.44-1.9		
Glass. Borosilicate	NIST-SRM 1820	1.487		436
Glass. Heavy Silicate Flint		1.65		589/656
Glass. Soda Lime	NIST-SRM 1822	1.529		436
Glass. Very Heavy Silicate Flint		1.89		589/656
Glauber's salt	$\text{Na}_2\text{SO}_4 \cdot 10\text{H}_2\text{O}$	1.394		
Goethite	$\text{FeO}(\text{OH})$	2.26-2.52		
Gold	$\text{Au}$	0.28	2.2	600
Gold	$\text{Au}$	0.31	2.7	650
Gold (electropolished)	$\text{Au}$	1.460		443
Gold (electropolished)	$\text{Au}$	0.180		590
Gold (electropolished)	$\text{Au}$	0.080		774
Gold (electropolished)	$\text{Au}$	0.080		886
Graham's salt	$(\text{NaPO}_3)_6$	1.482		
Graphite	$\text{C}$	1.8	0.6-0.8	633



Graphite	C	2.5	1.5	
Greenockite	CdS	2.51-2.53		
Grossularite		1.73-1.75		
Gutta percha a		1.514		
Gutta percha b		1.509		
Gypsum	CaSO <sub>4</sub> ·2H <sub>2</sub> O	1.52-1.53		
Hafnium fluoride	HfF <sub>4</sub>	1.56		
Hafnium (single crystal Ell c)	Hf	2.540		443
Hafnium (single crystal Ell c)	Hf	3.640		590
Hafnium (single crystal Ell c)	Hf	3.520		729
Hafnium (single crystal Ell c)	Hf	3.720		886
Hafnium (single crystal E.L c)	Hf	2.310		443
Hafnium (single crystal E.L c)	Hf	3.350		590
Hafnium (single crystal E.L c)	Hf	3.630		729
Hafnium (single crystal E.L c)	Hf	3.610		886
Halite	NaCl	1.544		
Hambergite		1.559-1.631		
Hausmannite	Mn <sub>3</sub> O <sub>4</sub>	2.46		
Hausmannite	Mn <sub>3</sub> O <sub>4</sub>	2.1-2.5		671
Hauynite		1.502		
Hematite	Fe <sub>2</sub> O <sub>3</sub>	2.9-3.2	0.01	
Hemimorphite	2ZnO·SiO <sub>2</sub> ·H <sub>2</sub> O	1.614-1.636		
Hiddenite		1.655-1.68		
Hopeite	Zn <sub>3</sub> (PO <sub>4</sub> ) <sub>2</sub> ·4H <sub>2</sub> O	1.572-1.574		
Howlite		1.586-1.609		
Hydraargilite	Al <sub>2</sub> O <sub>3</sub> ·3H <sub>2</sub> O	1.595		
Hydromagnesite	3MgCO <sub>3</sub> ·Mg(OH) <sub>2</sub> ·3H <sub>2</sub> O	1.527		
Hydroxyapatite	Ca <sub>10</sub> (PO <sub>4</sub> ) <sub>6</sub> B <sub>6</sub> H <sub>2</sub>	1.63		
Hydroxypropyl cellulose		1.337		
Ice Cylinders	H <sub>2</sub> O	1.308		
Idemitsu polycarbonate		1.585		
Illite (clay)		1.54-1.61		
Iodyrite	AgI	2.21		
Iolite		1.548		
Iridium	Ir	1.810		443
Iridium	Ir	2.400		590
Iridium	Ir	2.690		729
Iridium	Ir	2.720		886
Iron	Fe	2.120		443
Iron	Fe	2.800		590
Iron	Fe	1.7	1.8	668
Iron	Fe	2.980		729
Iron	Fe	3.120		886
Iron oxide	FeO	2.32		
Iron oxide magnetite	Fe <sub>3</sub> O <sub>4</sub>	2.42		
Iron perchlorate	Fe(ClO <sub>4</sub> ) <sub>2</sub> ·6H <sub>2</sub> O	1.493		
Iron sulfate	Fe <sub>2</sub> (SO <sub>4</sub> ) <sub>3</sub>	1.814		
Iron sulfate	FeSO <sub>4</sub> ·4H <sub>2</sub> O	1.533		
Ivory		1.54		

Jadeite		1.660-1.668		
Jarosite	$\text{KFe}_3(\text{SO}_4)_2(\text{OH})_6$	1.72-1.82		
Jasper		1.54		
Jet		1.66		
Kalinite	$\text{KAl}(\text{SO}_4)_2 \cdot 12\text{H}_2\text{O}$	1.454		
Kaliophilite	$\text{KAlSiO}_4$	1.532		
Kaolin clay		1.64		
Kaolinite	$\text{Al}_2\text{Si}_4\text{O}_{10}(\text{OH})_8$	1.53-1.57		
Kieserite	$\text{MgSO}_4 \cdot \text{H}_2\text{O}$	1.52-1.58		
Kornerupine		1.665-1.682		
Krausite	$\text{K}_2\text{SO}_4 \cdot \text{Fe}_2(\text{SO}_4)_3 \cdot 24\text{H}_2\text{O}$	1.482		
Kunzite		1.655-1.68		
Labradorite (feldspar)		1.565		
Lanarkite	$\text{PbSO}_4 \cdot \text{PbO}$	1.93		
Lansfordite	$\text{MgCO}_3 \cdot 5\text{H}_2\text{O}$	1.456		
Lanthanum fluoride	$\text{LaF}_3$	1.613		435
Lanthanum fluoride	$\text{LaF}_3$	1.602		546
Lanthanum sulfate	$\text{La}_2(\text{SO}_4)_3 \cdot 9\text{H}_2\text{O}$	1.564		
Lapis (gem)		1.5		
Lard (fresh pork fatty tissue)		1.448-1.460		
Lawrencite	$\text{FeCl}_2$	1.567		
Lazulite		1.615-1.645		
Lead	$\text{Pb}$	2.6		
Lead dioxide	$\text{PbO}_2$	2.3		
Lead dithionate	$\text{PbS}_2\text{O}_6 \cdot 4\text{H}_2\text{O}$	1.635		
Lead nitrate	$\text{Pb}(\text{NO}_3)_2$	1.782		
Lead orthophosphate	$\text{Pb}(\text{PO}_4)_2$	1.97		
Lead oxides	$\text{PbO}, \text{Pb}_3\text{O}_4, \text{PbO}_2$	2.3-2.7		
Lechatelierite	$\text{SiO}_2$	1.45		
Leonite	$\text{K}_2\text{SO}_4 \cdot \text{MgSO}_4 \cdot 4\text{H}_2\text{O}$	1.483		
Leucite	$\text{KAlSi}_2\text{O}_6$	1.508		
Lime	$\text{CaO}$	1.838		
Lithium acetate	$\text{LiC}_2\text{H}_3\text{O}_2 \cdot 2\text{H}_2\text{O}$	1.43-1.54		
Lithium carbonate	$\text{Li}_2\text{CO}_3$	1.42		
Lithium fluoride	$\text{LiF}$	1.399		400
Lithium fluoride	$\text{LiF}$	1.394		500
Lithium fluoride	$\text{LiF}$	1.392		600
Lithium fluoride	$\text{LiF}$	1.390		700
Lithium fluoride	$\text{LiF}$	1.389		800
Lithium fluoride	$\text{LiF}$	1.388		900
Lithium fluosilicate	$\text{Li}_2\text{SiF}_6 \cdot 2\text{H}_2\text{O}$	1.30		
Lithium hydroxide	$\text{LiOH}$	1.46		
Lithium oxide	$\text{LiO}_2$	1.64		
Lithopone		1.84		
Magnanite	$\text{MnO}(\text{OH})$	2.24		
Magnesite	$\text{MgCO}_3$	1.51-1.78		
Magnesium acetate	$\text{Mg}(\text{C}_2\text{H}_3\text{O}_2)_2 \cdot 4\text{H}_2\text{O}$	1.4		
Magnesium chloride	$\text{MgCl}_2$	1.675		
Magnesium fluoride	$\text{MgF}_2$	1.390		400

Magnesium fluoride	MgF <sub>2</sub>	1.385		546
Magnesium fluoride	MgF <sub>2</sub>	1.382		700
Magnesium silicate	MgSiO <sub>3</sub>	1.65		
Magnesium sulfate	MgSO <sub>4</sub>	1.568		
Magnesium sulfide	MgS	2.271		
Magnesium sulfite	MgSO <sub>3</sub> ·6H <sub>2</sub> O	1.511		
Magnetite	Fe <sub>3</sub> O <sub>4</sub>	2.42		
Malachite	Cu <sub>2</sub> (OH) <sub>2</sub> (CO <sub>3</sub> )	1.65-1.91		
Manganese	Mn	2.110		451
Manganese	Mn	2.470		582
Manganese	Mn	2.700		756
Manganese	Mn	2.970		892
Manganese fluosilicate	MnSiF <sub>6</sub> ·6H <sub>2</sub> O	1.357		
Manganese pyrophosphate	Mn <sub>2</sub> P <sub>2</sub> O <sub>7</sub>	1.695		
Manganese sulfate	MnSO <sub>4</sub> ·5H <sub>2</sub> O	1.495		
Manganese tantalate	Mn(TaO <sub>3</sub> ) <sub>2</sub>	2.22		
Mascagnite	(NH <sub>4</sub> ) <sub>2</sub> SO <sub>4</sub>	1.52-1.53		
Massicot	PbO	2.51		
Meerschaum		1.53		
Melamine		1.87		
Melanterite	Fe <sub>2</sub> SO <sub>4</sub> ·7H <sub>2</sub> O	1.471		
Mercallite	KHSO <sub>4</sub>	1.480		
Mercury	Hg	1.8		
Mercury chloride	HgCl <sub>2</sub>	1.8		
Mercury iodide	HgI <sub>2</sub>	2.5		
Mervnite	3CaOMgOSiO <sub>2</sub>	1.708		
Methanol	CH <sub>3</sub> OH	1.329		
Methyl cellulose		1.497		
Methyl ester of rosin		1.517-1.521		
Methylene iodide		1.74		
Mica		1.53-1.70		
Microcline	K <sub>2</sub> O·Al <sub>2</sub> O <sub>3</sub> ·6SiO <sub>2</sub>	1.522		
Moissanite	SiC	2.65-2.69		
Moldavite		1.5		
Molybdenum	Mo	3.080		443
Molybdenum	Mo	3.680		590
Molybdenum	Mo	3.840		729
Molybdenum	Mo	3.150		886
Monoazite	CePO <sub>4</sub>	1.795		
Moss agate		1.54-1.55		
Muscovite	K <sub>2</sub> O·Al <sub>2</sub> O <sub>3</sub> ·6SiO <sub>2</sub>	1.551		
Nantokite		1.93		
Naphthalene-formaldehyde rubber		1.696		
Natrolite		1.48-1.493		
Neodymium sulfate	Nd <sub>3</sub> (SO <sub>4</sub> ) <sub>3</sub> ·8H <sub>2</sub> O	1.41		
Nephelite	Na <sub>7</sub> O·Al <sub>2</sub> O <sub>3</sub> ·2SiO <sub>2</sub>	1.537		
Nephrite		1.6-1.63		
Nesquehonite	MgCO <sub>3</sub> ·3H <sub>2</sub> O	1.495		

Nickel	Ni	1.630		443
Nickel	Ni	1.850		590
Nickel	Ni	2.280		729
Nickel	Ni	2.650		886
Niobium	Nb	2.660		451
Niobium	Nb	2.890		605
Niobium	Nb	2.360		751
Niobium	Nb	1.760		918
Nitrobarite	Ba(NO <sub>3</sub> ) <sub>2</sub>	1.57		
Nylon 6 [Poly(caprolactam)]		1.53		
Nylon 6(3)T [Poly(trimethyl hexamethylene terephthalamide)]		1.566		
Nylon 6,10 [Poly(hexamethylene sebacamide)]		1.565		
Nylon 6,6 [Poly(hexamethylene adipamide)]		1.565		
Obsidian		1.48-1.51		
Octahedrite anatase	TiO <sub>2</sub>	2.554		
Oligoclase (feldspar)		1.539-1.547		
Onyx		1.486-1.658		
Opal	SiO <sub>2</sub> ·nH <sub>2</sub> O	1.41-1.46		
Optical Sapphire	Al <sub>2</sub> O <sub>3</sub>	1.771		539
Optical Sapphire	Al <sub>2</sub> O <sub>3</sub>	1.765		653
Optical Sapphire	Al <sub>2</sub> O <sub>3</sub>	1.761		775
Optical Sapphire	Al <sub>2</sub> O <sub>3</sub>	1.758		886
Orthoclase	KAlSi <sub>3</sub> O <sub>8</sub>	1.52-1.54		
Orthoclase feldspar		1.518-1.526		
Osmium (poly crystalline)	Os	5.070		443
Osmium (poly crystalline)	Os	4.260		590
Osmium (poly crystalline)	Os	3.700		729
Osmium (poly crystalline)	Os	2.490		886
Palladium	Pd	1.290		443
Palladium	Pd	1.670		590
Palladium	Pd	2.000		729
Palladium	Pd	2.340		886
Paraffin Oil		1.48		
Pearl		1.530-1.686		
Periclase	MgO	1.735		
Peridot		1.654-1.690		
Peristetite		1.525-1.536		
Perspex		1.495		
Petalite		1.502		
Phenakite		1.65-1.67		
Phenol-formaldehyde resin		1.7		
Phosphorus white	P <sub>4</sub>	2.144		
Plastic		1.46-1.7		
Platinum	Pt	1.830		443
Platinum	Pt	2.230		590
Platinum	Pt	2.2	2.1	633

Platinum	Pt	2.630	729
Platinum	Pt	3.100	886
Polyacetal		1.51	
Polycarbonate		1.59	687
Polycarbonate resin		1.586	
Polyethylene		1.51	
Polyethylene ionomer		1.51	
Polyethylene, high density		1.54	
Polyethylene, low density		1.51	
Polyhalite	$K_2Ca_2Mg(SO_4)_4 \cdot 2H_2O$	1.548	
Polypropylene, isotactic		1.49	
Polystyrene		1.59-1.60	
Polystyrene latex		1.59	
Polystyrene-butadiene		1.52-1.59	540/589
Polysulfone resin		1.633	
Polyvinyl alcohol (PVA)		1.51	
Polyvinylchloride (PVC)		1.52-1.55	
Potassium acid oxalate	$KHC_2O_4$	1.382	
Potassium acid oxalate-oxalic acid	$KHC_2O_4 \cdot H_2C_2O_4 \cdot 2H_2O$	1.56	
Potassium antimony tartrate	$KSbC_4H_4O_7 \cdot 1/2H_2O$	1.620	
Potassium bromide	KBr	1.572	486
Potassium bromide	KBr	1.559	589
Potassium bromide	KBr	1.556	643
Potassium bromide	KBr	1.552	706
Potassium carbonate	$K_2CO_3$	1.531	
Potassium carbonate	$K_2CO_3 \cdot 2H_2O$	1.380	
Potassium carbonate	$2K_2CO_3 \cdot 3H_2O$	1.380	
Potassium chlorate	$KClO_3$	1.409	
Potassium chloride	KCl	1.500	467
Potassium chloride	KCl	1.488	627
Potassium chloride	KCl	1.484	768
Potassium chromate	$K_2CrO_4$	1.74	
Potassium dichromate	$K_2Cr_2O_7$	1.738	
Potassium disilicate	$K_2Si_2O_5$	1.480-1.502	
Potassium fluoride	KF	1.363	
Potassium hydrocarbonate	$KHCO_3$	1.482	
Potassium iodide	KI	1.718	546
Potassium iodide	KI	1.677	589
Potassium iodide	KI	1.649	768
Potassium iron sulfate	$KFe(SO_4)_3 \cdot 12H_2O$	1.452	
Potassium iron sulfate	$K_2SO_4 \cdot FeSO_4 \cdot 6H_2O$	1.476	
Potassium metaborate		1.45	
Potassium metasilicate	$K_2SiO_3$	1.502-1.528	
Potassium oxalate	$K_2C_2O_4 \cdot H_2O$	1.440	
Potassium perchlorate	$KClO_4$	1.471	
Potassium permanganate	$KMnO_4$	1.59	
Potassium phosphate		1.50	
Potassium tetrasilicate	$K_2Si_4O_9 \cdot H_2O$	1.495-1.535	
Potassium thiocyanate	KNCS	1.66	

Prase		1.54-1.553		
Praseodymium sulfate	$\text{Pr}_2(\text{SO}_4)_3 \cdot 8\text{H}_2\text{O}$	1.54		
Prasiolite		1.54-1.553		
Prehnite		1.61-1.64		
Pyrochroite	$\text{Mn}(\text{OH})_2$	1.723		
Pyrope		1.746		
Quartz	$\text{SiO}_2$	1.54-1.55		589/768
Quartz	a- $\text{SiO}_2$	1.45-1.47		
Quartz	c- $\text{SiO}_2$	1.48		
Quartz (natural $\text{SiO}_2$ )	$\text{SiO}_2$	1.55		
Quartz (purple)		1.544-1.553		
Quartz (white, colorless)		1.544-1.553		
Quartz (crystal)	$\text{SiO}_2$	1.556		458
Quartz (crystal)	$\text{SiO}_2$	1.552		515
Quartz (crystal)	$\text{SiO}_2$	1.547		633
Quartz (crystal)	$\text{SiO}_2$	1.543		755
Quartz (yellow, golden)		1.544-1.553		
Rhenium (single crystal E $\perp$ c)	Re	3.570		443
Rhenium (single crystal E $\perp$ c)	Re	3.740		590
Rhenium (single crystal E $\perp$ c)	Re	3.380		729
Rhenium (single crystal E $\perp$ c)	Re	3.230		886
Rhenium (single crystal E $\parallel$ c)	Re	2.890		443
Rhenium (single crystal E $\parallel$ c)	Re	3.030		590
Rhenium (single crystal E $\parallel$ c)	Re	2.700		729
Rhenium (single crystal E $\parallel$ c)	Re	2.440		886
Rhodium	Rh	1.800		459
Rhodium	Rh	2.050		590
Rhodium	Rh	2.420		729
Rhodium	Rh	3.010		886
Rhodolite		1.76		
Rhodonite	$\text{MnSiO}_3$	1.733		
Rinneite	$3\text{KCl} \cdot \text{NaCl} \cdot \text{FeCl}_2$	1.589		
Rock crystal		1.544-1.553		
Rock Salt	$\text{NaCl}$	1.544/1.541		589/640
Rubber		1.591		
Rubidium bromide	$\text{RbBr}$	1.56		488
Rubidium bromide	$\text{RbBr}$	1.55		590
Rubidium bromide	$\text{RbBr}$	1.55		633
Rubidium chloride	$\text{RbCl}$	1.5		488
Rubidium chloride	$\text{RbCl}$	1.49		590
Rubidium chloride	$\text{RbCl}$	1.49		633
Rubidium fluoride	$\text{RbF}$	1.396		
Rubidium iodide	$\text{RbI}$	1.67		488
Rubidium iodide	$\text{RbI}$	1.65		590
Rubidium iodide	$\text{RbI}$	1.64		633
Ruby	$\text{Al}_2\text{O}_3$	1.76-1.77		589/668
Ruthenium (single crystal E $\perp$ c)	Ru	2.990		443
Ruthenium (single crystal E $\perp$ c)	Ru	4.210		590
Ruthenium (single crystal E $\perp$ c)	Ru	5.120		729

Ruthenium (single crystal Elc)	Ru	4.860		886
Ruthenium (single crystal Elc)	Ru	2.540		443
Ruthenium (single crystal Elc)	Ru	3.690		590
Ruthenium (single crystal Elc)	Ru	4.420		729
Ruthenium (single crystal Elc)	Ru	4.020		886
Rutile	TiO <sub>2</sub>	2.56-2.90		589/691
Sanidine		1.522		
Sapphire	Al <sub>2</sub> O <sub>3</sub>	1.774		458
Sapphire	Al <sub>2</sub> O <sub>3</sub>	1.764		590
Sapphire	Al <sub>2</sub> O <sub>3</sub>	1.757		755
Sapphire	Al <sub>2</sub> O <sub>3</sub>	1.752		980
Scapolite		1.54-1.56		
Scapolite (yellow)		1.555		
Scorodite	FeAsO <sub>4</sub> ·2H <sub>2</sub> O	1.765		
Selenium oxide	SeO <sub>2</sub>	1.76		
Serpentine	Mg <sub>3</sub> Si <sub>2</sub> O <sub>5</sub> (OH) <sub>4</sub>	1.53-1.57		
SF10 Schott glass		1.748		480
SF10 Schott glass		1.734		546
SF10 Schott glass		1.728		589
SF10 Schott glass		1.722		644
SF10 Schott glass		1.717		707
SF10 Schott glass		1.709		852
Shell		1.53-1.686		
Siderite	FeCO <sub>3</sub>	1.875		
Siderotil	FeSO <sub>4</sub> ·5H <sub>2</sub> O	1.526		
Silica	SiO <sub>2</sub>	1.466		450
Silica	SiO <sub>2</sub>	1.458		600
Silica	SiO <sub>2</sub>	1.454		750
Silica	SiO <sub>2</sub>	1.452		900
Silica (fused)	SiO <sub>n</sub>	1.46		589/644
Silicon	Si	4.2	0.1	
Silicon carbide	SiC	2.64-2.65		589/616
Silicon nitride	Si <sub>3</sub> N <sub>4</sub>	1.97		
Sillimanite		1.658-1.678		
Silver	Ag	0.230		413
Silver	Ag	0.270		620
Silver	Ag	0.2	19.5	630
Silver	Ag	0.270		827
Silver bromide	AgBr	2.33		476
Silver bromide	AgBr	2.313		496
Silver bromide	AgBr	2.27		550
Silver bromide	AgBr	2.25		600
Silver bromide	AgBr	2.24		650
Silver bromide	AgBr	2.205		781
Silver chloride	AgCl	2.097		500
Silver nitrate	AgNO <sub>3</sub>	1.729		
Silver sulfate	Ag <sub>2</sub> SO <sub>4</sub>	1.758		
Smaragdite		1.608-1.63		
Soda niter	NaNO <sub>3</sub>	1.587		

Sodalite		1.483		
Sodium	Na	4.22		
Sodium acetate	$\text{NaC}_2\text{H}_3\text{O}_2$	1.464		
Sodium acid tartrate	$\text{NaHC}_4\text{H}_4\text{O}_6$	1.53		
Sodium aluminum sulfate	$\text{NaAl}(\text{SO}_4)_2 \cdot 12\text{H}_2\text{O}$	1.439		
Sodium borohydride	$\text{NaBH}_4$	1.542		
Sodium bromide	$\text{NaBr}$	1.64		
Sodium chloride	$\text{NaCl}$	1.541		640
Sodium chloride	$\text{NaCl}$	1.537		760
Sodium chloride	$\text{NaCl}$	1.534		903
Sodium cyanide	$\text{NaCN}$	1.452		
Sodium dithionate	$\text{Na}_2\text{S}_2\text{O}_4 \cdot 2\text{H}_2\text{O}$	1.482		
Sodium fluoride	$\text{NaF}$	1.328		486
Sodium fluoride	$\text{NaF}$	1.325		589
Sodium fluoride	$\text{NaF}$	1.324		707
Sodium fluoride	$\text{NaF}$	1.322		912
Sodium fluosilicate	$\text{Na}_2\text{SiF}_6$	1.312		
Sodium hypophosphate	$\text{Na}_4\text{P}_2\text{O}_6 \cdot 10\text{H}_2\text{O}$	1.477		
Sodium iodide	$\text{NaI}$	1.774		
Sodium iron sulfate	$3\text{Na}_2\text{SO}_4 \cdot \text{Fe}_2(\text{SO}_4)_3 \cdot 6\text{H}_2\text{O}$	1.558		
Sodium metaaluminate	$\text{NaAlO}_2$	1.566		
Sodium orthophosphate	$\text{Na}_3\text{PO}_4 \cdot 12\text{H}_2\text{O}$	1.446		
Sodium perchlorate	$\text{NaClO}_4$	1.460		
Sodium sulfate (anhydrous)	$\text{Na}_2\text{SO}_4$	1.485		
Sodium sulfite	$\text{Na}_2\text{SO}_3$	1.564		
Sodium tetraborate	$\text{Na}_2\text{B}_4\text{O}_7$	1.50		
Sodium thioarsenate	$\text{Na}_3\text{AsS}_4 \cdot 8\text{H}_2\text{O}$	1.680		
Sodium uranyl acetate	$(\text{C}_2\text{H}_3\text{O}_2)_3\text{NaUO}_2$	1.501		
Soot		1.7	0.7	
Spessartite		1.810		
Spinel	$\text{MgAl}_2\text{O}_4$	1.71-1.72		589/656
Spodumene		1.65-1.68		
Starch		1.530		
Stealite		1.539-1.589		
Stichtite		1.52-1.55		
Stolzite	$\text{PbWO}_4$	2.269		
Strontium carbonate	$\text{SrCO}_3$	1.61		
Strontium chloride	$\text{SrCl}_2 \cdot 2\text{H}_2\text{O}$	1.594		
Strontium fluoride	$\text{SrF}_2$	1.442		
Strontium fluoride	$\text{SrF}_2$	1.439		550
Strontium hydrosulfide	$\text{Sr}(\text{HS})_3$	2.107		
Strontium nitrite	$\text{Sr}(\text{NO}_2)_2 \cdot \text{H}_2\text{O}$	1.588		
Strontium oxide	$\text{SrO}$	1.810		
Styrene/acrylonitrile copolymer		1.57		
Styrene/maleic anhydride copolymer		1.564		
Suet (bovines fresh fatty tissue)		1.448-1.460		
Sugar (sucrose)		1.54		



Sugar of lead	$\text{Pb}(\text{C}_2\text{H}_3\text{O}_2)_2 \cdot 3\text{H}_2\text{O}$	1.567		
Sulfur	$\text{S}_6$	1.957		
Sulfur	S	1.96-2.25		
Sulfur dichloride	$\text{SCl}_2$	1.557		
Sulfur monochloride	$\text{S}_2\text{Cl}_2$	1.666		
Sylvite	KCl	1.490		
Synthetic emerald(flux)		1.561-1.564		
Synthetic emerald(hydro)		1.568-1.573		
Szmikite	$\text{MnSO}_4 \cdot \text{H}_2\text{O}$	1.562		
Talc	$3\text{MgO} \cdot 4\text{SiO}_2 \cdot \text{H}_2\text{O}$	1.54-1.60		
Tantalum	Ta	2.850		443
Tantalum	Ta	2.100		590
Tantalum	Ta	1.240		729
Tantalum	Ta	1.040		887
Tapiolite	$\text{Fe}(\text{TaO}_3)_2$	2.27		
Tanzanite (purple/blue)		1.69-1.70		
Tellurium	Te	1.002		
Tenorite	$\text{CuO}$	2.63		
Thallium bromide	TlBr	2.652		438
Thallium bromide	TlBr	2.418		589
Thallium bromide	TlBr	2.35		750
Thallium bromide-Thallium chloride (KRS-6 Crystal)	TlBr-TlCl	2.329		600
Thallium bromide-Thallium chloride (KRS-6 Crystal)	TlBr-TlCl	2.298		700
Thallium bromide-Thallium chloride (KRS-6 Crystal)	TlBr-TlCl	2.266		800
Thallium bromide-Thallium chloride (KRS-6 Crystal)	TlBr-TlCl	2.251		900
Thallium bromide-Thallium iodide (KRS-5 Crystal)	TlBr-TlI	2.681		540
Thallium chloride	TlCl	2.4		436
Thallium chloride	TlCl	2.247		589
Thallium chloride	TlCl	2.198		750
Thermonatrite	$\text{Na}_2\text{CO}_3 \cdot \text{H}_2\text{O}$	1.506		
Thomsonite		1.53		
Tiger eye		1.544-1.553		
Tiona (RCL-472)		2.7		
Titanium dioxide	$\text{TiO}_2$	2.6-2.9		
Titanium tetrachloride	$\text{TiCl}_4$	1.61		
Titanium (polycrystalline)	Ti	2.540		729
Titanium (polycrystalline)	Ti	1.680		443
Titanium (polycrystalline)	Ti	2.010		590
Titanium (polycrystalline)	Ti	3.170		886
Topaz	$\text{Al}_2\text{SiO}_5(\text{OH},\text{F})_2$	1.61-1.64		
Topaz (white, colorless)	$\text{Al}_2\text{SiO}_5(\text{OH},\text{F})_2$	1.619-1.627		
Topaz (blue)	$\text{Al}_2\text{SiO}_5(\text{OH},\text{F})_2$	1.61		
Topaz (pink, yellow)	$\text{Al}_2\text{SiO}_5(\text{OH},\text{F})_2$	1.62		
Topaz (white)	$\text{Al}_2\text{SiO}_5(\text{OH},\text{F})_2$	1.63		

Tourmaline		1.616-1.652		
Tremolite		1.6-1.62		
Tridymite	SiO	1.469		
Tridymite	SiO <sub>n</sub>	1.47-1.48		
Tugtupite		1.496-1.5		
Tungsten	W	3.310		443
Tungsten	W	2.76	1.0	578
Tungsten	W	3.540		590
Tungsten	W	3.840		729
Tungsten	W	3.290		886
Turquoise		1.61-1.65		
Turquoise (gem)		1.61		
Ulexite		1.49-1.52		
Urea formaldehyde		1.43		
UV Grade fused silica		1.464		480
UV Grade fused silica		1.460		546
UV Grade fused silica		1.457		644
UV Grade fused silica		1.455		707
UV Grade fused silica		1.452		852
Vanadium	V	1.610		443
Vanadium	V	2.310		590
Vanadium	V	2.520		729
Vanadium	V	2.480		886
Vanadium pentaoxide	V <sub>2</sub> O <sub>5</sub>	1.46		
Various glasses	SiO <sub>n</sub>	1.49-1.89		436-656
Variscite		1.55-1.59		
Vaterite	CaCO <sub>3</sub>	1.55-1.65		
Verdigris	Cu(C <sub>2</sub> H <sub>3</sub> O <sub>2</sub> ) <sub>2</sub> ·H <sub>2</sub> O	1.545		
Vivianite		1.58-1.627		
Wardite		1.59-1.599		
Washing soda	Na <sub>2</sub> CO <sub>3</sub> ·10H <sub>2</sub> O	1.405		
Witherite	BaCO <sub>3</sub>	1.53-1.68		
Wollastonite	CaSiO <sub>3</sub>	1.62-1.65		
Wurtzite	ZnS	2.35		
Yeast		1.49-1.53		
Yellow prussiate of soda	Na <sub>4</sub> Fe(CN) <sub>6</sub> ·10H <sub>2</sub> O	1.519		
Yttrium sulfate	Y <sub>2</sub> (SO <sub>4</sub> ) <sub>3</sub> ·8H <sub>2</sub> O	1.543		
Zinc acetate	Zn(C <sub>2</sub> H <sub>3</sub> O <sub>2</sub> ) <sub>2</sub> ·2H <sub>2</sub> O	1.494		
Zinc borate (ZB-467)		1.59		
Zinc bromate	Zn(BrO <sub>3</sub> ) <sub>2</sub> ·6H <sub>2</sub> O	1.545		
Zinc chloride	ZnCl <sub>2</sub>	1.681		
Zinc oxide	ZnO	2.029		
Zinc selenide	ZnSe	2.599		620
Zinc selenide	ZnSe	2.542		740
Zinc selenide	ZnSe	2.503		900
Zinc sulfide	ZnS	2.449		467
Zinc sulfide	ZnS	2.347		643
Zinc sulfide	ZnS	2.317		780
Zinc sulfide	ZnS	2.302		894

Zinc sulfide	ZnS	2.297		940
Zincite		2.008		
Zircon	ZrSiO <sub>4</sub>	1.92-2.02		
Zircon (colorless) (high)		1.925-1.984		
Zircon (colorless) (medium)		1.875-1.905		
Zirconium nitrate	Zr(NO <sub>3</sub> ) <sub>4</sub> ·5H <sub>2</sub> O	1.60		
Zirconium silicate		1.97		
Zirconium (polycrystalline)	Zr	1.400		443
Zirconium (polycrystalline)	Zr	1.990		590
Zirconium (polycrystalline)	Zr	2.680		729
Zirconium (polycrystalline)	Zr	3.100		886
Zoisite		1.691-1.704		

Note:

- The wavelength is 589 nm for the blanks in the fifth column. The values are either unknown or zero for the blanks in the fourth column.
- The content of this appendix is adopted from "*Some Physical Constants Used in Particle Characterization*" by Particle Characterization, Beckman Coulter, Inc., Miami, by permission.

## AUTHOR INDEX

---

The unbracketed numbers give the reference location (page number) in the text. The numbers in brackets give the chapter number followed by the number of the reference in that chapter.

---

### A

Aberle, L. B., 279 (5.98)  
 Abeynayake, C., 258 (5.57)  
 Abramson, H. A., 307 (6.34)  
 Abramson, L. R., 216 (4.44)  
 Accomazzo, M. A., 217 (4.45)  
 Adamson, A. W., 25 (1.43)  
 Agarwal, J. K., 191 (4.13)  
 Agrawal, Y. C., 153 (3.35)  
 Aharonson, E. F., 97 (2.98)  
 Ahn, K. H., 217 (4.48)  
 Ahrens, J., 277 (5.96)  
 Ahseng, C., 159 (3.46)  
 Akers, R. J., 209 (4.33)  
 Alberty, R. A., 298 (6.25)  
 Al-Chalabi, S. A. M., 74 (2.75),  
 173(3.84)  
 Alderliesten, M., 28 (1.50), 37  
 (1.54)  
 Alexander, K., 80 (2.76)  
 Alexander, N. E., 184 (4.5)  
 Alien, T., 12 (1.12), 7 (1.2)  
 Amal, R., 174 (3.86)  
 Anderson, J. L., 297 (6.9), 297  
 (6.19)  
 Anisimov, M., 183 (4.4)  
 Annapragada, A., 98 (2.100)  
 Ansari, R. R., 272 (5.83), 274  
 (5.89)  
 Aragon, S. R., 260 (5.62)  
 Arbouille, D., 167 (3.63)  
 Arsenin, V. Y., 152 (3.26)  
 Artaxo, P., 182 (4.1)  
 Asakura, T., 100 (2.107)  
 Asano, S., 65 (2.61)

Auweter, H., 273 (5.85)

### B

Bachalo, W. D., 60 (2.44), 60  
 (2.47)  
 Bacon, C., 99 (2.106)  
 Baert, L., 240 (5.22), 269 (5.77)  
 Baker, J. P., 141 (3.16)  
 Balgi, G. V., 60, 100 (2.51)  
 Baloch, K. M., 60 (2.22)  
 Barreiros, F. M., 169 (3.68)  
 Barthel, H., 175 (3.88)  
 Bassini, A., 98 (2.101), 154 (3.36)  
 Bauckhage, K., 103 (2.114), 103  
 (2.116)  
 Bauckhage, K., 60 (2.45)  
 Baudet, G., 172 (3.78)  
 Bayvel, L. P., 153 (3.31)  
 Bazzi, G., 98 (2.100)  
 Beenakker, C. W. J., 273 (5.84)  
 Beniams, H., 307 (6.36)  
 Benneyworth, P. R., 338 (6.66)  
 Berg, J. C., 265 (5.70)  
 Berglund, R. N., 208 (4.30)  
 Berne, B. J., 60, 224, 259 (2.30)  
 Berner, A., 21 (1.31)  
 Bernhardt, C., 7 (1.3)  
 Berry, G. C., 93 (2.91)  
 Bertero, M., 237 (5.18), 252 (5.36),  
 252 (5.37)  
 Bevington, P. R., 250 (5.27)  
 Bischof, O., 167 (3.64)  
 Bizi, M., 172 (3.78)  
 Blees, M. H., 26 (1.47)  
 Bly, D. D., 19 (1.23)

Boatner, L. A., 14 (1.16)  
 Boccacci, P., 237 (5.18), 252  
     (5.36), 252 (5.37)  
 Boerner, M., 26 (1.45)  
 Bogaert, H., 269 (5.77)  
 Bohren, C. F., 60, 69 (2.12), 60,  
     224 (2.28), 69 (2.65)  
 Bott, S. E., 119 (3.4), 119 (3.5),  
     119(3.6), 128 (3.8), 131 (3.9),  
     257 (5.51)  
 Bottlinger, M., 171 (3.76), 212  
     (4.40), 212 (4.41)  
 Bowen, P., 171 (3.74)  
 Boxman, A., 154 (3.41)  
 Brandolin, A., 60 (2.20)  
 Bremer, L. G. B., 275 (5.94)  
 Brenci, M., 275 (5.90)  
 Brock, J. R., 81 (2.84)  
 Brown, D. J., 80 (2.76), 136 (3.14)  
 Brown, R. G. W., 234, 273 (5.16),  
     273 (5.86)  
 Brunauer, S., 24 (1.41)  
 Bryant, G., 257, 258 (5.54), 258  
     (5.57)  
 Buchhave, P., 60 (2.46), 103  
     (2.112)  
 Buck, W., 229 (5.9)  
 Burchard, W., 259 (5.58)  
 Burkholz, A., 166 (3.62)  
 Burnett, J. G., 273 (5.86)  
 Burns, N. L., 311 (6.44), 313, 314  
     (6.46)  
 Bushell, G. C., 174 (3.86)  
 Buttner, H., 208 (4.29), 210 (4.34)

## C

Cai, X.-S., 98 (2.103)  
 Candel, S. M., 153 (3.30)  
 Cannon, D. W., 23 (1.38), 24 (1.39)  
 Cao, J., 80 (2.76), 148 (3.24)  
 Cerni, T. A., 98 (2.105)  
 Cerussi, A. E., 100 (2.109)

Chae, S. K., 211 (4.37)  
 Chaikin, P. M., 281 (5.101)  
 Chein, H., 208 (4.31)  
 Chen, S. B., 297 (6.16)  
 Chernyshev, A. V., 60, 224 (2.27)  
 Chigier, N. A., 159(3.46)  
 Chin, J. H., 153 (3.27)  
 Choi, M. K., 81 (2.84)  
 Chou, C. C. K., 208 (4.31)  
 Chow, K., 273 (5.86)  
 Chu, B., 60, 87, 224, 225, 242, 259  
     (2.38), 224 (5.6), 227 (5.8), 229  
     (5.9), 229 (5.10), 239 (5.20), 250  
     (5.28), 252 (5.34), 252 (5.41),  
     254 (5.47), 259, 269 (5.61), 261  
     (5.63), 269 (5.74), 269 (5.75)  
 Ciach, T., 203 (4.22)  
 Clauwaert, 1,233 (5.14), 272  
     (5.82)  
 Clifton, B. J., 338 (6.66)  
 Coghill, P. J., 23 (1.37)  
 Cohen Stuart, M. A., 195, 196  
     (4.17)  
 Collings, P., 60 (2.25)  
 Conklin, W. B., 134 (3.11)  
 Cooper, S. J., 97 (2.96)  
 Corbin, F., 63 (2.56)  
 Cornillault, J., 165 (3.61)  
 Coulter, W. H., 12 (1.13)  
 Cowley, J., 170 (3.72)  
 Cummins, H. Z., 223 (5.3)  
 Cuzzi, J. N., 173 (3.85)

## D

Dahneke, B. E., 60 (2.53), 60 (2.54)  
 Dapkunas, S., 171, 172 (3.80)  
 Davenport Jr., W. B., 330 (6.61)  
 De Boer, G. B. J., 135 (3.13)  
 de Groen, P., 252 (5.38), 257, 258  
     (5.52)

De Jaeger, N., 169 (3.69), 263 (5.68), 267 (5.72), 272 (5.81), 272 (5.82)  
 DeJuan, L., 21 (1.32)  
 DeKeizer, A., 297 (6.13)  
 de Kruif, C. G., 273 (5.88)  
 DeLaMora, J., 21 (1.32)  
 deSmet, J. G. A. E., 154 (3.42), 175, 176 (3.92)  
 De Vos, C., 258 (5.56)  
 deWeerd, C., 135 (3.13)  
 De Wispelaere, W., 169 (3.69), 272 (5.82)  
 Dean, P. N., 60, 224 (2.26)  
 Debye, P., 58, 66 (2.6), 306 (6.31)  
 DeFreez, R., 185 (4.9)  
 Deggelmann, M., 296 (6.7)  
 Delaye, M., 252 (5.40)  
 Delly, J. G., 16 (1.20)  
 Demeyere, H., 263 (5.68), 272 (5.82)  
 Den Tandt, Y., 169 (3.69)  
 Deriemaeker, L., 157 (3.43), 252 (5.38), 257, 258 (5.52), 258 (5.56), 272 (5.82), 275 (5.94), 314 (6.48)  
 Dhadwal, H. S., 227 (5.8), 239 (5.20), 250 (5.28), 252 (5.43), 274 (5.89)  
 Dhont, J. K. G., 273 (5.88)  
 Dick, W. D., 175 (3.90)  
 Dimas, N., 251 (5.30)  
 DiNapoli, A., 269 (5.74)  
 Dobbins, R. A., 99 (2.104)  
 Dogariu, A., 100 (2.107)  
 Doicu, A., 81 (2.81), 103 (2.113), 103 (2.114)  
 Doroshkin, A. A., 60, 224 (2.27)  
 Draine, B. T., 81 (2.85)  
 Drescher, S., 167 (3.64)  
 Drewel, M., 277 (5.96), 314 (6.51)  
 Dubinin, M. M., 25 (1.42)

Dukhin, A. S., 22 (1.34), 23 (1.35)  
 Dunn, R. C., 15 (1.18)  
 Durian, D. J., 281 (5.102)  
 Durst, F., 60 (2.43), 305 (6.29)  
 Dyson, R. D., 249 (5.25)

## E

Ebert, F., 103 (2.113), 175 (3.88), 208 (4.29), 210 (4.34)  
 Egelhaaf, S. U., 232 (5.13)  
 Eichler, T., 21 (1.32)  
 Einstein, A., 58 (2.7)  
 Elings, U. B., 191 (4.15)  
 Emmett, P. M., 24 (1.41)  
 Emoto, K., 310 (6.41)  
 Endoh, S., 170, 171 (3.75)  
 Eppmann, P., 60 (2.50)  
 Esposito, E., 153 (3.30)  
 Ettmuller, J., 100 (2.108)  
 Eustachi, W., 100 (2.108)  
 Evenstad, J., 103 (2.117)

## F

Facq, L., 307 (6.38)  
 Fair, M. C., 297 (6.19)  
 Fanderlik, I., 161 (3.50)  
 Fantini, S., M. A., 100 (2.109)  
 Farhadpour, F. A., 158 (3.44)  
 Felton, P. G., 136 (3.14), 159 (3.46)  
 Ferreira, P. J., 169 (3.68)  
 Ferri, F., 98 (2.101), 154 (3.36)  
 Figueiredo, M. M., 169 (3.68)  
 Finsy, R., 157 (3.43), 224 (5.5), 252 (5.38), 257, 258 (5.52), 258 (5.56), 263 (5.67), 263 (5.68), 267 (5.72), 272 (5.81), 272 (5.82), 275 (5.94), 314 (6.48)  
 Fisher, M. A., 184 (4.5)  
 Fishkin, J., 100 (2.109)  
 Flank, W. H., 171 (3.73)  
 Flatau, P. J., 81 (2.85)  
 Fleeer, G. J., 195, 196 (4.17)

Flögel, H. H., 60 (2.45)  
 Flygare, W. H., 299, 332, 335  
     (6.26)  
 Ford, J. R., 250 (5.28), 261 (5.63)  
 Ford, N., 229, 234 (5.12)  
 Fraunhofer, J., 74 (2.71)  
 Friehmelt, R., 208 (4.29)  
 Fujime, S., 259 (5.59), 259 (5.60)  
 Fukino, Y., 235 (5.17)  
 Furusawa, K., 26 (1.46), 308, 313,  
     323, 334 (6.40)

## G

Gang, Z., 98 (2.103)  
 Garcia-Rubio, L. H., 60, 98 (2.20),  
     99 (2.106)  
 Gebhart, J., 211 (4.39), 217 (4.47)  
 Gelade, E., 157 (3.43), 169 (3.69),  
     257, 258 (5.52), 272 (5.81), 272  
     (5.82), 275 (5.94)  
 Gerber, M., 60 (2.16), 96 (2.95)  
 Geurts, J. M., 26 (1.47)  
 Giddings, J. C., 20 (1.27), 21  
     (1.28), 21 (1.29)  
 Giglio, M., 154 (3.36)  
 Giles, C. L., 69 (2.64)  
 Gillioen, P., 272 (5.82)  
 Gimsa, T., 60 (2.50)  
 Girvin, K. L., 185 (4.9)  
 Glatter, O., 143, 163 (3.18), 161  
     (3.53), 252 (5.33)  
 Goetz, P. J., 22 (1.34), 23 (1.35)  
 Goldlin, A. A., 256 (5.50)  
 Goossens, H. W. J., 135 (3.13)  
 Gouesbet, G., 63 (2.56), 63 (2.57),  
     63 (2.58), 63 (2.59)  
 Gradon, L., 203 (4.22)  
 Graf, C., 296 (6.7)  
 Grant, D. C., 217 (4.45)  
 Gregg, S.J., 24 (1.40)  
 Gréhan, G., 63 (2.56), 63 (2.57), 63  
     (2.59), 103 (2.115)

Grell, E., 256 (5.49)  
 Grosberg, A. Y., 229 (5.10)  
 Grosse, C., 297 (6.8)  
 Gucker, F. T. Jr., 182 (4.3)  
 Gulari, Er., 98 (2.100), 252(5.34)  
 Gulari, Es., 98 (2.100), 252 (5.34)  
 Gull, S. F., 253 (5.44)  
 Gustavson, R. G., 307 (6.36)

## H

Haas, D. D., 60 (2.41), 299, 309,  
     336 (6.28), 308 (6.39)  
 Haestier, A., 272 (5.82)  
 Hagenbuchle, M., 296 (6.7)  
 Hagenow, A., 100 (2.108)  
 Hall, R. S., 265 (5.69)  
 Hamilton, J. D., 307 (6.37)  
 Hammond, D. C., 159 (3.45)  
 Hanson, R. J., 204 (4.25), 249  
     (5.25)  
 Hanus, L. H., 250 (5.29)  
 Hanusch, T., 203 (4.20)  
 Hareland, G. A., 172 (3.79)  
 Harris, J. M., 310 (6.41), 313, 314  
     (6.46)  
 Harrison, C. F., 188, 189, 193  
     (4.10)  
 Hart, W.H., 119 (3.4), 119(3.5),  
     119 (3.6), 128 (3.8), 131 (3.9)  
 Harvill, T. L., 83 (2.87), 164 (3.60)  
 Haugen, P., 103 (2.115)  
 HavardT., 229, 234 (5.12)  
 Hawkins, A. E., 46 (1.60)  
 Hayakawa, O., 60 (2.52), 170  
     (3.70), 170 (3.71)  
 Heffels, C. M. G., 74 (2.72), 169  
     (3.67), 176(3.91), 175, 176  
     (3.92), 176(3.93)  
 Heidenreich, S., 208 (4.29), 210  
     (4.34)  
 Heitzmann, D., 169 (3.67), 176  
     (3.91)

Heller, W., 98 (2.99)  
 Henry, D. C., 295 (6.4)  
 Hérard, C., 171 (3.74)  
 Herdan, G., 29 (1.51)  
 Hess, C. F., 60, 224 (2.29)  
 Heuer, M., 154 (3.40)  
 Heybroek, M., 183 (4.4)  
 Heywood, H., 7 (1.8)  
 Hideaki, I., 172 (3.81)  
 Hildebrand, H., 267 (5.73)  
 Hioki, R., 307 (6.33)  
 Hirleman, E. D., 60 (2.48), 83  
     (2.86), 148 (3.25), 154 (3.32),  
     163 (3.55), 163 (3.56), 163  
     (3.57), 169 (3.65), 176 (3.91)  
 Hirst, E., 174 (3.87)  
 Hitchen, C. J., 162 (3.54)  
 Hjerten, S., 314 (6.50)  
 Ho, K., 60 (2.52)  
 Hoff, C., 60 (2.15), 96 (2.94)  
 Holve, D. J., 83 (2.87), 164 (3.60),  
     164, 165 (3.58), 203 (4.23)  
 Hong, C., 98 (2.102)  
 Hoog, J. H., 83 (2.87), 164 (3.60)  
 Horn, D. F., 60 (2.55), 257 (5.55),  
     273 (5.85), 273 (5.87), 275  
     (5.91), 275 (5.92)  
 Houtmeyers, E., 169 (3.69)  
 Hubner, T., 170, 172 (3.82)  
 Huchins, D. K., 60 (2.53), 60 (2.54)  
 Huffman, D., 60, 69 (2.12)  
 Humphy-Baker, R., 171 (3.74)  
 Hunter, R., 294 (6.1), 294 (6.2)

**I**

Igushi, T., 115 (3.2)  
 Ikeda, C., 170, 171, 172 (3.75)  
 Ikegami, A., 259 (5.60)  
 Imae, T., 322 (6.58)  
 Inaba, K., 137 (3.15), 171 (3.77)  
 Inoue, S., 15 (1.19)  
 Irniger, V., 60 (2.23)

Isenberg, I., 249 (5.25)  
 Ishii, K., 281 (5.103)  
 Iwai, T., 281 (5.103)  
 Iwata, H., 170, 171, 172 (3.75)

**J**

Jacobasch, H.-J., 26 (1.45)  
 Jaenicke, R., 203 (4.20)  
 Jakeman, E., 239 (5.21)  
 Jennings, B. R., 60 (2.21), 72  
     (2.69), 72 (2.70)  
 Jizmagian, G. S., 99 (2.104)  
 Johnson, C. S. Jr., 265 (5.69)  
 Johnston, R. G., 60, 224 (2.28)  
 Jones, A. R., 74 (2.75), 169 (3.66),  
     173 (3.84)  
 Jones, R., 164 (3.59), 234 (5.15)  
 Joosten, J., 157 (3.43), 257, 258  
     (5.52), 275 (5.94)

**K**

Kaiser, T., 69 (2.66)  
 Kameyama, K., 311 (6.45), 322  
     (6.57)  
 Karasikov, N., 60 (2.17), 97 (2.98)  
 Kasper, G., 217 (4.46)  
 Katz, S., 184 (4.5)  
 Kaufman, S. L., 183 (4.4)  
 Kaye, B. H., 6 (1.1)  
 Kaye, P., 174 (3.87)  
 Keh, H. J., 297 (6.16)  
 Kellner, G., 143, 163 (3.18)  
 Kelly, J., 171, 172 (3.80)  
 Kerker, M., 60, 65, 66 (2.9), 69  
     (2.64)  
 Kern, J., 169 (3.69)  
 Khintchine, A., 88 (2.88)  
 Kidai, M., 311 (6.45)  
 Kim, S., 297 (6.17)  
 Kimura, Y., 60 (2.52)  
 Kinney, P. D., 97 (2.97)  
 Kirkland, J. J., 19 (1.23), 19 (1.24)



Klein, J. P., 60 (2.15), 96 (2.94)  
 Klingler, J. F., 60 (2.55)  
 Knable, N., 223 (5.3)  
 Knapp, J. Z., 216 (4.44)  
 Knight, J., 153 (3.31)  
 Knollenberg, R. G., 185, 191, 194,  
 195 (4.6), 185 (4.7), 185, 197,  
 208 (4.8), 190 (4.11), 191 (4.12),  
 198 (4.18), 210 (4.35)  
 Knollenberg, S. C., 190 (4.11)  
 Knox, R. J., 313, 314 (6.46), 323  
 (6.59)  
 Kohler, M., 60, 98 (2.20)  
 Köhler, W., 60 (2.24)  
 Kohno, T., 235 (5.17)  
 Komagata, S., 311 (6.43)  
 Komrska, J., 74 (2.73), 74 (2.74)  
 Koo, J. H., 153 (3.28)  
 Koppel, D. E., 249 (5.24)  
 Kornbrekke, R. E., 331 (6.62)  
 Koropchak, J. A., 183 (4.4)  
 Kouzelis, D., 153 (3.30)  
 Krahn, W., 224 (5.4)  
 Kratochvil, P., 60, 90 (2.13)  
 Krause, R., 296 (6.7)  
 Kubota, K., 259 (5.59), 259 (5.60)  
 Kuga, Y., 170, 171, 172 (3.75)  
 Kuo, C., 60, 98 (2.20)  
 Kusters, K. A., 80 (2.78)

## L

Laerum, O. D., 60, 224 (2.26)  
 Lange, H., 37 (1.53)  
 Lawson, C. L., 204 (4.25)  
 Lee, H. S., 211 (4.37)  
 Lehner, D., 143, 163 (3.18)  
 Leipertz, A., 172 (3.82), 229 (5.11)  
 Leith, D., 97 (2.96)  
 Leschonski, K., 40 (1.55), 141  
 (3.17)  
 Leyte, J. C., 26 (1.47)  
 Li, K., 69 (2.67)

Li, X., 159 (3.47)  
 Licinio, P., 252 (5.40)  
 Lieberman, A., 184 (4.5), 192, 193  
 (4.14)  
 Liebman, L. A., 81 (2.84)  
 Lilge, D., 257 (5.55)  
 Lindenthal, G., 205 (4.28)  
 Linder, A. O., 21 (1.31)  
 Lines, R. W., 13 (1.15)  
 Lisse, M. W., 307 (6.35)  
 List, J., 175 (3.89)  
 Liu, B. Y. H., 191 (4.13), 199  
 (4.19), 208 (4.30), 208 (4.32),  
 211 (4.37), 211, 215 (4.36), 217  
 (4.48)  
 Livesey, A. K., 252 (5.40)  
 Loeb, A. L., 296 (6.5)  
 Logiudice, P. J., 170 (3.72)  
 Loizeau, J.-L., 167 (3.63)  
 Lorenz, L. V., 58 (2.4)  
 Lucas, K., 224 (5.4)  
 Luckas, M., 224 (5.4)  
 Lüddecke, E., 257 (5.55)  
 Lyklema, J., 314 (6.52)  
 Lynch, M., 306 (6.30)

## M

Ma, Z., 154 (3.42)  
 MacDonald, I. P., 338 (6.66)  
 Mackowski, D. W., 81 (2.82)  
 Magnusson, L., 183 (4.4)  
 Maheu, B., 63 (2.56), 63 (2.57)  
 Maire, E., 296 (6.7)  
 Malghan, S., 171, 172 (3.80)  
 Maltsev, V. P., 60, 224 (2.27)  
 Marsh, J. F., 338 (6.66)  
 Massoli, P., 69 (2.67)  
 Matsumoto, K., 137 (3.15), 171  
 (3.77)  
 Mazumder, M. K., 306 (6.32)  
 Mazur, P., 273 (5.84)  
 McClements, D. J., 23 (1.36)

McCrone, W. C., 16 (1.20)  
 McMurry, P. H., 175 (3.90)  
 McNeil Watson, R., 252 (5.35)  
 McWhirter, J. G., 252, 254 (5.39)  
 Mees, L., 63 (2.59)  
 Melamed, M. R., 60, 224 (2.26)  
 Melling, A., 305 (6.29)  
 Mencaglia, A., 275 (5.90)  
 Menzel, R., 18 (1.22), 141 (3.17)  
 Merkus, H. G., 154 (3.41), 154  
 (3.42), 167 (3.64), 175, 176  
 (3.92), 275 (5.93)  
 Meyer, W. V., 274 (5.89)  
 Michoel, A., 169 (3.69)  
 Mie, G., 58 (2.5)  
 Mignani, A. G., 275 (5.90)  
 Millen, M., 123 (1.37)  
 Miller, J. R., 27 (1.48), 60 (2.49),  
 315, 316, 317, 339 (6.55), 337  
 (6.64), 337 (6.65), 338 (6.66)  
 Minor, M., 314 (6.52)  
 Mishchenko, M. I., 81 (2.82)  
 Moller, T., 15 (1.17)  
 Mölter, L., 205 (4.28)  
 Monnier, O., 60 (2.15), 96 (2.94)  
 Montague, C. E., 188, 189, 193  
 (4.10)  
 Morrison, F. A., 297 (6.15)  
 Morrison, I. D., 331 (6.62)  
 Mott, S. C., 141 (3.16)  
 Mroczka, J., 153 (3.32)  
 Mühlenweg, H., 148 (3.25), 153  
 (3.33), 169 (3.65), 204 (4.26)  
 Musazzi, S., 154 (3.36)

## N

Nakahira, K., 170 (3.70), 170  
 (3.71)  
 Naqwi, A. A., 103 (2.111), 103  
 (2.117)  
 Nashima T., 26 (1.46)  
 Nelson, R. D., 51 (1.62)

Newman, J., 269 (5.76)  
 Nguyen, T. H., 254 (5.45)  
 Nicoli, D. F., 191 (4.15)  
 Niehüser, R., 278 (5.97), 280 (5.99)  
 Nishi, N., 60 (2.52)  
 Niven, R. W., 60 (2.18)  
 Nyeo, S.-L., 252 (5.41), 254 (5.47)

## O

O'Brian, R. W., 24 (1.39), 296  
 (6.6), 297 (6.10), 297 (6.18)  
 O'Konski, C. T., 182 (4.3)  
 Oh, Y. S., 265 (5.69)  
 Ohbayashi, K., 235 (5.17)  
 Ohshima, H., 23 (1.35), 297 (6.11),  
 297 (6.12)  
 Ohya, H., 170, 171, 172 (3.75)  
 Oja, T., 23 (1.38), 331 (6.62)  
 Oka, K., 308, 313, 323, 334 (6.40),  
 311 (6.45), 322 (6.58)  
 Oliver, C. J., 234 (5.15), 239 (5.21)  
 Olivier, J. P., 134 (3.11)  
 Onofri, F., 103 (2.115)  
 Ooi, S., 60 (2.52)  
 Otani, W., 311 (6.45), 322 (6.58)  
 Otomo, J., 259 (5.60)  
 Overbeck, E., 278 (5.97), 280  
 (5.99)  
 Overbeek, J. Th. G., 296 (6.5), 297  
 (6.13)  
 Ovod, V. L., 194 (4.16)

## P

Paganini, E., 98 (2.101), 154 (3.36)  
 Paine, A. J., 42 (1.58)  
 Palberg, T., 278 (5.97), 280 (5.99),  
 296 (6.7)  
 Palmer, A. T., 170 (3.72)  
 Pasternack, R. F., 60 (2.25)  
 Patterson, H. S., 182 (4.2)  
 Pawar, Y., 297 (6.9)  
 Peacock, S. L., 217 (4.45)

Pecora, R., 60, 224, 259 (2.30), 223  
 (5.2), 260 (5.62)  
 Pedersen, J. S., 72, 91 (2.68), 357  
 Pei, P., 171, 172 (3.80)  
 Pelssers, E. G. M., 195, 196 (4.17)  
 Pennycook, S. J., 14 (1.16)  
 Perelman, A. Ya., 153 (3.29)  
 Perini, U. U., 154 (3.36)  
 Perrin, F., 64 (2.60)  
 Peters, C., 217 (4.47)  
 Petersen, G., 23 (1.38)  
 Phillies, G. D., 237 (5.19), 262  
 (5.65), 276 (5.95)  
 Phillips, B. L., 154 (3.37)  
 Pickard, H. B., 182 (4.3)  
 Pieraccini, M., 275 (5.90)  
 Pike, E. R., 234 (5.15), 237 (5.18),  
 239 (5.21), 252 (5.35), 252  
 (5.36), 252 (5.37), 252, 254  
 (5.39)  
 Pine, D. J., 280 (5.100), 281  
 (5.101), 281 (5.102)  
 Pitts, J. N., Jr., 182 (4.3)  
 Plantz, P. E., 60 (2.42)  
 Ploehn, H. J., 27 (1.48), 250 (5.29),  
 315, 316, 317, 339 (6.55)  
 Plomp, A., 21 (1.30)  
 Podgorski, A., 203 (4.22)  
 Podschus, U., 277 (5.96)  
 Pohl, D. W., 60 (2.23)  
 Pohl, H. A., 317 (6.56)  
 Polke, R., 49 (1.61), 100 (2.108),  
 166 (3.62), 175, 176 (3.93)  
 Pollack, J. B., 173 (3.85)  
 Pottsmith, H. C., 153 (3.35)  
 Prots, V. I., 60, 224 (2.27)  
 Provder, T., 60, 98 (2.20)  
 Provencher, S. W., 252 (5.42), 254  
 (5.46), 257, 258 (5.53)  
 Pruger, B., 60 (2.50)  
 Pui, D. Y. H., 97 (2.97), 208 (4.32)  
 Pusey, P. N., 239 (5.21), 263 (5.66)

**R**

Raasch, 1, 215 (4.43)  
 Radle, M., 100 (2.108), 175, 176  
 (3.93)  
 Raes, F., 21 (1.30)  
 Ramos, I. G. dos, 19 (1.26)  
 Raper, A., 174 (3.86)  
 Rarity, J. G., 273 (5.86)  
 Ratsimba, B., 60 (2.15), 96 (2.94)  
 Reichel, A., 60 (2.16), 96 (2.95)  
 Reischl, G. P., 21 (1.31)  
 Ren, K. F., 63 (2.59)  
 Renksizbulut, M., 159 (3.47)  
 Reuss, A., 297 (6.22)  
 Revillion, A., 19 (1.25)  
 Rheims, J., 103 (2.116)  
 Ribitsch, V., 26 (1.45)  
 Richter, S. M., 60, 100 (2.51)  
 Roberston, G., 153 (3.31)  
 Rohani, S., 96 (2.93)  
 Roitberg, M., 97 (2.98)  
 Rona, J. P., 172 (3.78)  
 Root, W. L., 330 (6.61)  
 Rosell, J., 21 (1.32)  
 Ross, D. A., 251 (5.30), 252 (5.43),  
 254 (5.45)  
 Rossmanith, P., 60 (2.24)  
 Roth, C., 217 (4.47)  
 Rothele, S., 114, 130 (3.1), 141  
 (3.17)  
 Row, G., 267 (5.73)  
 Rowlands, W., 24 (1.39)  
 Rozouvan, S., 60 (2.55)  
 Ruf, H., 251 (5.31), 256 (5.48), 256  
 (5.49)  
 Rushton, A. G., 209 (4.33)  
 Rutgers, A. J., 307 (6.38)

**S**

Sachweh, B., 175 (3.88), 175  
 (3.90), 175, 176 (3.93)

- Sadain, S., 183 (4.4)  
 Saffman, M., 60 (2.46)  
 Saleh, B., 89 (2.90)  
 Salzman, G. C., 60, 224 (2.28)  
 Santiago, S., 167 (3.63)  
 Sasaki, H., 26(1.46)  
 Scarlett, B., 45 (1.59), 154 (3.41),  
     154 (3.42), 167 (3.64), 169  
     (3.67), 175, 176 (3.92), 176  
     (3.91), 275 (5.93)  
 Schabel.S., 103 (2.113)  
 Schafer, M., 49 (1.61), 100 (2.108),  
     175, 176 (3.93)  
 Schatzel, K., 60 (2.49), 252 (5.32),  
     314 (6.51)  
 Schmidt, M., 261 (5.64)  
 Schmitz, B., 128 (3.8), 306 (6.30)  
 Schmitz, K., 60, 93, 224, 259 (2.36)  
 Schnablegger, H., 143, 163 (3.18),  
     161 (3.53), 252 (5.33)  
 Scholz, N., 49 (1.61), 175, 176  
     (3.93)  
 Schröer, W., 279 (5.98)  
 Schrof, W., 60 (2.55)  
 Schulz-DuBois, E. O., 89 (2.89)  
 Schurtenberger, P., 232 (5.13)  
 Schuster, B. G., 185 (4.7)  
 Schwartz, F. H., 60 (2.16), 96  
     (2.95)  
 Schwaz, S. E., 60 (2.23)  
 Schweiger, G., 69 (2.66)  
 Seaman, G. V. F., 313, 314 (6.46),  
     323 (6.59)  
 Sears, F.W., 306 (6.31)  
 Seebergh, J. E., 265 (5.70)  
 Sehrt, S., 217 (4.47)  
 Self, S. A., 203 (4.23)  
 Sevic-Muraca, E.M., 60, 100 (2.51)  
 Shamir, J., 97 (2.98)  
 Sharma, S. K., 80 (2.77)  
 Shen, J., 144 (3.19)  
 Shifrin, K. S., 153 (3.29)  
 Shik, H., 15 (1.18)  
 Shilov, V.N., 23 (1.35), 297 (6.8)  
 Shinde, R. R., 60, 100 (2.51)  
 Shofner, P.M., 18 (1.22)  
 Sieberer, J., 252 (5.33)  
 Silebi, C. A., 19 (1.26)  
 Sinclair, I., 209 (4.33)  
 Sing, K. S. W., 24 (1.40)  
 Singham, S. B., 60, 224 (2.28)  
 Sinn, C., 278 (5.97), 280 (5.99)  
 Skilling, J., 253 (5.44)  
 Smart, G., 313, 322 (6.47)  
 Smith, B. A., 314, 319 (6.49)  
 Smith, M. E., 307 (6.35)  
 Smoluchowski, M. v., 297 (6.20)  
 Sneyers, R., 169 (3.69), 263 (5.68),  
     272 (5.81), 272 (5.82)  
 So, P. T. C., 100 (2.109)  
 Sobotta, A., 314 (6.51)  
 Solomentsev, Y. E., 297 (6.9)  
 Sommer, H. T., 188, 189, 193  
     (4.10)  
 Sowerby, B. D., 23 (1.37)  
 Spliepcovich, C. M., 153 (3.27)  
 Staude, W., 279 (5.98)  
 Stelzer, E., 256 (5.49)  
 Stenhouse, J. I. T., 209 (4.33)  
 Štěpaněk, P., 248 (5.23), 257, 258  
     (5.53)  
 Stevens, T. J., 307 (6.37)  
 Stevenson, A. F., 98 (2.99)  
 Steyfkens, S., 272 (5.82)  
 Stieglmeier, M., 103 (2.115)  
 Stigter, D., 297 (6.14)  
 Stockmayer, W. H., 261 (5.64)  
 Stoeckli, H. F., 25 (1.42)  
 Stone-Masui, J., 272 (5.82)  
 Strickland, M. L., 134 (3.11)  
 Strutt, J. W. 58 (2.3)  
 Suh, K., 272 (5.83)  
 Suzuki, T., 307 (6.33)  
 Swinney, H. L., 269 (5.76)

Szychter, H., 134 (3.12), 175, 176  
(3.92)  
Szymanski, W. W., 199 (4.19), 203  
(4.21), 203 (4.22), 217 (4.48)

## T

Tadayyon, A., 96 (2.93)  
Taflove, A., 81 (2.83)  
Takagi, T., 298, 309 (6.23), 311  
(6.45), 322 (6.57)  
Tanford, C., 297 (6.21)  
Tanger, H., 60 (2.46)  
Tarantola, A., 154 (3.39)  
Teller, E., 24 (1.41)  
Terui, G., 235 (5.17)  
Thoenes, D., 80 (2.78), 135 (3.13)  
Thomas, J. C., 257, 258 (5.54), 258  
(5.57)  
Thornburg, J., 97 (2.96)  
Thorwirth, G., 60 (2.19)  
Tikhonov, A. N., 152 (3.26)  
Tiselius, A., 298 (6.24)  
Togawa, Y., 115 (3.2)  
Tominaga, Y., 259 (5.60)  
Tough, R., 263 (5.66)  
Toyoda, M., 125 (3.7)  
Trainer, M. N., 131 (3.10)  
Travis, L. D., 81 (2.82)  
Tribus, M., 153 (3.27)  
Troepe, C., 103 (2.115)  
Tscharnuter, W. W., 60 (2.17), 250  
(5.26), 340 (6.67)  
Tsubaki, J., 170 (3.70), 170 (3.71)  
Tsunasima, Y., 252 (5.34)  
Tüzüin, U., 158 (3.44)  
Twomey, S., 154 (3.38), 203 (4.24)  
Tyndall, J., 58 (2.2)

## U

Umhauer, H., 171 (3.76), 205  
(4.27), 212 (4.40), 212 (4.41),  
213 (4.42), 215 (4.43)

Ungut, A., 159 (3.46)  
Unterforsthuber, K., 257 (5.55)  
Uozumi, J., 100 (2.107)  
Uzgiris, E. E., 299 (6.27), 314, 315,  
336 (6.53), 315, 316, 335, 336  
(6.54), 334 (6.63)

## V

Van Alstine, J. M., 310 (6.41), 313,  
314 (6.46)  
van Amserdam, P., 169 (3.69)  
van Cotthem, L., 169 (3.69)  
van de Hurst, H. C., 60 (2.8)  
van de Ven, T. G. M., 60 (2.22)  
Van der Deelen, J., 272 (5.82)  
van der Drift, W. P. J. T., 297  
(6.13)  
van der Linde, A. J., 314 (6.52)  
Van der Meeren, P., 240 (5.22),  
263 (5.68), 269 (5.77), 272 (5.82)  
van der Minne, J. L., 307 (6.38)  
Van Dilla, M. A., 60, 224 (2.26)  
Van Keuren, E. R., 273 (5.87)  
Van Laethem, M., 252 (5.38), 263  
(5.68)  
van Leeuwen, H. P., 314 (6.52)  
Vanderdeelen, J., 240 (5.22), 263  
(5.68), 269 (5.77)  
Vanhoudt, J., 233 (5.14)  
Veal, D. L., 185, 191 (4.6)  
Velez, O., 27 (1.48), 315, 316, 317,  
339 (6.55)  
Verheijen, J. T., 154 (3.41)  
Verheijen, P. J. T., 154 (3.42), 169  
(3.67)  
Vernet, J.-P., 167 (3.63)  
Vincent, B., 60 (2.49), 338 (6.66)  
Vokram, C. S., 16 (1.21)  
Vomela, R. A., 211 (4.38)  
von Benzon, H., 103 (2.112)  
Vrij, A., 273 (5.88)

**W**

Waggeling, R., 60 (2.16), 96 (2.95)  
 Waisanen, S., 98 (2.105)  
 Wallach, M. L., 98 (2.99)  
 Wallas, P., 229, 234 (5.12)  
 Wang, D. S., 69 (2.64)  
 Wang, N., 98 (2.102), 98 (2.103),  
 144 (3.19)  
 Wang-Thomas, Z., 174 (3.87)  
 Ward, D. N., 297 (6.18)  
 Ward-Smith, S., 164 (3.59)  
 Ware, B. R., 60 (2.41), 299, 332,  
 335 (6.26), 299, 309, 336 (6.28),  
 308 (6.39), 314, 319 (6.49)  
 Watson, D., 148 (3.24), 252 (5.35)  
 Watson, R. M. J., 72 (2.69), 72  
 (2.70)  
 Weber, R., 296 (6.7)  
 Wedd, M. W., 164, 165 (3.58), 164  
 (3.59)  
 Wei, J., 98 (2.102)  
 Weichert, R., 153 (3.33), 175  
 (3.89), 204 (4.26)  
 Weiner, B. B., 60 (2.17), 250 (5.26)  
 Weise, W., 314 (6.51)  
 Weitz, D. A., 280 (5.100), 281  
 (5.101), 281 (5.102)  
 Wen, H. Y., 217 (4.46)  
 Whitby, K. T., 211 (4.38)  
 White, L. R., 296 (6.6)  
 White, P., 311 (6.42)  
 Whitelaw, J. H., 305 (6.29)  
 Whytlaw-Gray, R., 182 (4.2)  
 Wiegard, S., 279 (5.98)  
 Wiersema, P. H., 296 (6.5)  
 Wiese, H., 273 (5.87)  
 Wijers, J. G., 80 (2.78)  
 Will, S., 172 (3.82), 229 (5.11)  
 Willeke, K., 211, 215 (4.36)  
 Willemse, A. W., 275 (5.93)  
 Williams, P. S., 21 (1.29)  
 Winkelmayr, W., 21 (1.31)

Witt, W., 114, 130 (3.1)  
 Wriedt, T., 81 (2.80), 81 (2.81),  
 103 (2.114), 103 (2.116)  
 Wright, C. A., 141 (3.16)  
 Wu, C., 229 (5.9), 257 (5.55)  
 Wu, S. C. C., 27 (1.48), 315, 316,  
 317, 339 (6.55)  
 Wyatt, C. L., 56 (2.1)

**X**

Xu, R., 41 (1.57), 68, 79 (2.62), 80  
 (2.79), 116, 118, 122, 123, 124  
 (3.3), 146 (3.20), 224 (5.6), 239  
 (5.20), 254 (5.47), 259, 269  
 (5.61), 261 (5.63), 266 (5.71),  
 269 (5.74), 270 (5.79), 271  
 (5.80), 306 (6.30), 313, 322  
 (6.47), 314 (6.48), 329 (6.60)  
 Xu, T.-H., 103 (2.115)

**Y**

Yang, I., 172 (3.81)  
 Yang, X., 183 (4.4)  
 Yau, W. W., 19 (1.23)  
 Yeh, Y., 223 (5.3)  
 Ying, Q., 229 (5.10)  
 Yoon, B. J., 297 (6.17)  
 Young, H. D., 34 (1.52)  
 Yule, A. J., 159 (3.46)

**Z**

Zaré, M., 60 (2.43)  
 Zhang, H., 98 (2.102)  
 Zikikout, S., 153 (3.30)  
 Zimm, B. H., 94 (2.92)

## SUBJECT INDEX

---

### A

Absorption, 56, 60, 98, 160, 205, 265, 280  
Absorption effect, 264  
Accuracy, 41, 148, 166, 208, 213, 241, 298, 334  
    *round-robin*, 168  
Acoustic spectroscopy, 23  
Aerosol, 4, 21  
    *electrostatic classifier*, 208  
Air bubbles, 101, 150, 214  
Air-borne particles, 182, 194  
Alignment, 143, 150, 233  
Amplitude-weighted phase difference, 337  
Angular pattern, 66, 94, 115, 151, 174, 242  
    *map*, 68, 80  
    *monotonic*, 199, 211  
    *polytonic*, 199, 201, 209  
Anisotropic, 59, 259  
Anomalous diffraction, 80, 160  
Applied field, 295, 318, 337  
Arithmetic mean, 36, 39, 41  
ASTM, 8, 336  
Avalanche photodiode, 234, 273

### B

Back scattering measurement, 99  
BCR, 167, 172  
Bragg cell, 306  
Brownian motion, 11, 83, 239, 266, 300, 323, 332, 337

### C

Calibration, 143, 149, 188, 190, 208, 214, 323  
Capillary cell, 307, 322  
    *coating*, 314

*electroosmosis*, 310

*flow profile*, 310

*stationary layer*, 311, 329

### Characterization method

#### *acoustic*

    acoustic spectroscopy, 23

    electroacoustic spectroscopy, 23

#### *aerosol analysis*

    differential mobility, 21

    diffusion battery, 21

*back scattering measurement*, 99

*capillary porometer*, 25

*chromatographic*, 18

        field flow fractionation, 20

        hydrodynamic chromatography, 19

        size exclusion chromatography, 18, 229

*Coulter principle*, 12, 45, 168

*diffusing-wave spectroscopy*, 280

*electrical sensing zone* (*see*  
        *Coulter principle*)

*ensemble*, 4, 32, 168, 259

*focused beam reflectance*, 95

*frequency domain photon*

*migration*, 100

*gas sorption*, 24

*image analysis*, 15, 39

        holographic, 16

        microscopic, 44

*mercury porosimetry*, 25

*non-ensemble*, 6, 183

*phase Doppler anemometry*, 101

*sedimentation*, 10, 44, 165, 168

*sieve analysis*, 7, 114, 168

*streaming potential measurement*,  
        26, 295

*time-of-flight measurement*, 96

*time-of-transition measurement*,  
        97

*turbidimetry*, 98

- Charge-coupled device, 100, 134, 159
  - Chromatographic method, 18
  - Coherence
    - length*, 226, 280
    - time*, 226
  - Coils, 73, 94
  - Concentration effect, 83, 101, 163, 229, 262, 272
  - Condensation nucleus counter, 183
  - Conductivity
    - solution*, 316, 335
  - Constrained regularized method, 156
  - CONTIN, 254
  - Convolved distribution, 328
  - Cord length, 96
  - Correlation function, 86, 235, 242, 247, 299, 323, 335
    - analysis*
      - cumulants, 249
      - fingerprint, 267
      - functional fitting, 250
      - global, 257
      - Laplace inversion, 251
        - CONTIN, 254
      - maximum entropy method*, 252
    - baseline*, 242, 256, 263, 279
    - cross*, 86, 276
      - 3-D, 278
      - two-color, 277
    - delay time*, 87, 235, 241, 243, 281, 324
    - in concentrated suspension*, 273
    - Siebert relation*, 89
    - Wiener-Khinchine theorem*, 87
  - Correlator, 235, 241, 281, 321
    - cross*, 279
    - linear*, 236
    - non-linear*, 237
    - software*, 238
    - time-of-arrival*, 238
  - Coulter principle, 12, 45, 168
  - Counter
    - condensation nucleus*, 183
    - Coulter*, 12, 168
    - optical*, 186, 190
      - monitor, 185, 218
  - Cross correlation function, 86, 276
    - 3-D, 278
    - two-color, 277
  - Cross correlator, 279
  - Crossbeam measurement, 303, 337
  - Cumulants analysis, 249
  - Cumulative distribution, 31, 166, 218
- D**
- De Brouckere mean, 41
  - Debye-Huckel parameter, 291
  - Delay time, 87, 235, 241, 243, 281, 324
  - Depolarized scattering, 91, 259, 268
  - Detector
    - array*, 134, 143, 165, 174
    - fly-wing pattern*, 135
    - half-ring pattern*, 135
    - multichannel analyzer*, 198, 212
    - optode*, 273
    - photodiode*, 131, 174, 190, 233
      - avalanche, 234, 273
    - photomultiplier tube*, 233, 277, 321
    - Xpattern*, 135, 146
  - Differential distribution, 31, 217
  - Differential mobility analysis, 21
  - Diffraction
    - anomalous*, 80, 160
    - Fraunhofer*, 73, 111, 144, 152, 160, 173, 206
    - Fresnel*, 74, 102, 173
  - Diffusing-wave spectroscopy, 280
  - Diffusion battery method, 21
  - Diffusion coefficient
    - absorption effect*, 264



*hydrodynamic effect*, 265  
*rotational*, 259, 268  
 Discrete distribution, 28, 37, 81, 87,  
     152, 247, 252  
 Dispersion, 49, 141  
     *sonication*, 50, 143, 151  
     *surfactant*, 50  
 Distribution  
     *convoluted*, 328  
     *discrete*, 28, 37, 81, 87, 152, 247,  
         252  
     *function*, 28, 33  
         (normal) Gaussian, 33, 217  
         log-normal, 33, 204  
         Poisson, 214  
     *polydispersity index*, 249, 272  
     *presentation*  
         cumulative, 31, 166, 218  
         differential, 31, 217  
         fractional, 31, 254  
         histogram, 29, 40, 252, 326  
     *trimodal*, 122  
     *weighting*, 269  
 Doppler shift, 84, 299, 332  
 Double layer, 265, 290  
 Dynamic light scattering  
     *heterodyne*, 86  
     *homodyne*, 86, 276  
     *self-beating*, 86

**E**

Elastic scattering, 59  
 Electrical sensing zone method  
     (*see Coulter principle*)  
 Electroacoustic spectral analysis,  
     23  
 Electrokinetic sonic amplitude  
     effect, 23  
 Electroosmosis, 295, 310, 334  
 Electrophoresis cell  
     *capillary*, 307, 322  
         coating, 314  
         electroosmosis, 310  
         flow profile, 310

        stationary layer, 311, 329  
     *comparison*, 317  
     *parallel-plate*, 315  
 Electrophoretic mobility  
     *definition*, 295  
 Electrostatic classifier, 208  
 Extinction, 56, 98, 182, 187, 205  
     *efficiency*, 98, 205

**F**

Fiber optic frequency shifter, 305  
 Fiber, 126, 227, 230, 273, 305  
     *few-mode*, 232  
     *monomode*, 127, 232, 273  
     *multimode*, 232, 273  
 Field flow fractionation, 20  
 Fingerprint analysis, 267  
 Flow profile, 310  
 Fluorescence, 15, 57  
 Flux, 112, 149, 188, 203  
 Focused beam reflectance, 95  
 Forward scattering, (*see*  
     *Fraunhofer diffraction*)  
 Fourier optics, 128  
 Fourier transform, 74, 87, 134, 300,  
     326  
 Fractal dimension, 174  
 Fractional distribution, 31, 254  
 Fraunhofer diffraction, 73, 111,  
     144, 152, 160, 173, 206  
 Fredholm integration, 152  
 Frequency  
     *shifted*, 300  
     *shifter*, 85, 304  
         Bragg cell, 306  
         fiber optic, 305  
         moving mirror, 305  
         rotating grating, 306  
 Frequency domain photon  
     migration, 100  
 Fresnel diffraction, 74, 102, 173

**G**

Gas sorption, 24

Gaussian distribution, 33, 217

Geometric mean, 30, 41

Global analysis, 257

## H

He-Ne laser, 126, 185, 226, 305

Henry equation, 295

Heterodyne, 86

Histogram, 29, 40, 252, 326

Holographic method, 16

Homodyne, 86, 276

Horizontal polarization, 61, 118

Huckel equation, 297

Hydrodynamic chromatography, 19

Hydrodynamic effect, 265

Hydrodynamic size, 245, 264, 268

Hydro-focusing, 194

## I

Image analysis, 15, 39

Incandescent filament lamp, 185

In-line measurement, 99, 139, 272

Instrument

*alignment, 143, 150, 233*

*calibration, 143, 149, 188, 190, 208, 214, 323*

Interference, 56, 148, 241, 280, 301, 323

Irregularly shaped particles, 173

ISO, 8, 250

Isoelectric point, 294

## K

Kurtosis, 35

## L

Laplace inversion, 251

Laser diode, 126, 185, 226, 273

Light-beating spectroscopy, 85

Light source

*incandescent filament lamp, 185*

*laser*

*diode, 126, 185, 226, 273*

*He-Ne, 126, 185, 226, 305*

*multiple, 130*

*tungsten, 13*

*white light, 126*

Linear correlator, 236

Linewidth, 306, 326

Liquid-borne particles, 139, 150, 182, 194, 295

Local oscillator, 85, 233, 275

Log-normal distribution, 33, 204

Lorentzian spectrum, 300, 323

## M

Matrix conversion, 23

*constrained regularized method, 156*

*maximum entropy method, 156, 252*

*Phillips-Twomey method, 154, 203*

Maximum entropy method, 156, 252

Mean

*arithmetic, 36, 39, 41*

*De Brouckere, 41*

*geometric, 30, 41*

*moment, 40*

*moment-ratio, 37*

*Sauter, 41*

*weight-averaged, 91, 270*

*z-averaged, 93*

Measurement

*crossbeam, 303, 337*

*in-line, 99, 139, 272*

*multiangle, 232, 242, 257, 267, 319*

*fingerprint, 267*

*on-line, 22, 99, 139, 166, 272, 281*

*reference beam, 233, 301, 306, 326, 337*

- Median, 34  
Mercury porosimetry, 25  
Microelectrophoresis, 297, 307  
Microscopic method, 44  
Mie scattering, 66, 98, 111, 152,  
159, 173, 205, 243, 269  
Mode, 33  
Molecular weight, 18, 90, 270  
Monodisperse, 208, 327  
Moving mirror frequency shifter,  
305  
Multiangle measurement, 232, 242,  
257, 267, 319  
Multichannel analyzer, 198, 212  
Multiple scattering, 23, 82, 142,  
163, 240, 245, 262, 272, 322
- N**  
Non-spherical particles, 44, 103,  
166, 172, 211, 260, 268
- O**  
On-line measurement, 22, 99, 139,  
166, 272, 281  
Optically equivalent size, 210  
Optics  
  *fiber*, 126, 227, 230, 273, 305  
    few-mode, 232  
    monomode, 127, 232, 273  
    multimode, 232, 273  
  *Fourier*, 128  
  *reverse Fourier*, 132  
Optode, 273
- P**  
Parallel-plate cell, 315  
Particle counting, 182, 192  
Particles  
  *aerosol*, 4, 21  
  *air bubbles*, 101, 150, 214  
  *air-borne*, 182, 194  
  *liquid-borne*, 139, 150, 182, 194,  
295  
  *powder*, 4, 47, 141  
Peeling method, 329  
Phase analysis, 336  
Phase difference  
  *amplitude-weighted*, 337  
Phase Doppler anemometry, 101  
Phillips-Twomey method, 154, 203  
Photodiode, 131, 174, 190, 233  
  *avalanche*, 234, 273  
Photomultiplier tube, 233, 277, 321  
Plates, 7, 72, 78, 147, 171, 260, 268  
Point of zero charge, 294  
Poisson distribution, 214  
Polarization, 226  
  *horizontal*, 61, 118  
  *vertical*, 61, 67, 118  
Polarization intensity differential  
  scattering, 119, 131, 157  
Polydispersity index, 249, 272  
Polygons, 75  
Polystyrene latex, 115, 124, 158,  
208, 265, 271, 329, 334  
Porometer, 25  
Powder, 4, 47, 141  
Power spectrum, 323, 330  
  *broadening*, 157, 212, 304, 328,  
332  
  *linewidth*, 306, 326  
  *Lorentzian*, 300, 323  
  *peeling method*, 329
- Q**  
Quasi-elastic scattering, 59
- R**  
Radius of gyration, 72, 93, 174  
Rayleigh ratio, 92  
Rayleigh scattering, 69, 82, 163,  
250  
Rayleigh-Debye-Gans scattering,  
71, 82, 260, 266

Reference beam, 233, 301, 306,  
326, 337  
Reference reticle, 145, 147  
Refractive index, 57, 91, 116, 159,  
162, 199, 208, 258  
Regularly shaped particles, 43, 72,  
176, 260  
Resolution, 134, 154, 165, 199,  
211, 217, 258, 270, 328, 330  
Reverse Fourier optics, 132  
Rods, 43, 73, 171, 260, 268  
Rotating grating, 306  
Rotational diffusion coefficient,  
259, 268  
Round-robin test, 168

## S

Sample module, 139, 165, 229  
Sample reduction, 47  
Sampling, 41, 47, 52, 142, 150, 191  
*hydro-focusing*, 194  
*sample reduction*, 47  
*sheathflow*, 96, 197  
Sauter mean, 41  
Scattering  
*angular pattern*, 66, 94, 115, 151,  
174, 242  
map, 68, 80  
monotonic, 199, 211  
polytonic, 199, 201, 209  
*depolarized*, 91, 259, 268  
*elastic*, 59  
*extinction*, 56, 98, 182, 187, 205  
*geometry*, 61, 278  
*inelastic*, 59  
*multiple*, 23, 82, 142, 163, 240,  
245, 262, 272, 322  
*parameter*  
cross section, 65  
extinction efficiency, 98, 205  
Rayleigh ratio, 92  
scattering efficiency, 101, 163  
scattering factor, 71, 93, 260  
structure factor, 91, 262

*phase analysis*, 336  
*quasi-elastic*, 59  
*static*, 58, 90, 258  
*technologies*, 60  
*theory*  
diffraction  
*anomalous*, 80, 160  
*Fraunhofer*, 73, 111, 144, 152, 160,  
173, 206  
*Fresnel*, 74, 102, 173  
forward scattering (see Fraunhofer  
diffraction)  
Mie, 66, 98, 111, 152, 159, 173, 205,  
243, 269  
numerical  
*surface-based*, 81  
*volume-based*, 81  
Rayleigh, (see Rayleigh scattering)  
Rayleigh-Debye-Gans, (see Rayleigh-  
Debye-Gans scattering)  
*time-averaged*, 58, 61, 82, 90  
*vector*, 62, 99, 273, 276, 328, 337  
Scattering cross section, 65  
Scattering efficiency, 101, 163  
Scattering factor, 71, 93, 260  
Sedimentation, 10, 20, 165, 168,  
322  
Self-beating, 86  
Shape  
*coil*, 73, 94  
*irregular*, 173  
*non-spherical*, 44, 103, 166, 172,  
211, 260, 268  
*plate*, 7, 72, 78, 147, 171, 260,  
268  
*polygon*, 75  
*regular*, 43, 72, 176, 260  
*rod*, 43, 73, 171, 260, 268  
*sphere*, 43, 67, 75, 101, 144, 168,  
206, 268  
Sheath flow, 96, 197  
Siegert relation, 89  
Sieve analysis, 7, 114, 168  
Signal-to-noise ratio, 137, 165, 197,  
241, 321

- Size  
  *cord length*, 96  
  *fractal dimension*, 174  
  *hydrodynamic*, 245, 264, 268  
  *optically equivalent*, 210  
  *radius of gyration*, 72, 93, 174  
  *Stokes diameter*, 10, 63, 171  
Size exclusion chromatography, 18, 229  
Skewness, 34  
Smoluchowski equation, 297  
Software correlator, 238  
Sonication, 50, 143, 151  
Spatial filter, 127, 229, 278  
Specific surface area, 4, 25  
Spectrum analysis, 86, 235  
Spectrum analyzer, 299, 321  
Spheres, 43, 67, 75, 101, 144, 168, 206, 268  
SRM, 312, 323  
Standard  
  *ASTM*, 8, 336  
  *BCR*, 167, 172  
  *ISO*, 8, 250  
  *reference reticle*, 145, 147  
  *SRM*, 312, 323  
Standard deviation, 42  
Static scattering, 58, 90, 258  
Stationary layer, 311, 329  
Statistical parameters  
  *kurtosis*, 35  
  *mean*, (*see Mean*)  
  *median*, 34  
  *mode*, 33  
  *skewness*, 34  
  *standard deviation*, 42  
  *variance*, 34  
Stern layer, 290  
Stokes diameter, 10, 63, 171  
Streaming potential, 26, 295  
Structure factor, 91, 262  
Surface-based numerical method, 81  
Surfactant, 50  
**T**  
Time-of-arrival correlator, 238  
Time-of-flight measurement, 96  
Time-of-transition measurement, 97  
Tomographical transformation, 159  
Trimodal distribution, 122  
Tungsten light, 13  
Turbidity, 98, 163  
**V**  
van der Waals force, 263, 294  
Variance, 34  
Vector of momentum-transfer, 62, 99, 115, 249, 328, 337  
Vertical polarization, 61, 67, 118  
Volume-based numerical method, 81  
**W**  
Weight-averaged mean, 91, 270  
White light, 126  
Wiener-Khintchine theorem, 87  
**Z**  
z-averaged, 93  
Zeta potential  
  *Henry equation*, 295  
  *Hückel equation*, 297  
  *Smoluchowski equation*, 297  
Zimm plot, 94

## PARTICLE TECHNOLOGY SERIES

---

### FORMERLY POWDER TECHNOLOGY SERIES

1. H. Rumpf (Translated by F.A. Bull): *Particle Technology*. 1990  
ISBN 0-412-35230-3
2. S. Lowell and Joan E. Shields: *Powder Surface Area and Porosity* (Third Edition). 1991  
ISBN 0-412-39690-4
3. K. Heiskanen: *Particle Classification*. 1993  
ISBN 0-412-49300-4
4. O. Molerus: *Principles of Flow in Disperse Systems*. 1993  
ISBN 0-412-40630-6
5. I. Claus Bernhardt: *Particle Size Analysis*. Classification and Sedimentation Methods. 1994  
ISBN 0-412-55880-7
6. Yasuo Arai: *Chemistry of Powder Production*. 1996  
ISBN 0-412-39540-1
7. Terence Allen: *Particle Size Measurement* (Fifth Edition). 1996  
Volume 1: Surface area and pore size determination. ISBN 0-412-72950-4  
Volume 2: Powder sampling and particle size measurement.  
ISBN 0-412-75330-8  
Set of 2 vols., ISBN 0-412-75350-2
8. George E. Klinzing, Roy D. Marcus, Farid Rizk and L.S. Leung<sup>†</sup>: *Pneumatic Conveying of Solids*. A Theoretical and Practical Approach (Second Edition). 1997  
ISBN 0-412-72440-5
9. Jonathan P.K. Seville, Uğur Tüzün and Roland Clift: *Processing of Paniculate Solids*. 1997  
ISBN 0-7514-0376-8
10. B. Kaye: *Powder Mixing*. 1997  
ISBN 0-412-40340-4
11. O. Molerus and K.-E. Wirth: *Heat Transfer in Fluidized Beds*. 1997  
ISBN 0-412-60800-6
12. R. Weinekötter and H. Gericke: *Mixing of Solids*. 2000  
ISBN 0-7923-6229-2
13. R. Xu: *Particle Characterization: Light Scattering Methods*. 2000  
ISBN 0-7923-6300-0